JRJC 2021- Journées de Rencontres Jeunes Chercheurs. Book of Proceedings

Pauline Chambery, Mathieu de Bony de Lavergne, Matteo Pracchia, Kinson Vernet, Simon Chiche, Thomas Strebler, Mohamad Kanafani, Sacha Daumas-Tschopp, Claudia de Dominicis, Vlad Dedu, et al.

JRJC

Journées de Rencontres Jeunes Chercheurs

17-23 Octobre 2021

La Rochelle (17)

Village "La Fayette"

Avenue de Bourgogne CS 30809
17041 La Rochelle cedex 01

Société Française de Physique

Book of Proceedings

Comité d'organisation :

Pauline Ascher	(LP2i Bordeaux)
François Brun	(CEA Saclay)
Emmanuel Chauveau	(LP2i Bordeaux)
Rachel Delorme	(LPSC)
Romain Gaior	(LPNHE)
Julien Masbou	(SUBATECH)
Laure Massacrier	(IJCLab)
Antonio Uras [*]	(IP2I Lyon)
Dimitris Varouchas	(IJCLab)
Laura Zambelli	(LAPP)

[*] Editor of these proceedings

Secrétariat :

Isabelle Cossin	(LPNHE)

Contents

Part I

Astrophysics and Astroparticle physics

session chaired by Sami CAROFF

In search of TeV halos, new astrophysical objects to reveal our gamma-ray sky map

Pauline CHAMBERY

LP2i Bordeaux (Laboratoire de Physique des Deux Infinis de Bordeaux)

Abstract — TeV halos are astrophysical objects recently discovered by HAWC which extend around pulsars. These sources are electron and positron accelerators in interaction with the surrounding magnetic field. Their recent detection is due to the fact that they are so far only visible in the gamma-ray domain, their size represents several degrees in the sky and they are very faint. To study them, it is therefore necessary to have instruments that are both very sensitive and have a wide field of view, which is technically difficult to achieve. However, their study is important because they dominate TeV emissions in the galaxy and compete with dark matter in explaining the observation of the excess of positrons reaching Earth. Today some of these objects are revealed by the array of imaging atmospheric Cherenkov telescopes H.E.S.S. but the construction of the new array CTA, ten times more sensitive, and the implementation of an associated analysis system could reveal hundreds of them. Their omnipresence attests to the importance of better understanding these objects. This presentation aims to understand what is the nature of TeV halos, how do they evolve, with which instruments do we detect them and how do we analyze them? This will be done by approaching gamma astronomy and particle accelerators in astrophysics more broadly.

Introduction

Gamma-ray astronomy

Gamma-ray astronomy is the study of the most energetic photons in the electromagnetic spectrum, produced by the most violent events and the most powerful objects in our Universe such as active galaxy nuclei, gamma-ray bursts, pulsars, supernovae ... and in particular particle accelerators. Gamma photons are produced from non-thermal mechanisms that correspond to the interaction of very high energy particles with a magnetic or electric field, namely inverse Compton scattering, Bremsstrahlung emission, electron-positron annihilation and synchrotron emission. Due to their high energies upon arriving on Earth, they will interact with the atmosphere. They can therefore be detected directly by space telescopes or indirectly by using their reaction with the atmosphere. The main objectives of these gamma studies are to better understand astrophysical objects by obtaining more information, such as at what energies do they accelerate particles? Do they accelerate leptons or hadrons? What are their spectrum and morphology? But also to study certain objects which are detected only at these energies, such as the TeV halos that we are trying to analyze.

Observation and Instrumentation

We are studying these objects using data collected from imaging atmospheric Cherenkov telescope arrays. This detection technique is done indirectly, so on the ground. Indeed, when the gamma-ray coming from the astrophysical source arrives on Earth, it interacts in the vicinity of an atomic nucleus of the atmosphere and thus creates an electron-positron pair. The two charged particles continue to propagate in the atmosphere and by deflection by the electromagnetic field of other nuclei create gamma photons, which can in turn react to create pairs. A chain of these two processes follows and creates a particles shower that eventually exceed the speed of light in this medium. The consequence is the emission of a blue ring emission, qualitatively similar to the shock wave when exceeding the speed of sound, called the Cherenkov light. To detect this light we use a Cherenkov telescope. This type of telescope makes it possible to detect both a very short emission with a mount allowing to go quickly to the source and a high speed camera, and at the same time a faint emission with a very large mirror which focuses the photons and a thin pixelation. We use several of these telescopes organized in arrays for the detection because these electromagnetic showers are rare events. With one event per square meter per year for a bright source, the ground surface must be maximized. Furthermore, the objective is to reconstruct the energy and direction of the incident photon in order to return to the source.

The direction is obtained by combining the images from different cameras and the energy is evaluated from the intensity of the light collected in all cameras. Thus, the more telescopes there are, the more precise we can be on the study of the source. This is why today we are working on data from the HESS telescopes array located in Namibia and in operation since 2002 [1], and we are trying to improve the analysis of future data from the CTA telescopes array under construction. It will be located part in the Northern Hemisphere in La Palma and part in the Southern Hemisphere in Chile and will have much greater sensitivity and angular resolution [2].

TeV halos are very recent objects discovered about 5 years ago by High Altitude Water Cherenkov Experiment (HAWC) [3]. The latter is a gamma ray and cosmic ray observatory between 100 GeV and 100 TeV located at high altitude in Mexico. It detects particles from a shower created by a gamma photon or a cosmic ray arriving in the atmosphere thanks to water reservoirs where the Cherenkov light is triggered. HAWC has two advantages which allowed this detection, it can observe night and day (so twice much) and has a very large field of view due to the size and number of water tanks. Its disadvantage is its precision in reconstructing direction and energy, as compare to Cherenkov telescopes.

TeV halos

By reanalyzing the HESS data, we estimate to find between 10 and 50 TeV halos, but with the new CTA telescopes and HAWC, we could detect in total between 50 and 240 [4]. Their study with Cherenkov telescopes, in particular with the improvement of performance, is therefore essential because they should dominate the galactic sky at TeV. In addition, we observe an excess of positrons arriving on Earth with PAMELA and AMS-02 dark matter experiments [5]. A dark matter theory could explain this but the acceleration of particles in the TeV halos or its predecessors the pulsar wind nebulae (PWN) is a competing theory [6]. Finally, understanding their nature could provide us with more information on pulsars and the particle accelerators in general under different physical conditions than those already known, such as in supernova remanents (SNR).

Indeed, all these objects, which are the site of particle acceleration, are created at the death of the stars. From this moment, a huge explosion occurs and the shock wave created by the ejecta extends into the interstellar medium which corresponds to the SNR. But the heart of the star remains in the center, which will become a compact object rotating very quickly on itself called a pulsar. The latter creates a very strong magnetic field around it and by electromagnetic force will eject electrons and positrons. Because of the presence of this magnetic field, the charged particles will be accelerated and will radiate at TeV and thus form the symmetric PWN for about 10kyr. But the SNR extending into the interstellar medium will end up losing energy and the shock wave will be reflected. The reverse shock will disturb the PWN which will therefore be deformed and the electrons and positrons giving photons at TeV begin to escape between about 10kyr and 100kyr. After 100kyr, the pulsar with its own movement will escape from the SNR and the latter will disappear [7]. The electrons and positrons continue to escape from the asymmetric PWN and are confined in a much larger region where the particles follow only diffusion laws and by interaction radiate at TeV, this is called the TeV halo [3]. The three stages of the evolution of a PWN towards a halo are represented in Figure 1.

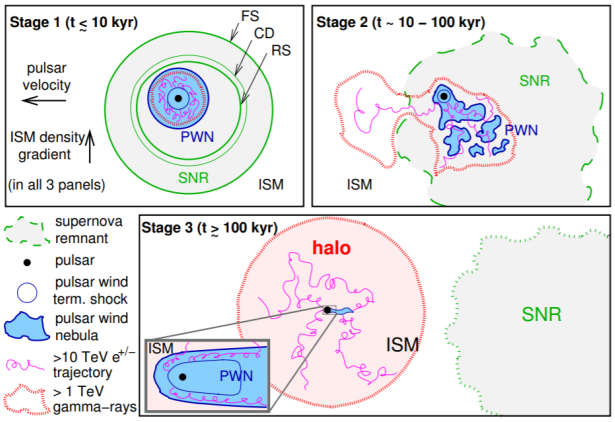

Figure 1: The three stages of the evolution of a PWN towards a TeV halo. Figure from [7].

Analysis method

The study of these astrophysical objects is done by looking at their morphology and their spectrum, that means their flux as a function of energy. In the case of the TeV halos, there are three analysis difficulties which are the strong dependence of their morphology on their energy, their faint flux, close to that of the galactic background, and their very large extension, larger than the telescope field of view.

The general idea of the analysis is to start from real (HESS) or simulated (CTA) data. We select the data in spatial coordinates around the source that we want to study and in the energy range in which we want to analyze the source. Then, we make sky maps of the chosen spatial region to see all the sources that are present. Close to the galactic center, the number of sources is very large and conversely this number is low when one moves away from it. With the help of these sky maps, we create a model that describes all the sources seen, whether they are from the extragalactic background, the galactic background or point or extended astrophysical objects on the map [8]. In this description of the sky, we have parameters which correspond to the morphology of the sources and to the spectra. The analysis will therefore consist of a fit to optimize all parameters with a maximum likelihood method, so until the model parameters best reproduce the data. Finally, we can compare the flux as a function of the energy of

the best model found, called the butterfly plot, with the flux separately calculated for small energy bands, called the spectral energy distribution. They allow a check of their consistency and better understand the physical phenomena at the origin of the source.

For the TeV halos, it is necessary to deepen these analyses to understand the object because of the difficulties it presents. For example, we can look more precisely at the slope of the spectrum from the pulsar to the edges of the source by spatially cutting the source into small boxes [9], as seen in Figure 5. In addition, we can also look at its spatial extension as a function of its energy [9]. For this, we calculate from the sky map of the object in each energy band the number of photons as a function of the distance to the pulsar, as can be seen in Figures 2 and 3. The blue rings in Figure 2 represent the direction in which we count the photons because this object is asymmetrical and also represents the beginning and the end of the interval of distance to the pulsar that we are looking at. We do not really start with the pulsar for reasons of fit difficulties but this is not important because we want to know the maximum extent of the PWN.

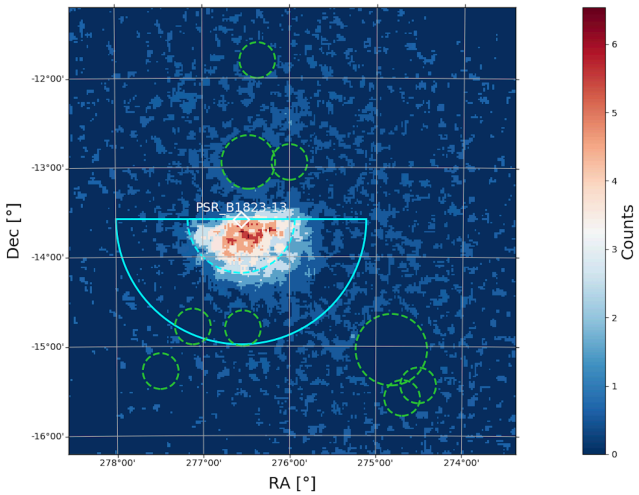

Figure 2: 5×5 sky map of the region around HESS J1825-137 in an energy band between 2TeV and 4TeV. The white diamond is the pulsar. The blue rings are the start and end of the interval where the photons are counted. And the green circles are masks on the other sources in the region.

In the first part of the thesis, we studied the HESS J1825-137 PWN with simulated data for CTA (see Figure 2). This map shows that the source is very extended but to better understand we can look at Figure 3. In this Figure, we can see the green vertical line which is the reference radius to talk about the extension of the source. Between 2 TeV and 4 TeV we see that the source has a radius of 0.85 and is asymmetrical. Knowing that the moon has a diameter of 0.55, it is about twice the full moon in the sky. In addition to its size, this source was chosen for our study because it is particularly bright for a PWN. Thereby, it was easier

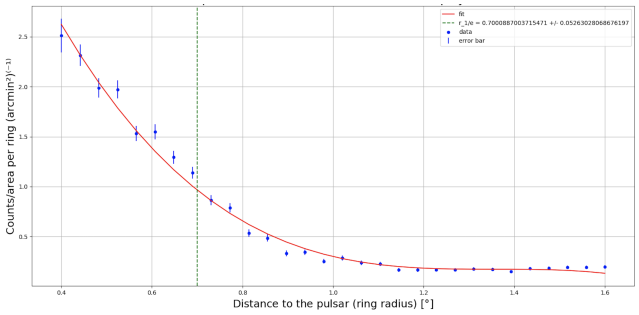

Figure 3: This graph shows the number of photons normalized as a function of the distance to the pulsar in an energy band between 2TeV and 4TeV. The blue points are the data, the red line is the fit and the vertical green line represents the value of the radius that is used to compare different methods to estimate the extension of the source.

to develop tools for analyzing extended sources with an energy dependant morphology. HESS J1825-137 is a known source which had already been studied with data from the Fermi satellite [10] and HESS data [9] and therefore allowed us to compare the results.

Results

The results, obtained on the CTA simulations of HESS J1825, are consistent with the studies done previously, on data from HESS [9] and from Fermi [10]. Moreover, these results have a significance of more than 5 sigmas. And finally, they are in agreement with the theoretical knowledge we have today on PWNs.

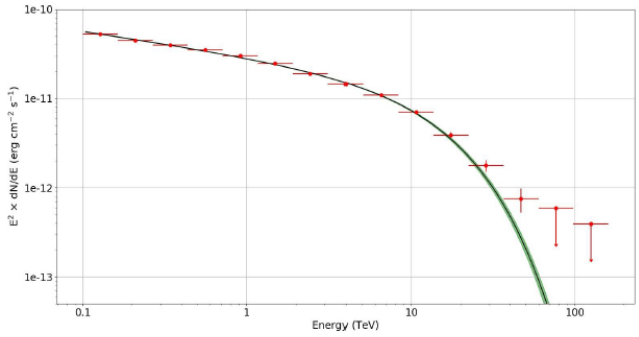

Figure 4: The butterfly plot, in green, and the spectral energy distribution, the red dots, of the best spatial and spectral model of HESS J1825-137 from 300 GeV to 160 TeV.

In Figure 4, the source is represented geometrically by an elliptical Gaussian and spectrally by an exponential cutoff power law. This Gaussian morphology corresponds well to this type of object because they are often very bright at the level of the pulsar which continues to supply high energy particles, on the other hand they quickly lose significance at the edges. And the ellipticity is due to the asymmetric shape of these

PWNe which were disturbed by the reverse shock of the SNR, and which in addition extend especially where the interstellar medium is the least dense, on the opposite side of the galactic plane (Figure 2). This spectral description is also logical, the power law shows that the more we go to high energies the less particles we have until having a clear cut because the particles have not had time to be accelerated beyond a certain energy threshold, due to its young age. In general, this study highlighted that the PWNe, but also the TeV halos, must be studied by taking into account the morphology and the spectrum at the same time because the two are very dependent on each other, even if it is very demanding in computing time.

Figure 5 shows the slope of the spectrum of the source which is more negative when one moves away from the pulsar. This means that there are less particles of high energies and indeed these have lost energy while propagating.

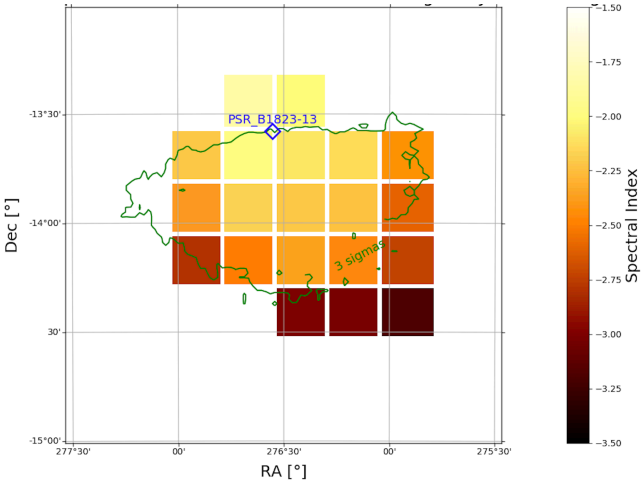

Figure 5: The map of the slopes of the spectra (called spectral index) of each box in power law, for the 20 boxes surrounding HESS J1825-137. The more negative the index is, the steeper the spectrum is and the more low energy photons are present compared to high energy photons.

In addition, in Figure 6, it can be seen that the radial extension decreases sharply with increasing energy after about 500 GeV. This is due to the fact that the particles have lost energy while propagating so there are fewer high energy particles which can therefore give such energetic photons, the source is seen to be smaller at these energies. Furthermore, the results of Figure 6 highlight a predominantly advection pattern. This effect is characteristic of young PWNe where the particles move in a flow. This clearly shows the difference with the old PWNe which evolve in TeV halos where the particles move with pure diffusion, that is to say a free motion of particles in the medium.

Finally, this study in addition to participating in the understanding of these objects was useful for the optimization of the layouts of the telescopes in the southern array of CTA [11]. With the data collected, we

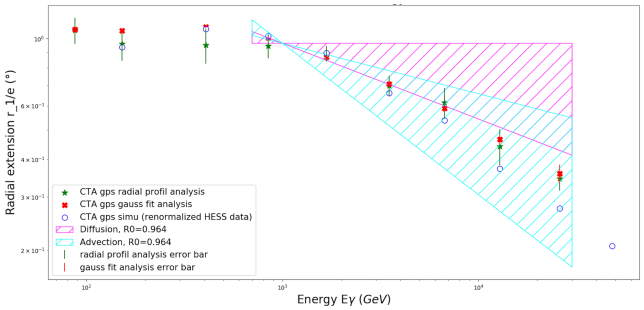

Figure 6: The radial extension of HESS J1825-137 as a function of energy, calculated with two different method and compared to the simulated data (blue dots), and the theoretical models of particle advection (in blue hatching) and diffusion (in pink hatching). The two different methods are the radial profile and the fit of a Gaussian.

were able to see which layout of the telescope array had greater accuracy in reconstructing the direction of events for the extended sources. Indeed, we have reproduced the study with these different layouts, in particular those with the slopes of the spectrum in the boxes (Figure 5). Looking in each box for the signification and the errors on the result, we then compared those errors for the different layouts and kept the one giving the most signification and the smallest errors. We can see an example of a graph obtained in Figure 7.

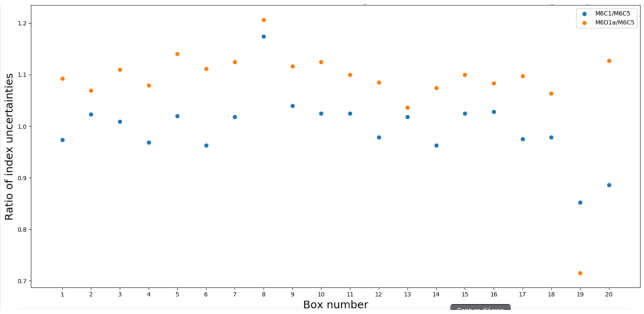

Figure 7: The ratio of the power law slope (index) uncertainties for different layouts of the 20 boxes surrounding HESS J1825-137. Figure from [11].

References

[1] H.E.S.S. collaboration, High Energy stereoscopic System, 2004-2021, https://www.mpi-hd.mpg.de/hfm/HESS/

[2] CTA collaboration, CTAO Performance, 2016, https://www.cta-observatory.org/science/ctao-performance/

[3] Linden et al., «Using HAWC to Discover Invisible Pulsars», Phys. Rev. D 96, 103016, 2017

[4] Sudoh et al., «TeV Halos are Everywhere: Prospects for New Discoveries», Phys. Rev. D 100, 043016, 2019

[5] O. Adriani et al., «Observation of an anomalous positron abundance in the cosmic radiation.», Nature, Vol. 458, pp. 607-609., 2009

[6] Abeysekara et al., «Extended gamma-ray sources around pulsars constrain the origin of the positron flux at Earth», Published in Science as DOI:10.1126/science.aan4880, 2017

[7] G. Giacinti et al., Astronomy & Astrophysics, «On the TeV Halo Fraction in gamma-ray bright Pulsar Wind Nebulae», 2019

[8] IRAP, Cherenkov Telescope science analysis software ctools, Sept 2021, http://cta.irap.omp.eu/ctools/

[9] H.E.S.S. collaboration et al., Astronomy & Astrophysics, «Particle transport within the pulsar wind nebula HESS J1825–137», 2018

[10] G. Principe et al., Astronomy & Astrophysics, «Energy dependent morphology of the pulsar wind nebula HESS J1825–137 with Fermi-LAT», 2020

[11] CTA Consortium Science Working Group and Roberta Zanin, CTA Observatory Project Scientist, «CTA-S alpha layout optimization», Oct 2021

First observations of Gamma-Ray Burst with the Large-Sized Telescope

Mathieu DE BONY DE LAVERGNE

LAPP (Laboratoire d'Annecy de Physique des Particules)

Abstract — The recent detection of Gamma-Ray Bursts in the Very High Energy domain by H.E.S.S. and MAGIC was the result of an intensive and long work by many physicists. These detections are important to have a better understanding of emission mechanism of the Gamma-Ray Bursts. With the development of multi-wavelength astronomy and now multi-messenger astronomy (with the detection of gravitational waves and neutrino), the future Cherenkov Telescope Array experiment will have an important role by observing them at Very High Energies which will help the comprehension of Gamma-Ray Bursts. As part of CTA, the Large-Sized Telescopes are the most important telescopes for the study of Gamma-Ray Bursts. Here are presented the first observations of Gamma-Ray Bursts with the first LST telescope.

Introduction

The first detection of a Gamma-Ray Burst (GRB) was made by a Vela satellite in 1967. The Vela satellites were military spy satellites dedicated to the detection of nuclear explosions caused by the test of nuclear warheads. They recorded bright bursts of gamma-rays lasting a few seconds coming from space [13].

Since this detection, gamma-ray bursts have been extensively studied. The BATSE instrument on-board of the CGRO spacecraft has led to significant discoveries. It was dedicated to the detection and localization of GRBs. One of the major results was the identification of two populations of GRBs, based on their duration. The GRBs lasting less than 2s are short GRBs and more than 2s are long GRBs. This instrument shows also that GRBs are isotropically distributed across the sky [15].

Another important piece of the comprehension of the phenomena was the detection of the first optical and X-Ray afterglow of a GRB with GRB 970228 [18] and the first association of a burst with a galaxy with GRB 970508 [9].

All these discoveries are well in agreement with the actual main theory for explaining the emissions of the GRBs, the "Fireball" model [16]. The long GRBs originated from the explosion of dying massive stars, while the short GRBs originate from the merger of two neutron stars. In both cases, the forming black hole will be the central engine for forming an ultra-relativistic jet. The prompt phase of the GRBs is due to internal shocks of different blobs of matters that are traveling at different speeds in the jets. The afterglow emission is then caused by the shock of the jet with the interstellar medium. This model predicts emission on the whole light energy spectrum, especially for the afterglow phase. The co-detection of GW 170817 both by gravitational wave detectors as a merger of two neutron stars and by Fermi/GBM as a short GRB was a nice confirmation of this theory [1].

As the prompt emission is the most easily detectable in the hard X-Ray to the soft Gamma-Ray band, it's originally the most studied energy for the emission of GRB. But detection and study of the emission of GRBs in other energy bands have been a goal since the start of the observation of GRBs. The first detection at High Energy has been made by EGRET with the observation of gamma-ray up to 1 GeV from GRB 930131 during its prompt phase [17]. Observation of HE prompt and afterglow emission from GRBs is now common with the instrument Fermi/LAT which has observed more than 180 bursts [6].

The detection of VHE energy emission from GRBs was a long quest as it could help to understand better the emission mechanism behind the HE emission. The first hint of emission with a $\sim 3\sigma$ excess during the prompt phase was reported on GRB 970417 by the Milagrito experiment [7]. Sixteen years later, The Fermi/LAT experiment detected photons up to 95 GeV from GRB 130427A, approaching the VHE energy domain (typically defined above 100 GeV). The different Imaging Atmospheric Cherenkov Telescope (IACT) experiments have been searching for more than 15 years VHE counterpart to GRBs. In 2018, H.E.S.S. detect the first GRBs at VHE with GRB 180720B [2]. This detection was followed by the detection of GRB 190114C [14] and GRB 201216C [10] by MAGIC and the detection of GRB 190829A by H.E.S.S. [12].

The observations of these GRBs help constrain some models but also raised a lot of questions, like in the case of GRB 190829A which is challenging to properly model. Detection of more GRBs at VHE could help to have a better view and understanding of the phenomena. Also, detection of afterglow emission from short GRBs and prompt emission of any kind of GRB has still to be achieved. In consequence, GRBs follow-up

and observations are major science programs for currents IACTs experiments and future experiments like Cherenkov Telescope Array (CTA).

GRBs observation by CTA/LST

CTA is the next generation of IACT instrument [11], which will increase sensitivity up to one order of magnitude and also increase the energy range compared to current experiments. IACTs work principle is to use the atmosphere as a calorimeter. When a VHE photon arrives in the upper atmosphere, they will interact and create an electron-positron pair. The element of this pair will then also interact and create through successive interactions an electromagnetic shower composed of electrons, positrons, and gamma-rays. The energy of the particles composing the shower is still very high, which will allow charged particles to travel faster than the speed of light in the atmosphere, which will then cause the emission of light by Cherenkov effects. It's this Cherenkov light that is observed by the telescopes. In consequence, the IACTs experiment needs telescopes with a very large reflector and with a camera able to work at a very high rate to catch the faint and brief flash of Cherenkov light.

The principle of the analysis of IACTs is then to use the images of the shower obtained with the telescopes to determine the origin of the particle, its energy, and its nature. One of the difficulties of this type of experiment is that cosmic-rays are also creating atmospheric showers, and need to be to hope to detect any kind of gamma-ray sources.

CTA will be composed of tens of telescopes spread across two sites, one at La Palma in Spain, and another one at Paranal in Chile. There will be three different types of telescope, each specialized in a given energy range : the Small-Sized Telescope (SST) from 1 TeV up to 300 TeV, the Medium-Sized Telescope (MST) from 80 GeV up to 50 TeV, and the Large-Sized Telescope (LST) from 20 GeV up to 3 TeV.

The LST prototype, LST-1 is currently under commissioning at La Palma [3] (Fig. **??**). Its low energy threshold (20 GeV) and its fast positioning capabilities, half turn in 30 s, make it a great instrument to search for counterparts from GRBs (Tab. 1).

Detecting a GRB in the FOV of the instrument during the observations is highly unlikely due to the small FOV of LST-1, in consequence, all the observations are done by doing follow-up of alerts emitted by other instruments to inform the community of the detection of an event. Most of these alerts come from instruments dedicated to GRB detection are onboard satellites. These instruments typically work in the hard X-Ray to soft Gamma-ray domains. Currently, we are mainly considering alerts that are coming from the instrument Swift/BAT, Fermi/GBM, Fermi/LAT, and INTEGRAL/IBIS.

[1] https://www.cta-observatory.org/project/technology/lst/

Figure 1: The LST-1 prototype at La Palma (Credit : Tomohiro Inada)

Energy range	20 GeV - 3 TeV
Energy range in which LSTs dominate CTA sensitivity	20 GeV - 150 GeV
Optical Design	Parabolic
Primary reflector diameter	23 m
Effective mirror area	370 m^2
Focal length	28 m
Total weight	103 t
Field of view	4.3
Number of pixel in Cherenkov camera	1855
Pixel size (imaging)	0.1
Photodetector type	Photomultiplier tubes
Telescope readout event rate	15 kHz
Telescope data rate	24 Gb/s
Positioning time to any point in the sky	30 s
Pointing precision	$<$ 14 arcseconds

Table 1: Specification of the LSTs telescopes [1]

So far, six GRBs have been observed by the LST-1 telescope (Tab. 2) (Fig. 2). The observations have been conducted under standard observation mode.

The analysis of the data has been performed using cta-lstchain [4] for the reconstruction and gammapy [8] for the high-level analysis. It's the current standard analysis pipeline for LST-1 data. No signals have been detected from any of these observations.

Discussion

The follow-up of GRBs with LST is only starting, and the telescope is still being commissioned so there is still a lot of development ongoing. Currently, the follow-up is done fully manually. This could lead to an additional delay in the follow-up or even miss occasions. A transient handler that will manage the automatic response to received alerts is currently under development [5].

Having a precise location is also important for the follow-up of GRBs. The opening angle of the gamma FOV of LST-1 is around 2.5 deg. Some instruments like

	T_0	T_{90} [s]	Redshift	Observation start time	Delay [min]	Zenith [deg]	Trigger Instrument
GRB 201216C	2020-12-16 23:07:31	16	1.1	2020-12-17 20:57:03	1310	40	Swift/BAT
GRB 210511B	2021-05-11 11:26:39	6	-	2021-05-12 03:37:54	971	42	Fermi/GBM
GRB 210704A	2021-07-04 21:14:53	1.06	-	2021-07-04 23:32:43	138	60	Fermi/GBM
GRB 210731A	2021-07-31 22:21:08	22.51	1.25	2021-07-31 23:02:22	41	60	Swift/BAT
GRB 210802A	2021-08-02 11:46:46	11	-	2021-08-03 22:13:30	2067	34	Fermi/GBM
GRB 210807A	2021-08-07 10:20:06	156.30	-	2021-08-08 03:55:14	1055	60	Swift/BAT

Table 2: List of all the Gamma-Ray Bursts observed by LST-1 up to the end of 2021

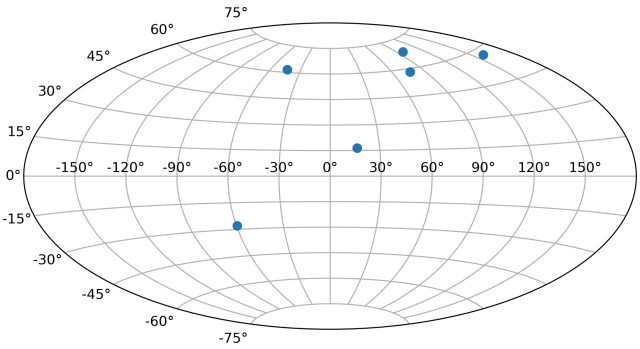

Figure 2: Positions in the sky of the GRBs observed by LST-1 up to the end of 2021

Swift/BAT and INTEGRAL/IBIS, provide alerts that are localized at the arcminute level which allow us to observe them like normal sources. Fermi/LAT provides alerts that are localized at the sub-degree level, this is precise enough to not affect too much the observation strategy, but on the other hand, alerts are emitted several hours after the burst which prevents any quick follow-up. Finally, Fermi/GBM provides alerts with several degrees of uncertainty on the position. This makes follow-up challenging as it exceeds the size of the FOV. As an example with GRB 210511B, only 43% of the probability region given in the alert is covered. In the case of GRB 210704A, a more precise localization from Swift/XRT arrived after the observations. This position is at the edge of the FOV, where the performance of the instrument is greatly decreased. Not following Fermi/GBM alerts would lead to fewer observations and especially of short GRBs as Fermi/GBM is the instrument that is providing most of the detection of localized short GRBs. ls In the future, to improve the follow-up of large uncertainty alert like the ones emitted by Fermi/GBM, follow-up will be done with multiple pointing by using the tilling observations method inspired from the follow-up of gravitational waves alert [5]. This would help to improve the probability region covered and also increase the chance that if a more precise localization arrives it would be closer to the center FOV of at least one pointing.

The observation will restart with the end of the volcanic eruption in La Palma. We could expect a lot more GRBs observation and increased time dedicated to these observations as the commissioning go to its end. GRBs observations with LST-1 are only starting and a lot could be expected in the future with the performance of the instrument and the construction of three additional LSTs that should increase the performance a lot.

References

[1] B. P. Abbott, et al. Multi-messenger Observations of a Binary Neutron Star Merger. *The Astrophysical Journal*, 848(2):L12, October 2017.

[2] H. Abdalla, et al. A very-high-energy component deep in the γ-ray burst afterglow. *Nature*, 575(7783):464–467, November 2019.

[3] Hyuga Abe, et al. Status and results of the prototype LST of CTA. In *Proceedings of 37th International Cosmic Ray Conference — PoS(ICRC2021)*, volume 395, page 872, 2021.

[4] Hyuga Abe, et al. Physics Performance of the Large Size Telescope prototype of the Cherenkov Telescope Array. In *Proceedings of 37th International Cosmic Ray Conference — PoS(ICRC2021)*, volume 395, page 806, 2021.

[5] Hyuga Abe, et al. First follow-up of transient events with the CTA Large Size Telescope prototype. In *Proceedings of 37th International Cosmic Ray Conference — PoS(ICRC2021)*, volume 395, page 838, 2021.

[6] M. Ajello, et al. A Decade of Gamma-Ray Bursts Observed by Fermi-LAT: The Second GRB Catalog. *The Astrophysical Journal*, 878(1):52, June 2019.

[7] R. Atkins, et al. Evidence for TeV emission from GRB 970417A. *The Astrophysical Journal*, 533(2):L119–L122, apr 2000.

[8] C. Deil, et al. Gammapy - A prototype for the CTA science tools. In *35th International Cosmic Ray Conference (ICRC2017)*, volume 301 of *International Cosmic Ray Conference*, page 766, January 2017.

[9] A. S. Fruchter, et al. HUBBLE SPACE TELESCOPE Observations of the Host Galaxy of GRB 970508. *The Astrophysical Journal*, 545(2):664–669, December 2000.

[10] Satoshi Fukami, et al. Very-high-energy gamma-ray emission from GRB 201216C detected by MAGIC. In *Proceedings of 37th International Cosmic Ray Conference — PoS(ICRC2021)*, volume 395, page 788, 2021.

[11] Orel Gueta. The Cherenkov Telescope Array: layout, design and performance. In *Proceedings of 37th International Cosmic Ray Conference — PoS(ICRC2021)*, volume 395, page 885, 2021.

[12] H. E. S. S. Collaboration, et al. Revealing x-ray and gamma ray temporal and spectral similarities in the GRB 190829A afterglow. *Science*, 372(6546):1081–1085, June 2021.

[13] Ray W. Klebesadel, Ian B. Strong, and Roy A. Olson. Observations of Gamma-Ray Bursts of Cosmic Origin. *The Astrophysical Journal*, 182:L85, June 1973.

[14] MAGIC Collaboration, et al. Teraelectronvolt emission from the γ-ray burst GRB 190114C. *Nature*, 575(7783):455–458, November 2019.

[15] William S. Paciesas, et al. The fourth BATSE gamma-ray burst catalog (revised). *The Astrophysical Journal Supplement Series*, 122(2):465–495, jun 1999.

[16] T. Piran. Gamma-ray bursts and the fireball model. *Physics Reports*, 314(6):575–667, June 1999.

[17] M. Sommer, et al. High-Energy Gamma Rays from the Intense 1993 January 31 Gamma-Ray Burst. *The Astrophysical Journal*, 422:L63, February 1994.

[18] J. van Paradijs, et al. Transient optical emission from the error box of the γ-ray burst of 28 February 1997. *Nature*, 386(6626):686–689, April 1997.

A joint GW-GRB Bayesian study for low-luminosity short GRB population

Matteo PRACCHIA *on behalf of the LIGO and the Virgo collaborations*

LAPP (Laboratoire dâAnnecy de Physique des Particules)

Abstract — A Bayesian joint analysis of gravitational waves and gamma-ray bursts (GW-GRB) is performed in order to put constraints on the low-luminosity end of the short gamma-ray burst (sGRB) population, exploiting the results of the modeled search for GW transients associated to short and ambiguous GRBs detected during the O1, O2, and O3 runs of the LIGO/Virgo network. A broken power law is used to describe the luminosity function of our sGRB population. These results provide estimates on the rate distribution of the low-luminosity sGRB population and on the joint detection rate between sGRB and GW for the future O4 run.

Introduction

Gamma-Ray Bursts (GRBs) are flash transients of high energy light, which are thought to be generated by cataclysmic astrophysical events. They are classified according to their observation time when they are detected:

- Long GRBs are observed with duration longer than 4 s and they have been associated mainly to core-collapse supernovae (CCS) events
- Short GRBs (sGRBs) are observed with duration less than 2 s and they are thought to be generated mainly in binary neutron stars (BNS) coalescences and neutron star/black hole (NSBH) coalescences
- Ambiguous GRBs are transients observed with duration between 2 and 4 seconds

There are several models which try to explain the emission mechanism and the jet profile (see fig.1), but the means we have don't allow yet to confirm any of these.

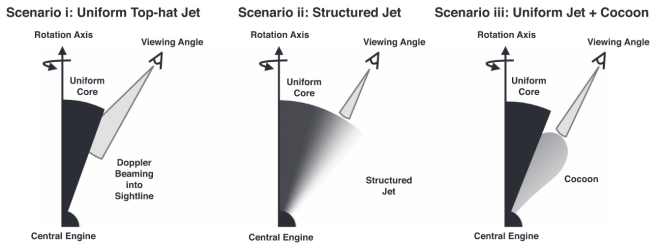

Figure 1: Different models of jet emission in a gamma-ray burst. On the left, an uniform top-hat jet, with a sharp monochromatic end. At the center, a structured jet with a profile which shades the further it gets from the rotation axis. On the right, an highly relativistic uniform jet surrounded by a mildly relativistic "cocoon". Source: [1].

The joint unambiguous detection of the gravitational wave (GW) event GW170817 and of the sGRB event GRB 170817A, confirmed that BNS can be a source for sGRBs. GRB 170817A was surprisingly close (redshift measured from GW170817 for NGC 4993, the host galaxy of the event $z_{\text{NGC 4993}} = \tilde{z} = 0.009783$ [2]) and had an unexpectedly low measured isotropic peak luminosity ($L_{\text{iso}}^{\text{GRB 170817A}} = \tilde{L} = (1.6 \pm 0.6) \times 10^{47}$ erg s^{-1} [1]). The low measured luminosity was most probably due to the off-axis observation of the jet.

This exceptional event required to modify the sGRB population models to include events which could be potentially observed off axis: we will refer to those as the low-luminosity part of the sGRB population. In this work, the sGRB population is described through a simple luminosity function model which follows [3], and it has been extended at low luminosities following the procedure described in [4]. The resulting luminosity distribution has the shape of a power law with two breaks

$$\phi_0(L_{\text{iso}}) \equiv \frac{\mathrm{d}P}{\mathrm{d}\log(L_{\text{iso}})} = \begin{cases} \left(\frac{L_{\text{iso}}}{L_{**}}\right)^{-\gamma_L} \left(\frac{L_{**}}{L_*}\right)^{-\alpha_L}, & L_0 \leq L_{\text{iso}} \leq L_{**} \\ \left(\frac{L_{\text{iso}}}{L_*}\right)^{-\alpha_L}, & L_{**} < L_{\text{iso}} \leq L_* \\ \left(\frac{L_{\text{iso}}}{L_*}\right)^{-\beta_L}, & L_{\text{iso}} > L_* \end{cases} \tag{1}$$

where $L_* = 2 \times 10^{52}$ erg s^{-1}, $L_{**} = 5 \times 10^{49}$ erg s^{-1}, $\alpha_L = 0.94$ and $\beta_L = 2$ [3]. The uncertainties are not taken into account for those fixed parameters, as the analysis would not be significantly influenced by them.

The goal of this work is to use the results obtained

from the GW followup modeled analysis of GRBs during the O1, O2 and O3 runs [5, 6, 17, 4, 7, 18] and the results on BNS rates from [8] to put constraints on the low-luminosity power index γ_L and the low-luminosity cutoff L_0 through a Bayesian analysis. For this purpose, we consider only BNS coalescences as progenitors for short GRBs. NSBH mergers could also be sGRB sources [9] under certain strict conditions [10], as well as local magnetar giant flares [11]. We don't take into account those possibilities due to their relative low rate. We use then the so obtained results to obtain an estimate on the rate distribution of the sGRB population and on the joint GW-sGRB detection rate for O4.

Bayesian Analysis

This section describes the computation of the prior $\mathrm{i}(\gamma_L, L_0)$ probability distribution function (PDF) and of the likelihood function $\mathfrak{L}(x|\gamma_L, L_0)$ as a function of γ_L, L_0 and of the observed data set x. These two elements yield the posterior PDF $P(\gamma_L, L_0|x)$ in the following form

$$P(\gamma_L, L_0|x) = \\ = \frac{\mathfrak{L}(x|\gamma_L, L_0)\mathrm{i}(\gamma_L, L_0)}{\int_{\gamma_L^{\min}}^{\gamma_L^{\max}} \int_{L_0^{\min}}^{L_0^{\max}} \mathfrak{L}(x|\gamma_L, L_0)\mathrm{i}(\gamma_L, L_0)\mathrm{d}\gamma_L \mathrm{d}L_0} \ , \quad (2)$$

with $[\gamma_L^{\min}, \gamma_L^{\max}] = [-5, 5]$ and $[L_0^{\min}, L_0^{\max}] = [10^{43}, 10^{47}]$ erg s^{-1}. All computations consider a flat ΛCDM cosmology with $h_0 = 0.7$, $\Omega_{\mathrm{m}} = 0.3$ and $\Omega_\Lambda = 0.7$, in order to be consistent with the analysis done in [3].

Prior PDF

We initially compute the observed cumulative rate distribution $C_R^{\mathrm{obs}}(z, \gamma_L, L_0)$ as function of redshift z, γ_L and L_0. We take into account the astrophysical rate density for short GRB explosions $\psi(z)$ in its form given in [3]. The short GRBs spectrum is modeled through a Band function [12] with power indices $\alpha_{\mathrm{Band}} = -0.5$, $\beta_{\mathrm{Band}} = -2.25$ and peak energy $E_{\mathrm{peak}} = 800$ keV. We use Eq. (1) as the isotropic luminosity probability distribution for our population of short GRBs and we consider as detectable in gamma-rays, at each redshift, the fraction of short GRBs which has a 64 ms peak photon flux above $P_{64}^{\mathrm{th}} = 2.37$ photons cm^{-2} s^{-1} in the energy window considered for *Fermi*/GBM, i.e. [50–300] keV. The cumulative observed rate distribution is then computed as

$$C_R^{\mathrm{obs}}(z, \gamma_L, L_0) = \int_0^z \frac{\mathrm{d}P_{\mathrm{obs}}^{\mathrm{GRB}}}{\mathrm{d}z'}\mathrm{d}z' \ , \quad (3)$$

where the differential probability of having an observed short GRB is defined as

$$\frac{\mathrm{d}P_{\mathrm{obs}}^{\mathrm{GRB}}}{\mathrm{d}z} \propto \frac{\psi(z)}{(1+z)}\frac{\mathrm{d}V}{\mathrm{d}z}\epsilon(z, \gamma_L, L_0) \ . \quad (4)$$

We denoted in Eq. (4) $\psi(z)$ as the short GRB redshift distribution, $\mathrm{d}V/\mathrm{d}z$ as the differential comoving volume and $\epsilon(z, \gamma_L, L_0)$ as the fraction of sGRBs luminous enough to be detected by *Fermi*/GBM as a function of redshift and of the low-luminosity parameters of the luminosity distribution.

Starting from $C_R^{\mathrm{obs}}(z, \gamma_L, L_0)$, an uninformative prior PDF $\mathrm{i}_u(\gamma_L, L_0)$ is built considering a flat probability distribution in the logarithms of the local observed rate density and of L_0. We impose then the total local sGRB rate to have the local BNS rate as an upper limit: using the measured posterior PDF on BNS local rate density $\mathcal{P}_{\mathrm{BNS}}(R_0^{\mathrm{BNS}})$ [8], we define

$$\mathfrak{f}(\gamma_L, L_0) = \int_0^{R_0^{\mathrm{GRB}}(\gamma_L, L_0)} \mathcal{P}_{\mathrm{BNS}}(R_0'^{\mathrm{BNS}})\mathrm{d}R_0'^{\mathrm{BNS}} \ , \quad (5)$$

where $R_0^{\mathrm{GRB}}(\gamma_L, L_0)$ is the sGRB local rate density given Eq. (1) as luminosity probability distribution and normalized considering the part of the population with $L_{\mathrm{iso}} > L_{**}$ to have a local rate density of $\rho_0^{GRB} = 4.1$ Gpc^{-3} s^{-1} [3]. The final informative prior is defined by rescaling the uninformative prior using $\mathfrak{f}(\gamma_L, L_0)$

$$\mathrm{i}(\gamma_L, L_0) = (1 - \mathfrak{f}(\gamma_L, L_0))\mathrm{i}_u(\gamma_L, L_0) \ . \quad (6)$$

Likelihood

The likelihood function $\mathfrak{L}(x|\gamma_L, L_0)$ is defined as the probability of detecting no GW transients associated with short or ambiguous GRBs during O1, and O3 and of detecting one single GW transient associated to a GRB observed during O2. We impose that the joint detection occurred at the redshift of NGC 4993 and the isotropic luminosity measured for the corresponding GRB to be in the range measured for GRB 170817A (see introduction). To reach this goal, we use the sets of GW efficiency curves computed through the modeled analysis of short and ambiguous GRBs detected during O1, O2 and O3.

Given a detected GRB i during O2, the probability of detecting a joint GW170817-like event is computed as

$$P_i^{\mathrm{det}}(\gamma_L, L_0) = \int_0^\infty \phi_0(L, \gamma_L, L_0) \ln \mathcal{N}_{\tilde{L}}(L)\mathrm{d}\ln L \\ \times \int_0^\infty \eta_i(z)\frac{\mathrm{d}P_{\mathrm{obs}}^{\mathrm{GRB}}}{\mathrm{d}z}\delta(z - \tilde{z})\mathrm{d}z \ , \quad (7)$$

where $\eta_i(z)$ is the efficiency curve corresponding to the given GRB and $\mathrm{d}P_{\mathrm{obs}}^{\mathrm{GRB}}/\mathrm{d}z$ is defined in Eq. (4). For the purpose of setting the joint detection to have the same luminosity of GRB 170817A and the same redshift of GW170817, we choose $\mathcal{N}_{\tilde{L}}(L)$ to be a log-normal distribution with mean $L_{\mathrm{GRB170817A}} = \tilde{L}$ with $\sigma_{\tilde{L}}$ being the error on the measurement of $\tilde{L}$, and we use a Dirac delta distribution $\delta(z - \tilde{z})$, being our analysis not sensitive to small variations in redshift.

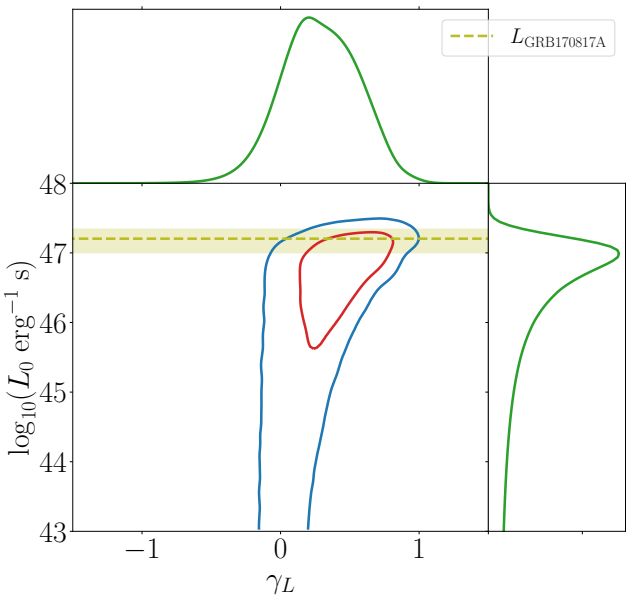

Figure 2: Posterior PDF as a function of γ_L (x-axis) and of $\log_{10} L_0$ (y-axis) with corresponding marginalized posterior curves (in green). Contours correspond to the 90% and 50% credible regions (respectively in blue and red) for the two parameters. The L_0 values for the bulk of those bounds regions lie below the measured isotropic luminosity from GRB 170817A (yellow dashed line with shaded area).

The probability of not having a joint GW detection associated to a given GRB detected during one of the observing runs can be computed in a similar way

$$P_i^{\text{no det}}(\gamma_L, L_0) = 1 - \int_0^\infty \eta_i(z) \frac{\mathrm{d}P_{\rm obs}^{\rm GRB}}{\mathrm{d}z} \mathrm{d}z \ . \tag{8}$$

The probability of a single joint detection during O2 is then obtained as

$$\mathbf{P}_{\rm O2}(\gamma_L, L_0) = \\ = \sum_i^{N_{\rm O2}^{\rm GRB}} \left(P_i^{\rm det}(\gamma_L, L_0) \prod_{j\neq i} P_j^{\text{no det}}(\gamma_L, L_0) \right) \tag{9}$$

and the probability of not having any joint detection during O1, O3a and O3b as

$$\mathbf{P}_{\rm O1+O3}(\gamma_L, L_0) = \\ = \prod_i^{N_{\rm O1}^{\rm GRB}} P_i^{\text{no det}}(\gamma_L, L_0) \prod_i^{N_{\rm O3}^{\rm GRB}} P_i^{\text{no det}}(\gamma_L, L_0) \tag{10}$$

and finally the likelihood is

$$\mathfrak{L}(x|\gamma_L, L_0) = \mathbf{P}_{\rm O2}(\gamma_L, L_0) \mathbf{P}_{\rm O1+O3}(\gamma_L, L_0) \ . \tag{11}$$

Posterior PDF

The posterior is computed as in Eq.(2), for which a contour plot is shown on Fig. 2, with contours in blue and red corresponding respectively to the posterior 90% and 50% credible regions and the marginalized posteriors shown in green. The shape of the posterior is shaped by the constant rate curves: for a fixed value of the rate, lower values for the low-luminosity power index γ_L favor lower values of the low-luminosity cutoff L_0. The marginalized posterior for L_0 peaks around the luminosity measured for GRB 170817A, as in the likelihood is required that the joint detection happened around that value. The values of L_0 in the credible region are compatible with the luminosity range measured for GRB 170817A, as the bulk of their values is lower than this last one. The 90% credible region curve does not close for low values of L_0: this is because we do not have any information about events down to those luminosities and for this reason we do not explore lower values for L_0. By marginalizing the posterior PDF over L_0, we obtain that, with a 90% confidence interval, $\gamma_L = 0.28 \pm 0.45$.

Results

In order to show the results in the luminosity function space, we build a sample of pairs of values (γ_L, L_0), according to the posterior distribution $P(\gamma_L, L_0|x)$. We then use this set of samples to compute a set of differential local rate density curves $\mathrm{d}R_0/\mathrm{d}\log_{10} L$, from which we obtain the median and the credible intervals on the luminosity distribution.

The plot in the top panel of Fig. 3 shows the $\mathrm{d}R_0/\mathrm{d}\log L$ 90% and 50% credible intervals as functions of $\log L$ and compares them to the same kind of functions estimated in other works [13, 14, 15]. The differential local rate density curves found in our work are consistent with other distributions derived after the observation of GRB 170817A. Furthermore, the short GRB luminosity functions in our model peaks around $L \sim L_{\rm GRB\ 170817A}$, considering this the only short GRB event observed at such a low luminosity.

The plot in the bottom panel of Fig. 3 shows the inverse cumulative short GRB rate density distribution $R_0(>L)$ as a function of the luminosity L. The credible intervals corresponding to the sampled curve are compatible with the BNS rate density measured for [8], but they are averagely lower. We can interpret this by saying that if the assumption that the rate of the sGRB other than BNS mergers is relatively negligible holds, there could be a fraction of BNS mergers that does not produce a sGRB and this fraction could be estimated through future more precise bounds.

Joint GW-GRB detection rate for O4

Given the present results on the low-luminosity short GRB population and the expected sensitivity for O4 [16], and only considering short GRBs detected by Fermi/GBM as onboard triggers, we can give an estimate for the joint GW-GRB detection rate we expect during the next data collecting period. This estimate highlights the effects of the low-luminosity part of the

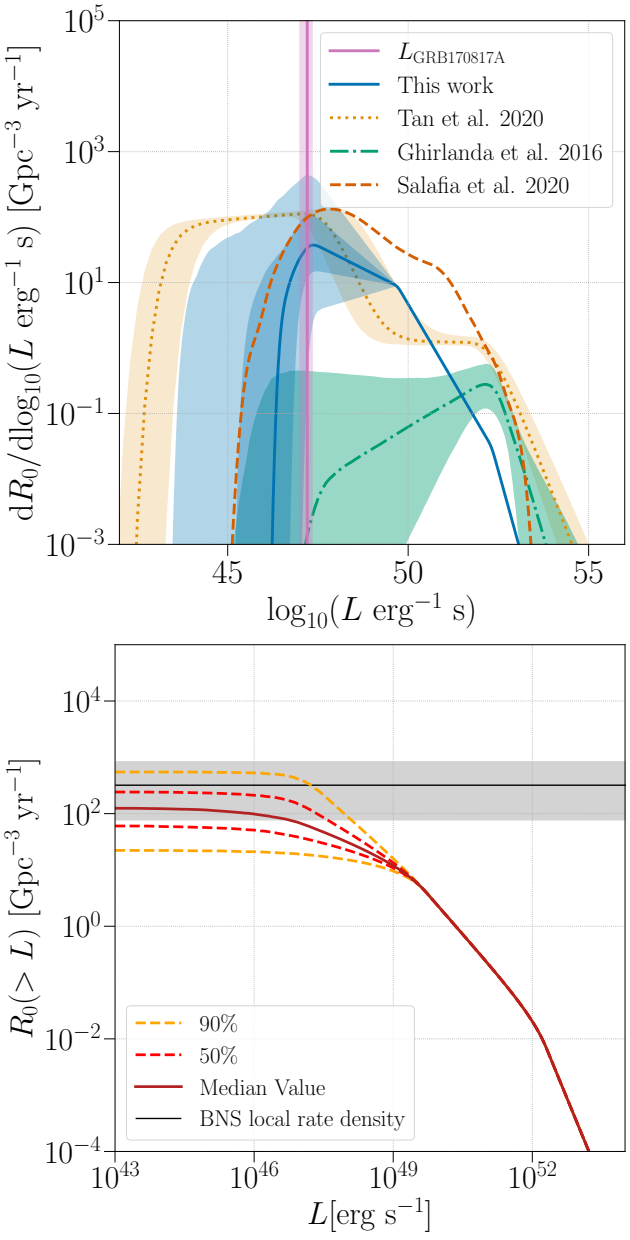

Figure 3: Differential local rate densities (top panel) and of the inverse cumulative rate density (bottom panel) as functions of luminosity. In the top plot, our set of curves is represented with the blue solid line (with shaded areas representing 90% and 50% credible intervals). For luminosities above $L_{**} = 5 \times 10^{49}\ erg\ \mathrm{s}^{-1}$, we do not represent the error bars, since in this analysis the parameters of the distribution above this value were set by the analysis from [3]. In the same plot we also show the luminosity functions from [13] (orange, dashed line), [14] (yellow, dotted line) and [15] (green, dash-dotted line). In the bottom plot we represent the median curve as a continuous brown line and the 90% and 50% credible intervals respectively as yellow and red dashed lines.

sGRB population on the rate of possible GW-GRB detections.

To have an estimate of the O4 network GW efficiency curve, we take the GW efficiency curves $\eta^{\rm GW}_{\rm O3}$ as functions of the luminosity distance ($d_{\rm L}$) obtained from the GW followup modeled analysis of the GRBs detected during O3. We then define an average O3 network efficiency curve as

$$\eta^{\rm GW}_{\rm O3}(d_{\rm L}) = \Omega_0 \frac{1}{N} \sum_{i=1}^{N} \eta^{\rm GW}_i(d_{\rm L})\ . \tag{12}$$

where $\Omega_0 \sim 0.95$ is the fraction of time when at least one of the three interferometers (IFOs) of the LIGO/Virgo network was operative during O3. Being that the modeled GW analysis has been performed on data transients corresponding to each GRB with different combinations of the (IFOs), we can safely assume that this averaged efficiency curve takes into account their different duty cycles. In order to rescale the curves to the O4 network sensitivity, we take into account the BNS ranges expected for the single IFOs r_i [16], combining them in the following way

$$\Upsilon = \sqrt{\frac{\sum_i r^2_{{\rm O4},i}}{\sum_j r^2_{{\rm O3},j}}} \tag{13}$$

and the estimated network efficiency curve for the O4 run is then

$$\eta^{\rm GW}_{\rm O4}(d_{\rm L}) = \eta^{\rm GW}_{\rm O3}(d_{\rm L}\Upsilon^{-1})\ . \tag{14}$$

Since for each detector we have that an upper and lower estimate for the O4 BNS range, we have an upper and a lower estimate for the O4 network efficiency curve, corresponding respectively to the foreseen best case and worst case scenarios.

Taken the sample of couples (γ_L, L_0) described at the beginning of the section, for each of those couples we compute a GW-GRB joint detection cumulative rate curve as function of redshift

$$R_{\rm GW-GRB}(<z) = R^{\rm GRB}_{\rm GBM} \frac{\int_0^z \frac{{\rm d}P_{\rm GRB}}{{\rm d}z'} \eta^{\rm GW}_{\rm O4}(d_{\rm L}(z')){\rm d}z'}{\int_0^\infty \frac{{\rm d}P_{\rm GRB}}{{\rm d}z'}{\rm d}z'}\ , \tag{15}$$

where $R^{\rm GRB}_{\rm GBM} = 39.5\ \mathrm{yr}^{-1}$ is the Fermi/GBM detection rate [19]. Considering the median value and the 90% credible interval for the sampled curves, the total expected joint detection rate is $R^{\rm O4}_{\rm GW-GRB} = 1.04^{+0.26}_{-0.27}\ \mathrm{yr}^{-1}$.

Conclusions

We used the results from the GW followup modeled analysis of the GRBs observed during the LIGO/Virgo observing runs [5, 6, 17, 4, 7, 18] and the results obtained on the BNS rates through the GW population analysis [8] to probe the low-luminosity part of the sGRB population. The aforementioned sGRB population has been described using a broken power law with

two breaks to shape the luminosity probability distribution, of which we constrained through Bayesian analysis the low-luminosity power index and the low-luminosity cutoff, while the other parameters were already determined in previous works [3]. The results we obtained provided an estimate on the sGRB local rate and its distribution as function of the luminosity. Although the credible intervals found are relatively large, the distribution is consistent with other distributions found after the observation of GRB 170817A [13, 14, 15]. Furthermore, the sGRB local rate density found tends to be slightly lower than the BNS local rate density, and with future more precise bounds, if the sGRB from sources other than BNS mergers have a relatively negligible rate, the fraction of BNS resulting in a sGRB could be estimated. Finally, we provided an estimate on the joint GW-sGRB rate we expect for the next GW data take, and on how much it depends on the low-luminosity part of the sGRB population. If we assume that those events follow a Poison statistics, we can expect to have, with a 90% of confidence, from 0 to 2 joint detections during O4.

References

[1] Abbott, B., Abbott, R., Abbott, T., Acernese, F., Ackley, K., Adams, C., Adams, T., Addesso, P., Adhikari, R., Adya, V., et al. Gravitational Waves and Gamma-Rays from a Binary Neutron Star Merger: GW170817 and GRB 170817A. *The Astrophysical Journal*. **848**, L13 (2017,10)

[2] Levan, A., Lyman, J., Tanvir, N., Hjorth, J., Mandel, I., Stanway, E., Steeghs, D., Fruchter, A., Troja, E., SchrÃ¸der, S., et al. The Environment of the Binary Neutron Star Merger GW170817. *The Astrophysical Journal*. **848**, L28 (2017,10)

[3] Wanderman, D. & Piran, T. The rate, luminosity function and time delay of non-Collapsar short GRBs. *Monthly Notices Of The Royal Astronomical Society*. **448**, 3026-3037 (2015,3)

[4] Abbott, B., Abbott, R., Abbott, T., Abraham, S., Acernese, F., Ackley, K., Adams, C., Adhikari, R., Adya, V., Affeldt, C., et al. Search for Gravitational-wave Signals Associated with Gamma-Ray Bursts during the Second Observing Run of Advanced LIGO and Advanced Virgo. *The Astrophysical Journal*. **886**, 75 (2019,11)

[5] Harry, I. & Fairhurst, S. Targeted coherent search for gravitational waves from compact binary coalescences. *Physical Review D*. **83** (2011,4)

[6] Williamson, A., Biwer, C., Fairhurst, S., Harry, I., Macdonald, E., Macleod, D. & Predoi, V. Improved methods for detecting gravitational waves associated with short gamma-ray bursts. *Physical Review D*. **90** (2014,12)

[7] Abbott, R., Abbott, T., Abraham, S., Acernese, F., Ackley, K., Adams, C., Adhikari, R., Adya, V., Affeldt, C., Agathos, M., et al. Search for Gravitational Waves Associated with Gamma-Ray Bursts Detected by Fermi and Swift during the LIGOâVirgo Run O3a. *The Astrophysical Journal*. **915**, 86 (2021,7)

[8] Abbott, R., Abbott, T., Abraham, S., Acernese, F., Ackley, K., Adams, A., Adams, C., Adhikari, R., Adya, V., Affeldt, C., et al. Population Properties of Compact Objects from the Second LIGOâVirgo Gravitational-Wave Transient Catalog. *The Astrophysical Journal Letters*. **913**, L7 (2021,5)

[9] Narayan, R., Paczynski, B. & Piran, T. Gamma-ray bursts as the death throes of massive binary stars. *The Astrophysical Journal*. **395** pp. L83 (1992,8)

[10] Pannarale, F. & Ohme, F. Population Properties of Compact Objects from the Second LIGO-Virgo Gravitational-Wave Transient Catalog. *The Astrophysical Journal*. **791**, L7 (2014,7)

[11] Burns, E., Svinkin, D., Hurley, K., Wadiasingh, Z., Negro, M., Younes, G., Hamburg, R., Ridnaia, A., Cook, D., Cenko, S., et al. Identification of a Local Sample of Gamma-Ray Bursts Consistent with a Magnetar Giant Flare Origin. *The Astrophysical Journal Letters*. **907**, L28 (2021,1)

[12] Band, D., Matteson, J., Ford, L., Schaefer, B., Palmer, D., Teegarden, B., Cline, T., Briggs, M., Paciesas, W., Pendleton, G., Fishman, G., Kouveliotou, C., Meegan, C., Wilson, R. & Lestrade, P. BATSE Observations of Gamma-Ray Burst Spectra. I. Spectral Diversity. . **413** pp. 281 (1993,8)

[13] Salafia, O., Barbieri, C., Ascenzi, S. & Toffano, M. Gamma-ray burst jet propagation, development of angular structure, and the luminosity function. *Astronomy Astrophysics*. **636** pp. A105 (2020,4)

[14] Tan, W. & Yu, Y. The Jet Structure and the Intrinsic Luminosity Function of Short Gamma-Ray Bursts. *The Astrophysical Journal*. **902**, 83 (2020,10)

[15] Ghirlanda, G., Salafia, O., Pescalli, A., Ghisellini, G., Salvaterra, R., ChassandeâMottin, E., Colpi, M., Nappo, F., DâAvanzo, P., Melandri, A., et al. Short gamma-ray bursts at the dawn of the gravitational wave era. *Astronomy Astrophysics*. **594** pp. A84 (2016,10)

[16] Abbott, B., Abbott, R., Abbott, T., Abraham, S., Acernese, F., Ackley, K., Adams, C., Adya, V., Affeldt, C., Agathos, M., et al. Prospects for observing and localizing gravitational-wave transients with Advanced LIGO, Advanced Virgo and KAGRA. *Living Reviews In Relativity*. **23** (2020,9)

[17] Abbott, B., Abbott, R., Abbott, T., Abernathy, M., Acernese, F., Ackley, K., Adams, C., Adams, T., Addesso, P., Adhikari, R., et al. Search for Gravitational Waves Associated with Gamma-Ray Bursts

during the First Advanced LIGO Observing Run and Implications for the Origin of GRB 150906B. *The Astrophysical Journal.* **841**, 89 (2017,5)

[18] Abbott, B., Abbott, R., Abbott, T., Abernathy, M., Acernese, F., Ackley, K., Adams, C., Adams, T., Addesso, P., Adhikari, R., et al. Search for Gravitational Waves Associated with Gamma-Ray Bursts Detected by Fermi and Swift During the LIGO-Virgo Run O3b. (2021,11)

[19] Kienlin, A., Meegan, C., Paciesas, W., Bhat, P., Bissaldi, E., Briggs, M., Burns, E., Cleveland, W., Gibby, M., Giles, M. & Al. The Fourth Fermi-GBM Gamma-Ray Burst Catalog: A Decade of Data. *The Astrophysical Journal.* **893**, 46 (2020,4)

3D Volcano Imaging Using Transmission Muography

Kinson VERNET

Laboratoire de Physique de Clermont / Université Clermont-Auvergne

Abstract — Muography is a recent technique in particle physics where atmospheric muons are used to study the interior of large targets such as volcanoes. The principle is the same as for radiography performed in hospitals. The density map of a target is inferred from the map of the radiation transmitted through it.

Introduction

Muography is a new technique in particle physics where atmospheric muons are used to study the interior of large targets such as volcanoes. In the case of transmission muography, a detector is used to count and track muons that survive after propagation through the target. To a first approximation, the number of muons that survive after propagation through the target depends directly on the amount of integrated matter along their path. The 2D map of the number of detected muons should be inverted into a 2D map of density. To achieve this, the number of muons measured with the detector in each direction is compared to the expected number of muons for different target models (in terms of density). For each direction, the inverted density is the simulated density that best reproduces the data.

Muography and other imaging techniques

The first imaging using radiation particles was realised by Wilhelm Rontgen in 1895 when he studied the fluorence of minerals[1]. He discovered a new type of "invisible" radiation, later named X-Rays as every unknown mathematical variable we would call x. A historical radiography of the bones of a human hand adorned with a ring on its third finger is showed in the figure 1. This type of radiation will be later on used to diagnose patients. The transmission muography is the same as radiography in hospitals, except that it uses atmospheric muons instead of X-rays. The atmospheric muons are well suited to image targets like volcanoes because they are very penetrating, easy to detect and exist naturally. They were also used in the past to measure overburden of tunnels[2]. Alvarez, in 1970, used this type of radiation to search for hidden chambers in pyramids [3]. The first radiographic observation of the ascent and descent of magma along a conduit utilizing atmospheric

FIG. 1.—Photograph of the bones in the fingers of a living human hand. The third finger has a ring upon it.

Figure 1: Photograph of the bones in the fingers of a living human hand. The third finger has a ring upon it[1]

muons has been reported[4]. In July 2020, some significant results on monitoring of the volcano-tectonic evolution of Mount Etna using atmospheric muons have been showed[5]. Muography provides a better resolution than the other conventional methods[6] (gravimetry for instance).

A standard measurement setup for imaging volcanoes is shown in figure 2. The direction of an incident muon can be described by two angles: the azimuth, β with respect to the geographic North, and the elevation α, that is the complement of the zenith angle.

The number of detected muons (equation 1) is given by the convolution of the transmitted muon flux with

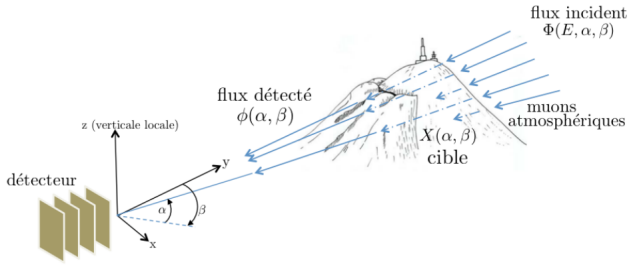

Figure 2: A standard measurement setup for imaging vulcanoes where the two angles used to map the volcano interior (α, β) are defined.

the effective surface of the detector multiplied by the duration of data collection :

$$N(\alpha,\beta) = \int_t \int_{E_\mu,\Omega(\alpha,\beta)} \phi(\alpha,\beta,E_\mu) \times S_{eff}(\alpha,\beta,E_\mu) dE_\mu d\Omega dt \quad (1)$$

where $\phi(\alpha, \beta, E_\mu)$ is the transmitted muon flux through the target and t the time. The effective surface, $S_{eff}(\alpha, \beta, E_\mu)$ combines the geometrical surface of the detector, the acceptance and the detection efficiency for muons with energy E_μ coming from the direction (α, β). It is therefore necessary to model the primary atmospheric muon flux, the target, the muon transport through the target and the effective surface of the detector in order to estimate the number of expected muons for a given model of volcano.

Modeling of atmospheric muon flux

When cosmic rays interact with matter in the upper atmosphere, they produce pions and kaons in atmospheric showers. They will subsequently decay into muons as shown in the figure 3. Nowadays, we can model the atmospheric muon flux at some altitude with respect to their energy and direction. CORSIKA simulation program[7] was used in this research to simulate the atmospheric muon flux at an altitude of 1.6 km. An estimation of the atmospheric muon flux at sea level with respect to the muon kinetic energy for three different directions is shown on figure 4. At high kinetic energies ($E\mu \geq 100$ GeV), the atmospheric muon flux does not vary significantly with the direction that is an advantage for transmission muography where high energy muons are needed to cross the target to reach more likely the detector.

Muon transport model and survival probability

To simulate the transport of atmospheric muons through the target, high resolution topographic data[8]

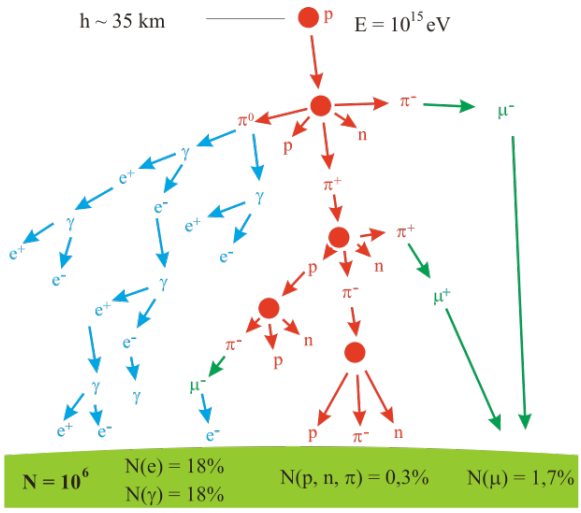

Figure 3: Example of a cascading shower from cosmic rays.

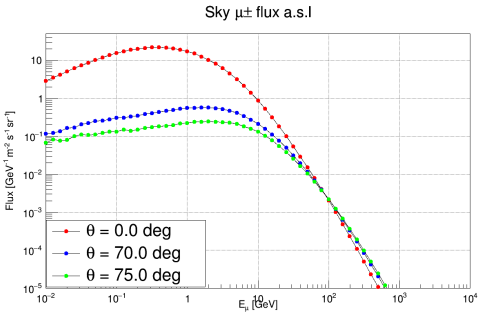

Figure 4: Sky $\mu\pm$ flux a.s.l

are crucial. Additional inputs are the chemical composition and the density, both assumed to be uniform across the target.

The survival probability of a muon depends, in first approximation, on the amount of integrated matter along its path. Many experiments use an analytical approximation called CSDA (Continuous Slow Down Approximation) giving the range of matter a particle may cross for a given energy[9]. In our case, a simulation code was developed to backward propagate muon and tau through a target described by a topographic data[10]. Use the CSDA approximation, thus neglect the stochastic character of the high-energy interactions of the particles with matter, underestimates their survival probability and thus induces systematics on the reconstructed density. The figure 5 shows in the range of kilometer of standard rock, the effect is about 3%.

Effective surface of the detector

The effective surface of the detector is defined according to the equation 2 where S_{geo}, $A(\alpha, \beta)$ and $\epsilon(\alpha, \beta, E_\mu)$ are respectively the geometrical surface, the acceptance and the efficiency of the detector to detect muons of

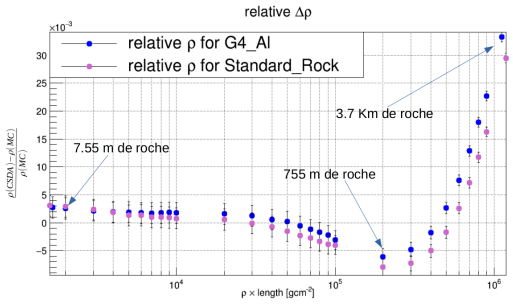

Figure 5: Systematic effects on density reconstruction using CSDA approximation

energy E_μ arriving in the direction (α, β).

$$S_{eff}(\alpha, \beta, E_\mu) = S_{geo} \times A(\alpha, \beta) \times \epsilon(\alpha, \beta, E_\mu) \quad (2)$$

The acceptance could be visualised as the perpendicular projection of the intersection of the detector layers on the muon's direction. The figure 6 shows an example of the acceptance for a $1m^3$ ideal[1] detector. The acceptance is maximal for muons arriving in the direction perpendicular to the detector layers ($\alpha_{det} = 0^o$, $\beta_{det} = 0^o$) and decreases with α_{det} or β_{det}.

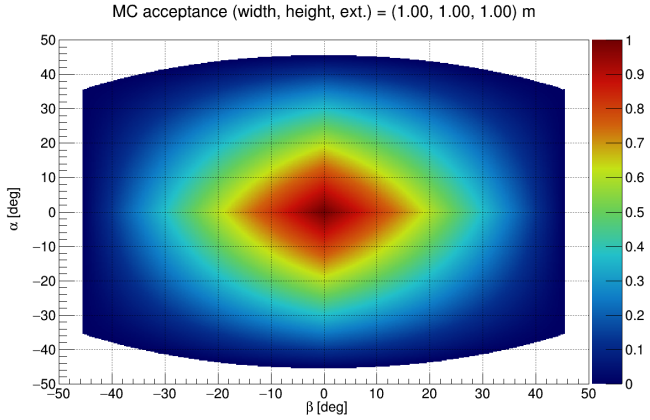

Figure 6: Acceptance of a $1m^3$ ideal detector

Density reconstruction of the Puy-de-Dome

The algorithm of the density reconstruction used during the research can be described as follows:

1. From a density interval $[\rho_{min}, \rho_{max}]$ obtained by other conventional geophysics
2. Shrink the interval until a given width ρ_w while remaining compatible with the measure

For each direction, the density center is thus an estimation of the reconstructed density.

[1]Efficiency of detection = 100% and without dead zones

The algorithm to reconstruct the density described above was applied on the Puy-de-Dome[2] and the density was reconstructed with a statistical uncertainty of 6.7%.

For 12 months of collection data with a $1m^3$ ideal detector located at latitude = 45.7699609^o and longitude = 2.9806875^o, the figure 7 shows an estimation of the detected muon crossed the PdD. For example in the direction (azimuth, elevation) = $(280.125^o, 22.125^o)$, we expect about 7.81 ± 0.03 muons with a $1m^3$ ideal detector in 12 months in a $0.25^o \times 0.25^o$ solid angle for muons with $E_\mu \geq 60$ MeV.

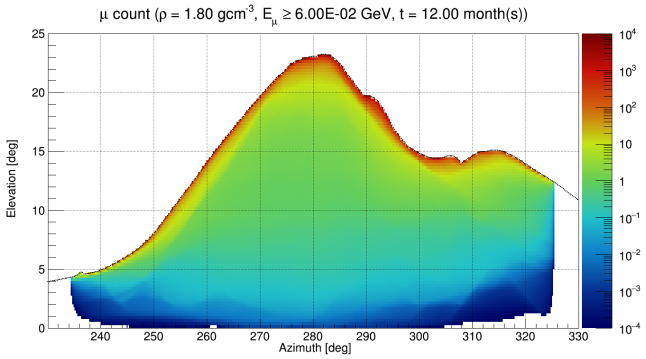

Figure 7: Expected number of muons through PdD with an ideal $1m^3$ detector and T = 1 year

The reconstructed density of the PdD in the direction (azimuth, elevation) = $(280.125^o, 22.125^o)$ assuming a uniform density of 1.8 gcm^{-3} is shown in the figure 8. The reconstructed density is $1.807 \pm sys(0.01) \pm stat(0.12)$ gcm^{-3} for muons with $E_\mu \geq 60$ MeV.

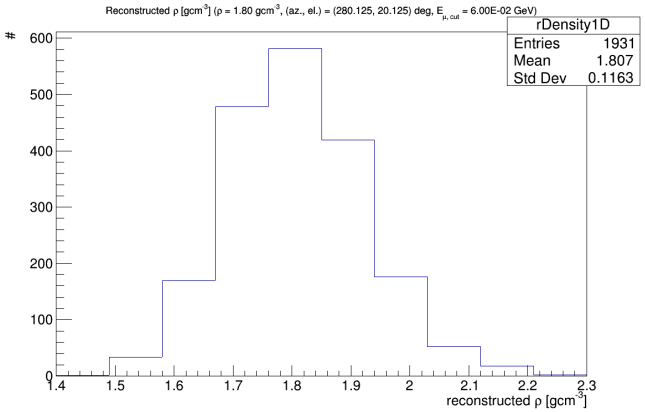

Figure 8: Reconstructed density with the algorithm for a hypothesis data

Conclusions

Muography is a good imaging technique to help in predicting volcanic crisis by reconstructing the density

[2]Puy-de-Dome is a volcano located in Clermont-Ferrand (France).

map of a volcano. With one telescope, a 2D map density could be created. With the progress of the current development of detectors used in particle physics, the muography offers better resolution than the other conventional methods. Using a treatment Monte Carlo instead of CSDA approximation gives a better precision on the reconstructed density.

References

[1] On a New Kind of Rays. Nature 53, 274-276 (1896). https://doi.org/10.1038/053274b0

[2] E.P. George. "Cosmic rays measure overburden of tunnel," in: Commonwealth Engineer (1955), pp. 455-457.

[3] Luis W. Alvarez et al. "Search for Hidden Chambers in the Pyramids". In: Science 167.3919 (1970), pp. 832-839. issn: 0036-8075. doi: 10.1126/science.167.3919.832.

[4] Tanaka, H., Kusagaya, T. & Shinohara, H. Radiographic visualization of magma dynamics in an erupting volcano. Nat Commun 5, 3381 (2014). https://doi.org/10.1038/ncomms4381

[5] Lo Presti, D., Riggi, F., Ferlito, C. et al. Muographic monitoring of the volcano-tectonic evolution of Mount Etna. Sci Rep 10, 11351 (2020). https://doi.org/10.1038/s41598-020-68435-y

[6] Raffaello D'Alessandro et al. Volcanoes in Italy and the role of muon radiography

[7] D. Heck, J. Knapp, J. N. Capdevielle, G. Schatz and T. Thouw, "CORSIKA: A Monte Carlo code to simulate extensive air showers," FZKA-6019.

[8] Kervyn, Matthieu & Ernst, G. & Goossens, Rudi & Jacobs, Patric. (2008). Mapping volcano topography with remote sensing: ASTER vs. SRTM. International Journal of Remote Sensing. 29. 6515-6538. 10.1080/01431160802167949.

[9] M. Tanabashi et al. (Particle Data Group), Phys. Rev. D 98, 030001 (2018).

[10] Backward Monte-Carlo applied to muon transport, https://doi.org/10.1016/j.cpc.2018.04.001

Radio-Morphing: a semi-analytic tool for a fast computation of air-shower radio signals

Simon CHICHE

Sorbonne Université, CNRS, UMR 7095, Institut d'Astrophysique de Paris, 98 bis bd Arago, 75014 Paris, France

Abstract — Radio detection of air-showers is a mature technique that has gained momentum over the past decades. With increasingly large-scale experiments, massive air-shower simulations are needed to evaluate the radio signal at each antenna position. Radio Morphing was developed for this purpose. It is a semi-analytical tool that enables a fast computation of the radio signal emitted by any air-shower at any location, from the simulation data of one single reference shower at given positions. It relies on simple electromagnetic scaling laws of the radio emission (i.e., electric field) at the antenna level and then an interpolation of the radio pulse at the desired positions. We present here major improvements on the Radio Morphing method that have been implemented recently. The upgraded version is based on revised and refined scaling laws, derived from physical principles. It also includes shower-to-shower fluctuations and a new spatial interpolation technique, thanks to which an excellent signal timing accuracy of a fraction of nanosecond can be reached. This new implementation, provides simulated signals with relative differences on the peak-to-peak amplitude of ZHAireS simulations below 10% (respectively 25%) for 91% (99%) of antennas while the computation time was reduced by more than 2 orders of magnitude compared to standard simulations. This makes Radio Morphing an efficient tool that allows for a fast and accurate computation of air-shower radio signals. Further implementation of Askaryan emission or enabling to use an input value of the geomagnetic field should reduce relative differences with ZHAireS by few percents and make the method more universal.

Introduction

The preparation of up-coming large-scale radio experiments (e.g., GRAND [6], AugerPrime-Radio [7], RNO [9], IceCube-Gen2-Radio [8]) requires to run a large number of air-shower simulations to evaluate their performances. While microscopic approaches such as Monte-Carlo simulations (ZHAireS [4], CoREAS [5]) provide an accurate way to model the radio-emission, these are highly time consuming with hours of computation needed to generate the radio signal of a single air-shower at the location of a hundred antennas. Macroscopic approaches are much faster but limited by our knowledge of the physical processes, particularly for very inclined arrival directions. Radio Morphing, originally introduced in [1], is a semi-analytic tool that allows for a fast computation of any air-shower at any position from a small set of ZHAireS simulations used as references. The method is based on the principle of the universality of air-showers which assumes that the radio emission can fully be inferred by characterizing the shower at $X_{\max}$, supposed point like, such as variations in the radio emission between different showers can directly be modeled by accounting for the variations at $X_{\max}$. The electric field (i.e., the radio signal) of a microscopically simulated reference shower is first scaled using simple electromagnetic scaling laws. It can then be evaluated at any 3D antenna position thanks to dedicated interpolation methods. We present the major improvements that enable to overcome serious limitations of the initial version [1], in particular in terms of scaling accuracy, radio signal timing.

Basic principles of the Radio Morphing

The Radio Morphing procedure consists in two steps (see Fig. 1): (1) Scaling: this step enables to infer the radio emission from any reference shower to any target shower with different parameters, but with same Xmax distance (i.e., distance between Xmax and the core of the shower in the shower plane). From a reference simulation run for a set of antennas located in a place perpendicular to the shower axis ("shower plane"), with given parameters (primary nature, energy and arrival direction) we apply simple scaling laws to the layout and the electric field traces and to their footprint. (2) Interpolation: we use the resulting traces of antennas in the scaled plane to interpolate the electric field at any other position in space.

The scaling process relies on physical principles to account for the variation of the electric field with shower

parameters such as the primary energy $\mathcal{E}$, azimuth Φ, and zenith angle θ. Following [1], we recall that the scaling of the electric field E with primary energy is given by $E^t = k_e E^r$ with $k_e = \mathcal{E}_t/\mathcal{E}_r$, where indices r and t refer to the reference and the target shower respectively. A scaling is justified by the fact the number of particles in air-shower scales linearly with the primary energy at the first order. The scaling with the azimuth angle is done by correcting for variations of the geomagnetic angle $\alpha = (\widehat{\mathbf{u_v}, \mathbf{u_B}})$, where $\mathbf{u_v}$ and $\mathbf{u_B}$ are respectively the direction of the shower axis and of the local magnetic field. As the geomagnetic emission is due to the Lorentz force, its electric field amplitude depends linearly on $\sin\alpha$, hence our scaling corrects the $\mathbf{v}\times\mathbf{B}$ component of the electric field by $E^t_{v\times B} = k_{\rm geo} E^r_{v\times B}$ with $k_{\rm geo} = \sin\alpha^t/\sin\alpha^r$. In practice, $E_{v\times B}$ contains also a minor charge excess or Askaryan component which does not scale with $\sin\alpha$. A more rigorous implementation taking this effect into account is under progress.

Scaling with the zenith angle

One of the main steps of Radio Morhping consists in modeling the effect of the zenith angle of the incoming air-shower direction on the electric field. We identified 3 mains contributions: (1) a change in the geomagnetic angle (described in the previous section) (2) a change in the refractive index at $X_{\rm max}$ and (3) a change in the density at $X_{\rm max}$. We detail below steps (2) and (3).

The variation of the refractive index n at $X_{\rm max}$ was already modeled in [1]. Such variations affect the Cerenkov feature of the radio-emission. It can be taken into account by applying a stretching factor to the antennas position: $\vec{x_t} = k_c \vec{x_r}$ where $k_c = \theta^t_c/\theta^r_c$ is given by the ratio of the Cerenkov angle of the target and of the reference shower. Due to energy conservation, the electric field traces can be expressed: $\vec{E^t}(\vec{x},t) = j_c \vec{E^t}(\vec{x},r)$ with $j_c = 1/k_c$.

Variations of the zenith angle will also change the density at $X_{\rm max}$ as inclined showers develop in thinner atmosphere than vertical ones. Yet, only scarce literature can be found about the dependency of the geomagnetic and charge excess emissions with air-density, in particular for very inclined air-showers. We study this dependency using a set of 11 000 ZHAireS simulations of cosmic-rays on a star-shape layout with zenith angles between 45° and 90°, energies between 0.01 EeV and 3.98 EeV and 4 azimuth angles $(0°, 90°, 180°, 270°)$. For each air-shower, we computed the geomagnetic and charge excess electric field amplitudes along the $\mathbf{v}\times\mathbf{v}\times\mathbf{B}$ baseline of antennas. Following Eq. 2.8 of [2] and assuming a radial symmetry of the radio emission, we reconstructed the charge excess and geomagnetic radiated energies $E_{\rm rad,\,ce}$ and $E_{\rm rad,\,geo}$. Finally, these energies were then corrected from any dependency on the primary particle energy and on the geomagnetic angle via the following operations: $\tilde{E}_{\rm rad,\,geo} = E_{\rm rad,\,geo}/(\mathcal{E}\times\sin\alpha)^2$ and $\tilde{E}_{\rm rad,\,ce} = E_{\rm rad,\,ce}/\mathcal{E}^2$. The residual dependency of $\tilde{E}_{\rm rad,\,geo}$ and $\tilde{E}_{\rm rad,\,ce}$ should then stem from density effects. Hence, assuming the atmospheric model of Linsley, we fit the geomagnetic and charge excess electric field amplitude dependency with air-density at $X_{\rm max}$, $f_{\rm geo}(\rho_{\rm xmax})$ and $f_{\rm ce}(\rho_{\rm xmax})$, which are illustrated in Fig. 2. Note that the dependency between the density at $X_{\rm max}$ and the shower zenith angle can be easily computed numerically from a given injection height, $X_{\rm max}$ value and atmospheric model. In the initial version of the Radio Morphing [1], a scaling of the geomagnetic electric field amplitude in $1/\sqrt{\rho(X_{\rm max})}$ was assumed. We find that this scaling is only valid up to $\theta < 70°$. For the most inclined showers however (i.e., above 70°), the amplitude of the geomagnetic electric field decreases with decreasing density, an unexpected feature that remains to be fully understood. The physical origin of this trend, likely due to lower number of particles in thinner atmospheres and hence milder resulting currents, is being investigated.

The $\mathbf{v}\times\mathbf{v}\times\mathbf{B}$ component of the electric field corresponds to charge excess only. Hence it can be directly scaled with $f_{\rm ce}$. The $\mathbf{v}\times\mathbf{B}$ component however consists of charge excess and geomagnetic contributions. A rigorous scaling would require to decompose $E_{v\times B}$ into contributions from both emissions and then independently scale each component. Yet, as such a decomposition is not possible for antennas close to the $\mathbf{v}\times\mathbf{B}$ baseline, we assume for simplicity that $E_{v\times B}$ is made of geomagnetic emission only, a reasonable hypothesis for showers in the range of zenith angles that we consider. As a consequence, one can scale the $\mathbf{v}\times\mathbf{B}$ component directly with $f_{\rm geo}$. Finally the scaling of the electric field with air-density can be expressed

$$E^t_{v\times B} = \frac{f_{\rm geo}(X_{\rm max^t})}{f_{\rm geo}(X_{\rm max^r})} E^r_{v\times B} \tag{1}$$

$$E^t_{v\times v\times B} = \frac{f_{\rm ce}(X_{\rm max^t})}{f_{\rm ce}(X_{\rm max^r})} E^r_{v\times v\times B}\ . \tag{2}$$

For more accuracy in the scaling procedure, a sample of reference showers can be used (e.g., 5 reference showers with zenith angles [67.8, 74.8, 81.3, 83.9, 86.5]), instead of a single one. A library with a denser sampling for inclined air-showers is favored, as small variations in zenith translate to large differences in terms of propagation. Using such a reference library, we were able to extend the validity range of the Radio Morphing from $\theta = 85°$ to $\theta = 90°$ in zenith angle (initial version) to $\theta = 60°$ to $\theta = 90°$ for this new version.

The scaling procedure was tested by computing the integral of the radio signal of Radio Morphed simulations and comparing them with the integral of the analogous ZHAireS simulations. The mean relative differences of the electric fields are of $\lesssim 10\%$.

Once the scaling process is completed, antennas of the scaled plane in Figure 1 are used to interpolate the radio emission at any position in space. We refer as 2D interpolation an interpolation performed inside of the scaled plane and 3D an interpolation at a position outside of that plane, both are presented in Section 5.

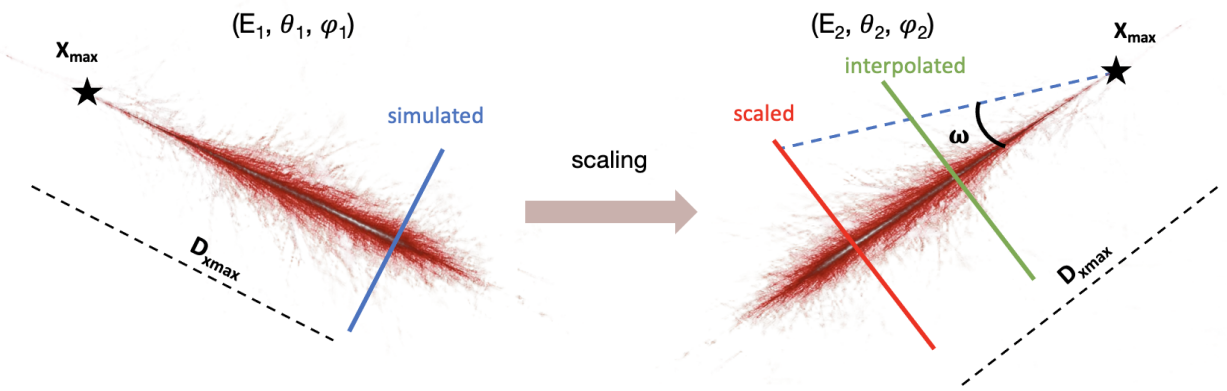

Figure 1: Sketch of the Radio Morphing procedure. The electric field from a reference ZHAireS simulation with parameter $(E_1, \theta_1, \Phi_1, d_{\mathrm{xmax}})$ is scaled towards a shower with $(E_2, \theta_2, \Phi_2, d_{\mathrm{xmax}})$, the resulting signal is then interpolated to infer the radio-emission at any position.

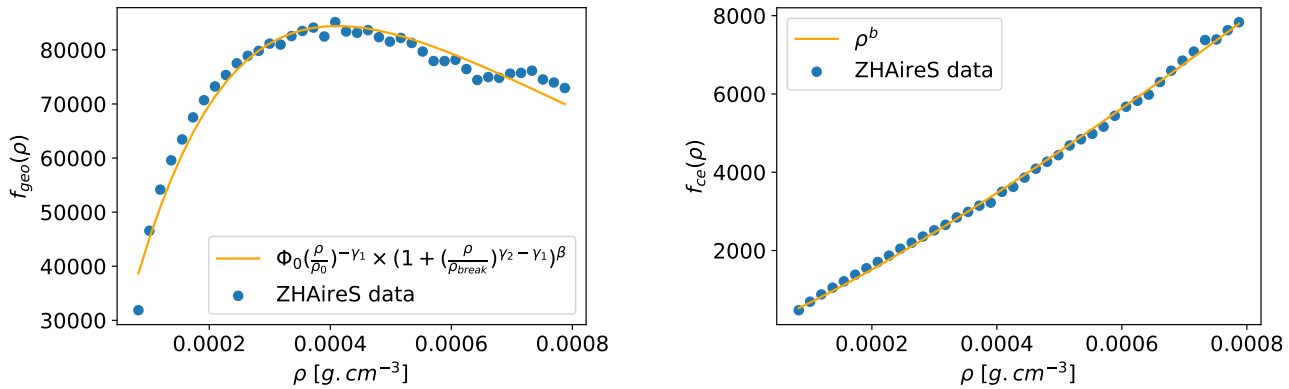

Figure 2: (*Left*) Fit of the geomagnetic electric field dependency with air-density with a broken a power law using $\phi_0 = 1010$, $\gamma_1 = -1.0047$, $\gamma_2 = 0.2222$, $\rho_{\mathrm{break}} = 3.5 \times 10^{-4}$, $\beta = 2.5$ and $\rho_0 = 1.87 \times 10^{-6}$. (*Right*) Fit of the charge excess electric field dependency with air-density with a simple power law using b = 1.195.

Interpolation

Once the scaling procedure is completed, the next step of the Radio Morphing consists in using the radio-emission from the scaled antennas to then interpolate the electric field amplitude at any given position. The interpolation in itself can be divided into two main steps, first a 2D interpolation to infer the signal at any position included in the plane of the scaled antennas and then a 3D extrapolation to infer the radio-emission at any position outside of that plane. We present below these 2 steps.

2D interpolation

We use a 2D interpolation use the 2D interpolation method presented in [3]. This method is performed in Fourier space where the electric field traces of antennas used for the interpolation are first decomposed into a phase and an amplitude, which are then linearly interpolated at the desired position. Finally, an inverse Fourier transform is performed to infer the desired traces. When considering antennas outside of the Cerenkov cone, this method provides relative differences with ZHAireS simulations of only a few percent on both the peak-to-peak amplitude and the integrated pulse. The interpolation method also provides a good agreement in timing with simulations, with an accuracy of less than 1 nanosecond. This is one of the important improvements of this version, compared to the initial Radio Morphing implementation [1] which was not providing a correct timing information.

3D: correcting for propagation effects

The 3D interpolation is mainly an extension of the 2D, extrapolating beyond the shower plane by correcting for propagation effects. In Fig. 1, $\omega = (\mathbf{u_v}, \widehat{\mathbf{u}_{\mathrm{antenna}}})$ represent the angle between the shower direction $\mathbf{u_v}$ and the direction that goes from X_{max} to a given antenna $\mathbf{u}_{\mathrm{antenna}}$. To infer the electric field of an antenna in the "interpolated" plane at a given ω, we first perform a 2D interpolation to infer the electric field of the antenna at the same ω in the "scaled" plane, and then correct from propagation effects between the 2 planes. The correction of the propagation effects consists in first accounting for the dilution of the radio signal between the 2 planes. This can simply be done

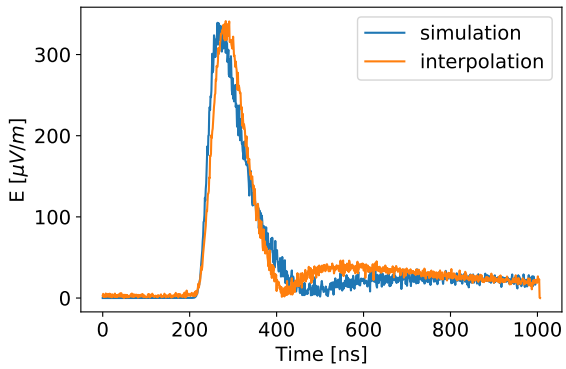

Figure 3: Example of an interpolated trace after a scaling procedure along the East-West channel of an antenna for a shower with $\mathcal{E} = 3.98\,EeV$, $\theta = 85°$, $\Phi = 270°$.

by applying a dilution factor $E_{\text{interpolated}} = k_d E_{\text{scaled}}$, where $k_d = D_{\text{scaled}}/D_{\text{interpolated}}$ corresponds to the ratio between the distance from $X_{\max}$ to the interpolated plane and the distance from $X_{\max}$ to the scaled plane. A second correction of the propagation consists in accounting for the difference in the integrated refractive index $\bar{n}$ between both planes. This is done by applying a stretching factor to the antennas positions and the traces $k_{\text{stretch}} = \theta_c^{\text{interpolated}}/\theta_c^{\text{scaled}} = (\arccos 1/\bar{n}_{\text{interpolated}})/(\arccos 1/\bar{n}_{\text{scaled}})$, similarly to what was done for the scaling with the zenith angle.

In Fig. 3, the comparison between a 3D interpolated signal for the East-West channel of a given antenna after scaling, and a ZHAireS simulation is presented. We found a good agreement between both signals with a relative difference of 0.4% on the peak-to-peak amplitudes.

Results

The results of the full Radio Morphing method are presented in Fig. 4. We considered a set of $\sim$ 1200 cosmic-ray simulations with energies between 0.1 EeV and 3.98 EeV, zenith angles between 60° and 90° and 4 azimuth angles $(0°, 90°, 180°, 270°)$. We consider planes of antennas perpendicular to the shower axis, the distance to $X_{\max}$ was chosen to have planes at $z \sim 1000\,m$ above see level. For each simulation, the electric field amplitude of 16 antennas was computed with Radio Morphing and then compared to the corresponding ZHAireS simulations. On the left plot, we present the relative differences on the peak-to-peak amplitude of the total electric field between ZHAireS and Radio Morphing as a function of the zenith angle of the target showers. The blue points correspond to the mean values and the orange stars to the RMS. We obtain an accuracy between 5 to 20% and a precision between 5 to 15% for most data bins, independently of the zenith angle. In the right-hand plot of Fig. 4, we show the normalized distributions of the mean errors for 3 different ranges of the total electric field amplitude. It appears that the largest errors come from This corresponds to antennas located on the Cerenkov cone for which the sharp amplitude variations limit the accuracy of the interpolation. We note however that the results presented here are full band, hence applying a frequency filter will reduce the Cerenkov features and improve the results. Also, the Radio Morphing method is sensitive to the reference library of showers that are also subject to shower to shower fluctuations. This limits the maximal precision that can be reached even with precise scaling procedure and interpolation. Nevertheless, the performances of this method are excellent, 91.5% the Radio-Morphed signals at the antenna level have a relative error on the peak amplitude below 10% and 99.1% below 25%.

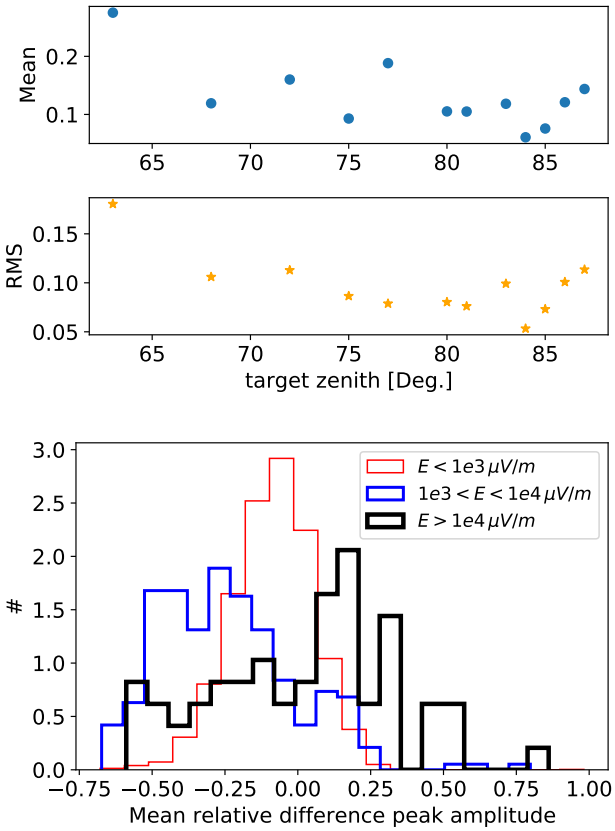

Figure 4: (*Top*) Relative differences on the peak-to-peak amplitude of Radio-Morphed antennas and corresponding ZHAireS simulations as a function of the target zenith angle for a set of 1200 showers with 16 interpolated antennas each. (*Bottom*) Normalized histogram of the distribution of the error on the peak amplitude for 3 different ranges of the total electric field amplitude E.

Conclusions

Radio Morphing is an innovative tool that allows for a fast computation of any air-shower at any given position from a small set of ZHAireS reference simulations. It relies on two main steps: a scaling procedure

based on simple physical principles to evaluate the impact of the parameters of the primary particle (nature, energy, arrival direction) on the amplitude of the electric field, and an interpolation which uses the signal of the scaled antennas to infer the radio-emission at any other position. We presented here novel implementations compared to the initial method presented in [1], to approach the experimental data. Specifically, the possibility to enable shower-to-shower fluctuations was added by parametrizing ZHAireS simulations. The scaling with the zenith angle of the shower arrival direction was also refined based on fits of the charge excess and geomagnetic emission dependencies with air density, extending the validity range of Radio Morphing to zenith angles of 60° to 90°. Finally, a new interpolation method was implemented leading to relative differences with ZHAireS simulations of few % on the amplitude, and timing accuracies of a fraction of nanosecond.

The full method (scaling + interpolation) provides results comparable to ZHAireS simulations, we find relative differences on the peak amplitude below 10% (respectively 25%) for 91.5% (99.1%) of antennas. In parallel, the computation time was reduced by several orders of magnitude compared to usual Monte-Carlo simulations. Further refinements such as correcting for the second order effects in the scaling with the geomagnetic angle, or enabling to use an input value for the geomagnetic field should provide an even more accurate and universal method.

References

[1] A. Zilles, O. Martineau-Huynh, K. Kotera, et al., Astropart. Phys. 114 (2020), 10.

[2] C. Glaser, M. Erdmann, J.R. Hörandel, T. Huege, J. Schulz, JCAP 09 (2016) 024.

[3] M. Tueros and A. Zilles 2021 JINST 16 P02031

[4] J. Alvarez-Muñiz, W. R. Carvalho, E. Zas, Astropart. Phys. 35 (2012), 325.

[5] T. Huege, M. Ludwig, C. W. James, AIP 1535 (2013), 128.

[6] J. Alvarez-Muñiz, R. Alves Batista, A. Balagopal V, et al., Science China Physics, Mechanics, and Astronomy 63 (2020), 219501.

[7] The Pierre Auger Collaboration, arXiv: Instrumentation and Methods for Astrophysics (2016), arXiv:1604.03637.

[8] The IceCube-Gen2 Collaboration, arXiv e-prints (2020), arXiv:2008.04323.

[9] J.A Aguilar, P. Allison, J.J. Beatty, et al., Journal of Instrumentation 16 (2021), P03025.

Part II

Beyond Standard Model

session chaired by Thomas STREBLER

Introduction to Beyond the Standard Model session

Thomas STREBLER

Aix-Marseille University, CNRS/IN2P3, CPPM, Marseille, France

Abstract — The aim of this contribution is to provide a short and pedagogical review of the topics discussed in the "Beyond Standard Model" session of the JRJC.

The Standard Model success story

The Standard Model (SM) is a Quantum Field Theory (QFT) which has been developed over the 1960s and 1970s to describe the elementary particles and their interactions. It describes matter and antimatter particles as fermionic fields, organised in three families of quarks and leptons. The fundamental interactions (electromagnetic, strong and weak) are associated spin-1 gauge bosons. The generation of the mass of the fermions and the W and Z bosons is produced through the electroweak symmetry breaking, possible thanks to the scalar Higgs field associated with the spin-0 Higgs boson. As this QFT is renormalizable, a finite set of measurements can be used to determine the 25 parameters of the theory, which can afterwards predict the cross-sections or kinematic distributions associated with any of the processes involving SM particles. Thanks to the large variety of processes accessible in proton collisions and the large dataset collected, many SM processes have been probed in particular at the Large Hadron Collider (LHC), as illustrated in Fig. 1. The measurements span processes covering almost 15 orders of magnitudes in cross-section and have been found to be consistent with the theory predictions over a wide range of energies and final states, making the SM one of the most predictive theories in science.

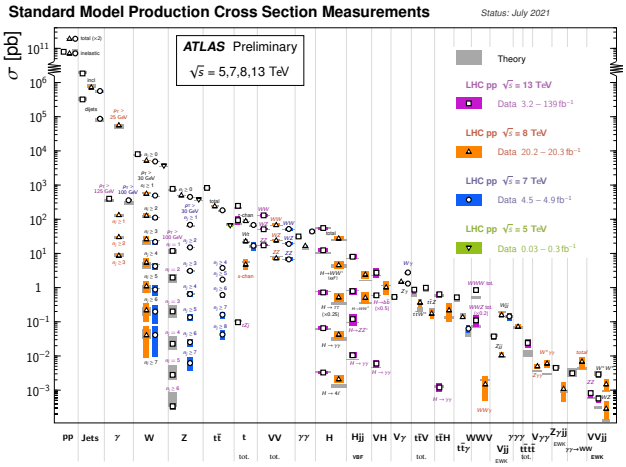

Figure 1: Summary of several Standard Model total and fiducial production cross-section measurements by the ATLAS collaboration at LHC [1].

Why going beyond the Standard Model?

Despite the many successes of the Standard Model, several experimental results over the last years have brought to light possible inconsistencies between those and the Standard Model predictions. This was for instance the case with the faster-than-light neutrino anomaly reported by OPERA in 2011 [2], the 750-GeV diphoton excess measured by ATLAS and CMS in 2015 LHC data [3, 4], the recent measurement of the muon anomalous magnetic moment by the Muon $g-2$ collaboration [5] or the recent tests of lepton-flavor universality in B-hadron decays by the LHCb collaboration [6, 7], illustrated in Fig 2. While all of those results could be interpreted as potential sign of new physics beyond the Standard Model (BSM) and prompted the release of many theory papers, not all of them successfully passed the test of time. The comparison between experimental results and theory predictions can indeed be sensitive to statistical fluctuations, inherent with the quantum nature of the processes probed, as well as underestimated theoretical or experimental systematic effects, which can potentially bias the reported results. Independent experimental confirmations or theoretical predictions are therefore often awaited with strong expectations from physicists to confirm potential signs of BSM physics.

Beyond experimental results, the SM is also thought to suffer from fundamental flaws, which let us think the SM might not be the most complete theory to describe elementary particles. With 25 free parameters, one might for instance argue that this theory is still relatively complex and set up in a very ad hoc way to fit all of the experimental observations, in the same way as the epicycle theory was set up to describe the trajectories of planets in the sky in geocentric models.

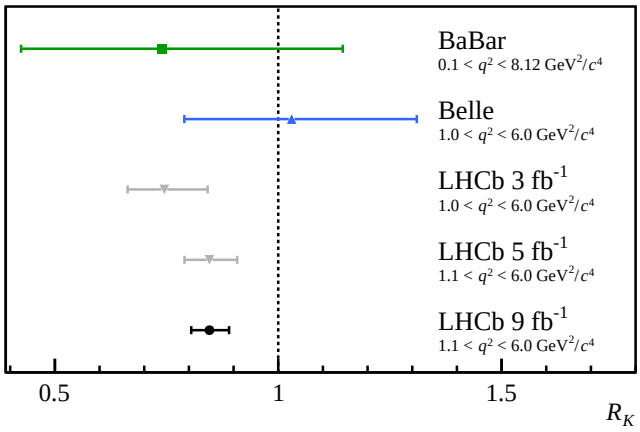

Figure 2: Recent measurements by the LHCb collaboration of the R_K parameter, corresponding to the ratio of the branching fractions of the $B^+ \to K^+\mu\mu$ and $B^+ \to K^+ee$ decays. Due to the flavor universality of the lepton couplings and the small masses of electrons and muons compared to the b quark, this parameter is expected to be close to unity within the SM [7].

At the same time, many fundamental questions are not addressed in the SM, such as follows:

- why are there three families of fermions?
- is there any connection between lepton and quark?
- why is there some CP-asymmetry in the weak interaction? why is there none in the strong interaction?
- why such a complex symmetry group $SU(3) \times SU(2) \times U(1)$? is some grand unification possible?
- are neutrinos Dirac's or Majorana's fermions?
- why is there such a large mass hierarchy between fermions?

Those questions and others are often used as motivations to develop new BSM models.

Finally, a theory describing in the same framework elementary particle interactions and gravitation is yet to be developed, as the Einstein's equations of general relativity cannot be embedded in a renormalizable QFT. Some astrophysical observations also point at new matter content in the Universe not described within the SM. This is for instance the case of dark matter (DM), whose presence is only detected thanks to its gravitational impact on the rotation speed of the galaxies or due to gravitational lenses effect in areas depleted from standard matter. The cosmological ΛCDM model also supports the existence of cold DM, together with dark energy, which accounts for the accelerating expansion speed of the Universe. While the dark energy can in principle be described as a cosmological constant or vacuum energy density, such as the one introduced with the non-zero vacuum expectation value (vev) of the Higgs field after electroweak symmetry breaking in the Standard Model, the difference between the measured value of the cosmological constant and the Higgs vev amounts to up to 60 orders of magnitude and points therefore at new sources of BSM physics.

Phenomenological framework

Searches for BSM physics are broadly carried on using two complementary approaches to interpret experimental results. On the one hand, model-dependent approaches exploit a UV-complete theory, embedding the Standard Model and trying to address some of the SM flaws or unanswered questions. This is for instance the case of the Minimal SuperSymmetric Standard Model (MSSM), which extends the SM particle content adding supersymmetric partners. This model offers in particular a potential DM candidate, the lightest supersymmetric particle, and solves the SM naturalness problem, associated with the unnatural fine-tuning required with the Higgs mass quantum corrections thanks to the new symmetry between fermions and bosons introduced. Developing such kinds of models require of course to make sure that model predictions do not contradict existing measurements, such as the non-observation of the proton decay or of flavor-changing neutral currents.

On the other hand, model-independent approaches, treating the SM as a low-energy Effective Field Theory (EFT) of some unknown UV-complete theory, can also be followed. With those frameworks, perturbations are introduced beyond the SM Lagrangian with non-renormalisable BSM operators as follows

$$\mathcal{L}_{SMEFT} = \mathcal{L}_{SM} + \frac{1}{\Lambda}\sum_i c_i^{(5)}\mathcal{O}_i^{D=5} + \frac{1}{\Lambda^2}\sum_i c_i^{(6)}\mathcal{O}_i^{D=6} + ... \quad (1)$$

with Λ the cut-off energy scale beyond which the expension break and $c_i^(n)$ numerical pre-factors for dimension-n BSM operators. There is a single dimension-5 operator, associated with Majorana's neutrinos, while the general basis for dimension-6 operators includes 2499 operators. Not of all of those operators respect the SM accidental symmetries, such as $B-L$ conservation or lepton-flavor universality, and assumptions are sometimes made to restrict the number of operators and break possible degeneracy by imposing some symmetries. This treatment remains valid as long as the energy-scale of the processes probed stay negligible in comparison to Λ, the scale at which non-perturbative new physics processes such as new resonances can happen. This approach is similar to Fermi's theory of weak interactions, describing the neutron-proton decay in radioactive atoms through a four-fermion interaction, as a low-energy approximation of diagrams involving a W boson.

Experimental searches

Considering the wide range of possible sources of BSM physics, no experiment can probe all of them simultaneously. Some experiments look for instance for BSM physics at the precision frontier in low-energy observables associated with β nuclear decays, such as the b-STILED or MORA experiments, set up to study respectively ^{6}He or heavier ions decays.

Several BSM models predict DM candidates with different masses and properties, such as sterile neutrinos, axions or weakly interactive massive particles (WIMP), which can be searched for using different processes. Collider experiments search for instance for processes where SM particles interact to produce DM particles associated to missing transverse energy in the detectors, while indirect detection experiments, such as AMS, look for the signature of DM-anti DM annihilation producing SM particules. Several generations of detectors aiming at direct DM detection, i.e. the observation of nuclear recoil from an interaction with a DM particle, have also been set up over the last years and put strong constraints on WIMP models presented in Fig. 3. Thanks to the use of different technologies, those detectors typically have different mass sensitivity and the new DAMIC-M detector in particular will help to further constrain models with a WIMP mass down to 1 GeV.

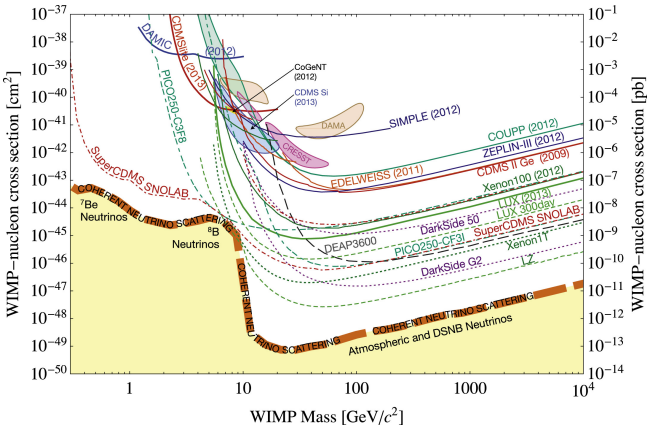

Figure 3: A compilation of WIMP nucleon spin-independent cross-section limits from current dark matter experiments and projections for planned direct detection DM experiments [9].

B hadron decays can also be used as a probe for BSM physics. These particles can be produced with a high luminosity in B factories in electron colliders, such as SuperKEKB for the Belle II experiment, or in hadron colliders, such as LHC for the LHCb experiment. Those processes indeed typically involve loop diagrams and can be sensitive to BSM particles running into the loop, which would be too heavy to directly produce in colliders. BSM physics can in that case either impact the decay rates or the angular properties of the B hadron decay products.

For resonances up to a few TeV, direct production can also be targeted in hadron colliders. Depending on the models, the search can go from simple bump search in a di-object mass spectrum to more complex MVA-based analyses, in case intermediate SM resonances, such as Higgs bosons, or even BSM resonances are involved. Given the absence of clear signal for BSM physics, physicists have also started to question whether some of the reconstruction or analysis techniques standardly used in LHC analyses might not be blind to some non-standard BSM signatures. Alternative techniques have therefore been developed recently to overcome those possible issues, in particular aiming at reconstructing and identifying long-lived particles decaying beyond the first tracking layers as illustrated in Fig. 4. Model-independent analysis techniques have also been developed, based in particular on unsupervised machine-learning techniques, to look for anomalies in data which do not fit the SM prediction but for which the relevant BSM model might still not be discovered.

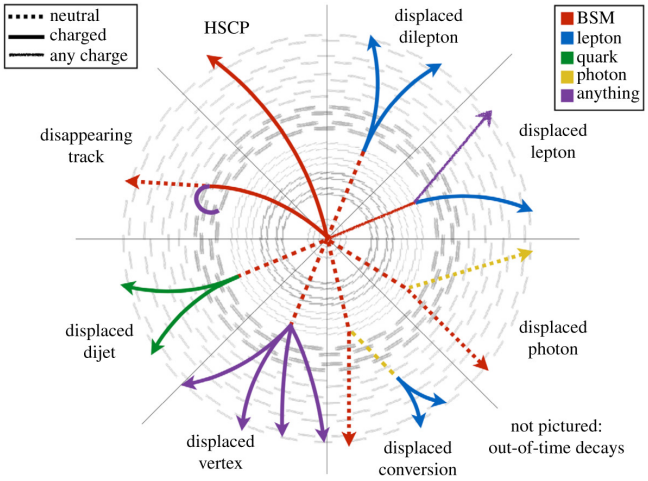

Figure 4: Several key topologies searched for by LHC experiments in the hunt for BSM long-lived particles [10].

Conclusions

We have several reasons to believe that the SM is not the ultimate theory to describe particle physics and new BSM physics might just sit around the corner. Many experimental avenues are still open and each one of them would deserve a dedicated focus. Some of them have been presented in the BSM session of the JRJC 2021 and will be summarized in the abstracts of this section.

References

[1] ATLAS Collaboration, ATL-PHYS-PUB-2021-032 (2021)

[2] OPERA Collaboration, JHEP **10** (2012) 093

[3] ATLAS Collaboration, JHEP **09** (2016) 001

[4] CMS Collaboration, Phys. Lett. B 767 (2017) 147

[5] Muon $g-2$ Collaboration, Phys. Rev. Lett. **126** (2021) 14

[6] LHCb Collaboration, JHEP **08** (2017) 055

[7] LHCb Collaboration, LHCb-PAPER-2021-004, Subm. to Nature Physics

[8] C. S. Wu et al, Phys Rev. **105** (1957) 1413

[9] J. Cooley, Physics of the Dark Universe **4** (2014) 92

[10] A. De Roeck, Phil. Trans. R. Soc. A. **377** (2019)

Search for exotic tensor couplings in the nuclear beta decay of ^{6}He

Mohamad KANAFANI

Normandie Université, ENSICAEN, UNICAEN, CNRS/IN2P3, LPC Caen, France

Abstract — Precision measurements are used to search for physics beyond the Standard Model. The b-STILED project aims to extract the Fierz interference term in the pure Gamow-Teller transition of ^{6}He with a total uncertainty of $\Delta b_{GT} = 10^{-3}$ at 1σ [1]. This contribution describes all the phases of b-STILED, especially the experimental setup used for the low energy experiment of the phase I of this project. The goals of this experiment are to extract the Fierz term with a precision of $\Delta b_{GT} = 4.10^{-3}$, and to measure the half-life of ^{6}He with a precision that is competitive with the most precise measured value so far.

Introduction

The Standard Model of particle physics is the most accurate description of elementary particles and fundamental forces. It has been a huge success, culminating with the discovery of the Higgs boson in 2012. However, despite all the successes, we have plenty of reasons to believe that it does not tell the whole story about our universe. For instance, it does not include gravity, which is one of the four fundamental forces; it also failed to explain the matter-antimatter asymmetry, in addition to the nature of dark matter and dark energy.

These reasons motivate physicists to search for a new theoretical framework that involves new physics beyond the Standard Model. This search is being held on three frontiers:

- The cosmological frontier that includes the direct probes of the cosmic microwave background as well as the indirect astrophysical search of dark matter.
- The high-energy frontier that consists of direct observation of new particles using powerful particles colliders like the Large Hadron Collider (LHC) at CERN.
- The high precision frontier that consists of executing high precision measurements at very low energy, aiming to detect any small deviations from the Standard Model's predictions, which if existed, will be a proof of new physics [2].

This work belongs to the last frontier where the aim is to study the nuclear beta decay of ^{6}He.

Nuclear beta decay

In analogy with electromagnetism, the beta decay interaction can be written as a product of a hadrons current and a leptons current:

$$H_\beta = \frac{G_F}{\sqrt{2}} J_H J_L \tag{1}$$

where G_F is the Fermi coupling constant. This Hamiltonian can be expanded as following [3]:

$$H_\beta = \frac{G_F}{\sqrt{2}} \sum_i (\bar{\psi}_p \mathcal{O}_i \psi_n)(\bar{\psi}_e \mathcal{O}_i (C_i + C_i' \gamma_5)\psi_\nu) + h.c. \tag{2}$$

where $\bar{\psi}_p, \psi_n, \bar{\psi}_e$ and ψ_ν are the spinors of the proton, neutron, electron and neutrino, $\mathcal{O}_i$ is the quantum operator of the Scalar, Vector, Tensor, Axial-vector and Pseudo-scalar interactions, and C_i (i = S, V, T, A and P) are the coupling constants for the five types of interactions. According to the Standard Model, the scalar, tensor and pseudo-scalar components are equal to zero, which indicates the non existence of their currents.

Many observables exist to probe new physics beyond the Standard Model, and the Fierz term b is one of them. It can be expressed for pure Fermi transitions and pure Gamow-Teller transitions as follows:

$$b_F \propto \gamma Re\left(\frac{C_S + C_S'}{C_V}\right) \tag{3}$$

$$b_{GT} \propto \gamma Re\left(\frac{C_T + C_T'}{C_A}\right) \tag{4}$$

Equations (3) and (4) shows that b depends linearly on the scalar and tensor coupling constants, and therefore its value is predicted to be zero by the Standard Model.

The Fierz term b can be measured precisely, by studying the shape of the beta energy spectrum, which can be expressed as following:

$$N(E) \propto (1+\eta) pE(E-E_0)^2 \left(1 + \frac{m}{E} b\right) \tag{5}$$

where η is a correction factor that includes several well known corrections like the Fermi function, $pE(E-E_0)^2$

is the phase space of the beta decay spectrum, and m is the mass of the electrons. Equation (5) shows that the shape of the spectrum is biased by the Fierz term especially at very low energy.

b-STILED

The b-STILED (b: **S**earch for **T**ensor **I**nteractions in nuc**L**ear b**E**ta **D**ecay) project that is taking place at LPC Caen aims to extract the Fierz interference term in a pure Gamow-Teller transition with a total uncertainty of $\Delta b_{GT} = 10^{-3}$ at 1σ [1]. The project is based on a precise measurement of the beta energy spectrum of ^{6}He, and it consists of two phases. For the phase I, the goal is to reach an uncertainty of the order of $\Delta b_{GT} = 4.10^{-3}$. For this phase, two experiments are planned with two different detection setups: the first uses a low energy beam of ^{6}He implanted on the surface of a YAP (Yttrium Aluminium Perovskite) crystal scintillator (Fig 1 left panel). Then another detector is placed in front of the first, in a way that insures the contact between the two scintillators in order to achieve a 4π detection geometry. For the second detection setup, a high energy beam of ^{6}He is implanted deep inside the volume of the scintillator to achieve the 4π detection geometry (Fig 1 right panel). With both setups, the 4π geometry suppress energy losses due to beta backscattering and the associated systematic error.

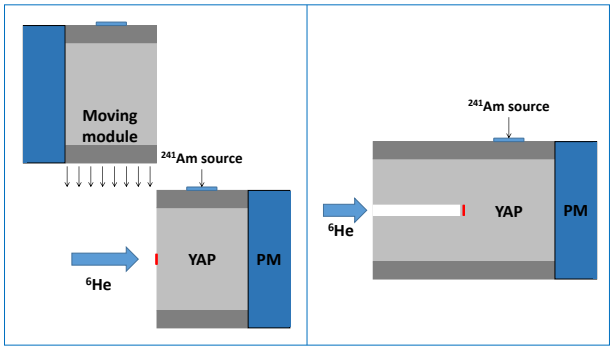

Figure 1: Left panel: sketch of the setup with a low energy beam. Right panel: sketch of the setup with a high energy beam [1].

For the phase II, the goal is to reach the final uncertainty of the project of $\Delta b_{GT} = 10^{-3}$, while using the optimal detection setup from the phase I. This work is oriented on the low energy experiment of the phase I.

Experimental setup

The low energy experiment of the phase I was performed at GANIL. We used two phoswich detectors as shown in Fig 1 (left panel). Each of them is composed of two different scintillators with different decay times coupled to a photomultiplier tube (Fig 2). The scintillator in the center is a 30 mm diameter, 30 mm long cylinder made of a crystal material with a slow decay time (YAP with $\tau = 25$ ns) surrounded by a hollow

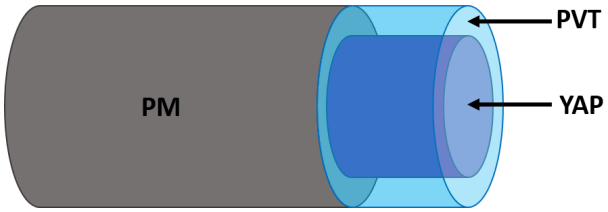

Figure 2: Schematic of the phoswich detector.

cylinder of the same length, with a 5 mm thickness made of Plastic scintillator with a significantly faster decay time (PVT with $\tau = 1.8$ ns). Such configuration will lead to the creation of two types of signals: the fast signals coming from particles interacting inside the PVT and the slow signals coming from particles interacting inside the YAP.

To distinguish between these signals, we used three integration windows (Fig 5): the baseline window [-30;-6] ns which we use to get the baseline, the fast window [-6;30] ns which by integrating the signal within it, we obtain what we call the fast charges Q_{fast}, and the total window [-6;300] ns which provides the total charges Q_{tot} by integrating the signal within it.

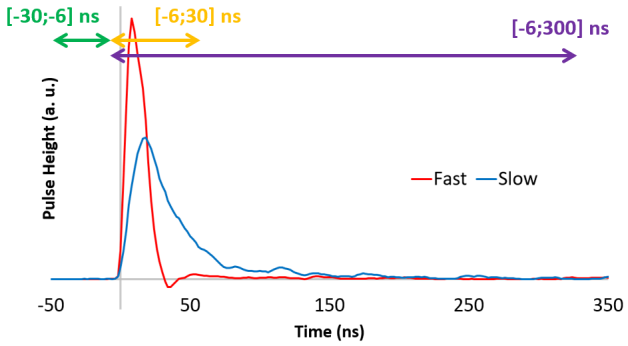

Figure 3: The two types of signals produced by phoswich detectors: the fast signal (in red) coming from particles interacting in the PVT, and the slow signals (in blue) coming from particles interacting in the YAP. The horizontal lines show the integration windows used during the data acquisition: the baseline window in green, the fast window in yellow, and the total window in purple.

During the experiment, one of the detectors was fixed along the beam axis, while the other was free to move inside and away from the beam trajectory (Fig 1). Its motion was synchronized with the beam according to fixed cycles of 16.3 sec: the low energy beam of ^{6}He is implanted on the center of the surface of the YAP scintillator while the free detector is away of the beam axis. Then the beam will be stopped, the free detector will move to be in contact with the fixed detector announcing the beginning of the acquisition stage which will last for 12 sec (more than 10 half-lives). At last,

the free detector will move out of the beam axis announcing the beginning of a new cycle.

The nominal polarization voltages of the photomultipliers were set to -1420 kV for the fixed detector and -1620 kV for the free detector. These values were chosen to ensure that the gain of the two photomultipliers were the same, and to ensure the linearity of their response functions up to 3.5 MeV. An ^{241}Am source was attached to the lateral surface of the plastic scintillator of each detector (Fig 1) which was used for the energy calibration and to monitor the gain variations of the two photomultipliers.

We executed several runs with different polarization voltages, double the cycles time, background runs and runs with several calibration sources (^{241}Am, ^{137}Cs, ^{60}Co and ^{22}Na) before and after the experiment. During the acquisition, the events were time stamped with a digital data acquisition system.

Data analysis

The electrons from the decay process will interact inside the YAP and therefore creating slow signals: To identify these signals we use the Q_{slow}/Q_{tot} ratio (Fig 3) where Q_{tot} is the sum of the fast and slow charges.

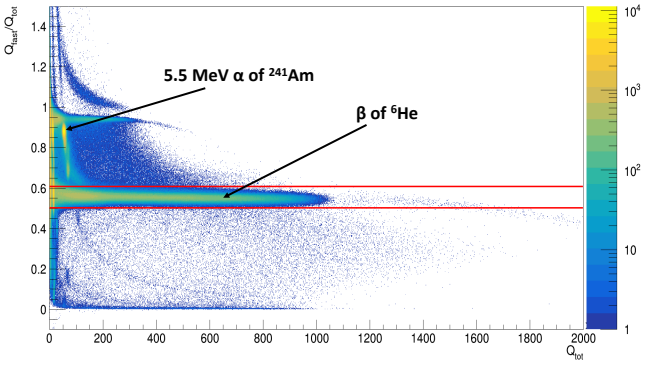

Figure 4: The Q_{fast}/Q_{tot} ratio vs the total charge for one of our detectors during a 1 hour run. This plot enables to identify the particles interacting inside the YAP scintillator (between the red lines) as well as the particles interacting inside the PVT, like the alphas of the ^{241}Am.

By choosing only the events having a Q_{slow}/Q_{tot} ratio between 0.5 and 0.62 (the events lying between the red lines in Fig 3), we isolate the events that happened inside the YAP including the electrons from the decay of the ^{6}He.

We used the 59.54 keV photopeak of the ^{2}41Am for the energy calibration and gain monitoring for each of the two detectors. The gain is affected by the count rate, and this can be seen by shifts of the position of the 59.54 keV photopeak with time (Fig 4), with an amplitude of about 1.5%. These gain shifts should be corrected if we want to achieve our precision goals. Therefore, we have to apply corrections to compensate the gain shifts for the data coming from each detector

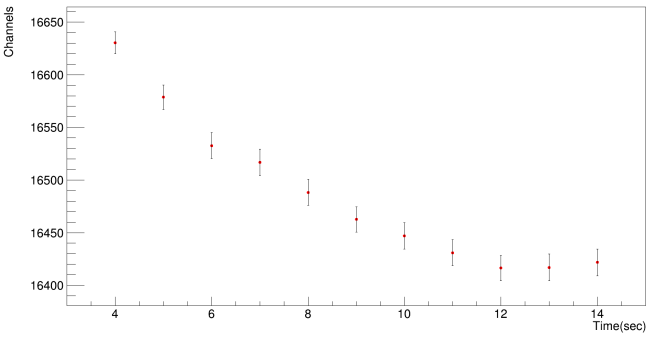

Figure 5: The position of the 59.54 keV gamma peak position vs the time within a cycle for the fixed detector.

before proceeding into the energy calibration for the whole detection system.

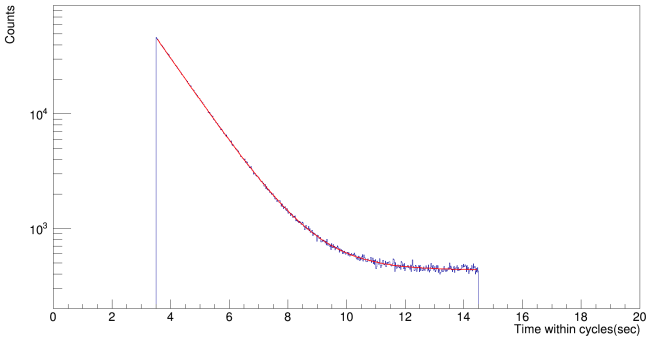

Figure 6: The count rate as function of time within the cycle during the acquisition stage (from 3.5 sec to 14.5 sec). The Background is dominated by the 59.54 keV photopeak of the ^{241}Am source

The statistics we recorded with this setup should allow us to measure the value of the half-life of ^{6}He with a precision of the order of 10^{-4}, which is competitive with the most precise value so far that was measured by Knecht et al. [4].

Summary

The precision measurement of the Fierz interference term b is one way to search for physics beyond the Standard model. The b-STILED project seeks to measure b with a precision of the order of $\Delta b_{GT} = 10^{-3}$, using YAP scintillators. Two different experimental setups will be tested with different beam energies during the phase I of this project, where the optimal setup will be qualified to be used for the phase II.

The experiment for the first setup with a low beam energy was performed successfully at GANIL. The analysis of this experiment's data was carried on, starting by the energy calibration for both of the used detectors, which showed a significant gain shifts that must be compensated in order to achieve the precision goal of the experiment.

In addition to the measurement of the Fierz term, the statistics acquired during the low energy experiment should allow us to measure the half-life of ^{6}He with a precision that is competitive with the world's most precise value.

References

[1] Naviliat-Cuncic O., Fléchard X., Liénard E., Mougeot X., Quéméner G., & Thomas J.C. (2020). Improved Search for Tensor Interactions in Nuclear Beta Decay. Proposal to the AAPG 2020, CE31.

[2] Cirigliano V., & Ramsey-Musolf M. (2013). Low Energy Probes of Physics Beyond the Standard Model. Prog. Part. Nucl. Phys., 71, 2-20.

[3] Severijns N. (2004). Weak Interaction Studies by Precision Experiments in Nuclear Beta Decay. In J. Al-Khalili & E. Roeckl (Reds), The Euroschool Lectures on Physics with Exotic Beams, Vol. I (bll 339-381).

[4] Knecht A., Hong R., Zumwalt D., Delbridge B., García A., Müller P., Swanson H., Towner I., Utsuno S., Williams W., & Wrede C. (2012). Precision Measurement of the ^{6}He Half-Life and the Weak Axial Current in Nuclei. Phys. Rev. Lett., 108, 122502.

Search for CP Violation: The MORA project

Sacha DAUMAS-TSCHOPP

LPC Caen

Abstract — The MORA (Matter's Origin from RadioActivity of trapped and oriented ions) project aims to measure with unprecedented precision the D correlation in the nuclear beta decay. Complementary to high-energy collision reactions performed to the LHC, MORA uses an innovative in-trap orientation technique at low-energy combining very optimised Paul trap and laser orientations. The commissioning of the trap and line is described in this contribution. The first milestone of this experiment is to measure the polarisation degree of the confined species before the first measurement of the D correlation. A first campaign of measurements will take place at JYFL before moving the set-up at GANIL, in the DESIR hall.

Introduction

Why are we living in a world of matter? What is the reason for the strong matter - antimatter asymmetry we observe in the Universe? A large CP violation has therefore to be discovered, at a level [1] beyond the CP violation predicted to occur in the Standard Model via the quark-mixing mechanism. The MORA project aims to search for new CP violations in beta decay thanks to the measurement of the triple D correlation, with an unprecedented precision to the order of 10^{-5} [2]. The MORA experiment uses an elegant nuclear polarisation technique, which implements the high efficiency of ion trapping [3] and the orientation of a laser. A ring of detectors allows the measurement of the coincidences between the beta particles and the recoil ions coming from the trapped radioactive ions beta decay. The D parameter can be determined by the asymmetry in the counting rate when inverting the polarisation. This measurement should also potentially enable, for the first time, a probe of the Final State Interaction effect which mimics a non-zero D correlation at or below 10^{-4}. The MORA apparatus is currently tested either at the LPC Caen or at GANIL before moving to JYFL, where adequate lasers are available for the polarization of ions, the $^{23}Mg^{+}$ being the first interesting candidate for the D measurement. MORA will be installed later in the DESIR hall at GANIL where better production rates are expected, offering the opportunities to reach unprecedented sensitivities to New Physics.

The Physics behind MORA

In nuclear beta decay, the CP violation can be inferred from the measurement of the triple D correlation described in the general beta decay rate function [4].

$$D\frac{<\vec{J}>}{J}.(\frac{\vec{p_e}}{E_e}\times\frac{\vec{p_\nu}}{E_\nu}) \quad (1)$$

Due to the scalar product between the nuclear spin J and the cross-product of the lepton momenta, a maximal correlation exists in a plan which is perpendicular to the nuclear spin direction. This plan has been chosen to be our detector plan, as shown on the figure 2. Due to the momentum conservation, the cross-product between the beta and neutrino is equivalent to the one between the beta and the recoil ion which is way simpler to detect. When the bunch of ions will enter inside the chamber, it will be confined inside a transparent Paul trap which has been numerically optimized [3]. While trapped, a circular polarized laser beam will orient the cloud either to the exit of the trap or to the injection line. A value of D can be deduced from an asymmetry in the counting such as:

$$D.P\alpha\frac{N_{coinc}^{+45^\circ}+N_{coinc}^{+135^\circ}-N_{coinc}^{-45^\circ}-N_{coinc}^{-135^\circ}}{N_{coinc}^{+45^\circ}+N_{coinc}^{+135^\circ}+N_{coinc}^{-45^\circ}+N_{coinc}^{-135^\circ}} \quad (2)$$

$N_{coinc}^{+45^\circ}$, $N_{coinc}^{+135^\circ}$, $N_{coinc}^{-45^\circ}$, $N_{coinc}^{-135^\circ}$ are corresponding to the number of recorded coincidences at a given average angle for the polarisation along the beam direction("+" sign) and for the reverse polarization ("-"sign).

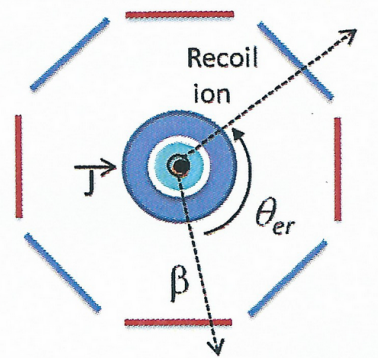

Figure 1: Simplified scheme of the detection plan of MORA. Red lines represent RIDE detectors and blue ones represent Phoswich detectors.

The detection system

MORA is composed of three kinds of detectors.

RIDE

Micro-channel plates associated to position sensitive anodes are used to detect the recoil ions. As shown in Fig.2 and 3, four such RIDE (Recoil Ion DEtectors) devices are placed on cardinal positions. Tests and characterization, performed at GANIL, are ongoing.

PhoSwich

To detect beta particles, four phoswich (phosphor sandwich) detectors are placed at inter cardinal positions (see on Figure 3). They are made of two plastic scintillators, transparent to their own light, of different sizes, one thin(0.5 mm) and one thick(5 cm) and with different time constant, a fast one for the thin (1.8 ns) and a slow one (285 ns) for the thick plastic. They are connected mechanically to a photomultiplier. We used a ^{207}Bi for the characterization of our detector. This source is very useful for that because of the multiple gammas and internal conversion electron rays, enabling to check the gamma-electron discrimination and to calibrate the detector in energy. We cannot exploit the raw spectrum however due to the correlation between the collected charges. The total charge Q_{tot} is the addition of the fast charge and the slow one. In order to decorelate the events, bidimentionnal spectra are analysed to remove the Qslow contribution in Qfast and then, the "corrected" Qfast contribution in Qtot. The obtained Qtot distribution can then be used for the final energy calibration. Geant4 simulations are ongoing to analyse in detail the electron spectra measured with the phoswich detectors in the trap chamber.

Silicon Detector

Silicon detectors, located downstream and upstream of the trap, are used for the polarisation degree determination, through the beta asymmetry parameter measurement.

Trapping commissioning

The commissioning of the trapping system has been performed with a stable surface ionization source of ^{23}Na, which appears to be polluted by other alkali elements (potassium and rubidium). We have added a tiny Radio-Frequency Quadrupole (RFQ) directly on the source in order to mimic the bunched behavior of the final line of MORA. This commissioning has been accompanied by a simulating work using the SIMION software to determine the timing of the ions inside the beam line. The line of MORA is composed of 2 lenses, 2 steerers and a MCP-phosphorus device to control the beam geometry. A pulse drift tube (PDT), located at the entrance of the trap chamber, is meant to slow down the beam, i.e to reduce its kinetic energy. The

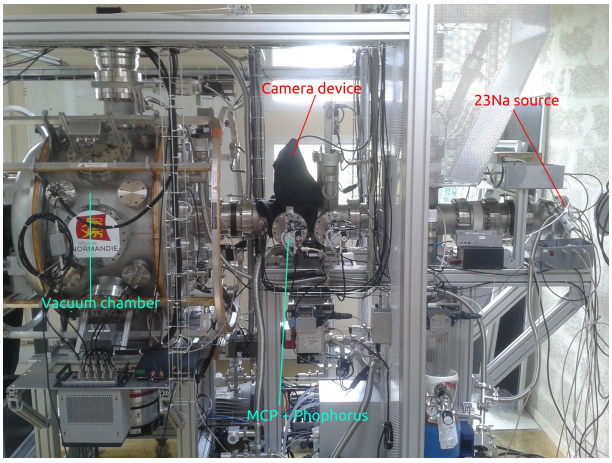

Figure 2: The MORA trap (on the left) and injection line. This line contains beam optics (lenses and steerers) and a MCP-phosphorus device to control the beam geometry. A pulse drift tube and other optics, located in the trap chamber, enable to optimize the trapping (see text for details).

ions bunch starts their journey by being ejected at 1.5 keV from the source. When they are entering in the PDT, they face a positive potential at 955 V, so by climbing that "hill" of potential, they will lose kinetic energy reaching down 545 eV. At a very specific timing (optimizing for Na ions), when they reach the center of the PDT, we apply a negative potential at - 445 V for two purposes:

- for slowing down the Na ions at the exit of the PDT.
- for focusing the beam.

Na ions are entering the trap at 110 eV and a positive potential is applied to an inner electrode of the trap to stop the ions in the middle of it. As a result, the ion bunch will be almost at 0 eV of kinetic energy at the center of the trap. They are then trapped by turning on the radio-frequency potential on the adequate electrodes.

Results

The trapping time is set at 60μs and progressively increased until reaching almost 0.5 s. The trapping efficiency is determined following this procedure:

1. After the trapping time, the ions are ejected (potential imposed on an inner trap electrode) and counted by a MCP detector located downstream of the trap.
2. The trap is turned off and the ions passing through it (Na, K, Rb) are counted on the MCP.
3. The contaminant contribution (K and Rb) is determined in another counting performed with a positive potential imposed on a grid located in front on

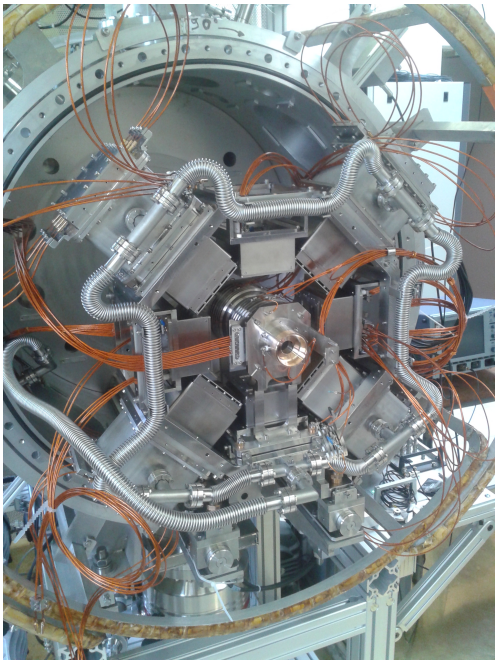

Figure 3: The MORA trap with the transparent paul trap in the center, Phoswich detectors at intercadinal positions and RIDE detectors at cardinal positions.

the MCP. This potential removes from the events the Na ions slowed down by the PDT.

4. Efficiency is deduced from the ratio

$$T_{efficiency} = \frac{number\ of\ trapped\ ^{23}\mathrm{Na}}{number\ of\ direct\ ^{23}\mathrm{Na}} \qquad (3)$$

Trapping efficiency	Trapping time
56%	60 μs
22%	90 ms
10%	450 ms

Table 1: We can see the decay of the ion cloud inside the trap. We have estimated the half-life of the cloud about 350 ms after 1 ms of evaporation of the most energetic ions.

The results presented in table 1 are quite impressive due to the fact that they have been achieved in two weeks of commissioning thanks to the precision of the beam line simulation. The MORA offline tests are promising and we are really confident for the first beam-time experiment which is scheduled for the 17th of February 2022. First, on-line trapping efficiency and the polarization degree will be measured. At JYFL, we hope collecting sufficient statistics for a first D determination during the years of stay before moving the setup at GANIL in the DESIR hall which is not built yet.

References

[1] A.Sakharov, JETP Letters, 5 (1967) 24.

[2] P. Delahaye et al., Hyperfine Interact 240 (2019) 63.

[3] M. Benali et al., Eur. Phys. J. A 56 (2020)163.

[4] M.Gonzalez-Alonso, O.Naviliat-Cuncic and N.Severijns, Prog. Part. Nucl. Phys. 104 (2019) 165.

Search for Light Dark Matter with DAMIC-M

Claudia DE DOMINICIS ***on behalf of the DAMIC-M collaboration***

SUBATECH, IMT Atlantique, CNRS-IN2P3

Abstract — DAMIC-M (Dark Matter in CCDs at Modane) is a near-future experiment that aims at searching for low-mass dark matter particles through their interactions with silicon atoms in the bulk of charge-coupled devices (CCDs). Pioneer in this technique was the DAMIC experiment at SNOLAB. Its successor, DAMIC-M, will have a detector mass 25 times larger and will employ a novel CCD technology (skipper amplifiers) to achieve sub-electron readout noise. Strengthened by these characteristics, DAMIC-M will reach unmatched sensitivity to the dark matter candidates of the so-called hidden sector. A challenging requirement is to control the radiogenic background down to the level of a fraction of events per keV per kg-day of target exposure. To meet this condition, Geant4 simulations are being exploited to optimize the detector design, drive the material selection and handling, and test background rejection techniques. This proceedings gives an overview of the project, including the estimated background, and the strategies implemented for its mitigation and characterization.

Introduction

The Standard Model can describe only the 5% of the energy-matter density of the Universe, while the 27% is considered to be composed by Dark Matter (DM) [1], the nature of which is still unknown. Many DM models and candidates have been proposed. One of the most popular candidates is a weakly interacting massive particle (WIMP), with a mass in the few GeV-TeV range. This particle would induce a nuclear recoil via a scattering process, producing a detectable signal. However, after decades of search, no WIMP signals have been detected and alternative candidates are becoming more and more popular. Among them there are the so-called hidden sector particles [2], which, in contrast with a WIMP candidate, would induce an electron recoil.

The DAMIC-M (Dark Matter In CCD at Modane) experiment will look for nuclear and electron recoils induced by dark matter particles in the silicon bulk of charge-coupled devices (CCDs). With its sub-electron resolution and low background, it will be leading the search of MeV-scale DM candidates in the hidden sector and eV-scale hidden photon. The CCDs are light sensors commonly used in digital cameras and astronomical telescopes. Their applicability in the search for DM was successfully demonstrated by DAMIC, the predecessor of DAMIC-M located at SNOLAB. DAMIC-M will be installed at the Laboratoire Souterrain de Modane (LSM) in France and it will introduce several novelties with respect to its predecessor. In fact, the detector mass will be 25 times lager and it will employ the so-called skipper CCDs, a novel type of CCD that achieves sub-electron resolution on the charge measurements [3]. Due to these features and to a low level of dark current, DAMIC-M will be extremely sensitive to very feeble ionization signals down to few eV, which are expected from DM interaction with nuclei or electrons in the silicon bulk. In particular the silicon's low nucleus mass ensures a good sensitivity to WIMPs with masses in the range 1-10 GeV, while its small band gap ($\sim$ 1.1 eV) provides sensitivity to hidden sector DM-electron interactions. The expected sensitivity to WIMP-nucleon interactions and to one possible hidden sector candidate is shown in Figure 1.

To reach these results, DAMIC-M will require a radiogenic background rate of a fraction of d.r.u[1], 100 times lower than DAMIC's one. Thus, an extensive campaign of innovation of the detector's technology and design is ongoing. Geant4 simulations are being exploited to optimise the detector design, drive the material selection and handling, and test background rejection techniques. In the following, the background mitigation strategies which DAMIC-M is going to adopt will be described. The estimated background level for one the latest investigated designs will be also provided.

Experimental setup

In its current design, DAMIC-M will employ 200 CCDs, which are fabricated from n-type, high-resistivity silicon wafers. Each CCD features a three-phase polysilicon gate structure with a buried p-channel and is fully depleted by applying a potential larger than 40 V to a thin back-side contact [4]. DAMIC-M CCDs will be characterized by 6k x 1.5k pixels over a 9 cm x 2.25 cm area, a thickness of at least 0.675 mm and a mass of about 5 g.

The operation of a CCD applied to the DM search is based on the creation of electron-hole pairs due to nuclear/electronic recoils in the silicon bulk. The produced ionization charges are drifted by the applied electric field and diffuse transversely with a spatial variance proportional to the transit time (or depth of the

[1] 1 d.r.u (differential day units) corresponds to 1 event/day/kg/keV.

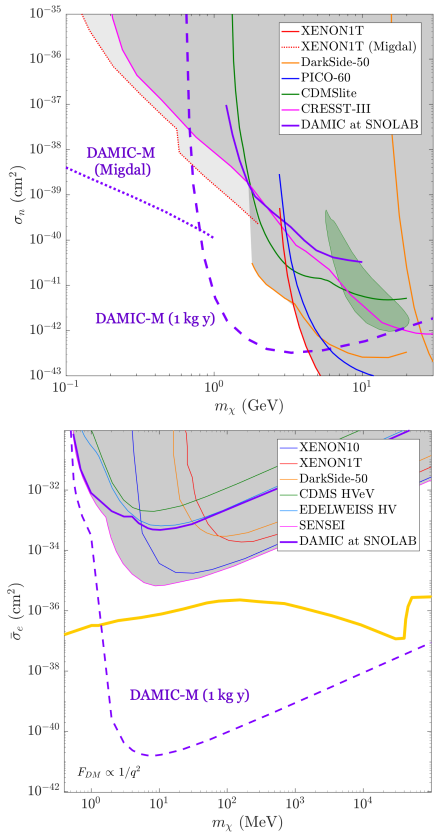

Figure 1: Examples of expected sensitivity of DAMIC-M [5] and exclusion limits compared to other dark matter searches and theoretical models. Up: exclusion limits for a WIMP-nucleon spin-independent scattering. The Midgal projection comes from [6]. Bottom: exclusion limit for a DM-electron interaction via a light dark photon mediator [2].

interaction). This allows a 3D reconstruction of the energy deposits. The charges are collected and held at a polysilicon gate until read out. The new DAMIC-M CCDs will be equipped with skipper amplifiers which will perform repeated, non-destructive measurements of the charge in each pixel, in order to damp the readout noise (usually about 2 e- rms/pix in conventional scientific CCDs) to a sub-electron level [3]. Continuous readout will be used to minimize the accumulation of charges from leakage current in a pixel before it is read out. The CCD clocks and output node signal will travel on low background kapton cables.

The detector design is ongoing. One of the latest designs is shown in Figure 3. A cryostat vessel houses the CCDs, hung on a copper support and surrounded by infrared (IR) shields. Cooling is provided by the use of liquid nitrogen, whose consumption will be optimized by the use of a heat exchanger. The working temperature is of about 140 K to ensure a low level of dark current. Most of the components are made of electro-formed (EF) copper, especially those nearest to the CCDs, given their very low content of radioactive isotopes. This material requires a long procedure to be grown and very high control of the background level to ensure its high purity. The farther volumes are instead made of oxygen-free high thermal conductivity (OFHC) copper which is widely used in cryogenics and is characterized by high chemical purity. A sandwich of electroformed copper and ancient lead disks is placed on top of the CCD stack to shield from the background events coming from the above detector components. Simulations were used to optimize the disks thickness. A polyethylene and ancient lead shields with a thickness of about 40 cm and 20 cm respectively surround the detector to screen it from external neutrons and γ-rays.

Background sources and detector simulations

In order to be sufficiently sensitive to the feeble interaction cross section of dark matter with ordinary matter, DAMIC-M has to reduce the background level to a fraction of d.r.u. All the particles able to produce a signal which mimics the one induced by a dark matter interaction are considered as background sources. The main ones are are γ-rays, electrons and neutrons of radiogenic or cosmogenic origins, from the materials surrounding the detector or in the silicon bulk.

Neutrons can be created by spallation of cosmic ray muons on nuclei in the materials around the experiment (prompt cosmogenic neutrons) or via radioactive processes. They can interact with the nuclei in the detector and induce nuclear recoils. To reduce the background from prompt neutrons, direct dark matter experiments are hosted in underground laboratories and are surrounded by a shield of high density polyethylene, which is an excellent neutron moderator. The radiogenic neutrons can instead be reduced by selecting materials with poor content of Uranium (^{238}U) and Thorium (^{232}Th).

Electrons and γ-rays are produced in the decays in the materials around and inside the experimental setup. γ-rays can produce electrons via photoelectric effect, Compton scattering and e+/e- pair production. Low energy electrons from Compton scattering are particularly critical at the energies of interest of DAMIC-M. Detailed measurements of Compton scattered electrons spectra in the bulk of skipper CCDs are currently being carried out [7]. The main sources of electrons and γ-rays are the ^{238}U and ^{232}Th chains, the ^{40}K and the cosmogenic isotopes. Cosmogenic isotopes are produced by spallation of cosmic rays in the detector components, like the copper or silicon ones. Particularly relevant is the case of tritium (^{3}H) contamination, as shown by DAMIC results [8]. The ^{3}H production rate at energies below 5 keV corresponds to an activity of roughly 0.002 decays/(keV$\cdot$kg$\cdot$day) per day of sea-level exposure [9]. Moreover, traces of ^{32}Si and ^{210}Pb can be found in the silicon bulk or surface. Their nuclei undergo sequential beta decays whose β spectra extend to the low-energy region considered for the DM search. Given the unique spatial resolution of DAMIC-M, analysis techniques looking for spatial correlated events in the silicon bulk allow to identify these decay chains [10]. To reduce

the radioactive isotopes contamination of the detector components, the DAMIC-M collaboration will employ high purity materials, and will limit the exposure time to cosmic rays by shielded transportation, underground storage, and handling in a radon free ambient. Finally, the flux of γ-rays from the environment is suppressed by about 20 cm of archaeological lead which has low level of contamination of ^{238}U and ^{232}Th.

Another approach that DAMIC-M may use to lower surface background events, due to ^{210}Pb contamination on CCD, is to remove about 10 μm from the backside surface of the silicon wafer. This technique would also result in the removal of the partial charge collection regions in the back of the CCD, which may lead to distortions in the low part of the energy spectrum [11]. Finally, further background rejection can be done at analysis level [12].

The ability to control the backgrounds to the expected level will be demonstrated by the DAMIC-M prototype, the so-called Low Background Chamber (LBC) which was installed at the LSM laboratory in December 2021 (Figure 2). The detector features two high-quality 6k $\times$ 4k skipper CCDs and is expected to achieve a background level of few d.r.u. The LBC will provide a first validation of the background model down to single electron resolution and some first results on the dark matter search using DAMIC-M skipper CCDs.

Figure 2: The Low Background Chamber prototype installed at the LSM.

As stated before, the DAMIC-M detector design is still under development. The proposed layouts are simulated to predict the corresponding background level and drive further design improvements.

The simulated components for the latest design are shown in Figure 3.

A Geant4 [13] based code has been developed to simulate the physics processes undergone by a particle passing through the experimental setup. A code written in python (WADERS) is then used to reproduce the detector response and provide the cluster[2] reconstruction.

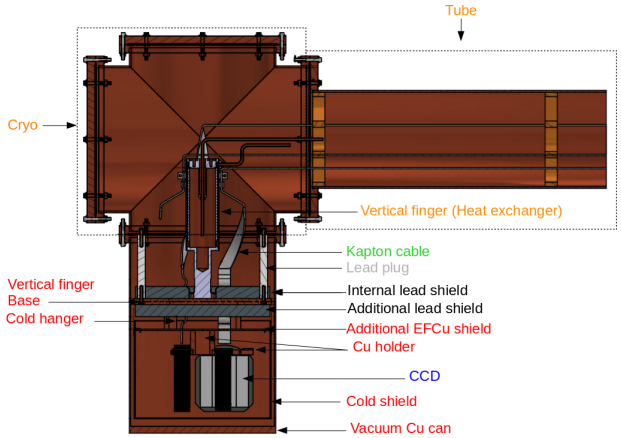

Figure 3: Latest simulated detector design. The different colors indicate the material used for the components: OFHC (orange), EF copper (red), lead (black), kapton (green), silicon (blue). The oring component, made of viton, is not visible in the figure and it is located between the Cryo and the Vacuum Cu can.

The radioactive isotopes are uniformly simulated in the bulk of the detector components, choosing only the proper ones depending on the volume material. The following isotopes from the ^{238}U and ^{232}Th chains are considered: ^{210}Pb, ^{210}Bi, ^{212}Pb, ^{212}Bi, ^{214}Pb, ^{214}Bi, ^{234}Th, ^{234}Pa, ^{228}Ac, ^{208}Tl. The cosmogenic isotopes from copper activation are included: ^{60}Co, ^{56}Co, ^{57}Co, ^{58}Co, ^{54}Mn, ^{59}Fe, ^{46}Sc. The ^{40}K and the ^{87}Rb isotopes are also considered because traces of them can be found in epoxy and copper. The components of a radioactive chain are simulated separately. The background rate is obtained for each isotope scaling the cluster energy spectrum by a proper scale factor f:

$$\mathrm{f} = \frac{\mathrm{n_{bins}} \cdot \mathrm{A_{iso}} \cdot \mathrm{m_{vol}}}{\Delta\mathrm{E} \cdot \mathrm{N_{decays}} \cdot \mathrm{M_{detector}}} \quad (1)$$

where $\mathrm{n_{bins}}/\Delta\mathrm{E}$ is the bin width, $\mathrm{A_{iso}}$ is the activity of the isotope in decays/kg/day, $\mathrm{m_{vol}}$ is the mass in kg of the volume of the detector in which the radioactive element is simulated, $\mathrm{M_{detector}}$ is the mass of the whole sensitive detector in kg and $\mathrm{N_{decays}}$ is the number of simulated events. The used isotope activities are measured at SNOLAB for the DAMIC experiment or provided by the material suppliers. An assay program is ongoing for all the DAMIC-M detector materials.

The activity of the cosmogenic isotopes is calculated based on the time of exposure to cosmic rays ($\mathrm{T_{exp}}$), the time spent underground before data collection ($\mathrm{T_{cool}}$) and the running time of the experiment ($\mathrm{T_{run}}$):

$$A = \mathrm{S}\cdot(1-\mathrm{e}^{-\lambda \mathrm{T_{exp}}})\cdot\mathrm{e}^{-\lambda \mathrm{T_{cool}}}\cdot(1-\mathrm{e}^{-\lambda \mathrm{T_{run}}})/(\lambda \mathrm{T_{run}}) \quad (2)$$

where $\lambda = \log(2)/\mathrm{t}_{1/2}$, $\mathrm{t}_{1/2}$ is the half life of the iso-

[2] A cluster is a set of charged contiguous pixels.

tope and S is the cosmogenic production rate [14]. The exposure time, cooling time and run time of the OFHC components were assumed of 3, 6 and 12 months respectively.

The rate of background events is estimated by a fit to a constant in the energy interval between 2-7.5 keV. This energy range is chosen to exclude the silicon and copper fluorescence Kα emission peaks at 1.7 keV and 8 keV, respectively. The total background estimation for the design showed in Figure 3 is reported in Figure 4 .

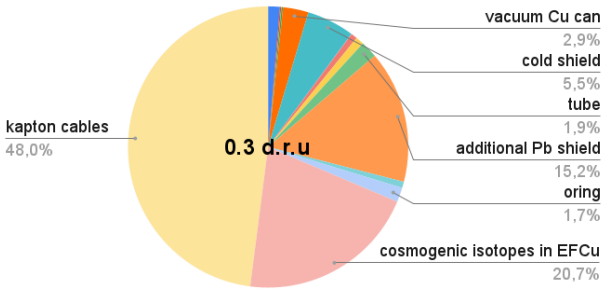

Figure 4: Contribution to the background rate of each detector component. A preliminary total background rate is 0.3 d.r.u. For the cosmogenic isotopes in the EF copper components, it was assumed T_{exp} = 10 days, T_{cool} = 6 months and T_{run}= 1 year. The external lead shield is not included in the simulated design.

The total background rate is less than 0.3 decays/day/keV/kg. The major contributors are the kapton cables, the additional lead shield and the cosmogenic isotopes in all the EF copper components. For the latter, it was assumed an exposure time of 10 days, a cooling time of 6 months and a running time of 1 year, resulting in a cosmogenic contribution of 0.06 d.r.u. This result decreases by a factor 10 if T_{exp}=1 day and increases by a factor 3 if T_{cool}=0.

The external shielding has not been designed yet. Preliminary simulations suggest that the external lead shield contribution would be comparable with the actual total background rate. Further investigations are ongoing to proper design it and damp its impact on the background budget.

Conclusions

DAMIC-M is a near-future experiment that aims at searching for low mass WIMP or hidden sector dark matter particles via their interactions in the bulk of CCDs. A major challenge for DAMIC-M is to lower the radiogenic background to a fraction of d.r.u. To this end, simulations are being performed to drive the detector design and the material selection and handling. The design is not yet finalized but current results show that the background level goal is within reach. The major contributors are the cables, the cosmogenic isotopes in the electro-formed copper components, and the additional lead shield. Pivotal to better background predictions are precise measurements of radiogenic isotope activities. An assay program is therefore ongoing. The validity of simulations, especially at low energies, will be tested with the LBC which has been successfully installed at the LSM at the end of 2021.

Acknowledgements

The author is supported by the CNRS-University of Chicago fellowship program. The DAMIC-M project has received funding from the European Research Council (ERC) under the European Union's Horizon 2020 research and innovation programme Grant Agreement No. 788137

References

[1] N. Aghanim *et al.* [Planck], Astron. Astrophys. **641** (2020), A6 [arXiv:1807.06209].

[2] R. Essig, J. Mardon and T. Volansky, Phys. Rev. D **85** (2012), 076007 [arXiv:1108.5383].

[3] J. Tiffenberg *et al.* [SENSEI], Phys. Rev. Lett. **119** (2017) no.13, 131802 [arXiv:1706.00028].

[4] A. Aguilar-Arevalo *et al.* [DAMIC], Phys. Rev. D **94** (2016), 082006 [arXiv:1607.07410].

[5] P. Privitera for the DAMIC-M collaboration, in proceedings of *TAUP Conference* (2019).

[6] S. Knapen, J. Kozaczuk and T. Lin, [arXiv:2011.09496].

[7] J. Cuevas-Zepeda, D. Norcini, P. Privitera, APS April Meeting (2021).

[8] A. Aguilar-Arevalo *et al.* [DAMIC], Phys. Rev. Lett. **125** (2020), 241803 [arXiv:2007.15622].

[9] R. Saldanha, R. Thomas, R. H. M. Tsang, A. E. Chavarria, R. Bunker, J. L. Burnett, S. R. Elliott, A. Matalon, P. Mitra and A. Piers, *et al.*Phys. Rev. D **102** (2020) no.10, 102006 [arXiv:2007.10584].

[10] A. Aguilar-Arevalo *et al.* [DAMIC], [arXiv:2011.12922].

[11] G. Fernandez-Moroni, K. Andersson, A. Botti, J. Estrada, D. Rodrigues and J. Tiffenberg, [arXiv:2007.04201].

[12] A. Aguilar-Arevalo *et al.* [DAMIC], [arXiv:2110.13133 [hep-ex]].

[13] S. Agostinelli *et al.* [GEANT4], Nucl. Instrum. Meth. A **506** (2003), 250-303.

[14] M. Laubenstein, G. Heusser, Appl Radiat Isot. **67** (2009), 750-754.

Measurement of *CP*-violating observables in $\overline{\mathrm{B}}^0 \to \mathrm{D}^{*+}\mu^-\overline{\nu}_\mu$ decays at the LHCb experiment

Vlad DEDU

Aix Marseille University, CNRS/IN2P3, CPPM, Marseille, France

Abstract — Hints on effects beyond the Standard Model (SM) have emerged lately in studies of $b \to c\ell\nu$ transitions. These discrepancies are present in the measurements of the ratios of branching fractions of the B mesons into final states with tau-leptons and muons such as R_D and R_{D^*}. Additional studied are needed to constrain and distinguish between the various NP models proposed to explain these anomalies. We aim to perform the first measurement of *CP*-violation in a semileptonic $b \to c\ell\nu$ transition, namely in $\overline{\mathrm{B}}^0 \to \mathrm{D}^{*+}\mu^-\overline{\nu}_\mu$ at the LHCb experiment. Due to the presence of NP, *CP*-violating effects can appear in the angular distribution. Here I report the first *CP*-violating sensitivity estimates, the technique employed for the kinematic recontruction of the decay and discuss the possible sources of systematic uncertainties.

Introduction

Intriguing hints on possible deviations from the predictions of the Standard Model (SM) are reported in the studies of the $b \to c\ell\nu$ transitions . At present, the discrepancies are present in the measurements of the ratios of branching fractions of the B mesons into the final states involving tau-lepton and muon, such as $R_{\mathrm{D}^*} \equiv \mathcal{B}(\overline{\mathrm{B}}^0 \to \mathrm{D}^{*+}\tau^-\overline{\nu}_\tau)/\mathcal{B}(\overline{\mathrm{B}}^0 \to \mathrm{D}^{*+}\mu^-\overline{\nu}_\mu)$ [1] and $R_{\mathrm{J/\psi}} \equiv \mathcal{B}(\mathrm{B}_\mathrm{c}^- \to \mathrm{J/\psi}\,\tau^-\overline{\nu}_\tau)/\mathcal{B}(\mathrm{B}_\mathrm{c}^- \to \mathrm{J/\psi}\,\mu^-\overline{\nu}_\mu)$ [2]. To confirm or disprove these deviations, as well as to distinguish between various New Physics (NP) models that could explain these anomalies, one has to study other experimental observables. *CP*-violating observables in the semileptonic decays were suggested as promising means to differentiate various NP scenarios.

In this analysis, we aim to perform the first study of the *CP*-violating observables in the $b \to c\ell\nu$ transitions, namely in the decay $\overline{\mathrm{B}}^0 \to \mathrm{D}^{*+}\mu^-\overline{\nu}_\mu$[3] using data collected by the LHCb detector at CERN.

The LHCb detector

The LHCb detector is one of the four main experiments at the LHC collider at CERN and its main purpose is to study and measure rare decays of beauty and charm hadrons and the *CP*-violation parameters these decays give access to. At the high centre-of-mass energy the LHC is operated at, proton-proton collisions produce $b\bar{b}$ quark pairs at small angles with respect to the beam axis, in forward or backward directions. The LHCb detector takes advantage of this by having a forward geometry, covering the pseudorapidity range $2 < \eta < 5$ [4]. With very efficient tracking and excellent particle identification, the LHCb detector is able to perform high precision measurements of *CP*-violation parameters and rare decays of beauty and charm hadrons.

Analysis overview

In the SM, semileptonic decays such as $\overline{\mathrm{B}}^0 \to \mathrm{D}^{*+}\mu^-\overline{\nu}_\mu$ proceed via a single $b \to c\ell\nu$ tree-level weak transition and can not violate *CP*, since *CP*-violation requires at least two interfering amplitudes with different weak and strong phases. However, even if additional NP amplitudes interfere with the SM one, for semileptonic decays the hadronic transition is the same $b \to c$ quark transition, such that the strong phase will be the same and there will still be no *CP*-asymmetry in the total rate of the decay. However, *CP*-violating effects in $\overline{\mathrm{B}}^0 \to \mathrm{D}^{*+}\mu^-\overline{\nu}_\mu$ decays are still possible in the angular distribution [3].

The differential decay rate of the $\overline{\mathrm{B}}^0 \to \mathrm{D}^{*+}\mu^-\overline{\nu}_\mu$ process is obtained by taking the spin-summed squared amplitude, where all possible contributions (SM + NP) are included in the total amplitude. This is achieved by taking the most general effective Hamiltonian with all NP Lorentz structures, given by:

$$\mathcal{H}_{eff}^{NP} = \frac{G_F V_{cb}}{\sqrt{2}} \sum_i g_i \mathcal{O}_i + \mathrm{h.c.}, \qquad \mathrm{i} = \mathrm{S,\ P,\ L,\ R,\ T}, \quad (1)$$

where the $\mathcal{O}_i$ operators with scalar (S), pseudoscalar (P), left-handed vector (L), right-handed vector (R) and tensor (T) Lorentz structures are given by:

$$\begin{aligned}
\mathcal{O}_S &= \overline{c}b\ \ell(1-\gamma_5)\nu \\
\mathcal{O}_P &= \overline{c}\gamma_5 b\ \ell(1-\gamma_5)\nu \\
\mathcal{O}_L &= \overline{c}\gamma^\mu(1-\gamma_5)b\ \ell\gamma_\mu(1-\gamma_5)\nu \\
\mathcal{O}_R &= \overline{c}\gamma^\mu(1+\gamma_5)b\ \ell\gamma_\mu(1-\gamma_5)\nu \\
\mathcal{O}_T &= \overline{c}\sigma^{\mu\nu}(1-\gamma_5)b\ \ell\sigma_{\mu\nu}(1-\gamma_5)\nu.
\end{aligned}$$

We note that in the SM, $\mathcal{H}_{eff}$ is only proportional to $\mathcal{O}_L$ while all the NP g_i couplings are zero. However, in general, the g_i couplings are non-zero and they can be complex.

The full angular distribution of the $\overline{\mathrm{B}}^0 \to \mathrm{D}^{*+}\mu^-\overline{\nu}_\mu$ decay with all possible NP contributions is derived and is given in Eq.2. The decay is considered as $\overline{\mathrm{B}}^0 \to \mathrm{D}^{*+}W^-$, where the D^{*+} decays to $\mathrm{D}^0\pi$ and the W^- decays to $\mu^-\overline{\nu}_\mu$.The angular distribution is expressed in terms of the three helicity angles θ_l, θ_D and χ, shown in Fig. 1, and q^2, the invariant mass squared of the two-lepton system. In Fig. 1, θ_D is defined as the polar angle of the D meson in the D^* rest frame, θ_l is the polar angle of the μ in the W^- rest frame, while χ is the azimuthal angle between the two decay planes.

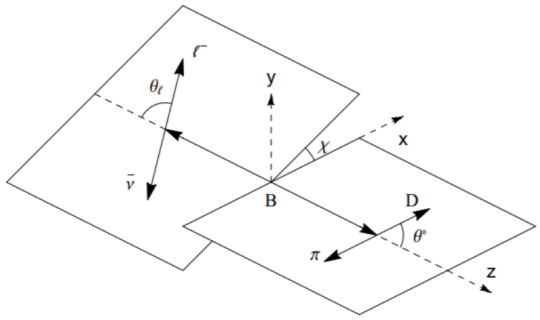

Figure 1: Definition of helicity angles in $\overline{\mathrm{B}}^0 \to \mathrm{D}^{*+}(\to \mathrm{D}^0\pi)\mu^-\overline{\nu}_\mu$

$$\frac{d^4\Gamma}{dq^2\, d\cos\theta_\ell\, d\cos\theta^*\, d\chi} = \frac{3}{8\pi}\frac{G_F^2|V_{cb}|^2(q^2-m_\ell^2)^2|p_{\mathrm{D}^*}|}{2^8\pi^3 m_B^2 q^2} \times \mathcal{B}(\mathrm{D}^{*+}\to \mathrm{D}^0\pi^+)\left(N_1 + \frac{m_\ell}{\sqrt{q^2}}N_2 + \frac{m_\ell^2}{q^2}N_3\right). \quad (2)$$

The angular distribution contains three types of angular terms: the unsuppressed ones, denoted by N_1 and the ones suppressed by factors of $m_\ell/\sqrt{q^2}$ and m_ℓ^2/q^2 denoted by N_2 and N_3, respectively. The unsuppressed angular terms are give in Table 1. The terms whose coefficients are $\mathrm{Im}(A_iA_j)$ are the *CP*-violating ones and they are all proportional to $\sin\chi$. Here, A_i and A_j are two different amplitudes. These angular terms must be looked at in decays of both B^0 and $\overline{\mathrm{B}}^0$, since by CP-conjugation both the weak phase and the azimuthal angle χ change sign. Therefore, if angular terms with the same sign proportional to $\mathrm{Im}(A_iA_j)$ are found for both the B^0 and its *CP*-conjugate decay, this would signal *CP*-violation.

Table 2 shows the *CP*-violating angular terms along with the NP couplings they are proportional to. From this table it can be seen that information about the g_R, g_P and g_T NP couplings can be extracted. For example, if the angular term $\sin 2\theta_\ell \sin 2\theta^* \sin\chi$ were measured to be nonzero it would imply that $\mathrm{Im}(\mathcal{A}_\perp\mathcal{A}_0^*) \neq 0$ such that $g_R \neq 0$ and that g_R has a different weak phase than $(1+g_L)$. Therefore, meaningful constraints can be placed upon the NP couplings which can be used to distinguish between different NP models that have been proposed to explain the b-anomalies, such as leptoquark models or $W^{'\pm}$ models.

Table 1: Terms in the N_1 part of the angular distribution [3]

Amplitude in N_1	Angular function
$\lvert\mathcal{A}_0\rvert^2$	$4\sin^2\theta_\ell\cos^2\theta^*$
$\lvert\mathcal{A}_\perp\rvert^2$	$2\sin^2\theta^*(\cos^2\chi + \cos^2\theta_\ell\sin^2\chi)$
$\lvert\mathcal{A}_\parallel\rvert^2$	$2\sin^2\theta^*(\cos^2\theta_\ell\cos^2\chi + \sin^2\chi)$
$\lvert\mathcal{A}_{\parallel,T}\rvert^2$	$32\sin^2\theta_\ell\sin^2\theta^*\cos^2\chi$
$\lvert\mathcal{A}_{\perp,T}\rvert^2$	$32\sin^2\theta_\ell\sin^2\theta^*\sin^2\chi$
$\lvert\mathcal{A}_{0,T}\rvert^2$	$64\cos^2\theta_\ell\cos^2\theta^*$
$\lvert\mathcal{A}_{SP}\rvert^2$	$4\cos^2\theta^*$
$\mathrm{Re}(\mathcal{A}_\parallel\mathcal{A}_\perp^*)$	$-4\cos\theta_\ell\sin^2\theta^*$
$\mathrm{Re}(\mathcal{A}_0\mathcal{A}_\parallel^*)$	$-\sqrt{2}\sin 2\theta_\ell\sin 2\theta^*\cos\chi$
$\mathrm{Re}(\mathcal{A}_0\mathcal{A}_\perp^*)$	$2\sqrt{2}\sin\theta_\ell\sin 2\theta^*\cos\chi$
$\mathrm{Re}(\mathcal{A}_{\parallel,T}\mathcal{A}_{SP}^*)$	$8\sqrt{2}\sin\theta_\ell\sin 2\theta^*\cos\chi$
$\mathrm{Re}(\mathcal{A}_{0,T}\mathcal{A}_{\parallel,T}^*)$	$16\sqrt{2}\sin 2\theta_\ell\sin 2\theta^*\cos\chi$
$\mathrm{Re}(\mathcal{A}_{0,T}\mathcal{A}_{SP}^*)$	$32\cos\theta_\ell\cos^2\theta^*$
$\mathrm{Im}(\mathcal{A}_\perp\mathcal{A}_0^*)$	$-\sqrt{2}\sin 2\theta_\ell\sin 2\theta^*\sin\chi$
$\mathrm{Im}(\mathcal{A}_\parallel\mathcal{A}_\perp^*)$	$2\sin^2\theta_\ell\sin^2\theta^*\sin 2\chi$
$\mathrm{Im}(\mathcal{A}_{SP}\mathcal{A}_{\perp,T}^*)$	$-8\sqrt{2}\sin\theta_\ell\sin 2\theta^*\sin\chi$
$\mathrm{Im}(\mathcal{A}_0\mathcal{A}_\parallel^*)$	$-2\sqrt{2}\sin\theta_\ell\sin 2\theta^*\sin\chi$

Table 2: Unsuppressed *CP*-violating terms in the angular distribution and their NP couplings [3]

Coupling	Angular function
$\mathrm{Im}[(1+g_L+g_R)(1+g_L-g_R)^*]$	$-\sqrt{2}\sin 2\theta_\ell\sin 2\theta^*\sin\chi$
$\mathrm{Im}[(1+g_L-g_R)(1+g_L+g_R)^*]$	$2\sin^2\theta_\ell\sin^2\theta^*\sin 2\chi$
$\mathrm{Im}(g_P g_T^*)$	$-8\sqrt{2}\sin\theta_\ell\sin 2\theta^*\sin\chi$
$\mathrm{Im}[(1+g_L-g_R)(1+g_L+g_R)^*]$	$-2\sqrt{2}\sin\theta_\ell\sin 2\theta^*\sin\chi$

In order to perform the measurement of the *CP*-violating terms in a model-independent way, instead of fitting, the distributions are projected onto the Fourier basis functions, i.e. sines and cosines of the three angles. In this way, the coefficients of the angular terms are obtained by taking the Fourier transform of the scattered data. This is equivalent to taking the discrete sum of the angular function f_i for each event k:

$$\begin{aligned} c_i &= \int P(\theta_\ell,\theta_D,\chi) f_i(\theta_\ell,\theta_D,\chi) d\theta_\ell d\theta_D d\chi \\ &= \sum_k f_i(\theta_\ell^{(k)},\theta_D^{(k)},\chi^{(k)}). \end{aligned} \quad (3)$$

Therefore, the coefficients of the Fourier expansion in the three angles will carry the information about the $\mathrm{Im}(A_iA_j)$ x which consequently carry the information about the NP couplings shown in Table 2.

Neutrino reconstruction

The semileptonic $\overline{\mathrm{B}}^0 \to \mathrm{D}^{*+}\mu^-\overline{\nu}_\mu$ decay has a neutrino in the final state which is not reconstructible in the detector. This causes a complication in reconstructing the helicity angles needed for this analysis. In order to reconstruct the neutrino, an approximation based on the decay topology using the B-meson line of flight between the primary vertex (PV) and the B-vertex is

employed. [5]

Although this method provides a way to estimate the B^0, or alternatively the ν momentum, it is still just an approximation. In order to improve this first approximation, the Decay Tree Fitter (DTF), an LHCb specific algorithm was used. The DTF makes a parameterization of the decay chain in terms of vertex positions, decay lengths and momenta and performs a refit of the decay tree in which some known parameters are constrained. The algorithm is described in [6]. In this analysis, the DTF is used to refit the full $\overline{B}^0 \to D^{*+}\mu^-\overline{\nu}_\mu$ decay chain including the first estimation for the neutrino momentum. The DTF uses the full information about the decay tree, including the correlations between the kinematic and topological parameters of the event. In this way, the precision in reconstructing the four kinematical parameters of the decay, three helicity angles and q^2 is improved.

Figures 2,3,4 and 5 show the resolution of these parameters before and after the refit. The effect of the DTF can be clearly seen, as it improves the resolution of the angles by about 10 %.

Sensitivity study

In order to study the sensitivity to measuring *CP*-violation in $\overline{B}^0 \to D^{*+}\mu^-\overline{\nu}_\mu$ at LHCb, a large simulation sample generated with a SM amplitude was used to calculate CP asymmetries in the SM as well as in different NP scenarios. For this purpose, the HAMMER tool [7] was used to reweigh the MC sample from the generation amplitude to any desired NP amplitudes. This is achieved by specifying a Form Factor (FF) scheme and the complex Wilson coefficients corresponding to the different complex couplings (g_i) in Eq.1. The basis of the NP operators is defined according to the following equation:

$$\mathcal{L} = \frac{4G_F}{\sqrt{2}} V_{cb} c_{XY} (\bar{c}\Gamma_X b)(\bar{\ell}\Gamma_Y \nu) \qquad (4)$$

where c_{XY} are the Wilson coefficients. The reweighing from the old to the new theory is done via a computation of the of the ratio of differential rates using true-level information:

$$w_i = \frac{\Gamma^{old}}{\Gamma^{new}} \frac{d\Gamma^{new}/dPS}{d\Gamma^{old}/dPS} \qquad (5)$$

where the 'new' theory can contain extra scalar, vector or tensor couplings, as shown in Eq. 1.

An example of the sensitivity is illustrated in Fig. 6, where the coefficient of the angular function $\sin 2\theta_\ell \sin 2\theta_D \sin\chi$ is shown as a function of the imaginary part of the g_R coupling. Using HAMMER, the MC sample was reweighed to the NP case where $\mathrm{Re}(g_R) = 0$

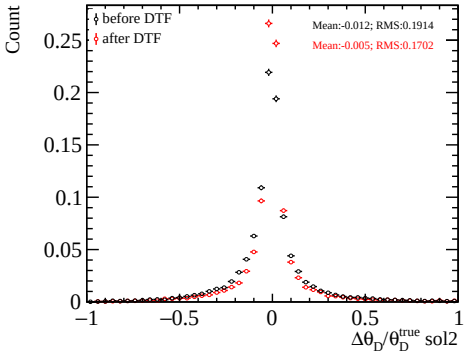

Figure 2: Resolutions of the helicity angle θ_D before (black) and after (red) the DTF.

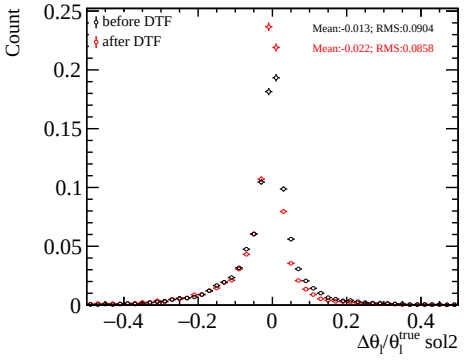

Figure 3: Resolutions of the helicity angle θ_{ell} before (black) and after (red) the DTF.

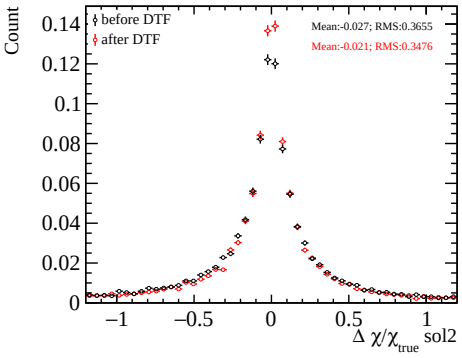

Figure 4: Resolutions of the helicity angle χ before (black) and after (red) the DTF.

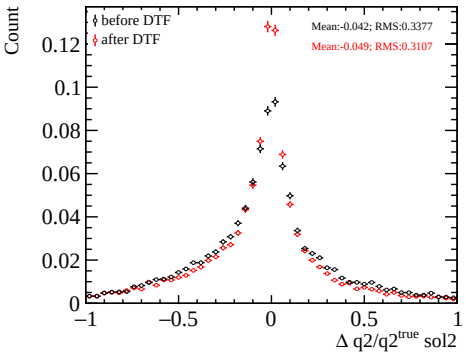

Figure 5: Resolutions of the q^2 before (black) and after (red) the DTF.

and $\mathrm{Im}(g_R)$ varying from $0.1i$ to $1i$. The coefficient of the angular function is calculated according to Eq. 3. The five different set of points in the plot show the coefficient of the angular term in different q^2 bins. This is done to make sure that the *CP*-asymmetry does not average out when integrating over q^2. The five q^2 bins, i.e. 0-1.5 GeV^2, 1.5-3 GeV^2, 3-5.5 GeV^2, 5.5-8 GeV^2 and 8-10 GeV^2 were chosen such that there is roughly the same amount of events in each of them.

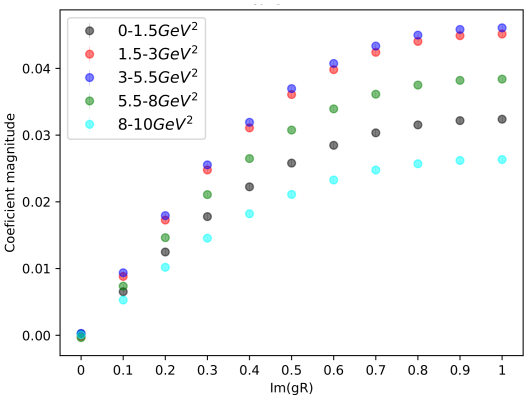

Figure 6: Sensitivity plot of *CP*-asymmetry due to presence of g_R NP coupling. The five sets of points show different q^2 bins. Y-axis shows the coefficient of the *CP*-violating angular term $\sin 2\theta_\ell \sin 2\theta_D \sin\chi$. X-axis shows the magnitude of the imaginary part of the g_R coupling.

The plot in Fig. 6 is based on a sample size of around three million simulated $\overline{\mathrm{B}}^0 \to \mathrm{D}^{*+}\mu^-\overline{\nu}_\mu$ events, which is roughly the yield of $\overline{\mathrm{B}}^0 \to \mathrm{D}^{*+}\mu^-\overline{\nu}_\mu$ in the currently available LHCb dataset collected in 2009-2018. The statistical error bars on the points are of the order of 0.1%, hence they are hardly visible in the plot. The first point in the plot, where $\mathrm{Im}(g_R) = 0$, is equivalent to the SM case where there is no *CP*-asymmetry, i.e. the coefficient of the angular term is zero. It can be seen that as the phase of the g_R coupling is increased, the *CP*-asymmetry becomes larger, up to about 4% in the case of the second and third q^2 bins.

Systematic uncertainties

Although this analysis is theoretically clean since there is no *CP*-violation in the SM, it is sensitive to effects that could fake *CP*-asymmetry. As seen in Sec. 10, all *CP*-violating terms are proportional to $\sin\chi$. Since the neutrino is reconstructed from the topology of the decay, i.e. PV and secondary vertices, nonzero angular terms proportional to $\sin\chi$ in fact reflect an asymmetry of the PV with respect to the observable $\mathrm{D}^0\mu^-\overline{\nu}_\mu$ plane. Experimental effects such as detector misalignments or non-uniformities in the tracking efficiency can introduce a bias in the *CP*-asymmetry. To address this, angular terms that should be zero even in the case of NP can be used to control these systematic effects at the 0.1% level. Another source of systematic uncertainties is the *CP*-violation in the backgrounds. In the case of semileptonic backgrounds, where there is no *CP*-violation in the SM, the magnitude of this systematic uncertainty can be estimated with HAMMER, in a similar manner as for the signal decay. The other possibility is *CP*-violation in double-charm backgrounds, such as $\overline{\mathrm{B}}^0 \to \mathrm{D}^+\mathrm{D}^-$. *CP*-violation in this type of decays is possible in the SM and their contribution can be either assigned an upper limit or be dealt with separately.

Conclusions

In order to constrain the current NP models that explain the discrepancies seen in $b \to cl\nu$ transitions, a measurement of the *CP*-asymmetries generated by NP in the angular distribution of the $\overline{\mathrm{B}}^0 \to \mathrm{D}^{*+}\mu^-\overline{\nu}_\mu$ decay is the scope of this analysis. In order to avoid being model dependant, instead of fitting, the measurement of the coefficients of the NP angular terms is realized by Fourier transform of the scattered data. An improvement of about 10% was achieved on the resolution on the kinematic parameters of the decay, three helicity angles and q^2. The sensitivity study showed a magnitude of *CP*-violation of about 4% with a statistical uncertainty of about 0.1%. Finally, since systematic effects that can introduce a bias in the *CP*-asymmetry need to be taken into account, a prospect on how we aim to control the various sources of systematics was given.

References

[1] LHCb Collaboration, Measurement of the ratio of the $\mathcal{B}(\mathrm{B}^0 \to \mathrm{D}^{*-}\tau^+\nu_\tau)$ and $\mathcal{B}(\mathrm{B}^0 \to \mathrm{D}^{*-}\mu^+\nu_\mu)$ branching fractions using three-prong τ-lepton decays, Phys. Rev. Lett. **120** (2018) 171802, arXiv:1708.08856.

[2] LHCb Collaboration, Measurement of the ratio of the $\mathcal{B}(\mathrm{B}_c^+ \to \mathrm{J}/\psi\tau^+\nu_\tau)/\mathcal{B}(\mathrm{B}_c^+ \to \mathrm{J}/\psi\,\mu^+\nu_\mu)$ branching fractions using three-prong τ-lepton decays, Phys. Rev. Lett. **120** (2018) 121801, arXiv:1711.05623.

[3] B. Bhattacharya, A. Datta, S. Kamali, and D. London, CP Violation in $\overline{\mathrm{B}}^0 \to \mathrm{D}^{*+}\mu^-\overline{\nu}_\mu$, JHEP **05** (2019) 191, arXiv:1903.02567.

[4] LHCb collaboration, The LHCb detector at the LHC, JINST **3** (2008) S08005.

[5] D. Hill, M. John, W. Ke, and A. Poluektov, Model-independent method for measuring the angular coefficients of $\mathrm{B}^0 \to \mathrm{D}^{*-}\tau^+\nu_\tau$ decays, JHEP **11** (2019) 133, arXiv:1908.04643.

[6] W. D. Hulsbergen, Decay chain fitting with a Kalman filter, Nucl. Instrum. Meth.155 **A552** (2005) 566, arXiv:physics/0503191.

[7] F. U. Bernlochner et al., Das ist der HAMMER: Consistent new physics interpretations of semileptonic decays, Eur. Phys. J. C **80** (2020) 883, arXiv:2002.00020.

Higgs pair production in $b\bar{b}\gamma\gamma$ final state with ATLAS Run 2 at LHC

Linghua GUO

Laboratoire de Physique des 2 Infinis Irène Joliot Curie

Abstract — The Higgs boson pair production is crucial for measuring the Higgs self-coupling and allows to search for new resonances. In this proceeding, the recent results of Higgs pair production in the two bottom quarks plus two photons final state [1] are introduced, using 139 fb^{-1} of proton-proton collision data at $\sqrt{s} = 13$ TeV recorded with the ATLAS detector with CERN Larger Hadron Collider. No clear signal is observed. Observed (expected) upper limit of non-resonant HH cross section is set to be 4.2 (5.7) times the SM prediction at 95% confidence level. The Higgs trilinear coupling modifier κ_λ is constrained to $[-1.5, 6.7]$ ($[-2.4, 7.7]$) for observed (expected) case at 95% confidence level. Observed (Expected) upper limits of new resonant spin-0 particle production cross section ($pp \to X \to HH$) under a narrow width approximation, are derived in function of m_X (251 GeV $< m_X <$ 1 TeV), ranging from 610 fb to 47 fb (360 fb to 43 fb) depending on mass hypothesis.

Introduction

The Higgs boson self-coupling provides information about the shape of the Higgs potential, and about stability of vacuum. A direct probe of the Higgs self-coupling is possible by studying Higgs boson pair production. In the Standard Model (SM) scenario, the Higgs potential is in form of a Mexican hat, and described by a scalar filed Φ, as shown in Eq. 1.

$$V = \mu^2\Phi^\dagger\Phi + \lambda(\Phi^\dagger\Phi)^2 \tag{1}$$

The special structure of the Higgs potential comes from $\mu^2 < 0$. It leads to the non-zero and degenerate vacuum bound states, lying on a ring in the horizontal plane, where each bound state is asymmetric under the rotation along the z-axis. The well-known Higgs mechanism successfully describes the mass generation for electroweak vector bosons and fermions, through a spontaneous symmetry breaking. The Higgs potential can be re-expressed in a new form in Eq. 2, by writing $\Phi = \frac{1}{\sqrt{2}}(v + h)$, where v is the vacuum expectation of the field, and h is the Higgs field.

$$V = \lambda v^2 h^2 + \lambda v h^3 + \frac{\lambda}{4}h^4 \tag{2}$$

$$v = \sqrt{\frac{-\mu^2}{\lambda}} \tag{3}$$

After the spontaneous symmetry breaking, the new Higgs potential predicts the Higgs mass and its self-couplings:

$$\begin{aligned} m_H &= \sqrt{2\lambda v^2} \\ \lambda_{3h} &= 3!\lambda v \\ \lambda_{4H} &= 3!\lambda \end{aligned} \tag{4}$$

The Higgs boson was discovered in 2012 by both the ATLAS and CMS experiments at LHC, with a mass measured around 125 GeV. If SM is powerful enough to be the ultimate theory of nature, the vacuum expectation value v is fixed by the Fermi constant G_F, i.e. $v = (\sqrt{2}G_F)^{-1/2} = 246$ GeV, thus giving a prediction of λ in SM of 0.13.

In experimental point of view, a direct measurement of λ is feasible by probing the Higgs trilinear coupling via pair production. At leading order (LO), the Higgs pair production is mainly produced via gluon-gluon fusion (ggF), with a minor contribution from vector boson fusion (VBF). As shown in Fig. 1 and Fig. 2, the ggF production involve a triangle and a box diagram. The Higgs self-coupling emerges in the triangle diagram, with $\kappa_\lambda = \lambda_{3h}/\lambda_{3h}^{SM}$ as self-coupling modifier defined to be the Higgs self-coupling normalized to the SM prediction. The SM predicts a destructive interference between the two ggF processes. The total cross section is predicted as 32.74 fb in the SM. Since no peak emerges in the di-Higgs invariant mass spectrum, such kind of process is denoted as non-resonant signal.

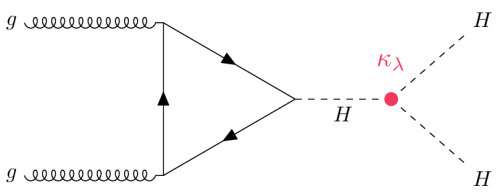

Figure 1: Triangle Feynman diagram of non-resonant HH production.

In some beyond-Standard-Model (BSM) scenarios, anomalous Higgs self-coupling would cause deviations with respect to the SM prediction, that may be within the sensitivity reach of the current pp collision data.

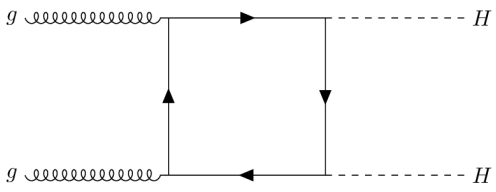

Figure 2: Box Feynman diagram of non-resonant HH production.

On the other hand, many BSM theories predict existence of new heavy scalar particle. Analysis has been performed by searching for new spin-0 particles with mass in range between 251 GeV and 1 TeV, under a narrow width approximation. In this case, the signal is denoted as resonant one. Fig. 3 shows the production of new scalar X via ggF, that afterwards decays into two SM Higgs bosons.

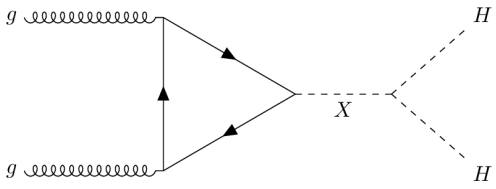

Figure 3: Feynman diagram of resonant HH production with a new scalar as intermediate particle.

In this proceeding, the Higgs pair production in two bottom quarks and two photons is introduced. Sec. 11 shows a brief introduction of the ATLAS detector, Sec. 11 introduces the signal and background samples, Sec. 11 summarizes the analysis selection and optimization. The results are presented in Sec. 11.

The ATLAS detector

The ATLAS detector at CERN consists of an inner detector (ID), surrounded by a 2 T magnetic field, a electromagnetic calorimeter (ECAL), a hadronic calorimeter (HCAL) and a muon spectrometer (MS), from the innermost to outermost radius. The detector covers almost the entire solid angle of the pp collisions.
The ID measures the transverse momentum of charged particles, with an insertable b-layer (IBL) designed for b-tagging. The calorimeter system covers the pseudorapidity range $|\eta| < 4.9$. The ECAL is used to measure energy of electrons and photons, the HCAL is provided by the steel/scintillator-tile calorimeter, in order to measure jet energy. The MS is incorporated with three large superconducting air-core toroidal magnets, and used to measure the transverse momentum of muons.
More details of the ATLAS detector are described in Ref. [2].

Data and simulated samples

For non-resonant analysis, signal samples with different κ_λ values are generated or emulated by a reweighting technique. The di-Higgs invariant mass distributions under different κ_λ hypotheses by gluon-gluon fusion production are shown in Fig. 4. For resonant, different m_X scenarios of the new scalar are studied, ranging from 251 GeV to 1 TeV.

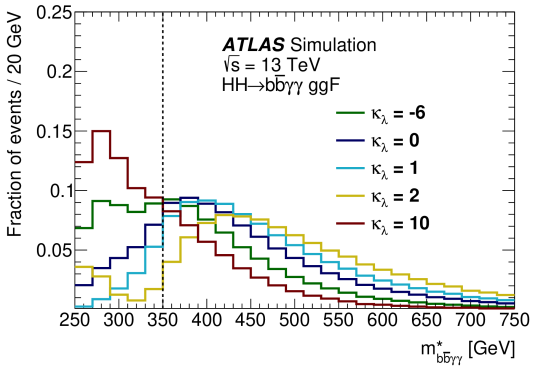

Figure 4: Invariant mass distributions of two photons and two b-jets under different κ_λ hypotheses, via gluon-gluon fusion.

The main background for both non-resonant and resonant analysis, is the diphoton plus additional jets process, denoted as $\gamma\gamma$ continuum. In this search, the single Higgs production also appears as a small fraction of background, including ggF, VBF, ttH, VH productions. For resonant analysis, the SM non-resonant production is considered as additional background as well.
The proton-proton collision data used in this search, is collected at a center of mass energy of 13 TeV, with an integrated luminosity of 139 fb^{-1}.

Event selection

The analysis firstly proceeds events with dedicated di-photon triggers.
Events with two photon candidates are selected, that photons are reconstructed in the ECAL, and a tight likelihood-based identification criteria is applied to distinguish photons with respect to other particles. Furthermore, in order to reject photons from hadrons decay, the selected photons are required to be isolated from other particles or activities in the detector. The two photons are afterwards used for constructing Higgs candidates, thus a cut is applied on diphoton invariant mass, i.e. $m_{\gamma\gamma} \in [105, 160]$ GeV.
b-jets are those coming from b quark hadronization, and a dedicated b-tagging algorithm is used to extract them from jets originated from light flavor quarks and gluons. In this analysis, events with two b-jets in the final state are selected.
Presence of leptons is forbidden by applying a lepton veto, specifically to reduce the top background.

Further selection is respectively optimized for non-resonant and resonant signals, using boosted decision trees (BDT). For non-resonant signal, according to Fig. 4, there is a clear dependency of the di-Higgs mass on κ_λ. Subsequently, two BDTs have been trained respectively in high mass and low mass regions splitting at 350 GeV. For high mass BDT, the SM ($\kappa_\lambda = 1$) is used for training, while $\kappa_\lambda = 10$ signal is used for low mass BDT. The high mass BDT score is shown in Fig. 5 for different κ_λ signals, backgrounds and observed data. Signal-enhanced regions are considered for the final results, and four categories are defined with optimized BDT cut.

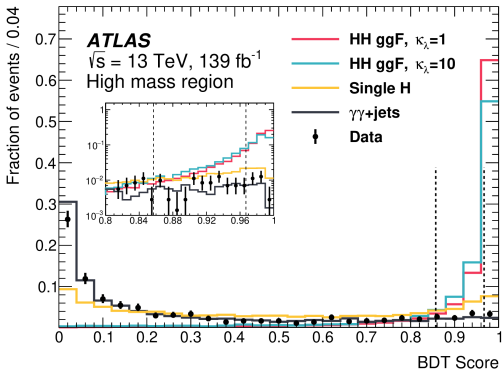

Figure 5: The BDT output in the high mass region.

For resonant case, BDTs are trained simultaneously for all the signals with different mass hypotheses, and respectively against $\gamma\gamma$ continuum and single Higgs background. A quadratic combination is performed for the two BDT outputs. The combined BDT score distribution is shown in Fig. 6 for mass hypothesis of 300 GeV. Eventually, a hypothesis-depend di-Higgs mass window cut is applied for each signal mass scenario.

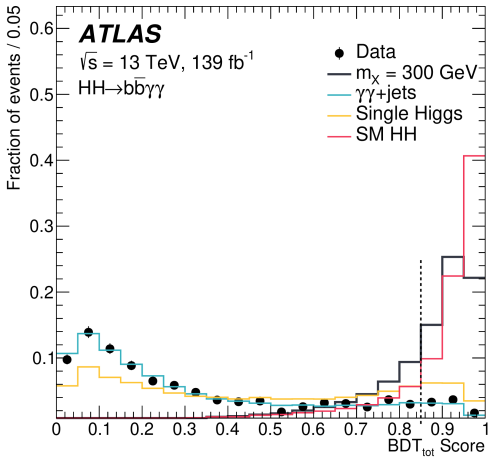

Figure 6: The BDT output for resonant signal $m_X = 300$ GeV.

Results

The statistical results are derived by performing a maximum likelihood fit with observed data, using the diphoton invariant mass as discriminant variable. Double sided crystal ball function is chosen to describe the $m_{\gamma\gamma}$ distribution of non-resonant and resonant signals, as well as single Higgs background. The $\gamma\gamma$ continuum background is modelled by an exponential function. For non-resonant case, a simultaneous fit is performed with all the four categories. For resonant analysis, each mass scenario is treated separately. The background-only fit results are shown in Fig. 7 for non-resonant analysis, and in Fig. 8 for resonant signal $m_X = 300$ GeV. No clear discrepancy has been found under the background-only hypothesis. Upper limit of the signal strength is derived at 95% confidence level (CL), using the CLs method, where the signal strength is defined as the production rate normalized to the SM prediction. Assuming the SM self-coupling, a 95% CL observed (expected) limit of 4.2 (5.7) on signal strength has been determined. In addition, the upper limits are derived in function of κ_λ, that further deduce an observed (expected) κ_λ limit interval as [-1.5, 6.7] ([-2.4, 7.7]) as shown in Fig. 9. The upper limits of cross section for resonant signals are presented in Fig. 10.

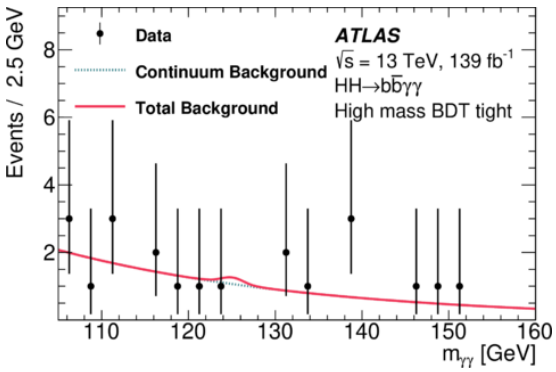

Figure 7: Background-only fit in the non-resonant high mass BDT tight category.

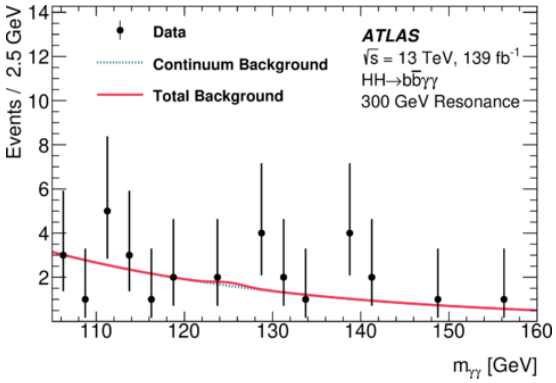

Figure 8: Background-only fit of resonant analysis for $m_X = 300$ GeV.

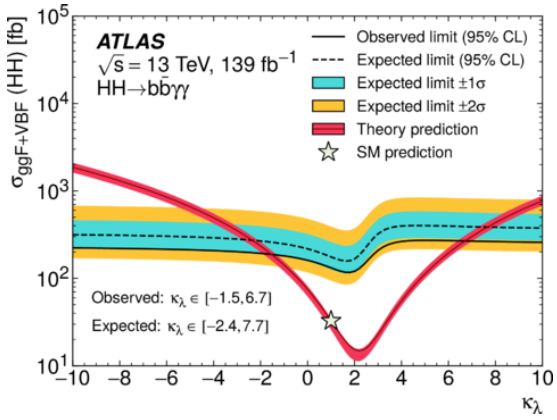

Figure 9: The cross section upper limits in function of κ_λ.

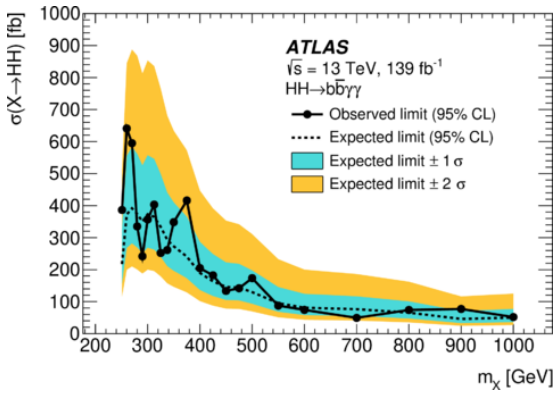

Figure 10: The cross section upper limits in function of m_X.

Conclusions

Searches for non-resonant and resonant Higgs boson pair production are performed in the $b\bar{b}\gamma\gamma$ final state using 139 fb^{-1} of 13 TeV pp collision data collected with the ATLAS detector at the LHC. No significant excess above the Standard Model background expectation is observed.

A 95% CL upper limit of 130 fb is set on the non-resonant production cross section, where the expected limit is 180 fb. The observed (expected) limit corresponds to 4.2 (5.7) times the cross section predicted by the Standard Model. Constraints on the Higgs boson self-coupling are also derived and limits of $-1.5 < \kappa_\lambda < 6.7$ are obtained, where $-2.4 < \kappa_\lambda < 7.7$ is expected. For resonant production of a scalar particle $X \to HH \to b\bar{b}\gamma\gamma$, upper limits on the production cross section are obtained for the narrow-width hypothesis as a function of m_X. The observed (expected) upper limits are in the range 610-47 fb (360-43 fb) for $251 \leq m_X \leq 1000$ GeV. Compared to the previous ATLAS result based on 36 fb^{-1} of 13 TeV pp collisions [3], a general factor of 5 improvement has been seen, which nearly benefits from the increase of luminosity, the improvement on flavour tagging and the selection optimization.

Outlook

Combinations have been performed with different HH decay channels, including $b\bar{b}\gamma\gamma$, $b\bar{b}\tau\tau$ and $b\bar{b}b\bar{b}$ with the current full Run 2 data [4].

A future upgraded accelerator called high luminosity LHC (HL-LHC) has been proposed, with an integrated luminosity of 3000 fb^{-1}, and an increase of the center of mass energy from 13 TeV to 14 TeV. The projection from the current 139 fb^{-1} results to HL-LHC has been made and recently published [5].

References

[1] G. Aad *et al.* [ATLAS], arXiv:2112.11876 [hep-ex].

[2] G. Aad *et al.* [ATLAS], JINST **3** (2008), S08003 doi:10.1088/1748-0221/3/08/S08003

[3] M. Aaboud *et al.* [ATLAS], JHEP **11** (2018), 040 doi:10.1007/JHEP11(2018)040 arXiv:1807.04873 [hep-ex].

[4] [ATLAS Collaboration], ATLAS-CONF-2021-052.

[5] [ATLAS Collaboration], ATL-PHYS-PUB-2022-001.

Search for New Physics with unsupervised Machine Learning

Louis VASLIN

Laboratoire de Physique de Clermont / Université Clermont-Auvergne

Abstract — The Standard Model of particle physics is the model that best describes our current knowledge of elementary particles and their interactions. However, it is not complete enough to explain everything. For this reason, experiments like ATLAS tries to find the constituents of New Physics beyond the Standard Model. In order to analyse the data produced by these experiments, Machine Learning is a very popular tool. We will present a new way to search for New Physics combining an anomaly detection algorithm based on unsupervised Machine Learning and a model independent bump hunting tool. A concrete example of application will be given using the data from the LHC Olympics 2020 challenge.

Introduction

The Standard Model (SM) is the most successful model in particle physics. It describes all the known particles and their interactions. The list of elementary particles and interactions is presented on figure 1. So far all the experimental results obtained in the past decades agree with the model predictions up to a high level of precision. But is this theory really complete ?

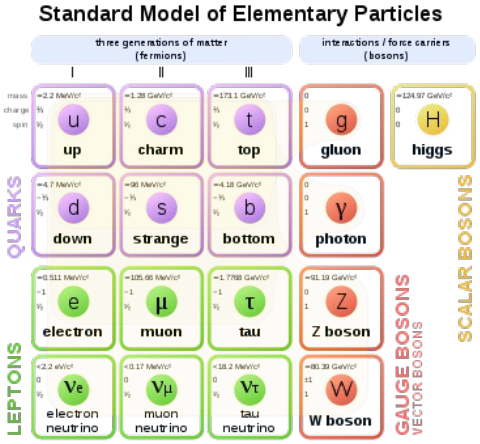

Figure 1: Figure representing all the generation of matter particles (fermions), the interaction mediators (gauge bosons) and the Higgs boson.

In fact, a fair number of observations reveal the limitation of the SM. For example, the gravitational force, as well as oysters, are not described in this theory. The same goes for the Dark Matter for which we have many indirect proof of existence. All these "missing pieces" in the SM tell us we need to find a more general theory Beyond the Standard Model (BSM).

In order to test the limit of the SM and to find the proof of such BSM theory, we need some experiments. The ATLAS experiment [1] is one of them (see schematics on figure 2). It is one of the 4 main experiments based along the Large Hadron Collider at CERN [2]. At the center of the detector, two beams of high energy particles (protons, heavy ions, ...) enter in a collision. From these collisions heavy particles are produced, and their decay products can be detected. ATLAS collects a huge amount of collision data and New Physics could be hidden somewhere in this data.

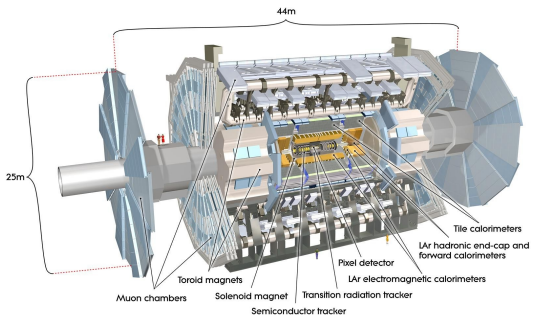

Figure 2: Schematics of The ATLAS detector.

This paper will present new techniques to search for New Physic in such a dataset. Then, these techniques will be included in a model independent analysis strategy. Finally, this strategy will be applied on a benchmark dataset provided by the LHC Olympics 2020 challenge [3].

Machine Learning and anomaly detection

A very popular tool in High Energy Physics (HEP) for the analysis of massive and complex datasets is Ma-

chine Learning (ML). This is an ensemble of algorithms that can be trained to perform a specific task. For the search of New Physics in collision data, there are 2 main ways of using ML.

The first one is to use a mix of background (SM) and signal (BSM) events in order to train a model to differentiate the two classes. This is called supervised ML. After training this model will tell us to which class unknown events belong. Such techniques imply that we know in advance what we are looking for. So we need both accurate background simulation and a signal hypothesis to train the model. But in the case of BSM searches, we have no way to know in advance if the signal hypothesis is a good one or not. There have been many attempts using supervised ML techniques, but no new particles have been found so far.

The second strategy is to train a model to learn the general behaviour of an unknown dataset. This is called unsupervised ML. After training, the model can tell us how anomalous new events are with respect to the norm it has learnt. In this case, we don't need to know exactly what we are looking for, making such a technique model independent. Also, this class of model can identify rarer events as being the more anomalous. This is what we call an anomaly detection algorithm. In our case, New Physics event can be seen as an anomaly with respect to the SM. This is this kind of technique that we will use in our strategy.

Analysis strategy

The strategy we developed is the following :

- Train an unsupervised ML model for anomaly detection
- Apply the trained model on unknown events in order to assess their anomaly score
- Select the most anomalous events (where the New Physic could be)
- Compare the distribution of selected events with the distribution before selection and look for a deviation

This strategy is based on the fact that New Physic event are very rare. Thus, they can't be identified as being the norm.

The first ML model that comes into mind for anomaly detection is the Auto-Encoder algorithm (AE). This is a Neural Network architecture composed of an input layer, a hidden layer of smaller size, and an output layer with the same size as the input. The objective of the AE is to learn how to reconstruct the input data by compressing its information into the hidden layer (latent space). In other words, the algorithm must learn the best latent representation in order to achieve the smallest reconstruction error. To train a Neural Network, we need a loss function that must be minimized by updating the weights of the model. This loss function gives the objective of the algorithm. In the case of the AE, the reconstruction error, which can be defined as the Euclidean distance between output and input, can be used as loss function. In order to apply this model to anomaly detection we also need an anomaly score that tells how anomalous an event is. Since the rarer events (anomaly) are not as well reconstructed as the others, the reconstruction error can also serve as anomaly score.

Based on the AE algorithm, we created a ML model called the GAN-AE (see schematics figure 3). It is composed of two Neural Networks : an AE, and a discriminant. The AE will try to reconstruct the original event as accurately as possible while the discriminant will try to distinguish the original event from the reconstructed ones. Thus, the two networks are trained with opposite objectives (adversarial training) so they can learn from each other. In this case, the loss function of the AE must include information from the discriminant in addition to the reconstruction error. The more the discriminant fails at fulfilling its objective, the more the AE succeeds. However, for the detection of anomalies, only the reconstruction error is used. The discriminant part is used only for the training as an additional constraint on the AE.

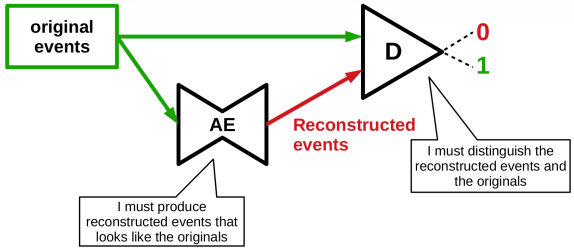

Figure 3: Schematics of GAN-AE architecture.

The GAN-AE algorithm can give us an anomaly score on which we apply a selection. But in order to find a deviation, we need the BumpHunter algorithm [4]. This algorithm compares a data histogram with a reference background. It will scan the distributions with a window of varying width in order to identify the interval with the most significant deviation of the data with respect to the background. The figure 4 illustrates this procedure. In the search for New Physics, we usually expect to find heavy new particles. Thus, the distribution that we will use to look for a deviation is the mass spectrum of the particle produced at the center of the detector.

For each tested interval, BumpHunter computes a local p-value that tells how far the data deviates from the reference. The interval with the smallest local p-value is identified as the one that deviates the most. Now, in order to tell the probability for this deviation to be a statistical fluctuation we must compute a global significance. For this purpose, the algorithm generates pseudo-data distributions by sampling from the reference background. Each of these distributions are scanned the same way in order to obtain a local p-value distribution corresponding to a background only distribution. The global p-value is then obtained by

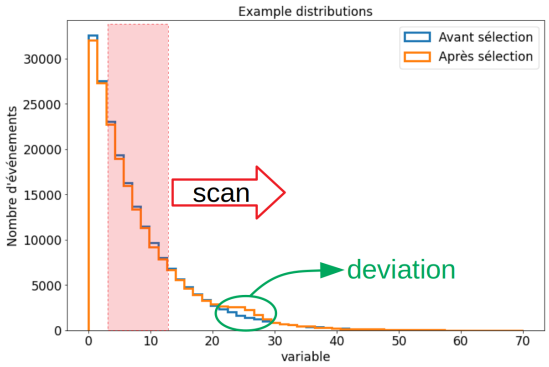

Figure 4: Figure illustrating the scan procedure of the BumpHunter algorithm.

comparing this background-only hypothesis with the data. We developed a public python version of this algorithm called pyBumpHunter. It includes several extensions of the algorithm and has been integrated into Scikit-HEP, an ensemble of tools dedicated to High Energy Physics analysis. pyBumpHunter is available on GitHub and PyPI [5].

However, if we want to use the BumpHunter algorithm in our analysis strategy, we need a reference background distribution which is valid after the selection of the most anomalous event. In our case, we know that the larger majority of events are SM background. Thus, the shape of the mass distribution before applying any selection could be assimilated as the shape of the background to use as reference. But is this background shape still a valid reference after applying a selection ? In fact, as illustrated on figure 5, applying a selection can change the shape of the mass distribution. This bias is due to the fact that the mass distribution is descending exponentially. Thus, low mass events are very numerous, so well reconstructed. On the other hand, high mass events are a minority, so they are not as well reconstructed. This phenomenon is called mass sculpting.

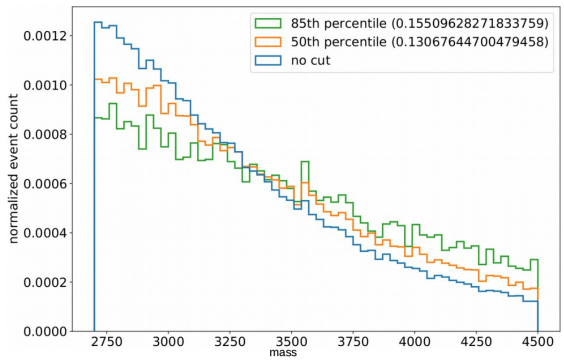

Figure 5: Normalized histograms of mass showing the mass sculpting. The blue histogram corresponds to the mass distribution before selection, and the others after different selections.

In order to correct this effect, we must ensure that applying a selection on the anomaly score will not affect the shape of the background. A possibility is to define

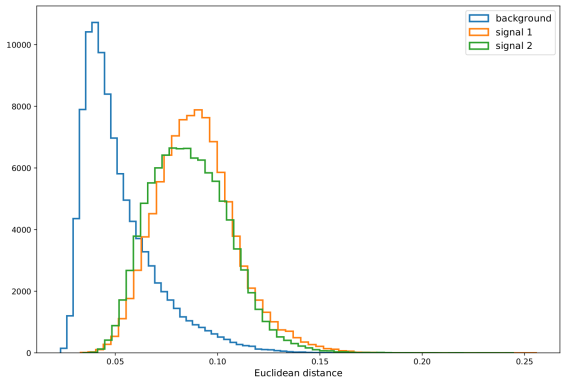

Figure 6: Histograms of Euclidean distance for the RnD background (blue) and the two RnD signals (orange and green).

an additional term in the loss function that enforces the decorrelation between the mass and the anomaly score. Another possibility is to reweight the events based on their mass. Lower mass events will have smaller weights while higher mass events will have bigger weights. Thus the model will see the mass distribution as being flat and will not be biased by its asymmetry. Combining these two techniques, we can greatly reduce the mass sculpting, allowing us to use the shape of the mass distribution prior to any selection as the reference background. This way, we can apply the BumpHunter algorithm using a fully data-driven background modeling.

Results

We have all the tools to apply our analysis strategy, now we need some data to test it. For this purpose, we used the data provided for the LHC Olympics challenge. This is an international challenge proposed to the High Energy Physics community. They provided two type of dataset :

- RnD dataset : Simulated background (QCD multijet) and signal (large radius dijet) events with labels
- Black-Box dataset : Unknown simulated events without labels (dijet)

The objective of the challenge was to assess if there is any new signal in the black boxes. Of course, since the events in the black-boxes are not the same as the ones in the RnD dataset, a supervised approach targeting the RnD signal will most likely fail. Thus, we had to develop an unsupervised anomaly detection technique to meet the objective.

A first step for this challenge was to use the RnD dataset in order to test and validate the GAN-AE model. For this purpose, the algorithm was trained using only the provided background, and applied both on background and signal. The figure 6 shows the distance distributions obtained for the background and two signals of the RnD dataset. We can see that these distributions are quite different.

In order to quantify the discriminating power of such distributions, ones can draw a ROC curve. This curve is built by looking at the percentage of rejected background and accepted signal for different selection thresholds. The ROC curves corresponding to the two signals are shown on figure 7. The goodness of a ROC curve can be evaluated by looking at the Area Under the Curve (AUC). The closer to 1, the more background we can reject while keeping a lot of signal. In our case, the AUC is around 0.92 for the two signals, which is a very good performance for an unsupervised model.

The last thing to check is the mass sculpting mitigation. For this purpose, one can look at the distribution of mass before and after applying a selection on the Euclidean distance. These distributions are shown on figure 8. We can see that the shape of the distributions are very similar. The mass sculpting has been reduced enough to allow the use of the pre-selection distribution shape as background model to use with BumpHunter.

Now that the GAN-AE model is working as expected, we can apply the full analysis strategy to the first black box dataset provided for the challenge. For this purpose, the GAN-AE was trained directly on the black box event. Then, a selection was applied on the distance distribution at the 99th percentile. And finally, the BumpHunter algorithm was used to look for a deviation using the mass distribution before selection as reference background, and the same distribution after selection as data. The result is shown on figure 9. We can see that BumpHunter has found a quite significant deviation localized around 3.8 TeV. The global significance of such deviation is over the 5σ threshold, and is compatible with a heavy oyster model. Outside of the bump area, the agreement between the data and the reference background seems to be good despite the fluctuations. This shows that our data-driven modeling is working as expected.

To conclude on this work, we developed a new analysis strategy for New Physic searches in particle physics. This strategy combined a new anomaly detection algorithm based on unsupervised ML (GAN-AE) and a model agnostic bump hunting tool (pyBumpHunter). It has been tested using the LHC Olympics 2020 data as a benchmark. The results of this test show a good potential at enhancing a new signal without any prior hypothesis, as well as the possibility to extract a background model directly from data.

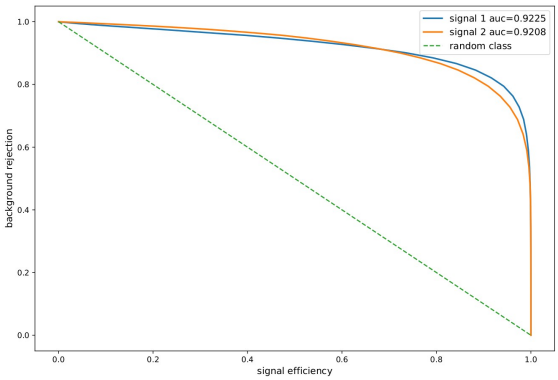

Figure 7: ROC curves of the two RnD signals.

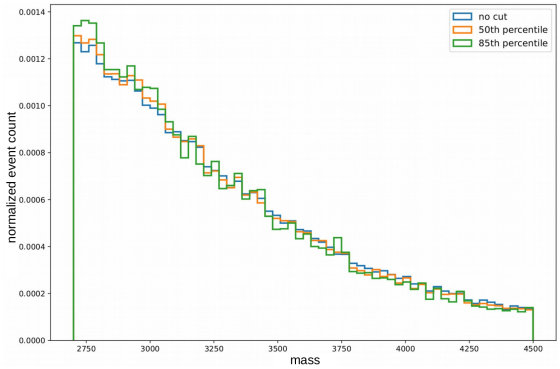

Figure 8: Normalized histograms of the RnD background mass distributions before selection (in blue) and after different selections (orange and green).

References

[1] ATLAS collaboration, *The ATLAS Experiment at the CERN Large Hadron Collider*, JINST 3 (2008) S08003

[2] L.R. Evans and P. Bryant, *LHC Machine*, JINST 3 (2008) S08001.

[3] G. Kasieczka and B. Nachman and D. Shih et al., *The LHC Olympics 2020 a community challenge for anomaly detection in high energy physics*, 2021 Rep. Prog. Phys. 84 124201

[4] G. Choudalakis, *On hypothesis testing, trials factor, hypertests and the BUMPHUNTER*, May 29, 2018, [arXiv:1101.0390]

[5] `https://github.com/scikit-hep/pyBumpHunter`, `https://pypi.org/project/pyBumpHunter/`

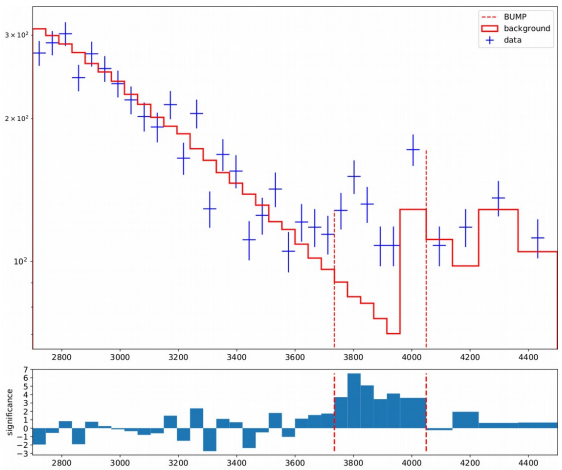

Figure 9: Result of BumpHunter on the first black box dataset. The top plot show the dijet invariant mass histograms of data and reference background, and the bottom plot show the local significance per bins.

Part III

Cosmology

session chaired by Florian RUPPIN

Black hole moving through a scalar field dark matter soliton

Alexis BOUDON

Université Paris-Saclay, CNRS, CEA, Institut de physique théorique, Gif-sur-Yvette, France

Abstract — The nature of dark matter is one of the most important problems in cosmology. This component has so far been detected only by its gravitational effects. The usual scenario is that of weakly interacting massive particles. However, such particles have still not been detected and the ΛCDM seems to encounter some difficulties in reporting data at galactic scales. This has revived interest in alternative scenarios, among which scalar field dark matter, and a way to prove them can be to calculate the dynamical friction. In this work, we focus on the study of the dynamical friction associated to a moving black hole inside a scalar field dark matter soliton, by considering or not self-interactions between the dark matter particles. We found that a free scalar field gives the same result as the classical case calculated by Chandrasekhar. While we do not obtain result for the self-interacting case, we characterize the induced dark matter wake and the associated velocity field.

Introduction

One of the pillars of the standard model of cosmology (ΛCDM) is dark matter (DM). Additional to baryonic matter and dark energy (Λ), it is considered to be a cold and perfect fluid. However its nature remains unknown, which leads to many hypotheses with masses ranging from 10^{-22} eV to several solar masses, going from fuzzy DM to primordial black holes [1].

As of today, many tensions remain in the ΛCDM model, especially at astrophysical scales, e.g. the core-cusp problem [2, 3, 4], the missing satellite problem and the too-big-to-fail [2, 5]. Although including baryonic feedback seems to alleviate those tensions, it is not yet certain that this fully resolves them. Moreover, the detection experiments on weakly interacting massive particles (WIMPs) do not seem to provide any conclusive results. Although WIMPs are not yet to be ruled out [6], it seems interesting today, more than ever, to study alternative models.

One of these models is the scalar field DM (SFDM), where DM is considered to be composed of spin-0 particles ranging from 10^{-22} eV to ~ 1 eV [7, 8]. In this model, since DM respects a Bose-Einstein distribution, a Bose-Einstein condensate, or the so-called soliton, appears at the center of halos. A way to verify and constrain the model is to calculate the dynamical friction, the loss of momentum of moving objects through gravitational interactions. This might help constraint the SFDM mass, e.g. Magellanic clouds induced wake [9] and gravitational wave emission [10, 11], and even help solve some cosmological tensions, e.g. the Fornax globular clusters timing problem [12].

An outline of the paper is as follows. We will firstly present the model and the associated equations of interest. Then we will focus on the free case, then on the self-interaction case. Finally, we will conclude and summarise on the results and prospects.

Scalar field dark matter

We study SFDM following the action

$$S_\phi = \int d^4x\sqrt{-g}\left[-\frac{1}{2}g^{\mu\nu}\partial_\mu\phi\partial_\nu\phi - V(\phi)\right], \qquad (1)$$

with a potential $V(\phi) = \frac{m^2}{2}\phi^2 + V_{\rm I}(\phi)$ with the self-interacting term $V_{\rm I}(\phi) = \frac{\lambda_4}{4}\phi^4$. Considering a non-relativistic regime, we can rewrite the scalar field ϕ as a complex field ψ, $\phi = \frac{1}{\sqrt{2m}}\left(e^{-imt}\psi + e^{imt}\psi^\star\right)$ where ψ obeys the Schrödinger equation,

$$i\,\dot{\psi} = -\frac{\nabla^2\psi}{2m} + m(\Phi_{\rm N} + \Phi_{\rm I})\psi, \qquad (2)$$

where $\Phi_{\rm N}$ and $\Phi_{\rm I}$ are respectively the Newtonian gravitational potential and the self-interaction potential, the self-interaction being $\Phi_{\rm I} = \frac{m|\psi|^2}{\rho_a}$ with $\rho_a = \frac{4m^4}{3\lambda_4}$. Using the Madelung transformation, $\psi = \sqrt{\frac{\rho}{m}}e^{is}$ with the amplitude ρ and the phase s. In this picture, the Schrödinger equation (2) give

$$\dot{\rho} + \nabla\cdot\left(\rho\frac{\nabla s}{m}\right) = 0\,, \qquad (3)$$

$$\frac{\dot{s}}{m} + \frac{(\nabla s)^2}{2m^2} = -(\Phi_{\rm N} + \Phi_{\rm I})\,, \qquad (4)$$

where we separated the real and imaginary parts. What is interesting to note is that we can neglect the quantum pressure $\Phi_{\rm Q} = -\frac{\nabla^2\sqrt{\rho}}{2m^2\sqrt{\rho}}$ since in the large-mass regime we have a small De Broglie wavelength $\lambda_{\rm dB} = 2\pi/mv$,

and so the wave effects, like interference, are negligible.

Thus, from Eq.(4) and considering the curl-free velocity field $\vec{v} = \frac{\vec{\nabla} s}{m}$, the equation of hydrostatic equilibrium is $\nabla(\Phi_{\rm N} + \Phi_{\rm I}) = 0$ which we can integrate as $\Phi_{\rm N} + \Phi_{\rm I} = \alpha$ with $\alpha = \Phi_{\rm N}(R_{\rm sol})$. Here we used the soliton radius $R_{\rm sol}$ with a spherical symmetric soliton. At this radius, the density becomes null and so $\Phi_{\rm I} = 0$, which permit us to determine the value of α. The contributions to the Newtonian gravitational potential are the central BH and the soliton self-gravity, $\Phi_{\rm N} = \Phi_{\rm BH} + \Phi_{\rm sg}$ with $\Phi_{\rm BH} = -\frac{r_{\rm s}}{2r}$, $\nabla^2 \Phi_{\rm sg} = 4\pi \mathcal{G} \rho$ and $r_{\rm s}$ begin the Schwarzschild radius.

As we neglect the gravitational backreaction of the soliton, we consider the Schwarzschild metric associated to a BH, $ds^2 = -f(r)\, dt^2 + h(r)\, (dr^2 + r^2\, d\vec{\Omega}^2)$. The isotropic metric functions read as $f(r) = \left(\frac{1 - r_s/(4r)}{1 + r_s/(4r)}\right)^2$ and $h(r) = (1 + r_s/(4r))^4$ while $\frac{r_s}{4} < r \ll r_{\rm sg}$, with the transition radius $r_{\rm sg} = r_s \frac{\rho_a}{\rho_0}$, and ρ_0 the soliton density. In this coordinates, the BH horizon is located at radius $r = r_{\rm s}/4$. At large radii $r \gg r_{\rm sg}$, in the weak-gravity regime, we have $f = 1 + 2\Phi_{\rm N}$ and $h = 1 - 2\Phi_{\rm N}$ with $\Phi_{\rm N} = \alpha - \frac{\rho_0}{\rho_{\rm a}} - \frac{r_{\rm s}}{2r}$.

For the following calculation, we consider as boundary conditions at large radii, a density equal to the soliton density ρ_0 and a relative velocity between the BH and the DM particules v_0 on z-axis.

Free case

Here, the self-interacting term is null and so, $V(\phi) = \frac{m^2}{2}\phi^2$. Considering a system in $(r,\, \theta)$, due to an axisymmetry, and searching for a stationary solution for the phase in the form $s = -Et + \hat{s}$, where $\hat{s}$ is time-independent, $E = \frac{k^2}{2m}$ and $k = m v_0$, and substituting in the Euler equation (4)

$$\frac{(\vec{\nabla}\hat{s})^2}{2m} - \frac{h}{f}\left(E + \frac{1-f}{2}m\right) = 0\,, \tag{5}$$

which looks like an Hamilton-Jacobi equation $\frac{d\hat{s}}{dt} + H(\vec{p}, \vec{r}) = 0$. Thus, we have the Hamilton equations $\dot{\vec{r}} = \frac{\partial H}{\partial \vec{p}} = \frac{\vec{p}}{m}$ and $\dot{\vec{p}} = -\frac{\partial H}{\partial \vec{r}} = -\frac{\partial V(\vec{r})}{\partial \vec{r}}$ which permit us to find, from the total derivative of $\hat{s}$,

$$s = -Et + \int_{t_0}^{t} dt \left(\frac{\vec{p}^2}{2m} - V(\vec{r})\right)\,. \tag{6}$$

Considering a central force potential, the momentum components are

$$p_\theta = L\,,\ |p_r| = m\sqrt{\frac{h}{f}}\sqrt{1 - f + v_0^2\left(1 - \frac{b^2}{r^2}\frac{f}{h}\right)}\,, \tag{7}$$

where $L = kb$ is a constant and $b = r\sin(\theta)$ is the impact parameter. Thus, defining $\hat{s}_0 = k z_0$

$$s = \hat{s}_0 + (\theta - \theta_0)L + \int_{t_0}^{t} dt \dot{r} p_{\rm r}\,. \tag{8}$$

Every particles pass through a minimum radius $r_{\rm min}$ specific to each trajectory. And so, we can define the angle at minimum radius $\theta_{\rm min} = \pi + L\int_{r_{min}}^{\infty} \frac{dr}{r^2 |p_r|}$ and the deflection angle at infinity $\theta_{\rm def} = \pi + 2L\int_{r_{min}}^{\infty} \frac{dr}{r^2|p_r|}$.

Considering mass conservation, the ratio between the density at final time ρ and the soliton density ρ_0 is given by

$$\frac{\rho}{\rho_0} = \frac{r_0^2 sin(\theta_0)}{r^2 sin(\theta)} J^{-1}\,, \tag{9}$$

with the Jacobian $J = \left|\frac{\partial r}{\partial r_0}\frac{\partial \theta}{\partial \theta_0} - \frac{\partial r}{\partial \theta_0}\frac{\partial \theta}{\partial r_0}\right|$. We can define $\widetilde{J} = \frac{J}{r_0^2 sin(\theta_0)}$ for convenience since its behavior is more intuitive than the one of J. This one can be rewritten as $\widetilde{J} = |p_{\rm r}|\left(\frac{\theta_{\rm def} - \theta}{bL} + \frac{1}{b|p_{\rm r_0}|}\frac{\partial \theta_{\rm def}}{\partial b} + \frac{L^2}{b}\int_r^\infty \frac{dr}{r^4 |p_{\rm r}|^3}\right)$. At infinity, for the trajectories that do not fall into the BH we have $|p_r| \to |p_{r_0}|$ and $\theta \to \theta_{\rm def}$. The Jacobian becomes $\widetilde{J}_\infty = \frac{1}{b}\frac{\partial \theta_{def}}{\partial b}$ and Eq.(9) reads

$$\left.\frac{\rho}{\rho_0}\right|_\infty = \left(\frac{r^2 \sin(\theta_{def})}{b}\frac{\partial \theta_{def}}{\partial b}\right)^{-1}\,. \tag{10}$$

The dynamical friction is defined as

$$\vec{F} = -\oint dS_{\rm j} T_{\rm jz} \vec{e_{\rm z}} = -\oint dx dy T_{\rm zz} \vec{e_{\rm z}}\,, \tag{11}$$

with $d\vec{S} = dxdy\vec{e}_{\rm z}$. However, the integration following dx and dy is not very convenient since the trajectories are deviated. Integrating over the impact parameter b seems more convenient since this one follows the trajectories. At $z \to -\infty$, we make the change of variable $(dx, dy) \to (db, d\varphi)$ which gives $dx \cdot dy = b db d\varphi$. At infinity after the BH, we can obtain a definition of b from $\theta_{\rm def}$ thus we make the change of variable $(dx, dy) \to (d\theta_{\rm def}, d\varphi)$ which gives $dx \cdot dy = z_\infty^2 \frac{\sin(\theta_{\rm def})}{\cos^3(\theta_{\rm def})} d\theta_{\rm def} d\varphi$ where $z_\infty = r\cos(\theta_{\rm def})$. Concerning the energy-momentum tensor, we obtain $T_{\rm zz} \approx \rho v_{\rm z}^2$ using the hydrodynamics approximation $v^4 \ll v_{\rm z}^2$. In Kepler approximation, the friction expression is thus

$$\begin{aligned} |F| &= -2\pi\rho_0 v_0^2 \left(\int_{b^-}^{b^+} b\cos(\theta_{\rm def}) db - \int_0^{b^+} b db\right)\,, \\ &= 2\pi\rho_0 v_0^2 \left[C^2 \ln\left(\frac{(b^+)^2 + C^2}{(b^-)^2 + C^2}\right) + \frac{(b^-)^2}{2}\right]\,, \end{aligned} \tag{12}$$

where $C = \frac{GM}{v_0^2}$ is a constant, b^- is the minimum impact parameter for a particle of mass m to not be absorbed by the BH and b^+ is a natural infrared cutoff. This result is the same as that obtained by Chandrasekhar in 1943 [13], at the exception of the second term $\propto \frac{(b^-)^2}{2}$ which corresponds to the force exerted on the BH by the particles absorbed by the latter.

Self-interacting case

Now we will consider self-interaction between particles with $\lambda_4 > 0$ to ensure an additional pressure. The

Klein-Gordon equation given by the action (1) is

$$\frac{\partial^2\phi}{\partial t^2} - \sqrt{\frac{f}{h^3}}\nabla\cdot(\sqrt{fh}\nabla\phi) + fm^2\phi + f\lambda_4\phi^3 = 0\,. \quad (13)$$

This equation is a cubic nonlinear one, with the form of the Duffing equation [14], with a solution

$$\phi = \phi_0(r,\theta)\,\mathrm{cn}[\omega(r,\theta)t - \mathbf{K}(r,\theta)\beta(r,\theta), k(r,\theta)]\,, \quad (14)$$

where $\mathbf{K}(r,\theta) \equiv \mathbf{K}[k(r,\theta)]$, $\mathrm{cn}(u,k)$ is the Jacobi elliptic function [15, 16] of argument u, modulus k, and period $4\mathbf{K}$, with the complete elliptic integral of the first kind $\mathbf{K}(k) = \int_0^{\pi/2} d\theta/\sqrt{1-k^2\sin^2\theta}$ for $0 \leq k < 1$ [15, 16]. This solution is in fact the leading-order approximation in the case $m \to \infty$, where we can consider that ψ_0 and k are much smaller than m. Here, we can recover the non-relativistic regime where $\mathrm{cn}(u,0) = \cos(u)$ if we consider the limit $k \to 0$.

As we need to ensure that spatial gradients stay constant with time, the field needs to oscillate in phase at each radius. Thus, $\omega(r,\theta)$ can be expressed as a function of $k(r,\theta)$, $\omega(r,\theta) = \frac{2\mathbf{K}(r,\theta)}{\pi}\omega_0$, to obtain a synchronization of the oscillators. The lowest frequency ω_0 will be determined using boundary conditions.

Considering only the leading order in the large-mass limit, the spatial derivatives are $\frac{\partial^2\phi}{\partial r^2} \approx \phi_0\left(\mathbf{K}\frac{\partial\beta}{\partial r}\right)^2\mathrm{cn}''$ and $\frac{\partial^2\phi}{\partial\theta^2} \approx \phi_0\left(\mathbf{K}\frac{\partial\beta}{\partial\theta}\right)^2\mathrm{cn}''$, where we noted $\mathrm{cn}'' = \frac{\partial^2\mathrm{cn}}{\partial u^2}$. Substituting into the Klein-Gordon equation (13) and using the property $\mathrm{cn}'' = (2k^2-1)\mathrm{cn} - 2k^2\mathrm{cn}^3$, we obtain the following conditions by separating the terms in cn and the ones in cn^3

$$(\nabla\beta)^2 = \frac{h}{f}\left(\frac{2\omega_0}{\pi}\right)^2 - \frac{hm^2}{(1-2k^2)\mathbf{K}^2}\,, \quad (15)$$

$$\frac{\lambda_4\phi_0^2}{m^2} = \frac{2k^2}{1-2k^2}\,, \quad (16)$$

To ensure that the steady state condition is respected, we need to take the average of the conservation equation over the oscillations of the solution (14), and so we have $\langle\nabla_\mu T_0^\mu\rangle = 0$. This gives the equation $\nabla\cdot(\rho_{\mathrm{eff}}\nabla\beta) = 0$ where we defined the effective density $\rho_{\mathrm{eff}} = \sqrt{fh}\phi_0^2\omega\mathbf{K}\langle\mathrm{cn}'^2\rangle$. This equation has the form of an effective continuity equation. Also, we can see that this constraint and Eq.(15) generalize to the strong-gravity regime the continuity equation (3) and the Hamilton-Jacobi equation (4), where we can interpret $\pi\beta/2$ as the phase s. In addition, we have the equation (16), which comes from the fact that we now have three fields to determine : the amplitude ϕ_0, the phase β, and the modulus k, the latter being coupled to ϕ_0 by this additional equation.

If we consider a radial accretion, the only spatial derivatives that we need to consider are the radial derivatives, and so the effective continuity equation can be integrated at once. Doing so, we obtain the constant flux $F = \rho_{\mathrm{eff}}\frac{d\beta}{dr}$. We can then express $\rho_{\mathrm{eff}}\frac{d\beta}{dr}$ as a function of $k(r)$ using Eqs.(15)-(16), and we obtain a condition on the flux of the form $F = \mathcal{F}(r,k)$. As in [17], for each radius, $\mathcal{F}(r,k)$ reaches a maximum $\mathcal{F}_{\max}(r)$ at a modulus $k_{\max}(r)$, then decreases to zero at a modulus $k_+(r)$, to turn negative at higher modulus. Thus, at each radius we have $0 \leq k \leq k_+$. In the case $F > \mathcal{F}_{\max}$ there is no solution, however if $F < \mathcal{F}_{\max}$ there is two separated solutions k_1 and k_2 defined as $k_1 < k_{\max} < k_2$. These solutions correspond respectively to a low-velocity and a high-velocity branch, the first one being close to free fall when the second one is supported by the self-interaction internal pressure. Considering the boundary conditions, we obtain that the high-velocity solution corresponds to small radii, because the internal pressure cannot prevent the DM to fall into the BH, and that the low-velocity solution corresponds to large radii as we need to match the static equilibrium of the soliton. To ensure a smooth transition between the two branches, we consider the critical flux F_c, given by the minimum of $\mathcal{F}_{\max}(r)$ reached at a critical radius r_c, which is of the order of the Schwarzschild radius. And so, the final solution is a combination of the two branches, k_2 at $r > r_c$ and k_1 at $r < r_c$.

Since here we consider a case which is not radial but axi-symmetric, the conservation equation cannot be integrated at once anymore due to a partial differential equation depending on r and θ. Nevertheless, if v_0 is small enough at large radii, which means much smaller than the speed of light, we expect the flow to match the radial case at radius much higher than the critical radius r_c. Thus, what we do is matching the flow to the radial case for radius lower than the matching radius r_m, with $r_m > r_c$, by taking the solution computed in [17]. Doing so, we now need to solve Eq.(15) and the conservation equation at larger radii, where we are on the low-velocity branch.

At large radii, $k \ll 1$ and we have a solution of the form $\phi = \phi_0\cos(\omega_0 - \pi\beta/2)$. This solution gives us the boundary conditions $\phi_0 = \frac{\sqrt{2\rho_0}}{m}$ and $\beta = \frac{2}{\pi}mv_0 z$ at radius $r \to \infty$ and the fundamental frequency $\omega_0 = (1+\alpha+v_0^2/2)m$. Then, from Eq.(16) we obtain the asymptotic value of k, $k^2 \simeq \frac{\lambda_4\phi_0^2}{2m^2} = \frac{4}{3}\Phi_{\mathrm{I}}$.

Since we have $k \simeq 0.4$ at r_{c}, the modulus k is small for $r > r_{\mathrm{c}}$. In this regime, the potential Φ_{N} is small too, and we have, from the system (16)-conservation equation, $\phi_0^2 = \frac{2m^2k^2}{\lambda_4}$ and $\rho_{\mathrm{eff}} = \frac{\pi m^2k^2}{2\lambda_4}\omega_0 \propto k^2$, while Eq.(15) can be rewritten as $\frac{\pi^2(\nabla\beta)^2}{4m^2} = 2\frac{\rho_0}{\rho_a} + \frac{r_{\mathrm{s}}}{r} + v_0^2 - \frac{3}{2}k^2$. Defining the dimensionless radius $\hat{r}$ and the rescaled phase $\hat{\beta}$ by $\hat{r} = \frac{r}{r_{\mathrm{s}}}$ and $\hat{\beta} = \frac{\pi}{2mr_{\mathrm{s}}}\beta$, this reads as $(\hat{\nabla}\hat{\beta})^2 = \frac{3}{2}k_0^2 + v_0^2 + \frac{1}{\hat{r}} - \frac{3}{2}k^2 = \frac{3}{2}\left[k_+(x)^2 - k^2\right]$ where we used $k_+(x)^2 = k_0^2 + \frac{2}{3}v_0^2 + \frac{2}{3\hat{r}}$. As in [17], the low-velocity branch corresponds to $k \simeq k_+$ and $v^2 \ll k_+^2$ where we defined the velocity $\vec{v}$ as $\vec{v} = \hat{\nabla}\hat{\beta}$. So, the conservation equation becomes

$$\hat{\nabla}\cdot\left[\left(k_+(x)^2 - \frac{2}{3}(\hat{\nabla}\hat{\beta})^2\right)\hat{\nabla}\hat{\beta}\right] = 0\,. \quad (17)$$

Far above the Schwarzschild radius but at sufficiently small radii, we are in the radial accretion regime and

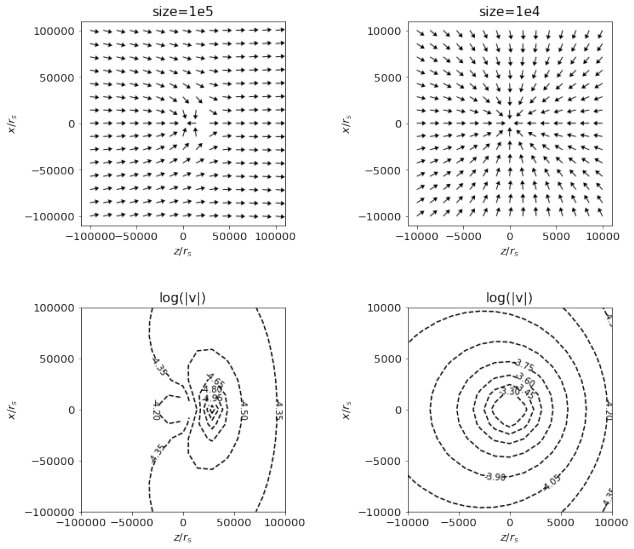

Figure 1: Plots of the "velocity" field at scales 10^5 and 10^4 for the normalised radius $\hat{r}$. The initial conditions are $v_0 = 10^{-4}$ and $k_0 = 10^{-3}$.

the term k_+^2 dominates over the term $(\hat{\nabla}\hat{\beta})^2$ in Eq.(17). At larger radii, where $\vec{v} \simeq \vec{v}_0$, this is still true if $v_0 \ll k_0$, where the relative velocity is much smaller than the speed of sound of the soliton.

It is useful to consider the linear flow associated with the linearized Eq.(17), $\hat{\nabla} \cdot \left[k_+(\hat{r})^2 \hat{\nabla}\hat{\beta}\right] = 0$, since it remains a good approximation at small radii. As k_+^2 has a spherical symmetry, the angular part of the linear modes can be expanded over spherical harmonics. The axi-symmetry implies that we only need the modes $Y_\ell^0(\theta, \varphi)$, also expressible in Legendre polynomials $P_\ell(\cos\theta)$. Then, the axi-symmetric modes $G_\ell(x, \theta)$ are $G_\ell(\hat{r}, \theta) = G_\ell(\hat{r})\, P_\ell(\cos\theta)$, with $\frac{d}{d\hat{r}}\left(\hat{r}^2 k_+^2 \frac{dG_\ell}{d\hat{r}}\right) - \ell(\ell+1)k_+^2 G_\ell = 0$.

At large radius $\hat{r} \to \infty$, we have $\vec{v} \to v_0\, \vec{e}_z$ which gives $\hat{\beta} = v_0\, \hat{r}\, \cos\theta$, while, at $\hat{r}_\mathrm{m}$, we have $v_r \simeq v_r(\hat{r}_\mathrm{m})$ which gives $\hat{r} = \hat{r}_\mathrm{m}$, $\frac{\partial\hat{\beta}}{\partial\hat{r}} \simeq v_r^\mathrm{m}$, $\frac{\partial\hat{\beta}}{\partial\theta} \simeq 0$. So, at the linear level, denoted by a upper L, we only need to consider the monopole and the dipole,

$$\hat{\beta}^L = \hat{\beta}_0^L(\hat{r}) + \hat{\beta}_1^L(\hat{r})\, \cos(\theta)\,, \tag{18}$$

From this, we know that the velocity decreases as $v_\mathrm{r} \sim 1/r$ where the flow is almost radial, as obtained in [17] for the radial accretion.

Now, we need to take nonlinear corrections from Eq.(17) into account to correct the linear flow. We define the parameter $\gamma = \frac{3k_0^2}{2} + v_0^2$ and $r_\gamma = 1/\gamma$. At radii $\hat{r} \gg \hat{r}_\gamma$ the coupling of the modes generates a constant wake for odd-order multipoles and a $1/r$ wake for even-order multipoles. These coefficients decay at high order multipoles if $v_0^2 < 3k_0^2/4$. Figure(1) shows the velocity field after 10 recursions for a velocity $v_0 \ll k_0$. At large enough scale, the flow of DM particles is almost not impacted by the BH, while at intermediate scale the trajectories are deformed by the gravity of the BH and form a wake behind it. This wake is located at the place where the particles turn around, at a certain distance from the BH, and is the reason why there is a non-zero dynamical friction in the system. Finally, on a small scale we find the radial case as expected. Due to the self-interaction and the appearance of a wake, we expect to have a lower dynamical friction than in the free case, and even lower as the coupling constant λ_4 increases since the density of the wake will decrease.

To consider a larger number of cases, we must also take into account larger values for the velocity, that is, $|v_0| \geq 3k_0^2/4$. In this regime, the flow changes from elliptic subsonic to hyperbolic supersonic. This change of behavior is due to the appearance of shocks from the hydrodynamical Euler equation, where in our case the speed of sound can be considered as $|v_\mathrm{s}| = \frac{\sqrt{3}}{2}k_0$. This behavior and the dynamical friction remain to be studied and calculated.

Conclusion and prospects

We have studied the dynamical friction produced in a system composed of a BH and a SFDM soliton, considering a free and then a self-interacting scalar field.

The free scalar field gives a result close to that of Chandrasekhar, aside that in our case the dynamical friction is impacted by the DM particles absorbed by the BH. However, we considered that the relativistic trajectories were negligible by performing the computation in the Keplerian approximation. Although this is a realistic approximation since particles close enough to the BH, and so relativistic, will have a free fall behavior, it would be interesting in future work to take these trajectories into account.

While we do not have yet the results for the dynamical friction in the self-interacting case, we were able to determine the appearance of a wake behind the BH and to characterize this one. This wake has a density that depends on the value of the coupling constant λ_4, the larger λ_4 is the lower the density of the wake is, and is the source of the dynamical friction. However, this characterization only works for velocities $v_0 < v_\mathrm{s}$ due to shocks appearing over this limit. The behavior beyond this limit remains to be studied.

For future works, some questions may be asked, as: How would the behavior of the system change if we considered, not a Schwarzschild BH but, a Kerr BH ? What would be the consequences if we consider a BH with a curved trajectory within the soliton ?

Acknowledgments

I would like to thank Patrick Valageas and Philippe Brax for their contribution to this research as well as for teaching me on the subject.

References

[1] K. Arun, S. B. Gudennavar, and C. Sivaram, Adv. Space Res. 60, 166 (2017), 1704.06155.

[2] A. Del Popolo and M. Le Delliou, Galaxies 5, 17 (2017), 1606.07790.

[3] L. Hui, Phys. Rev. Lett. 86, 3467 (2001).

[4] W. J. G. de Blok, Adv. Astron. 2010, 789293 (2010), 0910.3538.

[5] D. H. Weinberg, J. S. Bullock, F. Governato, R. Kuzio de Naray, and A. H. G. Peter, Proc. Nat. Acad. Sci. 112, 12249 (2015), ISSN 0027-8424, 1306.0913.

[6] G. Arcadi, M. Dutra, P. Ghosh, M. Lindner, Y. Mambrini, M. Pierre, S. Profumo, and F. S. Queiroz, Eur. Phys. J. C 78, 203 (2018), 1703.07364.

[7] E. G. M. Ferreira, Astron. Astrophys. Rev. 29, 7 (2021), 2005.03254.

[8] M. Battaglieri et al., in U.S. Cosmic Visions: New Ideas in Dark Matter (2017), 1707.04591.

[9] N. Garavito-Camargo, G. Besla, C. F. P. Laporte, K. V. Johnston, F. A. Gómez, and L. L. Watkins (2019), 1902.05089.

[10] F. Antonini and D. Merritt, Astrophys. J. 745, 83 (2012), 1108.1163.

[11] L. G. Gómez and J. A. Rueda, Phys. Rev. D 96, 063001 (2017).

[12] N. Bar, D. Blas, K. Blum, and H. Kim, Phys. Rev. D 104, 043021 (2021), 2102.11522.

[13] S. Chandrasekhar, Astrophys. J. 97, 255 (1943).

[14] I. Kovacic and M. Brennan, The Duffing Equation: Non-linear Oscillators and their Behaviour (Wiley, 2011).

[15] I. S. Gradshteyn and I. M. Ryzhik, Table of integrals, series, and products (New York Academic Press, 1965), 4th ed.

[16] P. Byrd and M. Friedman, Handbook of Elliptic Integrals for Engineers and Scientists (Springer, Berlin, Heidelberg, 1971).

[17] P. Brax, P. Valageas, and J. A. R. Cembranos (2019), 1909.02614.

Analysis of Single Gravitational Waves Detector Triggers

Vincent JUSTE

IPHC, Strasbourg

Abstract — The confidence in the early detection of gravitational waves events, starting in 2015, arised from the use of a network of detectors and the requirement to see the event in at least two of them. The last few years have seen upgrades of the interferometers which enabled many more detections and made the searches more reliable. The requirement of coincidences between detectors is thus not mandatory anymore and some pipelines have also started taking into account events that were seen in only one detector. The MBTA team has started working on the single detector triggers in order to make them public for the LIGO-Virgo O4 observing run scheduled to start at the end of 2022 and some of this work is presented here. It includes the definition of criteria for the selection of MBTA single detector triggers as well as the computation of a false alarm rate for those single detector triggers in order to quantify their significance.

Introduction

The discovery of gravitational waves back in 2015, with the detection of the black hole merger GW150914 [1], opened up a new era for cosmology and multi-messenger astronomy. Since then all observed gravitational waves events originate from compact binary systems coalescences (CBC). Figure 1 shows a representation of a CBC process. We have observed three types of CBC:

- Binary Neutron Star systems (BNS)
- Binary Black Hole systems (BBH)
- Neutron Star + Black Hole systems (NSBH)

Gravitational waves are detected using LIGO Handford (H1), LIGO Livingston (L1) and Virgo (V1), a total of three detectors based on the principle of the Michelson interferometer with kilometers-long arms. The passage of a gravitational wave will modify the distance between the mirrors of the interferometers ($\sim 10^{-19}$m), inducing a change in the interference pattern which can be measured. The network formed by the three detectors allows for more confident detections as well as a a better precision on the sky localization of the source.

The work presented here is part of an upgrade of the MBTA pipeline [2], a low-latency analysis pipeline looking for CBCs, for the 4th observing run of LIGO and Virgo. Events are initially required to be seen in at least two detectors to become astrophysical candidates. The three detectors are not always taking data simultaneously due to various reasons, meaning that the effective duty cycle for which we can detect astrophysical events is not 100% of the detectors duty cycle: for example a period of time where only L1 is taking data is lost. Similarly it's unlikely to meet the criteria

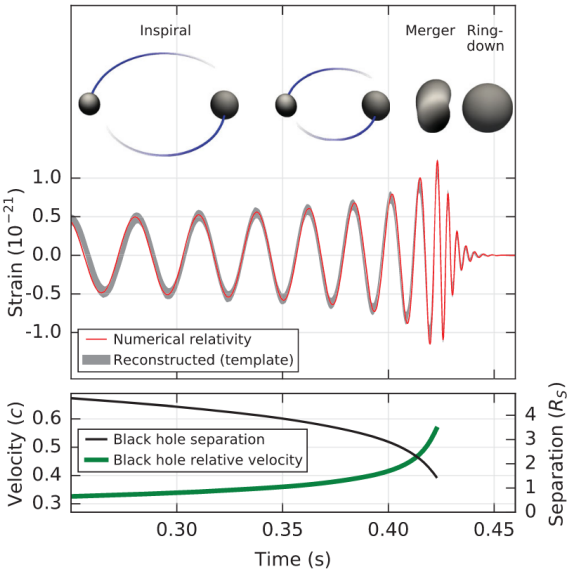

Figure 1: Gravitational strain, black hole separation and velocity reconstructed for GW150914. Original figure in [1].

of a simultaneous detection during a period where only L1 and V1 are online due to the lower sensitivity and different orientation of V1.

Gravitational waves are now well established, we have more sensitive detectors and better analysis pipelines and therefore more confident detections. The MBTA team therefore plans to release the single detector triggers (events seen in only 1 detector) during O4 to increase the number of observed astrophysical events. My work to reach this goal is to assess the significance of single detector triggers (which will sometimes be abbreviated as "singles") by computing a False Alarm Rate (FAR), as well as select the "good" triggers by finding selection criteria which could be used during O4.

Computation of a False Alarm Rate

Searching for known signal: matched filtering

The shape of the signal created by CBCs is known as it is predicted by the general relativity: we only need to find the right parameters. Waveforms are generated for different set of parameters. We then build a bank of templates (one template per set of parameters) and compare the templates to the data, this is called matched filtering. The comparison consist in the computation of a cross-correlation of the detector output with a template. The matched filtering output (MFO) is a time series of the signal-to-noise ratio, the maximum of the amplitude of the MFO is called the Signal-To-Noise Ratio (SNR) and is a measure of the significance of the signal.

Method for the computation of a FAR

The computation of a FAR for events found in coincidences in 2 detectors is done by first generating a background distribution by making random coincidences between the events observed by the two detectors at different times [2]. The FAR for a given SNR is defined as the expected number of background events with a SNR equal or greater than the given one.

For single detector triggers we want to do something similar by taking advantage of the structure of the MBTA pipeline. MBTA stands for Multi-Band Template Analysis. The pipeline uses two frequency bands, a Low Frequency (LF) band ranging usually from 25 Hz to 80 Hz and a High Frequency (HF) band from 80 Hz to 2048 Hz. When analyzing data the matched filtering is done in both frequency bands, which results in an MFO and an SNR for each band. Both MFOs are then combined. For an astrophysical signal the combination is coherent. The benefit of this method is to have a lower computational cost. This way of processing data allows us, with only one detector, to make random coincidences between the LF and HF bands at different times in order to generate a SNR distribution for background events in a single detector. We have to be careful when making the coincidences: the event in one of the band has to be a trigger, i.e. its SNR has to be above the single-band SNR threshold. The event taken in the other band for the coincidence is simply random noise. The two panels in Figure 2 show the distribution of single band SNR for the triggers and the random noises used in coincidences for each frequency band. The generated background SNR distribution is shown and compared to the observed background in figure 3. We can then compute the FAR in the same way as for coincidences.

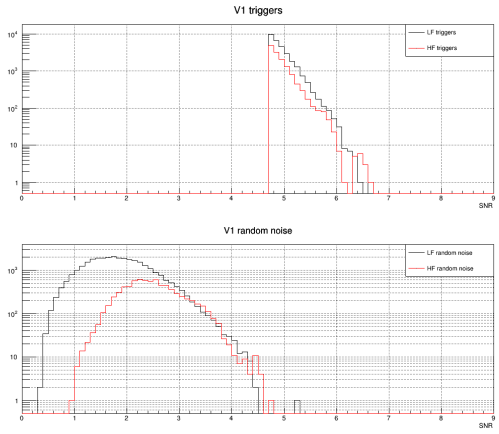

Figure 2: Single band triggers and random noise in V1.

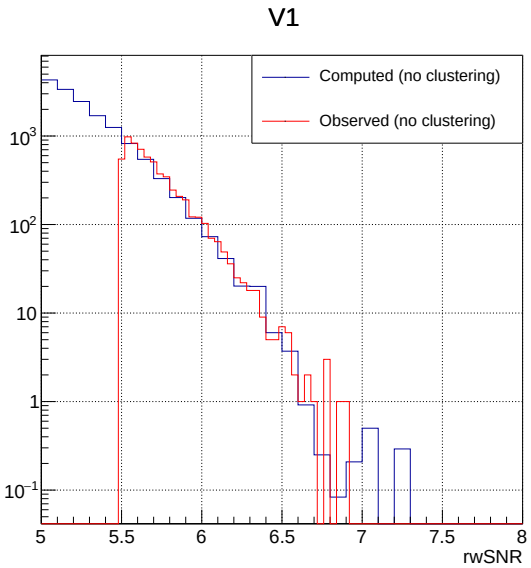

Figure 3: Comparison of the computed background with the one observed during O3 in V1.

Selection criteria for single detector triggers

The detector output is neither Gaussian nor stationary due to various reasons which will not be detailed here. The presence of short transients, called glitches, also

pollutes the data on a large frequency band at times. For the single detector triggers we want to focus on signals that we can properly identify and those that are the most interesting for astrophysics. Glitches are unlikely to mimic long signals. The duration of the signal is related to the masses of the objects forming the CBC: the higher the masses, the shorter the signal. Therefore a longer signal is more likely to originate from a CBC containing a neutron star (less massive than a black hole) and thus is more likely to have an electromagnetic counterpart (due to the presence of matter). We will refer to these as the EM bright population, that is the population of CBC which could have an electromagnetic counterpart based on their properties. The EM bright population is very interesting for online alerts since there are electromagnetic follow-ups looking for counterparts to gravitational waves events. Motivated by the LVC GRB results [3], we define the EM bright population as follows:

$$1\mathrm{M}_\odot \leq m_1 \leq 25\mathrm{M}_\odot, \quad (1)$$

$$1\mathrm{M}_\odot \leq m_2 \leq 2.8\mathrm{M}_\odot \quad (2)$$

The underlying idea is that we want at least 1 neutron star (matter) in the CBC system which imposes a small mass for the lighter object (m2) and either another neutron star or a small black hole such that tidal disruption is possible, this requires a not-too-large mass for the heavier object (m1). No constraints were put on the spins of the two object as it was shown that they were badly recovered. The distribution of the template in the m1 vs m2 plane is shown in figure 4 with the different mass regions. Figure 5 shows the comparison

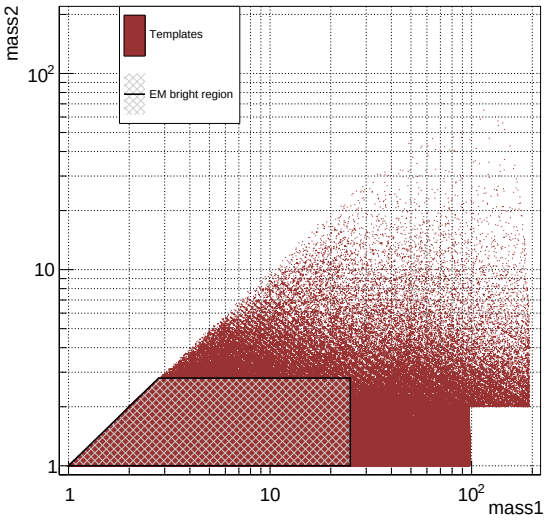

Figure 4: Templates distribution in the m1 vs m2 plane with the different search regions.

between the EM bright singles background of O3 with the overall O3 background, as well as the astrophysical candidates. We see that many non-EM bright events have a high SNR and most astrophysical candidates are indistinguishable while the EM bright background is cleaner. To improve this we can use pipeline-related

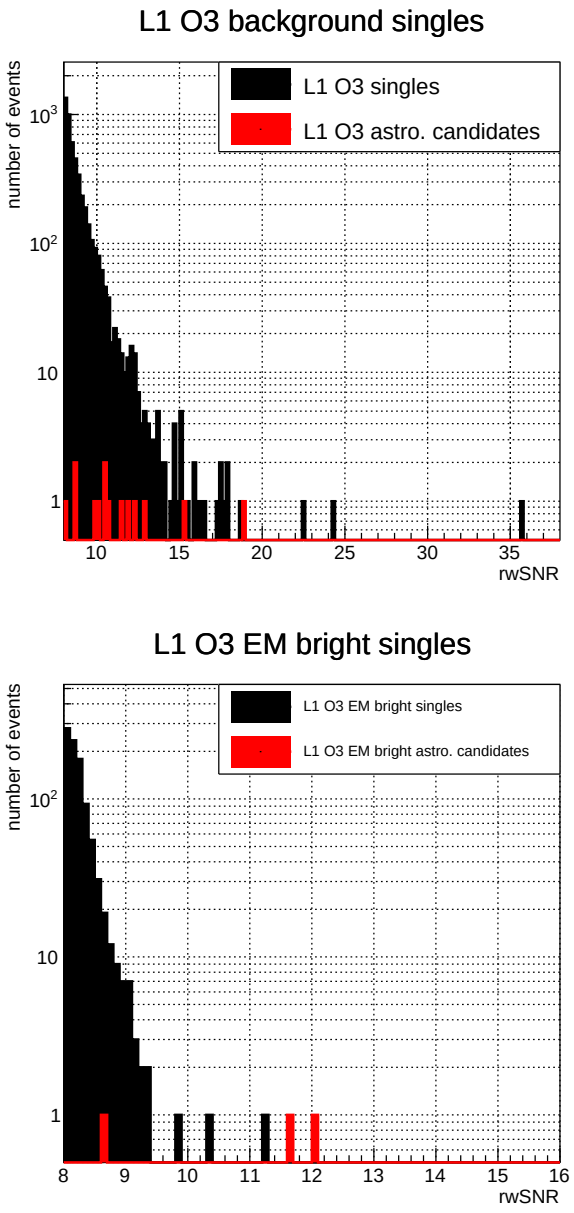

Figure 5: Top: O3 background and astrophysical candidates. Bottom: O3 EM bright background and astrophysical candidates. Mind the difference in horizontal axis scale for better readability.

quantities to discriminate against triggers of "poor" quality. One quantity that proved to be effective in selecting singles is the "excess rate". The excess rate is the ratio of trigger rate before and after quality checks. For astrophysical signals there can be a small excess of bad triggers during a few seconds, for noise it can be for longer duration. A penalty is applied to the SNR of a trigger if it came at a noisy time.

Figure 6 show the effect of a cut rejecting any trigger with an excess rate larger than 0.3 on the EM bright background along the astrophysical candidates reported in GWTC-2.1 [4] and GWTC-3 [5] (with parameter within the EM bright region and seen as singles by MBTA), we see that the candidates with large

SNRs are left untouched by the cut and stand out of the distribution.

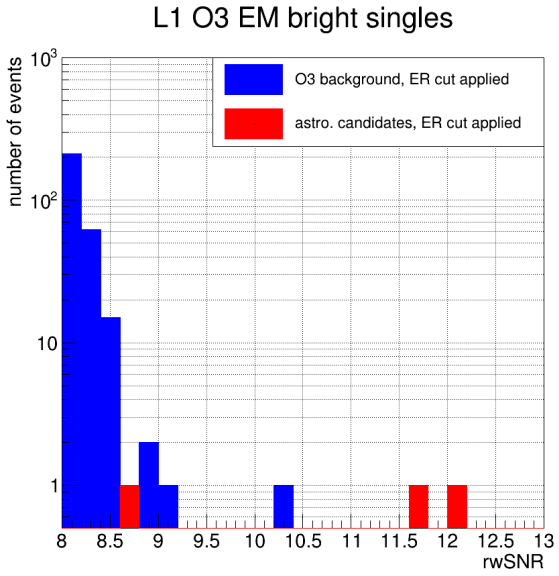

Figure 6: O3 EM bright background and astrophysical candidates after applying the cut on the excess rate.

Summary

We want to release the single detector triggers in order to increase the number of detections. We saw that focusing on triggers from the EM bright population already allows to have a cleaner background. For this same EM bright candidate population the excess rate allows for a nice selection of the single detector triggers, as was shown for a cut at ER= 0.3. To assess the significance of the single detector triggers we want to compute a FAR for each of them in the same way as for the coincidences. Taking advantage of MBTA multi-band structure we can proceed to random coincidences to generate a background SNR distribution for single detector triggers and compute a FAR. All of this provides guidelines that will be implemented in the MBTA pipeline for O4.

References

[1] Observation of Gravitational Waves from a Binary Black Hole Merger, B. P. Abbott et al. DOI: 10.1103/PhysRevLett.116.061102

[2] F. Aubin *et al.* "The MBTA pipeline for detecting compact binary coalescences in the third LIGO-Virgo observing run". In: Classical and Quantum Gravity 38.9 (Apr. 2021), p. 095004. issn: 1361-6382.doi:10.1088/1361-6382/abe913

[3] R. Abbott *et al.* "Search for Gravitational Waves Associated with Gamma-Ray Bursts Detected by Fermi and Swiftduring the LIGO-Virgo Run O3a". In: The Astrophysical Journal915.2 (July 2021), p. 86. issn: 1538-4357. doi: 10.3847/1538-4357/abee15

[4] R. Abbott *et al.* "GWTC-2.1: Deep Extended Catalog of Compact Binary Coalescences Observed by LIGO and Virgo During the First Half of the Third Observing Run" [LIGO Scientific and VIRGO], [arXiv:2108.01045 [gr-qc]].

[5] R. Abbott *et al.* "GWTC-3: Compact Binary Coalescences Observed by LIGO and Virgo During the Second Part of the Third Observing Run" [LIGO Scientific and VIRGO], [arXiv:2111.03606 [gr-qc]]

Power Spectrum Accuracy in N-body simulations using Scale Free cosmologies

Sara MALEUBRE, ***with D. Eisenstein, L. Garrison and M. Joyce***

Laboratoire de Physique Nucléaire et de Hautes Énergies, UPMC IN2P3 CNRS UMR 7585, Sorbonne Université

Abstract — We exploit a suite of large N-body simulations (up to N=4096^3), performed with Abacus, of scale-free models with a range of spectral indices n, to better understand and quantify convergence of the matter power spectrum. Using self-similarity to identify converged regions, we show that the maximal wavenumber resolved at a given level of accuracy increases monotonically as a function of time. At the 1% level it starts at early times from a fraction of k_Λ, the Nyquist wavenumber of the initial grid, and reaches at most $\sim 2-3k_\Lambda$ at the very latest times we evolve to, if the force softening is sufficiently small. At the 5% level, accuracy extends up to wavenumbers of order $5k_\Lambda$ at late times. Expressed as a suitable function of the scale-factor, accuracy shows a very simple n-dependence, allowing an extrapolation to place conservative bounds on the accuracy of N-body simulations of non-scale free models like ΛCDM.

Introduction

The power spectrum (PS) is one of the most basic statistical tools employed to characterise clustering at large scales in cosmology. Building a precise theoretical framework for their calculation is crucial in order to fully exploit observational data coming from the next generation surveys, such as DESI, Vera C. Rubin Observatory LSST or Euclid, that will open a new window in the era of "precision cosmology". In this context the nonlinear regime of gravitational evolution is of particular importance, as it will be a key to distinguish among the plethora of exotic dark energy and modified gravity models, as well as tightly constraining the ΛCDM scenario.

Studies have estimated that to fully exploit the observed data, the matter PS in the range of scales ($0.1 \lesssim k/h\mathrm{Mpc}^{-1} \lesssim 10$) needs to be determined to a $1-2\%$ accuracy, depending on the specifications of the survey. Calculation of predictions at these scales rely entirely on numerical simulations that use the N-body method. One important and unresolved issue in this context is the accuracy limitations on such simulations arising from the fact that they approximate the evolution of the dark matter phase space distribution using a finite particle sampling, as well as a regularisation at small scales of the gravitational force. Despite the extensive use and spectacular development of N-body cosmological simulations over the last several decades, no clear consensus exists in the literature about how achieved accuracy, even for the PS, depends on the relevant parameters in an N-body simulation.

Frequently, convergence is probed by comparing between two or more codes to assess the accuracy of their results, but this establishes only a *relative convergence* that can give confidence in the accuracy of the clustering calculation but does not take into account the effects of discretization and dependence on the N-body parameters. Alternatively, we propose a methodology based on Joyce (2020) [2], which uses the property of self-similarity of "scale-free" cosmological models to derive resolution limits to the PS with respect to particle density and gravitational softening.

Scale-Free cosmologies and Self Similarity

The value of scale-free models in the context of physical resolution of N-body simulations relies on the self-similarity of their evolution: *temporal evolution of clustering is equivalent to a well defined rescaling of the spatial coordinates.* This is the case because such models are characterised by just one length scale and one time scale: their initial (linear) PS of fluctuations is a simple power law $P(k) \propto k^n$, and the Universe follows an Einstein-de-Sitter (EdS) expansion law $a \propto t^{2/3}$ (where a is the scale factor). The single length scale can thus be defined as the non-linearity scale R_{NL} given by

$$\sigma^2_{lin}(R_{NL}, a) = 1 \xrightarrow{\text{linear theory}} R_{NL} \propto a^{\frac{2}{3+n}} \quad (1)$$

where σ^2_{lin} is the variance of normalized linear mass fluctuations in a sphere, while the time scale is fixed by the normalization of the Hubble law (i.e. by the mean mass density combined with Newton's constant G).

For the case of statistics such as the PS which are a function of wavenumber k and time, it follows simply by dimensional analysis that a suitable dimensionless definition of the statistic f can be written as a function of $k\,R_{NL}(a')$ where a' is some reference scale-factor

(left-hand side). As the reference scale-factor is itself arbitrary (because of the EdS expansion law) we can take $a' = a$ (right-hand side), and obtain:

$$f(k,a) = f(k\,R_{NL}(a'), a/a') = f_0(k\,R_{NL}(a))\,. \quad (2)$$

where f_0 is independent of time. For our study of the PS we use the canonical definition of the dimensionless PS, and thus self-similar behaviour corresponds to

$$\Delta^2(k,a) = \frac{k^3 P(k,a)}{2\pi^2} = \Delta_0^2(k\,R_{NL}(a))\,, \quad (3)$$

In N-body simulations of scale-free cosmologies, any deviations from this self-similar evolution can only be due to *unphysical scales*. Conversely results can represent the PS in the desired physical limit — which must be independent of these parameters — only to the extent that the rescaled dimensionless PS statistic becomes independent of time.

Numerical simulations

We have performed simulations using the Abacus N-body code [3]. It is designed for high-accuracy, high-performance cosmological N-body simulations, exploiting a high-order multipole method for the far-field force evaluation and GPU-accelerated pairwise evaluation for the near-field. The larger, $N = 4096^3$ simulations in this work were run as part of the AbacusSummit project [4] using the Summit supercomputer of the Oak Ridge Leadership Computing Facility.

We report results here based on the simulations listed in Table 1. We have simulated three different exponents for the PS ($n = -1.5, -2.0, -2.25$) in order to probe the range of exponents relevant to structure formation in a ΛCDM cosmology. The softening lengths have been chosen to include for each n at least one pair of simulations (with $N = 1024^3$) which differ only in this parameter (and for $n = -2.0$ a range of different softenings). Non-asterisk values of ϵ are fixed throughout the simulation in comoving units, while the ones with an asterisk are fixed in physical coordinates (i.e. $\epsilon/\Lambda \propto 1/a$) for $a > a_0$ and in comoving for $a < a_0$. In this study a_0 does not correspond to the scale factor today, but to the epoch at which fluctuations of peak-height $\nu \approx 3$ are expected to virialize in the spherical collapse model ($\sigma_{lin} \approx \delta_c/\nu$, with $\delta_c = 1.68$), and the first non-linear structures appear in the simulations.

$$\sigma_{lin}(\Lambda, a_0) = 0.56 \quad (4)$$

We have saved the outputs (full particle configurations) of our simulations starting from $a = a_0$ and then at subsequent times separated by intervals in which the characteristic non-linear mass M_{NL} grows by a factor of $\sqrt{2}$. Given that $M_{NL} \propto R_{NL}^3$, the scaling in Equation 1 implies that the outputs correspond to scale-factors a_i where

$$\log_2\left(\frac{M_{NL}(a_{i+1})}{M_{NL}(a_i)}\right) = \frac{1}{2} = \frac{6}{3+n}\log_2\left(\frac{a_{i+1}}{a_i}\right)\,. \quad (5)$$

n	N	ϵ/Λ	S_f	$\log_2(a_f/a_0)$
-1.5	4096^3	0.3*	29	3.625
-1.5	1024^3	0.3*	29	3.625
-1.5	1024^3	1/30	29	3.625
-2.0	4096^3	0.3*	35	2.917
-2.0	1024^3	0.3*	37	3.083
-2.0	1024^3	1/30	37	3.083
-2.0	1024^3	1/60	37	3.083
-2.0	1024^3	1/15	37	3.083
-2.25	4096^3	0.3*	35	2.1875
-2.25	1024^3	0.3*	37	2.3125
-2.25	1024^3	1/30	37	2.3125

Table 1: Summary of the N-body simulations used for the analysis in this paper. The first columns show the spectral index of the initial PS, n and the number of particles, N. The fourth column gives the ratio of the effective Plummer force smoothing length ϵ to mean inter-particle separation (equal to the initial grid spacing Λ), for $a < a_0$ (as defined by Equation 4, the time of our first output). For the cases without an asterisk this is its value at all times (i.e. the smoothing is fixed in comoving coordinates) while for the cases with an asterisk the smoothing for $a > a_0$ is fixed in proper coordinates. The last two columns give, respectively, the value of the time parameter S at the last snapshot and the final scale factor relative to that at first output. Note that given that the first output is at $S = 0$, the number of outputs for each simulation is $S_f + 1$.

It is convenient then to define the time variable S by

$$S = \frac{12}{3+n}\log_2\left(\frac{a_s}{a_0}\right) \quad (6)$$

with the outputs corresponding to $S = 0, 1, 2\ldots$. The final time S_f up to which we have integrated is dictated by two competing considerations. On one side there is a limitation on numerical cost arising from the use of a global time-step in Abacus which means that it can no longer integrate efficiently when the central densities of halos become too large. On the other hand finite box size effects become dominant at sufficiently long times. For $n = -1.5$, it is the former limitation which dictates the stopping time, while for $n = -2.25$ it is the latter. This will be illustrated explicitly in our analysis below.

Results

The accuracy and extent of self-similarity, and how it is limited by the different unphysical simulation parameters, can be seen in Fig. 1. It shows the behaviour of Δ^2 at the non-linear regime for $n = -1.5$, $n = -2.0$ and $n = -2.25$. At these small scales the results are insensitive to box size, but do show dependence on the softening (except for $n = -2.25$ where box-size effects wipe out this behaviour). The simulations with proper softening and those with the smaller comoving softening show the widest and most coincident regions of self-similarity, while the simulations with larger comoving

softening show a suppression of power relative to the self-similar value. Further the same $\epsilon = \Lambda/30$ comoving smoothing shows just marginal ($\sim 1\%$) deviation in the $n = -2.0$ simulation, but more significant ($\sim 3\%$) deviation for $n = -1.5$. Thus the limit on resolution at small scales at any time, corresponding to the largest k at which self-similarity may be attained, is determined by k_Λ alone (i.e. by the initial grid spacing, or mass resolution) provided the smoothing is chosen sufficiently small.

We can now determine the *estimated precision* of the PS at any scale and time, i.e. the difference between its measured value in a given simulation and the converged value for a given cosmology. Fig. 2 shows that *the precision of the measured PS at any given comoving k improves monotonically in time.* This reflects that the discretization on the lattice is the origin of imprecision (data is taken on a range of k/k_Λ unaffected by box-size effects and with an appropriate softening). It also illustrates the qualitative difference between the modes $k < k_\Lambda$ and $k > k_\Lambda$: the former are wavenumbers for which the PS is already resolved well in the initial conditions, and its behaviour depends on the exponent, as the mass variance of redder spectres dominates earlier over the effects of the lattice above k_Λ. For the latter the physical PS can only be resolved when the fluctuations from non-linear evolution dominate over the initial discreteness fluctuations at sub-grid scales. In addition, this regime seems *n-independent*, i.e. propagation of resolution migh be determined by the evolution of the comoving size of the first virialised structures.

Resolution limits for non scale-free cosmologies

While our method is valid for scale-free cosmologies, our underlying motivation is to quantify the resolution in simulations of non scale-free cosmologies such as ΛCDM or variants of it. Such cosmologies are not very different from scale-free cosmologies for what concerns their non-linear evolution: their PS can be considered to be an adiabatic interpolation of power-law spectra, with the modified expansion rate due to dark energy only coming into play at very low redshift.

We have anticipated this extrapolation of our results above by choosing to simulate, as far as practicable, scale-free models with n in the range relevant to ΛCDM, and focusing on the dependence of our results on these exponents. Further we have characterised how resolution depends on time in terms of a scale factor relative to a_0 which can be defined, as given in 4, for any cosmology, and has the simple physical meaning as the time when non-linear structures start to develop. Using the definition of the linear variance, we can find a one-to-one relation between redshift in a ΛCDM simulation with a specific interparticle distance and our time variable $\log_2(a/a_0)$.

Our analysis above shows that we have two quite different regimes for the evolution of small scale resolution. For the modes $k > k_\Lambda$, which are not modelled in the initial conditions and which always describe the strongly non-linear regime, resolution is approximately n independent as a function of $\log_2(a/a_0)$. For

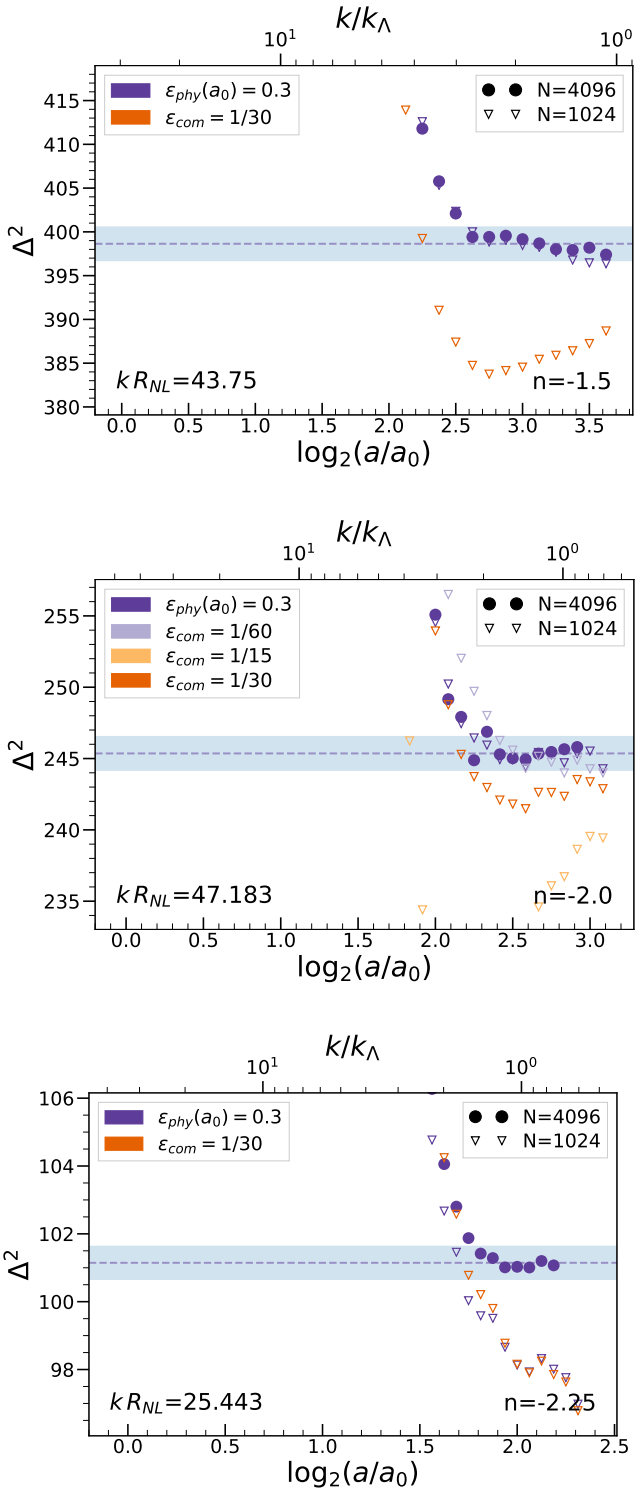

Figure 1: Evolution of Δ^2 as a function of logarithmic scale factor $\log_2(a/a_0)$ (lower x-axis) and as a function of k/k_Λ (upper x-axis) for rescaled bins labelled by their kR_{NL} value. From top to bottom we have $n = -1.5$, $n = -2.0$ and $n = -2.25$. The horizontal dashed line marks our estimated converged value determined in the largest simulation, and the blue shaded region indicates that within $\pm 0.5\%$ of this value.

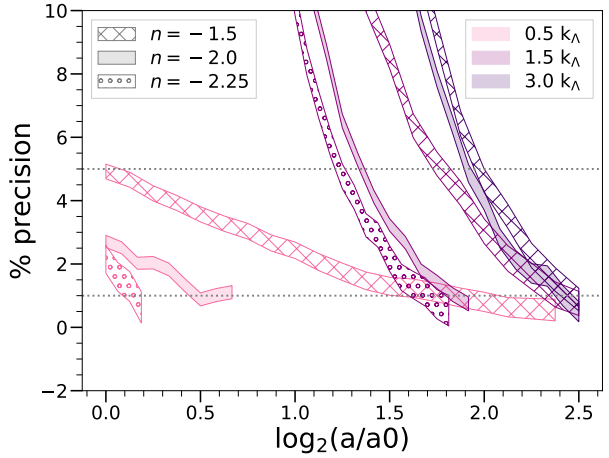

Figure 2: Estimated precision of the PS (in $N = 4096$ simulations) relative to its true physical value as a function of time, for different selected comoving scales. Confidence intervals show the expected error in the converged value. The horizontal dotted lines correspond to 1% and 5%.

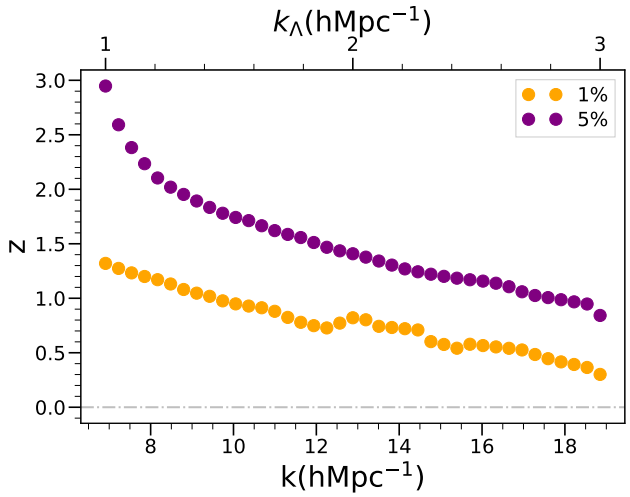

Figure 3: Resolved k as a function of redshift for a fixed value of the mean interparticle spacing $\Lambda = 0.5h^{-1}$Mpc, using a standard ΛCDM cosmology ("Planck 2013" [5]). Orange points correspond to 1% precision, while purple points represent a 5%. We have added an axis for the k_Λ of the hypothetical ΛCDM simulation for an easier extrapolation with 2.

these modes it seems very reasonable that we can carry over straight- forwardly our results from Fig. 2 (modulo small possible corrections due to non-EdS evolution) to resolution as a function of scale and redshift. Fig. 3 shows, for a $\Lambda = 0.5h^{-1}$Mpc simulation of a standard "Planck13" [5] cosmology, the smallest scale which we will have access to as a function of redshift at a 1% and 5% precision.

On the other hand, for the modes $k < k_\Lambda$ we have seen that the resolution as a function of time shows n-dependence. These differences can be understood as arising directly from the initial conditions, and are thus essentially dependent on the behaviour with scale of the mass variance around the initial grid spacing. For a generic ΛCDM type cosmological model with a slowly varying exponent we can thus expect to determine the resolution from that of a scale-free model which, at scales $\sim \Lambda$, approximates the behaviour of the variance. Such an effective exponent can be estimated as:

$$n_{\rm eff} = -3 - 2\,\frac{d\log\sigma}{d\log R}\bigg|_{R=\Lambda} \qquad (7)$$

Taking the aforementioned ΛCDM model ("Planck 2013"), its estimated $n_{\rm eff}$ is situated typically around or below our smallest simulated exponent, at least for interparticle distances of typical (current) N-body simulations, $n \sim (-2.5, -2)$ for $\Lambda \in [0.1, 1]$. The resolution of $n = -2.25$ shows the same tendency as $n = -2.0$, inferred from 2. We thus conclude that we can use our results for $n = -2.0$ to obtain conservative bounds on precision for numerical simulations of such models.

These statements assume of course implicitly that the method of setting up initial conditions is like that used in our simulations, that convergence has been established with respect to time-stepping and any all other numerical parameters, and that the box size is sufficiently large so that finite box effects are negligible at these scales considered.

Acknowledgments

This research used resources of the Oak Ridge Leadership Computing Facility at the Oak Ridge National Laboratory, which is supported by the Office of Science of the U.S. Department of Energy under Contract No. DE-AC05-00OR22725. The AbacusSummit simulations have been supported by OLCF projects AST135 and AST145, the latter through the Department of Energy ALCC program.

References

[1] S. Maleubre, D. Eisenstein, L. Garrison, M. Joyce, *MNRAS*51218292022

[2] M. Joyce, L. Garrison, D. Eisenstein, *MNRAS*50150512020

[3] L. Garrison, D. Eisenstein, D. Ferrer, N. Maksimova, P. Pinto, *MNRAS*5085752021

[4] N. Maksimova, L. Garrison, D. Eisenstein, B. Hadzhiyska, S. Bose, T. Satterthwaite, *MNRAS*50840172021

[5] Planck Collaboration et al., *A&A*571A162014

Detection of Compact Binary Coalescences and the Multi-Band Template Analysis

Elisa NITOGLIA

Institut de Physique des Deux Infinis de Lyon

Abstract — The Multi-Band Template Analysis (MBTA) is a pipeline suited for searching for gravitational waves (GWs) emitted by coalescing compact binary systems (CBCs) in LIGO-Virgo data. It has been used ever since the first generation of interferometric GW detectors in its online configuration, and over the past years it has been improved to provide contributions to GW transient catalogues by developing an offline configuration. MBTA performs a template-based search by splitting the analysis in two frequency bands to reduce computational costs. It has been used in both its offline and online configuration to analyse data from the third observing run (O3) in the standard search, investigating for signals emitted by coalescing Binary Black-Holes (BBHs), Neutron Star Binaries (BNSs) and Neutron-Star-Black-Hole Binaries (NSBHs). At the moment, MBTA is contributing in the Sub-Solar Mass (SSM) search, seeking for signals emitted by compact binaries with at least one component with mass smaller than the mass of the Sun.

Introduction

General Relativity, Einstein's theory of gravitation, was developed between 1907 and 1915 and according to it spacetime can bend because of the presence of masses and interactions between them. One of its predictions was the existence of Gravitational Waves (GWs), ripples in the curvature of spacetime generated by the acceleration of masses. The first attempts to directly detect GWs were made by Joseph Weber in 1960. Once emitted, a GW propagates virtually forever with an amplitude that decreases linearly in the distance from the emitting source. When these waves travel through an object, it experiences time varying stresses that can produce mechanical strains in an elastic solid. As a GW passes, the strain in the bar causes the piezoelectric crystals to expand and contract, producing an electric signal which could be amplified through low noise amplifiers. These early experiments reached sensitivities of 10^{21}, sufficiently low to detect supernovae explosions in our galaxy (which are rare events), but never achieved clear evidence of a GW detection. Modern detectors are laser interferometers which use laser light to measure relative changes in the lengths of two perpendicular arms of a Michelson interferometer. GWs which propagate perpendicularly to the detector plane will stretch and squeeze the armlengths of the interferometer, modulating the interference pattern at the output port of the instrument. On September 14, 2015 at 09 : 50 : 45 UTC the two Advanced LIGO interferometers simultaneously observed a transient GW signal: the first GW event, GW150914 [1], started the era of GW astronomy. It matched the waveform predicted by general relativity for the inspiral and merger of a binary black hole. The source was found to have component masses of $36^{+5}_{4} M_{\odot}$ and $29^{+4}_{4} M_{\odot}$, and the black hole resulting from their fusion has a mass of $62^{+4}_{4} M_{\odot}$. $3.0^{+0.5}_{0.5} M_{\odot} c^2$ were radiated in GWs.

Laser Interferometers

The change in the proper separation between test particles is the physical quantity that GW detectors are designed to measure in order to observe the passage of a gravitational wave. In interferometric detectors, like the ones that are currently operational, these changes in the proper separation are monitored by measuring the travel time of a laser beam travelling back and forth along the arms of a Michelson interferometer. The physical principle exploited by interferometric GW detectors is the interference between coherent light beams, which is generated by differences in the light travel time along the arms. At the moment, three interferometers are used to take data: LIGO Hanford, LIGO Livingston and Virgo. During the next observing run (O4) Kagra will join the data taking.

The output of the detectors is a time series which describes the oscillation state of the resonant masses; it is a combination of the GW signal $h(t)$, if present, and of noise $n(t)$.

$$s(t) = h(t) + n(t) \tag{1}$$

The detection problem is how to distinguish n(t) from h(t) and how to reduce the noise in a way that the gravitational wave signal becomes recognizable. The noise is a random process but, if stationary, as in short periods of time detection, it is possible to compute its expectation value. Noise is categorized as either displacement noise, which directly moves the suspended mirrors causing a differential change in the arm cavity lengths, or as sensing noise, which appears in the read-

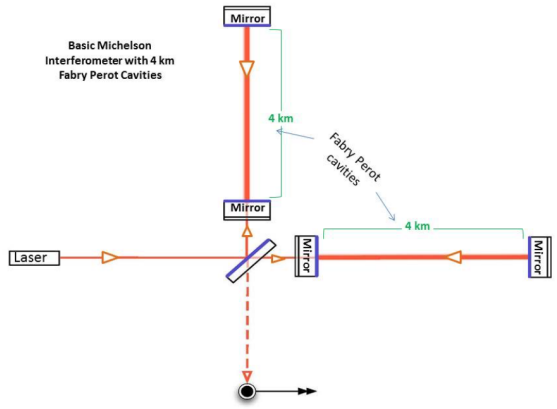

Figure 1: Illustration of a simplified Michelson interferometer

out signal but is not caused by a gravitational wave. The main noise sources are: seismic noise, thermal noise, photon shot noise, radiation pressure, quantum limit and the residual gas noise. The sensitivity of an interferometer is limited by various noise sources, as shown in Fig.(2), and the sensitivity band of current detectors is between 10Hz and 2000Hz.

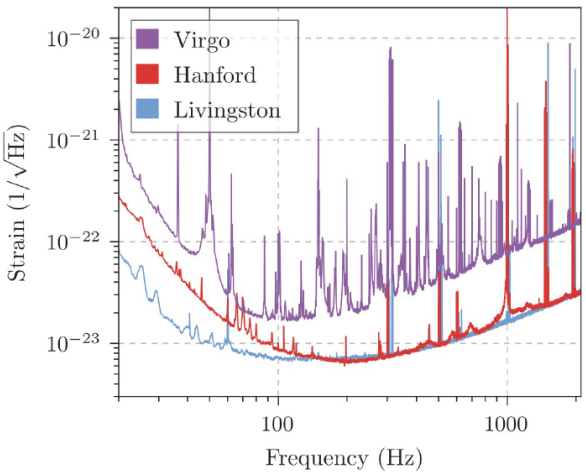

Figure 2: Simplified illustration of the sensitivities of current GW interferometers

Gravitational Wave Sources

Every non-symmetric, accelerated system emits GWs. In order to have detectable GWs, we need sources that are massive, compact and violent enough to induce a sufficiently strong gravitational field. Sources of this kind are necessarily of astrophysical origin, such as black holes (BHs), neutron stars (NSs) and supernovae (SN). There are four categories of data analysis. Four categories of GWs are defined, based on what generates them: continuous, coalescing compact binaries, stochastic and burst.

The MBTA pipeline is involved in the search for signals originated from Compact Binary Coalescences (CBC). Those are a class of sources composed by two compact objects, either NSs or BHs, which orbit around each other. These sources are further divided into binary black holes (BBHs), binary neutron stars (BNSs) and neutron star black hole binaries (NSBHs). The emission of GWs causes the system to lose energy and angular momentum, causing the two objects to spiral towards each other. The emitted signal can be divided into three stages: the inspiral, the merger and the ringdown or postmerger phase.

The inspiral phase is when the two objects are spiralling towards each other, losing orbital energy and angular momentum, causing the GW amplitude and frequency to increase as a function of time. Sources can remain in this phase for millions of years, but they can only be observed by ground-based detectors once the binaries reach their final orbital cycles. During this phase, gravitational fields and velocities are still relatively weak and the GWs emitted can be found through approximation methods such as the Post-Newtonian formalism. The following stage is the merger phase which occurs when the two objects are close enough that they start to merge into a single object. In this phase the gravitational fields are very strong and the GW emission can only be computed numerically. Once the two objects have merged, they enter a regime in which the newly formed object needs to settle down into a quiescent equilbrium state. For BBHs this happens via the BH ringdown. The GWs in the ringdown phase can be computed using the perturbation theory. The result consist of superpositions of damped sinusoids, known as quasi-normal modes. When NSs are involved, this final stage is more complicated and its description requires the use of numerical methods, because NSs may go through metastable, post-merger states.

The Search Method

The identification of GW candidates in data from ground-based interferometers presents three main challenges: the signal is weak compared to the noise from the detector, so it needs to be extracted from the data with efficient methods; the parameters describing the signal are unknown and, even if those parameters were known precisely, the shape of the GW signal $h(t)$ is not known exactly because the equations of General Relativity are highly non-linear, so that waveforms need to be approximated. The solution to the first problem is to use matched filtering to efficiently separate signals from noise, while the solution to the second problem is to compare the data against many different templates, built upon several combinations of parameters.

Although great efforts are carried out in order to reduce the overall noise affecting detectors, the GW signal is still buried in noisy data. Filtering is the process of separating the cleanest possible useful signal from the contaminated combination of signal and noise. The technique of matched filtering computes the correlation

between the signal buried into data and a reconstructed waveform, called template.

In order to detect in the data the presence of GW signals that may originate from binaries with a wide range of masses and spins, the filtering is carried out using a bank of templates that covers the desired portion of the mass-spin parameter space.

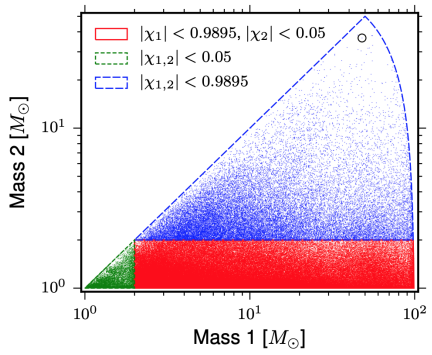

Figure 3: Simplified illustration of the template bank used in the first observing run (O1). The color code indicates mass regions with different limits on the dimensionless spins. Green, red, and blue correspond to BNS, NSBH, and BBH systems, respectively.

The bank is discrete, and this results in a loss of detection volume. The detector data is filtered with each waveform in the bank, so that any signal within the targetted range of masses and spins matches one of the templates within an error. The cross correlation between each template and the detector data is computed, shifting the former over time through the latter. Each template therefore produces an SNR timeseries; only values above a specified threshold are accepted for further analysis. These accepted data points are called triggers and denote times when a template in the bank correlates with the data at least at the level of the specified threshold: each trigger is a data instance in which a GW signal may be present and therefore warrants further investigation. The SNR value determines the probability of detection of the signal. The higher its value, the higher the probability of detection. The matched filtering has the property of maximizing the SNR, independently of the probability distribution of the noise.

The Multi-Band Template Analysis

The Multi-Band Template Analysis (MBTA) pipeline has been used to perform low-latency searches for CBCs ever since the late operation of the first generation of interferometric GW detectors. Over the past years, the MBTA pipeline has been improved in various ways, driven both by the specific needs of the low-latency search designed to enable electromagnetic (EM) follow-up of GW candidates and by the desire to use the pipeline offline to produce future GW transient catalogs. The MBTA offline pipeline performs a coincident analysis, so each detector in the network is analyzed separately before the results are combined to identify coincident events. It uses the matched filter technique, but splits it in two frequency bands to reduce the computational costs [2]. The performance of the offline analysis has been illustrated in [3] and, so far, it has been used to analyze data from the third observing run (O3), participating to the catalog paper of the first half of the third observing run (O3a) GWTC-2.1 [4], the catalog paper of the second half of third observing run (O3b) GWTC-3 [5], the NSBH discovery paper [6] and the Sub-Solar Mass (SSM) search performed on O3a data [7].

Candidate Event Significance

Candidate events are assigned a statistical significance, determined by the rate at which detector noise produces events as loud as a given candidate event. The False Alarm Rate (FAR) depends on the pipeline response to non-stationary and non-Gaussian noise, and, given the unpredictability of this noise, it is not possible to model it analytically, therefore it must be empirically derived. The FAR is evaluated using information from data.

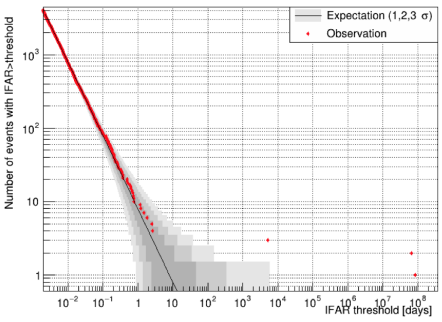

Figure 4: Inverse False Alarm Rate (IFAR) cumulative distribution for the MBTA offline running on the $O2$ data from August 13, 2017 06 : 09 : 42 to August 24, 2017 02 : 41 : 22. For a given IFAR threshold the red dots show the number of candidate events with IFAR equal or larger than the considered value. The black curve shows the expected number of events from background, and the grey bands represent the 1σ, 2σ, and 3σ statistical uncertainties around it (Poissonian errors are taken into account)

The Sub Solar Mass Search

In conventional stellar evolution models, the lightest ultracompact objects are formed when stellar remnants exceed the Chandrasekhar mass limit. The lightest remnants that exceed the Chandrasekhar mass limit form neutron stars. There is no widely accepted model for forming neutron stars below $1M_\odot$. Detecting ultracompact objects below one solar mass would challenge

our theories about stellar evolution, indicating a new formation mechanism, and potentially of new physic. One possible scenario for the formation of SSM black holes is the collapse of overdensities in the early universe, resulting in primordial black holes (PBHs).

So far, searches for compact binaries with at least one SSM component have been carried out in the O1 [8], O2 [9] and the first half of the third observing run (O3a) [7]. The lack of detections can be recast as an upper limit on the merger rate of compact binaries. The estimation of the merger rate can be done by computing the surveyed time-volume:

$$< VT >= T \int dz \frac{dV}{(1+z)dz} \epsilon(z) \quad (2)$$

where T is the analyzed time and $\epsilon(z)$ is the efficiency. The efficiency represents the fraction of astrophysical sources in the population which are detectable at a redshift z and it is estimated by simulating GW signals from a population of SSM compact binaries and adding them into the collected data. The search sensitivity is primarily a function of the chirp mass $\mathcal{M} = (m_1 m_2)^{3/5}/(m_1 + m_2)^{1/5}$, so that the population of simulated signals has been divided into 9 equally spaced bins. Each bin is treated as a separate population and the merger rate (at 90% confidence interval) is estimated as

$$R_{90,i} = \frac{2.3}{< VT >_i} \quad (3)$$

The final results are shown in Fig.4. Differences in background estimation lead to differences in the estimation of the merger rate by the involved pipelines.

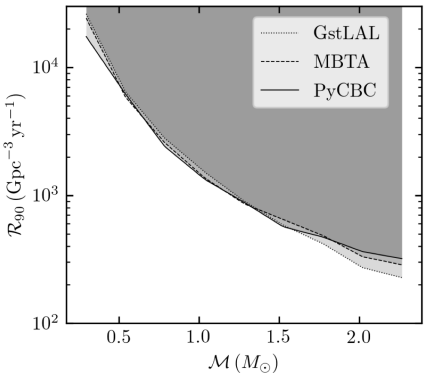

Figure 5: Upper limit on the merger rate of binaries with at least one SSM component as a function of source frame chirp mass. The dotted, dashed, and solid lines represent the 90% confidence limits obtained by the different pipelines involved in the search

Conclusions

During the Advanced LIGO and Advanced Virgo search for sub-solar mass ultra-compact objects in data from the first half of the third observing run, no unambiguous sub-solar mass gravitational wave candidates were identified by the three different algorithms employed in the search. The null result allowed us to place constraints on the abundance of such ultra-compact binaries and obtained upper limits on the merger rate of SSM black holes in the range $[220 - 24200] Gpc^{-3} yr^{-1}$. The upper limit depends on the chirp mass of the source as shown in Fig.4. For any astrophysical model that could generate SSM binaries, the merger rate upper limits can be used to set constraints on the model parameters. In this study we focused on two such models: formation of PBHs catalyzed by three-body interactions [10], and dark-matter black holes formed by late-time gravitational collapse of dark matter sub-structure [11]. Assuming PBHs produced at a single mass, and randomly distributed in space it has been found that the fraction of PBHs (as a fraction of the dark matter density) is $< 6\%$ for PBHs in equal-mass binaries with component objects in the range $[0.2 - 1.0] M_\odot$, while the upper limit on the fraction of the dissipative dark matter that ends up in black holes has is lowest limit at $1 M_\odot$, where it is $< 0.003\%$.

References

[1] Observation of Gravitational Waves from a Binary Black Hole Merger, Benjamin P. Abbott et al. in Phys. Rev. Lett., vol. 116, 2016

[2] Rencontres de Moriond Gravitational Waves and Experimental Gravity, F. Marion, 2003

[3] The MBTA pipeline for detecting compact binary coalescences in the third LIGO-Virgo observing run, Aubin, F and Brighenti, F and Chierici, R and Estevez, D and Greco, G and Guidi, G M and Juste, V and Marion, F and Mours, B and Nitoglia, E and et al., Classical and Quantum Gravity

[4] GWTC-2.1: Deep Extended Catalog of Compact Binary Coalescences Observed by LIGO and Virgo During the First Half of the Third Observing Run, The LIGO Scientific Collaboration and the Virgo Collaboration

[5] GWTC-3: Compact Binary Coalescences Observed by LIGO and Virgo During the Second Part of the Third Observing Run, The LIGO Scientific Collaboration and the Virgo Collaboration and the KAGRA Collaboration

[6] Observation of Gravitational Waves from Two Neutron Star-Black Hole Coalescences, R. Abbott, T. D. Abbott, S. Abraham et al, the Astrophysical Journal Letters

[7] Search for subsolar-mass binaries in the first half of Advanced LIGO and Virgo's third observing run, The LIGO Scientific Collaboration and the Virgo Collaboration and the KAGRA Collaboration

[8] Search for Subsolar-Mass Ultracompact Binaries in Advanced LIGO's First Observing Run, Abbott, B.P. and Abbott et al, Physical Review Letters

[9] Search for Subsolar Mass Ultracompact Binaries in Advanced LIGO's Second Observing Run, Abbott, B.P. and Abbott et al, Physical Review Letters

[10] Black hole binary formation in the expanding universe: Three body problem approximation, Ioka, Kunihito and Chiba, Takeshi and Tanaka, Takahiro and Nakamura, Takashi

[11] Gravitational Waves from Binary Mergers of Subsolar Mass Dark Black Holes, Shandera, Sarah and Jeong, Donghui and Gebhardt, Henry S. Grasshorn

Part IV

Hadronic Physics

session chaired by Maxime GUILBAUD

Multiplicity dependence of Υ production at forward rapidity in pp collisions at $\sqrt{s} = 13$ TeV with ALICE

Yanchun DING

Central China Normal University, Institut de Physique des Deux Infinis de Lyon

Abstract — In pp collisions at LHC energies, the production of heavy quarks happens during the hard scattering and then these quarks hadronize in either open heavy-flavour hadrons or quarkonia (e.g. J/ψ, ψ(2S), Υ). The study of quarkonium production as a function of charged-particle multiplicity links soft and hard processes and allows to study their interplay. While a linear increase of quarkonium production as a function of charged-particle multiplicity can be reasonably well understood in the context of multi-parton interactions, the observation of deviations with respect to a linear increase requires a more detailed description of the collision and the inclusion of additional mechanisms such as collective effects, color reconnection or percolation. In this contribution, we will present the latest ALICE measurements for J/ψ and Υ production as a function of charged-particle multiplicity in pp collisions at $\sqrt{s} = 13$ TeV. The self-normalized yield of J/ψ and Υ, defined as the ratio between the corresponding quarkonium yield in a given multiplicity interval to the multiplicity-integrated yield, are measured at forward rapidity ($2.5 < y < 4.0$) in the dimuon decay channel. The charged-particle multiplicity is measured in $|\eta| < 1$. The first measurement of the self-normalized yield ratios of Υ(2S) over Υ(1S) and J/ψ over Υ(1S) as a function of self-normalized charged-particle multiplicity will also be shown.

Introduction

The event-multiplicity dependent production of quarkonium and open heavy-flavor hadrons in small colliding systems such as pp and p–Pb is widely studied at the LHC. Indeed, it has the potential to give new insights on processes at the parton level and on the interplay between the hard and soft mechanisms in particle production. ALICE has studied the multiplicity dependence in pp collisions at $\sqrt{s} = 13$ TeV of inclusive J/ψ production at central rapidity [2], which shows a stronger than linear increasing trend. It is compared with various theoretical models, such as the coherent production model [3], the Color Glass Condensate (CGC) model [4], the 3-Pomeron CGC model[5], and PYTHIA 8.2 predictions [6, 7]. With similar motivations, the recent multiplicity dependence of Υ production at forward rapidity has been studied, aimed to improve the understanding of the underlying production mechanisms.

Analysis strategy

The Υ production at forward rapidity is studied as a function of charged-particle multiplicity measured at central rapidity. The Υ yield ($\mathrm{d}N_{\Upsilon}/\mathrm{d}y$) and the pseudorapidity charged-particle multiplicity density ($\mathrm{d}N_{\mathrm{ch}}/\mathrm{d}\eta$) are both measured for INEL>0 events. In this analysis, tracklets, i.e. track segments reconstructed in the ALICE Silicon Pixel detector (SPD) [1] with pseudorapidity $|\eta| < 1$, are used for the charged-particle multiplicity estimation. The pseudorapidity coverage of the SPD changes with the interaction vertex along z direction and with time, due to the varying number of dead channels. Therefore, a data-driven event-by-event correction is applied, similar to the one described in Ref.[8]. The first step of the multiplicity calibration is to correct for the detector inefficiency along the interaction vertex (z_{vtx}), by equalizing the number of tracklets variation as a function of z_{vtx} on an event-by-event basis. Then, using a Monte Carlo simulation based on the PYTHIA 8.2 [6] and EPOS-LHC [9] event generators, the correlation between the tracklet multiplicity (after the z_{vtx}-correction), $N_{\mathrm{trk}}^{\mathrm{corr}}$, and the generated primary charged particles N_{ch} is determined, as shown in Fig. 1. Finally, the self-normalized multiplicity is defined as the ratio between the charged-particle density ($\mathrm{d}N_{\mathrm{ch}}/\mathrm{d}\eta$) in a given multiplicity interval to the integrated one. The Υ is reconstructed in the rapidity range $2.5 < y < 4.0$ via the dimuon decay channel using the forward muon spectrometer [1]. The dimuon invariant mass distribution in the region relevant for Υ measurement is shown in Fig. 2 for the analyzed data sample. The number of Υ in each multiplicity interval is extracted from a log-likelihood fit to the corresponding invariant mass ($m_{\mu^+\mu^-}$) distribution. The signal shape is described by three Double Crystal Ball functions, one for each signal state, and the background shape is described by a Variable Width Gaussian function [10].

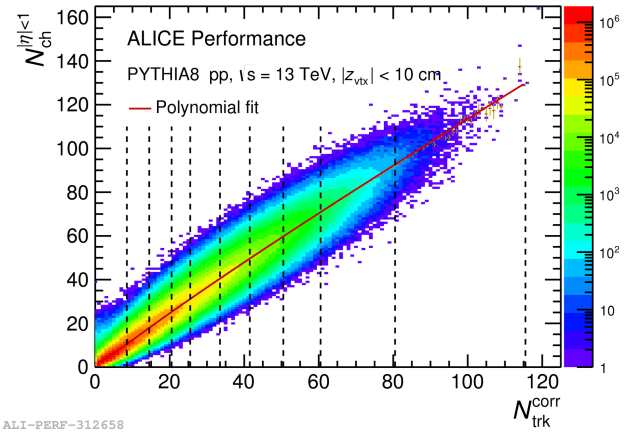

Figure 1: Number of charged particles $N_{\rm ch}$ as a function of trakclets $N_{\rm trk}^{\rm corr}$ as determined by a Monte Carlo simulation using PYTHIA 8.2 simulation with superimposed the best fit with a polynomial function.

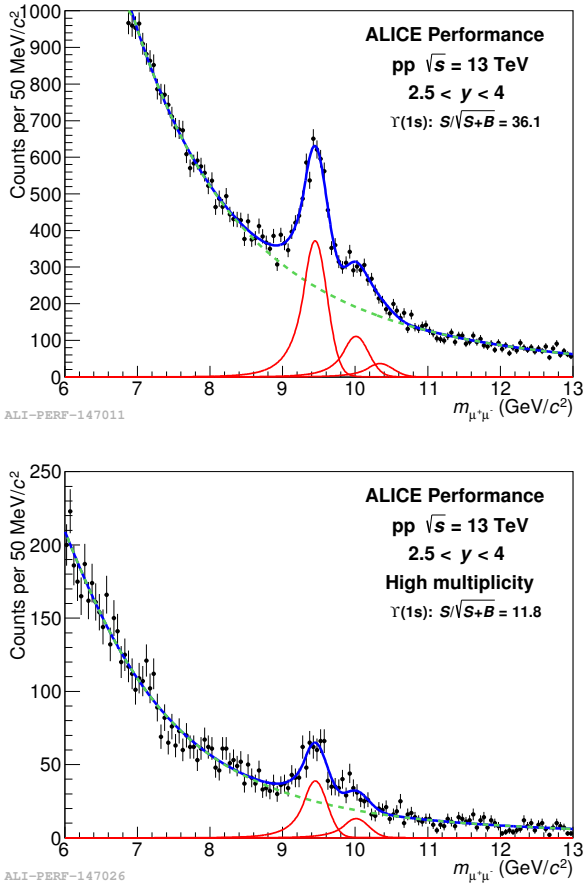

Figure 2: Dimuon invariant mass distribution for integrated over the multiplicity (top) and for high multiplicity pp collisions, corresponding to the $N_{\rm trk}^{\rm corr}$ interval bin $[34, 41]$ (bottom).

Results

The self-normalized yield of Υ is defined as the Υ yield in a given multiplicity interval to the multiplicity-integrated yield. As shown in Fig. 3, an approximately linear increasing behavior is observed for $\Upsilon(1S)$ (blue points), $\Upsilon(2S)$ (green points) and J/ψ (red points) at forward rapidity. However, a faster than linear increase is presented for J/ψ (purple points) at central rapidity, when there might be a correlation between the signal ($|y| < 0.9$) and the multiplicity estimator ($|\eta| < 1$). The different trends observed with the introduction of a rapidity gap might be explained as the result of largely eliminating the auto-correlation effects [7]. The self-normalized yield ratios of $\Upsilon(2S)$ over $\Upsilon(1S)$ and $\Upsilon(1S)$ over J/ψ, as shown in Fig. 4 and 5, respectively, are independent on multiplicity and compatible with unity within uncertainties. It reveals that there is no dependence on resonance mass and quark component within uncertainties.

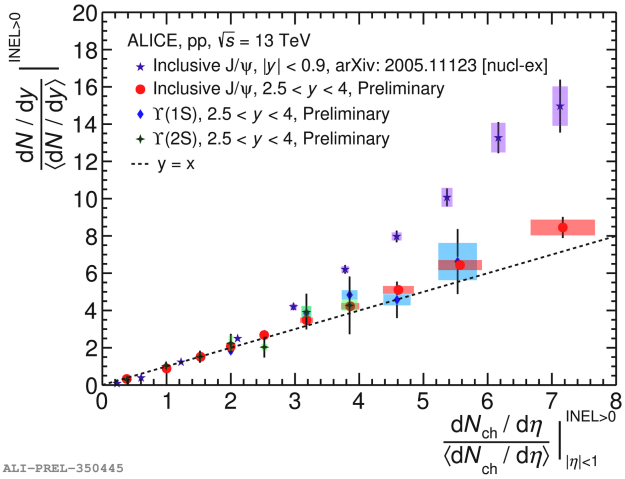

Figure 3: Self-normalized yield of Υ and J/ψ as a function of self-normalized charged-particle multiplicity. The error bars represent the statistical uncertainty on the quarkonium yields, while the quadratic sum of the point-by-point systematic uncertainties on the quarkonium yields as well as on $\mathrm{d}N_{\rm ch}/\mathrm{d}\eta$ / $\langle \mathrm{d}N_{\rm ch}/\mathrm{d}\eta \rangle$ is depicted as boxes.

Conclusions

In this contribution, the first results of the $\Upsilon(1S)$ and $\Upsilon(2S)$ production as a function of charged-particle multiplicity have been presented. A different behavior is observed compared with the J/ψ at central rapidity. In addition, the self-normalized yield ratios of $\Upsilon(1S)$ over J/ψ and $\Upsilon(2S)$ over $\Upsilon(1S)$ as a function of charged-particle multiplicity are found to be compatible with unity within uncertainties. Last but not least, it should be noted that the measurements suffer from limited statistical significance, so that it is hard to draw any firm conclusion on the quarkonium production. A lager data

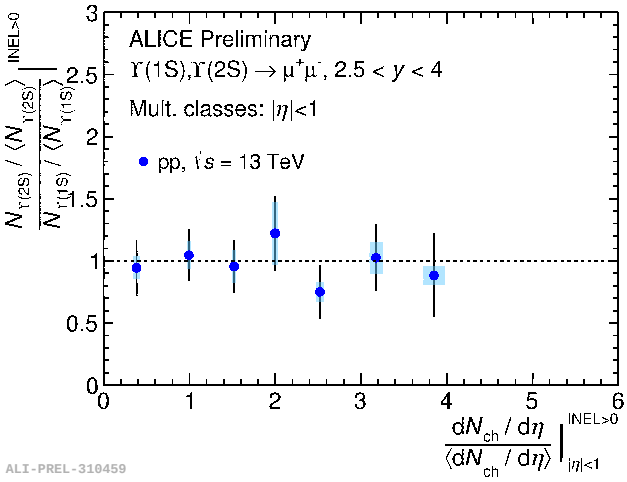

Figure 4: Self-normalized yield ratio of Υ(2S) over Υ(1S) as a function of self-normalized charged-particle multiplicity. The error bars represent the statistical uncertainty on the self-normalized yield ratio, while the quadratic sum of the point-by-point systematic uncertainties on the self-normalized yield ratio as well as on $\mathrm{d}N_{\mathrm{ch}}/\mathrm{d}\eta$ / $\langle \mathrm{d}N_{\mathrm{ch}}/\mathrm{d}\eta \rangle$ is depicted as boxes.

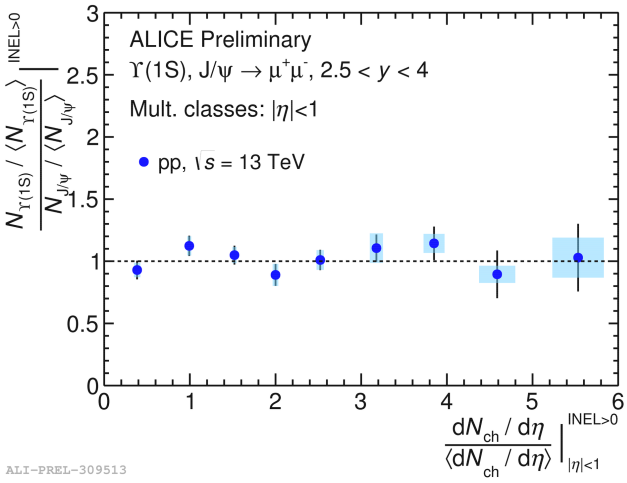

Figure 5: Self-normalized yield ratio of Υ(1S) over J/ψ as a function of self-normalized charged-particle multiplicity. The error bars represent the statistical uncertainty on the self-normalized yield ratio, while the quadratic sum of the point-by-point systematic uncertainties on the self-normalized yield ratio as well as on $\mathrm{d}N_{\mathrm{ch}}/\mathrm{d}\eta$ / $\langle \mathrm{d}N_{\mathrm{ch}}/\mathrm{d}\eta \rangle$ is depicted as boxes.

sample is required for this analysis to improve the precision of the measurements and to draw firm conclusions.

References

[1] B. B. Abelev *et al.*, ALICE Collaboration, Int. J. Mod. Phys. A **29**, 1430044 (2014)

[2] S. Acharya *et al.* ALICE Collaboration, Phys. Lett. B (2020) 135758

[3] B. Z. Kopeliovich, H. J. Pirner, I. K. Potashnikova, K. Reygers, and I. Schmidt, Phys. Rev. D 88 (2013) 116002

[4] Y. Q. Ma, P. Tribedy, R. Venugopalan, and K. Watanabe, Phys. Rev. D 98 (2018) 074025

[5] M.Siddikov, E. Levin, and I. Schmidt, Eur. Phys. J. C 80 (2020) 6, 560

[6] T. Sjöstrand, S. Ask, J. R. Christiansen, R. Corke, N. Desai, P. Ilten, S. Mrenna, S.Prestel, C. O. Rasmussen, and P. Z. Skands, Comput. Phys. Commun. 191 (2015) 159-177

[7] S. G. Weber, A. Dubla, A. Andronic, and A. Morsch, Eur. Phys. J. C 79 (2019) 36

[8] B. Abelev *et al.*, ALICE Collaboration, Phys. Lett. B **712**, 165-175 (2012)

[9] T. Pierog, Iu. Karpenko, J. M. Katzy, E. Yatsenko, and K. Werner, Phys. Rev. C 92, 034906

[10] ALICE Collaboration, Phys. Rev. Lett. 123, 192301 (2019)

MFT detector commisioning in ALICE and J/ψ polarisation measurement in ultra-peripheral Pb-Pb collisions at 5.02 TeV

Lucrezia Camilla MIGLIORIN

Institut de Physique des Deux Infinis de Lyon

Abstract — Ultra-relativistic heavy-ion collisions are an important tool to investigate the Quark-Gluon Plasma predicted by the theory of Quantum Chromo-Dynamics. It is also possible to use these collisions to study poorly known gluon shadowing effects at low Bjorken-x values. Indeed Ultra-Peripheral Collisions (UPC) between two lead nuclei, in which the impact parameter is larger than the sum of their radii, provide a useful way to study photonuclear reactions. In this paper, a study based of the angular modulation of the muons originating from decays of photoproduced J/ψ mesons is presented. It uses data collected during Run 2 by the ALICE Collaboration at forward rapidity. Finally, The addition and commissioning of the Muon Forward Tracker detector in ALICE for Run 3 and Run 4 at forward rapidity is discussed. This new detector will improve the spatial resolution and thus allow more precise studies of the photoproduction in UPC.

Introduction

The main goal of experimental physics is to test and constrain theories while raising new questions. One of the central questions concerns the origin of our Universe and the most commonly accepted "Big Bang" theory. Understanding the nature and the properties of the fundamental components of nuclear matter (called quarks and gluons) allows to better understand and describe the first moments of the Universe [1]. According to this theory, a few microseconds after the Big Bang, the medium was so dense and so hot that the quarks and gluons evolved freely with respect to each other; this state of matter is called Quark Gluon Plasma (QGP). The expansion of the Universe would then have led to its cooling and the confinement of quarks and gluons in the hadrons that make up ordinary nuclear matter.
The physics of ultra relativistic heavy ion collisions came from the questions raised by astrophysics and hadronic physics about the collective properties and the conditions of existence of the excited nuclear matter. The idea is to reproduce the conditions in which the Universe was a few moments after the Big Bang in order to characterize the QGP. Due to QGP's very brief lifetime ($\tau \sim 10$ fm/c), its properties cannot be accessed directly. Some observables, as *charmonia* ($c\bar{c}$ bound states), have been identified to probe and characterize the presence of QGP. Created during the first stages of the collision, these heavy quark hadrons experience the whole development of the hot QCD medium. To get a deeper understanding of the fundamental mechanisms of hot QCD plasma, it is obvious that a comprehensive evaluation of charmonia properties is important. Among the attributes that may be studied on charm hadrons is the polarisation, which can be investigated via so-called UPC.
Indeed, different types of interactions are possible in heavy ion collisions. The most prominent interaction mechanism is of the hadronic type, governed by the strong nuclear force and occur essentially between nucleons. Nevertheless, there is also the photon-nucleon interaction. This process is called and originate from the intense magnetic field surrounding the travelling ions *photoproduction*. Using the Weiszäcker-Williams approximation [3], the powerful electromagnetic field can be studied and it has been shown that the photon flux is proportional to the squared nuclear charge (Z^2) and the charge distribution. As the photoproduction results from a process that is simultaneously reliant on QED (photon flux) and QCD (photon-nuclear cross section), the overall cross-section is produced as a result of $n_\gamma(\pm y, b)$ and $\sigma_{\gamma A}(\pm y)$. As already mentioned above, the simplest way to observe this kind of interaction is given by UPC, *i.e.* collisions where the impact parameter is greater than the sum of the two radii of the nuclei ($b > R_1 + R_2$) and thus hadronic interactions are strongly suppressed. A quasi-real photon can oscillate into a quark anti-quark pair that will scatter off the second nucleus that produces vector mesons, like J/ψ. In the following, a study of photo-produced J/ψ polarization is presented.
Furthermore, starting from 2022, the Large Hadron Collider (LHC) [19] will enter a new era by achieving its maximum energy and luminosity. New detectors and technologies have been installed in the ALICE cavern to cope with the new accelerator condition and

improve the detectors performances. This newly installed systems in the ALICE experiments should improve the encouraging results obtained during Run 1 and 2. One of the new detectors is the Muon Forward Tracker (MFT) [4], calibrated in IP2I in Lyon. In the last part of this paper, this new system and its calibration will be presented.

UPC and incoherent J/ψ production

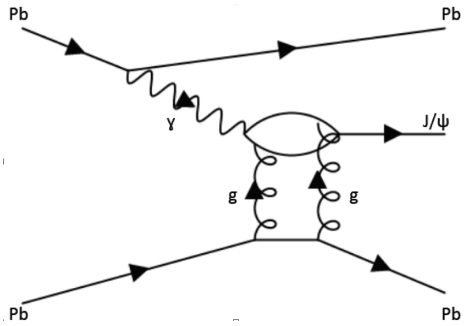

Figure 1: Mechanism of production of J/ψ mesons in UPC.

In Figure 1, the Feynman diagram represents the creation of J/ψ mesons in UPC. There are two types of physical processes behind UPCs: *coherent* creation, in which the photon interacts with the entire nucleus and *incoherent* creation, in which the photon interacts with a single nucleon. Coherent and incoherent J/ψ photoproduction can give answers to the calculation of cross section in gluon Parton Distribution Function within the target hadron [5]. The $\sigma_{\gamma A}$ should be proportional to the square of the gluon density in the nucleus at a value of Bjorken-x with $x(\pm y) = m_{J/\psi}/\sqrt{s_{\rm NN}}\exp(\pm y)$. In addition to this, ($\gamma$+Pb $\longrightarrow$ J/ψ $\longrightarrow$ $\mu\mu$) provides a powerful tool to study poorly known gluon shadowing effects at low Bjorken-x [6].
The vector meson average transverse momentum is inversely proportional to the nucleus radius i.e. $<p_{\rm T}>\propto 1/R_{\rm nucleus}$. This property explain why such production happens mostly at low p_T. Figure 2 shows the $p_{\rm T}$ distribution for opposite sign dimuons in UPC Pb-Pb measured with ALICE around the J/ψ mass. The coherent and incoherent processes are separated by $p_{\rm T}$ values: the coherent part dominates at a very low $p_{\rm T}$ and, the incoherent part is more important starting from 0.5 GeV/c in $p_{\rm T}$. Therefore, we can disentangle the two contribution and study them separately.

ALICE experiment

A Large Ion Collider Experiment (ALICE) [20] is one of the four big experiments at the LHC. This experiment is mainly dedicated to heavy-ion physics. Heavy-ion collisions are used to study the QGP state as the energy density achieved at the LHC allows the formation

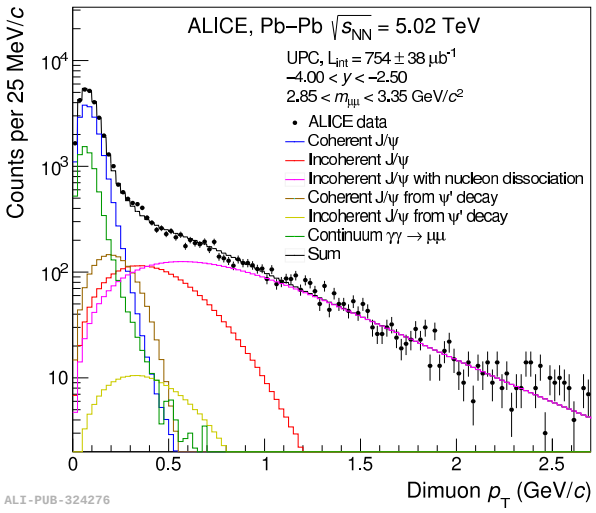

Figure 2: Transverse momentum distribution for muon pairs in the range 2.85 < $m_{\mu\mu}$ < 3.35 GeV/c^2(around the J/ψ mass) [from [7]].

of such a state. However, ALICE's physics program is not limited to Pb-Pb collisions as p-p and p-Pb measurements are performed to provide a reference to the Pb-Pb system and to study cold nuclear effects respectively.

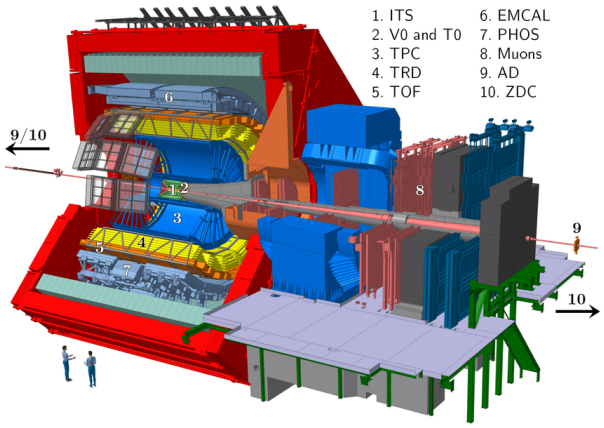

Figure 3: ALICE apparatus during the RUN2 of LHC.

In Figure 3 shows the ALICE detector. It is composed of two main parts : the central barrel around the interaction point and a forward rapidity muon spectrometer [21]. The later can be used to study quarkonia states via their dimuon decay channel. The muon spectrometer cover a pseudo-rapidity range of -4<η<2.5 and the full azimuth.
For the analysis of incoherent J/ψ mesons in UPC, the data selected are those reconstructed with the muon spectrometer in 2015 and 2018 in Pb-Pb collisions at $\sqrt{s_{\rm NN}}$ = 5.02 TeV, selecting all data with a dimuon $p_{\rm T}$ higher than 0.35 GeV/c.

Analysis purpose and results

The STAR Collaboration [22] discovered a transverse angular modulation [23] due to the extreme Lorentz

contraction of electromagnetic fields in UPC. Indeed, the photons are polarized *i.e.* they have a privileged distribution of orientation in space so they will scatter to produce vector mesons in a privileged direction. The angular modulation is defined by the $\Delta\varphi$ angle described in Figure 4.

The analysis is done in helicity frame direction, that implies the J/ψ are expected to be produced transversely in comparison to their own momentum direction. [8].

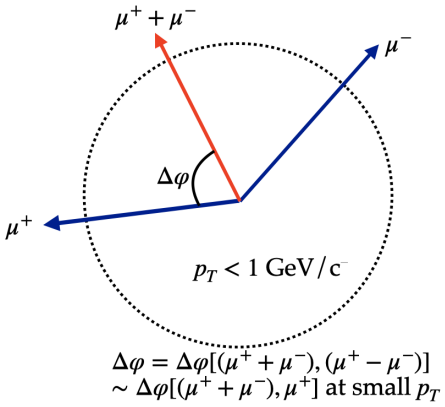

Figure 4: Definition of the angle that represents the angular modulation shown by STAR Collaboration [9]

In helicity frame, $\Delta\varphi$ is extremely correlated with φ angle: this implies that the amplitude of $\cos(\Delta\varphi)$ modulation is almost equivalent to the λ_φ polarization parameter. There are indeed three polarization parameters $(\lambda_\theta, \lambda_\varphi, \lambda_{\theta\varphi})$ from three angles $(\theta, \varphi, \widetilde{\varphi})$. The most general distribution of the helicity frame is reported in equation 1:

$$W(\cos\theta, \varphi) \propto \frac{1}{3+\lambda_\theta}(1+\lambda_\theta \cos^2\theta + + \lambda_\varphi \sin^2\theta \cos 2\varphi + \lambda_{\theta\varphi} \sin 2\theta \cos\varphi) \quad (1)$$

Starting from formula 1, J/ψ mesons have the same polarisation as the quasi-real photon that generates the photoproduction reaction but there are two possible scenarios:

1. $\lambda_\theta, \lambda_\varphi, \lambda_{\theta\varphi} = (1, 0, 0)$ transverse polarization;
2. $\lambda_\theta, \lambda_\varphi, \lambda_{\theta\varphi} = (-1, 0, 0)$ longitudinal polarization.

A first extraction of these polarization parameter have been attempted starting with the invariant mass spectrum given in Figure 5. This spectrum is produced using UPC events that were collected by the ALICE muon spectrometer in 2015 and 2018 period. An amount of 6081±97 reconstructed J/ψ mesons have measured. The polarisation parameter extraction is currently ongoing.

ALICE experiment after the LS2

Starting from Run 3, the LHC luminosity will be improved by a factor 10 to 100. During the year 2021, ALICE finalised its major upgrades in order to collect

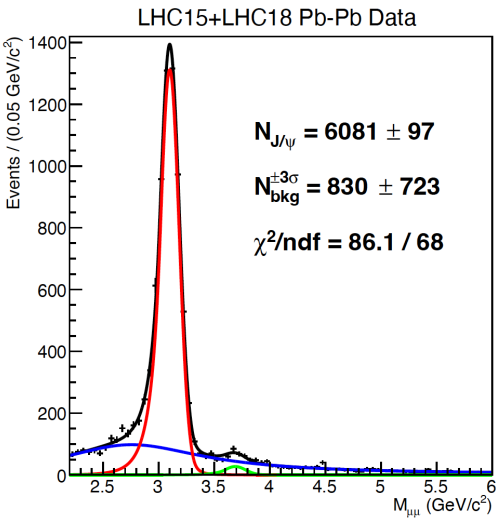

Figure 5: Invariant mass distribution of opposite dimuons for p_T>0.35 GeV/c and -4<y<-2.5 in ultra-peripheral Pb-Pb collisions at $\sqrt{s_{NN}}$=5.02 TeV.

interaction rates of 50 kHz in Pb-Pb collisions. Here, is the list of the most important detectors installed during this Long Shutdown 2 (LS2):

- The Gas Electron Multiplier (GEM) detectors have been installed in TPC [10];
- the Inner Tracker System (ITS) has been replaced by seven new layers of ALPIDE sensors [11] for an improved tracking efficiency and resolution;
- a *new forward rapidity tracker called MFT* has been installed in order to add vertexing capabilities to the current Muon Spectrometer.

The new MFT detector

The MFT detector is installed between the interaction point and the front absorber of the muon arm [12]. It is made of two half-MFT cones surrounding the beam pipe. Each half-MFT cone consists of 5 half-disks placed along the beam axis, in the direction of the muon spectrometer with the two first half-disks placed at $z = -46$ cm from the nominal interaction point. In each half-MFT, the first two half-disks are identical while the remaining three half-disks have a larger radius [13]. The basic detection element of the MFT is a silicon Monolithic Active Pixel Sensor (MAPS), identical to that of the new ALICE Inner Tracking System (ITS) [14, 15], called ALPIDE. Chosen for its granularity, material thickness, read-out speed, power consumption and radiation hardness, the chip ALPIDE contains a matrix of 512×1024 sensitive silicon pixels and it measures 30×15 mm^2. The sensor ladders consist of 2, 3, 4 or 5 silicon pixel sensors bonded to a Flexible Printed Circuit (FPC) with aluminium strips, covering an active total surface of 0.4 m^2.

Two major Physics goals of MFT have been highlighted by the Collaboration [16].

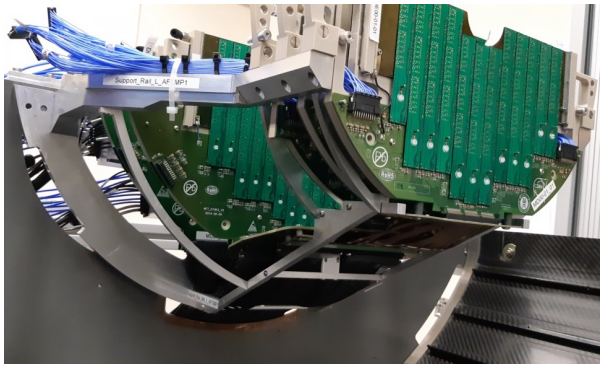

Figure 6: Picture of one assembled half-MFT during the commissioning at CERN.

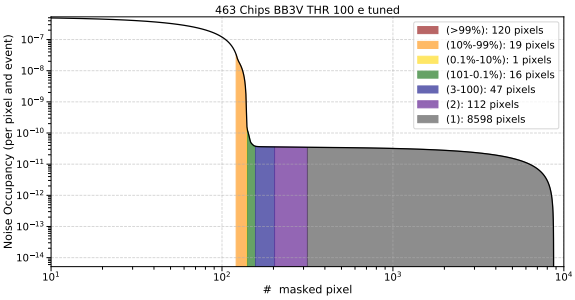

Figure 7: Evolution of the fake-hit rate for one half-cone with the back-bias applied ($V_{BB} = -3\,V$) as a function of the number of noisy pixels being masked, starting from the noisiest ones.

The first one is the charm and beauty hadron production separation. The measurement of non-prompt J/ψ production from is a well-established tool for beauty production measurement in high-energy nuclear collisions [17]. Thanks to the MFT, it will be possible to achieve the statistical separation between prompt and non-prompt J/ψ produced at the collision. This separation is based on the measurement of the distance between the primary vertex and the secondary vertex corresponding to B hadron decay.

Other goals have been identified when the MFT has been designed [18]. For example, using this new detector, a measurement of the QGP thermal radiation and the spectral structure of low-mass vector mesons can be conducted or the measurements of charm (semi-muonic decays) and beauty (semi-muonic and J/ψ decays) p_T-differential production yields will be used to explore the medium density and the mass dependency of in-medium parton energy loss [16]. The ALPIDE qualification was conducted at IP2I in Lyon. The functioning quality of the digital and analog parts of the ALPIDE sensors operated on the half-disk assemblies were studied in details. For each chip, a vote was cast based on the number of dead or ineffective pixels. A sensor with less of 50 defective pixels is considered gold; when the "broken" pixels are between 50 and 1500, the chip is called silver, finally if there are more than 1500 imperfect pixels, the sensor is bronze. Thanks to this work, it is fair to say that the MFT detector is a gold detector with silver areas. Only 3 sensor chips out of 936 have been classified as bronze and 6 ALPIDE have problems on the slow control lines, so the communication with them is impossible. As much as 99% of the surface covered with pixels is operational. Such good performances insure that the detector will fulfill its intended goals. In particular, it will be able to provide precision results for the study of the non-prompt decays in the forward rapidity region.

As an illustration of the MFT high performances, Figure 7 shows the pixel noise occupancy as a function of number of masked pixel. It is feasible to run the detector at a fake-hit rate of 10^{-10} evt^{-1} pixel^{-1}, *i.e.* several orders of magnitude below the design requirement.

The MFT detector was installed in December 2020 in ALICE cavern and is ready to record the new upcoming data expected during 2022.

Conclusion

Quarkonia are an excellent probe to study the QGP and its characteristics. J/ψ mesons produced in Pb-Pb UPC evebts are useful to understand the gluon density in the PDFs. Despite the fact that the results on the polarisation parameters cannot yet be compared with those reported in previous research, the analysis of the incoherent component is crucial in order to determine whether or not the experimental results and theoretical predictions are consistent. With the installation of the new MFT detector in the ALICE cavern, improved measurements of J/ψ are expected in order to understand the hadronic but also the photon-nucleon interactions. The first Run 3 collisions are expected to occur in spring 2022. Based on results obtained during the commissioning, the MFT should met its expected performances and produce high quality data to be analyzed within the ALICE Collaboration.

References

[1] Linder, EV, *Exploring the Expansion History of the Universe*, 2003, Phys. Rev. Lett. 90, 091301, `https://journals.aps.org/prl/abstract/10.1103/PhysRevLett.90.091301`

[2] Bjorken, JD, *Highly relativistic nucleus-nucleus collisions: The central rapidity region*, 1983, Phys. Rev. D 27, 140, `https://journals.aps.org/prd/abstract/10.1103/PhysRevD.27.140`

[3] Ahern, SC, *An Electroweak Weizsacker-Williams Method*, 2002, `https://arxiv.org/abs/hep-ph/0211133`

[4] ALICE Collaboration, *Technical Design Report for the Muon Forward Tracker*, 2015, `https://cds.cern.ch/record/1981898?ln=en`

[5] Ryskin, MG *et al.*, *Diffractive J/ψ photoproduction as a probe of the gluon density*, 1997, Zeitschrift für Physik C Particles and Fields, https://link.springer.com/article/10.1007/s002880050547

[6] Guzey, V *et al.*, *Evidence for nuclear gluon shadowing from the ALICE measurements of PbPb ultraperipheral exclusive J/ψ production*, 2013, Physics Letters B, https://arxiv.org/abs/1305.1724

[7] ALICE Collaboration, C*oherent J/ψ photoproduction at forward rapidity in ultra-peripheral Pb-Pb collisions at* $\sqrt{S}NN$*=5.02 TeV*, 2019, Phys.Lett. B798 (2019) 134926, https://arxiv.org/abs/1904.06272

[8] Li, C *et al.*, *Probing the linear polarization of photons in ultraperipheral heavy ion collisions*, 2019, https://arxiv.org/abs/1903.10084

[9] Brandenburg, D, *Probing the Nucleus with Linearly Polarized Photons*, 2021

[10] ALICE Collaboration, *Upgrade of the ALICE Time Projection Chamber for the LHC Run 3*, 2004, https://arxiv.org/abs/2004.10520

[11] Suljic, M, *ALPIDE: the Monolithic Active Pixel Sensor for the ALICE ITS upgrade*, 2018, https://www.researchgate.net/publication/303121925_ALPIDE_the_Monolithic_Active_Pixel_Sensor_for_the_ALICE_ITS_upgrade

[12] Uras, A, *ALICE MFT Project: Motivations and Epxectations*, 2012

[13] Slupecki, M, *ALICE forward rapidity upgrades*, 2018, PoS

[14] Rinella, G, *The ALPIDE pixel sensor chip for the upgrade of the ALICE Inner Tracking System*, 2018, Nuclear Instruments and Methods in Physics Research Section A: Accelerators, Spectrometers, Detectors and Associated Equipment

[15] Mager, M, *ALPIDE, the Monolithic Active Pixel Sensor for the ALICE ITS upgrade*, 2016, Nuclear Instruments and Methods in Physics Research Section A: Accelerators, Spectrometers, Detectors and Associated Equipment

[16] Tieulent, R, *ALICE Upgrades: Plans and Potentials*, 2015, arXiv:1512.02253

[17] CMS Collaboration, *Suppression of non-prompt J/psi, prompt J/psi, and Y (1S) in PbPb collisions at* $\sqrt{}$ *(sNN)= 2.76 TeV*, 2012, arXiv:1201.5069

[18] ALICE Collaboration, *Addendum of the Letter of Intent for the upgrade of the ALICE experiment : The Muon Forward Tracker*, 2013, https://cds.cern.ch/record/1592659?ln=en

[19] Lyndon Evans, *The large hadron collider*, 2007, New Journal of Physics, 10.1088/1367-2630/9/9/335/meta

[20] ALICE Collaboration, *The ALICE experiment at CERN LHC*, 2008, Journal of Instrumentation, 10.1088/1748-0221/3/08/S08002/meta

[21] Christian Finck, *The Muon Spectrometer of the ALICE*, 2006, Journal of Physics: Conference Series, 10.1088/1742-6596/50/1/056/meta

[22] STAR Collaboration, *The STAR Collaboration*, 2009, 10.1016/j.nuclphysa.2009.10.156

[23] STAR Collaboration, *Measurement of* e^+e *Momentum and Angular Distributions from Linearly Polarized Photon Collisions*, 2019, Phys. Rev. Lett. 127 (2021) 052302, 10.1103/PhysRevLett.127.052302

Cluster shape analysis and strangeness tracking for the ALICE upgrade

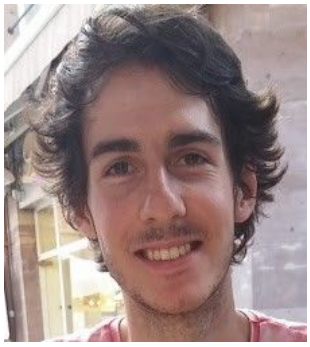

Alexandre BIGOT

IPHC, Université de Strasbourg

Abstract — ALICE (*A Large Ion Collider Experiment*) is one of the main experiments of the LHC (*Large Hadron Collider*) at CERN (*European Organization for Nuclear Research*). The purpose of ALICE is to study the properties of strongly interacting matter by performing different kinds of measurements in proton-proton, proton-nucleus and nucleus-nucleus collisions. In prevision of the Run 3 of the LHC, that will start in 2022, many detectors of ALICE were upgraded, the ITS (*Inner Tracking System*) being one of those. The ITS is built of ALPIDE (*ALICE Pixel Detector*) silicon sensors that allow particle detection by means of their pixels. When several neighbouring pixels are activated during the same particle crossing, they form a cluster. First, the shape of these clusters are studied with real data from the commissioning and simulation generated by the ALICE's Monte Carlo code. We investigate the dependence of cluster's shape on various parameters such as the dimensions of the pixels and especially the inclination of particle tracks with respect to the surface of sensors. In addition, using the recent upgrades of the ITS, a study of the decay channel: $\Xi_b^- \rightarrow (\Xi_c^0 \rightarrow \Xi^-\pi^+)\pi^-$ is performed. The goal is to create an analysis prototype using a state-of-the-art detector and a brand new technique called strangeness tracking. This technique is meant to improve the efficiency and precision of the reconstruction of weakly decaying particles (such as Ξ^- or hypertritons). The resulting gain in the precision of secondary vertex reconstruction will allow for a large suppression of combinatorial background when detecting short-living heavy-flavour baryons, such as Ξ_b^- decaying to Ξ_c^0 and π^-.

Introduction

The goal of the ALICE (*A Large Ion Collider Experiment*) experiment at the *Large Hadron Collider* (LHC) at CERN (*European Organization for Nuclear Research*) is to study strongly interacting matter created during collisions of heavy nuclei up to the center-of-mass energy of about 5 TeV per nucleon. Under these extreme conditions, a new phase of matter, named Quark Gluon Plasma (QGP), is formed. This plasma is believed to have prevailed during the first microseconds after the Big Bang [1].

The detection of heavy-flavour hadrons (charm and beauty) allows to probe QGP properties [1]. Heavy quarks are produced at the very beginning of the collision, during the most energetic (hard scattering) processes. Subsequently interacting with the QGP medium, heavy-flavour quarks finally hadronize. The production rate and kinematic characteristics of the resulting particles are thus modified by the medium, which can be measured and traced back to the QGP properties. The magnitude of these modifications depends, among other things, on the mass of the involved quarks. This makes the studies of production of heavy-flavour particles particularly advantageous. The detection of these particles need a detector fast and precise enough because they have a low production rate and a very short life time. In ALICE, the heavy-flavour particles are detected using the ITS that allows for track reconstruction[1] of charged particles as well as the positions of the primary and secondary interaction vertices[2]. The first version of the ITS, used during the Runs 1 and 2 of the LHC, presented some limitations on data read-out rate and the distinction between primary and secondary vertices. These technical limitations result in a lesser quantity and quality of the recorded data and therefore impact the physical interpretation of these data. In order to probe more deeply the QGP, upgrades were undertaken and gave birth to a new version of the Inner Tracking System [1].

The first part of the following document is about the ITS upgraded, its characteristics, its functioning and its validation with cosmic-ray data. The second part presented here, concerns the strangeness tracking with ALICE 3 [2] by studying a specific decay channel: $\Xi_b^- \rightarrow (\Xi_c^0 \rightarrow \Xi^-\pi^+)\pi^-$.

[1] The ITS performs *tracking* along with other ALICE detectors.

[2] The primary vertex is the location of the collision where particles are produced. The secondary vertex of a particle is the point where this particle decays.

Cluster shape analysis

During the ITS commissioning at CERN in 2020, series of measurements of cosmic particles (typically muons) were performed. The ITS is paved with ALPIDE (*ALICE Pixel Detector*) chips [3]. These silicon chips are composed of $512 \times 1\,024$ pixels activating when a charged particle crosses the semiconductor sensor, forming clusters of several shapes. The stored data contain information on the position of the fired pixels and the resulting cluster shape. The main purpose of this work was to study these cluster shapes as a function of several factors such as the inclination of the particle tracks with respect to the surface of the sensor. A track inclination in the direction of a row (resp. a column) of pixels is designated as angle λ (resp. ψ).

The study of the pixel cluster shapes and its impact on the tracking precision was studied. First, a calibration process needed to be implemented in order to suppress the omnipresent noise. The determination of noise maps and their subsequent use allowed us to get rid of a large noisy pixel amount. Then, track candidates are selected and defined as the association of three clusters (one on each detection layer) that fall onto a same straight line. They are studied to access the cluster shapes of clusters originating from particles.

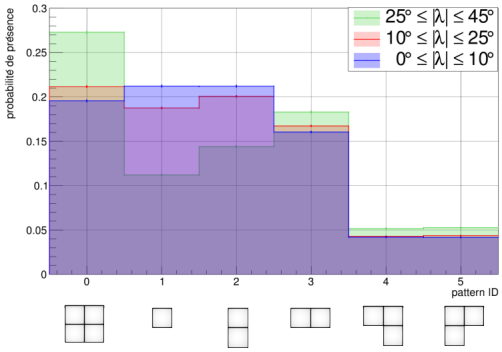

Figure 1: Probability of different cluster shapes as a function of track inclination λ.

The obtained results showed that the cluster shape depends on the track inclination angles λ and ψ and the pixels geometry. Indeed, one can conclude that the cluster's elongation along rows (resp. columns) becomes more important when the inclination angle λ (resp. ψ) increases in absolute value. The Figure 1 highlights this rising elongation, in the rows direction, for rising intervals of $|\lambda|$. Moreover, the elongation along columns is favored with respect to the one along rows. This appears as an immediate consequence of the pixels geometry as they are shorter along columns than along rows.

In the light of these results, real data coming from the ITS commissioning are compared with simulated data using the ALICE Monte Carlo code. For all the angle intervals studied, this code better reproduces the biased real data than the unbiased ones. Here, the bias corresponds to a potential difference applied to the semiconductor width of a chip in order to compensate the radiation damage underwent by the sensors through time. On top of that, the reliability of the Monte Carlo code diminishes while the track inclination rises. Therefore, some optimisation of this code free parameters is needed in order to bring the generated data in better agreement with real data.

This worked has opened new perspectives. The obtained dependence of cluster shapes on the track inclinations could be integrated in the tracking algorithm as some cluster shapes offer a better precision regarding particle detection. Besides, knowing the cluster shape distribution as a function of the track inclination can increase the probability that the algorithm assigns the cluster to the right track during the track reconstruction process. On top of that, the results coming from the comparison of real data and simulated data could be used to improve the ALICE Monte Carlo simulations in order to better describe the properties of the real detector. It is important to work with a reliable Monte Carlo code because this code induces systematic errors in the measurements when one uses it for physical corrections on real data.

Strangeness tracking in ALICE 3

Simulation of collisions

The data analyzed in the following are exclusively coming from a Monte-Carlo simulation[3] that can be summarised as follows: (i) a minimum bias Pythia[4] event with up to one particle on interest (Ξ_b^- here) added to the underlying event; (ii) propagating the generated particles with GEANT3; (iii) simulating hits with the experimental geometry (beam pipe + ALICE 3) and simulation of the detector response by digitizing these hits.
When generating Ξ_b^- particles, we require that these Ξ_b^- decay according to the wanted channel $\Xi_b^- \rightarrow \Xi_c^0(\Xi^-\pi^+)\pi^-$[5]. This is done by means of instructions inside the generator by using a specific syntax[6].

A quite large sample of simulated data was needed for these studies. Among 200 simulated events[7], a min-

[3]This allows us to go beyond the current geometry of ALICE and study collisions with the ITS3 (the future version of the ITS that should be installed during LS3 of LHC [4], [5]) whose innermost layer is positioned at 18 mm radial distance from the interaction point (even closer than ITS2). The foreseen geometry of ALICE after LS3 is called ALICE 3.

[4]Pythia is a simulation code used to simulate pp collisions.

[5]Then $\Xi^- \rightarrow \Lambda\pi^-$ with a branching ratio above 99.8% and Λ mainly decays into $p\pi^-$ with a branching ratio of about 64%.

[6]Each particle is identified by a "PDG code" [6] and specific command lines are used to declare (and possibly impose) a decay channel [7]. Information on the particles can be found in [8].

[7]An event is a collision that triggered the detection apparatus. We can have either zero event (no trigger) or one event (trigger) for a given collision, if pileup is not considered.

imum of 200 Ξ_b^- and 200 Ξ_c^0 particles were produced[8], meaning Pythia generated the wanted amount of particles[9] to study the decay channel of interest.

Reconstruction of a decay channel

In addition to a particle of interest, many other particles are produced in a collision. Random associations of tracks from "non-interesting" particles produce a large combinatorial background. Hence, an implemetation of a special procedure minimizing this background is needed, so called "topological reconstruction".

Ξ_b^- can decay via many channels, leading to a particle cascade. The whole cascade underpinned by Ξ_b^- is not reconstructed. Indeed, only a specific *branch* of this *family tree* by going from the tip of the *branch* to the roots of the *tree* is reconstructed. This specific *branch* corresponds to the decay channel presented Figure 2.

[scale=0.6]decay$_c$*hannel.svg*

Figure 2: Sketch of the decay channel $\Xi_b^- \rightarrow (\Xi_c^0 \rightarrow \Xi^-\pi^+)\pi^-$. The indicated flight distances are not at a right scale.

Via this channel, one aims at studying Ξ_b^- disintegrating according to $\Xi_b^-(\mathsf{dsb}) \rightarrow \Xi_c^0(\mathsf{dsc})\pi^-(\bar{\mathsf{u}}\bar{\mathsf{d}})$. Then the Ξ_c^0 decays in two particles with opposite charges such as $\Xi_c^0(\mathsf{dsc}) \rightarrow \Xi^-(\mathsf{dss})\pi^+(\bar{\mathsf{u}}\bar{\mathsf{d}})$. The Ξ_b^- cascade is composed of a succession of V shaped decays. In such a cascade, one could consider Ξ_b^- as a mother living over a distance of about 470 μm before giving birth to her daughters Ξ_c^0 and π^-. At this stage, only π^- is detected because of its non-zero electric charge (contrary to Ξ_c^0 that is electrically neutral, hence undetected[10]): it is called the *bachelor* particle. After travelling a distance of about 46 μm, the Ξ_c^0 becomes a mother[11], giving birth to Ξ^- and π^+ respectively called the *negative* and *positive* particle according to their electric charge. The distinction as a function of the electric charge sign is important because this sign affects the curvature of the particles, an observable accessible through the measurements and used during the topological reconstruction procedure.

Topological reconstruction aims at associating the tracks of the *negative* (Ξ^-) and *positive* (π^+) particles to reconstruct the undetected Ξ_c^0, that will itself be associated to a track of a *bachelor* particle (π^+) and eventually constitute a candidate to Ξ_b^-. The Ξ^- can directly be detected allowing for "strangeness tracking" with improved track reconstruction. This improvement

[8]More of these particles could have been produced directly by the collision or via decays taken into account by Pythia.

[9]Note that these numbers are obtained for a single data generation. This generation code was launched thousands of times during the project, to get a data sample big enough.

[10]The detection relies on the ionization of the medium composing the detection layers which is only possible if the particle passing through is electrically charged.

[11]Ξ_b^- is then promoted to the status of grand-mother.

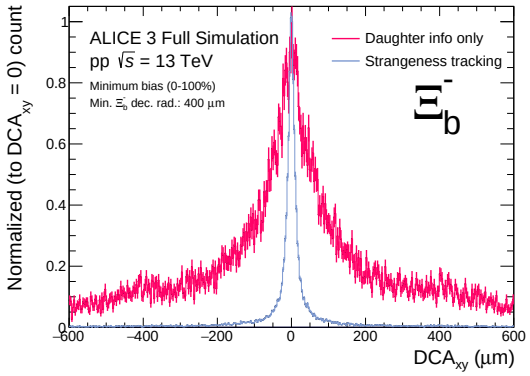

Figure 3: Comparison between topological reconstruction with (in blue) and without (in red) strangeness tracking in the distribution of DCA$_{xy}$ to primary vertex for Ξ_b^-.

can then be propagated to the reconstruction of Ξ_c^0 and then Ξ_b^-.
We don't describe all the details of this procedure in this report (Sections 6.2.3 and 6.6.4, [10]). Yet we can mention that the main goal of topological reconstruction is to find the point in space where the tracks of two potential daughters are the closest (this point becomes a vertex candidate) and then use momentum-energy conservation at this vertex to calculate the invariant mass of the particle of interest that supposedly decayed at this very point.

Once we reconstructed Ξ_c^0, we repeat the procedure presented previously but instead of associating *positive* and *negative* particles, we associate a *bachelor* with the freshly reconstructed Ξ_c^0 to eventually reconstruct the track of Ξ_b^-. This whole procedure is done in a piece of C++ code of about 2 000 lines running in the O2 environment[12]. Originally, this piece of code was written for a completely different decay channel. In this work, the code is adapted to reconstruct the decay channel of Ξ_b^-. The output files of this procedure contained a lot of information on the reconstructed particles and the associated tracks that can be used to go from the physics analysis results back to the Monte Carlo truth.

Data analysis and main results

More than two millions events were generated, containing more than two millions Ξ_b^- decaying in the channel of interest. Some background was simulated by generating Ξ_c^0 instead of Ξ_b^- and not imposing any decay channel. The same number of events was generated for background and signal data.

When we study a specific decay channel and/or a specific particle, we want to reduce the background and to do so, we have to know how topological observables

[12]O2, standing for Online-Offline, is the ALICE software and allows data treatment online (while the detection system is operating) as well as offline (after the recording of the data).

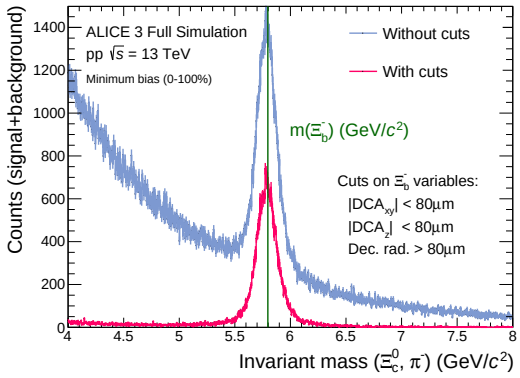

Figure 4: Invariant-mass distribution for the reconstructed Ξ_b^- candidates.

such as the decay radius[13] or the DCA[14] behave for the case of true signal an background candidates. These topological observables can be used to apply *topological cuts* on the data to constrain the reconstruction process and to suppress as much as possible the background.

The Figure 3 shows that strangeness tracking offers an improvement in DCA resolution (compared to the "standard" method), hence proving the usability of this new technique: strangeness tracking applied on Ξ^- reduces combinatorial background in the study of Ξ_b^-.

Finally, Figure 4 presents the main result of this project: the invariant mass plot for Ξ_b^- candidates. We can notice that the cuts on DCA and decay radius offer an important background suppression: our analysis prototype works. We managed to reconstruct the decay channel of Ξ_b^- until isolating this particle with a peak well centered around Ξ_b^- mass. Of course, the background here is strongly under-estimated. The cuts elaborated in this work will play an important role in the optimisation of signal-over-background ratio in the reconstruction of Ξ_b^- with the future ALICE 3 experiment.

References

[1] B. Abelev *et al* [ALICE Collaboration], J. Phys. G41, 087002 (2014), *Technical Design Report for the Upgrade of the ALICE Inner Tracking System*, `https://iopscience.iop.org/article/10.1088/0954-3899/41/8/087002/pdf`

[2] ALICE Collaboration, CERN-LHCC-2022-009, LHCC-I-038, *Letter of intent for ALICE 3: A next generation heavy-ion experiment at the LHC*, `https://cds.cern.ch/record/2803563`

[3] G. Aglieri Rinella [ALICE Collaboration], Nucl. Instrum. Meth. A 845 (2017) 583-587, *The ALPIDE pixel sensor chip for the upgrade of the ALICE Inner Tracking System*, `https://inspirehep.net/files/e879a9edbcc6860d0b77005f4781497c`

[4] ALICE Collaboration, Expression of Interest for an ALICE ITS Upgrade in LS3

[5] Longer term LHC schedule

[6] P.A. Zyla *et al.* (Particle Data Group), Prog. Theor. Exp. Phys. 2020, 083C01 (2020) and 2021 update, *Monte Carlo Particle Numbering Scheme*

[7] University of Arizona, *The Particle Data Scheme*

[8] P.A. Zyla *et al.* (Particle Data Group), Prog. Theor. Exp. Phys. 2020, 083C01 (2020) and 2021 update, PDG Live

[9] ALICE Collaboration, *Definition of the ALICE Coordinate System and Basic Rules for Sub-detector Components Numbering*

[10] ALICE Collaboration et al 2006 J. Phys. G: Nucl. Part. Phys. 32 1295, *ALICE: Physics Performance Report, Volume II*, `https://iopscience.iop.org/article/10.1088/0954-3899/32/10/001`

[13] The decay radius of a particle is the distance seperating the disintegration vertex of this particle and the center of the ALICE detector, in the transverse plane.

[14] The DCA is the algebraic *Distance of Closest Approach*. It can be evaluated between two particles or between a particle and a vertex. $|\mathrm{DCA}| = \sqrt{\mathrm{DCA}_{xy}^2 + \mathrm{DCA}_z^2}$ where DCA_{xy} (resp. DCA_z) is the DCA in the transverse plane (resp. the beam direction).

$\psi(2S)$ normalised yields as a function of charged-particle pseudorapidity density in pp and p–Pb collisions with the ALICE experiment at the LHC

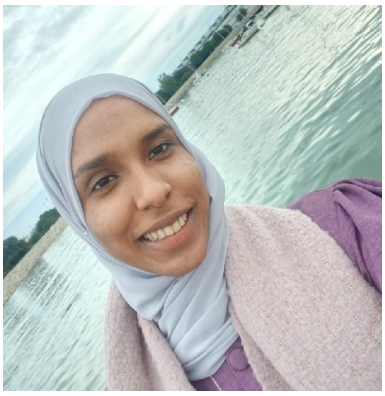

Theraa TORK

IJCLab, Paris-Saclay University

Abstract — The production of heavy quarkonia such as charmonium (bound state of charm and anti-charm quark) presents an excellent tool to test both perturbative and non-perturbative QCD, as charm production process can be described by perturbative QCD, but the formation of the bound state involves non-perturbative aspects. In ultrarelativistic heavy-ion collisions, a deconfined state of QCD matter, made of free quarks and gluons, called quark-gluon plasma (QGP) is expected to be formed. To probe such an environment, the study of charmonium is an important tool as it is produced during the initial stage and experiences the full evolution of the collision. An increase of the charmonium yields as a function of event charged-particle pseudorapidity density was observed in pp and p–Pb collisions with the ALICE experiment at the LHC. This proceeding shows the result of the $\psi(2S)$ yields normalised to their average values as a function of the pseudorapidity density of charged-particles in pp collision at $\sqrt{s} = 13$ TeV and p–Pb collisions at $\sqrt{s_{NN}} = 8.16$ TeV. The ratio of the excited state, $\psi(2S)$, to the ground state J/ψ as a function of the pseudorapidity density of charged-particles is shown as well.

Introduction

Lattice QCD predicts the existence of quark-gluon plasma (QGP), a deconfined state of quarks and gluons. In nature, QGP may have permeated the first microsecond of the universe [1], where extreme conditions of high energy density and high temperature exist. Such conditions are reproduced at the laboratory by colliding heavy ions at sufficient high energy.

In heavy-ion experiments several observables are used as a tool to probe and characterize the QGP. Besides QGP effects, the observables might be affected by the presence of nuclei, so-called cold nuclear matter effects. To disentangle the QGP influences from the cold nuclear matter effects, proton-nucleus collisions are used as a control system, since QGP effects are not expected to be formed.

Charmonia, bound states of charm anti-charm quarks, production is an excellent tool to study the QGP. Due to their heavy mass, the charmonia states are produced in the early stages of the collision and experience the full evolution of the collision. This makes charmonia widely used tools to understand the QGP and cold nuclear effects. A suppression of J/ψ production in p–Pb collisions, with respect to pp collisions, at forward rapidity region was reported by different experiments [2, 3]. This suppression was found to be consistent with theoretical models that includes cold nuclear matter effects in their calculations[4, 5].

The excited state, $\psi(2S)$, results show a larger suppression in p–Pb, with respect to pp, at both forward and backward rapidity regions. When compared with J/ψ values, a similar suppression was observed of $\psi(2S)$ at forward rapidity. This suppression was ascribed to initial state cold nuclear matter effects. On the other hand, at backward rapidity, $\psi(2S)$ experienced a significantly stronger suppression than J/ψ. This behaviour was reproduced by the comovers model, which considers a dissociation of the charmonia due to the interaction with the final state comoving particles [9].

In this proceeding, measurements of $\psi(2S)$ production in p–Pb and pp collisions as a function of charged-particle pseudorapidity density are reported. The ratio of $\psi(2S)$ to the J/ψ relative yields as a function of charged-particle pseudorapidity density is shown. In the presented measurements both charmonia yields and charged-particle pseudorapidity density are normalised to their average values.

Experimental apparatus

ALICE (A Large Ion Collider Experiment) is the dedicated heavy-ion LHC (Large Hadron Collider) experiment [10]. ALICE consists of 18 sub-detectors, which allow to study a broad range of observable. These sub-detectors can be classified into three main cate-

gories. First, global detectors measure general quantities such as particle multiplicity, luminosity, and collisions centrality. Second, central barrel detectors at mid-rapidity are important to reconstruct the trajectories of hadrons, photons and electrons. Third, the muon spectrometer [11] at forward rapidity which is designed to measure the production of heavy quark resonances, e.g J/ψ, $\psi(2S)$, open heavy flavor, with a sufficient mass resolution to separate all the states and down to zero transverse momentum p_T.

The analyzed data are recorded mainly using the muon spectrometer at forward rapidity $-4.0 < \eta_{\rm lab} < -2.5$. The spectrometer consists of: a set of absorbers essential to reduce the background from the decay of hadrons and beam-gas interactions; a dipole magnet provides an integrated magnetic field of 3 Tm used to deflect particles trajectories to measure their curvature, momentum and electric charge; five stations of muon tracking chambers and two stations of muon trigger chambers which are important to ensure the muon identification. Other detectors are used in this analysis, such as the silicon pixel detector (SPD), the V0 and the zero degree calorimeter (ZDC). The SPD [12] is the innermost part of the ALICE inner tracking system. It consists of two cylindrical silicon pixel detector layers covering a pseudorapidity range of $|\eta| < 2$. The SPD is essential for the reconstruction of primary vertices and measuring the charged-particle multiplicity at midrapidity. The V0 [13] is composed of two arrays of scintillator counters positioned on both sides of the interaction point, which serves as a minimum bias (MB) trigger in this analysis. The ZDC [14] is two sets of hadronic calorimeters placed at 116 m on either side of the interaction point. It is essential to reject the electromagnetic and beam-induced background.

Analysis

This analysis exploits the data sets of p–Pb collisions at $\sqrt{s_{\rm NN}} = 8.16$ TeV and pp collisions at $\sqrt{s} = 13$ TeV. The analyzed data was collected using two triggers: the MB trigger, and dimuon trigger in the muon trigger chambers (MUL). Two criteria are applied to data to remove events with multiple interaction per bunch crossing (pile-up). To ensure the unformities in the SPD acceptance, only events with z-vertex position $|z_{\rm vtx}| < 10$ cm are considered. The analysis steps done for the charged-particle pseudorapidity density and the $\psi(2S)$ normalised yields measurements are discussed in this section.

Charged-particle multiplicity

The charged-particle pseudorapidity density $\mathrm{d}N_{\rm ch}/\mathrm{d}\eta$ is evaluated by counting the number of tracklets, $N_{\rm tracklet}$, in the SPD detector. A tracklet is a track segment that connects two hits in the two layers of the SPD pointing to a primary vertex. To account for the limited acceptance of the SPD detector and its condition variation with time, a data-driven procedure was applied to correct the raw $N_{\rm tracklet}$. The correction is performed by renormalizing the $N_{\rm tracklet}$ distribution to the overall maximum, it ensures a uniform $N_{\rm tracklet}$ distribution. To account for possible fluctuation, the corrected $N_{\rm tracklet}$ is smeared with a Poissonion distribution. The correlation between the $\mathrm{d}N_{\rm ch}/\mathrm{d}\eta$ and $N_{\rm tracklet}$ is estimated using DPMJET [15] (PYTHIA6 [17]) Monte Carlo (MC) generator for p–Pb (pp) data set, and the transport of the particle through the detector is simulated using GEANT3 [16]. The correlation is found to follow a second-order polynomial trend. Several sources of systematic were investigated: possible deviation of the correlation from the second-order polynomial was evaluated by testing other types of correlation, the influence of the event generator was evaluated by compring the DPMJET simulations to the EPOS event generator simulations [**?**], the uncertainty on the residual dependence of the z-vertex position due to the difference between MC and data, and the uncertainty on the average charged-particle pseudorapidity density,$<\mathrm{d}N_{\rm ch}/\mathrm{d}\eta>$. The latter was found to be the main source of uncertainty, resulting in 4% for p–Pb data set and 1.4% for pp data set.

Normalised yield

The $\psi(2S)$ normalised yield, $Y^{R,i}_{\psi(2S)}$, is defined as the ratio of the yield in a multiplicity bin (i) to the integrated multiplicity bin (tot), and is computed as follows

$$Y^{R,i}_{\psi(2S)} = \frac{Y^{i}_{\psi(2S)}}{Y^{tot}_{\psi(2S)}} = \frac{N^{i}_{\psi(2S)}}{N^{tot}_{\psi(2S)}} \times \frac{N^{eq,tot}_{MB}}{N^{eq,i}_{MB}} \times \frac{(A\times\epsilon)^{tot}}{(A\times\epsilon)^{i}} \times \frac{\epsilon^{i}_{MB}}{\epsilon^{tot}_{MB}}$$

where, $N_{\psi(2S)}$ is the $\psi(2S)$ raw yield, N^{eq}_{MB} is the equivalent number of MB events, $(A\times\epsilon)$ is the $\psi(2S)$ detector acceptance and efficiency and ϵ_{MB} is the event selection efficiency of the MB trigger.

The muon tracks must fulfil the following requirements: their pseudorapidity is within the acceptance of the detector, their radial distance at the end of the front absorber is within 17.6 cm and 89.5 cm, and the multiplication of their momentum and the distance of closest approach is within 6σ. Moreover, to ensure the muon identification, the reconstructed muon track in the muon tracking chambers must match a track in the muon trigger chamber.

To reconstruct the J/ψ and $\psi(2S)$ candidates, the opposite-sign muons are combined and their invariant mass is computed. To extract the $\psi(2S)$ raw yields and uncertainties, the invariant-mass dimuon distribution is fitted. Several functions are used to model the signal and the background continuum. A Gaussian core with power-law mass tails function is used to fit the signal. The background of p–Pb data set is fitted either by a sum of two exponential or an exponential of first order convoluted with a fourth-order polynomial, while the pp background is parameterized using a sum of two exponential or pseudo-Gaussian function whose width varies linearly with the invariant mass. The $\psi(2S)$ yields and their statistical uncertainties are extracted

by evaluating the average of the results of the fit trials varying the signal function, the background function, and the invariant-mass fit interval. The systematic uncertainty due to the signal extraction was determined by evaluating the standard deviation of all the fit trials. An example of dimuon distribution fit is shown in Fig. 1.

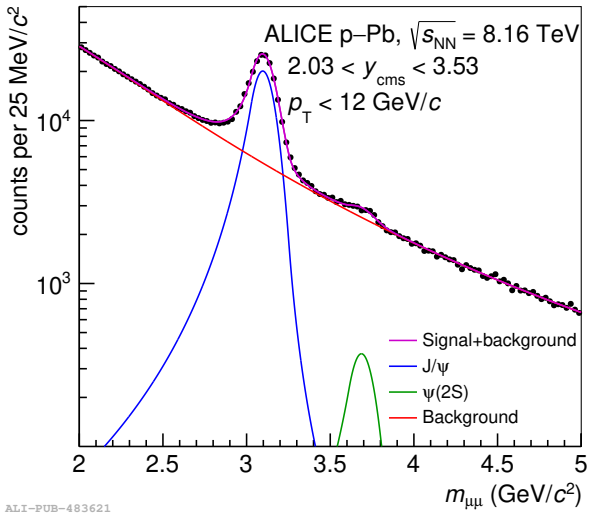

Figure 1: Example of p_{T} and y integrated mass spectrum for the forward rapidity p–Pb data sample. The contribution of the resonances and of the background are shown separately [7].

The analysis is done using the dimuon trigger data sample. A normalization factor, F_{norm}, is used to correct the measurements and convert the number of analyzed events to the number of equivalent MB events, N^{eq}_{MB}. Two methods are used to evaluate F_{norm}, both are based on comparing the MB sample to the dimuon trigger sample. The direct method is computed by finding the ratio of the MB trigger events to the MUL trigger events. The indirect method uses the single muon trigger as an intermediate trigger to evaluate F_{norm}.

The detector acceptance and efficiency $(A \times \epsilon)$ is studied as a function of charged-particle multiplicity. PYTHIA6[17] event generators coupled with GEANT3[16] were used to simulate the p_{T} and y distributions. These distributions were used as an input for the $(A \times \epsilon)$ determination. A data-driven procedure was performed to tune MC inputs on data. $(A \times \epsilon)$ is found to be independent as a function of multiplicity in p–Pb sample, while the pp data set shows a decreasing efficiency as multiplicity increases. Therefore, a correction due $(A \times \epsilon)$ is only applied to the pp data set.

$\psi(2S)$ yields are corrected for the efficiency of the MB trigger to select the events of the class, inelastic (INEL) > 0 for the pp data set or non-single diffractive (NSD) for the p–Pb data set. ϵ_{MB} is computed for each charged-particle multiplicity interval. The distribution of ϵ_{MB} is found to be independent of charged-particle multiplicity apart from the lowest interval, where a 1% correction was considered to the lowest interval.

The systematic uncertainty was obtained as the quadratic sum of the following contributions: signal extraction, the z-vetrtex normalization, pileup, Ntracklets correction, and event selection efficiency. The highest contribution is due to the signal extraction uncertainty, ranging 3.9%-5.2% for pp data and 4%-13% for p–Pb data. The higher value for p–Pb signal extraction systematic uncertainty is due to the smaller statistics data sample compared to the pp sample.

Results

The normalised yield of $\psi(2S)$ in pp collisions at 13 TeV and p–Pb collisions at 8.16 TeV as a function of charged-particle pseudorapidity density is presented in Fig. 2. The $\psi(2S)$ yields are measured at large rapidity, while the charged-particle multiplicity is evaluated at midrapidity. The plot shows an increase of $\psi(2S)$ yields with increasing multiplicity. This increase is compatible with linear (y=x), within uncertainties, depicted as a dashed line in the figure. The vertical bars represent the statistical uncertainty, while the boxes' height and width represent the systematic uncertainty for the $\psi(2S)$ yields and charged-particle pseudorapidity density, respectively.

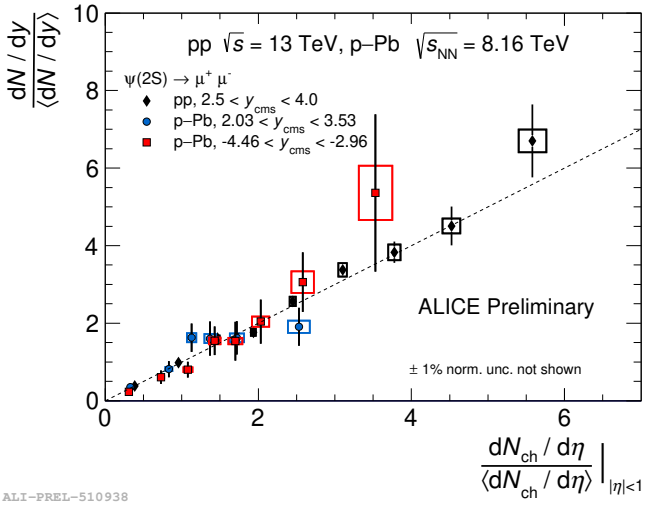

Figure 2: Normalised yields of inclusive $\psi(2S)$ yields as a function of charged-particle pseudorapidity density in pp collisions at $\sqrt{s}$= 13 TeV and p–Pb collisions at$\sqrt{s_{NN}}$= 8.16 TeV.

In Fig. 3, the $\psi(2S)$ to J/ψ normalised yields as a function of charged-particle pseudorapidity density in pp collisions at 13 TeV are presented. The result shows a behaviour compatible with linear distributions with either a null or negative slope, within the uncertainties. The comparison with the comovers model is shown in the same figure, predicting a stronger suppression of the $\psi(2S)$ with respect to the J/ψ at high multiplicity. In the comovers model, the quarkonia is expected to dissociate due to the interaction with the surrounding final state comoving particles. This effect will depend

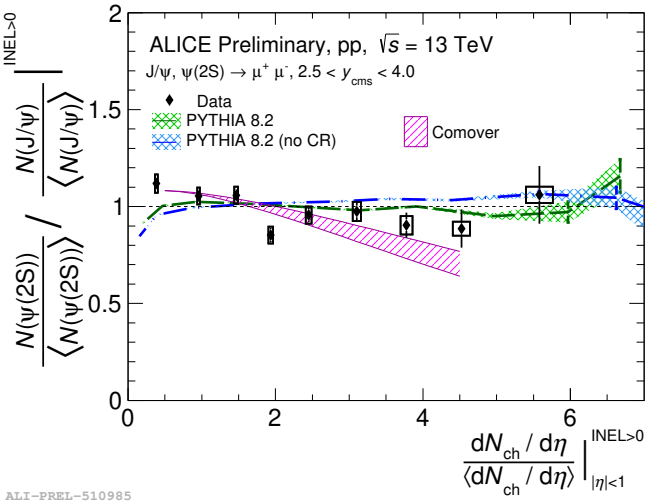

Figure 3: $\psi(2S)$ to J/ψ normalised yields as a function of charged-particle pseudorapidity density in pp collisions at $\sqrt{s}$ = 13 TeV with predictions from comovers model and PYHTIA 8.2 event generator.

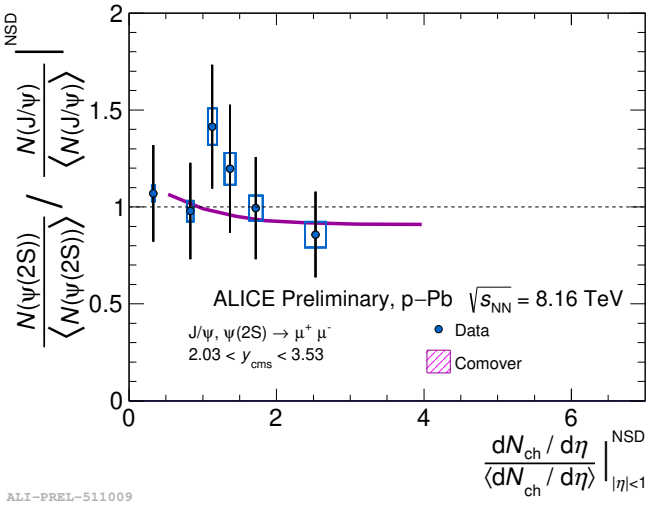

Figure 4: $\psi(2S)$ to J/ψ normalised yield as a function of charged-particle pseudorapidity density in p–Pb collisions at $\sqrt{s_{NN}}$ = 8.16 TeV in the rapidity region 2.03 < y_{cms} < 3.53. The yields are compared to the comovers model calculation.

on the quarkonia state binding energy and the density of the comoving particles. Due to the lower binding energy, the $\psi(2S)$ state is more probable to dissociate than J/ψ. The probability will increase with charged-particle multiplicity due to the increase of the comovers density. In this model, the uncertainty is evaluated by the density of comoving particles. The $\psi(2S)$ to J/ψ production can be simulated using the PYTHA 8.2 event generator [18], as shown in Fig. 3. PYTHIA 8.2 calculation allows the production of the charm quark to occur in the hard QCD processes and also during the hard QCD multiparton interactions (MPI). MPI refers to the several parton-parton interactions that take place in a single hadron-hadron collision. The MPI implementation in PYTHA 8.2 predict a direct proportionality between the charged-particle multiplicity and the number of hard processes. The result in Fig. 3 shows a small tension between the $\psi(2S)$ to J/ψ double ratio and PYTHIA 8.2 simulation in the low and intermediate multiplicity intervals.

In Figs. 4 and 5, the normalised yields of $\psi(2S)$ to J/ψ as a function of charged-particle multiplicity are presented for the forward and backward rapidity regions, respectively. The results show a distribution compatible with unity within uncertainties for both p–Pb configurations. The measurements are compared to the comovers model calculations. The results, within their large uncertainty, are consistent with the comovers scenario, which predict a stronger suppression at backward rapidity than at forward rapidity.

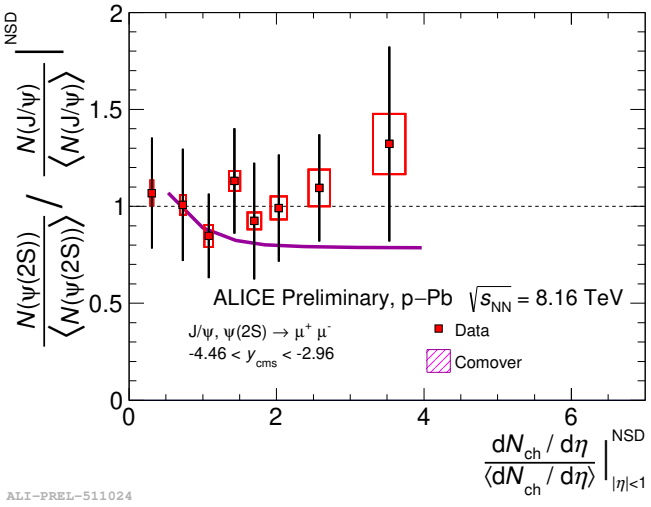

Figure 5: $\psi(2S)$ to J/ψ normalised yield as a function of charged-particle pseudorapidity density in p–Pb collisions at $\sqrt{s_{NN}}$ = 8.16 TeV in the rapidity region -4.46 < y_{cms} <-2.96. The yields are compared to the comovers model calculation.

Conclusion

The measurements of $\psi(2S)$ production within the muon spectrometer in p–Pb collisions at $\sqrt{s_{NN}}$ = 8.16 TeV and pp collisions at $\sqrt{s}$ =13 TeV as a function of

charged-particle pseudorapidity density were discussed. The results show an increase in the relative yield as the charged-particle pseudorapidity density increases for pp and p–Pb data sets. The double ratio of the $\psi(2S)$ to J/ψ yield as function of charged particle pseudorapidity density, is reported for pp and p–Pb collisions. The co-movers model described the excited to the ground state ratio in both configurations, expecting a stronger dissociation of $\psi(2S)$ than the J/ψ. PYTHIA 8.2 event generator calculations expected a flat distribution of the $\psi(2S)$ to J/ψ as a function of multiplicity in pp collisions. This behaviour is compatible with the data within uncertainties.

References

[1] P.Braun-Munzinger & J.Stachel. "The quest of quark-gluon plasma", Nature 448,302,309 (2007).

[2] ALICE collaboration, S. Acharya *et al.*, "Inclusive J/ψ production at forward and backward rapidity in p-Pb collisions at $\sqrt{s_{\rm NN}} = 8.16$ TeV", JHEP **07**, 160 (2018) arXiv:1805.04381 [nucl-ex].

[3] LHCb collaboration., Aaij, R., Adeva, B. et al. "Prompt and nonprompt J/ψ(2S) production and nuclear modification factor in pPb collisions at $\sqrt{s_{\rm NN}}$= 8.16 TeV", PLB 774(2017) 159.

[4] R. Vogt "Shadowing and absorption effects on J/ψ production in dA collisions", Phys. Rev. C 71, (May-2005)054902.

[5] B. Ducloue, T. Lappi, and H. Mäntysaari "Forward J/ψ production at high energy: Centrality dependence and mean transverse momentum", Phys. Rev. D 94, (Oct-2016)07403.

[6] LHCb collaboration., Aaij, R., Abellán Beteta, C. *et al.* "Study of ψ(2S) production and cold nuclear matter effects in pPb collisions at $\sqrt{s_{\rm NN}} = 5$ TeV", JHEP 2016, 133 (2016).

[7] ALICE collaboration, S. Acharya *et al.*, "Measurement of nuclear effects on ψ(2S) production in p-Pb collisions at $\sqrt{s_{\rm NN}} = 8.16$ TeV", JHEP **07**, 237 (2020).

[8] ALICE collaboration, "Suppression of $\psi(2S)$ production in p–Pb collisions at $\sqrt{s_{NN}} = 5.02$ TeV", JHEP 12 (2014) 073.

[9] E. G. Ferreiro, "Excited charmonium suppression in proton-nucleus collisions as a consequence of co-movers", arXiv:1411.0549 [hep-ph]

[10] The ALICE Collaboration, K.Aamodt et al. "The ALICE experiment at the CERN LHC" 2008 JINST 3 S08002.

[11] The ALICE Collaboration, "ALICE dimuon forward spectrometer : addendum to the Technical Design Report". CERN, Geneva.

[12] The ALICE Collaboration, K. Aamodt et al., "Alignment of the ALICE Inner Tracking System with cosmic-ray tracks". JINST 5 P03003.

[13] The ALICE Collaboration, E. Abbas et al., "Performance of the ALICE VZERO system". JINST 8 P10016.

[14] The ALICE Collaboration, M.Gallio et al.,"ALICE Zero-Degree Calorimeter (ZDC): Technical Design Report". CERN, Geneva.

[15] S. Roesler, R. Engel, and J. Ranft, "The Monte Carlo Event Generator DPMJET-III", arXiv:hep-ph/0012252.

[16] R.Brun, F.Bruyant, F.Carminati, S. Giani, , M. Maire, A. McPherson, G. Patrick, and L.Urban, "GEANT: Detector Description and Simulation Tool; Oct 1994", https://cds.cern.ch/record/1082634.

[17] T. Sjostrand, S.Mrenna, P.Skands,"PYTHIA 6.4 Physics and Manual", JHEP 0605:026,2006.

[18] T. Sjostrand et al., "An Introduction to PYTHIA 8.2", Computer Physics Communications,Volume 191,2015.

Dynamical Thermalization In Heavy-Ion Collisions

Mahbobeh JAFARPOUR[1], ***with K. Werner*** [1], ***E. Bratkovskaya*** [2,3] ***and V. Voronyuk*** [4]

[1] *Subatech, Nantes University - IMT Atlantique - IN2P3/CNRS, Nantes, France*
[2] *GSI Helmholtzzentrum fur Schwerionenforschung, Darmstadt, Germany*
[3] *Institute for Theoretical Physics, Johann Wolfgang Goethe University, Frankfurt am Main, Germany*
[4] *Joint Institute for Nuclear Research, Dubna, Moscow region, Russia*

Abstract — In this paper, we will present the EPOSi+PHSDe approach, where we employ EPOS to determine the initial distribution of matter (partons/hadrons) and then use PHSD for the evolution of the matter in a non-equilibrium transport approach. We will compare EPOSi+PHSDe results with EPOS, which amounts to essentially comparing two different dynamical descriptions with the same initial condition. We also show pure PHSD simulations because here, the initial conditions are different for the same evolution compared to EPOSi+PHSDe. We will show results concerning transverse momentum spectra and elliptic flow.

Introduction

Ultrarelativistic Heavy-Ion Collisions (HICs) at the Relativistic Heavy-Ion Collider (RHIC) and the Large Hadron Collider (LHC) provide a hot and ultra-dense form of the matter composed of unconfined quarks and gluons, named Quark-Gluon Plasma (QGP) [1, 2, 3]. The space-time evolution of HICs can be modelized by the Bjorken scenario [4]. If we follow the evolution of the initial state, the matter evolves according to these steps: Pre-equilibrium, QGP or Hydrodynamic phase, Mixed state, Hadronic gas, and Freeze-out. Although using HICs we have learned many things both on theoretical and phenomenological aspects, there is still a large amount of uncertainty in particular concerning the thermalization of the system. The dynamics are pretty sophisticated; hence, various stages should be considered. The first is the primary scattering which defines the large extent of the matter distribution in the phase-space. The second is the partonic phase that will evolve in space and time until the system is sufficiently hadronized. Therefore, we need models with different degrees of sophistication concerning the various stages (initial, evolution, and hadronization). In this context, we find out that EPOS [5, 6, 7, 8] and PHSD [9, 10, 11, 12, 13, 14, 15, 16, 17] models are among the successful models to investigate the space-time evolution of such HICs.

When comparing two models, like EPOS and PHSD, looking at numerous observables, is not always clear to what extent the two parts, the initial phase (i) and the expansion (e), contribute to the final results. Therefore, the idea to combine the initial EPOS phase (EPOSi) and the evolution from PHSD (PHSDe), giving rise to the **EPOSi+PHSDe** model. In this way, comparing EPOSi+PHSDe and pure EPOS, we compare two models with the identical initial condition but different evolution. However, when comparing EPOSi+PHSDe and pure PHSD, we compare two models with different initial conditions but the same evolution. So we can clearly separate "initial" and "evolution" effects.

The following is the outline of this paper: in sections 1 and 2, we have a brief look at EPOS and PHSD models and those parts of these two models that we employ in EPOSi+PHSDe. The following section includes the summary of the new approach, and the last section contains the results. Finally, we will wrap up our results in the end.

EPOS

EPOS (Energy conserving multiple scattering Partons, parton ladder and strings Off-shell remnants Saturation) is a model for the initial phase of the HICs based on a multiple scattering S-matrix within the Gribov Reggeon Field Theory formalism of the pomeron exchange. The initial phase of EPOS (EPOSi) amounts to multiple scatterings based on PBGRT, whereas the following dynamics has been realized so far by assuming that a fast equilibration occurs followed by a hydrodynamical evolution (EPOSe).

EPOSi: An entirely quantitative representation of the experimental data needs sensible initial conditions. In relativistic nucleus-nucleus collisions, the geometry of the initial overlap region is determined in the final momentum space distributions of the produced particles [18]. An essential part of defining the initial con-

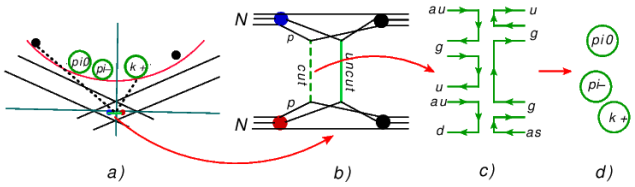

Figure 1: From Pomerons to string segments in the hyperbola. a) Evolution of the matter in the light-cone coordinate. b) Elementary diagrams of the Nucleon-Nucleon collision in the PBGRT using the cut ladder (dashed green line) and the uncut ladder (full green line). c) Color flow diagram from the cut ladder. d) Produced particles in the hypersurface.

dition is correctly modeling the incoming nuclei's (projectile and target) geometry. This is achieved within Monte Carlo simulations (MC) where each nucleus is created using a finite amount of nucleons distributed with a density ρ specified by a Woods-Saxon distribution. In EPOS, we determine the cartesian coordinates of nucleons for both projectile and target with Woods-Saxon distribution. In the main theory inside the EPOS, Parton-based Gribov Regge Theory (PBGRT) [5], the pomeron or parton ladder represents an elementary interaction between two hadrons or two partons from projectile and target sides. The principal concept to form this theory is to treat both hard and soft processes during a collision. The collision can happen between proton-proton, proton-nucleus, and nucleus-nucleus. The PBGRT constitutes a strategy to determine the cross-sections and the particle production taking into account the uncut and cut ladders, respectively, with respect to the energy conservation. The two kinds of ladders can be seen in Fig. 1b. One can produce the hadrons (or string segments like π^0, π^-, and K^+) on the hyperbola from the cut ladders using the color flow diagram (see Fig. 1c). In EPOS, we consider the energy loss of each string segment on the hyperbola at a given time τ as [19]:

$$P_t^{new} = P_t - f_{Eloss} \int_\gamma \rho dL, \qquad (1)$$

where γ and P_t are the trajectory and transverse momentum of the string segment, respectively. f_{Eloss} is a nonzero constant, and ρ is the local string density. If the P_t^{new} is positive, the string segment can escape from the dense area, and it is categorized as a **"corona particle"**. If the P_t^{new} is negative, however, the string segment loses all its energy and is unable to leave, thus it will remain in the dense area and called **"core particle"**.

EPOSe: Only the core particles are concerned in the next stage, the **hydrodynamic expansion**. Then, the system expands hydrodynamically using relativistic viscous hydrodynamic equations with $\eta/s = 0.08$ [20]. The microcanonical method describes the hadronization of the matter from the core part [21]. The corona particles have hadronized before these steps, using the string phenomenological model [22]. After hadronization of both core and corona parts, the system continues to interact via hadronic scattering and we employ the UrQMD model [23] to investigate this scattering at high enough hadron density.

PHSD

PHSD is a microscopic covariant dynamical approach for the strongly interacting systems formulated based on the Kadanoff-Baym equations. This approach consistently describes the whole evolution of a relativistic HICs. For the initial collisions of PHSD (**PHSDi**), the Pythia and the Lund string models are used. The created hadrons (or pre-hadrons) are then inserted into the QGP when fulfilling an energy density condition (starting the **PHSDe**). The DQPM and the equation of motions are used to study the properties and dynamics of QGP. As the system expands and cools, the energy density and temperature decrease, and the system transforms from partonic to hadronic degrees of freedom, a process known as hadronization. In this process, the colored off-shell partons fused into color-neutral off-shell hadrons. This transition is described by local covariant transition rates [29] in PHSD. Produced hadrons interact with each other elastically or inelastically after hadronization in the final stage of the collision. In the following, we will introduce the new approach that combines EPOSi and PHSDe.

EPOSi+PHSDe

After creating string segments using **EPOSi**, one can consider the dense area where the string segments must entirely or partially overlap. The overlapping part of the strings is called **rope segments** or fused strings that have the longitudinal color fields as ordinary strings but with changed properties. The rope segments are treated as strings with larger string tension, leading to a larger transverse momentum value than the ordinary strings. The dense area of rope segments is called **clusters** and their energy and flavor content are entirely determined by the corresponding string segments [25].

To prepare the evolution for PHSD, we need to decay the rope segments into **quasiparticles or pre-hadrons**. In EPOS, the statistical method to decay the cluster or a practical object with mass M at rest is using by Microcanonical decay [26]. We use the pre-hadron because we want to distinguish between the hadrons from hadronization before and after QGP. The pre-hadronization procedure happens at some early "initial time" quickly after the nuclei pass through each other. The produced pre-hadrons from the decay of the clusters are technically called **Core pre-hadrons**, and the rest of them are called **Corona pre-hadrons**.

After producing the pre-hadrons on the hyperbola in EPOS, we need to insert all the pre-hadrons with their carried momenta, flavor content, and position at the given proper time to the PHSD arrays.

The principal difficulties in the realization are related to

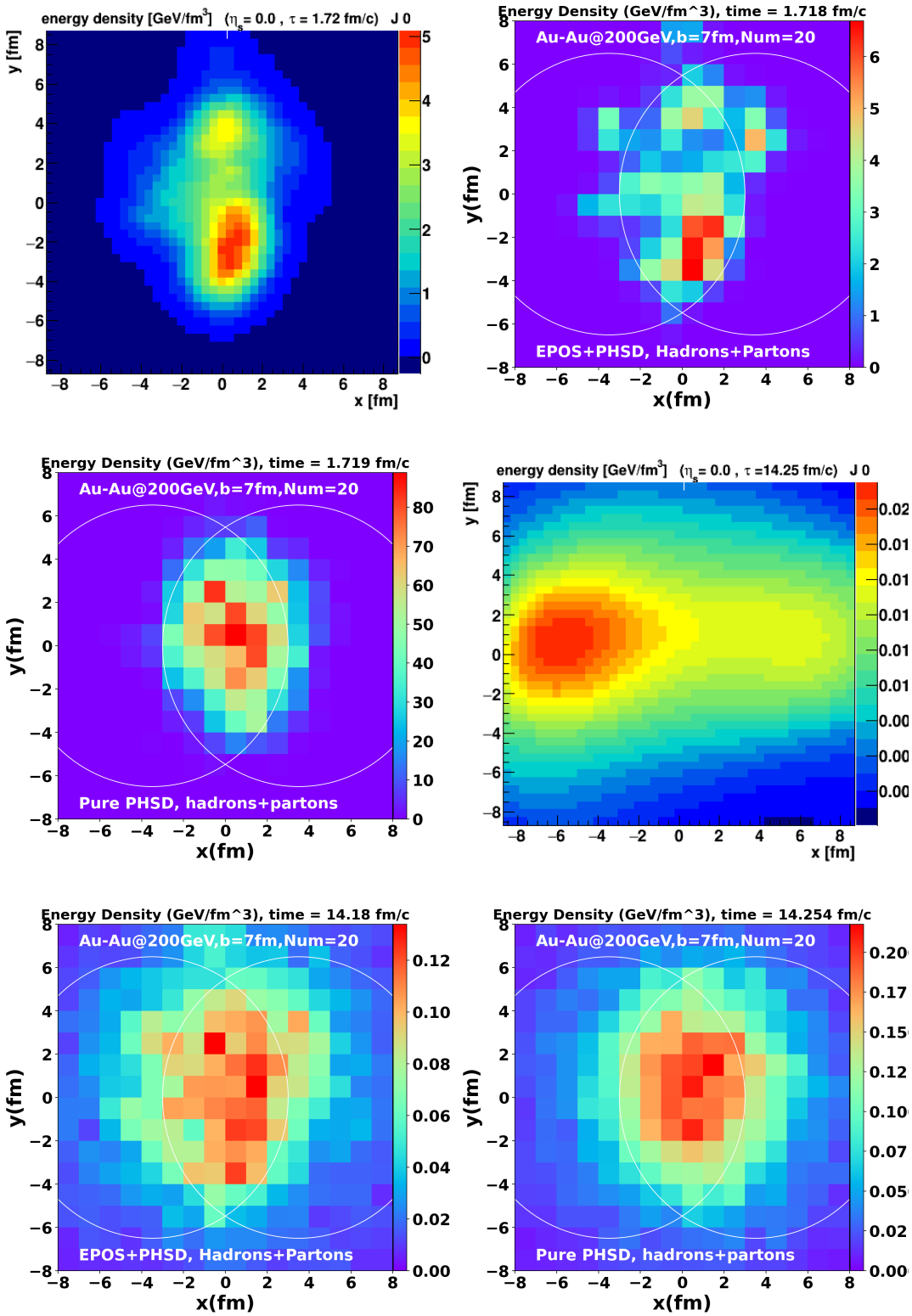

Figure 2: Time evolution of the energy density in the transverse plane (at z=0) for Au-Au collisions at 200 GeV with an impact parameter of 7 fm, for three models, considering events with the same initial matter distribution (at 1.7 fm/c). We show from left to right EPOS, EPOSi+PHSDe, and pure PHSD models, and from top to bottom the times (in fm/c) 1.7 ,and 14.1.

the fact that EPOS uses the light-cone dynamics (in the Milne coordinates). In contrast, PHSD employs real-time dynamics (in the Minkowski space-time). Thus, inserting particles from EPOS into PHSD arrays is complicated since the pre-hadrons in EPOS are produced on the hyperbola in space-time and they need to be extrapolated back to the start time of PHSD. We propose a particular EPOS2PHSD interface to allow the transition between the code of the two models. In the interface, we initially store all pre-hadrons from EPOS, then interpolate them into the PHSD arrays. In this step, we should consider the **"melting condition"**. The melting condition is defined when particle energy density exceeds the critical energy density of 0.5 GeV/fm^3. Therefore, these particles are melted into the QGP phase. It is worth noting that we only consider the energy density of core pre-hadrons.

After injecting pre-hadrons as input to the PHSD arrays, the following evolution of the matter is done by the PHSD non-equilibrium dynamics (**PHSDe**).

To see the differences between these three models, EPOS, EPOSi+PHSDe, and pure PHSD, we study the radial expansions via energy density evolutions. To compute the energy density, we use the energy-momentum tensor $T^{\mu\nu}$ from kinetic theory [27], where the energy density is given as T^{00} in the comoving frame. The energy density evolutions for semi-peripheral Au-Au collisions at 200 GeV in three models have been presented in Fig. 2. The left, middle, and right panels are related to the EPOS, EPOSi+PHSDe, and pure PHSD energy density profiles. One can see that the evolutions behave in fundamentally different ways, EPOS on one side and both EPOSi+PHSDe and pure PHSD on the other side. From the energy density evolutions (see Fig. 2), we observe that the systems in EPOSi+PHSDe and pure PHSD expand slowly compared to EPOS, which expands strongly in the transverse plane. The system expansions drastically affect observables like transverse momentum (p_T) and elliptic flow. The transverse momentum spectra and elliptic flow results of these three simulations will be compared in the next section.

Results

One of the key observables in our investigation is p_T. The invariant yields of charged hadrons as a function of transverse momentum p_T and centrality classes, and elliptic flow as a function of transverse momentum in three different models will be presented and compared to each other and experimental data in Figs. 3 and 4. EPOS accurately reproduces data from charged particle spectra, particularly at intermediate p_T rates (see Fig. 3). This is because the system expands substantially in the transverse plane, resulting in a large transverse flow, which immediately translates to enhanced particle production at larger p_T. All of this is predicated on the assumption that the system thermalized quickly and that hydrodynamics can be used to simulate the following evolution. Most notably, large gradients (in energy density) at early periods translate into a large transverse flow in the case of a hydrodynamically expanding expansion.

In comparison to the experimental data and EPOS, EPOSi+PHSDe and pure PHSDe are unable to reproduce sufficient particles at intermediate and high p_T (see Fig. 3). Because there is no assumption of equilibration in EPOSi+PHSDe and pure PHSD, it is necessary to evolve via parton-parton scatterings. However, obviously these interactions are not strong enough; there is no transverse expansion, and as a result, the shift of particles towards intermediate p_T values is missing. This provides a clear picture: the significant gradients in EPOSi+PHSDe and pure PHSD do not convert into the transverse flow, implying that the system does not reach equilibrium at an early stage.

We looked at flow anisotropies to confirm this picture. In EPOS, large asymmetries (via v_2) are observed both at low (< 1 GeV/c) and high (> 1 GeV/c) p_T, very similar to the experimental data, see blue curve in Fig. 4. However, in EPOSi+PHSDe (red curve in Fig. 4) and pure PHSD (green curve in Fig. 4), only low p_T results agree with the data, whereas at high p_T, the values are far too low. This is somehow expected, since from p_T spectra we know already, that these two models show too little transverse flow, and transverse flow

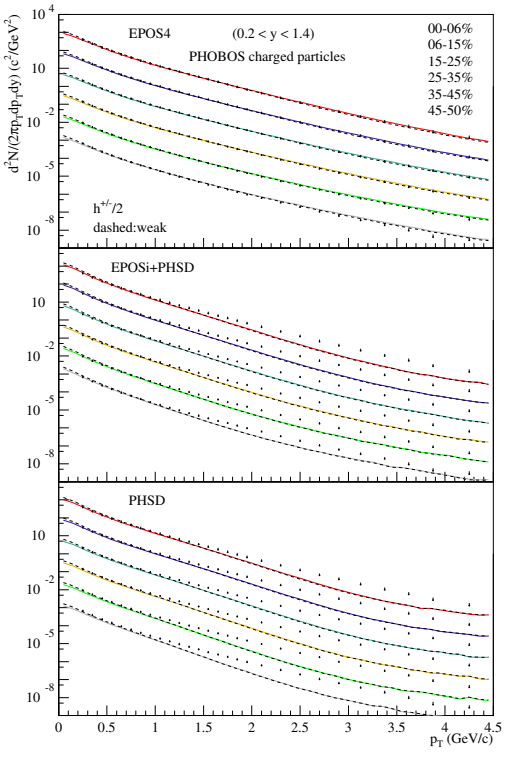

Figure 3: Invariant yields for charged hadrons as a function of p_T for 6 centrality bins in a rapidity range of $0.2 < y < 1.4$ in Au-Au collisions at $\sqrt{s_{NN}}$=200 GeV in different simulations, EPOS (upper panel), EPOSi+PHSD (middle panel), and pure PHSD (lower panel). The contribution of weak decays are plotted with the dashed lines. The experimental data are taken from PHOBOS [30] with black points.

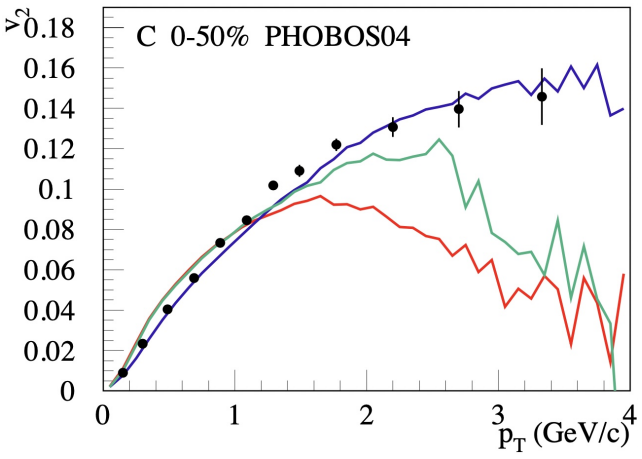

Figure 4: Elliptic flow as a function of transverse momentum ($v_2(p_T)$) for charged hadrons in Au-Au collisions at $\sqrt{s_{NN}}$=200 GeV for 0-50 % centrality collisions. Blue, red, green colors, and dots indicate EPOS, EPOSi+PHSD, pure PHSD results, and PHOBOS [31] experimental data, respectively.

is a necessary condition to have asymmetric transverse flow.

Conclusions

With the current results, one can answer to this question: "What is the difference between pure EPOS and pure PHSD?" The distinctions between these two models are related to their **"evolutions"**, whereas differences in the initial conditions play a minor role. More precisely, the development of radial flow is fundamentally different, the partonic scatterings do not provide sufficient "thermalization".

References

[1] H. Vanhees *et al.*, Phys. Rev. C **73**, 034913 (2006).

[2] H. Song *et al.*, Phys. Rev. Lett. **106**, 192301 (2011).

[3] M. Asakawa *et al.*, Phys. Rev. Lett. **96**, 252301 (2006).

[4] J. D. Bjorken, Phys. Rev. D **27**, 140 (1983).

[5] H. J. Drescher *et al.*, Phys. Rept. **350**, 93 (2001).

[6] M. Bleicher *et al.*, J. Phys. G **25**, 1859 (1999).

[7] T. Pierog *et al.*, Phys. Rev. C **92**, 034906 (2015).

[8] K. Werner *et al.*, Phys. Rev. C **89**, 064903 (2014).

[9] W. Cassing and E. L. Bratkovskaya, Phys. Rev. C **78**, 034919 (2008).

[10] W. Cassing and E. L. Bratkovskaya, Nucl. Phys. A **831**, 215 (2009).

[11] W. Cassing, Eur. Phys. J. ST **168**, 3 (2009).

[12] E. L. Bratkovskaya **et al.**, Nucl. Phys. A **856**, 162 (2011).

[13] V. P. Konchakovski *et al.*, Phys. Rev. C **85**, 011902 (2012).

[14] T. Song *et al.*, Phys. Rev. C **92**, 014910 (2015).

[15] E. L. Bratkovskaya *et al.*, J. Phys. Conf. Ser. **878**, 012018 (2017).

[16] O. Linnyk *et al.*, Prog. Part. Nucl. Phys. **87**, 50 (2016).

[17] P. Moreau *et al.*, Phys. Rev. C **100**, 014911 (2019).

[18] J. Y. Ollitrault, Phys. Rev. D **46**, 229 (1992).

[19] K. Werner et al, Phys. Rev. C **89**, 064903 (2014).

[20] K. Werner, Phys. Rev. C **82**, 044904 (2010).

[21] K. Werner, COST THOR Working Group I and II and GDRI Meeting (2018).

[22] Bo. Andersson, Phys. Rep. **97**, 31-145 (1983).

[23] H. Petersen, et al, Phys. Rev. C **78**, 044901 (2008).

[24] K. Werner, Nucl. Phys. B Proc. Suppl. **175**, 81 (2008).

[25] K. Werner, Phys. Rev. Lett. **98**, 152301 (2007).

[26] K. Werner and J. Aichelin, Phys. Rev. C **52**, 1584 (1995).

[27] H. J. Drescher *et al.*, Phys. Rev. C **65**, 054902 (2002).

[28] R. Marty *et al.*, Phys. Rev. C **92**, 015201 (2015).

[29] W. Cassing *et al.*, Phys. Rev. C **78**, 034919 (2008).

[30] BB. Back *et al.*, Phys. Lett. B **578**, 297-303 (2004).

[31] BB. Back *et al.*, Phys. Rev. C **72**, 051901 (2005).

Study of baryonic resonances in $\pi^- + C$ reaction at 0.69 GeV/c

Fatima HOJEIJ

IJCLab, Orsay

Abstract — Various exit channel topologies ($p\pi^-$, $p\pi^-\pi^-$ and $p\pi^-\pi^+$) for the $\pi^- + C$ reaction have been studied with the High Acceptance Dielectron Spectrometer (HADES) setup, using the GSI pion beam at an incident pion momentum of 0.69 GeV/c. Pion and proton spectra are compared to predictions of the INCL++ cascade and PLUTO event generator. The results allow to test selectively the capacity of such models to describe the various reaction mechanisms (quasi-elastic scattering, multipion production, rescatterings). The sensitivity of the data measured in the quasi-elastic channel to short range correlations is also investigated.

Introduction

One of the motivations to study high-energy nuclear collisions is to explore the QCD phase diagram. This diagram can be characterized by the temperature (T) and the baryon chemical potential (μ_B) as shown in Fig.1, where different regions can be reached experimentally by changing the beam energy. Experiments at the Large Hadron Collider (LHC)[1] study the region with high temperature and low baryon chemical potential, while very few experiments are studying high μ_B and moderate temperatures. One of the objectives of these studies is to explore the microscopic structure of baryon dominated matter in the domain where baryon resonances play an important role.

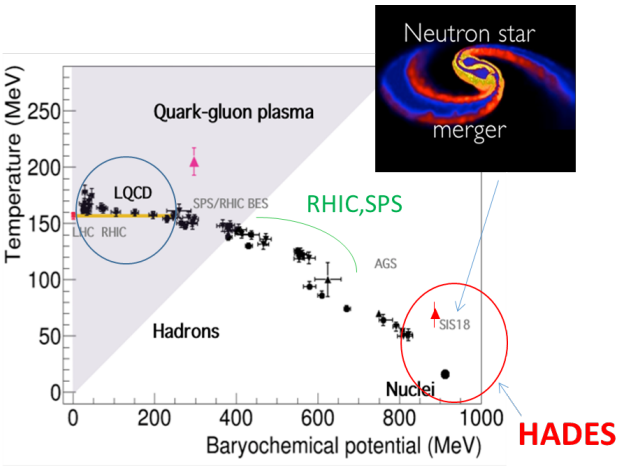

Figure 1: The QCD phase diagram. The black symbols are the chemical freeze-out points deduced from hadron abundances. The yellow curve displays the lattice QCD predictions for the phase boundary. Red triangles are the points measured from the invariant-mass slope of dimuons by the NA60 collaboration [2] and of dielectrons by the HADES experiment [3].

The pion-nucleus reaction is an important source of information about hadronic matter. In particular, at incident momenta below 2 GeV/c, it gives access in a very unique way to the properties of baryonic resonances in the nuclear medium. While the region of the $\Delta(1232)$ resonance, corresponding to incident pion beam momenta of about 300 MeV/c, was studied in detail in the past [4, 5], only very scarce measurements were provided at higher energies, e.g. in the second resonance region (N(1440), N(1520), N(1535),..). Such information is however needed in the context of dense hadronic matter studies for the description of heavy-ion reactions at a few GeV/nucleon, where pion-nucleus dynamics play a crucial role. More generally, measurements of proton and pion differential spectra in pion induced reactions is needed to validate transport models or hadronic cascades used in GEANT4 for various applications involving pion detection. We focus here on the analysis of the proton and pion spectra in different exclusive channels ($p\pi^-$, $p\pi^-\pi^-$ and $p\pi^-\pi^+$) measured in the $\pi^- + C$ reaction at an incident pion momentum of 690 MeV/c.

The HADES experiment

The High-Acceptance Di-Electron Spectrometer (HADES) [6] is a fixed target experiment located at the SIS18 accelerator at the Helmholtzzentrum für Schwerionenenforschung (GSI) in Darmstadt. It is divided into six sectors around the beam axis covering 85% of azimuthal angles and polar angles between 18° and 85° as shown in Fig.2. Charged hadrons (p, π^-, π^+) are tracked using four Multiwire Drift Chambers, placed before and after a superconducting toroidal magnet, allowing for the measurement of the momentum. Particle identification via dE/dx and time of flight is performed using two plastic scintillators TOF ($\theta > 45°$) and RPC ($\theta < 45°$).

The experiment took place in August 2014 using a

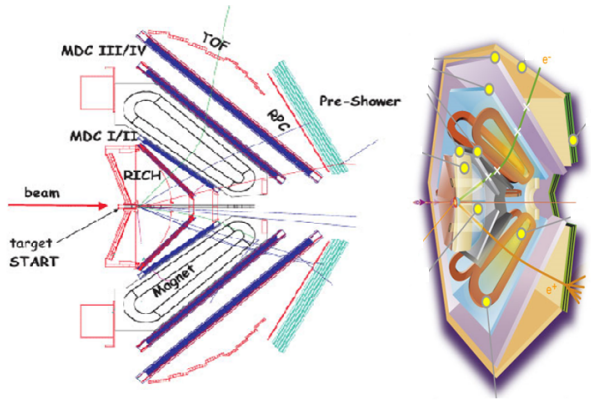

Figure 2: Schematic layout of the HADES detector.

secondary pion beam on polyethylene and carbon targets. Data on carbon were mainly used for subtraction of $\pi^- + C$ interactions in CH_2 target to study free $\pi^- + p$ collisions. In this work, we present dedicated analysis using the large available statistics for hadronic channels (π^-, π^+ and p) production in the $\pi^- + C$ reaction.

To normalize the data measured on the CH_2 and carbon targets, the analysis of the $\pi^- + p$ elastic scattering is used, as described in [11].

Simulations

As discussed below, the results are compared to predictions of the INCL (Intranuclear Cascade model) [7] and of PLUTO [8], a Monte Carlo simulation framework developed by the HADES collaboration for heavy ion and hadronic-physics reactions. These two models are different in their construction.

Simulated events are filtered using acceptance and efficiency matrices depending on particle momenta and angles. These matrices, which were calculated using GEANT simulations reflect our detector's response and allow for a realistic comparison of simulations to the data. INCL++ provides normalized distributions, while only relative yields are available from PLUTO, thus all spectra compared to PLUTO will be normalized to the area.

PLUTO

The incident pion interacts with the carbon target described as an off-shell participant proton moving with a momentum distribution which follows an effective spectral function taken from (e,e'p) results [9], and an on-shell spectator nucleus (^{11}B). Only defined quasi-free channels can be included and no further interactions are taken into account.

INCL

The carbon target is described as a nucleon Fermi gas where all nucleons are moving and on-shell. The incident pion interacts with the target nucleus by transferring part of its energy and momentum to it, through binary pion-nucleon or nucleon-nucleon collisions, successive and well separated in space and time, then ejecting few nucleons and/or pions from the carbon target. The nucleon-nucleon distance is large compared to the mean free path λ of the incident pion in the target nucleus. It is then considered that the different binary collisions are independent of each other. A nucleon mean field is acting on products. Excitation, decay and absorption of the $\Delta(1232)$ resonance is also taken into account through reactions of the type : $\pi N \longleftrightarrow \Delta(1232)$ or $NN \longleftrightarrow N\Delta(1232)$. However, no higher lying baryon resonances is included. Multi-pion production is treated using parameterizations of elementary cross sections [10]. De-excitation of the excited residual nucleus is treated in the evaporation step.

Quasi-elastic analysis

0.1 Selection of the quasi-elastic channel

To select the quasi-elastic channel, first events with one proton and one π^- were selected. The Fig. 3 shows how Quasi-elastic (QE) events were further selected. A cut on the momentum correlation of the π^- and proton in the laboratory frame (red line) is applied and the coplanarity condition ($150° < \Delta\phi < 210°$) is enforced. For comparison, calculations for the free process $\pi^- + p \to \pi^- + p$ has been drawn (black line).

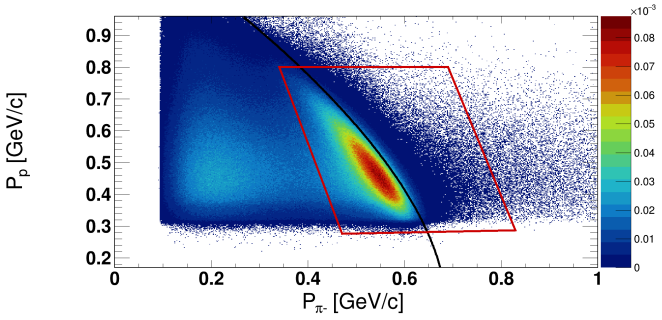

Figure 3: Momentum correlation between detected protons and pions showing two well separated correlations (inelastic on the left and quasi-elastic on the right). The black line corresponds to the momentum correlation between detected proton and π^- for the free binary reaction $p + \pi^- \to p + \pi^-$. The red line shows the selection used for quasi-elastic events.

Comparison with simulations

To make a relevant comparison with the data, QE cuts are also applied to simulations.

The angular distribution of detected pions, in the center of mass frame of a $\pi^- + p$ reaction with a proton at rest, is shown in Fig.4. The mean value of pion

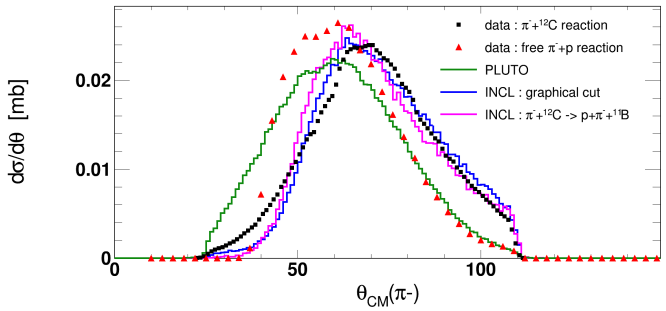

Figure 4: Angular distribution of the π^- from QE events. The distribution is shown in the center-of-mass frame of a $\pi^- + p$ reaction with a proton at rest.

angular distribution for data measured on the carbon target is shifted to higher values w.r.t data on free proton (red triangles in Fig.4). INCL describes the pion angular distribution much better than PLUTO, which predicts a distribution close to free proton scattering. However, the difference between PLUTO and INCL does not seem to be due to rescatterings. This is checked, by selecting from all simulated INCL events, those produced in a pure quasi-elastic process without rescatterings (magenta curve in Fig.4). The pion angular distribution seems indeed not to be very sensitive to the rescattering.

Investigation of Short Range Correlations (SRC)

The missing momentum is compared to both models in Fig.5. It is calculated as :

$$\vec{P}_{miss} = \vec{P}_{beam} - \vec{P}_{p} - \vec{P}_{\pi^-} \quad (1)$$

where $\vec{P}_{beam}$, $\vec{P}_{p}$ and $\vec{P}_{\pi^-}$ are the beam, proton and pion momentum vector, respectively.

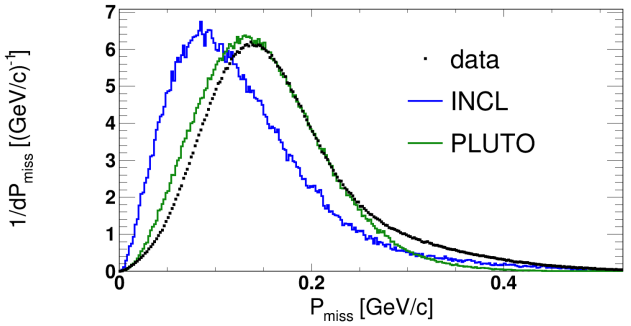

Figure 5: Missing momentum distribution for QE $\pi^- + p$ events compared to PLUTO and INCL predictions.

For a pure quasi-elastic process, the missing momentum corresponds to the momentum of the participant proton in the nucleus. With the effective proton momentum distribution reproducing (e,e') scattering data [9], PLUTO describes this missing momentum distribution very well up to 250 MeV/c, while the INCL distribution, which is based on the Fermi gas model is shifted to lower values. This distribution is sensitive to the "local energy" parameter used in INCL to reduce the momentum of the participant particle close to the surface of the nucleus. This helps to get realistic cross sections in such case, where interaction cross sections vary rapidly with the momentum [12].

Data shows a long tail for high proton momenta. This can be due to rescattering effects, resolutions of the detector or SRC. SRC are nucleon pairs that are close together in the nucleus and have high relative and low center-of-mass momentum, compared to the Fermi momentum [13, 14]. INCL is exploited in order to test the possibility to suppress rescattering effects from data and increase the sensitivity to SRC. Figure 6 shows the distributions of missing momentum (top) and missing mass for the reaction $\pi^- + {}^{12}C \rightarrow \pi^- + p + X$ (bottom) with different event selection.

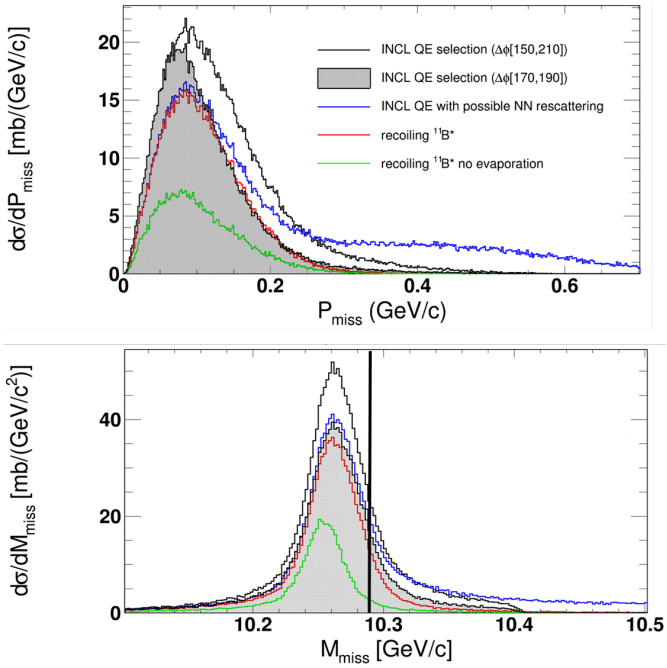

Figure 6: Missing momentum (top) and missing mass distributions (bottom) for different event selection in INCL : Our "QE" selection (black line), our "QE" selection with strict coplanarity condition (black filled area), pure QE (red), QE+rescattering (blue) and pure QE with excitation energy lower than nucleon emission threshold of the ^{11}B remnant (green).

We first consider INCL++ events corresponding to a first $\pi^- + p$ quasi-elastic collision. The difference between blue and red curves corresponds to rescattering effects in INCL, which extends the distribution towards large missing momenta and large missing masses. In addition, it can be observed that for more than 50% of the pure quasi-elastic events (i.e. without rescattering), the recoiling nucleus is excited above the nucleon emission threshold. Then, by comparing $\pi^- + p$ events obtained after applying the QE selection criteria (shown as a black curve) to the pure quasi-elastic

events, one can study the validity of our selection. It can be checked that events with high missing momenta due to rescatterings are efficiently suppressed. A tight $\Delta\phi$ ($180°\pm10°$) cut is needed to further suppress rescatterings and gets closer to the pure quasi-elastic distribution. However, an excess of events with low missing momentum can still be observed, which needs to be further investigated. To suppress scattering effects, that prevent from the investigation of Short Range Correlation effects, while keeping most of the pure quasi-elastic events, we propose to make a cut on the missing mass variable ($M_{miss} < 10.29$ GeV/c^2) or to narrow the $\Delta\phi$ selection. Studies are on-going to check that such cuts do not suppress the expected Short Range Correlation effects.

Inelastic channels : Two pion production

We also show results for exit channels with a pion emitted in addition to a $\pi^- + p$ pair : $p\pi^-\pi^-$ and $p\pi^-\pi^+$.

The sequential emission of the two pions (quasi elastic step $\pi^- N \rightarrow \pi^- N$ followed by $NN \rightarrow NN\pi$) is suppressed, due to the detection of the π^- in the forward hemisphere and, hence, the too small energy of the backward emitted nucleon in the quasi-elastic step. Both channels are therefore mainly produced in two pion production reactions, either in a single collision ($\pi^- n \rightarrow \pi^-\pi^- p$ or $\pi^- p \rightarrow \pi^-\pi^+ p$, with a smaller cross-section for the latter), or followed or preceeded by a quasi-elastic step ($\pi^- N \rightarrow \pi^- N$) or charge exchange ($\pi^- p \longleftrightarrow \pi^0 n$).

$\pi^- + C \rightarrow \pi^- + \pi^- + p + X$

We show in Fig.7 the normalized missing mass spectrum (in the reaction $\pi^- + ^{12}C \rightarrow \pi^- + \pi^- + p + X$).

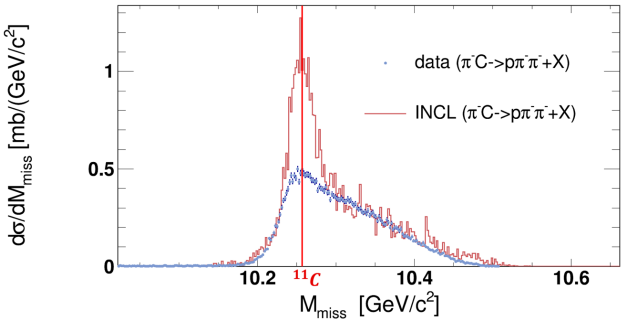

Figure 7: Missing mass of the $\pi^- + ^{12}C \rightarrow \pi^- + \pi^- + p + X$ reaction.

Events with invariant masses close to the ^{11}C mass are due to a pure quasi-free double pion production process. The broad distribution for higher missing mass values represents the excitation energy of the remnant and it comes from the rescattering of pions/nucleons in the nucleus. INCL++ overestimates by 40% the number of $p\pi^-\pi^-$ events. In addition, data shows a much larger effect of rescattering than predicted by INCL.

$\pi^- + C \rightarrow \pi^- + \pi^+ + p + X$

The normalized spectrum of missing mass variable is also shown for $\pi^- + ^{12}C \rightarrow \pi^- + \pi^+ + p + X$ in Fig.8

The absence of a peak close to the low invariant masses in this $p\pi^-\pi^+$ channel confirms that it is not produced from a single collision and a charge-exchange step is needed. Therefore, this channel allows us to make a selective study of rescattering processes. The yields of this channel are overestimated by INCL (by 60%), like for $p\pi^-\pi^-$. This confirms that the two pion production cross sections seem to be overestimated in INCL++.

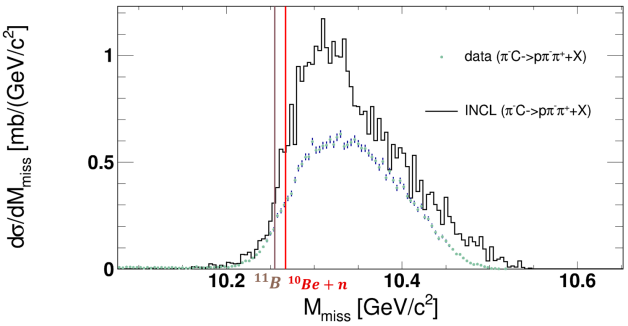

Figure 8: Missing mass of the $\pi^- + ^{12}C \rightarrow \pi^- + \pi^+ + p + X$ reaction.

Conclusion and outlook

We have presented an analysis of some exclusive channels : quasi-elastic ($\pi^- p$) and two pion production ($\pi^-\pi^- p$ and $\pi^-\pi^+ p$). The high statistics data allow for a test of model predictions. For the quasi-elastic process, we presented studies with the INCL++ code, which allow to better understand rescattering processes. The aim is to optimize cuts used to select events from the pure quasi-elastic process. Studies are on going to quantify the effect of Short Range Correlations in our data. The analysis of $p\pi^-\pi^-$ and $p\pi^-\pi^+$ events was also confronted to INCL++ predictions, pointing to too large double pion production cross sections in the model. Discussions are on-going with INCL++ experts to adjust parameters of the model to better reproduce the data. An important step will also consist in the estimation of the experimental systematic errors. We also started to investigate new exit channels ($\pi^-\pi^-$, $\pi^-\pi^+$, $p\pi^+$, pp...) and to test other models including $N^*(1440)$, $N^*(1520)$, ... baryon resonances in addition to $\Delta(1232)$ (SMASH, rQMD...).

References

[1] Kenta Shigaki [ALICE Collaboration], Progress of Theoretical Physics Supplement 186, (2010) doi:10.1143/ptps.186.427

[2] H. J. Specht [NA60 Collab.], AIP Conf. Proc. 1322, (2010) 1.

[3] J. Adamczewski-Musch et al. (HADES Collaboration), Nature Phys. 15 (2019) 1040.

[4] S. Teis et al., Z. Phys., A356 :421, 1997.

[5] D. Ashery et al. True absorption and scattering of pions on nuclei. Phys. Rev. C 23, 2173 (1981).

[6] G. Agakishiev et al. (HADES collaboration), Eur. Phys. J. A41, 243-277 (2009).

[7] S. Leray et al. J. Phys. Conf. Series 420 (2013) 012065.

[8] I. Frohlich et al., PoS ACAT 076 (2007) doi:10.22323/1.050.0076 [arXiv:0708.2382 [nucl-ex]].

[9] K. Nakamura et al. The reaction $^{1}2C(e, e'p)$ at 700 MeV and DWIA Analysis. Nucl. Phys. A, 268 (1976), 381.

[10] Th. Aoust and J. Cugnon. Phys. Rev. C 74, 064607 (2006).

[11] J. Adamczewski-Musch et al. (HADES collaboration), Phys. Rev. C102 (2020) 024001.

[12] A. Boudard et al. Phys. Rev. C 87, 014606 (2013).

[13] M. Patsyuk et al., Nat. Phys. 17, 693 (2021).

[14] A. Schmidt et al., Nat. Phys. 578, 540 (2020).

Impact of hadronic cascades on the 2nd order net-charge cumulant proxies studied for Au+Au at $\sqrt{s_{NN}} = 200$ GeV/A with EPOS 4

Johannès JAHAN[1], ***with with K. Werner*** [1], ***T. Pierog*** [2] ***and M. Stefaniak*** [3,4]

[1] *Subatech, Nantes Université - IMT Atlantique - IN2P3/CNRS, Nantes, France*
[2] *KIT Campus North, Institut für Kernphysik, Karlsruhe, Germany*
[3] *Warsaw University of Technology, Warsaw, Poland*
[4] *GSI Helmholtzzentrum für Schwerionenforschung, Darmstadt, Germany*

Abstract — The susceptibilities are useful theoretical tools to probe the existence of a 1st order phase transition and a possible critical endpoint of nuclear matter phase diagram. In this context, STAR collaboration recently published some measurements of their experimental equivalents, the 2nd order cumulants for net-electric charge (Q), net-protons and net-kaons in Au+Au collisions, across many energies of the Beam Energy Scan (BES) program.
Hence, we plan to simulate those collisions with the event generator EPOS, in order to reproduce STAR analyses, and especially study the impact of hadronisation process and hadronic cascades on these observables. We show here our first results for collisions at $\sqrt{s_{NN}} = 200$ GeV/A, obtained with a preliminary version of EPOS 4.

Introduction

Since the creation of a deconfined state of the nuclear matter, called Quark-Gluon Plasma (QGP), has been indirectly observed in ultra-relativistic heavy-ion collisions almost 20 years ago [1, 2, 3, 4], tremendous efforts have been made to learn more about its properties. One of the main goals is to precisely map the phase diagram of Quantum Chromo-Dynamics (QCD). On the theoretical side, many models have been used to make predictions about its structure, an important result being the prediction of a potential 1st order phase transition and a critical endpoint (CEP) [5] between the QGP and hadronic phase. On the experimental side, those predictions have motivated the creation of Beam Energy Scan (BES) program [6], which aims to explore this diagram by colliding heavy-ions in a large range in energy, from few to several hundreds of GeV/A. The search for signatures of criticality is since a very active field of research, using notably the measured event-by-event fluctuations of net-multiplicity distributions for different particles, which are related to the thermodynamic susceptibilities [7, 8, 9, 10]. These observables are connected to the susceptibilities, and thus to the derivatives of the equation of state (EoS). Consequently, they reflect the magnitude of the thermal fluctuations which will diverge near a possibly existing CEP.

However, heavy-ion collisions are very complex processes, from which many aspects are still not clearly understood [11, 12, 13]. Also, if there were to be any critical behaviour of the matter created in such collisions, it is not precisely known yet how important would be the signatures of this criticality, and how the amplitude of the signal would be modified by the other stages of the event [14]. Some phenomenological studies have already been achieved to clarify this point [15, 16, 17], but always within specific frameworks. To perform such study by taking into account the complete background of the collision, we propose to use EPOS [18], an event generator dedicated to heavy-ion physics that uses hydrodynamical evolution of the bulk matter, which can be assimilated to a QGP droplet [19].

In this proceeding, we will first of all introduce the susceptibilities, as well as their experimental counterparts, *i.e.* net-number cumulants of the proxies used by the STAR experiment. Then, after a short presentation of the different ingredients used to simulate events within the EPOS event generator, we will give a review of the new features introduced with the last version EPOS 4, and present the motivations of our work. Finally, we will present the first results of our investigations on the impact of hadronic cascades on these cumulants of the 2nd order, compared with STAR data for Au-Au collisions at $\sqrt{s_{NN}} = 200$ GeV.

This work takes place in the larger process of evaluating EPOS 4 validity in the energy range of the BES program, which is essential before its public release.

Susceptibilities and net-charge cumulants

In the grand-canonical (GC) ensemble, susceptibilities are theoretical tools that quantify how the partition

function of the system changes under the variation of chemical potentials. In the search for radical changes in the state of the nuclear matter, like CEP or 1st order phase transition, these quantities should diverge in the presence of such critical behaviour [20].

In a system of volume V and temperature T, the susceptibilities are defined as the derivatives of the pressure P with respect to the reduced chemical potentials $\hat{\mu} = \mu/T$ of the charge considered, here electric charge (Q), baryonic number (B) and strangeness (S). Considering that pressure is connected with the logarithm of the QCD partition function $Z(T, V, \mu_B, \mu_Q, \mu_S)$, one can write [8] :

$$\chi^{B,Q,S}_{i,j,k} = \frac{\partial^{i+j+k}(P/T^4)}{(\partial\hat{\mu}_B)^i(\partial\hat{\mu}_Q)^j(\partial\hat{\mu}_S)^k} = \frac{1}{VT^3}\cdot\frac{\partial^{i+j+k}\ln Z(T,V,\mu_B,\mu_Q,\mu_S)}{(\partial\hat{\mu}_B)^i(\partial\hat{\mu}_Q)^j(\partial\hat{\mu}_S)^k} .$$

In this work, we will focus on the 2nd order susceptibilities, imposing thus $i + j + k = 2$ in the previous equation. These susceptibilities can be linked to event-by-event fluctuations of the corresponding conserved charges, *i.e.* 2nd order cumulants of these net-charges via

$$\chi^{X,Y}_{1,1} = \frac{1}{VT^3}.\sigma^{1,1}_{X,Y} = \frac{1}{VT^3}(\langle N_X N_Y\rangle - \langle N_X\rangle\langle N_Y\rangle),$$

$$\chi^{X}_{2} = \frac{1}{VT^3}.\sigma^{2}_{X} = \frac{1}{VT^3}(\langle {N_X}^2\rangle - \langle N_X\rangle^2),$$

with the net-multiplicities $N_{X,Y} = n_{X,Y} - n_{\overline{X},\overline{Y}}$, and X, Y being B, Q or S [8].

However, experiments are facing the impossibility to measure directly net-B and net-S, because they can only access distributions of charged particles, pions, kaons, protons and Λ with enough precision to allow cumulants analyses. Moreover, calculate susceptibilities would require to evaluate V and T, which are very difficult to access experimentally. For this reason, ratios are generally used to get rid of the T and V dependence, even though the cancellation is not exact as these quantities also fluctuate event-by-event [14].

In this respect, the STAR collaboration has recently provided experimental measurements of variances and covariances of net-pions, net-protons and net-kaons (proxies for net-Q, net-B and net-S), for Au-Au collisions in the whole energy range of the BES program [21]. These (co)variances have been measured as a function of the pseudorapidity acceptance and of the number of participants in the collision N_{part}, which is related to the centrality of the collision. They have also been used to construct the following ratios :

$$C_{Qp} = \frac{\sigma^{11}_{Qp}}{\sigma^2_p} \qquad C_{QK} = \frac{\sigma^{11}_{QK}}{\sigma^2_K} \qquad C_{pK} = \frac{\sigma^{11}_{pK}}{\sigma^2_K}$$

still shown as a function of N_{part}, but also integrated and plotted as a function of $\sqrt{s_{NN}}$. Note that proxy ratios for Q are built using covariances of identified particles, like $C_{Q\alpha} = (\sigma^{11}_{\pi\alpha} + \sigma^{11}_{p\alpha} + \sigma^{11}_{k\alpha})/\sigma^2_\alpha$. Data were taken for particles within $|\eta| < 0.5$ and with momentum $0.4 < p_T < 1.6$ GeV/c, while N_{part} is estimated from the charged multiplicity distribution of the events with the Glauber model [22], using particles with $0.5 < |\eta| < 1$ and $p_T > 0.15$ GeV/c. The study presented in this proceeding uses these results as a baseline.

EPOS

Monte-Carlo event generators are widely used, for many years now, to model hadronic interactions and help to understand the underlying mechanisms taking place in high-energy hadronic collisions. In the catalogue of general purpose event generators, EPOS [23] is one of the approaches capable of successfully describe data from both collider experiments [24, 25, 26] and high-energy cosmic rays induced air showers [27, 28, 29].

EPOS relies on the parton-based Gribov-Regge theory (PBGRT) [30], a marriage of perturbative QCD with Gribov-Regge theory of multiple interaction [31] which can be applied to many systems, from lepton-proton deep-inelastic scattering (e-p) to nucleus-nucleus collisions (A-A). In this formalism, the elementary scatterings happening simultaneously in parallel between the participating partons are modeled by theoretical objects called Pomerons, each of them providing their own contribution to the total T-matrix of the reaction. They can be composed of a soft part, a parametrised T-matrix element corresponding to an exchange of low-virtuality gluons, and/or a hard part, corresponding to high-virtuality partons whose T-matrix contribution is computed using DGLAP evolution equation. The Pomerons, which are physically equivalent to parton ladders, can be either cut and then used for particle production, or uncut, giving interference terms in the total cross-section calculations. A schematic representation of a multiple Pomerons exchange for a nucleus-nucleus collision can be seen in Fig. 1 ; more details about the approach are given in [30]. Saturation effects [32] are also taken into account, with a saturation scale Q_s calculated for each individual Pomeron ; we will discuss it with a bit more details later. Once the configuration of parton ladders produced by the primary interactions is established, each chain made of a quark-antiquark pair linked by gluon(s) is identified with a relativistic string, which evolves following the dynamics of a gauge-invariant Lagrangian [33] and fragment into hadrons by producing pairs of (di)quark-anti(di)quark [34].

In heavy-ion collisions, as well as in high-multiplicity collisions of small systems (p-p, p-A), the density of strings reached is so important that they cannot possibly evolve and decay independently from each other. In such situation, we separate at a certain early time τ_0 the region with a high string segments density, which will constitute a bulk matter called "core", from the escaping segments with a high-p_T which will compose the "corona". This "core-corona" procedure is applied by evaluating, for each string segment, if it has enough

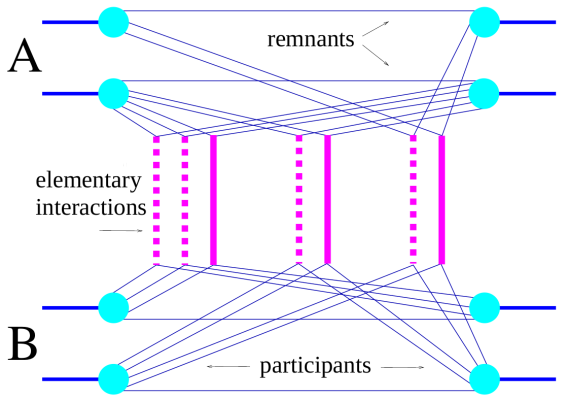

Figure 1: *Diagrammatic view of a multiple Pomeron exchange in the PBGRT for a A-A collision*

initial transverse momentum (p_T) to escape the region with a local string density ρ, following the formula :

$$p_T^{esc} = p_T - f_{E_{loss}}(p_T) \int_\gamma \rho.dL$$

where γ is the trajectory of the segment, and $f_{E_{loss}}(p_T)$ the linear energy loss which is function of the initial p_T of the segment considered [18]. If the value of p_T^{esc} is positive, the segment will be considered as part of the corona, and will follow the classical string evolution described previously ; otherwise, it will stay in the core. The latter one will then be used, assuming fast thermalization, as initial condition for a viscous 3+1D hydrodynamic evolution [35], using a cross-over transition equation of state with 3 flavours conservation (B, Q, S). This flowing medium will cool down while expanding and eventually turn to hadrons via a statistical hadronisation procedure, using until now the GC Cooper-Frye formulae [36], when reaching a critical temperature T_H (taken as $T_H = 166$ MeV [37]). Finally, the formed hadrons will still interact between each other via hadronic scatterings using the UrQMD model [38], in what is generally called hadronic cascades, until complete freeze-out of the system.

Motivations

All characteristics of the model presented so far are valid for EPOS 3, but the substantial developments achieved during the past years on several aspects of the event generator has led to a new version : EPOS 4. The first major upgrade concerns the saturation scale used in the evolution of the parton ladders, in the initial state. While in the early versions of EPOS, a constant was used [39], Q_s now depends on both number of participants N_{part} interacting in the collision, and number of Pomerons exchanged N_{Pom}, the latter one being important in p-p events as it is the only one to vary with the event activity [40].

Another significant change is the possibility to use a new equation of state (EoS) in the hydrodynamic evolution of the core, that include a 1st order phase transition and a CEP (taken from [20]), instead of the cross-over transition one used previously. This new feature could justify, at first sight, to study how final-state observables used to probe criticality are modified by the presence of a CEP. However, because we use a non-stochastic formulation of hydrodynamics that doesn't include any ingredient mimicking thermal fluctuation (see discussion about such work in [14]), we expect that most of the fluctuations originate from initial state, hadronisation and hadronic cascades.

The last important modification relates to the hadronisation process of the core part. Because in small systems the core can be relatively small, using a GC approach may not conserve energy and flavours properly, as discussed in [41]. Therefore, a microcanonical procedure is now employed in EPOS 4, which is equivalent to the previously employed GC one for large masses, but differs significantly for small masses. More detailed information are provided in [42].

Thus, even though EPOS is not appropriate to study the presence of a CEP because of the hydrodynamics framework it employs,this new feature can motivate the study presented in this paper, whose goal is to investigate how hadronisation and hadronic cascades impact the net-particle cumulants presented in the first section, for the energy range of the BES program. To do so, we will evaluate these cumulants before and after the hadronic cascade, taking advantage of the fact that EPOS gives such possibility, to quantify how they are modified by the last stage of the collision. The results presented in the next section will be especially related to this topic.

Results & discussion

All the results shown here have been obtained from 1.5M events of Au-Au collisions at $\sqrt{s_{NN}} = 200$ GeV, simulated with EPOS v3.424. We compare them with results measured by the STAR collaboration from [21], using the same kinematic cuts. The only difference with the experimental analysis is that we plot the cumulants directly as a function of N_{part}, which we can access for each event via Glauber model calculations. The centrality bin-width effect, inducing trivial volume fluctuations to the signal, is in fact not supposed to have any impact on the 2nd order cumulants (discussed in [43], and verified in our case although we don't show it here).

We show in Fig. 2 the (co)variances of net-π, net-p and net-K as a function of N_{part}, measured from EPOS simulations before the hadronic cascade (*i.e.* just after hadronisation of the core) and for full events simulated, compared with STAR data. Focusing first on the results for full events, we see that EPOS does reproduce qualitatively well the centrality dependence observed by STAR, even for σ^{11}_{pK} where the UrQMD model alone fails [21]. EPOS is even able to match the data in a quantitative way for σ^2_p and σ^{11}_{pK}, but slightly overshoots the measured amplitudes for σ^2_π, σ^2_K, σ^{11}_{Qp} and σ^{11}_{QK}. For the latter ones, the discrepancies are simply due to a global overproduction or an imbalance between

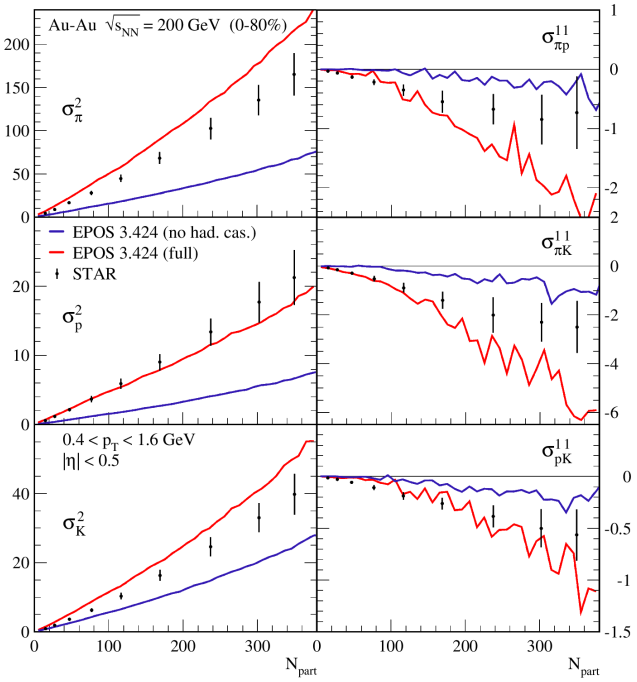

Figure 2: *Centrality dependence of variances and covariances of net-Q, net-p and net-k for Au-Au collisions at* $\sqrt{s_{NN}} = 200$ *GeV/A. Different results from EPOS are compared with STAR data [21].*

the positively and negatively charged particles for the species of interest, as the variances are directly proportional to the net-multiplicity numbers.

When comparing now with the results obtained just after hadronisation, we observe a significant increase of the amplitude for all (co)variances due to the hadronic cascades. The signal is doubled to tripled for variances, and even most of it originates from the hadronic phase for the covariances. The rise of the signal amplitude can be explained by the increase of the involved hadronic species multiplicities during this stage, due to the decays of heavy resonances and inelastic scatterings. For the covariances in particular, the major part of the correlation originates effectively from these processes as the particles can be produced together via scatterings (*e.g.* $X + Y \to \pi + p$) or decays (*e.g.* $X \to K + p$).

Fig. 3 displays the ratios C_{Qp}, C_{Qk} and C_{pk} introduced at the end of the first section, still as a function of N_{part} measured for both full EPOS simulations and before hadronic cascades, and compared with STAR data. As a result of the differences with the experimental data observed for (co)variances, we observe discrepancies with the data for ratios too. For C_{pk} in particular, we see that EPOS is able to reproduce the small signal for the most central collisions, contrary to UrQMD.

The important conclusion, coming from the comparison between the calculation achieved before the hadronic cascades and for full events, is that the hadronic stage have little impact on the value of the ratios, despite modifying significantly the amplitude of the (co)variances signals. This is particularly true for C_{pK} where the amplitude is almost not modified by the hadronic cascade, while there is still a variation of about ~ 0.1 for C_{Qp} and C_{QK}.

Summary & outlooks

We present a study of the impact of hadronic cascades on the 2$^{\text{nd}}$ order cumulants of net-charge, net-protons and net-kaons in Au-Au collisions at $\sqrt{s_{NN}} = 200$ GeV/A, led with a preliminary version of the event generator EPOS 4. Our motivation is to study how the last stage of the collision affect their ratios, which are related to the ratios of thermodynamic susceptibilities of the associated conserved charges, and that are thus used to probe the existence of a possible CEP in the QCD phase diagram. The main takeaway message of the results shown here is that hadronic cascades seems to have a very small impact on the signal ratios, in spite of their impact on the variances and covariances themselves.

The next step of our project is of course to go to lower energies in order to scan the whole range of the BES program and investigate the energy dependence of these ratios. In parallel, we also want to extend our study to some "enhanced" proxies (using more species like Λ, Ξ and Ω baryons) proposed in [15], and eventually to some higher-order cumulants. Finally, we plan to study the impact of different hadronisation processes, thanks to the new features of EPOS discussed in our motivations.

References

[1] BRAHMS collaboration, *Nucl. Phys. A* **757** (2005), arXiv:nucl-ex/0410020 [nucl-ex]

[2] PHOBOS collaboration, *Nucl. Phys. A* **757** (2005), arXiv:nucl-ex/0410022 [nucl-ex]

[3] STAR collaboration, *Nucl. Phys. A* **757** (2005), arXiv:nucl-ex/0501009 [nucl-ex]

[4] PHENIX collaboration, *Nucl. Phys. A* **757** (2005), arXiv:nucl-ex/0410003 [nucl-ex]

[5] M. Stephanov, K. Rajagopal & E. Shuryak, *Phys. Rev. Lett.* **81** (1998), arXiv:hep-ph/9806219 [hep-ph]

[6] STAR collaboration, e-print (2010), arXiv:1007.2613 [nucl-ex]

[7] M.A. Stephanov, *Phys. Rev. Lett.* **102** (2009), arXiv:0809.3450 [hep-th]

[8] M. Cheng et al., *Phys. Rev. D* **79** (2009), arXiv:0811.1006 [hep-lat]

[9] M. Asakawa, S. Ejiri & M. Kitazawa, *Phys. Rev. Lett.* **103** (2009), arXiv:0904.2089 [nucl-th]

[10] B. Friman, F. Karsch, K. Redlich & V. Skokov *Eur. Phys. J. C* **71** (2011), arXiv:1103.3511 [hep-ph]

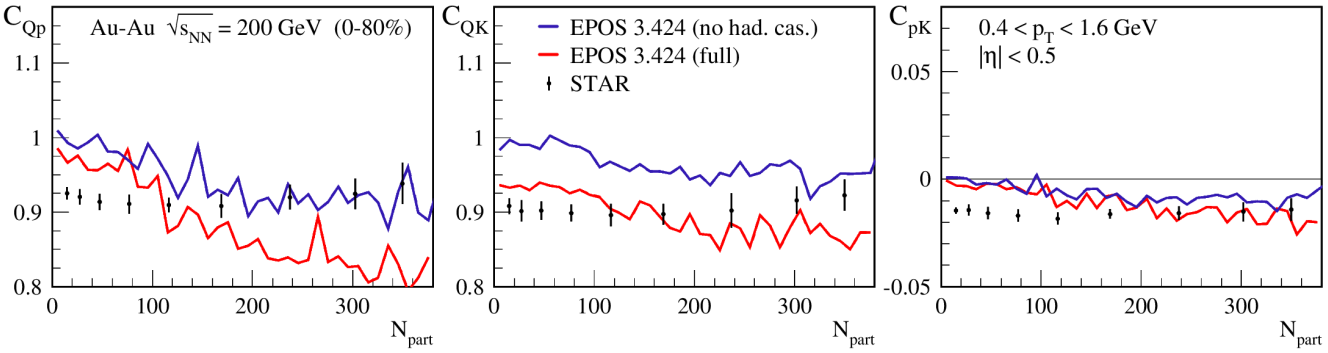

Figure 3: *Centrality dependence of covariances to variances ratios of net-Q, net-p and net-k for Au-Au collisions at* $\sqrt{s_{NN}} = 200$ *GeV/A. Different results from EPOS are compared with STAR data [21].*

[11] A. Mazeliauskas, *Nucl. Phys. A* **982** (2019), arXiv:1807.05586 [nucl-th]

[12] J.N. Guenther, *Eur. Phys. J. A* **57** No.4 (2021), arXiv:2010.15503 [hep-lat]

[13] S. Cao & X.-N. Wang, *Rept. Prog. Phys.* **84** (2021), arXiv:2002.04028 [hep-ph]

[14] M. Bluhm et al., *Nucl. Phys. A* **1003** (2020), arXiv:2001.08831 [nucl-th]

[15] R. Bellwied et al., *Phys. Rev. D* **101** (2020), arXiv:1910.14592 [hep-lat]

[16] P. Braun-Munzinger, A. Rustamov & J. Stachel, *Nucl. Phys. A* **960** (2017), arXiv:1612.00702 [nucl-th]

[17] J. Steinheimer, V. Vochenko, J. Aichelin, M. Bleicher & H. Stöcker, *Phys.Lett.B* **776** (2018), arXiv:1608.03737 [nucl-th]

[18] K. Werner, B. Guiot, I. Karpenko & T. Pierog, *Phys. Rev. C* **89** (2014), arXiv:1312.1233 [nucl-th]

[19] U. W. Heinz, *Workshop on Extreme QCD* **3-12** (2005), arXiv:nucl-th/0512051 [nucl-th]

[20] P. Parotto et al., *Phys. Rev. C* **101** (2020), arXiv:1805.05249 [hep-ph]

[21] STAR collaboration, *Phys. Rev. C* **100** (2019), arXiv:1903.05370v2 [nucl-ex]

[22] STAR collaboration, *Phys. Rev. C* **79** (2009), arXiv:0808.2041 [nucl-ex]

[23] K. Werner, F.M. Liu & T. Pierog, *Phys. Rev. C* **74** (2006), arXiv:hep-ph/0506232 [hep-ph]

[24] N. Armesto, N. Borghini, S. Jeon, U.A. Wiedemann et al., *J. Phys. G* **35** (2008), arXiv:0711.0974 [hep-ph]

[25] T. Pierog, I. Karpenko, J.M. Katzy, E. Yatsenko & K. Werner, *Phys. Rev. C* **92** (2015), arXiv:1306.0121 [hep-ph]

[26] J. Aichelin et al., *Nucl. Phys. A* **956** (2016), DOI:10.1016/j.nuclphysa.2016.04.019

[27] T. Pierog & K. Werner, *Phys. Rev. Lett.* **101** (2008), arXiv:astro-ph/0611311 [astro-ph]

[28] T. Pierog & K. Werner, Nucl. *Phys. B Proc. Suppl.* **196** (2009), arXiv:0905.1198 [hep-ph]

[29] T. Pierog et al., *Proc. of Sc.* **ICRC 2021** (2021), arXiv:2105.06148 [astro-ph]

[30] H.J. Drescher, M. Hladik, S. Ostapchenko, T. Pierog & K. Werner, *Phys. Rept.* **350** (2001), arXiv:hep-ph/0007198 [hep-ph]

[31] V.N. Gribov, *Zh. Eksp. Teor. Fiz.* **53** (1967)

[32] L. McLerran & R. Venugopalan, *Phys. Rev. D* **49** (1994) 2233 ; *Phys. Rev. D* **49** (1994) 3352 ; *Phys. Rev. D* **50** (1994) 2225

[33] X. Artru, *Phys. Rep.* **97** (1983), DOI:10.1016/0370-1573(83)90080-7

[34] D.A. Morris, *Nucl. Phys. B* **288** (1987), DOI:10.1016/0550-3213(87)90235-5

[35] I. Karpenko, P. Huovinen & M. Bleicher, *Comput. Phys. Commun.* **185** (2014), arXiv:1312.4160 [nucl-th]

[36] F. Cooper & G. Frye, *Phys. Rev. D* **10** (1974), DOI:10.1103/PhysRevD.10.186

[37] K. Werner, I. Karpenko, T. Pierog, M. Bleicher & K. Mikhailov, *Phys. Rev. C* **83** (2011), arXiv:1010.0400 [nucl-th]

[38] M. Bleicher et al., *J. Phys. G* **25** (1999), arXiv:hep-ph/9909407 [hep-ph]

[39] K. Werner, I. Karpenko, T. Pierog, M. Bleicher & K. Mikhailov, *Phys. Rev. C* **82** (2010), arXiv:1004.0805 [nucl-th]

[40] K. Werner, *XVIII GDRE Workshop on Heavy Ions at Relativistic Energies* (2016), hal-02444682

[41] K. Werner, *KSETA Topical Courses* (2019), hal-02434245

[42] K. Werner, T. Pierog, B. Guiot & J. Jahan, *Phys. Atom. Nucl.* **84** No.6 (2021), DOI:10.1134/S106377882113041X

[43] N.R. Sahoo, S. De & T.K. Nayak, *Phys. Rev. C* **87** (2013), arXiv:1210.7206 [nucl-ex]

[44] V. Vovchenko & V. Koch, *Nucl.Phys.A* **1010** (2021), arXiv:2101.02182 [nucl-th]

[45] STAR collaboration, *Phys. Rev. C* **105** (2021), arXiv:1903.05370v3 [nucl-ex]

Part V

Instrumentation

session chaired by Sabrina SACERDOTI

Machine Learning for Real-Time Processing of ATLAS Liquid Argon Calorimeter Signals with FPGAs

Nemer CHIEDDE

Aix-Marseille University, CNRS/IN2P3, CPPM, Marseille, France

Abstract — The ATLAS experiment at the Large Hadron Collider (LHC) is operated at CERN and measures the energy deposited by particles produced in proton-proton (p-p) collisions with a repetition frequency of 40 MHz. The readout electronics of liquid-argon (LAr) calorimeters are being prepared for high luminosity-LHC (HL-LHC) operation as part of the phase-II upgrade, anticipating a pileup of up to 200 simultaneous p-p interactions. The increase of the number of p-p interactions implies the calorimeters have higher probability of having consecutive signals in the same cell within 25 bunch crossing (BC), making energy reconstruction more challenging. Field-programmable gate arrays (FPGAs) are used to process digitized pulses sampled at 40 MHz in real time and different machine learning approaches are being investigated to deal with signal pileup. The convolutional and recurrent neural networks outperform the optimal signal filter currently in use, both in terms of assigning the reconstructed energy to the correct proton BC and in terms of energy resolution. The enhancements are focused on energy obtained from overlapping pulses. Because the neural networks are implemented on an FPGA, the number of parameters, resource usage, latency and operation frequency must be carefully analysed.

Introduction

The ATLAS detector [1] is placed at the Large Hadron Collider [2] (LHC) and is used to detect particles generated in high-energy p-p collisions. Every 25 ns, the proton bunches collide, resulting in a collision frequency of 40 MHz. Scheduled to begin with Run-4 in 2027, the next high-luminosity phase of the LHC (HL-LHC) is projected to achieve instantaneous luminosities of 5-7x$10^{34} cm^{-2} s^{-1}$. This corresponds to 140-200 p-p interactions occurring at the same time. The ATLAS LAr calorimeter mainly exploits the ionisation signals to measure the energy of electromagnetic showers of photons, electrons, and positrons. The fact that up to 25 signal pulses produced in successive LHC BCs might overlap, resulting in an out-of-time pileup, significantly decrease the energy resolution of the LAr calorimeter.

Each of the 182,000 calorimeter cells is required to reconstruct the deposited energy at the correct BC with high energy resolution. The calorimeter is expected to provide real time energy reconstruction to the ATLAS trigger system, thus continuous data processing is required. As a result, the digital processing of LAr calorimeter signals in run 4 must be able to manage continuous data. Due to the huge input data bandwidth of about 250 Tbps delivered through serial connections with 36,000 optical fibers, FPGA technology was chosen over alternative processing devices. In the current design options, one Intel Stratix-10 FPGA [3], with a latency requirement of about 150 ns [4, 5], will process 384 or 512 LAr calorimeter cells, which corresponds to data measured by three or four so-called front-end boards (FEBs), respectively.

Energy reconstruction in the ATLAS liquid argon Calorimeter

The current readout electronics of the LAr calorimeters digitize the electrical pulse from the calorimeter at 40 MHz and apply an optimum filter [6] (OF) algorithm to compute the energy in each cell. The use of a linear combination of up to five digitized pulse samples reduces electronic noise and signal pileup. A peak finder is used to allocate energy to the appropriate BCs. When the pulse is distorted by earlier events the performance of the OF algorithm, that expects a perfect pulse shape, is significantly degraded. In this situation, the peak finder fails to assign the energy to the relevant BC.

To increase the energy resolution at the HL-LHC, we developed Artificial Neural Network (ANN) based approaches. The ANNs are trained using simulated HL-LHC data from AREUS [7]. AERUS simulates electronic noise in the detector which is added to low-energy deposits (up to 1 GeV) from particles created in inelastic p-p collisions that represent pileup. A homogeneous transverse energy spectrum is randomly superimposed to simulate hard-scattering events, with maximum energy deposits of 5 GeV at a mean interval of 30 BC and a standard deviation of 10 BC. The simulation is run for one cell in the LAr calorimeter's barrel section, with an average pileup (mu)=140.

Neural network

For energy reconstruction, two neural network topologies based on Convolutional and Recurrent Neural Networks (CNNs, RNNs) are evaluated. The ANNs are developed and trained using Keras [8] and TensorFlow [9]. This paper will concentrate on the RNNs, more details about CNNs can be found in reference [15].

Recurrent neural networks

RNN is a type of neural network that is used to process time series data. It comprises of an internal neural network that processes current input in conjunction with previously processed states. They are excellent candidates for quantifying deposited energy from time-ordered digitized LAr signals. The two RNN architectures investigated are Vanilla-RNN [11] and Long Short-Term Memory (LSTM) [12]. The vanilla-RNN is a network architecture with fewer parameters and only one activation function, which was chosen to be the ReLU activation function in our scenario. The LSTM, on the other hand, has a complex internal structure that gates the flow of information to the next timestep using neural network layers with sigmoid and tanh activation functions. As a result, LSTM can handle longer sequences and may be used in two ways. The sliding window approach (figure 1) divides the digitized signal from the calorimeter into overlapping sub-sequences with a single reconstructed energy for each sub-part. The second option is a single cell, which involves continuous information processing at each timestamp without the need of a sequence interval. Due to their simplicity, the Vanilla-RNN only works with the sliding window technique.

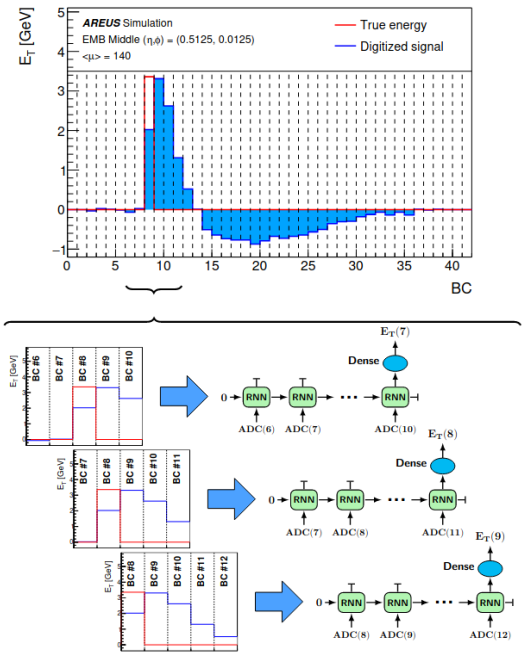

Figure 1: RNN processing of calorimeter samples with the sliding window architecture [15].

FPGA architecture and advantages

The energy reconstruction is done on the LAr Signal Processor (LASP). This board transmits the results (at 40 MHz) to the trigger and data acquisition systems. Startix-10 FPGAs are used in the LASP due to their low processing latency compared to CPU/GPU and also due to the on chip memory blocks and configurable logic components.

Neural network performance

The energy resolution of several NN algorithms is compared to the OF algorithm in Figure 2. Only energy deposits greater than 3σ the noise thresholds are taken into account. The performance of the five ANNs outperforms that of the OF.

The energy resolution is plotted as a function of the time gap between subsequent energy deposits in Figure 6. The OF performances decline dramatically when the gap is small, leading to overlapping pulses. In this low-gap zone, NNs are capable of restoring the performance.

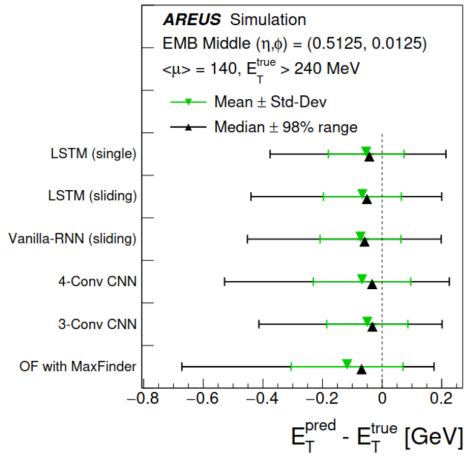

Figure 2: Energy resolution for different algorithms [15].

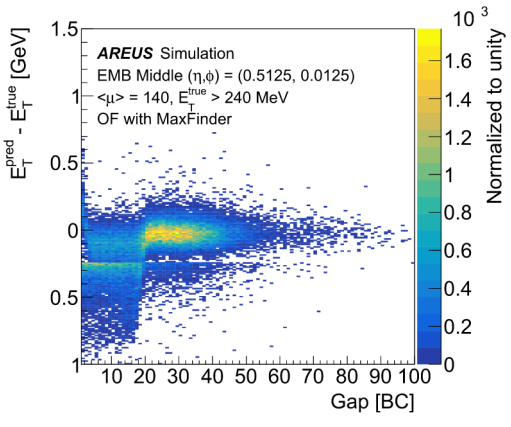

Figure 3: Energy resolution as function of the distance to previous high energy deposit for the OF with maximum finder algorithm [15].

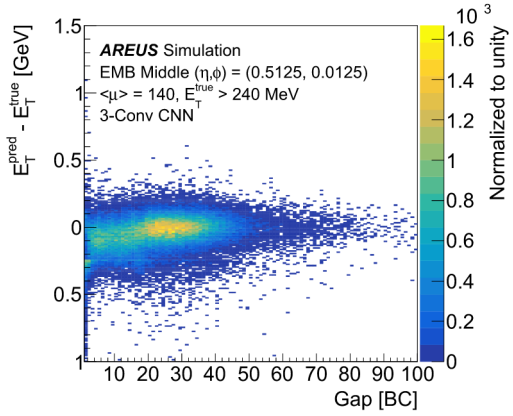

Figure 4: Energy resolution as function of the distance to previous high energy deposit for the 3-Conv CNN algorithm [15].

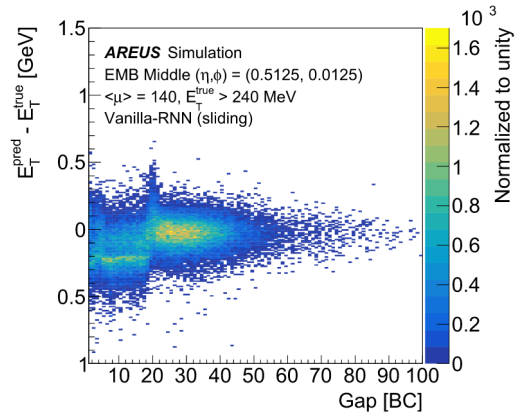

Figure 5: Energy resolution as function of the distance to previous high energy deposit for the Vanilla-RNN algorithm [15].

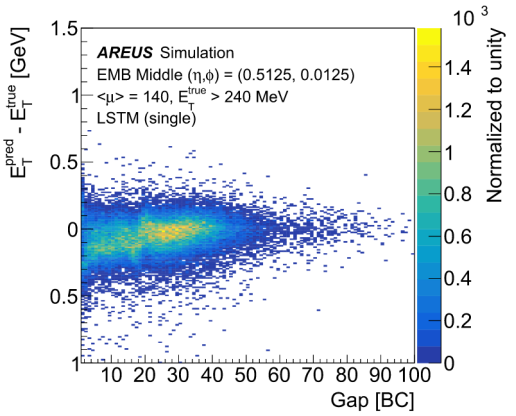

Figure 6: Energy resolution as function of the distance to previous high energy deposit for the LSTM algorithm [15].

FPGA performance

The CNNs and RNNs implementations were made with different hardware description languages. Very High-speed integrated circuit hardware Description Language (VHDL) is used to implement CNNs and High Level Synthesis (HLS) is used for RNNs. Those implementations are simulated in Quartus 20.4 [13] and Questa Sim 10.7c [14] respectively and their output is compared to the one from Keras. The small differences between the software and firmware implementations observed in figure 7 are caused by quantization and by the LUT-based realisation of the activation functions.

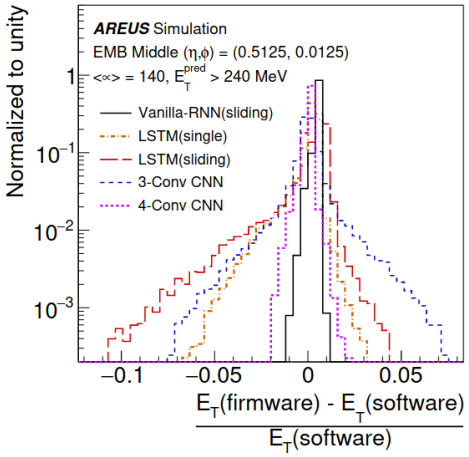

Figure 7: Relative deviation of the firmware and software results [15].

Table 1 and 2 show the maximum execution frequency, latency, initiation interval and resource usage on a Stratix-10 FPGA for a single data input channel in terms of number of digital signal processing (DSP) and adaptive logic modules (ALM). The maximum achievable processing frequency for all implementations is in the range of 480-600 MHz. The LHC data is received at 40 MHz which allows to implement networks with fifteen fold time multiplexing of the input data for vanilla RNN and six-fold for CNNs. Table 3 shows the properties of these multiplexed networks. The VHDL implementation of the CNNs targets mainly low latency for fast execution. The HLS implementation of the RNNs targets high frequency to allow higher multiplexing. This is reflected in the performance shown in table 3. Optimization of both implementation is ongoing to find an acceptable compromise between the high frequency and the low latency to fit the readout requirements for the LAr phase-II upgrade.

Table 1: Maximum achievable frequency, latency, initiation interval and resource usage of the RNNs (in HLS) on a Stratix-10 FPGA for an implementation with a single channel [15].

	Vanilla (**)	**LSTM (*)**	**LSTM (**)**
Max Frequency [MHz]	641	560	517
Clock (Cycle)	206	220	363
Initiation (Interval)	1	220	1
Resource Usage (DSPs / ALMs)	0.6% / 1.4%	3.1% / 1.9%	12.8% / 7.5%

(*)Single (**)Sliding

Table 2: Maximum achievable frequency, latency, initiation interval and resource usage of the CNNs (in VHDL) on a Stratix-10 FPGA for an implementation with a single channel [15].

	3-Conv	4-Conv
Max Frequency [MHz]	493	480
Clock (Cycle)	62	58
Initiation (Interval)	1	1
Resource Usage (DSPs / ALMs)	0.8% / 0.6%	0.7% / 0.6%

Table 3: Maximum achievable frequency, latency, initiation interval and resource usag of the multiplexed NNs implementation on a Stratix-10 FPGA [15].

	3-Conv	4-Conv	Vanilla
Multiplicity	6	6	15
Max Frequency [MHz]	334	334	640
Clock (Cycle)	81	62	120
Max LAr (Channels)	390	352	576
Resource Usage (DSPs / ALMs)	0.8% / 1.5%	0.7% / 1.7%	2.6% / 0.6%

Conclusions

CNNs and RNNs outperform the optimum filter method in reconstructing the energies deposited in the LAr calorimeter under HL-LHC conditions. The LAr's real-time processing requirements are successfully covered through multiplexed networks with latencies of roughly 200 ns and maximum execution frequencies of 344-640 MHz. At high luminosities, the adoption of ANNs on FPGAs has the potential to considerably improve ATLAS LAr calorimeter energy reconstruction, allowing for even more sensitive physics investigations and more efficient event selection by the ATLAS trigger system.

Acknowledgments

This work was in part supported by the German Federal Ministry of Education and Research within the research infrastructure project 05H19ODCA9. The project leading to this publication has received funding from Excellence Initiative of Aix-Marseille Université - A*MIDEX, a French âInvestissements dâAvenirâ programme, AMX-18-INT-006.

References

[1] ATLAS Collaboration, *The ATLAS experiment at the CERN large hadron collider*, JINST 3:S08003, Publisher (2008).

[2] Evans L, Bryant Ph, *LHC machine*, JINST 3:S08001, Publisher (2008).

[3] Intel Corporation, *Intel stratix-10 device datasheet*, Version 2020.12.24 Publisher (2020).

[4] ATLAS Collaboration, *Technical design report for the phase-II upgrade of the ATLAS TDAQ system, https://cds.cern.ch/record/2285584/*, CERN-LHCC-2017-020, ATLAS-TDR-029, Publisher (2017).

[5] ATLAS Collaboration, *Technical design report for the phase-II upgrade of the ATLAS LAr calorimeter, https://cds.cern.ch/record/2285582/*, CERN-LHCC-2017-018, ATLAS-TDR-027, Publisher (2017).

[6] Cleland WE, Stern EG, *Signal processing considerations for liquid ionization calorimeters in a high rate environment*, NIM A 338:467â49, Publisher (1994).

[7] Madysa N, *AREUS: a software framework for ATLAS readout electronics upgrade simulation*, EPJ Web Conf 214:02006, Publisher (2019).

[8] Chollet, François et al., *Keras, https://keras.io*, Accessed (Feb 2021).

[9] Martín A, Ashish A, Paul B et al., *TensorFlow: Large-Scale Machine Learning on Heterogeneous Systems, https://www.tensorflow.org/*, Accessed (Feb 2021).

[10] LeCun Y et al, *Backpropagation applied to handwritten zip code recognition*, Neural Comput 1(4):541â551, Publisher (1989).

[11] Sherstinky A, *Fundamentals of recurrent neural network (RNN) and long short-term memory (LSTM) network*, physd. 2019. 132306, Publisher (2020).

[12] Hochreiter S et al., *Long short-term memory. Neural*, neco. 1997.9. 8. 1735, Publisher (1997).

[13] Intel, *Quartus, ModelSim and HLS tools,*, https:// www. intel. com., Accessed (Feb 2021).

[14] Siemens, *Questa Sim*, Accessed (Jun 2021).

[15] Aad G, Berthold A, Calvet T, Chiedde N et al., *Artificial Neural Networks on FPGAs for Real-Time Energy Reconstruction of the ATLAS LAr Calorimeters, https://cds.cern.ch/record/2775033/*, ATL-LARG-PROC-2021-001, Publisher (2021).

Silicon trackers for neutrino tagging

Bianca DE MARTINO

Aix Marseille Univ, CNRS/IN2P3, CPPM, Marseille, France

Abstract — The recent progress in silicon detector technology opens the possibility to use these devices in neutrino beam lines. Such detectors would allow to kinematically reconstruct the neutrinos at production in the $\pi \to \mu\nu$ decays. This information would greatly benefit neutrino oscillation studies. The key aspects of the technique, referred to as neutrino tagging, are described in this article. The time resolution of the trackers appears to be critical as it determines the ability to resolve particles in very intense beams. The article presents an experimental study of the fundamental processes driving this resolution. The results of a test beam conducted with silicon planar sensors readout with the TDCPix chip are reported. The time resolution is measured for both p-on-n and n-on-p sensors and at different bias voltages. The impact of the pixel geometry is also studied. Finally perspectives are presented on a possible demonstration of the neutrino tagging using the existing NA62 experiment.

Introduction: neutrino tagging

The key measurements of the next decade for accelerator based neutrino experiments will be the neutrino mass ordering and the study of the charge-parity symmetry violation in the neutrino sector. These measurements require a large statistics and low systematic uncertainties.
In this context, an interesting option[1] could be to use a megaton scale natural water Cherenkov neutrino detector with a tagged neutrino beam. In such an experimental setup, the beam line would be instrumented with silicon trackers. These trackers would allows to reconstruct the neutrino produced in the $\pi \to \mu\nu$ decay based on the tracks of the incoming and outgoing charged particles. The tracker capabilities are limiting the beam intensity; it is possible to overcome this limitation by exploiting the very large size of the neutrino detector, in order to collect very large neutrino samples. For comparison, KM3NeT/ORCA, under construction off-shore Toulon will be 2 orders of magnitude larger than DUNE or HK. The aim is to perform a one-to-one match between the missing energy of the neutrino reconstructed by the tracker (the "tagged" neutrino) and the neutrinos interacting at the far detector.
The tracking of such a high intensity beam is the most challenging aspect of the neutrino tagging. For this purpose it is crucial to study and understand all the contributions that add up to the time resolution of silicon sensors. A study of the time resolution in silicon sensors performed on data from a beam test is described in the first two sections of this paper, while the last section contains a discussion on the possibility to demonstrate the tagging feasibility in an existing experiment.

Silicon sensors time resolution

Silicon pixel detectors' functioning principle is based on the p-n junction: the electrons near the p-n interface drift towards the p doped Silicon, while the holes drift towards the n doped Silicon. This separation creates a region that is free of charges, the depletion region. The width of the depletion region increases if a reverse bias voltage is applied across the junction, with the square root of the voltage. The signal is induced by the motions of electrons and holes produced by a ionizing particle crossing the sensor inside the depletion region and towards the electrodes, giving place to the particle detection[2]. The voltage bias affects not only the width of the depletion region in the p-n junction, but also the drift velocity of the charge carriers[10]:

$$\begin{aligned} v_n &= -\mu_n E, \\ v_p &= \mu_p E \end{aligned} \tag{1}$$

where v_n and v_p are the drift velocities of electrons and holes, E is the intensity of the electric field across the sensor, μ_n and μ_p the respective mobilities that depend on dopant and charge carrier concentration and temperature. For electric field values below 1 kV/cm, mobilities in silicon can be considered constant. When the electric field increases, the mobility becomes gradually more field-dependent and drift velocity tends to become constant, reaching a saturation value[10]. Depending on the doping of implants and bulk, there are several sensor types, such as n-on-p sensors (n implant on p bulk) and p-on-n sensors (p implant on n bulk). The sensors are bump-bonded to a readout chips.
The time resolution σ_t can be expressed as the sum of

several terms [3]:

$$\sigma_t^2 = \sigma_{\text{jitter}}^2 + \sigma_{\text{straggling}}^2 + \sigma_{\text{distortion}}^2 + \sigma_{\text{Time Walk}}^2 \quad (2)$$

. where:

- the term σ_{jitter} represents the time resolution contribution induced by the early or late firing of the comparator, due to the presence of noise. It is proportional to the inverse of the slope of the signal around the threshold value.
- the term $\sigma_{straggling}$ represents the time resolution contribution induced by the variation of charge deposit created by a crossing ionizing particle through the sensor, on an event-by-event basis. This produces an irregular signal that ultimately degrades the resolution.
- the term $\sigma_{distortion}$ originates from the non-uniformity of the weighting potential. The latter can be obtained by applying a unit potential to an electrode while grounding the neighbouring electrodes[9], and its shape is shown in Figure 1. The weighting field (WF) is the opposite the gradient of the weighting potential (WP), and depends on the distance between the pixel electrode to the backplane electrode, the pixel implant width and the distance to the neighbouring electrodes. As a result, the signal shape at the pixel center is different from the signal shape at the pixel edge, that spoils the time resolution.

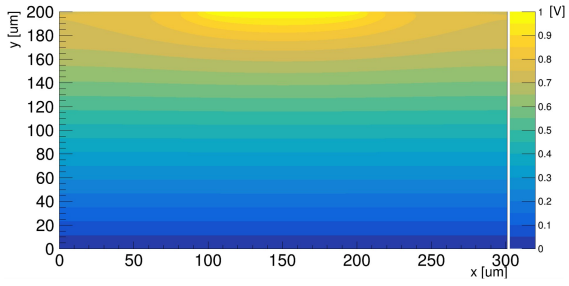

Figure 1: The weighting potential on the cross section of a p-in-n sensor on a $300\mu m \times 300\mu m \times 200\mu m$ pixel in a simulation from WeightField2[4]. The potential is more intense at the center than at the edges, and more uniform at the bottom than at the top.

- $\sigma_{TimeWalk}$ is a term that represents the time walk (TW), that affects the output of discriminators generating a delay on the firing of the discriminator. This effect is shown in Figure 2. This delay of detection depends on the signal amplitude: for signals arriving simultaneously, the time needed to cross the threshold is shorter for signals with larger amplitudes than for signals with smaller ones.

In order to study how these factors affect the time resolution of silicon pixel detectors a beam test was performed with planar silicon sensors (n-on-p and p-on-n) readout out with the TDCPix chip. This chip contains 40×45 pixels with a dimension of $300 \times 300\mu m^2$ integrates time digital converters with a 97 ps bin [6]. The chip was developed for the need of the NA62 experiment beam spectrometer called the GigaTracker[5].

Beam test data analysis

The beam test that has been analyzed has been performed at CERN SPS in 2017 with π^+ at 180 GeV/c, with the aim of studying the different contributions to the time resolution. The experimental setup includes three tracking planes made of planar sensors readout with TDCPix chips (the devices under test, DUT), and the LHCb VELO TimePix3 telescope[7]. This telescope has a high spatial resolution which allows to precisely determine the position at which the particle crossed the DUT. The data was collected with the two sensors types and with different bias voltages applied to them.

Time walk correction

A first coarse estimate of the TW corrections of each DUT was determined by using another DUT as time reference. Then, few iterations were performed in which the TW corrections were used to improve the precision of the time reference thus allowing to refine the TW correction of the DUT as function of the Time over Threshold (ToT). The ToT is the difference between the rising time and the falling time at threshold, and it is used as a proxy for the signal amplitude. Indeed, as shown in Figure 2, larger amplitudes correspond to larger ToT and a shorter delay of detection. The delay of detection as a function of the ToT is derived for each ToT bin thanks to the plots of $\Delta t = t_2 - t_1$ (where t_1 and t_2 are the rising times respectively of the first plane and of the second plane of the DUT) as function of ToT that are shown in Figure 3. The effect of the correction is to shrink and flatten the distribution.

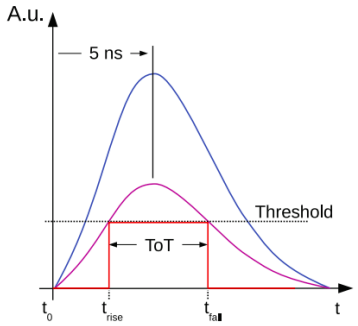

Figure 2: Signal amplitude as a function of time. For the same time of arrival, signals with larger amplitudes cross the threshold earlier when rising and later when falling than signals with smaller amplitudes. This translates in a larger ToT and a smaller time walk.

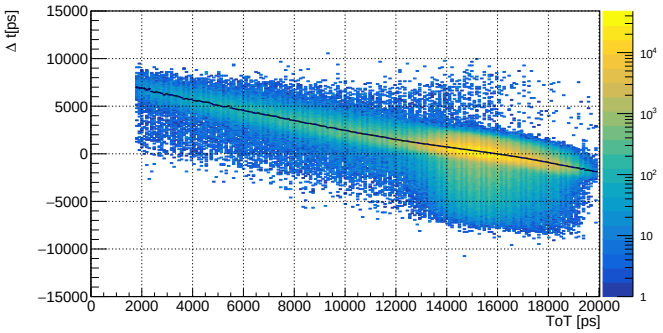

(a) Δt as function of ToT histogram before the correction.

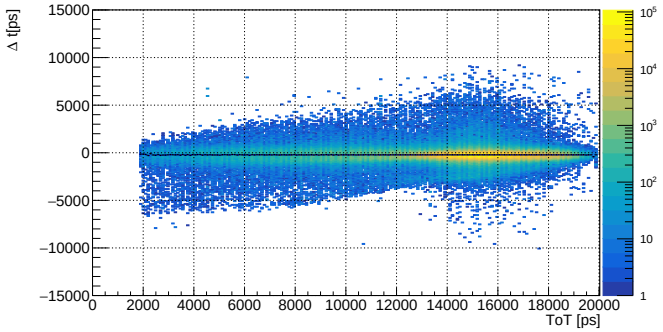

(b) Δt as function of ToT histogram after three iterations of correction.

Figure 3: The Δt as function of ToT plot (colors) with the mean values of Δt for each ToT bin (black dots), for planes 2 and 1, before and after the three rounds of iterations.

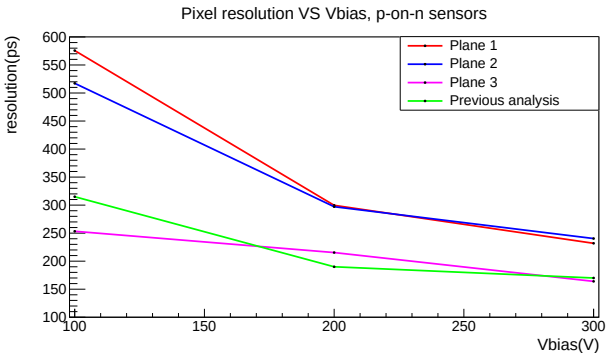

(a)

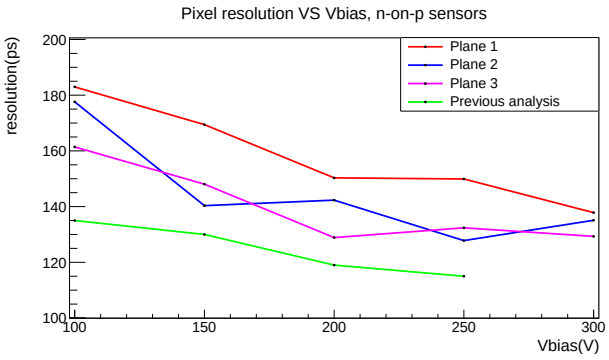

(b)

Figure 4: Resolution as a function of voltage bias for p-on-n (Figure 4a) and n-on-p (Figure 4b sensors: plane 1 is in red, plane 2 in blue and plane 3 in pink. The green line shows the results from previous tests.

Resolution as function of bias voltage and sensor type

The time resolution is obtained by fitting a Gaussian to the $\Delta t = t_i - t_j$ distribution, where t_i and t_j are the rising times of the two selected DUT modules. Assuming that the width of the Gaussian, σ_{i-j}, is the sum in quadrature of the two resolutions, σ_i and σ_j, the resolution of a single module can be extracted as:

$$\sigma_i = \sqrt{\frac{1}{2}(\sigma_{i-j}^2 + \sigma_{i-k}^2 - \sigma_{j-k}^2)}. \quad (3)$$

Figure 4 shows the time resolution as a function of the voltage bias. The n-on-p sensor time resolution, shown in Figure 4b, appears to be significantly better than the one of p-in-n, shown in Figure 4a. The signal induced by a crossing particle is made of two signals, the electrons-induced and the holes-induced signal; according to Ramo's theorem[8] the current induced in the electrodes by a charge carrier c is:

$$i_c = e\vec{E_W} \cdot \vec{v_c} = \mu_c e\vec{E_W} \cdot \vec{E} \quad (4)$$

where $\vec{E_W}$ is the WF and $\vec{E}$ is the electric field in the sensor. The mobility of the electrons is larger than the one of the holes, making the electrons the main contribution to the total induced current. In p-on-n sensors, electrons are collected in the part of the sensor where the WF is less intense. In n-on-p sensors, electrons derive towards the pixel electrode where the WF is more intense [9]; here the product of the WF and the electric field is maximum, making their contribution larger than in p-on-n sensors[2]. On the other hand, the charges moving towards the part where the WP falls to zero will not contribute to the signal[9], making the electrons contribution in p-on-n less intense. Moreover, the results show that the time resolution improves with a higher voltage bias, which was expected. The drift velocity of the charge carriers is directly proportional to the intensity of the drift electric field [10]. However, the results obtained in the present analysis are worse that the ones from the previous analysis[11][12]; this difference is of around ~ 20 ps in the case of n-on-p sensors, while it is in average much larger in the case of p-on-n sensors. Investigations are on-going to understand the reason of this difference.

Resolution as function of position inside the pixel

To investigate the effects of the WF, the time resolution was also measured as a function of the position inside the pixel. For this purpose, the TimePix3 telescope has been used to reconstruct the particles trajectory and determine the position at which they cross the pixels of the DUT. After having determined the offset in space and time between the DUTs and the

TimePix3 telescope, the hits in the DUTs were associated to the tracks reconstructed with the telescope. The spatial resolution to determine the particle position at the DUT has been computed using hits that fire two pixels. The firing of two adjacent pixels happens when a particle pass through the DUT pixel within 5μm from the edge. [1] Using these hits to compute the residual (that is the difference between the track coordinate and the hit coordinate) has the advantage of eliminating the main contribution to the spatial resolution given by the size of the DUT pixels. The spatial resolution is found to be $\sim 50\mu$m on the y coordinate and $\sim 30\mu$m on the x coordinate.
The pixel area of the DUT were divided in 3x10 regions as shown in Figure 5. The region to which a hit belongs is determined thanks to the position of the track associated to the hit. Only the central slice in y has been considered for the time being, as shown in Figure 5. The time resolution in a given region was derived us-

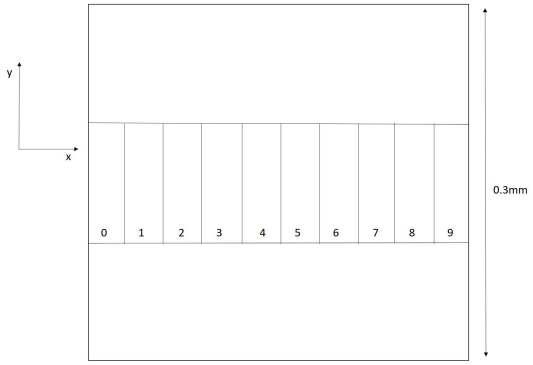

Figure 5: Sketch of slicing of plane 1 pixel.

ing the hits associated to the tracks intercepting this region on the DUT. The distribution of the time difference between these hits and the ones on the reference time DUT was fitted with a Gaussian. From the width of the Gaussian, σ_s, and the reference time resolution, σ_r, the time resolution for the region was estimate as:

$$\sigma_{1S} = \sqrt{\sigma_s^2 - \sigma_r^2} \tag{5}$$

In Figure 6 are plotted the resolution as a function of the position for the run taken at 250V for the n-on-p sensor. At the moment, it is not possible to resolve the WF effect. Further beam tests with an external time reference are foreseen in the near future, on planar sensors at different thicknesses and on new technologies such as LGADs. Hopefully those will yield to quantitative results as far as the WF effect is concerned.

Neutrino tagging feasibility study

A feasibility study of the neutrino tagging can be done using the data collected by the NA62 experiment[13].

[1] Also δ rays can fire two adjacent pixels. δ rays are not MIPs: they present large ToTs, which makes it possible to eliminate their contribution to the spatial resolution.

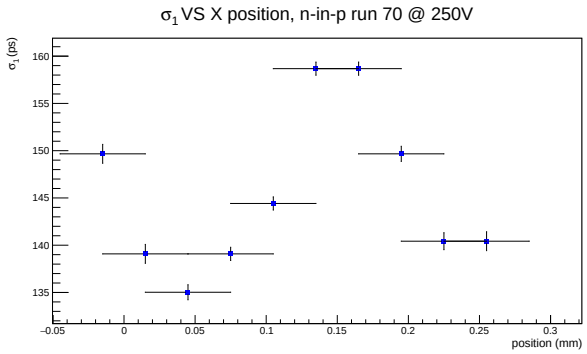

Figure 6: The resolution of plane 1 as a function of the position inside the pixel.

NA62 is a fixed-target particle physics experiment in the North Area of the SPS accelerator at CERN. Its purpose is to study rare kaon decays. The main Kaon decay mode, $K^+ \to \mu^+\nu$ can be exploited to demonstrate the neutrino tagging feasibility. The GigaTracker, the time resolved Silicon tracker of the experiment, in green in Figure 7, can precisely reconstruct the tracks from kaons. The STRAW spectrometer (in red in Figure 7) measures the trajectories and the momenta of the charged particles produced in the kaon decay such as muons. The muon neutrino produced in the decay can interact via a charged current interaction in the liquid Krypton calorimeter (LKr, on the right in blue in Figure 7), producing another muon and an hadronic shower. The two in-time muons (the one produced in the decay and the one generated by the Charged Current interaction of the neutrino) are then detected by the MUV3 (in orange in Figure 7), after passing through two hadronic calorimeters and the iron wall. A dedicated trigger line has been developed using the 2-muons topology and the energy deposited in the LKr. The neutrino interacting in the LKr can then be associated to a neutrino reconstructed with the kaon and the muon. This would demostrate the neutrino tagging feasibility.
This analysis has recently started; at nominal beam intensity, we expect ~ 60 neutrinos per year to interact in the calorimeter.

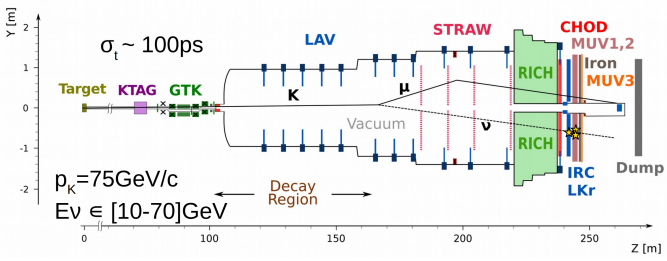

Figure 7: A view of the NA62 experiment; superposed in black the decay of a kaon in muon and neutrino. For a full description of the experiment the reader is reported to [13].

Conclusion

Neutrino tagging has the potential to change the way neutrino physics is done in the next decade. However it presents many challenges, one of them being the extremely high rate of particles at the tracker. For this reason it is necessary to study the time resolution of Silicon trackers, that plays a crucial role in the tagging and the matching of the neutrinos. It was showed that the time resolution of Si trackers depends on the voltage bias and on the sensor type. More studies are required to experimentaly characterise the WF effect. In addition to that, a feasibility study of the tagging on the $K^+ \to \mu^+\nu$ decay can provide important insight on the neutrino tagging method.

References

[1] M. Perrin-Terrin, Neutrino Tagging: a new tool for accelerator based neutrino experimentss, arXiv:2112.12848v1, Dec 2021

[2] Tsopelas, Panagiotis, A silicon pixel detector for LHCb, CERN-THESIS-2016-196

[3] N. Cartiglia, et al., Tracking in 4 dimensions, Nucl. Instrum. Methods Phys. Res., Sect. A, http://dx.doi.org/10.1016/j.nima.2016.05.078, May 2016

[4] F. Cenna et al., Weightfield2: A fast simulator for silicon and diamond solid state detector. In: Nucl. Instrum. Methods Phys. Res., Sect. A, https://doi.org/10.1016/j.nima.2015.04.015, Apr 2015

[5] M. Perrin-Terrin et al., The NA62 GigaTracKer: a low mass high intensity beam 4D tracker with 65 ps time resolution on tracks, Journal of Instrumentation, arXiv:1904.12837v3, Apr 2019

[6] G. Aglieri Rinella et al., The TDCpix readout ASIC: a 75 ps resolution timing front-end for the Gigatracker of the NA62 experiment, Physics Procedia 37, 2011

[7] Akiba et al, LHCb VELO Timepix3 telescope, Journal of Instrumentation, 10.1088/1748-0221/14/05/p05026, May 2019

[8] S. Ramo, "Currents Induced by Electron Motion," in Proceedings of the IRE, vol. 27, no. 9, pp. 584-585, Sept. 1939, doi: 10.1109/JRPROC.1939.228757.

[9] W. Riegler, G. Aglieri Rinella, Time resolution of silicon pixel sensors, Journal of Instrumentation, 10.1088/1748-0221/12/11/P11017, Jun 2017

[10] F. Cenna, Design and Test of Sensors and Front-End Electronics for Fast Timing in High Energy Physics, Thesis at Università degli Studi di Torino

[11] Noy M. et al., Characterisation of the NA62 GigaTracker end of column demonstrator hybrid pixel detector. Journal of Instrumentation, DOI:10.1088/1748-0221/6/11/C11025, 2011

[12] G. Aglieri Rinella et al., Test-beam results of a silicon pixel detector with Time-over-Threshold readout having ultra-precise time resolution, DOI: 10.1088/1748-0221/10/12/P12016, 2015

[13] The NA62 collaboration, The beam and detector of the NA62 experiment at CERN, May 2017, Journal of Instrumentation, DOI: 10.1088/1748-0221/12/05/P05025

Conception of a prompt-gamma detector for online proton therapy monitoring

Maxime JACQUET

Université Grenoble Alpes, CNRS, Grenoble INP, LPSC-IN2P3 UMR 5821, 38000 Grenoble, France

Abstract — Proton therapy is a tumor treatment taking advantage of the highly localized energy deposition at the end of the particle range, i.e the Bragg Peak. However, the determination of the Bragg peak position is subjected to uncertainties that require the establishment of safety margins during the irradiation of the patient, therefore decreasing the targeting efficiency. An online monitoring of proton therapy would allow real-time localization of the position of the Bragg peak, thus maximizing the treatment accuracy. Proton range measurement can be provided by the detection of Prompt Gammas (PGs), secondary particles generated almost instantaneously following a proton-matter nuclear collision. We propose a new approach for real-time imaging of the Bragg Peak, based on the time-of-flight measurement of PGs: the Prompt Gamma Time Imaging (PGTI). The precision on the Bragg peak location is directly related to the time resolution of our detection system, and simulations proved that a 100 ps rms time resolution would lead to a millimetric monitoring precision. Experimental tests using a ^{60}Co source permitted the characterisation of a prototype module achieving 190 ps rms of time resolution, paving the way for a PG detection with 100 ps of accuracy on the Time-Of-Flight (TOF) measurement.

Introduction

Protons have the benefit of presenting a very sharp dose depth profile, thereby offering an irradiation that can be precisely delimited to the tumor volume. Therefore, proton therapy presents a high targeting efficiency with a reduced dose deposition on healthy tissues. However, this high ballistic precision is impacted by the uncertainties in the measurement of the Bragg peak position, which can lead to significant overdosing of healthy tissue and underdosing of the targeted tumour. The sources of these uncertainties are multi factorial [**?**] and lead to the implementation of safety margins, which can be as large as 1 cm in case of deep-seated tumour.

In order to deal with these uncertainties, a real-time estimation of the Bragg peak position was proposed, through the development of a large variety of monitoring systems and methods ([**?**, **?**]). They take advantage of the correlation between the proton range and the spatial distribution of secondary particles produced by nuclear interactions within the patient [**?**]. These systems can infer information on the beam path in the distal (Bragg peak position) and/or transverse directions from the secondary particles detected. One of this method is the Prompt Gamma Timing (PGT), based on the time correlation between the PG TOF and the proton range [**?**]. This method relies on the use of very fast gamma-ray detectors ($LaBr_3$, BaF_2) [**?**] to measure the PG TOF with respect to the beam RF. Thus, the TOF precision ultimately achievable depends on the time-width of the proton bunches emitted by the accelerator, which is well above the time resolution of PG detection devices [**?**]. It was nevertheless stated that a 5 mm sensitivity on the proton range can be obtained with a proton bunch time-width of 2 ns FWHM and 10^4 PGs recorded [**?**]. More recently, the CLARYS collaboration showed that the PGT sensitivity can be improved using a fast gamma detector read in time-coincidence with a fast beam-tagging detector operated at a reduced beam intensity of 1 proton per bunch (single proton regime) ([**?**, **?**, **?**]), thus achieving 101 ps rms time resolution [**?**].

Based on these results, we propose to develop a detection system made of $\sim$ 30 small pixel detectors, closely arranged around a target, to measure in real-time the PGs TOF and their hit coordinates. This system, called TIARA, for Time of-flight Imaging ArRAy, will be read in time coincidence with a fast beam monitor. Each pixel will be composed of a Cerenkov radiator read out by a Silicon PhotoMultiplier (SiPM). Cerenkov cristals have higher density and they are inherently faster than classic scintillators, potentially providing better detection efficiency and time resolution. We propose to reconstruct the PG vertex through the resolution of an inverse problem where the only physical parameters of interest are the PG + proton TOF and the pixel position. We defined this method the Prompt Gamma Time Imaging (PGTI) [**?**]. PGTI is based on the solution of the following equation :

$$\mathrm{TOF} = \mathrm{T}_{\mathrm{proton}}(\mathbf{r}_v) + \frac{1}{c}\|\mathbf{r}_d - \mathbf{r}_v\| \qquad (1)$$

where the unknown is the PG vertex position ($\mathbf{r}_v$). $\mathrm{T}_{\mathrm{proton}}$ represents the proton transit time obtained via the Bethe Bloch equation, $\mathbf{r}_d$ corresponds to the PG hit

coordinates and $\frac{1}{c}\|\mathbf{r}_d - \mathbf{r}_v\|$ is the PG TOF. Therefore, a measurement of the overall TOF combined with the knowledge of the irradiated geometry and the pixel position is enough to determine the PG position of emission. To exploit the full potential of this detection system, we will focus on the control of the very first few irradiation spots in single proton regime, thus performing a proton range reconstruction helping clinicians to react in real-time in case of a beam displacement detection.

Simulation: capabilities of PG vertex reconstruction method

To explore the vertex reconstruction capabilities, Monte Carlo simulations were performed (GEANT4 10.4 release with the QGSP_BIC_HP_EMY physics list). Each simulation includes a spherical head of 10 cm radius, with 9.3 cm of homogeneous brain and 0.7 cm of skull thickness. This geometry was irradiated with a 6 mm radius pencil beam of 10^8 protons at 100 MeV. Thirty squared detection areas of 1 cm^2 were placed on the head surface. For each detection area, a 100 ps rms of time resolution, 26.6 % of detection efficiency (probability of interaction for a 4.4 MeV gamma-ray in a 1 cm thick PbF_2), and 1 MeV rms of energy resolution were assumed.

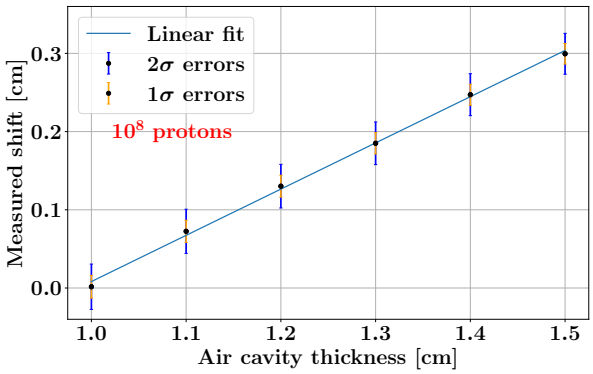

Figure 1: Correlation between the actual air cavity thickness and the corresponding beam displacement measured in the case of a 100 ps rms time resolution and 10^8 incident protons. The fit highlights the linear behaviour of our reconstruction method.

A simplified algorithm based on the Equation 1 was developed to estimate the potential of the reconstruction method. Therefore, the expected sensitivity for the detection of a longitudinal proton range shift, and for a lateral proton beam displacement were studied separately [**?**].

A variable thickness air cavity placed 4.5 cm after the head entrance was included to study the longitudinal sensitivity at a proton range shift. Then, the shift induced by the air cavity was measured as a function of the air cavity thickness (Figure 1) , revealing that a millimetric longitudinal displacement is measurable at 2σ.

The transverse sensitivity was assessed through a lateral beam displacement from 0 to 0.5 cm. For each beam displacement implemented, the shift was measured and compared to the actual beam position. The results are presented in Figure 2, showing that the method has a sensitivity of 2 mm at 2σ to detect a transverse beam translation.

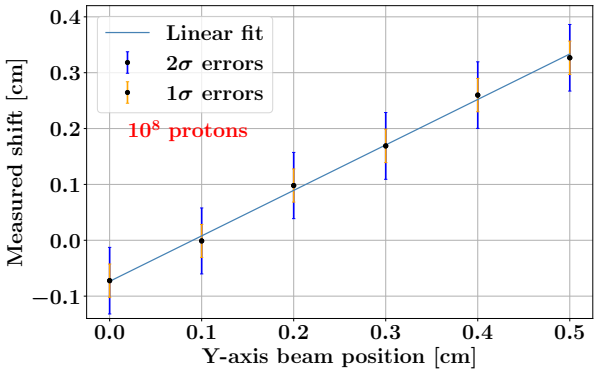

Figure 2: Correlation between the actual beam position and the corresponding beam translation measured in the case of a 100 ps rms of time resolution and 10^8 incident protons. The fit highlights the linear behaviour of the method implemented in this range.

The longitudinal and transverse sensitivity was investigated for different proton statistics. These results are summarised in table 1

Beam deviation	Longitudinal		Transverse
Nb. of Protons	10^7	10^8	10^8
Nb. of detected PG	3×10^3	3×10^4	3×10^4
1σ sensitivity (mm)	2	1	1
2σ sensitivity (mm)	3	**1**	**2**

Table 1: Summary of the 1σ and 2σ sensitivities obtained with the reconstruction methods described in the text. Values in bold correspond to the data presented in Figure 1 and Figure 2

Characterisation of pixel detectors

The pixel detector development is based on two main steps. The first is to characterize intrinsic SiPMs performances, in order to chose the best device in terms of time resolution and spectroscopic information. The second is to estimate the performance of a pixel detector composed of a Cerenkov crystal and a SiPM to detect gamma-rays. For this application, two Hamamatsu SiPMs were tested: Hamamatsu 13360-3050-CS and Hamamatsu 13360-3075-CS. Both are 3 mm^2 SiPM, the difference between the two SiPM being the micro cell size, which is of 50 μm for the former and 75 μm for the

latter. Each of those SiPM was read out by an ASD-EP-EB-PZ preamplifier board from Advansid. One of the main criteria guiding the SiPM choice is the Single Photon Time Resolution (SPTR) of the SiPM, i.e the time resolution of the SiPM when it detects one photon. The set-up to estimate the SiPM SPTR was the following: two identical SiPMs were illuminated by a Hamamatsu 48 ps FWHM pulse laser diode. Only the 1 photon signal detected by both SiPMs within the same pulse were selected. All signal acquisitions were realized using a Lecroy Oscilloscope with 1 GHz bandwidth, 10 Gs/s, and 12 bits ADC. The time difference was estimated between the 2 SiPMs signals with the std dev of this time difference distribution representing the coincidence SPTR. In order to obtain the SPTR, these value were divided by a factor $\sqrt{2}$. The results of SiPM SPTR are presented as a function of the SiPM overvoltage (Bias voltage above the breakdown voltage) in Figure 3.

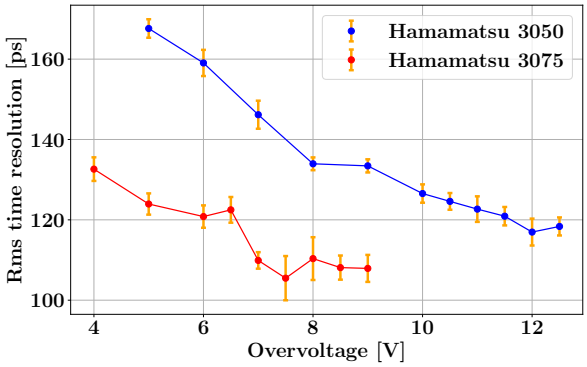

Figure 3: Single Photon Time Resolution of Hamamatsu SiPM 3050 and 3075 as a function of the SiPM bias voltage.

Figure 3 shows that the best overvoltage in terms of SPTR is different for each SiPMs, but the time resolutions achievable with SiPM + preamplifier are nearly SiPM independant. Therefore, Hamamatsu 3050 was chosen because of its better discrimination in term of number of photon detected.

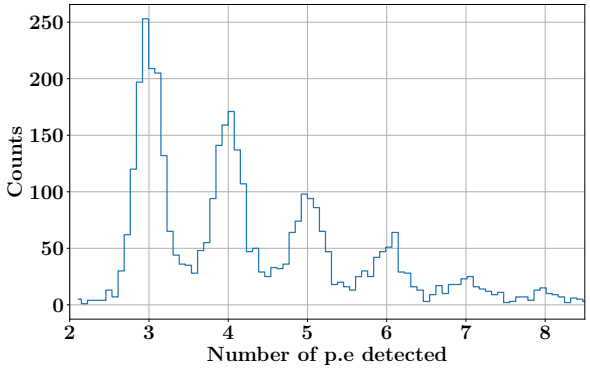

Figure 4: Number of photo-electrons recorded by the pixel detector with a threshold set at 2.5 photo-electrons.

Once the SiPM is chosen, it is crucial to estimate the time resolution of the whole pixel detector, i.e of a Cerenkov crystal coupled with a SiPM. The crystal selected is a 1 cm^3 PbF_2 radiator. The optical grease BC-630 from Saint Gobain was used to realise the optical coupling between the PbF2 and the SiPM. A ^{60}Co source enabled to estimate the time resolution in coincidence between two identical pixels. To reduce the SiPM dark counts, a 2.5 photo-electrons (p.e) threshold was applied to each detection block and the SiPM bias voltage was reduced to 7 V of overvoltage. Figure 4 represents the number of detectable p.e with a 2.5 p.e threshold. It means that for a 1.17 or 1.33 MeV gamma-ray, our detection system is able to detect up to 8 photons. Using the p.e spectrum, the time resolution was calculated as a function of the number of p.e detected, as shown in Figure 5.

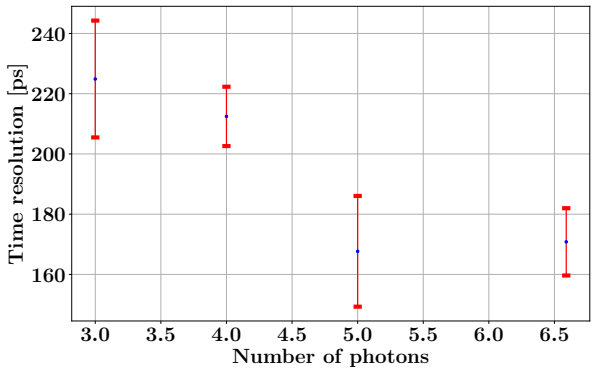

Figure 5: Time resolution of the detection pixel function of the number of photo-electrons detected. The value of 6.6 photo-electrons is the weighted average of the photo-electrons detected from 6.

Figure 5 proves that the time resolution improves according to the number of detected photon up to a value of about 170 ps rms. Since the time resolution roughly evolves in the same way as the Signal to Noise Ratio (SNR), a growth of the number of p.e detected should result in an improvement of the time resolution.

Discussion and conclusion

We propose a new approach for the determination of the PG vertex distribution based on the PG TOF measurement with a 100 ps rms time resolution. The method is based on the solution of an inverse problem that takes as input the PG detection time and hit coordinates. Simulations showed that the proton range can be measured with millimetric precision considering 10^8 incident protons. We also demonstrated the feasibility to detect 1 MeV gamma-ray with a technology combining Cerenkov radiator and SiPM. With the current amplifier, this block detector showed a time resolution down to 170 ps rms. Since the energy spectrum of PGs ranges from 1-2 MeV up to 10 MeV, the secondary electrons generated by the PG interaction will

have a higher kinetic energy than those generated by the gamma-ray interaction resulting from the decay of ^{60}Co. It implies a higher production of p.e, increasing the SNR, enhancing the time resolution ultimately achievable.

Acknowledgements

This work was partially supported by the ANR project ANR-15-IDEX-02 and by INSERM Cancer. This work was performed within the framework of the LABEX PRIMES (ANR-11-LABX-0063) of Université de Lyon.

[heading=subbibliography]

Development of a monolithic diamond ΔE-E telescope for particle identification and characterization of diamond detectors using the ToF-eBIC technique

Alexandre PORTIER

Laboratoire de Physique Subatomique et Cosmologie (LPSC Grenoble)
Institut Néel

Abstract — The diamond-based ΔE-E telescope detector device is obtained by Chemical Vapor Deposition of a thin epitaxic diamond layer (few microns) on a thick single crystal diamond substrate, including a metallic p^{++} boron doped layer in between. After an etching of the thin diamond layer in order to reach the p^{++} layer, electrical contacts are set at each surface layer. The combined measurement of energy loss in the thin layer and calorimetry in the thicker layer makes possible the identification of the various kinds of radiations, and charge and mass identification in the case of ionic projectiles. The dimensions of the two prototype detection stages have been optimized by simulation using the SRIM (The Stopping and Range of Ions in Matter) software. In parallel with this work, a very innovative characterization method that will be used for diamond detectors characterization has been set up: the time-resolved electron Beam Induced Current (TOF-eBIC) technique which enables a 2D mapping of a detector response to a well-focused electron beam.

Introduction

Semiconductor detectors are very commonly used to detect particles in physic experiments. Indeed, they have a higher efficiency and a faster response compared to gaseous detectors, and they have a far better energy resolution compared to scintillators. However, they are also easily damaged under charged particle irradiation. For this reason, more resistant semiconductors have been studied in order to develop the next generation of detectors.

Diamond is an ultra-wide bandgap semiconductor, which has been recently studied as a nuclear radiation detector [1, 2]. Because of its very high resistivity, its excellent charge transport properties, and its high radiation hardness, diamond is an ideal material to detect charged particles such as α particles, ions or Fission Fragments (FF) [3]. In order to identify ions with a simpler process requiring only one measurement, a monolithic diamond ΔE-E telescope is being developed. To better understand the charge transport properties of diamond detectors, α particle tests were conducted at laboratory with an ^{241}Am source, and a Time of Flight - electron Beam Induced Current (ToF-eBIC) setup was developed.

ΔE-E telescope

To identify a charged particle, it is necessary to measure the charge and the mass of said particle. To acquire these measurements, a multi-layer diamond detector based on the architecture of the ΔE-E telescope was developed (see Fig. 1). The detector was specifically designed so that when a charged particle interacts with the detector medium, the particle deposes part of its energy (proportional to Q^2/v^2) in the first layer (the ΔE stage) before stopping in a second layer (the E stage) and depositing its remaining energy. Thus, through this detector design, there is a correlation between the energy deposited in the ΔE layer and the total energy of the particle (proportional to $A.v^2$), which can be calculated by adding the energy quantities deposited in the two layers. Thus, by measuring the energy deposited in both layers, it may be possible to identify the particle which interacted in the detector. To acquire these measurements relating to the two detection stages, it is technically necessary to have an intermediate electrode. The challenge of this project lies in the design of a diamond electrode made of a layer of diamond highly doped with boron.

This kind of detector has already been used to detect light ions (in silicon: [4], in diamond: [6]) and FF particles (in silicon: [4, 5]). This project aims to create a diamond monolithic ΔE-E telescope used to detect α particles. To go further, the design could be adapted in order to detect FF particles.

The technique chosen to create this detector centers on a synthetic diamond substrate, from which a thin, highly-doped, and conductive diamond layer (the p^{++} layer or middle electrode) grows. As this second diamond layer grows, its growth creates a third diamond

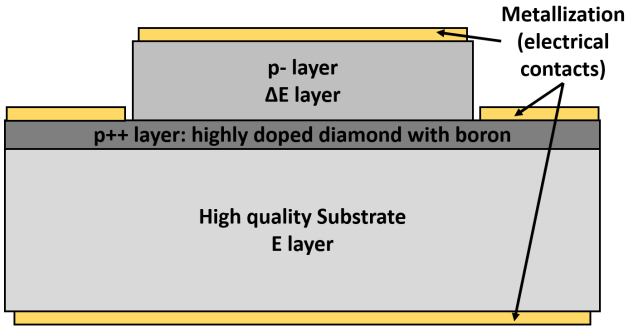

Figure 1: ΔE-E telescope scheme

layer (the p^- diamond layer). In order to maximize charge collection in the detector, the substrate and the p^- layer must be as pure as possible. Indeed, the impurities and dislocations lead to a recombination of the charge carriers and thus a lower charge collection [7]. As a result, an Element 6 (E6) single-crystal CVD diamond [8] with the purest crystalline quality (electric-grade) was chosen. In this diamond, the nitrogen concentration is about 5 ppb, and the boron concentration is about 1 ppb. Finally, for the doping of the p^{++} layer, a concentration of approximately 10^{20} cm^{-3} of boron is necessary to make the layer conductive.

To determine the thickness of the layers, the substrate needs to be thick enough in order to ensure that the incident particles stop inside of the substrate. The 550 μm thickness of E6 diamonds is more than sufficient to stop any ions with an energy of 10 MeV or less and every FF particles (SRIM simulation [10])). The p^{++} layer is a dead area of detection, so it must be as thin as possible. After discussion with the DiamFab startup of the Neel Institute [9], a thickness of 500 nm was chosen due to some technical requirements related to the growth of the layer. Determining the thickness of the p^- layer proved difficult: the p^- layer had to be thick enough to measure the energy deposited in the layer; however, if the p^- layer were too thick, it would be impossible to accurately measure the energy deposited in the substrate layer. To determine a thickness of the p^- layer which would allow for accurate measurements in both the p^- layer and the substrate, simulations were conducted with SRIM software, which is specifically adapted to simulate the energy deposition of ions in matter.

From simulation to manufacturing

To build the simulation, the ΔE-E telescope was recreated in the SRIM simulation software. The substrate was considered to be a carbon layer with a density of 3.52 $g.cm^{-3}$ (diamond density), a displacement energy of 43.0 eV, a lattice biding energy of 7.1 eV, and a surface binding energy of 7.41 eV ([11]). In the rest of this report, a layer with these characteristics will be referred to as a "diamond layer." Even if most of the ions have small ranges, the diamond substrate is considered to be 550 μm thick. Indeed, reducing the thickness does not significantly affect the simulation speed, so there are no known negatives associated with this choice. Regarding the p^{++} layer, the simulation proved that, as expected, doping does not significantly affect the energy deposit in the layer. As a result, the p^{++} layer was determined to be a simple diamond layer in this simulation. The p^- layer was also considered to be a diamond layer, and as explained in the previous paragraph, the thickness of the p^- layer was variable during simulations. The thickness of this p^- layer was represented throughout simulations as the variable th_{p^-}. In different simulations, th_{p^-} varied from a few hundred of nanometers to 10 μm. Different types of incident ions were also simulated, including light ions (proton, deuterium, tricium, helium 3 and 4) with an energy range of 1 to 35 MeV.

Regarding the simulation done on the light ions, the results are similar to the one we were expected: the mass ordering was respected for the five light ions tested. It was decided to optimized the first design on 5-6 MeV helium 4 simulation, because it is easy to study 5.5 MeV α particles in the laboratory using a radioactive source such as a ^{241}Am source.

The Figure 2 represents the simulated energy deposited in the p^- layer versus the total incident energy of the particle for different value of th_{p^-}. In order to determine an optimal th_{p^-}, some criteria were chosen: the energy deposition in the p^- layer needs to be superior to 1 MeV and inferior to the half of the particle initial energy. As a result, a value of 5 μm was chosen for the first design of the detector.

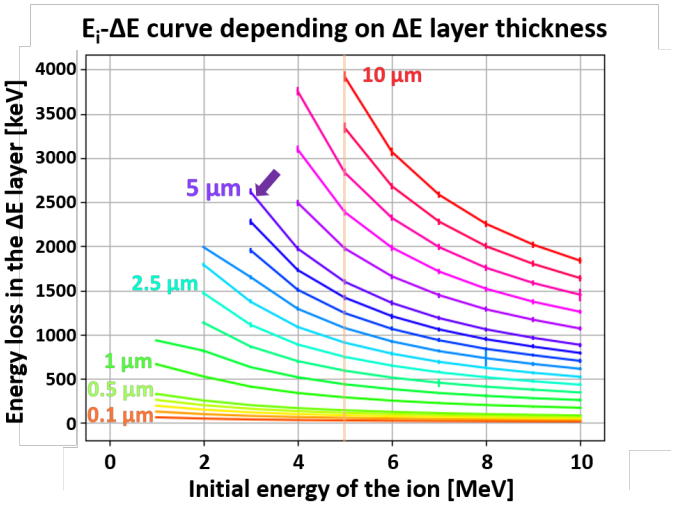

Figure 2: SRIM simulation results - energy deposited in the p^- layer by α particles of various energies for different p^- layer thickness th_{p^-}.

A test, sample was used to test the etching process. After some tests and discussions with the DiamFab staff, the following procedure has been chosen [12]:

- creation of the first mask by insulating a photosensitive resist deposited on the detector (laser lithography).

- deposition of a metallic mask (5 nm of titanium + 300 μm of aluminium) and lift-off of the resist.
- etching using an oxygen plasma with a DRIE (Deep Reactive Ion Etching).
- metallic mask removal.

Thanks to the good results of those tests, a first sample is being manufactured. The first p^{++} layer was done and the p^{-} layer will be done soon in early 2022. At first, the etching will be done in order to metalize the p^{++} layer. Then, some tests will be done with an ^{241}Am source at the LPSC and under alpha micro beam at AIFIRA.

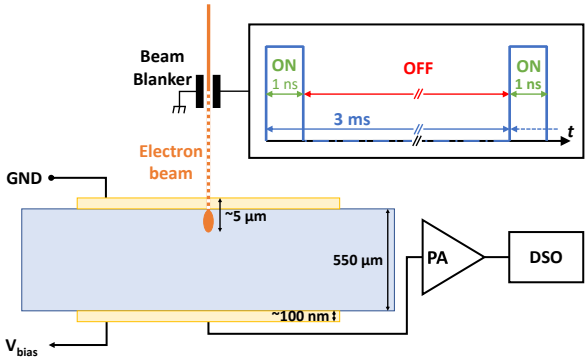

Figure 3: ToF-eBIC setup

Time-of-Flight electron Beam Induced Current

In parallel of those activities, some E6 high quality substrates were qualified thanks to a new very innovative setup: the Time-of-Flight electron Beam Induced Current (ToF-eBIC) setup at Institut NÃ©el in Grenoble. This setup used a pulsed electron beam in order to generate electron/hole pairs close to the surface. Compared to other setup using charged particles (such as α particles), the ToF-eBIC setup has a lot of advantages: an external trigger can be used in order to start the acquisition, the rate can be set directly by the user, the energy deposited by each pulse can be monitored and the spatial position of the beam can be controlled very precisely (micrometric resolution). This last point is particularly important in order to study the homogeneity of the current response of the detector and the polarization effect which is observed in diamond detector. Finally, the electrons of the pulse do not damage the diamond lattice.

The experiment is conducted in the following way (see Figure 3): a surface-metallized diamond sample is placed in a vacuum chamber of a Scanning Electron Microscope (SEM) and, the electron beam is focused on the diamond. The beam pass through a fast Beam Blanker (BB), which can be considered as a gap that can be biased on and off thanks to a voltage source. When there is no bias applied on the BB, the beam reach the sample (beam on). However, when a bias is applied on the BB, the electron beam is deflected and the beam do not reach the sample (beam off). As a results it is possible to generate pulses of electrons with a pulse width of about 1 ns and a period of 3 ms. Those pulses of 30 keV electrons will generate electron-hole pair in micrometric volume close to the surface (about 5 μm), and, because of the electric field, the charge carrier will drift toward the electrodes and induce a current that can be measured.

To qualify the setup, Transient Current Measurement were carried out. Those measurements consist to study the current induced by the drift of the charge carriers at different electric fields. Indeed, when the charge carriers started to drift because of the electric field, they induced a current as describe by the Shockley-Ramo theorem [14, 13] with a duration equal to their drift time and an amplitude equal to the total charge induced divided by the drift time. Consequently, the fastest the charge carrier is, the shortest the current induced width is and the highest the current induced amplitude is. That property lead to the fact that when the charge carriers are created just next to one electrode (~5 μm), one charge carrier is collected instantaneously (less than 100 ps) whereas the other charge carrier will drift along all the diamond thickness (550 μm) for several nanoseconds (typically from 10 to 50 ns). As a result, the signal induced by one charge carrier will be filtered by the read-out electronic, and so one charge carrier will be studied at the time.

Some traces obtained for holes at room temperature are shown Figure 4. It is clearly visible that when the bias increase, the signal becomes shorter. That can be explained easily by the fact that when the electric field increases, the drift velocity increases and so the drift time (which is equal to the signal width) is shorter. Concerning the amplitude, α and β spectroscopy measurements at lab has proven that the charge is entirely collected for electric field higher than 2000 V/cm (about 100 V) [15]. As a result, for those biases, the area of the pulses remains the same, and so if the width of the pulse decrease, the amplitude have to increase. One can notice that, with this explanation, the phenomenon is even more pronounced for the low biases where the area of the pulses become lower.

By measuring the drift time for different electric field, it is then possible to study the drift velocity versus the electric field. With this kind of study, some parameters such as the low field mobility and the saturation drift velocity can be calculated by fitting the drift velocity curve with this fit function:

$$v_{drift}(E) = \frac{\mu_0 E}{1 + \frac{\mu_0 E}{v_{sat}}} \quad (1)$$

With μ_0 the low field mobility and v_{sat} the saturation drift velocity. The value for holes are very close to the one obtained with α TCT measurements at lab or in literature. The differences in the results can be

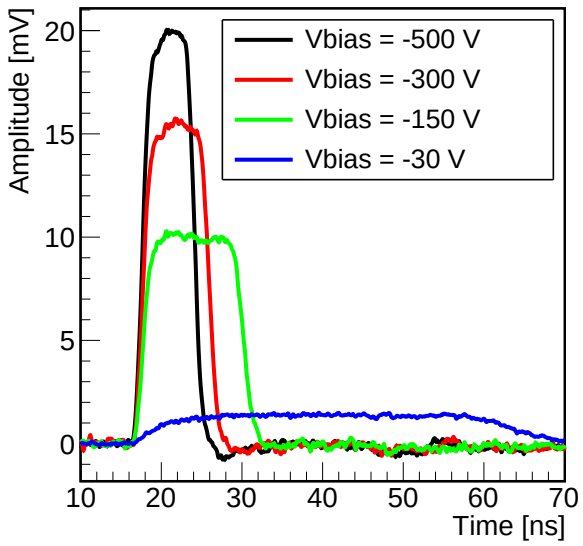

Figure 4: ToF-eBIC waveforms obtained for different biases. The y-axis represents the amplitude of the induced signals after the current preamplifier.

explained by the difficulty of measuring precisely these values because of the polarization effects and the limited electric field in some cases.

Holes		
Technique	μ_0 $[cm^2/(\text{V.s})]$	v_{sat} [10^6 cm/s]
ToF-eBIC	2334 ± 10	13.1 ± 0.1
α source	2380 ± 20	12.1 ± 0.1
α source (CEA LIST) [16]	2349 ± 28	14.1 ± 0.3

Table 1: Low field mobility and saturation drift velocity obtained with scCVD diamond in this work (first two lines) and by the CEA LIST (bottom line).

Conclusion

In order, to study charge particles a diamond monolithic ΔE-E telescope is currently under development. This detector will be adapted to detect light ions such as protons or α particles. In order to made this detector, a collaboration with the startup DiamFab was necessary to made the two epitaxial growths from a very pure scCVD E6 diamond substrate:

- the p^{++} layer, heavy doped ([B] $> 10^{20}$ cm^{-3} and very thin). This layer is used as a middle electrode
- the p^{-} layer with is used to detect the particle. This layer need to be very pure in order to avoid incomplete charge collection. Thanks to some simulation done with the software SRIM, an optimal thickness of 5 μm have been chosen.

A first sample will be tested in April under α beam at AIFIRA. In the meantime, a ToF-eBIC setup has been designed in order to study diamond devices. This setup has been used in order to compute the low field mobility and the saturation drift velocity of diamond detectors and study the polarisation effect. Some measurements at very low temperatures not presented in this proceeding have also been carried out.

References

[1] C. Canali et al., Nuclear Instruments and Methods, Volume 160, Issue 1, p. 73-77, 1979. doi: 10.1016/0029-554X(79)90167-8

[2] The RD42 Collaboration, RD Proposal, DRDC/P56, CERN/DRDC 94-21, May 1994. `https://cds.cern.ch/record/5473?ln=fr`

[3] ML. Gallin-Martel et al., Front. Phys 9:732730 (2021). doi: 10.3389/fphy.2021.732730

[4] K Gunzert-Marx et al, New Journal of Physics **10** 075003 (2008). doi: 10.1088/1367-2630/10/7/075003

[5] A. Singh et al., IEEE Transactions on Nuclear Science, vol. 62, no. 1, pp. 264-271, Feb. 2015. doi: 10.1109/TNS.2015.2390218

[6] S. Cesaroni et al., Nuclear Inst. and Methods in Physics Research, A **947** (2019) 162744. doi: 10.1016/j.nima.2019.162744

[7] H. Pernegger et al., Journal of Applied Physics **97**, 073704 (2005). doi: 10.1063/1.1863417

[8] `https://www.e6.com/en/products/optics`, Element 6 website

[9] `https://diamfab.com/`, DiamFab website

[10] `http://www.srim.org/`, SRIM software website

[11] M. T. Yin and Marvin L. Cohen, Physical Review B **24**, 6121 (1981) doi: 10.1103/PhysRevB.24.6121

[12] J. Letellier, PhD thesis, 2019. HAL Id: tel-02929023

[13] W. Shockley, Journal of Applied Physics **9**, 635 (1938). doi: 10.1063/1.1710367

[14] S. Ramo, Proceedings of the IRE. **27** (9), 584-585 (1939). doi: 10.1109/JRPROC.1939.228757

[15] S. Curtoni, PhD thesis, 2020. HAL Id: tel-03150715

[16] F. Marsolat, PhD Thesis, 2014. HAL Id: tel-00957871

Characterization of Light Scattering Point Defects in High Performance Mirrors For Gravitational Wave Detectors

Sihem SAYAH

Plateforme Nationale LMA - IP2I Lyon

Abstract — The highly-reflective mirrors of the gravitational waves detectors Advanced LIGO & Advanced Virgo present in the coating many micrometer size defects that scatter the light in the interferometer. This scattered light induces a loss of the laser power of the order of a few tens of parts per million (ppm) and a phase noise because of the recombination with the main beam after reflection on the tube walls. This phenomenon limits the sensitivity of the detector and impacts the ability to detect astrophysical events. A reduction of the scattered light is thus required in order to improve the optical performances of the coatings for the new mirrors of the Advanced LIGO+ and Advanced Virgo+ upgrade. For this purpose we studied the point defects for each material and we analyzed the impact of different parameters in order to compare the density and the size distribution of the defects.

Introduction of Gravitational Waves

Predicted by Albert Einstein in 1916, gravitational waves are defined as a space-time distorsion generated by the acceleration of masses [1]. The waveform depends on the astrophysical source emission which could be coalescence of two massive objects, supernovae, pulsars or cosmic microwave background. Using a giant Michelson interferometer as a detector is particularly well adapted because it allows to measure a differential change in length of the two arms because of the gravitational wave. Indeed, the latter will change in a differential way the phase of the light in the two arms as follows :

$$\delta L = \frac{h \cdot L}{2} \tag{1}$$

with L the arm distance and h being the amplitude of the gravitational wave. This deformation is very small and with the current performance of the detectors we can detect a relative shift in order of 10^{-20}.

The ground based detector Advanced Virgo located in Pisa, Italy, is composed of two tunnels of 3 km long under vacuum and super mirrors placed at each end of the arms. The figure 1 show a schema of the interferometer. It is composed of a laser, two Fabry cavities, a beamsplitter and several mirrors placed at each end of the arms. Interferometer principle is light making several round trips in the cavities before being recombined and directed to a photodetector which measures the interference pattern between the two beams. For my work we focus mainly on the mirrors of the cavity.

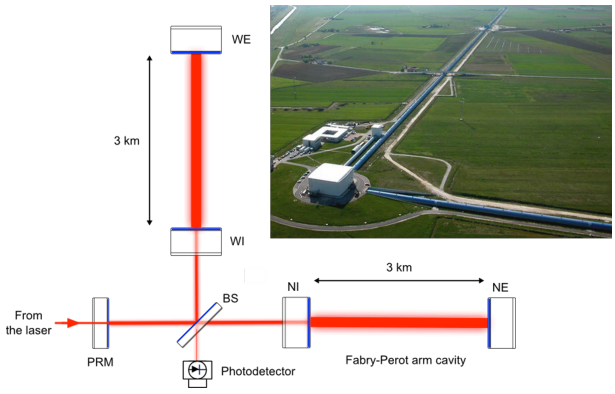

Figure 1: Simplified optical layout of the ground based detector Advanced Virgo and a picture of an aerial view of the detector in Pisa (Italy). credit : CNRS/Virgo

Gravitational Wave Mirrors

All the mirrors of current ground based detectors LIGO, Advanced Virgo and KAGRA were produced at LMA (Laboratoire des Matèriaux Avancès in Lyon). The large mirrors of gravitational wave detectors are large block of fused silica on which a coating of thin layers is deposited to make the mirror reflective [2]. The surface coating which is deposited at the LMA is a stack of optical thin films. We alternate between two materials of different refractive index. The greater the index contrast between the 2 materials, the more

it reflects the light. This forms a dielectric mirror and allows to reflect all the power of the laser light in the interferometer.

Fabry-Perot cavity

Fabry Perot cavities consist of two mirrors, one in front of the other separated by a distance L. There is creation of light interference inside the cavity, increasing or cancelling the electric field between the two mirrors. The most important problem with gravitational wave detectors is the loss of light in the Fabry Perot cavities: it is within these cavities that there is the most laser power and light losses means less laser power which reduces the sensitivty of the instrument [3]. For example, in the ideal case, if we have no loss : we send 1 W of laser power, we should recover 1 W. The optical losses measured on the Virgo site are 50 ppm (including the various losses). Because of these 50 ppm, we recover only 0.98 Watt at the cavity output. The Fabry-Perot cavities amplify the signal but also amplify the losses. Losses of 2%, that can appear very small but are enough to decrease the reflection of the cavity. These optical losses are mainly due to absorption, transmission by the mirrors and scattering. This work is focused on the scattering light by the imperfections of the mirror.

Sample and Experimental Procedure

So for our study, we used 2 materials tantala and silica and we prepared 8 samples using the ion beam sputtering technique for coating deposition [2]. We deposited the coating on ϕ 1" fused silica micropoly substrates because they have a low defect density and because the roughness of these substrates is less than 1 Å. We have good quality substrates and we do not have significant contributions from the substrates in our study. So we measure only defects in thin films.

At LMA, we process large blocks of fused silica on a deposition machine that operates under vacuum in which a reflective coating is deposited. An ion beam is sent from the source to the target of the material to be deposited on the surface and pulls the atoms from the target by collision cascades. The sputtered material forms a plume above the target and then condenses on the rotating substrate for a more homogeneous layer. This process creates unfortunately point defects in the coating.

These point defects are present inside the coating. To illustrate, here are real pictures of a Virgo mirror 2. We observed the mirror with three increasing laser powers. We can clearly see all the imperfections of the deposit highlighted by the incident beam. If the imperfections are illuminated it is because they are scattering. The more the defects, the more the optical losses in the cavities. This is a phenomenon that we have known for several years and which becomes a limiting factor for future detectors. To understand this phenomenon, I study the point defects in the coating of mirrors.

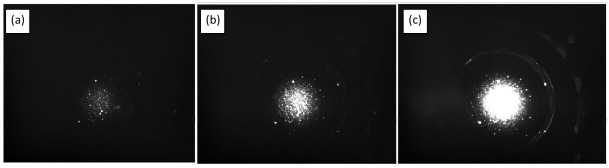

Figure 2: Photos of the end mirror of the West arm of the Advanced Virgo interferometer under different laser powers 0.1 kW, 10 kW and 80kW respectively. Credits: J.Degallaix LMA.

Defect detection instrument

After deposition, the samples are analyzed using an optical profilometer that has been customized for defect detection in dark field illumination. The detection principle works in dark field: the profilometer illuminates along a cone, in grazing light, basically no light is collected by the lens, and on the other hand when it passes over a defect, the defect will diffuse light that will be collected by the lens. The profilometer scans the surfaces and when it detects a difference in contrast in the field, the image is recorded. The instrument gives a cartography with the spatial distribution of the defects, the number of defects and images. It then classifies the defects in three size categories. But it is important to notice that the profilometer software does not provide information on the individual size of these defects, except that it is between 1 and 5 micrometers. A post-processing software has then been specifically developed for this purpose.

Image processing

We notice that the counting is not necessarily correct. Depending on the threshold value set, we see that not all defects are detected. In figure 3 we can see many defects marked in red that are detected and others that are not. The images stored by the profilometer are processed with an home-made image recognition software, to determine the radius of the detected defects. The software is a python code [4] which allows after image processing to circle all the defects present on the image field. This work allowed us to improve the defect counting and to determine the size of the defects with precision.

Optical Scattering

At LMA, the scattered light is measured by a Scatterometer Complete Angle Scan Instrument (CASI). This instrument, composed of a laser and a detector, allows to measure the scattered light at different scattering angles. The sample is illuminated at variable incidences and the detector scans the plane to measure the bidirectional reflectance distribution function (BRDF) [5]. The integrated value considers a pure isotropic emission, then this integrated value is given in parts per million (ppm). For this study the measurements are made with a laser source at 1064 nm,

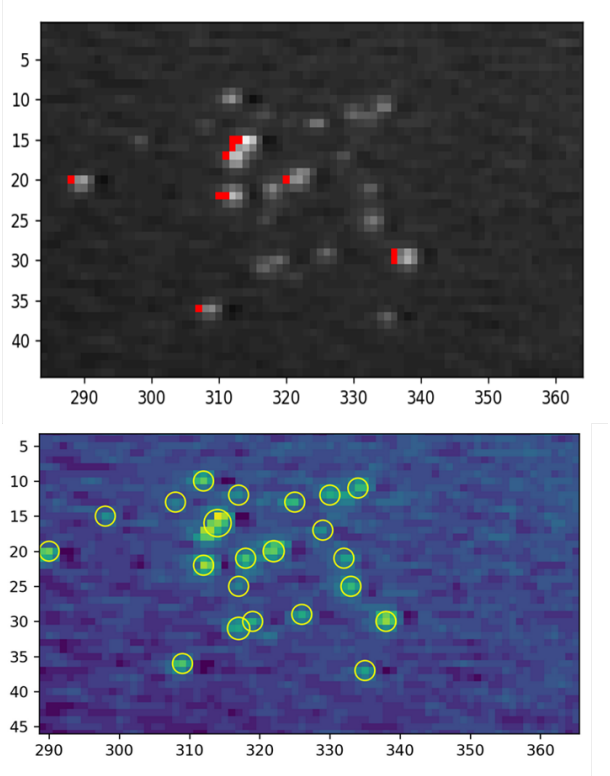

Figure 3: Image post-processing. Example of an image field with some defects detected and others not (top) and the image after analysis with processing image (bottom).

because it is the same wavelength used by the interferometers Advanced LIGO and Advanced Virgo.

Defect Study

Two parameters are studied the influence of the layer thicknesses during the deposition process and the post deposition annealing .

Influence of the Thickness

The figure 4 presents the number of defects with respect to the layer thickness for the two materials. It shows that the number of defects generated in the silica samples is much lower than in the Ta_2O_5. In addition, we notice that the behavior is different for the two materials. For silica, the number of defects depends linearly on the thickness of the layer, while for Ta_2O_5 it follows a power law [6].

Influence of the annealing

The impact of post-deposition annealing on the number of defects was also studied. All samples were annealed at 500°C corresponding to the green point in figure 4. Post-deposition annealing allows to reduce significantly the number of defects about 40-50%.

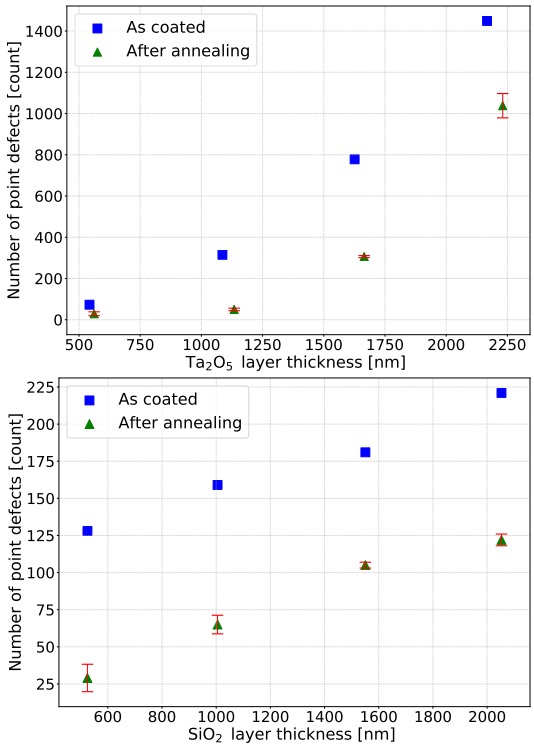

Figure 4: Number of point-like scatterers in SiO_2 layers (bottom) and Ta_2O_5 (top) as a function of the layer thickness. Results are shown for materials as coated (in blue) and after annealing (in green).

Results

Through image processing we obtained the different sizes of defects for the different samples in two histogram which are presented in figure 5. These figures show the defect sizes for the thicker samples Ta_2O_5 and SiO_2, for which we have the largest number of defects. Thus, after annealing, the median defect size is 3.66 μm for SiO_2 and 2.96 μm for Ta2O5, respectively. This shows that the defect size is smaller for Ta2O5 than for SiO_2.

Moreover the annealing seems to slightly decrease the size of the defects for Ta_2O_5, while the opposite is observed for SiO_2 but the statistic is quite low and further experiments are required in order to draw a conclusion.

To quantify the impact of defects on the scattered light, we measured the 8 samples with CASI after annealing. The figure 6 shows the light scattering of the two materials as a function of the layer thickness. The Ta_2O_5 coating seems to have a stable scattering for the first three thinnest layers that increases for the thickest layer. It is interesting to mention that the uncoated substrates used in this study has an optical scattering level below 3 ppm. The coating of the thin film and especially the addition of defects contributes to the scattered light. Regarding the silica, although there is ten times less of defects between the thickest silica sample and the tantala, the scattered light is comparable. This tends to show that the defects present in the Ta_2O_5 layers scatter less light than the defects present in the SiO_2.

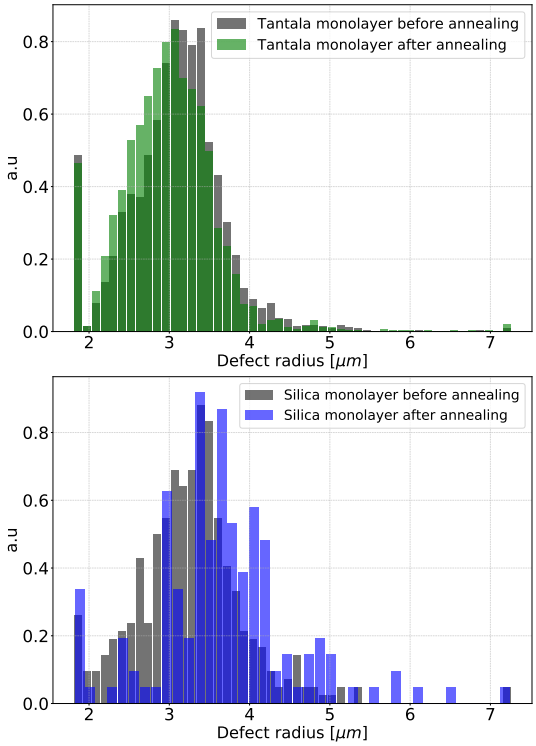

Figure 5: Defect size for the thickest samples of the two materials, SiO_2 (bottom) and Ta_2O_5 (top), before and after annealing. The distributions have been normalized to ease the shape comparison.

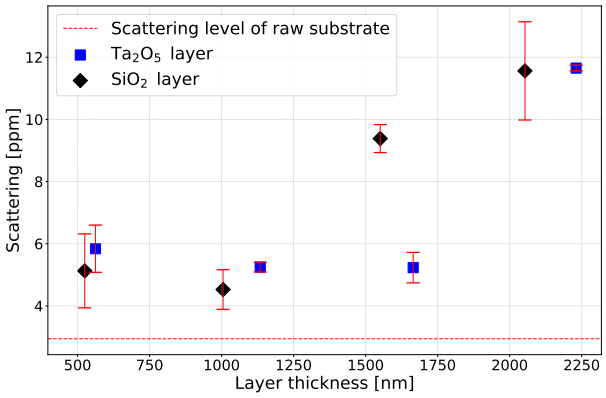

Figure 6: Scattering light for the two materials Ta_2O_5 and SiO_2 as a function of the layer thickness. The measured scattered light for a sample where the substrate was put in the IBS machine under the normal deposition conditions, but no deposition was performed (ghost deposition), is consistent with the value measured on raw substrate (within typical repeatability uncertainties, although the value being slightly lower can also be explained by small fluctuations in the substrate quality).

Conclusion

In conclusion, we show that we need a development of a reliable image processing. We demonstrate that we have more defects in tantala monolayers than in silica monolayers (about a factor 10). Concerning the influence of the thickness parameter, the thicker layer, the more the defects. We have also shown that annealing reduces the defect density by a factor of two. And we have determined that the median defect size is about 3 um for each material. We now need to work on the scattered light simulation to understand how the defects influence the scattering in the interferometer.

References

[1] A.Einstein, *Die grundlage der allgemeinen relativitats theorie*, Annalen der Physik, vol. 7, p. 769 to 822 (1916)

[2] L. Pinard et al., *Mirrors used in the LIGO interferometers for first detection of gravitational waves*, Appl. Opt. 56, C11-C15 (2017)

[3] J.Degallaix et al., *Large and extremely low loss: the unique challenges of gravitational wave mirrors*, J. Opt. Soc. Am. A 36, C85-C94 (2019)

[4] Van Der Walt et al., the scikit-image contributors. 2014. *scikit-image: image processing in Python*, PeerJ 2:e453 (2014)

[5] J. C. Stover, Optical Scattering Measurement And Analysis (SPIE Optical Engineering) (1995)

[6] S.Sayah et al., *Point defects in IBS coating for very low loss mirrors*, Appl. Opt. 60, 4068-4073 (2021)

Recurrent Neural Networks for Real-Time Processing of ATLAS Liquid Argon Calorimeter Signals with FPGAs

Lauri LAATU

CPPM, Aix-Marseille University, CNRS/IN2P3

Abstract — The readout electronics of the ATLAS Liquid Argon (LAr) Calorimeters will be replaced to be able to process high luminosity with pileup of up to 200 simultaneous proton-proton interactions as part of the Phase-II upgrade of the LHC. Due to the design of the calorimeter the signals can have an overlap of up to 25 events, which increases the difficulty of energy reconstruction. The real-time processing, which consists mainly of the reconstruction of the energy deposited in the calorimeter, is done using FPGAs at a frequency of 40HMz. This work evaluates recurrent neural networks as a replacement for the legacy optimal filter-based energy reconstruction. The developed recurrent neural networks provide performance increase in the case where the performance of optimal filtering suffers the most: overlapping events causing decreased energy resolution and assignment of energies to wrong bunch crossings. Furthermore the recurrent neural networks show stability over changing instantaneous luminosity.

Introduction

The ATLAS detector [1] is one of the general purpose detectors at the Large Hadron Collider [2] (LHC) measuring the properties of the particles produced in high-energy proton-proton collisions that happen every 25 ns (40 MHz).

In the Run-4 of the LHC starting in 2027, also known as the high-luminosity phase of LHC (HL-LHC), the machine is expected to produce instantaneous luminosities of 5 to $7\times10^{34}\,\mathrm{cm^{-2}s^{-1}}$ corresponding to 140 to 200 simultaneous proton-proton interactions. The liquid-argon (LAr) calorimeters of ATLAS mainly measure the energy of electromagnetically interacting particles using their ionization signal that causes an electronic pulse. This pulse is shaped to a bi-polar shape that spans up to 25 bunch crossings (BCs) as shown in Figure 1. This can lead to overlap between consecutive pulses known as out-of-time pileup. The out-of-time pileup probability increases significantly in HL-LHC conditions.

A new method capable of continuous energy reconstruction and identification of the corresponding collision event is required for the LAr calorimeter for the HL-LHC era [3]. The energy reconstruction is done by field-programmable gate arrays (FPGAs) for the 182 000 calorimeter cells with 384 or 512 LAr calorimeter cells per one Intel Stratix-10 FPGA [4] with a latency requirement of about 150 ns [3, 5]. Different Recurrent Neural Network [6] (RNN) types are developed to replace the current optimal filtering [7] (OF) algorithm.

Energy Reconstruction

The energy reconstruction method currently used in the LAr calorimeter is based on the optimal filtering algorithm. This is combined with a peak finder to find the correct BC for the energy deposit. While this method generally works well, due to the increased simultaneous p-p collisions, there are two major shortcomings that need to be addressed for the HL-LHC era. The first is the energy resolution decrease due to the fact that the optimal filtering algorithm assumes perfect pulse shape while this shape is distorted by previous pulses. The second comes from the peak finder's inability to assign the energy to correct BC if the pulse shape is distorted. By using an energy reconstruction method based on RNNs, it is possible to mitigate both of these effects.

The data used for training the neural networks is a simulation of a single calorimeter cell in the middle layer of the calorimeter ($\eta = 0.5125$, $\phi = 0.0125$) created using AREUS [8] with HL-LHC pileup. It contains injected energy deposits of up to 5 GeV combined with low energy deposits from inelastic proton-proton collisions as well as electronics noise. The higher energy deposits are injected randomly with a mean interval of 30BCs. The average pileup used is $\langle\mu\rangle = 100$, $\langle\mu\rangle = 140$ or $\langle\mu\rangle = 200$.

Energy Reconstruction with Recurrent Neural Networks

RNNs are a type of neural network designed for time-series processing. In this work two RNN types are

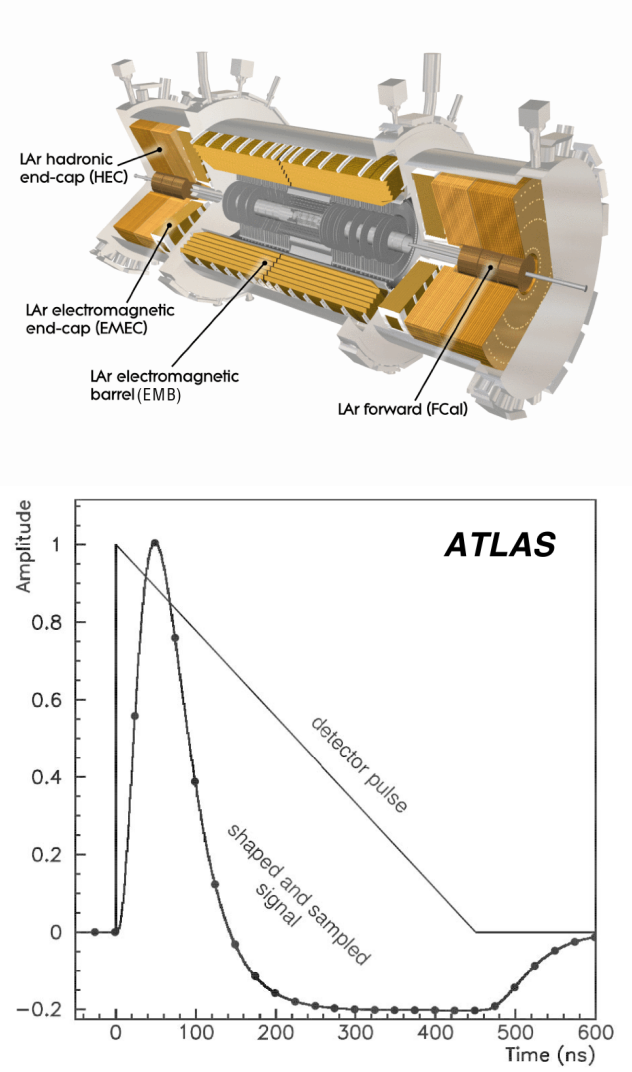

Figure 1: Top - cutout of the LAr calorimeter, bottom - shaped and digitized LAr calorimeter pulse [1].

evaluated: Long Short Term Memory (LSTM) [9] and vanilla RNN [10]. LSTM contains gated structure to control the flow of information through time using sigmoid and tanh activation functions. This network can be applied in two ways: sliding window in which the full time series is split in overlapping sequences, that consist of 5 BCs in this work, each corresponding to a single output energy, as shown in Figure 2 or in a single cell approach where the full time series is processed as a stream and each intermediate state corresponds to an output energy, as shown in Figure 3. The second type is vanilla RNN which contains only one internal neural network with ReLU activation function in this work. Vanilla RNN can only be applied in the sliding window way due to its simplicity.

The energy resolution for all energy deposits above 240 MeV is shown in Figure 45. All RNNs outperform the legacy OFMax algorithm. This performance increase is mainly due to the ability to correct for overlapping events. Figure 5 shows the energy resolution as function of the gap to the previous high energy pulse for optimal filtering with max finder. In the low gap region where the pulse is overlapping with the previous one, the energy resolution of the optimal filtering is significantly reduced. This effect can be mitigated by RNNs that utilize samples before the pulse peak. As seen in Figures 6 and 7 using sequence lenght of 5, where one sample is before the start of the pulse the network learns to correct for the overlapping effect. In the case of the single cell LSTM shown in Figure 8 the effect is almost fully corrected for.

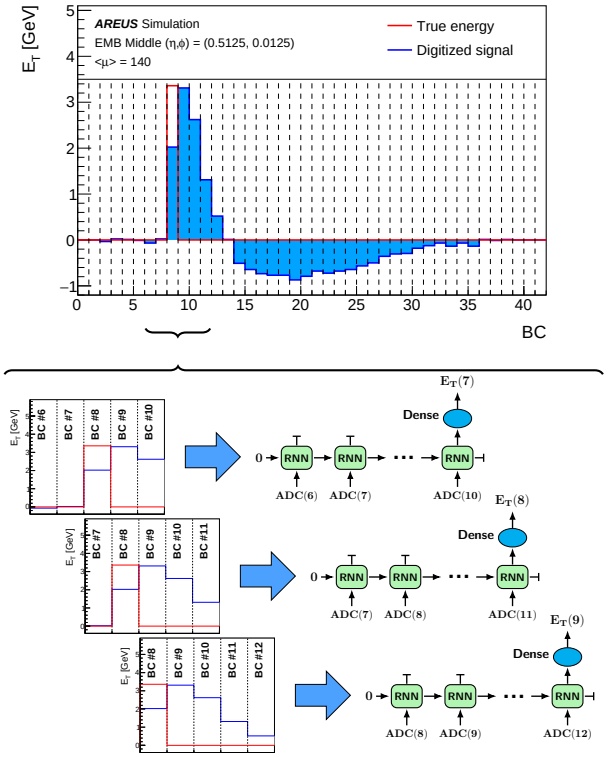

Figure 2: Sliding window application of RNNs [13].

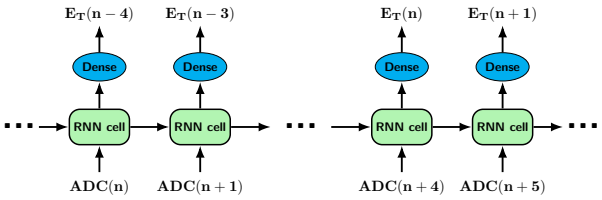

Figure 3: Single cell application of RNNs [13].

Stability

The performance of RNNs is better than of the optimal filtering based energy reconstruction. However for RNNs to be a viable option for the real-time energy reconstruction, the networks need to be capable of coping with the varying conditions in the detector. This includes the changes in the instantaneous luminosity, the varying pulse shapes in different regions of the detector as well as changing pulse shape for a specific

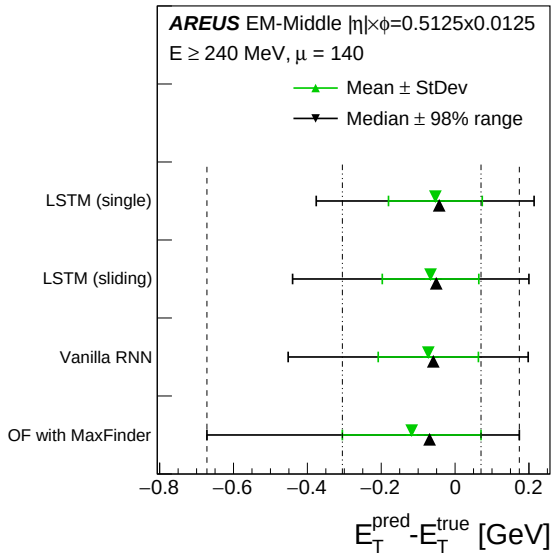

Figure 4: Comparison of the energy resolution for energy deposits 3σ above noise level.

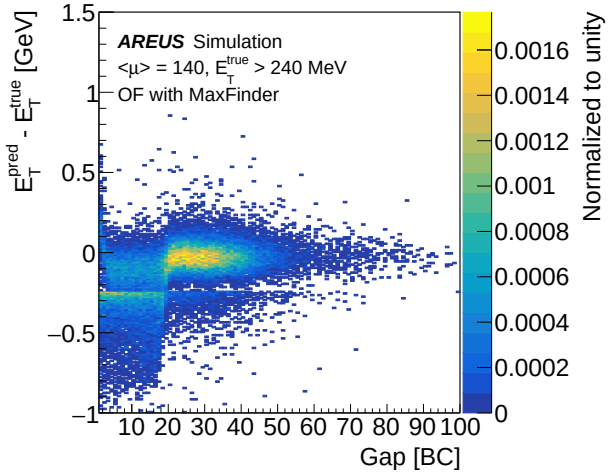

Figure 5: Energy resolution as a distance to the previous high energy energy deposit (gap) for OF.

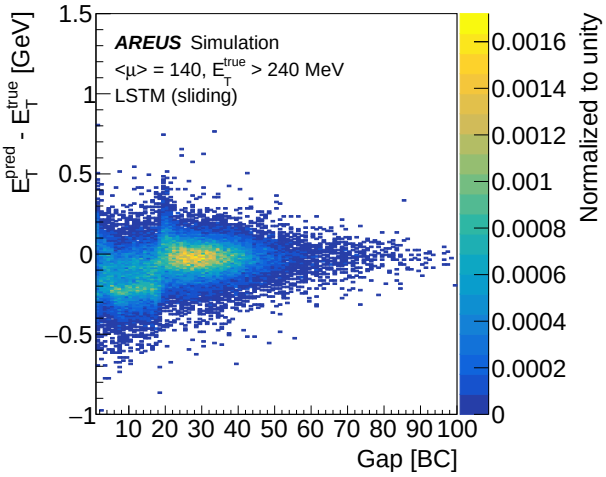

Figure 6: Energy resolution as a distance to the previous high energy energy deposit (gap) LSTM Sliding Window.

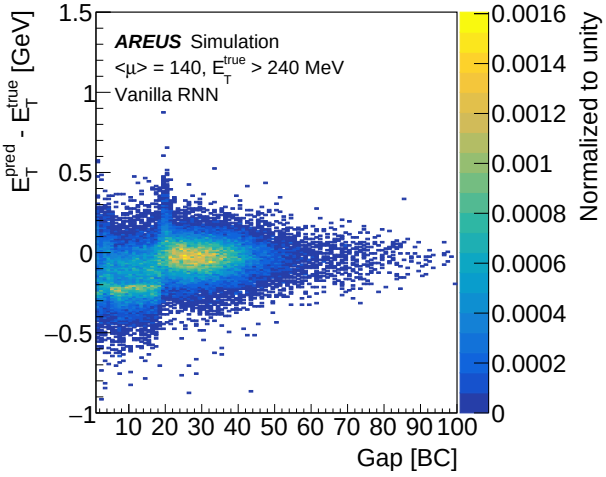

Figure 7: Energy resolution as a distance to the previous high energy energy deposit (gap) for Vanilla RNN.

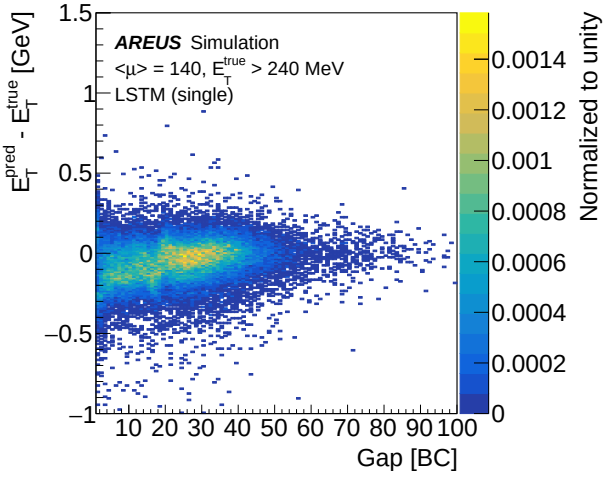

Figure 8: Energy resolution as a distance to the previous high energy energy deposit (gap) for LSTM Single Cell.

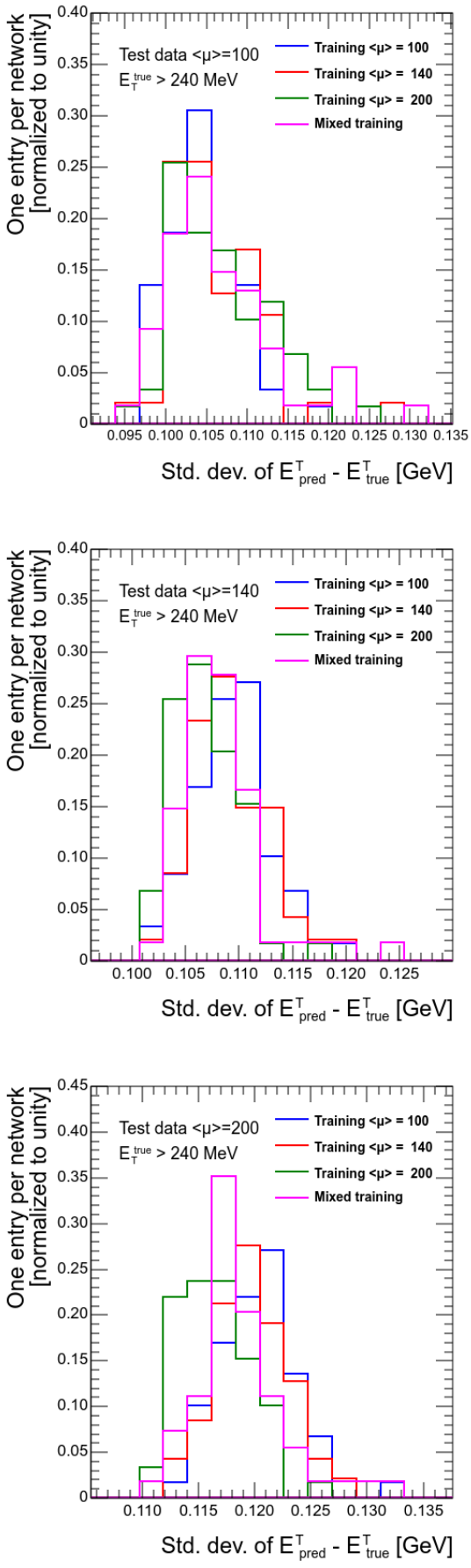

Figure 9: Comparison of the resolutions for energy deposits 3σ above the noise level for networks trained with different pileup composition.

cell over time. To evaluate the stability of the networks with respect to changing instantaneous luminosity, several networks are trained with different pileup rates of $\mu = 100$, $\mu = 140$ and $\mu = 200$ as well as a dataset that mixes one third of each μ value. In addition, the dependence of the NNs on the initialization during the training is quantified by repeating each training 70 times with randomly changing the initialization values for each dataset. This is done for the vanilla RNN as it is the only RNN type that is able to reach the latency and occupancy requirements of the LASP board [13].

The results on the robustness of the networks are shown in Figure 9. This figure shows the energy resolution in samples with $\mu = 100$, $\mu = 140$ and $\mu = 200$. For each of these samples a comparison is done using networks trained with different μ values. Changing the pileup rate of the training sample induce an energy resolution difference which is comparable to variations due to the statistical component which is probed by retraining the NNs with different initialization. Mixing training data does not show improvements in the results.

Results

RNNs perform better than optimal filtering for energy reconstruction in the case of overlapping signals. With a streaming architecture LSTM is able to almost fully correct for the effect of overlapping signals. For a sliding window architecture with a sequence length of five both LSTM and vanilla RNN partially correct for the energy resolution degradation in the low gap region. The vanilla RNN robustness against changing instantaneous luminosity is evaluated. It shows stable energy reconstruction resolution when varying the pileup rates ranging from $\mu = 100$ to $\mu = 200$ independently for the training and evaluation samples.

Acknowledgements

This work was in part supported by the German Federal Ministry of Education and Research within the research infrastructure project 05H19ODCA9. The project leading to this publication has received funding from Excellence Initiative of Aix-Marseille Université - A*MIDEX, a French "Investissements d'Avenir" programme, AMX-18-INT-006.

References

[1] ATLAS Collaboration (2008) The ATLAS Experiment at the CERN Large Hadron Collider, JINST 3:S08003. https://doi.org/10.1088/1748-0221/3/08/S08003

[2] Evans L, Bryant Ph, eds. (2008) LHC machine. JINST 3:S08001. https://doi.org/10.1088/1748-0221/3/08/S08001

[3] ATLAS Collaboration (2017) Technical Design Report for the Phase-II Upgrade of the ATLAS TDAQ System, CERN-LHCC-2017-020, ATLAS-TDR-029. https://cds.cern.ch/record/2285584

[4] Intel Corporation (2020) Intel Stratix-10 Device Datasheet, Version 2020.12.24

[5] ATLAS Collaboration (2017) Technical Design Report for the Phase-II Upgrade of the ATLAS LAr Calorimeter, CERN-LHCC-2017-018, ATLAS-TDR-027. https://cds.cern.ch/record/2285582

[6] Sherstinky A (2020) Fundamentals of Recurrent Neural Network (RNN) and Long Short-Term Memory (LSTM) network, Physica D: Nonlinear Phenomena 404:132306. https://doi.org/10.1016/j.physd.2019.132306

[7] Cleland W E, Stern E G (1994) Signal processing considerations for liquid ionization calorimeters in a high rate environment, NIM A Volume 338:467-497. https://doi.org/10.1016/0168-9002(94)91332-3

[8] Madysa N (2019) AREUS: A Software Framework for ATLAS Readout Electronics Upgrade Simulation, EPJ Web Conf. 214:02006. https://doi.org/10.1051/epjconf/201921402006

[9] Hochreiter S, Schmidhuber J (1997) Long Short-Term Memory Neural Computation 9:1735-1780. https://doi.org/10.1162/neco.1997.9.8.1735

[10] J. L. Elman (1990) Finding structure in time Cognitive science, vol. 14, no. 2, pp. 179-211

https://onlinelibrary.wiley.com/doi/abs/10.1207/s15516709cog1402_1

[11] Quartus, ModelSim and HLS tools available from https://www.intel.com; Accessed: 2021-02-18

[12] Questa Sim available from https://eda.sw.siemens.com/; Accessed: 2021-06-20

[13] Aad, G., Berthold, AS., Calvet, T. et al. (2021) Artificial Neural Networks on FPGAs for Real-Time Energy Reconstruction of the ATLAS LAr Calorimeters. Comput Softw Big Sci 5, 19 https://doi.org/10.1007/s41781-021-00066-y

Improvement of the vertex detector resolution in the Belle II experiment

Lucas MARTEL

University of Strasbourg

Abstract — The Belle II Silicon Vertex Detector (SVD) is part of the Super B factory composed of the asymmetric energy e^+e^- collider SuperKEKB and the Belle II experiment and is used to reconstruct tracks and decay vertices as well as provide particle identification information. In order to correctly reconstruct tracks, the position of the hits created by charged particles passing through the detector needs to be known with precision. It is also important to estimate the resolution of the hit position measurement, in order to correctly propagate the error on hit position to track fitting, as well as developing methods to optimize this resolution. Since 2019 and the start of the data taking, the SVD has demonstrated a reliable and highly efficient operation, even running in an environment with harsh beam backgrounds that are induced by the world's highest instantaneous luminosity. The cluster position resolution has been estimated first with simulated events, then on data using a dataset representing an integrated luminosity collected by Belle II of about 16 fb^{-1}. While the SVD performance is already very good, there is still room for improvement of the estimation of the cluster position resolution. Here we will present the latest studies to improve the hit position estimation in the vertex detector by correcting charge couplings between silicon strips, in order to improve data and simulation agreement.

Introduction

The SVD [1] is made of 172 double-sided silicon strip sensors arranged in 4 concentric layers, labelled L3 - L6 (from the closest to the interaction point to the farthest)(fig.1). Layer 3 is made of small rectangular sensors (*HPK small*) while L4, L5 and L6 are made of large rectangular sensors (*HPK large*) and trapezoidal ones (*wedge*) in the forward region. Table 1 contains the characteristics relevant for this study for each type of sensor.

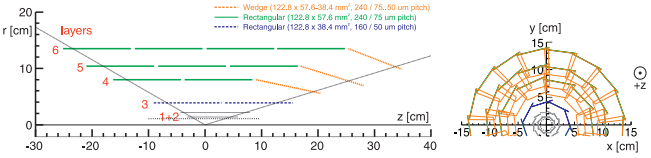

Figure 1: Layout of the detector.

On each sensor v/N - side strips measure the position along the z axis while u/P strips measure $r\phi$ position. A set of 128 strips are read by one APV25 chip[2], which provides six digitized samples of the response curve.

Cluster reconstruction

In order to identify their trajectory, signal left by charged particles crossing the detector is collected and a *cluster* is created corresponding to this signal. The SVD cluster provides estimations of:

sensor	layer	pitch v/N (μm)	pitch u/P (μm)
HPK small	3	160	50
HPK large	4,5,6	240	75
wedge	4,5,6	240	50-75

Table 1: Relevant characteristics of the three types of SVD sensors.

- The charge S collected by the sensor.
- The position x of the hit and its error.
- The time t of the hit and its error.

The cluster is a 1D object constructed using strips that have been fired by the passage of a particle. In order to be taken into account to build the cluster, strips are required to have a signal of 3 $\times$ the strip noise (N_i), this means that the strip signal to noise ratio (SNR_i) has to be greater than 3 (evaluated for each strip). A collection of strips passing the threshold also needs to contain a strip with a signal greater than 5 $\times N_i$ (called the *seed strip*) to be associated to a cluster.
For each retained strip we have access to:

- The six sampled amplitude of the APV response.
- The strip noise (from calibration on data).
- The strip gain (from calibration on data).

We take as value for the strip charge the maximum amplitude of the six samples.

Estimation of cluster position

In order to estimate the position x were the particle crossed the detector , we need to compute the position x_{CL} of the cluster associated to it. The position and its error Δx_{CL} are computed using the charges S_i and the positions x_i of the strips constituting the cluster.
For a cluster of size 1 *i.e. made of one strip* we have:

$$x_{CL} = x \tag{1}$$

For clusters of size > 1 x_{CL} is estimated with a center-of-gravity algorithm :

$$x_{CL} = \frac{\sum x_i S_i}{\sum S_i} \tag{2}$$

The error is estimated for all clusters by :

$$\Delta x_{CL} = p\sqrt{(\frac{a_1}{\xi + a_2})^2 + (b\xi)^2 + c^2} \tag{3}$$

Where $\xi = \sqrt{size} \times SNR_i$. The parameters a_1, a_2, b and c depend on the cluster size for clusters up to size $= 5$. For larger clusters, the values for cluster size $= 5$ are used.

Correction of coupling effects : unfolding method

During test runs, a charge is injected in one of the APV channels. A small signal is seen on the adjacent channel with a lower time (around 7/8 APV clock $\simeq$ 27 ns), showing a coupling between the two channels (Fig2). This effect is not expected to occur and can potentially skew the observed strip charge. Preliminary assessment shows that the observed adjacent strip charge could be underestimated by $\simeq 6\%$ of the seed strip charge.

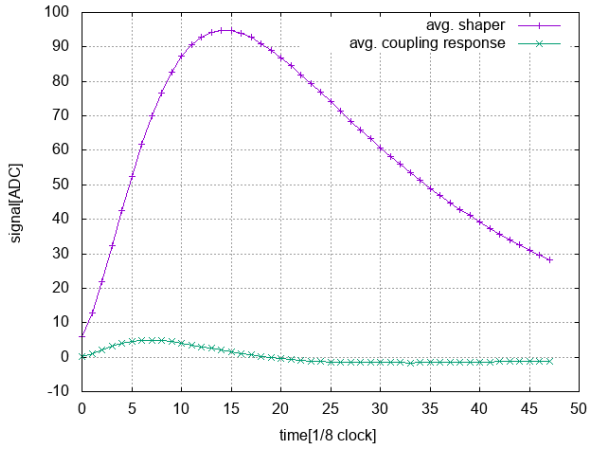

Figure 2: Response from an APV channel to which a signal was injected (purple) and from its adjacent channel (green) showing a coupling response.

Because the strip charge is used in the computation of x_{CL} this effect can worsen the estimation of cluster-position.

We aim at developing a method to correct this issue. We suppose that :

- Each strip in the cluster loses $\simeq 6\%$ of its collected charge which is transferred to one neighbour on each side (for a total loss of $\simeq 12\%$ of the initial charge).
- Strips at the edge of the cluster lose $\simeq 6\%$ of their charge by transferring it with strips that do not pass the charge requirement to be included in the cluster.
- Edge strips do not gain charge from strips that do not pass the charge threshold.
- These charge transfers happen simultaneously.

We propose to compute the *corrected* strip charges from the *observed* strip charges and then compute the cluster position and compare its values for both sets of charges.
Because of our hypotheses on the behavior of the edge strips, the total charge is not expected to be conserved between the *corrected* and *observed* clusters. In addition, both clusters are expected to have the same size.
To each *observed* cluster of size n, constructed with the strips of charges a_i, $i \in (0; n-1)$, we want to associate the corresponding *real* cluster composed by the strips of charges A_i. We define the *unfolding matrix* M of size $n \times n$ such as :

$$\begin{cases} M_{ij} = 1 - 2c & \text{if } i = j; \\ M_{ij} = c & \text{if } \mid i - j \mid = 1; \\ M_{ij} = 0 & \text{for all others } (i, j); \end{cases} \tag{4}$$

With $i, j \in (0, n-1)$ and the *Unfolding Coefficient* $c = 0.06$ (corresponding to the expected 6% loss of charge for a given strip).
The *corrected* strip charges A_i are then computed as :

$$\begin{pmatrix} A_0 \\ A_1 \\ \dots \\ A_{n-1} \end{pmatrix} = M^{-1} \begin{pmatrix} a_0 \\ a_1 \\ \dots \\ a_{n-1} \end{pmatrix} \tag{5}$$

Results

In order to gauge the possible improvements from the unfolding method, we performed a study on 1 fb^{-1} of data collected between October 2020 and December 2020. In addition 500k Monte-Carlo simulated events have been studied with the generic cluster reconstruction algorithm (i.e. without the unfolding method) in order to provide comparison. The unfolding method is not applied in the case of the simulation because the bias observed on the strip charge and discussed here is due to effects of cross-talks that are not simulated. Simulated events are not biased and therefore not fixed. Both datasets consist of $e^+e^- \longrightarrow \mu^+\mu^-$ events.

To assess the impact of our correction, we compute the resolution on x_{CL} observed in data with the generic reconstruction and we compare it with the resolution computed with the corrected cluster reconstruction for $c \in [0, 0.20]$. We repeat this analysis for all type of sensors listed in Table 1 to check if the optimal c value depends on the sensor specifications.

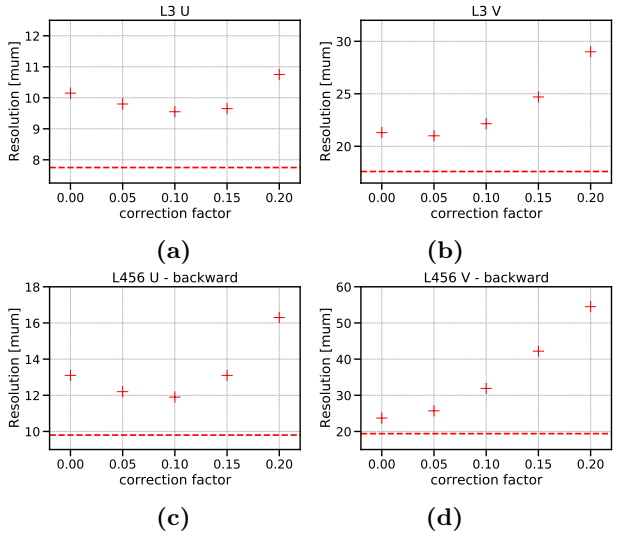

Figure 3: Cluster position resolution obtained with different values of the correction factor c (0 corresponds to the generic reconstruction), for the Layer 3 u/P-side (a) and v/N-side (b) and Layer 4,5 and 6 u/P-side (c) and v/N-side (d). The dashed line corresponds to the resolution observed in Monte-Carlo with generic reconstruction.

As shown in Fig.4,the correction improves the cluster position resolution for u/P - side sensors while it does not seem to improve it for v/N - side sensors.
We observe (see Table 2) that the lowest (=best) resolution is achieved for $c = 0.1$ for all types of u/P - side sensors.

Sensors - U side	c = 0	c = 0.05	c = 0.1
L3.1 small	9.6	9.3	9.1
L3.2 small	10.7	10.3	10
L456 backward	13.1	12.2	11.9
L456 origami	12.6	11.8	11.5
l456 slanted	11.6	10.9	10.7
Sensors - U side	**c = 0.15**	**c = 0.20**	**MC**
L3.1 small	9.3	10.7	7.2
L3.2 small	10	10.8	8.3
L456 backward	13.1	16.3	9.8
L456 origami	12.6	15.2	9.1
l456 slanted	12	14.8	8.9

Table 2: Cluster position resolution in μm for different values of the correction factor c, for each type of u/P - side sensor. v/N - side sensors are not shown here because the correction does not improve their resolution.

Conclusions

We have shown that the impact of the observed charge transfer between strips of the Belle II Silicon Vertex Detector can be mitigated. The correction we implemented led to an improvement of 5-10 % of the spatial resolution for u/P sides of the sensors, while no effect was observed for v/N sides. The corrections depends on the unfolding parameter c. The value of $c = 0.1$ allows to achieve the best resolution. This value is close to what was expected ($c = 0.06$) from preliminary assessment, albeit higher. This discrepancy could be explained by additional biases than those we studied here (charge transfer between strips) and that have not been yet identified.

This work is part of a global effort within the Belle II collaboration to improve the agreement between SVD performances on data and simulation that has been carried out by the SVD offline software working group between 2020 and 2021. Additional work is ongoing to close the remaining gap between data and simulation resolution (Fig.4), with the spatial resolution simulated being better than the one observed in data. The correction by the unfolding method has been implemented in the Belle II analysis software[3] since the summer of 2021.

The evolution with time and instantaneous luminosity conditions of the effect studied here and its correction is not yet known, thus this study will need to be conducted again in order to ensure an optimal correction to the cluster position resolution.
In the future, the Belle II detector will undergo changes of its vertexing system as well as a possible replacement of the SVD, prompting the need for this type of studies on new hardware.

Acknowledgements

This work was conducted with Giulia Casarosa, Francesco Tenchini and Guliana Rizzo (INFN Pisa, Pisa, Italy), Laura Zani, Robin Leboucher and Léonard Polat (CPPM, Marseille, France), Giulio Dujany and Christian Finck (IPHC, Strasbourg, France) within the Belle II collaboration.We thank Isabelle Ripp and Jerôme Baudot for fruitful discussions.

References

[1] T.Abe et. al., Belle II Technical Design Report, 1011.0352.

[2] M. J. French et al., Design and results from the APV25, a deep sub-micron CMOS front-end chip for the CMS tracker, Nucl. Instrum. Meth. A466 (2001) 359.

[3] T. Kuhr, C. Pulvermacher, M. Ritter, T. Hauth and N. Braun, The belle ii core software, Computing and Software for Big Science 3 (2018) 1.

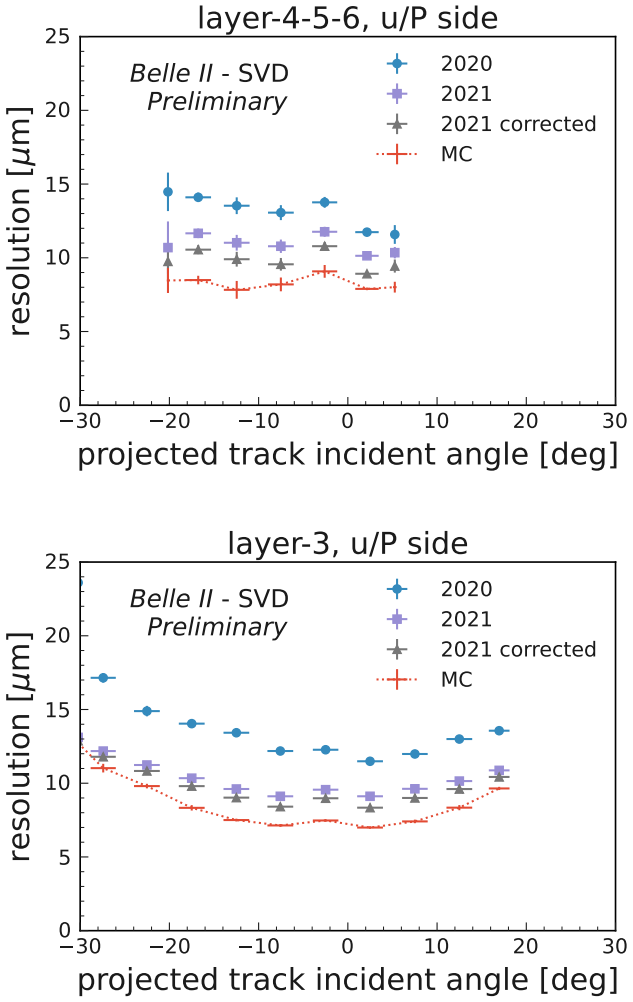

Figure 4: Spatial resolution on x_{CL} as a function of the incident angle of the track evaluated with the standard reconstruction algorithm in 2020, 2021 and the reconstruction corrected with the unfolding method, compared to the resolution evaluated with simulated events. The results are shown for all u/P sensors of L3 and all sensors of L4-6. Data - Monte-Carlo agreement is improved by our correction.

Simulation and instrumentation for the future Electron-Ion Collider

Pu-Kai WANG

IJCLab

Abstract — In order to study the internal structure of nucleons and nuclei and address some important outstanding questions in nuclear physics, a new Electron-Ion Collider (EIC) is planned to be built at Brookhaven National Lab (NY, USA). The EIC will collide a high energy proton/ion beam with a high energy electron beam. High performance detectors will be used to detect the particles created in the collisions. Detailed simulations and instrumentation developments are still required to better define the detectors that will soon start to be constructed[1]

Introduction

The Electron-Ion Collider (EIC) is a new particle accelerator facility planned for construction at Brookhaven National Laboratory (NY, USA). It will collide highly polarized electron and proton beams, as well as ion beams from deuterons to heavy nuclei. With a center-of-mass energy between 20 and 100 GeV, and luminosity as high as 10^{34} cm^{-2}·s^{-1}, it will address some of the most fundamental questions in science including the nucleon mass, the nucleon spin, and the emergent properties of a dense system of gluons.

One of the flagship processes that will be studied at EIC is Deep Virtual Compton Scattering (DVCS). DVCS can access the General Parton Distributions (GPD) of the nucleon scattering an electron off a parton inside the nucleon. In order to measure DVCS one needs to detect the scattered electron, the recoil proton and emitted photon of the DVCS reaction, which can be described in the following way:

$$e^- + p^+ \rightarrow e^- + \gamma + p^+$$

Figure 1 shows the layout of an EIC detector, including a central detector region and a far-forward detector system. In the case of the DVCS reaction, the scattered electron and emitted photon will go to the backward end-cap of the central detector. The recoil proton will be detected in the far-forward region very close to the beam line. Thus, two particular sub-detector systems, the end-cap electromagnetic calorimeter (EEMC) and the Roman Pots (RP), are of particular interest for DVCS. The RP are detectors placed very close to the hadron beam line and very far from the interaction region, and they allow to measure particles scattered at extremely low angles (<5 mrad).

The following sections will present our study concerning these two detector subsystems: the EEMC and the RP.

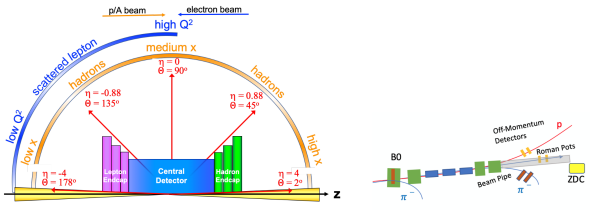

(a) (b)

Figure 1: Central EIC detector (a) and far-forward detector region (b). The Roman Pots are located at around 26 m from the interaction point.

Radiation hardness and light yield of lead tungsten crystals

Most scattered electrons and emitted photons from DVCS would be detected by the EEMC, which will contain thousands of lead tungsten crystals 2×2×20 cm^3 in size, in order to measure the energy and position of the incoming particles. The advantages of lead tungsten crystals are high light yield, small Moliere radius, fast response and high radiation hardness.

Since EIC will have a high intensity electron beam, the annual radiation dose in the EEMC will be around 30 Gy. It is important to know that the radiation hardness of the crystals will meet the required criteria. We have performed radiation hardness measurements in a subset of lead tungsten crystals using a high activity ^{60}Co source. Figure 2 shows the experimental setup. The radiation dose rate can be varied by changing the the distance between crystals and radiation source. We typically irradiated crystals at a dose rate of 1 Gy/min for a duration of 30 min, even though higher radiation rates and times were also used during our studies. Figure 3 shows the optical transmittance of the crystals along their longitudinal axis as a function of the wavelength, before and after irradiation. At the peak of the scintillating light spectrum (around 430 nm), we can observe a loss of transmittance of about 10% for 30 Gy

and about 15–20% after 10 kGy.

This small damage in optical transmittance can be recovered by annealing the crystals using blue light or by high temperature (around 250 °C).

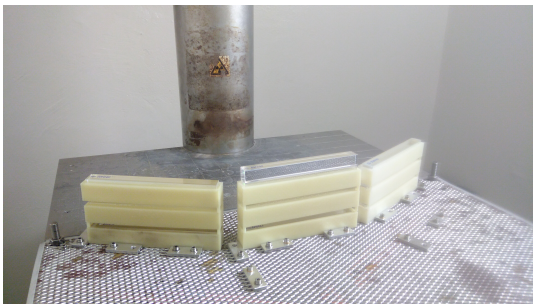

Figure 2: Experimental setup for radiation hardness measurements. The crystals are placed in front of a strong ^{60}Co source, which is inside the vertical cylinder. Different radiation dose rates can be achieved by changing the distance between crystals and the ^{60}Co source.

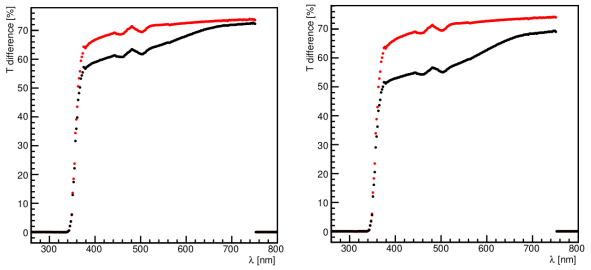

(a) (b)

Figure 3: Results of 30 (a) and 10000 (b) Gy radiation exposition. The horizontal axes show the wavelength in [nm]. Crystals lost around 15% of their transparency with 30 Gy and around 35% with 10000 Gy.

The light yield is also another important property of crystals that need to be quantified. Crystal were wrapped with VM2000 reflector to collect almost all scintillation light. We used a well-known energy radioactive source, ^{137}Cs and ^{22}Na, to measure the crystal light yield. The source was attached to the end of the crystal and we used a calibrated PMT to determine the light yield of the crystals, which is shown in Fig. 4. The light yield is calculated from the calibrated 1 photo-electron peak of the PMT. The light yield of 10 crystals is shown in Fig. 5. All crystals light yield are consistent with one another and meet the criteria of EEMC, which is 20 photo-electrons/MeV.

Calorimeter resolution study

When an electron or a photon hits a high density material they will lose their energy by generating an electromagnetic shower, which can be used to measure the impact position and energy of the particle. In order to have good position and energy resolutions, the crystal

Figure 4: Setup of the light yield test. The crystal wrapped with VM2000 and attached to a PMT. Everything is placed in a dark box The radioactive source was attached to the end of the crystal.

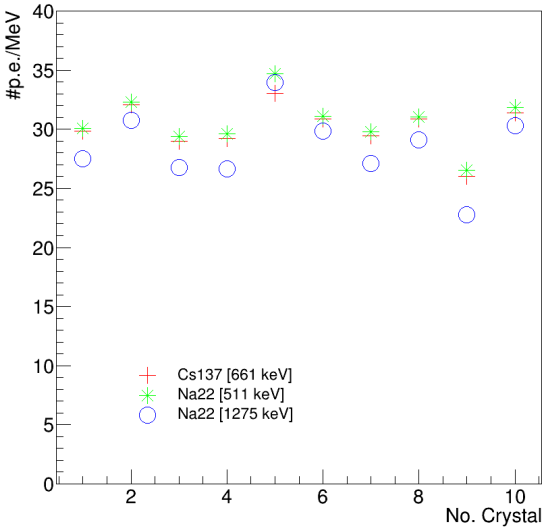

Figure 5: Light yield of 10 crystals with radioactive sources. We can see the good consistency of the light yield among all crystals.

size is designed to keep 90% of shower in one single crystal and 10% sharing by nearby crystals.

We have built the simulation setup of EEMC shown in Fig. 6. The blue ring structure on the left of the figure is the EEMC. We used a single photon generator in the simulation to study the position and energy resolution. Results show that we can have a position resolution better than 10% of the crystal size as shown in Fig. 7.

The energy resolution of the EEMC can be described by the following formula:

$$\frac{\sigma}{E} = \alpha \oplus \frac{\beta}{\sqrt{E}} \oplus \frac{\gamma}{E}$$

The α and β terms are related to the calorimeter design such as its geometry or its thickness. Fig. 8 shows the energy resolution of our EEMC design. The results meet the requirement of the EIC. In addition

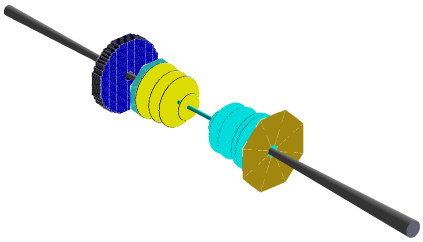

Figure 6: The blue ring structure on the left is the EEMC, which is around 1.8 m away from the interaction point. The inner and outer radius of the EEMC is 10 and 52 cm, respectively.

to the design of the EEMC, the clustering algorithm of the shower also plays an important role in these studies, which are currently still ongoing.

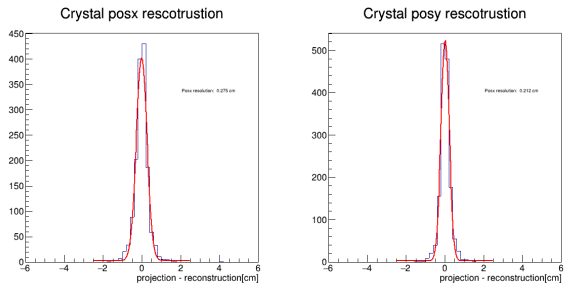

Figure 7: The crystal size is 2 x 2 x 20 cm^3 in the simulation setup. The position resolution is around 10% of the crystal width.

Test bench of AC-LGAD and ALTIROC

AC-coupled Low Gain Avalanche Diodes (AC-LGADs) are a new type of the silicon sensors designed by BNL, which are adapted from DC-LGADs used in the High-Granularity Timing Detector (HGTD) of the ATLAS experiment at CERN. The main difference between AC-LGADs and DC-LGADs is that metal electrodes are placed over an insulator at a fine pitch, and signals are capacitively induced on these electrodes, which is illustrated in Fig. 10. This feature not only allows AC-LGADs to keep its fast timing and low noise ability, but also offer better position information[2].

In order to characterize the readout performance of AC-LGADs and the signal sharing between neighboring channels, we setup a testbench using the ATLAS HGTD readout chip (ALTIROC) to read the signals from AC-LGADs. The ASIC was wire-bonded to the sensor. ALTIROC has 2 TDCs to measure the time-of-arrival and the time-over-threshold of the signal (which is related to its charge). In addition to this, 2 different type of preamplifiers, a voltage pre-amplifier (VPA) and a trans-impedance (TZ) pre-amplifier are available

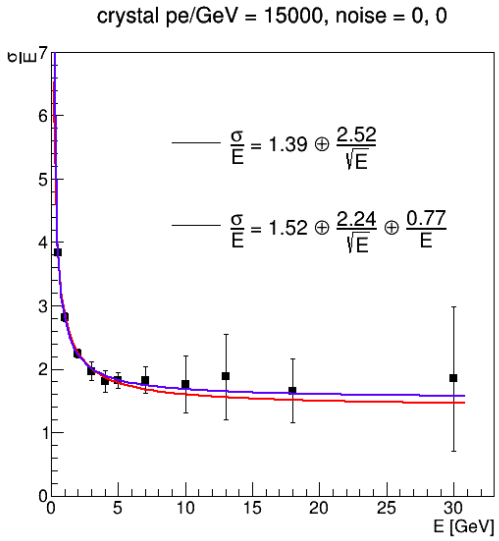

Figure 8: The energy resolution of EEMC design. The α term is around 1.5% and the β term is around 2.4% in both fits. The horizontal axis is the cluster energy of the incoming particles.

in the chip. We used both in this study in order to know which one is better for our future readout system. In order to reduce the background as much as possible, the test board is put inside a dark box, which is shown in Fig. 9.

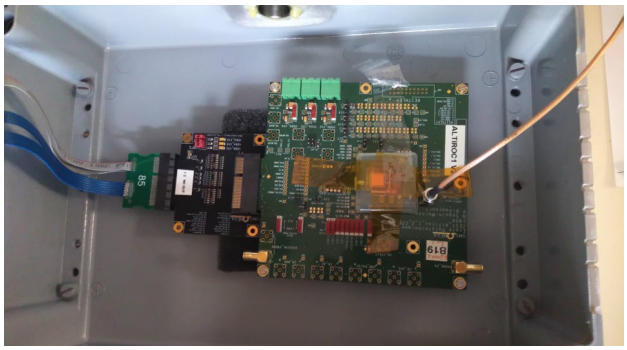

Figure 9: Test board with an AC-LGAD sensor and the ALTIROC readot chip placed inside the dark box.

We measured each channel response when all others are turned off. Later, we turned on all channels to measure all their responses when we inject a charge into each individual channel. The signal sharing map is shown in Fig. 11. In average, we have 20% of charge sharing with the VPA pre-amplifier and 10% of sharing with the TZ pre-amplifier. This is because the VPA has a higher gain than the TZ pre-amplifier. However, it also means that VPA may have a saturation issue for large signals and could induce a worse position resolution than the TZ pre-amplifier.

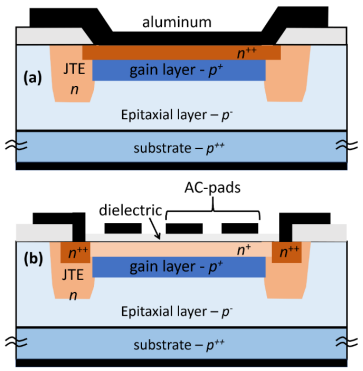

Figure 10: Top: DC-LGAD sensor. Bottom: AC-LGAD sensor. The metal pads with the dielectric layer in the AC-LGAD allow the charge sharing which improves the position resolution.

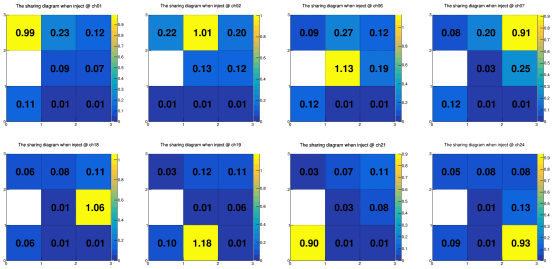

Figure 11: Top: signal sharing as we inject charge into the VPA pre-amplifier. Bottom: charge sharing for the TZ pre-amplifier. The maps show 20% of sharing among VPA channels and 10% sharing among TZ channels.

Position resolution study of future Roman Pot readout chip

In the future Roman Pot readout chip, 1 Analog-to-Digital Converter (ADC) and 1 Time-to-Digital Converter (TDC) would provide precised position and time measurements. However, ADCs have larger size and power consumption than TDCs and these go higher as we increase the number of bits of the ADC. The purpose of this study is to know the position resolution difference under different ADC number of bits. The simulation is based on the TZ type pre-amplifier and the charge is injected between 2 channels of the sensor. Several electronics and physics properties are also simulated in order to get results as close as possible to reality. For example, white noise, smearing of the injected charge with a Landau distribution, a detection threshold, probability of saturation of the ADC, are some of the effects that were simulated. Since the charge sharing only happens around the injection position, and rest of the channels only show the white noise, it is reasonable to just consider the nearby channels around the injected point in the position reconstruction. Based on the above, we simulated the position reconstruction algorithm and obtained the position resolution versus different number of bits of the ADC. Results are shown in Fig. 12. We find that there is no significant position resolution difference between 8, 10, and 12 bits, so an ADC with 8 bits would be adopted for our goal.

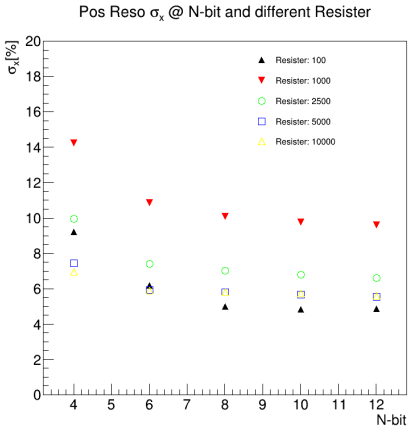

Figure 12: Position resolution as a function of the number of bits in the ADC. Rsheet represents the resistor value (in ohms) of the dielectric layer which affects the charge sharing. We find that there is no significant position resolution difference between 8, 10 and 12 bits.

Conclusion

We have presented some studies concerning the design of the EIC backward endcap electromagnetic calorimeter and the Roman pots.

Lead tungten crystals are shown to meet the criteria for radiation hardness, with small transmittance loss after 30 Gy of radiation dose. Their light yield are very uniform from one crystal to another. The energy and position resolution were simulated and found to meet the requirements needed for physics measurements at EIC.

Concerning the Roman pots measurements, the signal sharing of the AC-LGAD sensors was determined and the design of the ALTIROC readout chip seems to be a good starting point for a dedicated readout ASIC for EIC. An ADC will replace one of the TDCs of ALTIROC. We decided to use 8 bits in this ADC in order to get good position resolution while minimizing the power dissipation of the circuit. A new ASIC prototype will be produced later this year and we plan to characterize its performance in a similar way that we have done using ALTIROC.

References

[1] EIC Yellow Report, arXiv:2103.05419v3

[2] Fabrication and performance of AC-coupled LGADs, `https://www.osti.gov/servlets/purl/1571434`

Part VI

Neutrino Physics

session chaired by Benjamin QUILAIN

Study and calibration of SuperNEMO calorimeter

Xalbat AGUERRE

LP2i Bordeaux (Laboratoire de Physique des Deux Infinis de Bordeaux)

Abstract — The neutrino is the most abundant particle of matter in the Universe, but also the most mysterious, as such fundamental properties as its nature (Dirac or Majorana?) or its mass are still unknown. The SuperNEMO project aims to provide answers to these questions by searching for double beta decay without neutrino emission. This reaction, forbidden by the Standard Model, is only possible with a Majorana neutrino, and the signal corresponds to the emission of two electrons carrying all the reaction energy. To detect this decay, the SuperNEMO project uses a unique technology combining a tracker and a calorimeter that allows it to unambiguously identify the two electrons and measure their energy with the calorimeter. My thesis work consists of calibrating the energy of this calorimeter and following its evolution over time using different techniques: analysis and simulations of ambient background spectra, use of an LED light injection system for a relative calibration of the calorimeter and an absolute calibration using a ^{207}Bi source.

Introduction

Much has been learned about the neutrino since it was postulated by Wolfgang Pauli in 1930. Today it's know that the neutrino is a neutral lepton that can only interact by weak interaction, that there are three neutrino flavours (ν_e, ν_μ ν_τ and contrary to the Standard Model expectation, that the neutrino is a massive particle. This last property was proved by the neutrino oscillation discovery. Indeed, when the neutrino is propagating, its flavour changes and that's only possible if the neutrino is a massive particle. But there are many questions left unanswered about the neutrino. There are only limits on the mass value, and the mass ordering of the three flavours is still unknown. It's also known there are three flavours of neutrinos, but there are many experiments searching for possible other sterile neutrinos.

The nature of the neutrino is not yet known too. Neutrinos can be Dirac or Majorana particles. In other words, it's unknown if neutrinos and antineutrinos are different particles (Dirac) or same particles (Majorana). The knowledge of the neutrino nature would have large consequences on fundamental questions like the neutrino mass generation mechanism or for example on the origin of the matter/antimatter asymmetry in the Universe. The only practical way to answer this question is the study of the neutrinoless double beta decay ($\beta\beta0\nu$). Double beta decay with neutrino emission ($\beta\beta2\nu$) consisting of two simultaneous beta decays has already been observed. In this case, two electrons and two neutrinos are emitted simultaneously. In the case of the $\beta\beta0\nu$ only electrons are emitted as the first emitted neutrino is absorbed as antineutrino at the second vertex of the decay. This reaction is only possible if the neutrino is a Majorana particle. If this decay is observed, it would prove the Majorana nature of the neutrino. To observe it, it's needed to measure the sum of the energy of the two electrons, which correspond to the total reaction energy. The $\beta\beta0\nu$ is really challenging to observe as its half-life is estimated to be more than 10^{25} years.

SuperNEMO demonstrator

The SuperNEMO (Super Neutrino Ettore Majorana Observatory) experiment aims to observe $\beta\beta0\nu$ decay to prove the Majorana nature of the neutrino [1]. To achieve this objective, a tracker-calorimeter technology is used, which should allow to observe the trajectory of the two electrons of the $\beta\beta0\nu$ decay and to measure their individual energy. At the center of the detector, there is a source foil composed of ^{82}Se, a $\beta\beta$ emitter candidate. It is possible to change the source foil to accommodate other $\beta\beta0\nu$ emitter candidates. The tracker is placed around the source foil. This tracker is composed of 2034 Geiger cells. When a charged particle crosses the tracker, it ionizes the tracker gas (Helium) and the trajectory of the particle can be reconstructed using the fired Geiger cells. To measure the energy of the electrons, a calorimeter is located all around the tracker [2]. This calorimeter is made of 712 optical modules (OM), each composed of a photomultiplier coupled to a plastic scintillator. This calorimeter is divided in six different walls:

- 2 Main Walls (MW): 2x260 OMs in front of each side of the source foil (FWHM 8% at 1 MeV).
- 2 sides Walls (XW): 2x64 OMs with lower performances to tag background events.

- 2 Gamma Veto (GV): 2x32 OMs in top and bottom of the detector acting as a veto for the γ-rays.

A view of the detector is shown on figure 1.

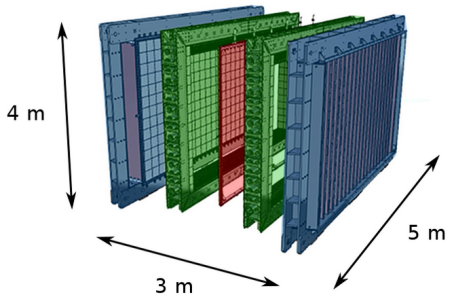

Figure 1: SuperNEMO demonstrator. In red the source foil, in green the tracker and in blue the calorimeter.

As the $\beta\beta$ 0 decay is a very rare event, it's necessary to be able to distinguish it from the background, especially from $\beta\beta2\nu$ one, as the two electrons of this decay can have an energy very close to the one from the $\beta\beta0\nu$. To decrease the background, the detector is installed at the Laboratoire Souterrain de Modane (LSM), under 4800 m water equivalent. The components of the detector were also chosen for their high radiopurity. Combining a tracker and a calorimeter provide also efficient event reconstruction to reject large part of backgrounds. In addition, good energy calibration and energy resolution are needed specially to improve the $\beta\beta0\nu$ and $\beta\beta2\nu$ distinction

To calibrate the calorimeter, different methods are used [3]. The nominal method is to use ^{207}Bi sources that are introduced into the detector near the $\beta\beta$ foils. This method needs the use of the tracker in order to identify the internal conversion electrons emitted by the ^{207}Bi. Unfortunately, the tracker is not currently fully operational other calibration methods have been developed and will be described in the two following sections.

Absolute energy calibration with ambient background

First method: fit with ambient background data

To calibrate the calorimeter, background runs taken in the LSM laboratory are used. The distribution of the background energy spectrum is well known above 1.2 MeV and is due to ^{40}K, ^{214}Bi and ^{208}Tl decays. In this first method, the objective is to fit the Compton edge of the ^{208}Tl located at 2.6 MeV. The fit uses the equation 1. There are two parts in this equation. The first one includes the error function to fit the Compton edge with N_evt being the number of events of the energy distribution at the beginning of the fit window, σ is the width of the error function and Mean corresponds to the amplitude where the slope is maximum. This point will be taken as reference to calibrate each OM. The second part of the equation 1 is exponential to fit rare high-energy events coming from neutron backgrounds. An example of this fit for a background run in one Main Wall OM can be seen in the figure 2.

$$\frac{N\_evt}{2}(1+erf\left(\frac{(Mean-x)}{\sigma\sqrt{2}}\right))+Nbg*exp(-\lambda x) \quad (1)$$

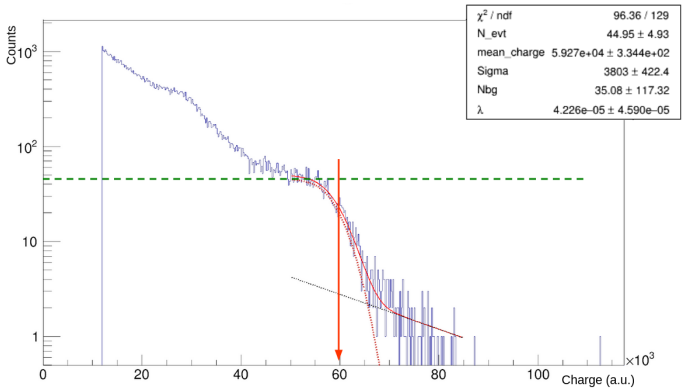

Figure 2: Amplitude distribution of one Main Wall OM for a background run fitted with the equation 1. The dotted brown curve represents the error function contribution, the black curve the decreasing exponential and the red curve is the sum of the two contributions. The green horizontal line represents the value of N_evt and the red vertical line the Mean value.

This method of fit works well for the Main Wall of the calorimeter and a first calibration was done with it. But problems appear with XW and GV OMs. Indeed, OMs of these walls have a worse energy resolution and the Compton edge of the ^{208}Tl is not well distinguishable, as it can be seen on figure 3. So the conclusion was that this method is useful for the calibration of the Main Wall, but is not really usable for the XW and GV. A second method has been developed.

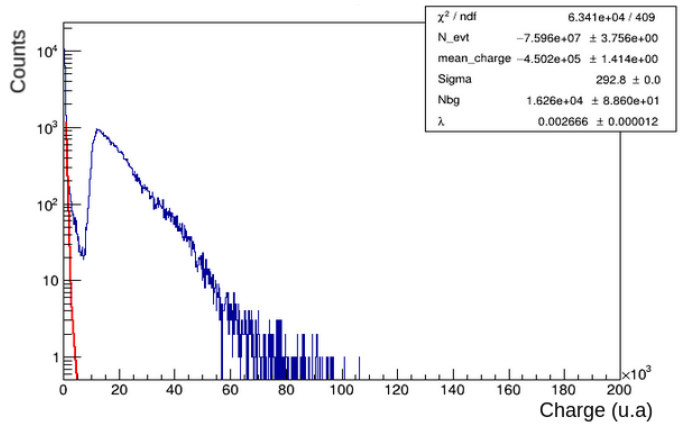

Figure 3: Charge distribution of one Main Wall OM for a background run of one OM of the GV. The fit method is not usable in this spectrum.

Second method: fit with simulated data

The three main components of ambient background have been simulated (^{40}K, ^{214}Bi and ^{208}Tl) to reconstruct the measured background spectra. The simulation was performed with the simulation software of the SuperNEMO collaboration: Falaise based on GEANT4. The output of the simulation is an energy spectrum where the energy resolution has been forced to be equal to zero. The energy resolution, the OM gain and the relative contribution of each component of the background (^{40}K, ^{214}Bi and ^{208}Tl) are then adjusted to match the simulated spectrum with the real data. An example of this method is shown on figure 4

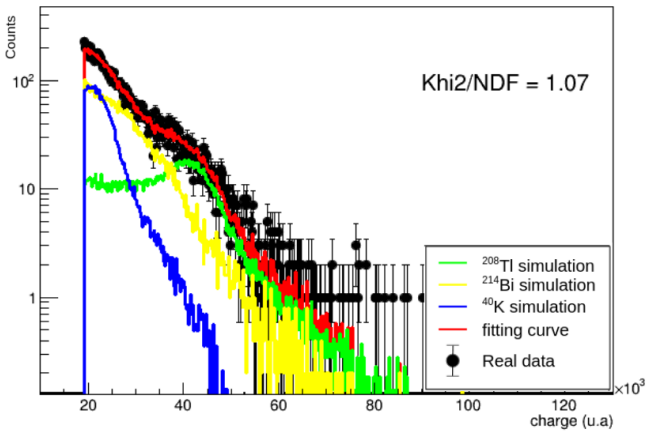

Figure 4: Charge distribution of one GV OM for a background run using the full spectra fit method. The blue curve represents the simulation of the ^{40}K, the yellow the ^{214}Bi, the green the ^{208}Tl, the red is the sum of the three simulations and the black points are the real data.

As expected it has been shown that optical corrections including Birks and Cherenkov effects, that are non-linearity effects with energy, needed to be applied on simulated spectra to reproduce the data. Geometrical corrections need also to be taken into account. Indeed, if a particle deposits its energy at the entrance of the scintillator or just in front of the photomultiplier, there will be differences in the light collection. Thus, there are non-linear effects with the position of the interaction within the scintillator volume. All these corrections were calculated and simulated by another PhD student [4]. I applied them to this fit method and demonstrated that they are necessary to perform a good fit.

This method allows now to calculate the gain of all the OMs, including the XW and GV ones and has been used to calibrate the detector for current studies. Unfortunately, it wasn't possible to extract the energy resolution of each OM, as this effect is hidden by the optical effects. Nevertheless, it has been possible to estimate the contribution of each component of the spectra (^{40}K, ^{214}Bi and ^{208}Tl) for each OM in order to calculate the corresponding activities for each OM. This work is in progress and will be useful to check the radioactivity level detected by the calorimeter.

Relative energy calibration: Light Injection System

A relative energy calibration is also planned using a Light Injection system (LI) with LED [5]. This relative calibration will be used in addition to the absolute calibration with ^{207}Bi sources. Indeed, this absolute calibration which will be used as soon as the tracker will be operational needs a lot of time, 20 h, and thus can't be done on a daily basis. It's planned to do this absolute calibration every 3 weeks. So the Light Injection System will provide the way to do a daily calibration survey.

This system consists of a monochromatic LED light that illuminates each OM. There are 10 LEDs lighting up about 70 OMs each and reference OMs. The reference OMs are placed outside the detector with an embedded ^{207}Bi source for a continuous calibration in order to monitor the LED light intensity. Once the LED light variations are corrected, it is possible to extract the gain variation of each OM. A LI run is done in 20 minutes, so it can be done twice a day without losing too much physics data taking, in addition to the absolute calibration.

Another advantage of this system is that high energy are reachable (10 MeV). With ^{207}Bi, the limit is 1.77 MeV. So with the LI system, the linearity of the OMs can be studied at higher energy. To do that, light is sent to the OMs with six different LED intensities. An example of linearity test is shown in figure 5 for one Main Wall OM. In this example, it is clearly visible that the linearity is not good. The same result is obtained for all the OMs. It is inconsistent with the tests done before the OMs installation into SuperNEMO showing a good linearity. So the hypothesis is that the non-linearity measured with the LED light is caused by the Light Injection system itself.

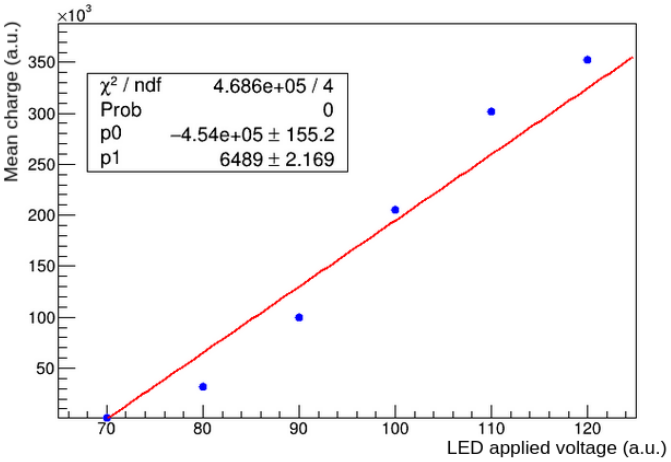

Figure 5: Example of a linearity fit obtained with the Light Injection System. The error bars are included but are too small to be seen.

To verify this assumption, it is possible to look at the deviation between the linear fit and the measured charge peaks related to one LED intensity for all the

70 OMs fired by this same LED. The figure 6 show this deviation distribution for 66 OMs associated to the same LED. A Gaussian distribution is clearly visible, meaning that the observed non-linearity is correlated to the LED itself.

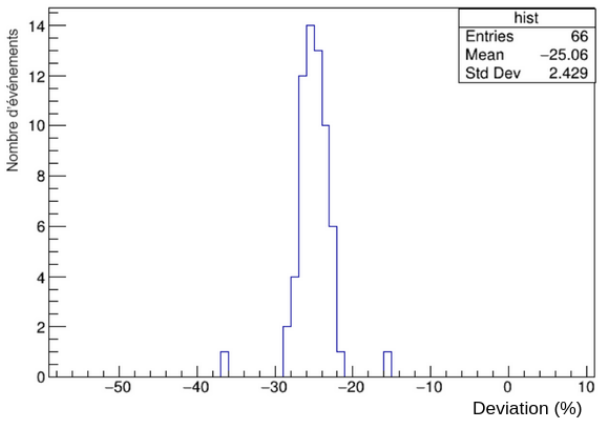

Figure 6: Example of deviation between the linear fit and a charge peak related to one LED intensity for all 66 OMs related to this LED.

In fact, there are still big uncertainties on the voltage applied to the LED which are under evaluation and correction.

Conclusion

In conclusion, SuperNEMO is an experiment aiming to detect the $\beta\beta0\nu$ decay to answer the question about the nature of the neutrino. SuperNEMO will soon be fully operational.

My work on this project is on the calibration of the calorimeter. For that, I used ambient background runs. I first fitted the Compton edge of the ^{208}Tl to obtain the energy calibration, but it wasn't adapted for the largest OMs. So we developed a new method of fit, using the simulation of the different background components. This method seems to be efficient for all OMs and has been applied to calibrate all the calorimeter. With this method, we should also be able to estimate the activity of each simulated background component for each OM.

I also worked on a relative energy calibration system using LED light allowing daily calibration survey and linearity measurements. A preliminary linearity study has been done and shown that there were still some uncertainties on the LED intensity which will be corrected soon.

References

[1] Arnold, R., Augier, C., Baker, J. et al. Probing new physics models of neutrinoless double beta decay with SuperNEMO. Eur. Phys. J. C 70, 927-943 (2010). https://doi.org/10.1140/epjc/s10052-010-1481-5

[2] Barabash, A. S., Basharina-Freshville, A., Blot, S., Bongrand, M., Bourgeois, C., Breton, D., . . . Žukauskas, A. (2017). Calorimeter development for the SuperNEMO double beta decay experiment. Nuclear Instruments and Methods in Physics Research, Section A: Accelerators, Spectrometers, Detectors and Associated Equipment, 868, 98-108. doi:10.1016/j.nima.2017.06.044

[3] Christine Marquet. La décroissance double bêta et les grandes questions sur le neutrino - Contributions aux calorimètres NEMO3 et SuperNEMO, Habilitation à diriger des recherches, Université de Bordeaux, Juin 2019

[4] Axel Pin. Recherche de la nature du neutrino via la décroissance double bêta sans émission de neutrinos : Caractérisation et optimisation du calorimètre SuperNEMO et impact sur la recherche de la décroissance du 82Se : Développement du premier prototype LiquidO. Astrophysique [astro-ph]. Université de Bordeaux, 2020. Français. NNT : 2020BORD0277. tel-03149593

[5] R.Salazar, "Calibration and Monitoring Systems for Neutrinoless Double Beta Decay Searches in the SuperNEMO Experiment", Thesis, The Univeristy of Texas at Austin, 2021.

R2D2 R&D : development of a Spherical Proportional Counter for the neutrinoless double beta decay search

Vincent CECCHINI

CENBG, Université de Bordeaux, SUBATECH, IMT-Atlantique, Université de Nantes, CNRS-IN2P3, France

Abstract — The R2D2 project is an R&D to assess the feasibility of a neutrinoless double beta decay search program by using the Spherical Proportional Counter (SPC) technology [1]. The first prototype purpose is to demonstrate the energy resolution capabilities of such a detector, as well as develop its electronics components. In this proceedings, after a presentation of the experimental setup, we will show some energy resolution measurements as well as drift-time measurements obtained combining the SPC charge readout to an additional light readout.

Introduction

The neutrinoless double beta decay ($\beta\beta0\nu$) search is currently a high interest field of study, since it is a way to probe physics beyond the standard model. Various method are under study, such bolometers, liquid TPC or high-pressure gaseous TPC. The Rare Decays with Radial Detector (R2D2) project is part of those R&D efforts, attempting to build a suitable detector for the neutrinoless double beta decay.
The $\beta\beta0\nu$ is characterised by the transformation of two neutrons into two protons with the emission of two electrons only (fig. 1, center), leading to a measurement of a discrete energy spectrum (fig. 1, right). This is the main experimental difference with the standard model allowed double beta decay ($\beta\beta2\nu$, fig. 1, left), which has two neutrinos in addition to the two electrons. Since it is barely impossible to calorimetrize the neutrino energy, the measured energy spectrum for the $\beta\beta2\nu$ is continuous.

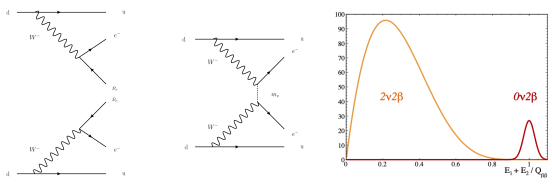

Figure 1: Left: $\beta\beta2\nu$, Center: $\beta\beta0\nu$., Right: Illustration of the expected energy spectrum shape for both $\beta\beta2\nu$ and $\beta\beta0\nu$.

This continuous spectrum being a background for the $\beta\beta0\nu$ detection, an excellent energy resolution has to be reached by the detector, at the order of 1% FWHM. Since the $\beta\beta0\nu$ is an extremely rare phenomena, a large isotope mass at the level of the ton scale is needed to fully probe the inverted mass hierarchy region, and the background should ideally be background free. A two track recognition ability is an additional asset to validate the observation of a $\beta\beta$ decay.
Following a simulation which indicate that a 1 m radius SPC filled with enriched ^{136}Xe could match those requirements [2], the R2D2 project is ongoing to build a proof of concept.
The R&D process follows a staged approach with a first small size prototype (20 cm radius), currently in use, to demonstrate the energy resolution capabilities profiting from a new designed electronics, and validating feedthrough and readout. Then a second prototype will follow, with radiopurity capabilities, and finally a tone scale experiment should be built.

SPC Principles

The spherical proportional counter is a gaseous detector with spherical shape and a small metallic ball used as anode at the center, functioning in proportional regime, as illustrated in fig. 2. This mean that when a charged particle ionizes the gas, the electrons are drifted to the central anode, where an avalanche occurs. That avalanche is induce by the high electric field in the region surrounding the anode. Indeed, the Gauss law imply that the electric field is proportional to

$$E(r) \propto \frac{V_0}{r^2} r_a \tag{1}$$

with V_0 the potential applied on anode, r_a the anode radius and r the radial distance.
We get the signal by monitoring the charge on the anode. This signal goes through a charge preamplifier (integrator), is digitized and saved, meaning that SPC is a one channel charge readout detector.
In addition to ionization of the medium, a charged

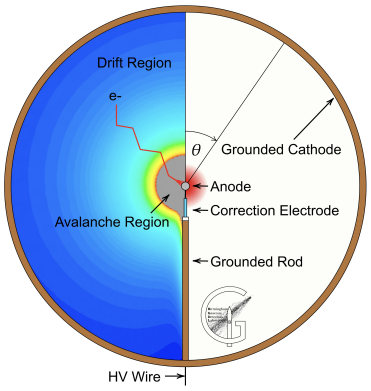

Figure 2: SPC generic design.

particle loses energy by excitation. The de-excitation results in light emission. The use of the emitted light for calorimetry is quite complicated since it requires a large photodetection coverage impacting the detector background, but the detection of a fraction of the light can be useful. Indeed, excitation light being produced by both primary charged particle interaction and by the avalanche, the measurement of the elapsed time between those two phenomena is a direct measurement of the electron drift-time. For this reason, adding a light readout could be an interesting feature that will be studied in our R&D.

Experimental Setup

The prototype in use (fig. 3) is a 20 cm radius sphere with a 1 mm radius anode. The anode is maintained by a road from the top of the detector and a ^{210}Po alpha source of 5.3 MeV is place at the bottom hedge of the vessel (fig. 4 shows the source holder). A top flange gives access to the anode and a bottom flange allows to manipulate the source. Lateral flanges are used for gas filling, pressure monitoring and vacuum system.
A particular attention was paid on the noise reduction. The mechanical noise has been reduced by adding anti-vibration pad, a low noise electronics has been developed thanks to the OWEN grant, and a meticulous grounding and cable electromagnetic screening results in a substantial reduction of low frequency noise.

The prototype is built in stainless steel *i.e.* non-radiopure material, but it has stringent requirements on the sealing. Indeed, the focus of this first step being on the energy resolution, it require to avoid external gas contamination. Before each data taking, the detector is pumped to a vacuum of the order of 10^{-5} mbar.
The gas use in the early stage was ArgonP2 (98% Ar + 2% CH_4) for resolution measurements, and pure Argon (99.9999% given by manufacturer) for drift-time measurements.

In addition to this setup, a Silicon PhotoMultiplier

Figure 3: Prototype in use at LP2IB facility.

(SiPM) was placed in the source holder. The Argon excitation light being emitted at 128 nm, we use a 6×6 mm^2 S13370 Hamamatsu VUV4 familly SiPM. It has a 14% photon detection efficiency at 128 nm.
Since the SiPM bias voltage (55 V) induces an electric field disturbing the one from SPC, we had to make a Faraday cage around the SiPM. For this reason, the source holder was machined to insert the SiPM and a grid was installed above it (fig. 4). To maintain a low

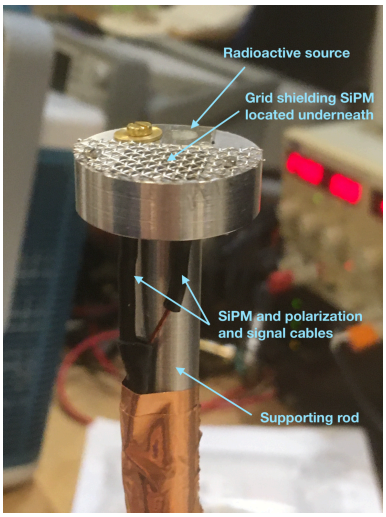

Figure 4: SiPM and α source holder, with the grid shielding SiPM electric field.

amount of additional material inside the detector, the SiPM electronics was placed outside, at about 20 cm distance. This resulted in a not suitable operation condition due to long cable used to connect the SiPM to its electronics. To minimize the noise, we use a single coaxial cable to transmit signal (core cable) and bias voltage (sleeve cable). In addition, a 10 MHz low-pass filter CLPFL-0010-124 BNC from CRYSTEK was used to suppress the high frequency noise.

Results

At the time of measurements, the detector did not received yet the certification to operate at pressure higher than the atmospheric one. Because we want a source with energy in the same order of magnitude than the ^{136}Xe $Q_{\beta\beta}$ value, β source was prohibited. Indeed, their small energy loss at atmospheric pressure prevents all attempt to a full calorimetrization. For this reason, we used an α source of ^{210}Po. At atmospheric pressure alpha tracks have a length of about 3 to 4 cm, while we can get longer tracks by lowering the pressure. The bottom threshold being a maximum track length of 20 cm, reached for pressure below 200 mbar.

Resolution Measurements

The resolution was measured under various conditions, to study the track length effect and the track direction effect. The results were presented in detail in [3].
As mentioned above, the track length effect was studied by varying the pressure. Two runs of data taking was performed in early 2020. The first one at 200 mbar with 720 V applied on the anode, resulting in tracks from 15 cm to 20 cm, in the same order of magnitude than β particles at 10 bar. The second one was taken at 1100 mbar and 2000 V resulting in tracks of few centimeters (3 to 4).
The resolution is measured on the signal integral distribution and the results are shown in fig. 4. 1.1% of energy resolution at full width at half-maximum (FWHM) was reached for more than 15 cm tracks, and at 1100 mbar we obtained 1.2% FWHM energy resolution. Those results indicate that neither the track length, nor the pressure, affect sizeably the energy resolution.

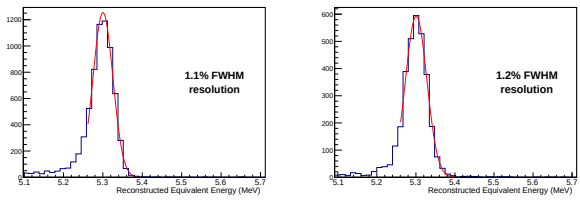

Figure 5: Left: signal integral for 200 mbar data; Right: signal integral for 1100 mbar data.

For what concern the track direction effects, we had to do a simulation of the detector to determine if some signal variables (like total duration, width at half-maximum or rise-time) could be linked to the direction of the track. As a matter of fact, we do not have the direct information of track direction in the experiment, but it is accessible in a simulation. It appears that the total duration of signal, called Dt, allows track direction discrimination, as showed in fig. 5. Thus, from simulation we determine Dt cuts values (green lines on the figure) to make subsamples of data, ordered by track direction. In the simulation plot (fig. 5, right), the color scale indicates the cosine of angle between the track and the vertical of the detector, -1 corresponding to track going toward the anode.
Fig. 6 show gaussian fit of each subsamples (red lines),

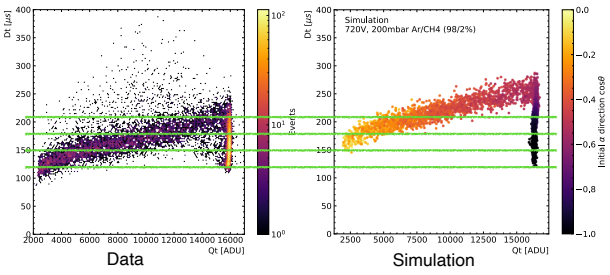

Figure 6: Total signal duration (Dt) VS charge (Qt) plots, with Dt cuts (green) allowing for track direction selection.

with a similar energy resolution of 1.1% to 1.2% FWHM for each selected direction, centered around a similar mean value. Therefore, we can say that the track direction does not affect the energy resolution (taking into account statistical uncertainties).

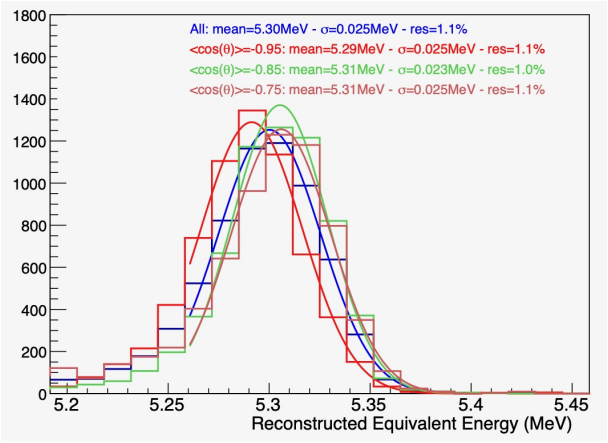

Figure 7: Energy distribution for different Dt subsambles.

Drift-time Measurements

The objectives of those measurements was to validate the minimal setup and confirm the possibility to get a drift-time measurements in an SPC. The finality, whether we would use the light signal directly in the experiment, or only as calibration tool, is not defined yet.
The drift-time was measured in pure argon gas to avoid the absorption of VUV light by Penning mixture. To allow a sufficient geometrical acceptance by the SiPM, we keep the α track close to it by operating the detector at 1100 mbar.
We define the drift-time Δt as the time interval between the maximum of the blue (light readout) and the yellow (SPC readout) signals from fig 8.

We repeat the measure at different voltage (900V,

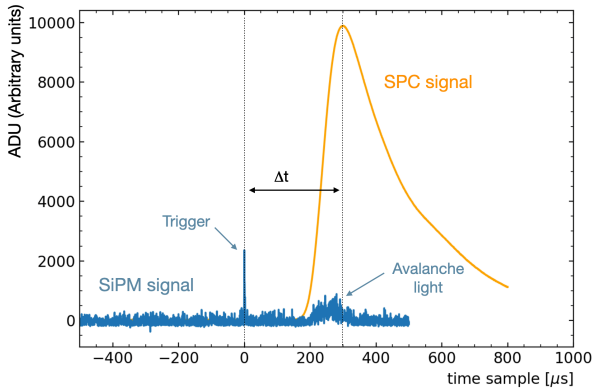

Figure 8: SPC generic design.

1350V, 1800V and 2200V) to compare results with the simulation in fig. 9. The errors bars on the data (dots) are given by the standard deviation of the distribution from the Drift-time distribution. As expected, the drift-time is increasing while voltage decrease and the shape is in good agreement with the simulation.

A Geant4 simulation shows a mean deposit energy

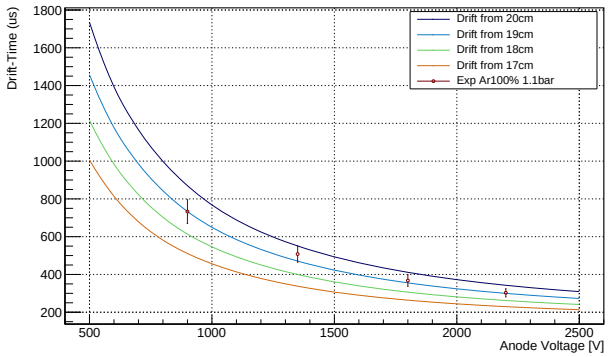

Figure 9: Simulated drift-time for 17 cm to 20 cm initial radial distances (lines) over voltage range from 500 V to 2500 V, and measured drift-time for 900 V, 1350 V, 1800 V and 2200 V anode voltages.

position at 19.15 cm in 1.1 bar pure Argon, which is in good agreement with results of fig. 9.
With those measurements we were able to validate the use of SiPM and its acquisition chain, as well as the simulated drift-time. More details can be found in Ref. [4].

Conclusion

The R2D2 R&D has shown some promising results, like 1.1% of FWHM energy resolution at 5.3 MeV and the independence of the energy resolution with respect to the track length or to the track direction. It has also allowed us to improve our knowledge on the detector response. And finally, it has demonstrate the possibility to measure the drift-time by using a Silicon Photomultiplier.
Nevertheless, important works has still to be done. About the analysis, we have to look for correlation of the light readout information to the SPC signal to improve the event reconstruction. About the detector itself, it recently received the agreement to operate pressurized, we will repeat the resolution measurement higher pressure. A gas recycling system will also be installed to do measurements by using xenon, which is our gas target for the experiment.

References

[1] A novel large-volume spherical detector with proportional amplification read-out, Giomataris I. *et al.*, J. Inst. 3 P09007 (2008).

[2] Study of a spherical Xenon gas TPC for neutrinoless double beta detection, Meregaglia A. *et al.*, J. Inst. 13 P01009 (2018).

[3] R2D2 spherical TPC: first energy resolution results, Bouet R. *et al.*, J. Inst. 16 P03012 (2021).

[4] Simultaneous scintillation light and charge readout of a pure argon filled Spherical Proportional Counter, Bouet R. *et al.*, Nuclear Inst. and Methods in Physics Research, A (2022)

Performing Time Calibration on the SuperNEMO Demonstrator Calorimeter and Extracting the Time Resolution for γs at 1 MeV

Malak HOBALLAH

Laboratoire de Physique des 2 Infinis Irene Joliot Curie (IJCLab)

Abstract — The SuperNEMO experiment aims to search for the neutrinoless double beta decay which is a hypothetical process that is forbidden by the Standard model. The observation of the signal of this decay would prove the Majorana nature of neutrinos. The final full detector goal of the experiment is to reach a sensitivity of 10^{26} years on the $0\nu\beta\beta$ decay half-life, i.e an effective Majorana neutrino mass of 50 - 100 meV. The first module of the full SuperNEMO experiment is under installation at Laboratoire Souterrain de Modane, with 6.23 kg of ^{82}Se as a double beta source. It is made of source foils that emit two electrons, wire tracking chamber that reconstructs the charged particle tracks, calorimeter walls made of photomultipliers to measure the individual particle energies and arrival times. The commissioning of the SuperNEMO calorimeter began in 2018, it is made of 712 optical modules of mostly 8" photomultipliers. This article reviews over the methods followed to extract the time resolution of γs at $\sim$ 1 MeV and the performing of time calibration and synchronization of the calorimeter walls using a Cobalt source. The results gave a time resolution of $\sim$ 600 ps for 8" PMTs and $\sim$ 800 ps for 5" PMTs, and a calibration with a precision on time less than 0.2 [ns].

Introduction

SuperNEMO is an experiment that inherits its instrumentation and principle from the NEMO experiments, and will carry out a search for the neutrinoless double beta ($0\nu\beta\beta$) decay using a tracker-calorimeter technique. This technique allows a full topological reconstruction of particles, and a measurement of the individual particles' energies and time-of-flight, which allows a unique identification of the different backgrounds enabling high particle rejection and an ultra-low background level.
With such tracker-calorimeter technique, and in the case of detection of the $0\nu\beta\beta$ signel, we would be able to study the decay mechanism that the isotope went through by reconstructing the full kinemetics (single electron energy and angular distribution) of the $\beta\beta$ events. And in the case of the normal two neutrino double beta decay ($2\nu\beta\beta$), the following studies will be possible:

- The quenching of the axial vector coupling constant (g_A^{eff}) that goes into the calculation of the $2\nu\beta\beta$ half-life as in equation 1, where g_A^{eff} is the effective axial vector coupling constant, $M^{2\nu}_{GT-3}$ is the Gamow-Teller nuclear matrix element, $G_0^{2\nu}$ and $G_2^{2\nu}$ are two phase space factors with different kinematics and ξ_{31} is a parameter. At the nuclear level, β decay can be considered as a mutual interaction of the hadronic and leptonic currents mediated by massive vector bosons $W^{\pm}$, that can be expressed as mixtures of vector and axial-vector couplings, g_V and g_A respectively. These couplings contribution enter the theory when the hadronic current is renormalized at the nucleon level [1]. The conserved vector-current hypothesis and partially conserved axial-vector-current hypothesis yield the free-nucleon values $g_V = 1.00$ and $g_A = 1.27$ [1]. But the value of g_A is affected, inside nuclear matter, by many-nucleon correlations.

It is well known that the theoretically calculated strengths of Gamow-Teller beta decay transitions to individual final states are significantly larger than the experimental ones. The effect is known as the axial-vector current matrix elements quenching [2]

$$(T^{2\nu}_{1/2})^{-1} \simeq (g_A^{eff})^4 |M^{2\nu}_{GT-3}|^2 \frac{1}{|\xi^{2\nu}_{31}|^2} |G_0^{2\nu} + \xi^{2\nu}_{31} G_2^{2\nu}| \quad (1)$$

- Information on whether the decay went through higher state dominance (HSD) or single state dominance (SSD), and this is related to the intermediate states of the decay. If one single intermediate state dominates the transition, then the process is said to be SSD. On the other hand, if the process proceeds through many higher intermediate excited states, it is said to be HSD. A precise study of single-electron energy distributions with high-statistics can be used to distinguish between these two models. This kind of study affects the final measured half-life of the $2\nu\beta\beta$ decay because a higher number of lower energy electrons in the SSD model is expected and this reduces the detection efficiency.

A first module of SuperNEMO, called Demonstrator, is under construction and testing at the Labo-

ratoire Souterrain de Modane (LSM) at 4800 m.w.e. depth. The Demonstrator aims to reach a sensitivity of $T^{0\nu}_{1/2} > 6.5\times10^{24}$ y corresponding to $\langle m_\nu \rangle < (260 - 500)$ meV with 17.5 kg.y exposure of ^{82}Se. With this Demonstrator, we can also prove that a SuperNEMO module can reach the background specifications for source radio-purity : ^{214}Bi < 2 μBq/kg and ^{208}Tl < 10 μBq/kg and Radon activity : ^{222}Rn < 0.15 mBq/m^3).

The SuperNEMO Demonstrator

The SuperNEMO Demonstrator is composed of three main components: the source foils, the tracker and the calorimeter (see Figure 1).

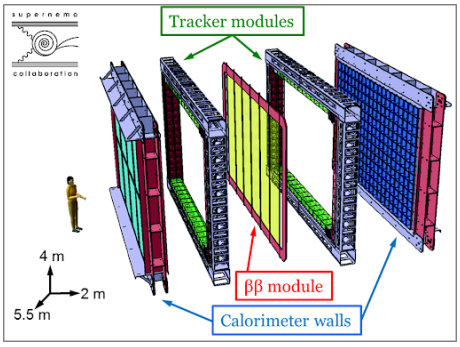

Figure 1: Scheme showing the different components of the SuperNEMO demonstrator, man as a scale. The numbers to the bottom left shows the dimensions of the demonstrator.

The detection method is presented in the scheme in figure 2 which shows the source foils situated in the middle of the detector that will undergo $2\nu\beta\beta$ decays emitting two electron, they will then travel through the detector hitting the tracker cell wires allowing for reconstruction of the decay topology. The particles will be under the effect of a magnetic field that curves the tracks of charged particles and allows particle discrimination. Finally, they will reach the segmented calorimeter wall made of photomultipliers where each particle energy will be measured individually.

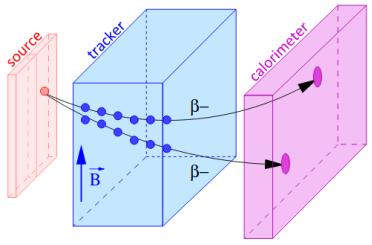

Figure 2: Scheme showing the principle of detection of the SuperNEMO experiment. Two electrons are emitted from the source foils, their tracks get detected by the tracker wires and finally their energy measure by the calorimeter walls.

Source

The demonstrator source is made of 6.23 kg of ^{82}Se separated into 34 ultra pure thin source foils. The choice of ^{82}Se was made following these reasons:

1- Having a relatively high $Q_{\beta\beta}$ value of 2.99 MeV, decreasing the β γ natural radioactive background effects.

2- Having a relatively high $2\nu\beta\beta$ half-life at 9.4 $\times10^{19}$, decreasing the $2\nu\beta\beta$ background with respect to the $0\nu\beta\beta$ signal.

3- Having high natural abundance, which allows a production of the isotopes in large quantities.

4- Ability to reach high purification values through the available techniques.

The choice of using thin source foils is to allow low energy electrons to be emitted from the foils and into the detectors without re-absorption. The second reason is to minimize energy loss inside the the foil, which reduces fluctuations in the energy spectrum and thus an improvement to the detectors' energy resolution. Using thin foils also eases the job of switching to another source to study its double beta properties.

Tracker

The tracker is a wire chamber made of 2034 drift cells operating in Geiger mode. The source foils are placed in the middle of the chamber which is filled with a gas mixture of 95% He, 4% ethanol and 1% Ar. Such position highlights the need to have less materials surrounding the foils to decrease particle energy loss. The tracker allows a differentiation between different particles and performs high background rejection to select eventually only two e^- events. A main aim is reconstructing particle tracks and full 3D topology, hence a good spatial resolution is required for a good vertex reconstruction. A correct reconstruction of the two electrons back to the same vertex, or at the minimum, to the same source foil is a key feature of the experiment.

The tracekr first signal was taken in September 2021.

Calorimeter

This whole setup is enveloped with a calorimeter of 712 optical modules (OM), of which 440 are 8" OMs and having an energy resolution of 8% FWHM at 1 MeV, and a time resolution of $\sigma < 400$ ps for 1 MeV electrons. The Calorimeter is made of 6 OM walls separated into 3 categories depending on their designated work: The main walls which are two walls standing in parallel to the source foils and made mainly of the 8" OMs, these are the walls that will be used for signal detection. The two other categories are concerned with background rejection and fully made of 5" OMs. The aim of the calorimeter walls is to measure each individual particle energy and register the detection time. A precise calibration of the OMs in time allows a calculation of the time of flight of the particles which in hand allows additional background rejection.

The plastic scintillators are composed dominantly from polystyrene. Inside, the interaction point of gammas differ from that of the electrons. By performing studies on attenuation of photons and stopping power of electrons inside polystyrene, it is found that the electrons at 1 MeV stop at the surface of the scintillation block (few mm inside), while gammas at 1 MeV can travel up to 10 cm inside the block. This creates an uncertainty on the calculated time resolution for gammas, contrary to that of electrons.

The calorimeter has been commissioned and taking data since 2018.

Shielding

A coil producing a 25 G magnetic field has been installed recently to distinguish the different charged particles and directions of travel. Future installations will include: An anti-radon tent to prevent Radon from diffusing from the laboratory towards the tracker, an iron shield of 20 cm thickness to protect against gamma rays from the laboratory and a second shield consisting of polyethylene water tanks and boron polyethylene plates to thermalize and capture neutrons emitted outside the detector.

Time Calibration and Time Resolution of the SuperNEMO demonstrator Calorimeter

At the time of conducting of the study, the Calorimeter was the only module that was commissioned in the demonstrator. There was no shielding installed and the tracker was turned off.

A cobalt (^{60}Co) source with an activity of 184 kBq was placed behind each calorimeter wall (two main walls and 4 secondary walls). The source then emits two gammas of energies 1.17 MeV and 1.33 MeV with a time difference on the order of less than a picosecond, so we consider then to be emitted simultaneously. The two particles will then be detected at the calorimeter wall at two different OMs, and in turn these OMs will register the energy of each gamma and the time of each particle in coincidence. The two registered times will then be subtracted from each other to produce a unique Gaussian distribution for each two OMs in coincidence, which we will call the Δ(t) distribution. The distribution will be fitted and we extract the mean and sigma. The mean of the fit will be used to synchronize in time the calorimeter OMs, while the sigma will be used to find the time resolution of gammas at 1 MeV.

Since our study is with gammas, the uncertainty on the time of flight of the γ resulting from the interaction point inside the scintillation block will lead to a broadening of the Δ(t) distribution, hence, increasing the value of the sigma, which will decrease our calculated time resolution. To be conservative about the interaction point of the γs, we will schematically assume that they will stop at exactly the center of the scintillation block, this will create a time delay of 1.25 ns for a scintillation gamma that traveled from the interaction point to the front surface of the block and then reflected back to the PMT, as shown in figure (3). For electrons, this delay is negligible .

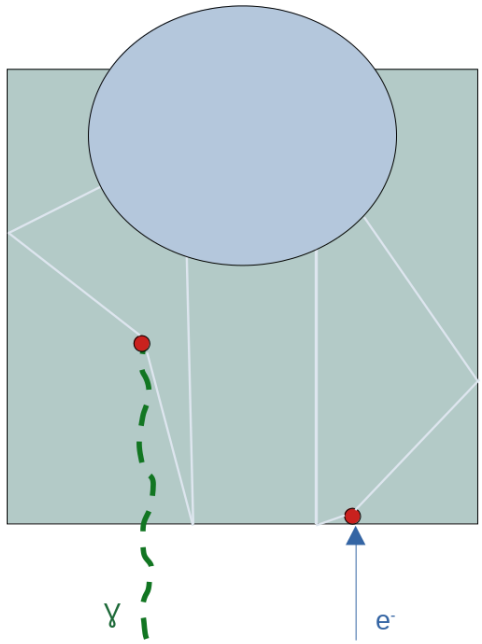

Figure 3: Scheme showing the scintillation block in light green and the PMT in light blue colors and the scintillation photons reflected inside the scintillation block, denoted as light colored lines. The red dot represents the interaction point, the dotted green line a gamma and blue line an electron.

Time Calibration As the two γs are emitted simultaneously from the cobalt source, the time difference between the two registered hits should be equal to zero using equation 2

$$t_{i]} = t_{\gamma,i} - TOF_i - \epsilon_i \quad (2)$$

Where t_i represent the corrected time of detection, $t_{\gamma,i}$ the time of detection at the PMT, TOF is the time of flight of the particle from the source position to the OM, and this is a known value. ϵ represents the time offset of each OM, it is a unique quantity of each OM, unknown and fixed. Since this offset is completely unknown, a calibration can be done by measuring this offset with respect to a chosen reference OM by applying t_i - $t_j = 0$. Applying this equation to the different OMs and then propagating the offset and errors with respect to a final reference OM will calibrate the calorimeter is time.

Time Resolution To get the time resolution, we get the sigma of the $\Delta(t)$ distributions mentioned before. By taking the coincidence between three OMs, we will then be able to extract the individual OM time resolution through the following equations:

$$\sigma_{01}^2 = \frac{\sigma_0^2}{E_{01}} + \frac{\sigma_1^2}{E_{10}}$$
$$\sigma_{02}^2 = \frac{\sigma_0^2}{E_{02}} + \frac{\sigma_2^2}{E_{20}} \quad (3)$$
$$\sigma_{12}^2 = \frac{\sigma_1^2}{E_{12}} + \frac{\sigma_2^2}{E_{21}}$$

Where σ_{ij} are the sigma of the $\Delta(t)$ distributions of the coincidences between the three OMs. E_{02} is the mean of energy deposited inside each OM and σ_i is the time resolution of each OM. The only unknown is the time resolution.

Results

Time Calibration Time calibration is performed for the full calorimeter (712 OMs) and the results are presented in figure 4 for a single main wall. The values in this wall are propagated to a single OM chosen. A clear color gradient is observed, which corresponds to the time delay created by the cables connected from each PMT to the electronics board, so the closer the PMT is to the boards the shorter this delay will be.

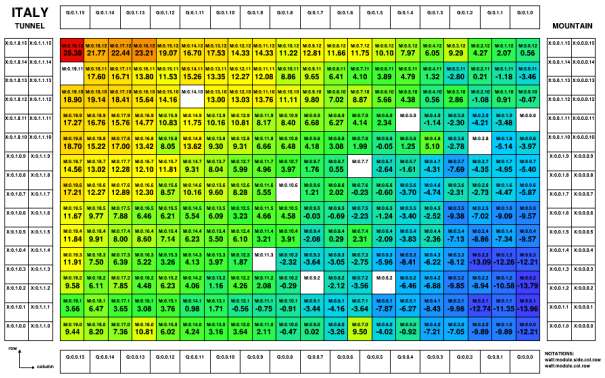

Figure 4: Each square in the figure represents an OM. The final offset values for the main wall facing the Italian borders are shown, and the values are referenced to a certain OM. The colorless squares on the sides have values that are not shown in this figure. While the colorless squares in the middle of the wall are dead OMs. The color gradiant represents the time delay created by the connected cables.

The time correction applied on each OM showed no change in the errors from the fits. The final precision obtained on the corrections is less than 0.2 [ns], which is good to perform background rejection using time of flight calculations.

Time Resolution The time resolution calculations was performed separately for 8" and 5" OMs. The performing of a weighted average on all the OMs in each category yielded a time resolution of 0.614 ± 0.02 (stat) + 0.064 (sys) - 0.00 (sys) [ns] for 8" OMs. While for 5" OMs the time resolution is 0.814 ± 0.006 (stat) + 0.073 (sys) - 0.000 (sys) [ns]. This degradation in the resolution for 5" OMs is expected because the size of the scintillation block stays the same while the OM shrinks in size, hence we acquire less light collection and lower energy resolution. As for the asymmetry of the systematic errors observed with a dominance on the increase on errors, it can be explained by the fact that: when applying the different cuts the background was taken into account (there is no shielding installed) so the cuts were optimized so that we gain the best signal/background ratio, increasing this cut will cut out large number of signal events and hence less statistics which increased the errors, and lowering this cut will decrease the signal/background ratio (more statistics but also more random coincidences), the latter did not have a significant effect on the error.

Conclusions

The SuperNEMO Demonstrator was presented with its specification, different components and the detection method. The method followed to perform time calibration of the calorimeter wall was presented along with the method to extract time resolution. The results were presented showing the achieved calibration with less than 0.2 [ns] precision on timing which is good to perform background rejection usign time of flight calculations. The time resolution results were presented for γs at 1 MeV to be 614 [ps] for 8" OMs.

Future work will be conducted on extracting the time resolution for electrons at 1 MeV, using the integrated calibration system, which includes ^{207}Bi sources that emit an electron at 976 keV. The study is intended to be performed when the tracker is fully operational.

References

[1] Jouni T. Suhonen, Value of the Axial-Vector Coupling Strength in β and $\beta\beta$ Decays: A Review, Frontiers in Physics vol. 5 2017, DOI=10.3389/fphy.2017.00055.

[2] J. D. Vergados, H. Ejiri, F. Simkovic, Theory of neutrinoless double beta decay arXiv:1205.0649v2 [hep-ph], 5 Jun 2012.

Analysis and R&D preparation for Hyper-Kamiokande experiment towards precise measurement of neutrino oscillation parameters

Lucile MELLET

LPNHE, Sorbonne Université, Paris

Abstract — Neutrinos and their oscillations have been a hot topic for over 30 years now and remain at the heart of many open questions such as how they obtain their mass (beyond standard model), matter/antimatter asymmetry, or supernovae explosion mechanisms... Long baseline neutrino beam experiments allow to perform high precision measurements of oscillation parameters by controlling the beam energy and flavor composition. Tokaï to Kamioka (T2K) is one of those and has published a first constraint on leptonic CP symmetry violation in 2020 which could play a role in matter/antimatter asymmetry. To improve these results, it is needed to reduce systematic uncertainties by both studies and an upgrade of the near detector with data taking foreseen for 2023. More specifically, I will focus on the nucleon binding energy uncertainty at interaction, depending on nuclear models. Moreover, the construction of the next generation final detector Hyper-Kamiokande (HK) with a 10 times larger fiducial volume and increased detection performances has started ,data taking being planned for 2027. I am involved in the R&D and associated sensitivity studies for its time synchronization system which will be based on atomic clocks and GNSS signal receptors. Time precision is indeed crucial for events reconstruction by coincidence but also for other purposes such as contributing to a worldwide supernovae explosion alert system.

Introduction

Neutrinos are very light (m_β $\leq$1.1 eV, 90 % CL [1]) and weakly interacting elementary particles. One of their property; the one we study with our experiment, is that their Eigenstates of mass and flavour do not correspond so that a mixing happens during propagation. As a result neutrino flavour can change after a certain distance: this is the neutrino oscillation phenomena. The probability of this oscillation depends on parameters such as mixing angles, squared differences of mass and one CP violation phase, all encoded in the mixing matrix PMNS[2]. T2K aims at obtaining strong constraints on some of the mixing angles and some Δ^2_m and potentially discovering CP violation in the leptonic sector.

To that end, T2K produces a beam of muon (anti-) neutrinos at a known energy of 600 MeV, seeks precision by characterizing the fluxes, composition and cross sections with a near detector and then detects neutrinos with an off-axis final Cherenkov light detector after a fixed 295km distance of flight. This allows for high precision measurement of the probability of oscillation thanks to Frequentist and Bayesian statistical analysis from which we can infer constraints on involved parameters. In order to reach better precision than so far [3] and discover CP violation at 5σ, it is needed to reduce systematic uncertainties especially on detection and reconstruction: examples of both short term and long term analysis to contribute to this effort will be presented here. It is also required to increase statistics, and for this a new final detector, larger and with better detection performances will be built in the next years: Hyper-Kamiokande [4]. A specific focus on time synchronization system R&D will be discussed here.

Systematic uncertainty in oscillation analysis : the nucleon binding energy

Preparing for the future experiment Hyper-Kamiokande (HK) means preparing for higher statistics. For now the total uncertainty is dominated by the statistical errors even though systematic errors play a more and more important role. While increasing statistics, we will reach a point where reducing systematic uncertainties will become crucial for the oscillation analysis. This is why there is an important ongoing effort to have a better understanding of the phenomena that lead to those uncertainties. Among these, the nuclear models used to estimate the cross-sections and thus the predicted number of neutrinos in analysis bins (against which we compare data) are of major interest. Several studies are being made at the near detector level to constrain those probabilities of interaction with data. However, some assumptions still need to be made and I will focus here on one specific parameter that needs to be estimated in the analysis: the binding

energy (Eb) of the nucleon involved in the Charged Current Quasi Elastic interaction (CCQE) which is the major interaction that leads to detection at the far detector. Indeed, there is not any possible hadronic state detection after interaction in a Cherenkov light detector so we can not infer directly from a measurement what the binding energy was and so what the probability of this interaction was. This is because the binding energy is one of the parameters allowing us to reconstruct the neutrino initial energy from the lepton kinematics after a CCQE interaction according to

$$E_{rec}^{CCQE} = \frac{m_p^2 - (m_n - E_b)^2 - m_l^2 + 2(m_n - E_b)E_l}{2(m_n - E_b - E_l + p_l \cos\theta_l)} \quad (1)$$

where indices p,n,and l refer to proton , neutron, and lepton and θ_l is the angle between the lepton outgoing direction and the beam direction.

The preferred nuclear model used for the newest analysis is the 'spectral function' model but it does not predict any outgoing lepton kinematics dependence of the Eb value. Another model ('relativistic Mean-field' model: RMF) does however predict a strong 3-momentum transfer ($Q3$) dependence. We therefore add this dependence to the corresponding Eb systematic parameter on top of the spectral function given information. The predicted additional Eb shift from nominal value ($Eb_{nominal} = 27MeV$ on Oxygen) for an event with a $Q3$ value of momentum transfer is given by

$$\Delta_{E_b} = \alpha(m \times Q_3 + c) \quad (2)$$

where m and c are constant estimated by dedicated fit studies and α is the strength of the correction (between 0 and 1).

The first proposed implementation is to use a fixed strength α so that we directly add the shift to the parameter Eb before going on with the rest of the pipeline that consists in using the Eb value to compute migration of events between analysis bins (this is how the Eb systematic parameter is applied). We obtain the preliminary result that can be seen on figure 1 where we see that this additional variation has indeed an impact on spectra, even though this is not yet validated at low energies. Another implementation that will come is a full variation where the α strength of the correction is itself a systematic parameter that is varied during analysis. This is ongoing work.
As a conclusion of this first section, here was detailed an example of new short-term implementation done for the 2021 T2K analysis to improve our knowledge and our capacity to refine the analysis. This is motivated by more theoretical work done by specific working groups.We would like to stress the fact that it is important to perform as much of those implementations as possible during the end of T2K era even if we are not yet driven by systematic uncertainties because it prepares our analysis pipeline for the next exciting step that is Hyper-Kamiokande.

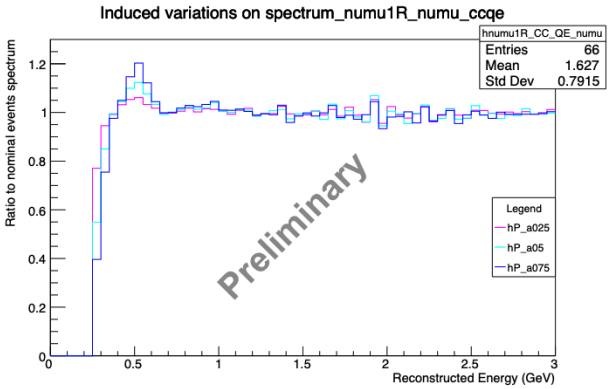

Figure 1: ratio to nominal spectra for different alpha variations

Systematic effects study with MCMC algorithm

In this section I introduce an ongoing prospective work that tries to build a single method to estimate all detector systematic parameters in the oscillation analysis. The motivation comes from the observation that in the current method, different independent studies and exterior experiments provide information for those which allows for precision in itself but makes the estimation of correlations between systematic parameters difficult. Moreover, the context of the beginning of this project was a Joint analysis between the two collaborations Super-Kamiokande (atmospheric neutrinos, same detector) and T2K, so that the idea was to unify the method between both sets of data. The preferred method in SK, also used for some parameters in T2K was to use a Markov-Chain MonteCarlo (MCMC) algorithm to modify distributions of likelihoods; those likelihoods being the variables on which the 'cuts' are made to attribute an analysis sample to an event. Our proposed method is to use an MCMC but with more upstream variables (direct output of the reconstruction algorithm such as momentum, direction,etc...)rather than computed likelihoods in order to take into account effects as close as possible to actual detection bias.There are 9 cuts, 7 of which are based on continuous variables and there are 17 of these variables. We assign a pair of parameters to each of the 17 variables: a multiplicative one α and an additive one β to account for both shifts but also smearing of the variable distribution at detection.At each step, the MCMC picks randomly a pair α/β for each variable, goes through the whole pipeline of assigning events in the 5 samples and computes a likelihood by comparing the final distributions of events in each sample to the nominal ones.The Metropolis-Hastings criteria for accepting a step in the MCMC is applied to this likelihood.
This procedure has been performed on atmospheric MonteCarlo 'data' with T2K samples only for now.So far, the method is not validated, the goal being more a proof of concept, and the preliminary results show final

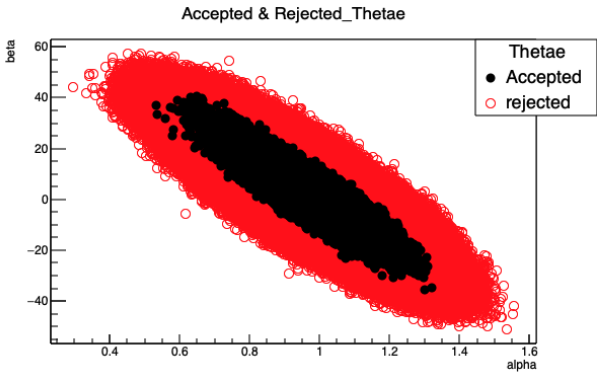

Figure 2: Accepted and rejected steps for θ_e parameter in the $\alpha\beta$ plane

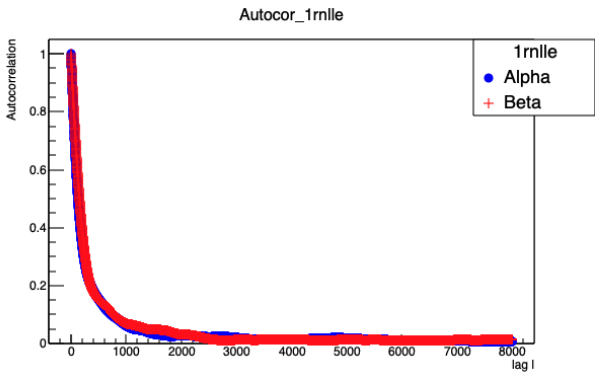

Figure 3: Autocorrelation plot for the 1Rnlle parameter

correlations between samples about one order of magnitude too small compared to current method, this being explained by the fact that the attempted new method is less detailed. However, further investigations are limited by the performances of the algorithm. It is slow and the acceptance rate is low, partly due to correlations between parameters. To improve this, a more sophisticated random picking of values at each step has been implemented; it is based on a Cholesky decomposition of the parameters correlation matrix extracted from the previous run of the code and allows to take into account those correlations instead of pure gaussian distributions, increasing the acceptance rate by a factor 10. As shown on figure 2, the red dots (refused steps) follow the same distribution as the black dots(accepted steps) meaning the correlation is taken into account at picking of values time so that values with a very low probability of being accepted are not even tried.

But something else limits the performance of the algorithm:it is a Markov Chain, so by definition all steps must be independent from each other (except to their direct neighbours $(N \pm 1)$) to get an unbiased result.Otherwise, we need to undersample the accepted steps which results in lowering the effective acceptance.The autocorrelation ρ_{lag} as a function of the distance between steps (lag) can be computed with

$$\rho_{lag} = \frac{\sum_i^{N-lag}(\theta_i - \bar{\theta})(\theta_{i+lag} - \bar{\theta})}{\sum_i^N (\theta_i - \bar{\theta})^2} \qquad (3)$$

and we can see on figure 3 that it does not quite get to 0 as fast as it should be to be efficient. Some solutions exist such as using a Hamiltonian MC but those are computing time consuming and not so easy to implement with such a custom likelihood calculation as we have. As a conclusion, this is a preliminary proof of concept that is for now limited by algorithm performances.

HK time synchronization system

As said before, another way of preparing the future of our long baseline experiment is to directly contribute to the development and characterization of new systems for Hyper-Kamiokande. More precisely, we are working on the new clocks synchronization system. The idea,

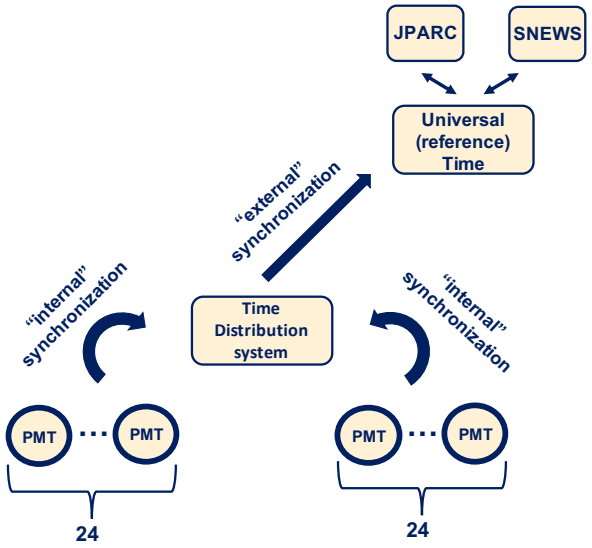

Figure 4: General clocks synchronization needs scheme

illustrated in figure 4, is to have a very stable time base common to all Photo-multipliers (PMTs) because the reconstruction of the signal - Cherenkov rings - is based on coincidence between PMTs hits and the whole measurement is based on particle identification through analysis of the shape and spreading of the ring. This is what we call "internal synchronization" and its requirement is expressed in terms of phase jitter [7] J.This is a number quantifying the time-domain stability deviations from a pure signal and it can be computed over a period tau as a function of the power spectral density $S(f)$,f being the fractional frequency offset with respect to the "ideal" frequency f_0 :

$$J = \frac{1}{2\pi f_0}\sqrt{\int_0^\infty S(f)\left(\frac{\sin(\pi\tau f)}{\pi\tau f}\right)^2 df} \qquad (4)$$

We aim at a Jitter lower than $100ps$ at $\tau = 1$s.

On top of that, we need "external synchronization" with a universal time, ie:UTC, for two purposes. One

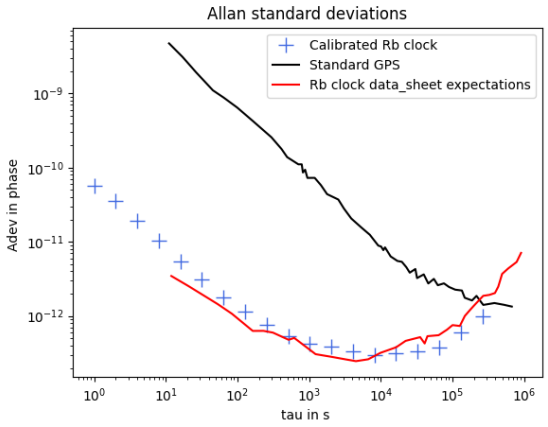

Figure 5: ASD for calibrated Rb clock compared to expectations (datasheet) and standard GPS signal

is that we want to be able to give a time stamp to bunches of particles comparing with when they were emitted at the beam start. The other is that our final detector HK (just like SuperK before) can also be used as an astrophysical neutrinos observatory, and in particular detect the neutrino signal of a nearby (until 50kpc) supernova explosion which arrives to earth around 3h before the photon signal. SK observed the last near enough explosion in 1987 [5] but with only a few neutrinos. With higher rates and high time precision, it is possible for HK to be apart of a global supernova explosion alert system (SNEWS) which aims at, by triangulating the time differences of detection between neutrino observatories around the globe (such as Icecube, SNO+,Dune, KamLAND,etc), defining a smaller region in the sky where telescopes should look for the photon signal. This could help observing the explosion at an earlier stage and as a result learn more about the phenomenon.

To achieve this, we aim at a precision of at least $100ns$ with respect to universal time. The best way to achieve very good short term stability is to use atomic clocks. We will be testing two types: a Rubidium standard and a passive hydrogen maser.However, for long term stability, we need to correct the drift of the chosen atomic clock (driven at long term by a random walk noise) with a GNSS signal directly linked to a UTC-like reference. To evaluate stability we use a specific statistics tool called Allan standard deviation (ASD) [6] that basically computes variances on different averaging times τ :

$$\sigma_y^2(\tau) = \frac{1}{2} < (\bar{y}_{n+1} - \bar{y}_n)^2 > \quad (5)$$

so that we can discriminate between different types of noises/drifts and evaluate the evolution of stability over time.

As it can be seen on figure 5 , the proposed the solution is to correct the clock time stamp when its ASD curve (in free running, the red line) crosses the GPS (or GNSS to be more general) one (black line) so that we combine the short term performance of the clock with the long term performance of GNSS signals.
We are currently investigating what might be an ideal system and how to combine both information by installing a test bench at our laboratory. So far we improved the rubidium clock stability after one round of calibration. We performed this calibration by comparison with another source of frequency that we know is more stable, setting then a parameter controlling a small magnetic field that we use to offset the output frequency of the clock. Doing so, we recover the behaviour and orders of magnitude for the ASD(see figure 5, blue crosses are our measurement) that were advertised by the clock data sheet (red line)) which will allow us to pursue our studies knowing the performances of our clock.

The goal is to test and characterize different equipment so as to choose the appropriate solution given the requirements. We also aim at developing the data acquisition software and perform sensitivity studies of the impact of time delays in the HK electronics on the physics performance.

Conclusion and perspectives

To conclude, we have shown three different types of ongoing contributions to prepare the next stage for long baseline neutrino oscillation experiments in Japan. We firstly detailed the importance of short-term improvements in taking into account systematic uncertainties in our analysis. We specifically illustrated this with the example of the nucleon binding energy at interaction time which requires the variation of systematic parameters with various inputs. We then presented a more prospective long term study to explore new ways of computing and combining detector systematic uncertainties in the framework of a joint analysis between atmospheric and beam neutrino data which will be the only kind of analysis in Hyper-Kamiokande. We showed the challenges that this can represent in terms of computational performances that are the main limitations to those studies when it comes to using a large number of parameters. Finally, we introduced our just started R&D efforts to build a new time synchronization system for Hyper-Kamiokande which will allow for precision reconstruction of events and hopefully supernova explosion detection. Sensitivity studies will also be added to this work so as to prepare the exciting next years for research on neutrino oscillations.

References

[1] M. Aker et al., An improved upper limit on the neutrino mass from a direct kinematic method by KATRIN, Phys. Rev. Lett., vol. 123, no. 22, p. 221802, Nov. 2019, doi: 10.1103/PhysRevLett.123.221802.

[2] B. Pontecorvo, Inverse beta-processes and lepton charge nonconservation, Zh. Eksp. Teor. Fiz., vol. 34, p. 247, 1957.

[3] The T2K Collaboration. Constraint on the matter antimatter symmetry-violating phase in neutrino oscillations. Nature 580, 339â344 (2020). https://doi.org/10.1038/s41586-020-2177-0

[4] K. Abe et al., Hyper-Kamiokande Design Report, 2016. KEK Preprint 2016-21.

[5] Observation of a neutrino burst from the supernova SN1987A K. Hirata, T. Kajita, M. Koshiba, M. Nakahata, Y. Oyama, N. Sato, A. Suzuki, M. Takita, Y. Totsuka, T. Kifune, T. Suda, K. Takahashi, T. Tanimori, K. Miyano, M. Yamada, E. W. Beier, L. R. Feldscher, S. B. Kim, A. K. Mann, F. M. Newcomer, R. Van, W. Zhang, and B. G. Cortez Phys. Rev. Lett. 58, 1490 â Published 6 April 1987.

[6] Statistics of Atomic Frequency Standards, D. W. Allan, Proceedings of the IEEE, 54 2 221-230, Feb. 1966, doi: 10.1109/PROC.1966.4634.

[7] Oscillator phase noise and sampling clock jitter, Rethnakaran Pulikkoonattu, ST Microelectronics, (Genesis Microchip) Bangalore, India, 2007 June 12

Neutrinoless double beta decay search in Xenon dual-phase Time Projection Chambers

Maxime PIERRE

SUBATECH, IMT Atlantique, CNRS/IN2P3, Universite de Nantes,
4 rue Alfred Kastler, 44307 Nantes, France

Abstract — Rare events physics experiments developed by the XENON Collaboration are primarly devoted to the direct detection of Dark Matter via its scattering with xenon target nuclei in a dual-phase time projection chamber detector. The unprecedented low level of background reached by XENON1T demonstrated this detector technology to be suitable also for other exciting rare-events searches among which the neutrinoless double beta decay of ^{136}Xe. In the context of the advancement of the XENON program the fourth generation of experiment XENONnT is currently collecting its first scientific data in the underground INFN Laboratori Nazionali del Gran Sasso, in Italy. In this proceeding, I will discuss how XENON1T and XENONnT will be able to simultaneously search for Dark Matter and neutrinoless double beta decay.

Introduction

The search for direct detection of Dark Matter (DM) candidates such as Weakly Interacting Massive Particles (WIMPs) is the main goal of the XENON Collaboration which developed experiments primarily devoted to the observation of the possible scattering of a WIMP off xenon nuclei. Dual-phase xenon Time Projection Chambers (TPCs) have proven to be the best technology for WIMPs direct detection above 6 GeV/c^2 [1]. Thanks to the improvement of the background reduction and the increase of their target mass, experiments based on this technology start to be sensitive to other rare events physics processes on a wide energy range spanning from few keV to MeV [2, 3, 4]. The search for neutrinoless double beta decay ($0\nu\beta\beta$) of ^{136}Xe carried on by the XENON Collaboration, is among the most compelling ones: its discovery would be an indication of physics beyond the Standard Model (SM) of particle physics.

While the two-neutrino double beta decay ($2\nu\beta\beta$) is a rare nuclear transition allowed in the SM, the $0\nu\beta\beta$ decay is forbidden as it leads to the violation of the lepton number in the process. Its observation could shed light on the nature of neutrinos indicating that they are Majorana fermions, i.e. their own anti-particles. The $2\nu\beta\beta$ was first suggested by M. Goeppert-Mayer in 1935 [5]: it consists in a nucleus emitting two electrons and two antineutrinos ($\bar{\nu_e}$) and it has been already observed in several isotopes. The $0\nu\beta\beta$ decay has been theorised by W. Furry [6] and the most studied mechanism is the exchange of a light Majorana neutrino. The ^{136}Xe is one of the most studied isotopes in the quest for the $0\nu\beta\beta$ decay. Its natural abundance in the targets of the XENON detectors corresponds to ∼8.9%. This isotope has already shown to undergo $2\nu\beta\beta$ with a half-life of $(2.165 \pm 0.016^{(stat)} \pm 0.059^{(sys)}) \times 10^{21}$ years and a Q value of (2457.83 ± 0.37) keV [7, 8].The most stringent limit on the half-life of the $0\nu\beta\beta$ decay of ^{136}Xe is hold by the KamLAND-Zen experiment with a $T^{0\nu}_{1/2} > 1.07 \times 10^{26}$ years [9].

In this proceeding I will firstly present the design of the XENON1T and XENONnT experiments and their working principle, in section 36. The signal and backgrounds models considered for the $0\nu\beta\beta$ decay search will be introduced in section 36. The development of the $0\nu\beta\beta$ decay data analysis for XENON1T and the sensitivity projection study for XENONnT will be covered in section 36. I will finally conclude with a summary and future prospects for the search of $0\nu\beta\beta$.

The XENON project: dual-phase Xe TPCs

The XENON dark matter program consists in conceiving and operating increasingly sensitive detectors. The program started with XENON10, it has continued with XENON100 which has been followed by XENON1T [10, 11, 12]. Those experiments were operating at the Instituto Nazionale di Fisica Nucleare (INFN) Laboratori Nazionali del Gran Sasso (LNGS) in Italy, an underground laboratory with a 3600 m.w.e depth that reduces the surface muon flux by a factor of 10^6. Currently, the fourth generation experiment, XENONnT, is collecting its first scientific data. All the above mentioned experiments are based on the same detection technology consisting of a dual-phase Time Projection Chamber (TPC) filled with Liquid (LXe) and Gaseous Xenon (GXe).

The working principle of such detector is illustrated

in Fig. 1 on the left and can be summarized as follows: when a particle interacts with the detector target, it can either scatter off LXe nuclei (in case of WIMPs, neutrons or neutrinos) or atomic electrons (γ rays, charged particles and electronic neutrinos), generating Nuclear (NR) or Electronic Recoils (ER), respectively. The transferred energy induced by the recoil will excite and ionize the atoms in the target medium, while a negligible part will be dissipated into heat. The processes of excitation and ionization will result in the release of quanta of light and charge whose proportion will depend on the type and energy of the incident particle. Photons will firstly be detected via Photomultipliers tubes (PMTs) on the top and the bottom of the TPC: this prompt scintillation signal is called S1. Ionized electrons will follow the electric field within the TPC, drifting towards the liquid-gas interface where a second stronger electric field will extract them into the gaseous phase. This will lead to the emission of a second scintillation signal, called S2. The primary position of the events can be reconstructed in three dimensions using the drift time between S1 and S2 to reconstruct the z coordinate and the S2 hit pattern on the top PMT array for the (x,y) coordinates. The S1/S2 ratio can be used to distinguish between the two different types of recoils which is primordial to discriminate background events from the expected WIMP signals. Thanks to its high stopping power for gamma and beta radiations (resulting in a self-shielding from external backgrounds) and to the low contamination of long-lived radioactive isotopes (which minimizes internal backgrounds), LXe represents an ideal target for rare events physics searches.

XENON1T

XENON1T is the third generation of experiments of the XENON collaboration operating from 2016 to 2018. The heart of XENON1T is the TPC which measures 97 cm in height and 96 cm in diameter, designed to contain 2 tonnes of LXe used as a target in the instrumented active volume. Its boundaries are delimited by 24 polytetrafluoroethylene (PTFE) reflectors panels at the side and by gate and cathode electrodes at the top and bottom, respectively, that generate the drift field inside the liquid part of the detector. The extraction field is generated between the gate and an anode placed in the GXe phase. A Stainless Steel (StS) diving bell is used to control the liquid-gas interface in the TPC. Two arrays of 127 and 121 Hamamatsu R11410-21 3" PMTs are arranged above and below the sensitive volume of the TPC, respectively. They were chosen for their low radioactivity and high quantum efficiency [13]. The TPC is encapsulated in a double-walled vacuum-isolated StS cryostat surrounded by an active water Cherenkov muon veto system [14] also used as a passive shield for external backgrounds sources. Cooling and purification of the xenon is ensured by the cryogenic and GXe purification systems located outside of the water tank and connected to the cryostat by a large vacuum-insulated cryogenic pipe. In case of emergency, a dedicated xenon-storage system called ReStoX (Recovery and Storage of Xenon), has been conceived and realized to store up to 7.6 tonnes of xenon in liquid or in gas phase and to ensure a fast recovery of the xenon. The ReStoX system can also be used to fill the xenon into the detector vessel in high purity conditions.

XENONnT

The XENON1T experiment has been conceived having already in mind its successor XENONnT. Therefore, several subsystems such as the water tank, the muon veto, the outer cryostat vessel and the GXe purification system were designed to be capable to lately host XENONnT and to allow a quick transition between the two experiments. With the design of the XENONnT TPC, shown in Fig. 1 on the right, the size of the detector itself has increased up to 148 cm in height and 137 cm in diameter, with an active region of 5.9 tons of LXe. The purity level of the xenon target mass is improved with respect to XENON1T thanks to a radon distillation column conceived to further suppress radon backgrounds and a novel liquid purification system that allows for a continuous circulation of the LXe. In addition to the water Cherenkov muon veto system, a new neutron veto has been installed, surrounding the cryostat which enables the identification and rejection of the otherwise irreducible neutron backgrounds, for WIMP searches, in the target volume. Given the larger xenon inventory, a second storage and recovery system of LXe, ReStoX2, has been installed.
The expected sensitivity to spin-independent WIMP-nucleon interactions for XENONnT with an exposure goal of 20 ty is $1.4 \times 10^{-48}\, cm^2$ for a $50\, GeV/c^2$ mass WIMP at 90% confidence level [15].

Signal and Background models

The expected signature of the $0\nu\beta\beta$ decay in the XENON detectors is a Single Scatter (or Single Site, SS) event whose energy corresponds to the sum of the two emitted electrons at the Q value of the process, noted $Q_{\beta\beta}$. Due to the high stopping power of LXe, the electrons penetration length in LXe is $\mathcal{O}(mm)$: this explains why a SS event is expected. However, Bremsstrahlung photons and β-electrons might generate multiple energy depositions giving rise to Multiple Site (or Multi Scatter, MS) topology events. Monte-Carlo (MC) simulations have shown that the energy of the expected signal within an optimized Fiducial Volume (FV) and after having accounted for energy resolution effects and removed MS events, follows a gaussian distribution centered at the $Q_{\beta\beta}$. As for the backgrounds, depending on their origin, it is possible to categorize two different types of sources in our detector: the external and the internal ones.

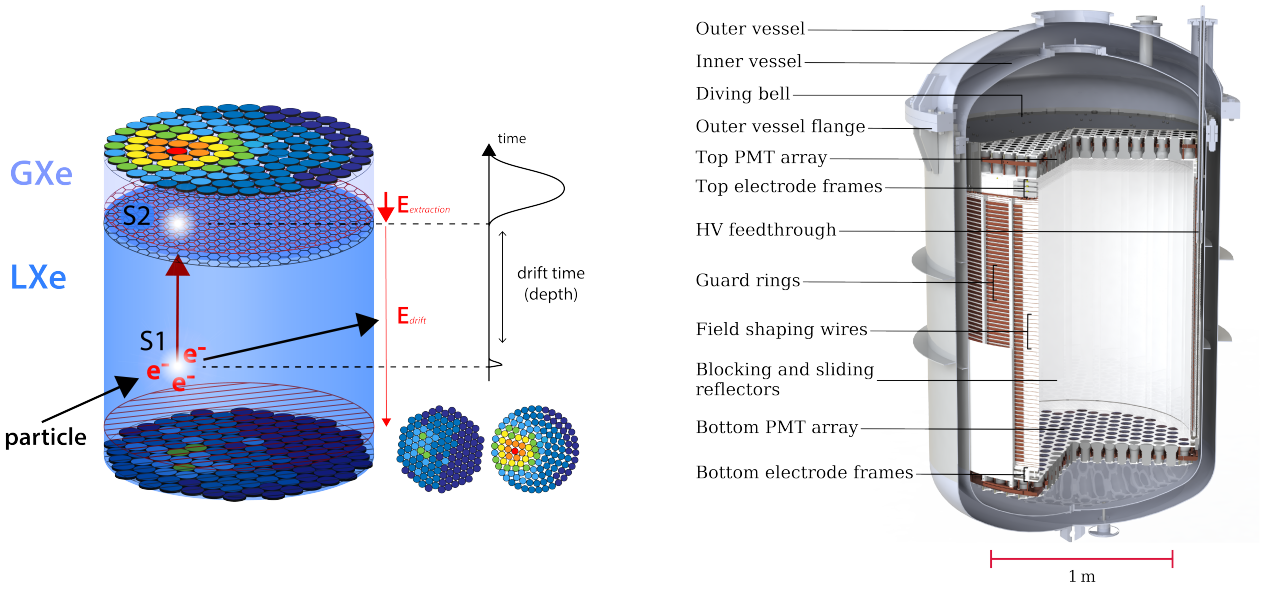

Figure 1: **(Left)** Working principle of a dual-phase TPC. **(Right)** CAD rendering of the XENONnT cryostat and TPC.

External Backgrounds

The detector materials contain long-lived radionuclides in trace amount that might emanate into the target and introduce background. The material contaminants in XENON1T and XENONnT originate from the ^{238}U and ^{232}Th natural decay chains. They might introduce ER background in the $0\nu\beta\beta$ energy Region Of Interest (ROI) in the form of γ-rays that can produce low energy Compton scatters and their interaction in LXe can mimic the signature of a $0\nu\beta\beta$ decay. In particular the ^{214}Bi and ^{208}Tl γ lines (^{238}U and ^{232}Th daugthers) at 2447.9 keV and 2614.5 keV respectively, are close to the $Q_{\beta\beta}$ of ^{136}Xe. Another source of background,that has been studied and proven to be negligible in XENON1T and XENONnT, is represented by the ^{60}Co decaying in two gammas with energies of 1173.2 keV and 1332.5 keV respectively. The two peaks could pile up and be reconstructed as a unique signal at 2505.7 keV, within the $0\nu\beta\beta$ ROI.
To be noticed that the XENON1T and XENONnT detectors materials were carefuly chosen, based on their radiopurity, in order to minimize as much as possible the induced background for the WIMP search in the low energy region. For this purpose, dedicated screening campaigns have been carried on for both experiments [16, 17].

Internal Backgrounds

Internal backgrounds either arise from the interaction between cosmogenic particles and the xenon target or from the isotopes present in the noble gas itself. Among them, the dominant one in the energy ROI for the $0\nu\beta\beta$ search is represented by the ^{222}Rn. Radon, that originates from the ^{238}U primordial decay chain, emanates from the detector materials and induces an intrinsic contribution into the LXe target in addition to the one from materials. One of the daughter nuclei of the ^{222}Rn decay chain relevant for our background model is the ^{214}Bi which offers a peculiar event topology thanks to the ^{214}Bi β-decays into ^{214}Po quickly followed by an α emission of ^{214}Po decaying into ^{210}Pb. We can identify and thus reject this type of events occurring within the instrumented detector, using the so called BiPo tagging technique. This technique can reach a rejection power larger than 99.8% [18]. However, when the decays happen in the non-instrumented LXe, the BiPo tagging cannot be applied, resulting in a 2.45 MeV γ emission from the ^{214}Bi decay within the FV that will constitute a non negligible source of background.
The β-decay of ^{137}Xe represents the second most relevant internal background within the ROI for $0\nu\beta\beta$ decay search. With a Q value of 4.17 MeV far beyond the $Q_{\beta\beta}$, it is a relevant source of ER background. ^{137}Xe is produced through neutron capture process on ^{136}Xe occurring either within the TPC itself or in the non-shielded parts (placed outside the water tank) of the purification systems. The muon-induced neutrons produced in the LXe are the principle responsibles for the production of ^{137}Xe in the TPC, while the thermal neutrons flux induced by radiogenic decays from the rocks, concrete and materials has the stronger impact on the production of ^{137}Xe in the purification system.
A source of irreducible background in our detectors comes from the ν-electron scattering. This ER background starts to become problematic for $0\nu\beta\beta$ decay search when the incident neutrino flux and energy are sufficiently high[19]. On the other hand, the background coming from atmospheric neutrinos, diffuse supernovae neutrinos, or geo-neutrinos are negligible since either their flux or their energy are too small to generate a background signal in the ROI for $0\nu\beta\beta$ search. The contribution from ^{8}B solar neutri-

nos can instead be relevant, but still subdominant in the current generation dual-phase LXe TPC compared to the others background sources discussed above. Finally, the $2\nu\beta\beta$ of ^{136}Xe is a natural background to the $0\nu\beta\beta$ decay search with its continuous energy spectrum that ends at the $Q_{\beta\beta}$ of ^{136}Xe. The modelisation of this background is based on theoretical calculations from J. Kotila and F. Iachello [20]. Thanks to the sub-percent energy resolution at $Q_{\beta\beta}$ demonstrated in XENON1T [21], its contribution in the $\pm1\sigma$ ROI is negligible with respect to the dominant backgrounds in both XENON1T and XENONnT.

$0\nu\beta\beta$ decay search in XENON1T and XENONnT

Xenon dual-phase TPCs experiments initially designed to search for WIMP DM candidates, have been optimised to work in the few keV electron recoil energy range. The saturation of the signals measured by the PMTs at energies above ∼100 keV impact the energy reconstruction of the detectors. Several improvements, especially concerning the reconstruction and correction of high energy signals, have to be made in the MeV region in order to allow the XENON experiments to simultaneously search for DM and $0\nu\beta\beta$ decay of ^{136}Xe. In XENON1T these improvements led to the world leading energy resolution at $Q_{\beta\beta}$ of 0.8% (σ/E) in a xenon dual-phase TPC [21]. Following this promising result, a blinded analysis using XENON1T data is currently being performed to search for $0\nu\beta\beta$ decay. The signature in our detector of a $0\nu\beta\beta$ signal is expected to be a ER event reconstructed as a SS, as discussed in section 36. Selection criteria based on data quality checks, signals properties and reconstructions have been developed in order to maximize the signal acceptance while rejecting potential background interactions. Among them, a key element is the optimization of the FV (that depends on the background rate in the volume and the target mass) to increase the signal over background ratio and thus improve the experimental sensitivity. The final post-unblinding results of the $0\nu\beta\beta$ decay analysis in XENON1T will soon be published. A projection study is ongoing to estimate the sensitivity of XENONnT to the $0\nu\beta\beta$ decay search. A significant increase in the expected sensitivity is expected with respect to its predecessor thanks to a larger LXe active mass ($\times$ 3) and a significant expected background reduction ($\times$ 1/10). Results of this sensitivity projection study for XENONnT will also be published soon.

Summary

The XENON project has proven throught its results the excellent capabilities of dual-phase liquid xenon Time Projection Chambers in searching for rare events on a broad energy range from keV to MeV. Among the most interesting search that is possible to perform with such a technology, there is the search for neutrinoless double beta decay. This process is of fundamental interest since its discovery will shed light on the nature of neutrinos. In this proceeding I presented the current status of the search for the $0\nu\beta\beta$ decay of ^{136}Xe in XENON1T and future perspectives in XENONnT. Despite not being competitive with currently leading $0\nu\beta\beta$ dedicated experiments, it has been shown that LXe dual-phase TPCs open the path towards a simultaneous search for DM and $0\nu\beta\beta$ decay with current and next generation detectors, such as XENONnT or DARWIN [22].

References

[1] E. Aprile et al. (XENON Collaboration), *Phys. Rev. Lett.* **121** 111302, (2018) [1805.12562].

[2] E. Aprile et al. (XENON Collaboration), *Nature* **568** 532, (2019) [1904.11002].

[3] E. Aprile et al. (XENON Collaboration), *Phys. Rev. Lett.* **126** 091301, (2021) [2012.02846].

[4] E. Aprile et al. (XENON Collaboration), *Phys. Rev. D* **102** 072004, (2020) [2006.09721].

[5] M. Goeppert-Mayer, *Phys. Rev.* **48** 512, (1935).

[6] W. H. Furry, *Phys. Rev.* **56** 1184, (1939).

[7] J. B. Albert et al. (EXO Collaboration), *Phys. Rev. C* **89** 015502, (2014) [1306.6106].

[8] M. Redshaw et al., *Phys. Rev. Lett.* **98** 053003, (2007).

[9] A. Gando et al. (KamLAND-Zen Collaboration), *Phys. Rev. Lett.* **117** 082503, (2014) [1605.02889].

[10] E. Aprile et al. (XENON Collaboration), *Astropart. Phys.* **34** 679, (2011) [1001.2834].

[11] E. Aprile et al. (XENON Collaboration), *Astropart. Phys.* **35** 573, (2012) [1107.2155].

[12] E. Aprile et al. (XENON Collaboration), *Eur. Phys. J. C* **77** 881, (2017) [1708.07051].

[13] E. Aprile et al. (XENON Collaboration), *Eur. Phys. J. C* **75** 546, (2015) [1503.07698].

[14] E. Aprile et al. (XENON Collaboration), *JINST* **9** P11006, (2014) [1406.2374].

[15] E. Aprile et al. (XENON Collaboration), *JCAP* **11** 031, (2020) [2007.08796].

[16] E. Aprile et al. (XENON Collaboration), *Eur. Phys. J. C* **77** 890, (2017) [1705.01828].

[17] E. Aprile et al. (XENON Collaboration), *Radiopurity* **XX** XXX, (2021) [XXXX.XXXXX].

[18] L. Baudis et al., *JCAP* **01** 044, (2014) [1309.7024].

[19] E. Vitagliano et al., *Rev. Mod. Phys* **92** 045006, (2020) [1910.11878].

[20] J. Kotila and F. Iachello, *Phys. Rev. C* **85** 034316, (2012) [1209.5722].

[21] E. Aprile et al. (XENON Collaboration), *Eur. Phys. J. C* **80** 785, (2020) [2003.03825].

[22] F. Agostini et al. (DARWIN Collaboration), *Eur. Phys. J. C* **80** 808, (2020). [2003.13407].

Core-Collapse Supernovae Neutrino Detection with the 3" PMT System of the JUNO Experiment

Victor LEBRIN ***on behalf of the JUNO Collaboration***

Subatech, Université de Nantes, IMT Atlantique, CNRS-IN2P3, Nantes, France

Abstract — Core-Collapse Supernovae (CCSNe) are gigantic and luminous explosions which occur when a massive star ($M \geq 8M_{\odot}$) comes to death. Many questions remain unanswered about the mechanisms which lead to such a violent explosion. Thirty-four years ago, for the first and only time, a few dozen of neutrinos from a Core-Collapse Supernova (CCSN) - SN1987A - were detected by three neutrino observatories, marking the beginning of a new era in the study of supernovae. The Jiangmen Underground Neutrino Observatory (JUNO) is a 20-kton liquid scintillator detector under construction in China. Two photomultiplier tube (PMT) systems, the first one made of ∼17612 20" PMTs and the second one made of ∼25600 3" PMTs, will collect the light produced by the neutrino interaction. JUNO is dedicated to Mass Ordering and precise oscillation parameter measurements. However, thanks to its large detection volume, it will be able to detect a burst of $\sim 10^4$ neutrinos for a typical 10 kpc (kilo-parsec) away galactic CCSN. Such high statistics will alow to constrain the supernovae explosion models and more generally to improve our knowledge in neutrino physics and nuclear physics.

Introduction

Core-Collapse Supernovae have been observed and studied for several hundreds of years. During the last 50 years, theoretical models have been developed in order to simulate the phenomenon based on fundamental principles, from the collapse ignition to the supernova remnant formation. The most widely accepted models state that when the iron (Fe) core of the progenitor star reaches the Chandrasekhar mass ($M \geq 1.4M_{\odot}$), it collapses and bounces[1]. An out-warding shock wave is then formed, but it quickly turns into a stalled accretion shock - ∼100-200 km away from the core - due to the in-falling matter that slows down its course. How the shock is revived to give birth to the final explosion is a question that remains open. In the neutrino-driven supernovae explosion assumption[2], the neutrinos, which represent 99% of the binding energy of the collapsing star, will heat the stalling shock region by an efficient energy deposition and eventually revive the shock wave. In this assumption, the neutrino signal from the CCSNe is expected to be time-dependent and to have specific flavor-dependent (i.e. electronic, muonic and tauic) energy spectra. The detection of CCSNe neutrinos with high statistics represent an excellent way to probe the microscopic physics of CCSNe. However, the rate of CCSNe in the Milky Way is ∼1.63±0.46 per century[3] and only one event (SN1987A) offered the opportunity to test the models. The detection of a few dozens of neutrinos by several neutrino experiments (Kamiokande[4], IMB[5], Baksan[6] and possibly LSD[7]) corroborated many points of the neutrino-driven paradigm, but way more statistics would have been required to fully constrain the models. JUNO[8][9] and other large neutrino detectors currently under development (DUNE[10], KM3NET[11], HK[12]) will be able to detect several thousands of neutrinos from the next galactic CCSN, offering a unique opportunity to scrutinise the CCSNe process. This contribution is organised as follows, section 37 briefly presents the JUNO experiment, section 37 presents the CCSNe neutrino detection in JUNO and section 37 the methodology used to reconstruct the CCSNe neutrino events.

The JUNO Experiment

The JUNO detector is a 20 kton (kilo-ton) Liquid Scintillator (LS) neutrino detector currently under construction in southern China, in the Guangdong province. It aims to determine the neutrino Mass Ordering (NMO) at the 3 sigma level in six years of data taking by detecting the electron anti-neutrinos ($\overline{\nu_e}$) from the Yangjiang and Taishan nuclear power plants *via* the Inverse Beta Decay (IBD) interaction channel. The Normal or Inverted Ordering will be inferred from the fine structure of the $\overline{\nu_e}$ spectrum, which requires a 3% energy resolution at 1 MeV (E_{vis})[13]. JUNO will also be able to measure three neutrino oscillation parameters at the sub-percent level: θ_{12}, Δm^2_{21} and $|\Delta m^2_{32}|$. This precision will allow to constrain the unitarity violation of the mixing matrix of the three neutrino flavor eigenstates with the three mass eigenstates[14][15]. Thanks to its huge detection volume, JUNO will also be able to detect a burst of neutrinos from a CCSN event as well as to

put new stringent limits on the Diffuse Supernovae Neutrino Background (DSNB), detect solar neutrinos, atmospheric neutrinos, geo-neutrinos, study the proton decay etc. The physics program of JUNO is fully reviewed in[8][9].

The JUNO detector consists in three main parts. The first one is the **C**entral **D**etector (**CD**). It consists in a 35.4 m diameter acrylic spherical vessel containing 20 kton of LS and supported by a stainless steel structure. It is the neutrino-target. The LS of JUNO is designed to produce ∼11,500 scintillation photons for 1 MeV of deposited energy. In order to collect these photons, the CD is instrumented with 17,612 20" PMTs that will allow to achieve a 75% photo-coverage. In addition, 25,600 3" PMTs[16] will be placed alternately with the 20" PMTs (Fig.1), with a corresponding photo-coverage of 3%. A 1.42 m thick water buffer separates the acrylic sphere from the PMTs in order to protect the target from the PMTs natural radioactivity. The 20" PMTs will allow to collect a great amount of light to reach ∼1345 photoelectrons (p.e)/MeV[8] while the 3" PMTs will work in photo-counting regime and will have ∼40 p.e/MeV. The 3" PMTs will allow to increase the energy dynamic range of the detector and mitigate the potential non-linearity and saturation effects in the 20" PMTs. The saturation may occur for high energy events (muons with an average energy $\overline{E} \simeq$ 200 GeV), for events at the detector borders (saturation of the PMTs in the vicinity of the vertex) or even when the event rate is to high, typically for a very close CCSN. In addition, the 3" PMTs will allow to perform quasi-independent physics analyses (solar parameters measurement, CCSNe neutrinos detection and proton decay) as well as enhance the muon-tracking capability.

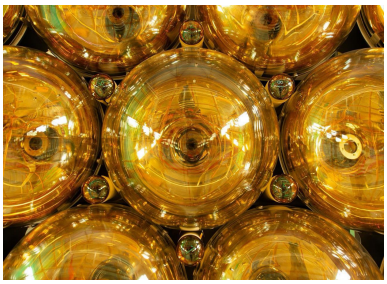

Figure 1: *Photograph showing a real size mock-up of the 3" PMTs placed in-between the 20" ones.*

The second part of the detector is the **W**ater **P**ool (**WP**) in which the CD is immersed, as shown on Fig.2. It is a cylindrical vessel with a diameter of 43.5 m and a height of 44.0 m. It will contain ∼35 kton of ultra pure water (< 0.2 Bq/m^3) instrumented with 2,400 20" PMTs (veto PMTs). It aims to reconstruct the tracks of the incoming cosmic muons and also constitutes a shield against the surrounding rock radioactivity. The third part is the **T**op **T**racker (**TT**), it is placed on top of the CD and WP. It consists of three planes of Plastic Scintillator (47.0 m x 20.0 m each) also dedicated to the reconstruction of the tracks of the cosmic muons entering the detector. Indeed, the muons represent a non-negligible source of correlated background for the NMO analysis and it needs to be carefully addressed. The expected median angular resolution is of ∼0.20° [17].

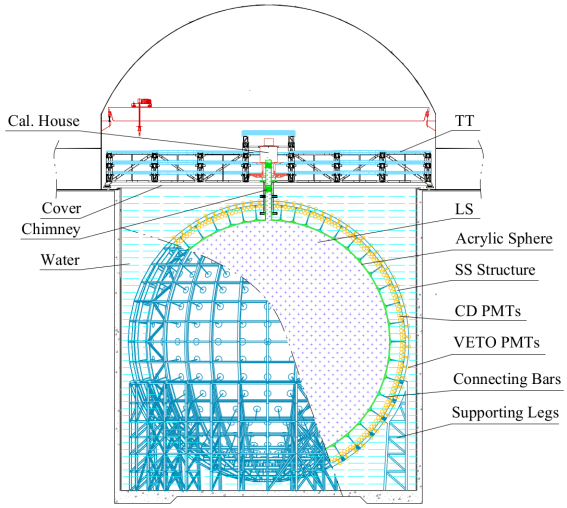

Figure 2: *Schematic view of the JUNO detector.*

Supernovae Neutrino Detection in JUNO

A CCSN will produce a 10 seconds long neutrino burst in JUNO, with ∼60% of the events in the very first second. In comparison to the rates of events of the other neutrino sources and their corresponding energy range [9], the CCSNe neutrinos detection can be considered as background free in a first approximation. The neutrinos will interact *via* six different channels, listed in Table 1[8]. The number of events is computed considering an energy threshold of 0.7 MeV.

Neutrinos interaction channels in JUNO

Interaction Chan.	Type	Num. evts (D=10kpc)
$\overline{\nu}_e + p \rightarrow e^+ + n$	CC	∼5000
$\nu + p \rightarrow \nu + p$	NC	∼2000
$\nu + e^- \rightarrow \nu + e^-$	NC	∼300
$\nu + {}^{12}C \rightarrow \nu + {}^{12}C^*$	NC	∼300
$\nu_e + {}^{12}C \rightarrow e^- + {}^{12}N$	CC	∼100
$\overline{\nu}_e + {}^{12}C \rightarrow e^+ + {}^{12}B$	CC	∼100

Table 1: *Numbers of neutrino events in JUNO with their corresponding interaction channels, where ν collectively stands for neutrinos and anti-neutrinos of all flavors. The corresponding distance to the CCSN is 10 kpc.*

The three main interaction channels are the IBD, the neutrino-proton elastic scattering (pES) and the neutrino-electron elastic scattering (eES). The first one will be a unique way to precisely determine the $\overline{\nu_e}$ energy spectra. The detection will be based on the powerful discriminating power provided by the temporal and spatial coincidence between two

signals: the first one produced by the positron and the annihilation gammas, and the second one induced by the neutron when it is captured. In addition, this channel gives a direct access to the incident $\overline{\nu_e}$ energy such as: $E_{\overline{\nu_e}} = E_{vis} + 0.782$, with E_{vis} being the reconstructed (visible) energy. The pES channel will allow to partially extract the ν_x (i.e. ν_μ, ν_τ, $\overline{\nu_\mu}$ and $\overline{\nu_\tau}$) energy spectra[18][19] while the eES channel will be predominantly sensitive to the ν_e due to the larger cross-section [20][8]. More information on the three other interaction channels involving ^{12}C can be found in[19].

The visible energy spectra for the different channels are shown in Fig.3. It ranges from 0.2 to 100 MeV with an average energy of ∼20 MeV for the IBD, <1 MeV for the pES and ∼10 MeV for the eES. The pES and IBD channels are dominating in the ranges 0-2 MeV and 2-100 MeV, respectively, which is a great advantage when it comes to select the events using energy cuts.

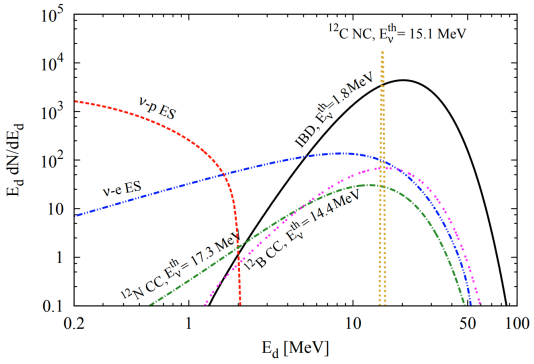

Figure 3: *The neutrino events spectra with respect to the visible energy E_d in the JUNO detector for a CCSN at 10 kpc. Taken from [8]*

As shown in Fig.4, the most probable position of the next CCSN is close to the Galactic Center (∼10 kpc) since it is a more active star forming region. Given the time resolution of the detector and considering a Data Acquisition (DAQ) time window of 1.25μs as it will be the case in JUNO, at this distance, only 1-2% of the events will pile-up (i.e. overlap in the time distribution of their respective scintillation photons). These events will not necessarily be lost and could be partly recovered by taking advantage of the size of the CD (e.g. by searching for clusters of fired PMTs). However, it's not impossible that a closer CCSN explodes, which would represent a real challenge for the readout electronics and DAQ with several hundreds of thousands of events to process and way more event pile-up (e.g. ∼10-15% for a 3 kpc away CCSN). In these specific cases, we expect the 3" PMT system not to saturate and to be able to get an event-by-event observation even if the rate is very high. Studies with the official JUNO simulation software are underway. A nearby CCSN would also represent an important data volume to transfer to the DAQ. In order to avoid data loss during the transferring, the front-end electronics is equipped with Dual Data-Rate (DDR) memories that can be used to temporally store the data in case of overflow (2 GigaBytes shared by 3 20" PMTs[8] and 1 GigaBytes shared by 128 3" PMTs).

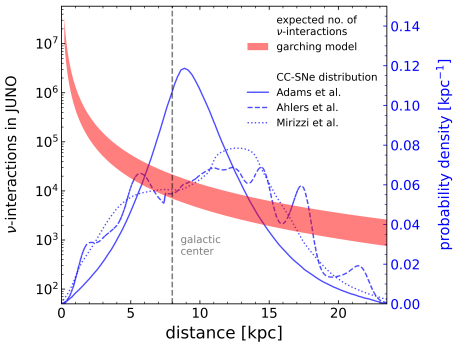

Figure 4: *The expected number of neutrino interactions events in JUNO as a function of the distance to the CCSN (red curve). The galactic CCSNe probability as a function of the distance is also shown (blue curves).*

Event reconstruction

In this section, we focus on the reconstruction of the events. The methodology is described and some orders of magnitude are given from the preliminary studies. The final results will come out in a later publication.

The ultimate goal of the CCSNe neutrino detection is to reconstruct the energy spectra as well as the time and flavor evolution of the neutrino flux (also called the neutrino light curves[21]). They will eventually be compared to the predictions from different models in order to infer the CCSN progenitor parameters. In this context, the reconstruction of the events, namely their vertex and energy, is of crucial importance. The reconstruction of the vertex will serve two main purposes. The first one is the correction of the detector non-uniformity when reconstructing the energy of the events. The second one is the selection of the IBD events among the other sources of background using the spatial coincidence mentioned in section 37. The energy of the events is also a crucial observable for the selection of the events and most importantly, it gives access to the neutrino energy spectra.

The algorithm developed takes advantage of the good time resolution of the 3" PMTs (the Transit Time Spread is 1.6 ns (σ))[16] as well as that of their readout electronics (0.5 ns accuracy, 0.2 ns RMS)[22]. The estimation of the vertex is done with a maximum likelihood method, using the first hit time of the fired 3" PMTs as well as their position. First, a probability density function (p.d.f.) $\mathcal{P}(t_{res,i})$ of the residual time (t_{res}) is built using Monte-Carlo (MC) simulation data:

$$t_{res} = t' - tof - t_0$$

where t' is the first hit time, tof is the time of flight of the scintillation photon from the vertex to the PMT and t_0 is the absolute starting time of the event. Then, the p.d.f. is used to construct a likelihood function such as:

$$\mathcal{L}(t_{res,1}, t_{res,2}..., t_{res,N}|\vec{r}, t_0) = -\log\left(\prod_{hits} \underbrace{\mathcal{P}(t_{res,i}|\vec{r}, t_0)}_{p.d.f}\right)$$

For a given vertex ($\vec{r}$) and initial time (t_0), the product of the probability to get the residual times ($t_{res,i}$) at the i-th PMT fired is computed. The algorithm looks for the vertex that maximizes the product of the probabilities (or minimizes its negative logarithm). The corresponding vertex is the more likely to be the true vertex of the event. The minimization is done using the MIGRAD algorithm of the TMinuit package[23] provided by ROOT[24].

The resolution obtained is of the order of a few tens of centimeters in the lower energy range (1-3 MeV) and is better than 20 cm in the higher energy range. These orders of magnitude are satisfactory in a detector whose radius is of the order of 10 m. However, the efficiency of the algorithm is not 100%. The efficiency corresponds to the fraction of events of the sample that were identified as well reconstructed. This identification is done based on the value of the likelihood function at the end of the minimisation. Some of the events occurring close to the border are badly reconstructed (i.e. several meters away from the true vertex) because of reflections undergone by the scintillation photons at the LS/water interface. The value of the likelihood function is higher for such events, which can be rejected with a simple cut. The average energy of most of the events from CCSNe neutrinos is above 10 MeV. In this energy region, the algorithm efficiency is >97% and the resolution is ∼10 cm.

An energy reconstruction algorithm has also been developed using the charge information provided by the 3" PMT system. The algorithm was first tested in the reactor neutrino energy range (0-10 MeV) and the consistency with the expected "abc" energy resolution model[25] was verified. The energy is reconstructed such as:

$$E_{rec} = \frac{nPE(R_{rec}, \theta_{rec}) - N_{DC}}{Y_0 \times f_{corr}(R_{rec}, \theta_{rec})}$$

where nPE(R_{rec}, θ_{rec}) is the number of p.e, R_{rec} and θ_{rec} are the reconstructed radius and zenithal angle, respectively. N_{DC} is the average number of dark counts (DC) expected during an event trigger time window (1.25μs), Y_0 is the number of p.e per MeV at the center of the detector, and $f_{corr}(R_{rec}, \theta_{rec})$ is the non-uniformity correction based on the reconstructed vertex. The reconstructed energy is also corrected from the intrinsic LS non-linearity (quenching effects and cherenkov light). When the visible energy is larger than 10 MeV, the energy resolution is better than 5%, which is satisfactory to achieve a precise reconstruction of part of the CCSNe neutrino energy spectra. Indeed, the measurement of the energy of the pES events - for which the visible energy is < 1 MeV - will suffer from the poor energy resolution of the 3" PMT system in this range.

Conclusion & Outlooks

Future large scale neutrino detectors like JUNO will be able to detect a burst of neutrinos from the next galactic CCSN. The reconstruction of the neutrino energy spectra and light curves will allow to probe the microscopic physics of CCSN and test the neutrino-driven explosion models. JUNO will have the opportunity to perform the analysis using two complementary PMT systems. The work presented here is focused on the 3" PMT system but other studies are currently being conducted using the 20" PMT system. As described in the previous sections, event reconstruction algorithms have been developed and showed satisfactory results. They're currently being used to perform the event selection and unfolding necessary to determine the CCSNe neutrino energy spectra.

References

[1] H.A Bethe, Supernova mechanisms. Rev. Mod. Phys. 62, 801, October 1990.

[2] B. Müller, Neutrino Emission as Diagnostics of Core-Collapse Supernovae, Annu. Rev. Nucl. Part. Sci. 2019.69:253-278, August 2019.

[3] K. Rozwadowska et. al, On the rate of core collapse supernovae in the Milky Way, New Astronomy 83(2):101498, August 2020.

[4] K. Hirata et. al, Observation in the Kamiokande-II detector of the neutrino burst from supernova SN1987A. Phys. Rev. Lett. 58, 1490, April 1987.

[5] R. M. Bionta et. al, Observation of a Neutrino Burst in Coincidence with Supernova 1987A in the Large Magellanic Cloud. Phys. Rev. Lett. 58, 1494, July 1987.

[6] E. N. Alekseev et. al, Properties of the Supernova 1987A Neutrino Signal Recorded by the Baksan Underground Scintillation Telescope. Sov. Astr. Lett. 14, 1988.

[7] V. L. Dadykin et. al, The signal recorded by the Mont Blanc underground neutrino detector on 23 February 1987. Sov. Astr. Lett. 14, 1988.

[8] A. Abusleme et. al, JUNO Physics and Detector, Progr. Part. Nucl. Phys. (2021) 103927, DOI: 10.1016/j.ppnp.2021.103927

[9] A. Fengpeng et al., Neutrino Physics with JUNO, J. Phys. G: Nucl. Part. Phys. 43, (2016) 030401.

[10] D. Brailsford. DUNE Status and Perspectives, arXiv:1804.04979, April 2018.

[11] S. Aiello et. al, The KM3NeT potential for the next core-collapse supernova observation with neutrinos, Eur. Phys. J. C 81, 445, May 2021.

[12] K. Abe et. al. Letter of Intent: The Hyper-Kamiokande Experiment - Detector Design and Physics Potential. arXiv:1109.3262, September 2011.

[13] A. Abusleme et al., Calibration strategy of the JUNO experiment, J. High Energy Phys. 03, (2021) 004.

[14] M. Sakata et. al, Remarks on the unified model of elementary particles. Progress of Theoretical Physics, Vol. 28, No. 5, pp. 870-880, November 1962.

[15] Chee Sheng Fong, Hisakazu Minakata and Hiroshi Nunokawa, Unitarity Tests of the Neutrino Mixing Matrix, JHEP02(2017)114, February 2017.

[16] C. Cao et. al Mass production and characterization of 3-inch PMTs for the JUNO experiment, Nucl. Instrum. Meth. A 1005 (2021) 165347, July 2021.

[17] Q. Hang and J.P.A.M de Andre on behalf of the JUNO Collaboration. Current status of JUNO Top Tracker. European Physical Society Conference on High Energy Physics, Jul 2019, Ghent, Belgium, October 2019.

[18] J.F Beacom et. al, Detection of supernova neutrinos by neutrino-proton elastic scattering, Phys. Rev. D 66, 033001, August 2002.

[19] Jia-Shu Lu, Yu-Feng Li, and Shun Zhou, Getting the most from the detection of Galactic supernova neutrinos in future large liquid-scintillator detectors. Phys. Rev. D 94, 023006, July 2016.

[20] W.J Marciano and Z. Parsa, Neutrino-electron scattering theory. J. Phys. G: Nucl. Part. Phys. 29 2629, 2003

[21] K. Nakazato et. al, Supernova Neutrino Light Curves and Spectra for Various Progenitor Stars: From Core Collapse to Proto-neutron Star Cooling, Astrophys. J. Suppl. 205, 2013.

[22] S. Comforti et. al, CATIROC: an integrated chip for neutrino experiments using photomultiplier tubes. Journal of Instrumentation, IOP Publishing, 2021, 16 (05), pp.P05010.

[23] R. Brun et. al, TMinuit Class Reference. https://root.cern.ch/doc/master/classTMinuit.html.

[24] R. Brun and F. Rademakers, ROOT - An object oriented data analysis framework. Nuclear Instruments and Methods in Physics Research Section A: Accelerators, Spectrometers, Detectors and Associated Equipment, Volume 389, April 1997, Pages 81-86.

[25] The JUNO collaboration., A. Abusleme et al. Calibration strategy of the JUNO experiment. J. High Energ. Phys. 2021, 4.

Performances of the ProtoDUNE Dual Phase experiment

Pablo Kunzé

Laboratoire d'Annecy de Physique des Particules

Abstract — Neutrinos still have well-kept secrets. What is the mass hierarchy? What are the precise values of the oscillation parameters? Or yet, is there a matter/antimatter asymmetry in the neutrino area? The future experiment DUNE will intend to answer these questions. Technologies used and large dimensions require to first build prototypes, such as ProtoDUNE Dual Phase.
The ProtoDUNE Dual Phase detector is a Liquid Argon Time Projection Chamber (LAr TPC) prototype with a liquid phase in which electrons drift and a gas phase used to amplify the signal. Cosmic rays data taken by this detector at CERN in 2019 and 2020 will allow us to characterize it and evaluate performances of this technology. For example we can evaluate the liquid Argon purity, measure the gain of the charge amplifier (LEMs) and characterize the gain dependence to the different detector settings. We will show the studies we are performing as well as the first results obtained on these topics.

Introduction

The future long-baseline neutrino oscillation experiments will allow to answer remaining questions in neutrino physics. The two main ones are the determination of the neutrino mass hierarchy and the CP asymmetry in the neutrino area.

One of these experiments is called DUNE for Deep Underground Neutrino Experiment [1], and will be possible thanks to a $\nu_\mu/\bar{\nu}_\mu$ beam provided by the FermiLab and 4 Liquid Argon TPC (LArTPC) modules of 17 kt and $60 \times 12 \times 12$ m^3 each, 1300 km away.

Before building such large-scale LAr-TPC detectors, two liquid Argon TPC prototypes, ProtoDUNE Single Phase and Dual phase, have been built at the Neutrino Platform at CERN. Both prototypes have similar sizes, ($\sim 6 \times 6 \times 6$ m^3 and $\sim$300 t) and investigate different technologies. The one we are interested in here is the Dual Phase technology.

The ProtoDUNE Dual Phase dectector

Principle

The ProtoDUNE Dual Phase dectector has taken data from 2019 to 2020 and might take data again at the begining of 2022 at the Neutrino Platform at CERN. The active volume of this prototype is $6 \times 6 \times 6$ m^3, resulting in 300 t of liquid Argon. The detector is made by a cathode (at the bottom), an anode (at the top) and a field cage (on the sides). All three produces a uniform drift field. Charged particles crossing the liquid Argon volume will ionize Argon producing e^- that will either recombine to an Argon ion or drift towards the anode (the ratio of e^- that drift over the total of e^- created is called the recombination factor) . The Dual Phase technology has a gaseous Argon layer just before the collection plane (Figure 1). When reaching the surface, ionization electrons are extracted from the liquid into the gas, thanks to the extraction field created by the grid and the LEMs (Large Electron Multipliers), then amplified inside the LEMs and collected on the anode equipped with orthogonal strips, or views. All the charge detection system is called CRP for Charge Readout Plane. Additionally, at the bottom of the detectors, are placed 36 Photmultipliler tubes (PMTs) with wavelength shifter to detect the UV-scitillation light created by the passage of a charged particles in the liquid.

In order to obtain a drift of electrons over 6 m and a high gain, powerful electric fields are needed. The drift field is chosen to be of 500 V/cm over 6 m and uniform, meaning that the cathode has to be operated at -300 kV.

Charge Readout Planes and Large Electron Multiplier

The first goal of the CRPs (Figure 2) is to extract electrons from the liquid to the gas. In order to do so, a grid is placed in the liquid and a potential difference is applied between the grid and the LEMs. It has been shown that an electric field of 2 kV/cm is needed to have an extraction efficiency of at least 80% [2]. LEMs are PCB plates with metal layers on both side, on which 500 μm holes are perforated spaced by 800 μm.

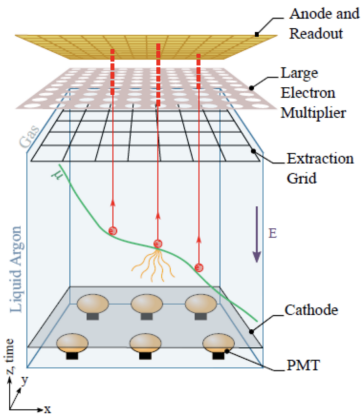

Figure 1: Schematic view of a dual phase liquid Argon TPC

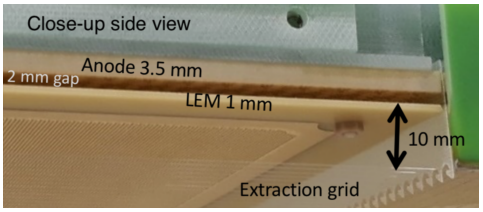

Figure 2: Close-up view of a CRP from the side

The electrons are guided through LEMs' holes where a high electric field ($\sim$ 30 kV/cm) is applied to create a Townsend avalanche. The electrons are then collected on the anode with the induction field and equally distributed on the two perpendicular views.

Inside ProtoDUNE Dual Phase, there are 4 CRPs. Two of them, CRP0 and CRP1, are fully instrumented, with 36 LEMs each, CRP3 has only 4 anodes without amplification and the CRP2 is completely un-instrumented. (Figure 3)

At the very begining of the data taking, a short happened between the supply chain of the cathode and the field cage. As a consequence, the drift field inside protoDUNE DP became non-uniform and the e^- could only drift over $\sim$1.2 m. All data has been collected in this condition, but the effect of the non uniform drift field is corrected offline.

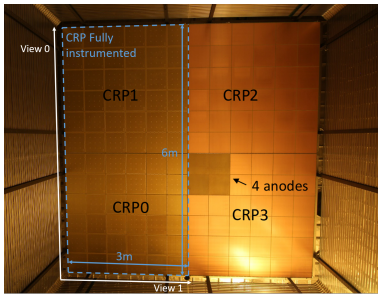

Figure 3: View of the CRPs from the bottom of ProtoDUNE Dual Phase

Analysis of charge signal from cosmics in ProtoDUNE Dual Phase

As said before, there are two types of signal in ProtoDUNE DP, the scintillation light and the ionization electrons. We will focus here on the charge signal.

The charge signal

The signal is collected on the anode. Each CRP has 960 channels separated by 3.125 mm. Cosmic events are triggered randomly in a window of 4 ms (10000 time bins). An event display can be seen in Figure 4 and we see that noises are mainly removed. Tracks from cosmic rays are also visible, a reconstruction code identify them, associate them in 3D tracks and provide the charge and positions.

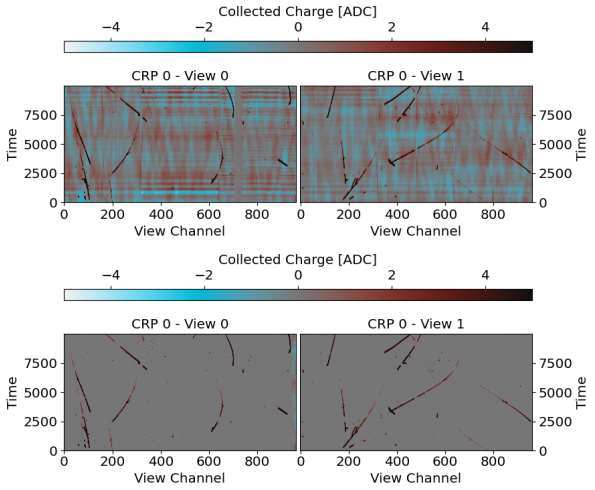

Figure 4: Top: Example of a raw event display for the two views of CRP0. The x axis is the channel number (the position) and the y axis is the time (in number of points). Bottom: Same event but with noise filtered.

In the following analysis, we select the muon-like tracks. First of all, we want only "late" tracks entering in the detector after the trigger and entering from the top of the detector, this is to ensure that we know the depth of each points of the tracks. Then we select the tracks on different quality criteria, their length ($> 30cm$), their number of hits associated (>15), their zenital angle ($95^o < \theta < 178^o$).

Measurement of the liquid Argon purity

The first analysis estimates the purity of the liquid Argon with cosmic tracks. When the electrons drift toward the anode they have a chance to be captured by impurities according to $e^{-t/\tau}$, with t the drift time and τ the electron lifetime. The purity and electron lifetime are related as follow: $\rho[\text{ppt}] \sim \frac{300}{\tau[\text{ms}]}$. A purity of 3 ms was a recquirement of protoDUNE DP.

The reconstruction provides the charge collected by

unit length along the track. This is

$$\frac{dQ}{ds}|_{\text{collected}} = G \cdot R(E_{\text{drift}}) \cdot \frac{dQ}{ds}|_{\text{created}} e^{-t/\tau}$$

with G, the effective gain, R(E) the recombination factor, $\frac{dQ}{ds}|_{\text{created}}$ the charge by unit length deposed by the particle and $e^{-t/\tau}$ due to impurities. So if we fit the distribution of $\frac{dQ}{ds}|_{collected}$ vs t we have access to τ the electron lifetime. For a run taken at a specific voltage configuration, the fit is performed on all LEMs and views, 144 fits in total. Then, to determine the electron lifetime value of the run, the gaussian mean of all τ values is taken (Figure 5).

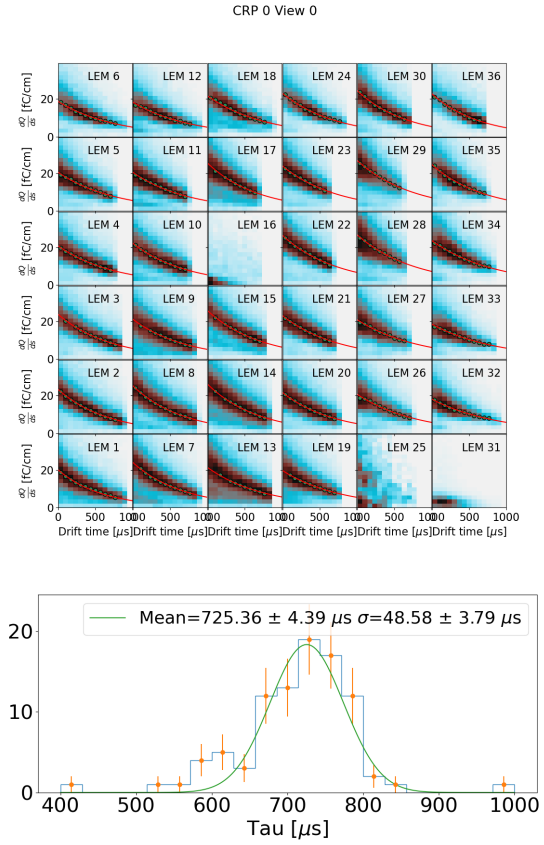

Figure 5: Top: Example of exponential fits on a run taken in October 2019. For clarity, only one CRP and one view is shown. Missing fits are LEMs not working. Bottom: Gaussian fit on the distribution of all τ values, resulting of a mean value of $\tau = 725.36 \pm 48.58$ μs

Cosmic data has been taken only for a few days in September, October, November 2019 and January 2020. In parallel, several times per day, the electron lifetime in the liquid Argon was monitored by two purity monitors located at the bottom and the middle of the detector (Figure 6). We see that the values we found are in good agreement with the values from the purity monitors and reach in January 2020 ∼3.5 ms.

Measurement of the effective gain

Now that we know the electron lifetime for each run, we have access to the effective gain. Indeed, as said

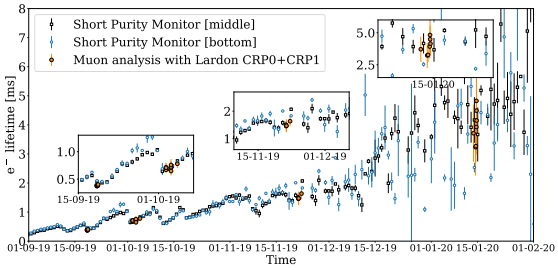

Figure 6: Comparison of electron lifetime from the cosmic analysis (orange) and from the purity monitors (blue and black).

before, we measure

$$\frac{dQ}{ds}|_{\text{collected}} = G \cdot R(E_{\text{drift}}) \cdot \frac{dQ}{ds}|_{\text{created}} e^{-t/\tau}$$

and we just found τ, the most probable value of $\frac{dQ}{ds}|_{\text{created}}$ for a muon is estimated at 12.24 fC/cm in liquid Argon and $R(E_{\text{drift}})$ has been parametrized by ICARUS [3].

To evaluate the effect of the LEMs amplification field on the gain, several runs at different amplification fields have been taken, from 25 kV/cm to 31 kV/cm, and at different period (in September, October, November 2019 and January 2020) (Figure 7). First of all, we see that the effective gain increases with the LEMs amplification field as expected. Then, we see that at a given amplification field, the effective gain decreases with time, an effect known for LEMs systems as the charging-up effect.

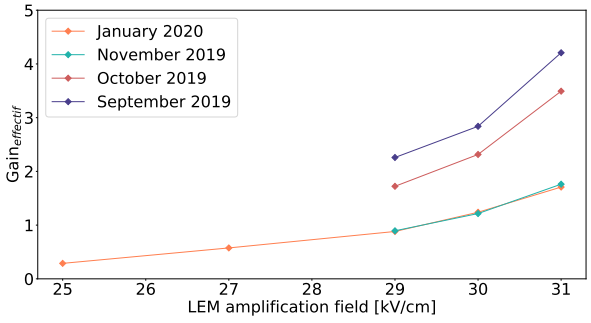

Figure 7: Effective gain as a function of the LEMs amplification field for one LEMs. In purple, September 2019, in red, October 2019, in green, November 2019 and in orange, January 2020.

Charging-up effect

The charging-up effect [4] is caused by charges attached on the plastic part of the LEMs modifying the amplification field and thus reducing the gain for a same voltage difference.

In September 2019, data has been collected in stable conditions for more than 5h. The effective gain for each LEMs has been computed in slices of 10 minutes, see Figure 8. We can clearly see a decrease of the gain with

time. Studies are on ongoing to associate this decrease with the charging-up effect.

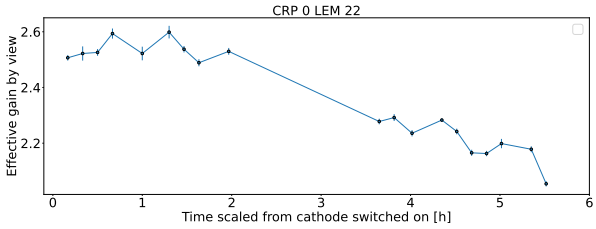

Figure 8: Effective gain at 29 kV/cm of amplification as a function of time from the turning on of the cathode for one LEM of CRP 0.

Conclusions

The ProtoDune Dual Phase detector took data in 2019 and 2020. The data taken are still under analysis but we could derive interesting observables. First, the electron lifetime could be estimated with cosmic tracks reaching 3.5 ms in January 2020 and in agreement with purity monitors. After that we could estimate the effective gain as a function of the amplification field. We also saw the effect of time on the gain due to the charging-up effect. Simulations of charging-up are ongoing.

References

[1] Volume I. Introduction to DUNE, B. Abi et al 2020 JINST 15 T08008

[2] Emission of "hot" electrons from liquid and solid Argon and Xenon, Gushchin E, Kruglov A., Obodovskii I., J Exp. Theor. Phys 1982 Vol. 55, Issue 5, p.860

[3] Study of electron recombination in liquid argon with the ICARUS TPC, S. Amoruso and al., Nucl.Instrum.Meth.A 523 (2004) 275-286

[4] Simulation of the dielectric charging-up effect in a GEM detector, M.Alfonsia, G.Crocia, S.Duarte Pinto, E.Rocco, L.Ropelewski, F.Sauli, R.Veenhof, M.Villa, Nucl.Instrum.Meth.A 671 (2012) 6-9

Part VII

Nuclear Physics & Multidisciplinary Topics

session chaired by Diego GRUYER

Charge-Exchange Excitations Beyond Gamow-Teller

Arthur BELOEUVRE[1], ***with S.Péru***[2,3], ***M. Martini***[4,5], ***M. Estienne***[1], ***M. Fallot***[1]

[1] *Subatech (CNRS/IN2P3), IMT Atlantique, Université de Nantes, 44307, Nantes, France*
[2] *CEA, DAM, DIF, F-91297 Arpajon, France*
[3] *Université Paris-Saclay, CEA, LMCE, 91680 Bruyères-le-Châtel, France*
[4] *IPSA-DRII, 63 boulevard de Brandebourg, 94200 Ivry-sur-Seine, France*
[5] *Sorbonne Université, Université Paris Diderot, CNRS/IN2P3, Laboratoire de Physique Nucléaire et de Hautes Energies (LPNHE), Paris, France*

Abstract — Charge-exchange excitations corresponding to first forbidden beta-decay transitions in nuclei have been studied in the self-consistent proton-neutron quasiparticle random-phase approximation (pnQRPA) using the finite-range Gogny interaction. No parameters beyond those of the effective nuclear force are included. Axial deformations are taken into account for both the ground state and charge-exchange excitations. With this formalism, nuclear matrix elements have been computed for operators derived from the multipole expansion of the weak current: spin-dipole, anti-analog dipole. They are needed in order to give a complete description of first-forbidden β-decays. A comparison of the predicted strength distributions to the existing experimental data is presented for those operators in the case of the ^{208}Pb.

Introduction

First-forbidden beta decays play an important role in several domains of physics. First, in astrophysics, where nuclear data such as the half-life govern stellar evolution and nucleosynthesis [1]. Second, they are of interest for nuclear reactors physics as first highlighted in 2014 [2]. In first-forbidden β-decays, the form factors of the leptonic spectra are not equal to one as for allowed decays [3]. It has been shown that it could have a non negligible impact on the shape of the antineutrino energy spectra. Among the models developed since then, which do not all tend to agree [4, 5, 6, 7], some even state that it could solve the reactor antineutrino shape anomaly. New theoretical calculations of the first-forbidden form factors associated to summation calculations [8] and dedicated experimental measurements would be useful to corroborate or negate already existing predictions.

In order to study first-forbidden antineutrino spectra, nuclear matrices elements obtained through the action of operators derived from the multipole expansion of the weak current [9], namely the Anti-Analog Dipole operator, Spin-Dipole operators, pseudoscalar-axial vector operator and tensor-polar vector operator, are needed to calculate the shape factor [3].

In this work, the Anti-Analog Dipole operator and the Spin-Dipole operators are calculated in the context of the pnQRPA (proton-neutron Quasiparticle Random-Phase Approximation), an approach first introduced in [10]. It is a mean-field based approach of the many-body problem to treat charge-exchange reactions. In order to give reliable predictions, it has to be able to treat deformed nuclei and use a unique effective nuclear force for all nuclei to describe their ground and excited states. The latter property is also called the self-consistency of the calculations. The number of pnQRPA models [11, 12, 13, 14, 15, 16, 17, 18, 19, 20, 21, 22, 23] able to do both remains small. Furthermore, even in the limited number of self-consistent calculations performed either with the zero-range Skyrme-type forces or in the relativistic mean-field framework, there often remains a coupling constant, typically in the particle-particle channel, which is treated as a free parameter and is usually adjusted to data of interest. Nuclear deformation has to be taken into account for nuclear reactor antineutrino spectra since they are produced mainly by deformed neutron-rich nuclei.

Here, we present a fully self-consistent axially symmetric-deformed pnQRPA calculation without any additional parameters other than those characterizing the effective nuclear force, Gogny D1M [24] in our case. Within this approach the isobaric analog strength and Gamow-Teller strength have already been studied [25]. First, we detail the pnQRPA formalism as well as the different operators and their sum rules. Then, the resulting strengths are calculated in the case of the ^{208}Pb, a well-known nucleus for which experimental data exist. Finally, conclusions and perspectives are given.

pnQRPA Formalism

The pnQRPA approach is used to treat charge-exchange excitations. The solutions are built on top of axially-deformed quasiparticle states from HFB

(Hartree-Fock Bogoliubov) calculations. Single fermion wave functions are expanded in a finite-sized orthogonal set of harmonic oscillator functions. In an axial symmetry, K, defined as the projection of the angular momentum J on the symmetry axis, and π, the parity, are good quantum numbers. Hence, pnQRPA calculations are performed in each K^π blocks.
In the following, the axially-symmetric-deformed pnQRPA states $|\theta_\alpha, K\rangle$ will be labeled with the angular momentum projection K. They are obtained by the action of the phonon operator $\theta^\dagger_{\alpha,K}$ on the pnQRPA ground state $|0_{\rm def}\rangle$, i.e.:

$$\theta^\dagger_{\alpha,K}\,|0_{def}\rangle = |\theta_\alpha, K\rangle \tag{1}$$

with

$$\theta_{\alpha,K} = \sum_{pn} X^{pn}_{\alpha,K}\eta^\dagger_p\eta^\dagger_n - (-)^K Y^{pn}_{\alpha,K}\eta_n\eta_p. \tag{2}$$

In the above formula $\eta^\dagger$ and η are the quasiparticle operators related to the fermion creation $c^\dagger$ and annihilation c operators through the u and v Bogoliubov transformation matrices with the relation:

$$\eta^\dagger = u_{p\pi}c^\dagger_\pi - v_{p\pi}c_\pi, \tag{3}$$

where repeated indices denote a sum over them. p and n refer to a proton and neutron quasiparticle respectively while π and ν denote harmonic oscillator states. pnQRPA eigenvectors X and Y are obtained through the well-known eigenvalue equation:

$$\begin{pmatrix} A & B \\ B & A \end{pmatrix}\begin{pmatrix} X_{\alpha,K} \\ Y_{\alpha,K} \end{pmatrix} = \omega_{\alpha,K}\begin{pmatrix} X^n \\ -Y^n \end{pmatrix}, \tag{4}$$

where the matrices A and B take the following form:

$$\begin{aligned} A_{pn,p'n'} &= (\epsilon_p+\epsilon_n)\delta_{pp'}\delta_{nn'} \\ &+ u_{p\pi}v_{n\nu}u_{p'\pi'}v_{n'\nu'}(\langle\pi\nu'|V|\nu\pi'\rangle - \langle\pi\nu'|V|\pi'\nu\rangle) \\ &+ v_{p\pi}u_{n\nu}v_{p'\pi'}u_{n'\nu'}(\langle\nu\pi'|V|\pi\nu'\rangle - \langle\nu\pi'|V|\nu'\pi\rangle) \\ &+ u_{p\pi}u_{n\nu}u_{p'\pi'}u_{n'\nu'}(\langle\pi\nu|V|\pi'\nu'\rangle - \langle\pi\nu|V|\nu'\pi'\rangle) \\ &+ v_{p\pi}v_{n\nu}v_{p'\pi'}v_{n'\nu'}(\langle\pi'\nu'|V|\pi\nu\rangle - \langle\pi'\nu'|V|\nu\pi\rangle) \end{aligned} \tag{5}$$

and

$$\begin{aligned} B_{pn,p'n'} &= u_{p\pi}v_{n\nu}v_{p'\pi'}u_{n'\nu'}(\langle\pi\nu'|V|\nu\pi'\rangle - \langle\pi\nu'|V|\pi'\nu\rangle) \\ &+ v_{p\pi}u_{n\nu}u_{p'\pi'}v_{n'\nu'}(\langle\nu\pi'|V|\pi\nu'\rangle - \langle\nu\pi'|V|\nu'\pi\rangle) \\ &+ u_{p\pi}u_{n\nu}v_{p'\pi'}v_{n'\nu'}(\langle\pi\nu|V|\nu'\pi'\rangle - \langle\pi\nu|V|\pi'\nu'\rangle) \\ &+ v_{p\pi}v_{n\nu}u_{p'\pi'}u_{n'\nu'}(\langle\pi'\nu'|V|\nu\pi\rangle - \langle\pi'\nu'|V|\pi\nu\rangle). \end{aligned} \tag{6}$$

Charge-exchange operators

The strength $B(\hat{O}_\lambda; J_i \to J_f)$ of an operator $\hat{O}_\lambda$, i.e. the response to an excitation is given through the square matrix element, according to the following formula:

$$B(\hat{O}_\lambda; J_i \to J_f) = \sum_K |\,\langle J_fK_f||\,\hat{O}_\lambda\,||J_iK_i\rangle\,|^2, \tag{7}$$

where $\langle J_fK_f||\,\hat{O}_\lambda\,||J_iK_i\rangle$ is given by the Wigner-Eckart theorem:

$$\begin{aligned} &\langle J_fK_f||\,\hat{O}_\lambda\,||J_iK_i\rangle = \\ &\frac{\sqrt{2J_f+1}}{\langle J_iM_i\lambda\mu|J_fM_f\rangle}\,\langle J_fM_fK_f|\,\hat{O}_{\lambda\mu}\,|J_iM_iK_i\rangle\,. \end{aligned} \tag{8}$$

States $|JM(K)_n\rangle$ $(K>0)$ are obtained by projecting the excitation on $|\theta_n, K\rangle$ according to [26]:

$$\begin{aligned} |JM(K)_n\rangle &= \frac{\sqrt{2J+1}}{4\pi}\int d\Omega\,\mathcal{D}^J_{MK}(\Omega)R(\Omega)\,|\theta_n, K\rangle \\ &+ (-)^{J-K}\mathcal{D}^J_{M\,-K}(\Omega)R(\Omega)\,|\theta_{\overline{n}}, -K\rangle\,, \end{aligned} \tag{9}$$

where Ω are the Euler angles, $\mathcal{D}$ the Wigner rotation matrix, and R the three-dimensional rotation operator. The nuclear ground-state $(J^\pi = 0)$ in the laboratory frame $|\widetilde{O}\rangle$ is related to the pnQRPA intrinsic deformed ground state $|0_{\rm def}\rangle$:

$$|\widetilde{O}\rangle = \frac{1}{2\pi}\int d\Omega\mathcal{D}^0_{00}(\Omega)R(\Omega)\,|0_{\rm def}\rangle\,. \tag{10}$$

The final expression of the matrix element is obtained through manipulations of the equations above:

$$\begin{aligned} &\langle\widetilde{O}|\hat{O}_{\lambda\mu}|JM(K)_n\rangle = \sqrt{2J+1}\sum_{\mu'} \\ &(-)^{\mu-\mu'}\,\langle 0_{\rm def}|\hat{O}_{\lambda\mu'}|\theta_n, K\rangle\begin{pmatrix} 0 & \lambda & J \\ 0 & -\mu & M \end{pmatrix}\begin{pmatrix} 0 & \lambda & J \\ 0 & -\mu' & K \end{pmatrix} \\ &+ (-)^{J-K+\mu-\mu'}\,\langle 0_{\rm def}|\hat{O}_{\lambda\mu'}|\theta_{\overline{n}}, -K\rangle \\ &\cdot\begin{pmatrix} 0 & \lambda & J \\ 0 & -\mu & M \end{pmatrix}\begin{pmatrix} 0 & \lambda & J \\ 0 & -\mu' & -K \end{pmatrix}. \end{aligned} \tag{11}$$

The simplest charge-exchange excitations operators are the Fermi, responsible for the Isobaric Analog Resonance ($\hat{O}^{IAR} = \tau_\pm$), and the Gamow-Teller operators ($\hat{O}^{GT}_\mu = \sigma_\mu\tau_\pm$). Those operators have already been studied within this model [25].
Here we consider operators associated with forbidden β-decays here. First, there is the operator associated to the Anti-Analog Dipole Resonance (AADR):

$$\hat{O}^{AAD}_\mu = rY_{1\mu}\tau_\pm, \tag{12}$$

which leads to an electric dipole excitation coupled with the third isospin component lowering or raising operator. Second, the spin-dipole operators

$$\hat{O}^{SD}_{\lambda\mu} = r\,[Y_1\otimes\sigma]_{\lambda\mu}\,\tau_\pm, \tag{13}$$

where $\lambda = 0,\ 1,\ 2$ refers to the change of spin in the nucleus. Those operators are defined by a dyadic product between an electric dipole excitation represented by the spherical harmonic tensor and the spin spherical tensor.

To give a complete description of first-forbidden beta

decays, two other operators are needed in addition to the AAD and SD: the pseudoscalar-axial vector operator [9]

$$\hat{O}^{P-A} = \sigma \cdot \nabla \tau_{\pm} \tag{14}$$

and tensor-polar vector operator

$$\hat{O}^{T-V}_{\mu} = [Y_0 \otimes \nabla]_{1\mu}\, \tau_{\pm}. \tag{15}$$

Higher degree variation of the AAD and SD operators are also taken into account such as the Analog Quadripole Resonance operator ($\hat{O}^{AQ}_{\mu} = r^2 Y_{2\mu}\tau_{\pm}$), the spin-quadripole operators ($\hat{O}^{SQ}_{\lambda\mu} = r^2\,[Y_2 \otimes \sigma]_{\lambda\mu}\,\tau_{\pm}$, $\lambda = 1, 2, 3$), the Anti-Analog Octupole Resonance operator ($\hat{O}^{AAO}_{\mu} = r^3 Y_{3\mu}\tau_{\pm}$) and the spin-octupole operators ($\hat{O}^{SO}_{\lambda\mu} = r^3\,[Y_3 \otimes \sigma]_{\lambda\mu}\,\tau_{\pm}$, $\lambda = 2, 3, 4$). Those operators correspond to second and third forbidden β decays.

The action of those operators have been calculated within the Gogny pnQRPA framework. In order to verify the calculation of the strength, it is useful to compare it with the model-independent sum rules for both the anti-analog dipole operator as well as the spin-dipole operators given, for spherical nuclei, by [27]:

$$B(\hat{O}^{AAD})_- - B(\hat{O}^{AAD})_+ = 3\frac{N\langle r^2\rangle_N - Z\langle r^2\rangle_P}{4\pi} \tag{16}$$

for the Anti-Analog Dipole and [28]

$$B(\hat{O}^{SD}_{\lambda})_- - B(\hat{O}^{SD}_{\lambda})_+ = (2\lambda+1)\frac{N\langle r^2\rangle_N - Z\langle r^2\rangle_P}{4\pi} \tag{17}$$

for the Spin-Dipole, where Z and N are the number of protons and neutrons in the mother nuclei, $\langle r^2\rangle_{N,P}$ is the squared mean neutron/proton radius, and the $\pm$ subscript denotes the operators related to a $\beta^{\pm}$ channel.

Results

In this section, charge-exchange excitations of the closed proton and neutron shells ^{208}Pb are presented for the Anti-Analog Dipole and Spin-Dipole excitation operators. The numerical calculation follows the same procedure as the one employed for the treatment of the IAR and GT strengths for this nucleus and others, as presented in Ref.[25]. Similar studies of the SD strength of ^{208}Pb have already been carried out in Refs. [29, 30, 31, 32, 33] with other models. The ^{208}Pb is a spherical nucleus, so for a given parity, all the K ($K \in (-J, ..., 0, ..., J)$) values will be degenerated and the $K = 0^{\pi}$ component is thus enough to determine any strength. D1M theoretical results for the SD operators are compared with experimental results from ^{208}Pb$(p,n)^{208}$Bi reactions [34] in figure 1. Results for the AAD operator are presented in the figure 2.

The calculations are performed with a cut in the 2-qp states at 70 MeV, which is enough to exhaust the sum rules. The operators strengths are expressed as a function of the excitation energy in the daughter nucleus

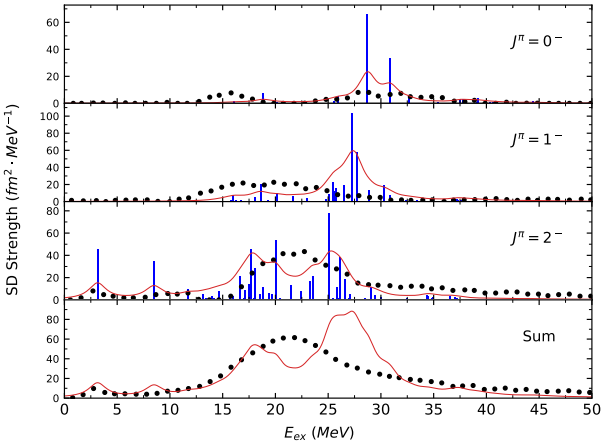

Figure 1: ^{208}Pb Spin-Dipole strengths for each multipolarity. The bars in blue are the pnQRPA strengths, the line in red is the folded Spin-Dipole strength and the points in black are the available experimental data [34].

E_{ex}. It is obtained by subtracting a reference energy E_0 from the pnQRPA phonon excitation energy $\omega_{\alpha,K}$:

$$E_{\mathrm{ex}} = \omega_{\alpha,K} - E_0. \tag{18}$$

The reference energy corresponds to the lowest 2-qp excitation associated with the ground state of the odd-odd daughter nucleus in which the quantum numbers of the single qp proton and neutron states are calculated with a self-consistent HFB approach of the odd-odd system. The operators strengths are then calculated for each pnQRPA level and then folded with a Lorentzian with a 2 MeV width.

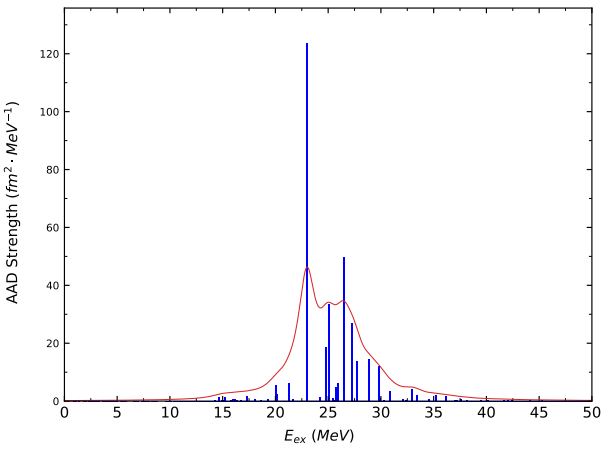

Figure 2: Predicted ^{208}Pb Anti-Analog Dipole strength.

The SD 0^- strength is experimentally divided into two peaks, but the pnQRPA only reproduces the sec-

ond one at the right position around 29 MeV.
The SD 1^- resonance obtained through calculations has not been experimentally observed at 27.5 MeV, but the strength has only been seen at lower energies, which is not reproduced by our model. The extra strength observed at lower energies could be explained by the contamination of the anti-analog dipole mode in the reaction. The AAD strength is predicted in the figure 2 and has a broad distribution between 20 and 30 MeV. Concerning the SD 2^- strength, our model predicts that the strength is split between two main peaks at 17.5 and 25 MeV respectively, whereas the experience has observed a continuous distribution of the strength around 22.5 MeV.
Looking at the total spin-dipole strength, which was the one observed directly in the experiment, the location and intensity of the strength is reasonably reproduced until 20 MeV, but a part of the strength, as explained before, has not been observed between 21 to 32.5 MeV.

The predicted strengths are however in agreement with the expected sum rules given in the table 1 with a maximum overestimation of 4%.

$\hat{O}$	$B(\hat{O})_-$	$B(\hat{O})_+$	Sum Rule	Expected
AAD	348.80	7.16	341.64	328.32
SD 0^-	140.30	26.58	113.71	109.44
SD 1^-	386.40	45.00	341.40	328.32
SD 2^-	601.95	32.56	569.40	547.20

Table 1: Total strength and sum rules values obtained from pnQRPA calculations in fm^2. Expected sum rules values are calculated from equations (16) and (17) with $\langle r \rangle_P = 5.408681$ fm and $\langle r \rangle_N = 5.472931$ fm obtained from HFB calculations.

Conclusion & Outlook

We have presented here a fully self-consistent pnQRPA calculation of four of the six operators needed to describe first-forbidden beta decays. The obtained results are in reasonable agreement with experimental data. With those operators, together with the pseudoscalar-axial vector and the tensor-polar vector ones it will be possible to calculate more accurately half-lives of nuclei that are predominantly decaying through forbidden transitions and it will be possible to calculate antineutrino spectra shape factor, a work that is currently ongoing.

References

[1] Arnould, M. et al. The r-process of stellar nucleosynthesis: Astrophysics and nuclear physics achievements and mysteries, Phys. Rept. 450, 2007

[2] Hayes, A. C. et al., Systematic Uncertainties in the Analysis of the Reactor Neutrino Anomaly, Phys. Rev. Lett. 112,2014

[3] H. O. Behrens and Wolfgang Bühring, Electron radial wave functions and nuclear beta-decay, 1982

[4] Fang et al., Effect of first forbidden decays on the shape of neutrino spectra, Phys. Rev. C 93, 2016

[5] Wang, X. et al., Weak magnetism correction to allowed β decay for reactor antineutrino spectra, Phys. Rev. C 95, 2017

[6] Wang, X. et al., Nuclear Zemach moments and finite-size corrections to allowed β decay, Phys. Rev. C 94, 2016

[7] Petković, J. et al., Self-consistent calculation of the reactor antineutrino spectra including forbidden transitions, J. Phys. G 46, 2019

[8] Estienne M. et al., Updated Summation Model: An Improved Agreement with the Daya Bay Antineutrino Fluxes, Phys. Rev. Lett. 123, 2019

[9] Bohr, Aage and Mottelson, Ben R, Nuclear Structure, World Scientific Publishing Company, 1998

[10] John A. Halbleib et al., Gamow-Teller beta decay in heavy spherical nuclei and the unlike particle-hole RPA, Nuclear Physics A 98, 1967

[11] J. Krumlinde et al., Calculation of Gamow-Teller β-strength functions in the rubidium region in the RPA approximation with Nilsson-model wave functions, Nuclear Physics A 417, 1984

[12] J. Hirsch et al., Gamow-Teller strength functions and two-neutrino double-beta decay, Nuclear Physics A, 1990

[13] A.A. Raduta et al., The $2\nu\beta\beta$ decay rate within a higher RPA approach, Physics Letters B 254, 1991

[14] Toivanen, J. et al., Renormalized Proton-Neutron Quasiparticle Random-Phase Approximation and Its Application to Double Beta Decay, Phys. Rev. Lett. 75, 1995

[15] P. Sarriguren et al., β decay and shape isomerism in 74Kr, Nuclear Physics A 635, 1998

[16] Bender, M. et al., Gamow-Teller strength and the spin-isospin coupling constants of the Skyrme energy functional, Phys. Rev. C 65, 2002

[17] Vretenar, D. et al., Spin-Isospin Resonances and the Neutron Skin of Nuclei, Phys. Rev. Lett. 91, 2003

[18] Paar, N. et al., Quasiparticle random phase approximation based on the relativistic Hartree-Bogoliubov model. II. Nuclear spin and isospin excitations, Phys. Rev. C 69, 2004

[19] Fracasso, S. et al., Fully self-consistent charge-exchange quasiparticle random-phase approximation and its application to isobaric analog resonances, Phys. Rev. C 72, 2005

[20] H. Liang et al., Spin-Isospin Resonances: A Self-Consistent Covariant Description, Phys. Rev. Lett. 101, 2008

[21] Minato, F. et al., Impact of Tensor Force on *beta* Decay of Magic and Semimagic Nuclei, Phys. Rev. Lett. 110, 2013

[22] K. Yoshida, Spin-isospin response of deformed neutron-rich nuclei in a self-consistent Skyrme energy-density-functional approach, Progress of Theoretical and Experimental Physics 11, 2013

[23] Mustonen, M. et al., Large-scale calculations of the double-β decay of ^{76}Ge,^{130}Te,^{136}Xe, and ^{150}Nd in the deformed self-consistent Skyrme quasiparticle random-phase approximation, Phys. Rev. C 87, 2013

[24] Goriely, S. et al., First Gogny-Hartree-Fock-Bogoliubov Nuclear Mass Model, Phys. Rev. Lett. 102, 2009

[25] Martini, M. et al., Gamow-Teller strength in deformed nuclei within the self-consistent charge-exchange quasiparticle random-phase approximation with the Gogny force, Phys. Rev. C 89, 2014

[26] Péru, S. and Martini, M., Mean field based calculations with the Gogny force: Some theoretical tools to explore the nuclear structure, The European Physical Journal A 50, 2014

[27] Cao, Li-Gang et al., Constraints on the neutron skin and symmetry energy from the anti-analog giant dipole resonance in Pb208, Physical Review C 92, 2015

[28] Gaarde, C., Excitation of giant spin-isospin multipole vibrations, Nuclear Physics A, 1981

[29] K. Yoshida, Charge-exchange dipole excitations in deformed nuclei. 08 2020.

[30] S. Fracasso et al., Spin-isospin nuclear response using the existing microscopic skyrme functionals. Physical Review C 76, Oct 2007.

[31] V. De Donno et al., Self-consistent continuum random-phase approximation with finite-range interactions for charge-exchange excitations. Phys. Rev. C, 93:034320, Mar 2016.

[32] Li-Gang Cao et al., Quenching factor of gamow-teller and spin dipole giant resonances. Physical Review C, 100(5), Nov 2019.

[33] A. Krasznahorkay et al., Excitation of isovector spin-dipole resonances and neutron skin of nuclei. Phys. Rev. Lett., Apr 1999.

[34] T. Wakasa, Spin-dipole strengths and tensor correlation effects for ^{208}Pb(p,n) at 295 MeV, 2010

Confronting the nucleonic hypothesis with current neutron star observations from GW170817 and PSR J0740+6620

Hoa DINH THI, ***with C. Mondal, F. Gulminelli***

Laboratoire de Physique Corpusculaire (LPC), CNRS, ENSICAEN, UMR6534, Université de Caen Normandie, F-14050 Caen Cedex, France

Abstract — The nuclear matter equation of state is relatively well constrained at sub-saturation densities thanks to the knowledge from nuclear physics. However, studying its behavior at supra-saturation densities is a challenging task. Fortunately, the extraordinary progress recently made in observations of neutron stars and neutron star mergers has provided us with unique opportunities to unfold the properties of dense matter. Under the assumption that nucleons are the only constituents of neutron star cores, we perform a Bayesian inference using the so-called meta-modeling technique with a nuclear-physics-informed prior. The latest information from the GW170817 event by the LIGO-Virgo Collaboration (LVC) and from the radius measurement of the heaviest known neutron star PSR J0740+6620 by the Neutron Star Interior Composition Explorer (NICER) telescope and X-ray Multi-Mirror (XMM-Newton) are taken into account as likelihoods in the analysis. The impacts of different constraints on the equation of state as well as on the predictions of neutron star properties are discussed. The obtained posterior reveals that all the current observations are fully compatible with the nucleonic hypothesis. Strong disagreements between our results with future data can be identified as a signal for the existence of exotic degrees of freedom.

Introduction

The knowledge of equation of state (EoS) at several times the nuclear saturation density ($\rho_{\rm sat} = 2.8 \times 10^{14}$ g cm^{-3}) is not yet accessible in terrestrial laboratories. Nonetheless, these densities can be explored in neutron star (NS) cores [1]. Together with the growth of multi-messenger astronomy, over the last few years, we have witnessed several breakthroughs in NS observations. For instance, astrophysicists are able to determine heavy pulsar masses with high precision via radio timing, e.g. PSR J0348+0432 ($M = 2.01 \pm 0.04 M_\odot$) [2] and PSR J0740+6620 ($M = 2.08 \pm 0.07 M_\odot$) [3], where $M_\odot$ is solar mass. Moreover, in August 2017, gravitational waves from the merger of a binary NS system (GW170817) were detected by LVC, delivering the very first information about the tidal deformability of NS [4, 5, 6]. Additionally, the development of X-ray timing telescope brings us information about the joint mass-radius distributions of the millisecond pulsars PSR J0030+0451 (NICER data) [7, 8] and PSR J0740+6620 (NICER+XMM-Newton data) [9, 10]. Due to the one-to-one correspondence between the EoS and NS static observables [11], these measurements together with the upcoming data [12] can be transformed into valuable information on matter at extreme conditions that cannot be reproduced on Earth. Thus, they are expected to be very promising tools to uncover the open questions about dense matter, such as whether or not exotic degrees of freedom exist in the cores of NS [13].

In this work, we assume that the only baryonic constituents of NS cores are nucleons, which are in weak equilibrium with electrons and muons. Under this hypothesis, the energy functional is described using the so-called meta-modeling technique [14, 15]. With the metamodel, the nuclear matter energy can be characterized by empirical parameters through a simple parameterization. In our Bayesian inference, the range of these parameters in the prior distribution is chosen such that they are compatible with the current nuclear physics knowledge [14, 15, 16, 17, 18], hence the name nuclear-physics-informed prior. This analysis can be considered as a way of transforming information from nuclear physics experiments and calculations as well as from astrophysical observations into empirical parameters in order to guide the elaboration of phenomenological and microscopic nuclear models. Additionally, it can be used as a null hypothesis to search for exotic degrees of freedom.

In the next section, we briefly recall the formalism described in Ref. [18]. Then, we discuss the posterior results from the Bayesian analysis. Finally, we present our conclusions. The main results of this study are published in Ref. [18].

Method

Meta-modeling technique

The meta-modeling for the EoS, proposed in Margueron et al. (2018) [14], is inspired from the Taylor

expansion around the saturation density $n_{\rm sat}$ of nuclear matter energy. It was shown in Ref. [14] that any nucleonic EoS can be reproduced satisfactorily by truncating the series expansion at the fourth order. The energy per nucleon at density $n = n_n + n_p$ and asymmetry $\delta = (n_n - n_p)/n$, therefore, can be written as

$$e(n,\delta) \approx \sum_{m=0}^{4} \frac{1}{m!} \left(\frac{d^m e_{\rm sat}}{dx^m}\bigg|_{x=0} + \frac{d^m e_{\rm sym}}{dx^m}\bigg|_{x=0} \delta^2 \right) x^m, \quad (1)$$

where n_n, n_p are the neutron and proton densities, $x = (n - n_{\rm sat})/(3n_{\rm sat})$, $e_{\rm sat}$ is the energy per nucleon of symmetric matter, and $e_{\rm sym}$ is called the symmetry energy, which is the difference between the energy per baryon of pure neutron matter and that of symmetric matter. In addition, the energy functional also includes the isoscalar effective mass and effective mass splitting in the kinetic energy and a parameter governing the energy functional at the zero-density limit. Thus, in total, the bulk energy is characterized by 13 parameters. To describe NS crusts, we complement these bulk parameters with 5 surface and curvature parameters within a compressible liquid drop model [17]. For each set of uniform matter parameters, these surface and curvature parameters are obtained by the optimal fit to the experimental Atomic Mass Evaluation 2016 (AME2016) nuclear mass table [19].

Statistical analysis

Here, we recall the main points in the Bayesian analysis performed in Ref. [18].

According to the Bayes' theorem, the posterior probability of the bulk parameter set $\mathbf{X}$ at given constraints $\mathbf{c}$ can be written as:

$$P(\mathbf{X}|\mathbf{c}) = \mathcal{N} P(\mathbf{X}) \prod_k P(c_k|\mathbf{X}), \quad (2)$$

with $\mathcal{N}$ being a normalization factor. $P(\mathbf{X})$ and $P(c_k|\mathbf{X})$ are called prior and likelihood, respectively. The constraints implemented in this work take into account both information at low density from nuclear mass measurements in the AME2016 mass table [19] and many-body perturbation theory (MBPT) calculations [20] and at high density from astrophysical observations [2, 6, 8, 10].

Considering an observable Y, the posterior distribution of Y can be calculated as

$$P(Y|\mathbf{c}) = \prod_{k=1}^{N} \int_{X_k^{min}}^{X_k^{max}} dX_k \, P(\mathbf{X}|\mathbf{c}) \delta\left(Y - Y(\mathbf{X})\right). \quad (3)$$

In Equation 3, $N = 13$ is the number of bulk parameters, $X_k^{\rm min(max)}$ is the parameter minimum (maximum) value chosen based on the current nuclear physics knowledge [14, 16], and $Y(\mathbf{X})$ is the value obtained with the parameter set $\mathbf{X}$ of the observable Y.

With the aim of studying the effects of different constraints on the nuclear-physics-informed prior, we present our results in four distributions as follows:

1. *Prior*: Models in the prior distribution are compatible with nuclear physics and represent the most general predictions within the nucleonic hypothesis. The weight of each parameter set $\mathbf{X}$ is determined by the quality of the optimization of the surface and curvature parameters to fit the nuclear masses in the AME2016 table [19].

2. *LD*: The information from ab-initio calculation is included. Particularly, models are selected by a pass-band filter which is the chiral EFT calculation for the energy per nucleon of symmetric matter and pure neutron matter in Ref. [20]. The filter is applied in the density interval $[0.02, 0.2]$ fm^{-3}.

3. *HD+LVC*: In this distribution, models are required to satisfy the following criteria: causality, thermodynamic stability, and non-negative symmetry energy at all densities. Then, the weight of each parameter set $\mathbf{X}$ is evaluated using two measurements: (1) mass measurement of PSR J0348+0432 [2], which is interpreted as a cumulative Gaussian distribution function with mean value $\mu = 2.01$ and standard deviation $\sigma = 0.04$, in the unit of $M_\odot$. This condition is used on the maximum NS mass obtained for each EoS; (2) joint distribution of tidal deformability and mass ratio inferred from the GW170817 by LVC as in Refs. [6, 21].

4. *All*: This includes the constraints mentioned above together with the likelihoods from the two mass-radius measurements from Refs. [8, 10]. This separation allows us to identify the effect from the new radius measurement of PSR J0740+6620 [10].

The model rejection (or acceptance) rate depends on the filter implemented. In each figure shown in the following section, similar statistics are used in the four distributions to make sure that the difference among them originate from the physical constraints. Moreover, the chosen statistics is checked to be sufficient so that convergence can be reached.

Results and Discussions

NS crustal and global properties

As we have shown in Ref. [18], the ab-initio nuclear physics calculation and the astrophysical data have distinct impacts on NS properties. To be more specific, the tightness of these constraints depends upon whether the crustal or global properties are considered.

For the crustal properties, Figure 1 displays the 68% confidence intervals (CI) of the NS crust thickness $R_{\rm crust}$ as a function of NS mass M in the prior and three posterior distributions. By construction, this quantity has a direct correlation to the location of the crust-core transition. In Ref. [18], it was shown that the chiral EFT calculation strictly constrains both the crust-core transition density, n_{CC}, and pressure, P_{CC}, while the

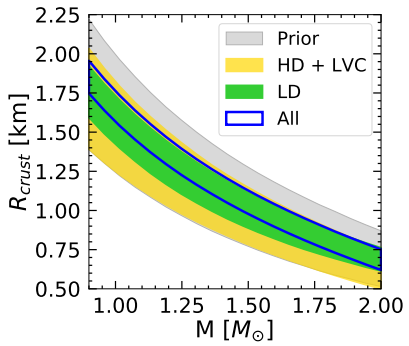

Figure 1: 68% confidence intervals of crustal thickness $R_{\rm crust}$ as a function of NS mass M in the four distributions: Prior (gray), HD+LVC (yellow), LD (green), and All (blue).

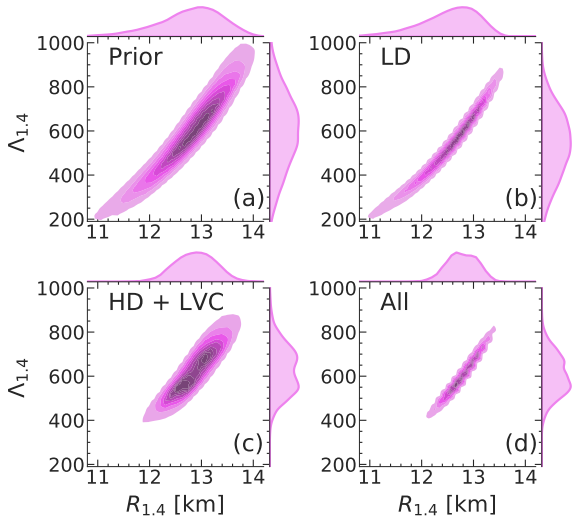

Figure 2: Joint probability density plots of NS dimensionless tidal deformability Λ and NS radius R at $M = 1.4M_\odot$ in the four distributions: Prior (panel **a**), LD (panel **b**), HD+LVC (panel **c**), and All (panel **d**).

astrophysical observations only disfavor very high P_{CC}. Therefore, we expect that the results of $R_{\rm crust}$ should reflect very similar effects. Indeed, as it can be seen in Figure 1, the 68% CI band in the "LD" distribution (green) is evidently thinner than the one in the "Prior" distribution (gray). On the other hand, in the "HD+LVC" distribution (yellow), only the upper limit of $R_{\rm crust}$ is impacted. As it was already pointed out in Ref. [18], these models which result in high $R_{\rm crust}$, or equivalently high P_{CC}, are associated to the violation of at least one of the following requirements: causality, thermodynamics stability, and non-negative symmetry energy. Accordingly, we can safely deduce that the constraints from GW170817 and the mass measurement of the heavy pulsar PSR J0348+0432 have negligible impacts on the crustal observables. When all the filters are combined together with the two NICER measurements (blue), we obtain a narrow band for the crust thickness, in which the effect from the chiral EFT calculation is dominant. The final relative uncertainties in the "All" distribution is up to $\sim 10\%$. The study of NS crustal properties is important because of the crust role in explaining pulsar phenomena, such as the "glitches" [22]. Thus, further constraints in the low-density region is of great relevance.

For the global properties, we plot in Figure 2 the joint distributions of NS dimensionless tidal deformability and radius at the canonical mass $M = 1.4M_\odot$, $\Lambda_{1.4}$ and $R_{1.4}$. In each panel, on the axes we display the marginalized probability density distributions of $\Lambda_{1.4}$ and $R_{1.4}$, while the plot in the center shows the correlation between them. From panel **b**, it is clear that the chiral EFT calculation constrains only slightly the upper limits of these two quantities. In addition, the correlation between $R_{1.4}$ and $\Lambda_{1.4}$ is enhanced in this case. In the "HD+LVC" distribution (panel **c**), the uncertainties in both $R_{1.4}$ and $\Lambda_{1.4}$ are significantly reduced. Specifically, the constraint from the GW170817 event prefers soft EoS, hence lowering the upper limit of $\Lambda_{1.4}$ and $R_{1.4}$. Contrarily, the NS mass measurement favors stiff EoS. Consequently, models resulting in very low $\Lambda_{1.4}$ and $R_{1.4}$ are eliminated. The combination of these two effects in the "HD+LVC" distribution, therefore, leads to narrow radius and tidal deformability distributions. Finally, when all constraints are put together (panel **d**), the correlation between the two quantities becomes even more well-defined, while the uncertainties remain roughly the same as in case of the "HD+LVC" distribution. This indicates that even for global properties of NS the results are insensitive to the constraints from the NICER mass-radius measurements. We will discuss this point more thoroughly in the next section. Concerning the correlation, in Ref. [18], we found the Pearson correlation coefficient between $R_{1.4}$ and $\Lambda_{1.4}$ to be 0.97, which is almost a perfect positive linear relationship. This linear correlation is also discussed in several works in literature [23, 24, 25, 26].

Comparison with NS observations from NICER and LVC

The validity of the nucleonic hypothesis can be checked by confronting the marginalized posteriors resulted from our Bayesian analysis with recent astrophysical observations.

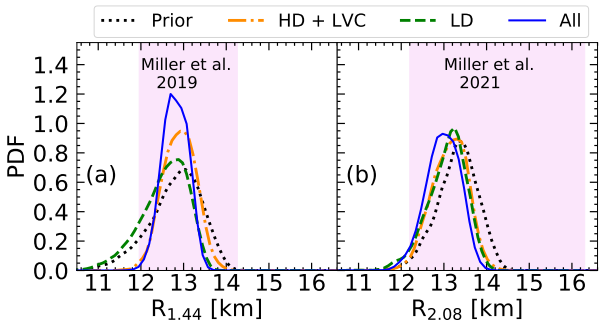

Figure 3: Probability density distributions of NS radii in the four distributions: Prior (black dotted lines), HD+LVC (orange dash-dotted lines), LD (green dashed lines), and All (blue solid lines). Panel **a**: $M = 1.44M_\odot$. The violet shaded rectangle shows radius measurement at 68% confidence interval of the pulsar PSR J0030+0451 by [8]. Panel **b**: $M = 2.08M_\odot$. The violet shaded rectangle shows the radius measurement at 68% confidence interval of the pulsar PSR J0740+6620 by [10].

Figure 3 displays the probability density distributions of NS radii at $M = 1.44M_\odot$ and $M = 2.08M_\odot$, which are respectively the masses (at median values) of pulsars PSR J0030+0451 [8] and PSR J0740+6620 [10]. Considering the first case (panel **a**), we can see that the "HD+LVC" distribution (dash-dotted orange line) is noticeably narrower than the "LD" distribution (dashed green line). This is similar to what we have discussed in Figure 2. As a result, the "All" distribution (blue solid line) is chiefly constrained by the NS mass and tidal deformability measurements from Refs. [2, 6]. On the other hand, in panel **b**, we do not observe noteworthy difference among the four distributions. This is because in this case all EoSs are required to be hard enough to support the mass $2.08M_\odot$. Consequently, the lower limits of $R_{2.08}$ in all distributions are strongly restricted as very soft EoSs are filtered out. Furthermore, this condition makes the requirement for the maximum NS mass in the "HD+LVC" distribution redundant. Therefore, the deviation between the "Prior" and the "HD+LVC" distributions appears mainly due to the constraint from GW170817 by LVC. Although the effects of the ab-initio nuclear physics calculation and the tidal deformability measurement on the upper limits of $R_{2.08}$ look similar (see the green dashed line and dash-dotted orange line in panel **b**), these two constraints dominate very different regions in NS properties. Particularly, the former governs the crust thickness, whereas the latter determines the global radius,

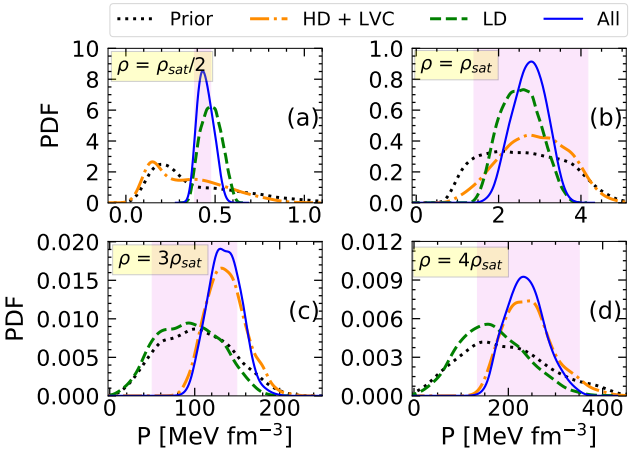

Figure 4: Probability density distributions of pressure in the four distributions at densities $\rho = \rho_{sat}/2$ (panel **a**), $\rho = \rho_{sat}$ (panel **b**), $\rho = 3\rho_{sat}$ (panel **c**), and $\rho = 4\rho_{sat}$ (panel **d**). The violet shaded rectangles display the corresponding pressure at 90% confidence interval inferred from the GW170817 event by Abbott et al. 2018 [5].

as we have already seen in Figures 1 and 2.

In both cases, our posterior distributions are in excellent agreement with the mass-radius measurements from Refs. [8, 10] (violet shaded rectangles). Here, the two referred results are presented at 68% CI. From the compatibility between our predictions and NICER measurements, we can infer that these dense matter observations can still be accounted for by the nucleonic EoS. Similar conclusions were made in Refs. [27, 28], where the authors computed the Bayes factors and found that the hadronic composition is favoured over the strong phase transition to quark matter. However, notice that this does not eliminate the possibility of having exotic degrees of freedom. In order to have a conclusive establishment in this regard, we need more stringent measurements.

In Figure 4, we plot the probability density distributions of pressure at four chosen densities: $\rho = \rho_{\rm sat}/2$ (panel **a**), $\rho = \rho_{\rm sat}$ (panel **b**), $\rho = 3\rho_{\rm sat}$ (panel **c**), and $\rho = 4\rho_{\rm sat}$ (panel **d**). As it is mentioned in the previous section, the prior distribution in our Bayesian analysis is generated in consistency with nuclear physics experiments and theory [14]. The prior marginalized distributions for pressure in Figure 4 are presented by black dotted lines. It is clear from the figure that our "Prior" distributions encompass the 90% CI inferred from GW170817 by LVC [5] (violet shaded rectangles). At low densities (panels **a** and **b**), the pressure is primarily constrained by the chiral EFT calculation (green dashed lines). On the contrary, at high densities, the pressure is mostly impacted by the constraints in the "HD+LVC" distributions (dash-dotted orange lines). These results show that the low-density part of the EoS is mainly influenced by nuclear physics inputs, whereas the high-density region is significantly constrained by

astrophysical data. By comparison with the posterior pressure obtained from LVC [5], we can conclude our final distributions (blue solid lines) are consistent with their results.

Last but not least, the similarity between the "HD+LVC" and "All" distributions also implies that the two NICER measurements does not have stringent impacts on the EoS and NS properties. This is due to the fact that the uncertainties from these measurements remains sizable. Additionally, these radius measurements almost entirely overlap our prior distributions (see Figure 1). These are the two factors for which the NICER measurements are not constraining.

Conclusion

To summarize, we have studied the impacts of different constraints from nuclear physics as well as astrophysical data on NS properties and nuclear matter EoS. Under the assumption that NS cores only consist of nucleons, we have carried out a Bayesian analysis using the meta-modeling technique with a nuclear-physics-informed prior. We have found that information from nuclear physics calculation tightly constrains the low-density parts of the EoS, hence controlling the crustal properties. Conversely, the high-density regions of the EoS, and therefore the global properties of NS, are more constrained by astrophysical data. Finally, we have shown that our results agree very well with both data from LVC and NICER. As a result, the nucleonic hypothesis cannot be ruled out.

References

[1] P. Haensel, A. Y. Potekhin, D. G. Yakovlev. Neutron Stars 1. Equation of state and structure. *Springer New York* **2007**.

[2] Antoniadis, J.; Freire, P. C. C.; Wex, N.; Tauris, T. M.; Lynch, R. S.; van Kerkwijk, M. H.; Kramer, M.; Bassa, C.; Dhillon, V. S.; Driebe, T.; et al. A Massive Pulsar in a Compact Relativistic Binary. *Science* **2013**, *340*, DOI: 10.1126/science.1233232.

[3] Fonseca, E.; Cromartie, H. T.; Pennucci, T. T.; Ray, P. S.; Kirichenko, A. Y.; Ransom, S. M.; Demorest, P. B.; Stairs, I. H.; Arzoumanian, Z.; Guillemot, L.; et al. Refined Mass and Geometric Measurements of the High-Mass PSR J0740+6620. *Astrophys. J. Lett.* **2021**, *915*, L12, DOI: 10.3847/2041-8213/ac03b8.

[4] Abbott, B. P.; Abbott, R.; Abbott, T. D.; Acernese, F.; Ackley, K.; Adams, C.; Adams, T.; Addesso, P.; Adhikari, R. X.; Adya, V. B.; et al. GW170817: Observation of Gravitational Waves from a Binary Neutron Star Inspiral. *Phys. Rev. Lett.* **2017**, *119*, 161101, DOI: 10.1103/PhysRevLett.119.161101.

[5] Abbott, B. P.; Abbott, R.; Abbott, T. D.; Acernese, F.; Ackley, K.; Adams, C.; Adams, T.; Addesso, P.; Adhikari, R. X.; Adya, V. B.; et al. GW170817: Measurements of Neutron Star Radii and Equation of State. *Phys. Rev. Lett.* **2018**, *121*, 161101, DOI: 10.1103/PhysRevLett.121.161101.

[6] Abbott, B. P.; Abbott, R.; Abbott, T. D.; Acernese, F.; Ackley, K.; Adams, C.; Adams, T.; Addesso, P.; Adhikari, R. X.; Adya, V. B.; et al. Properties of the Binary Neutron Star Merger GW170817. *Phys. Rev. X* **2019**, *9*, 011001, DOI: 10.1103/PhysRevX.9.011001

[7] Riley, T. E.; Watts, A. L.; Bogdanov, S.; Ray, P. S.; Ludlam, R. M.; Guillot, S.; Arzoumanian, Z.; Baker, C. L.; Bilous, A. V.; Chakrabarty, D.; et al. A NICER View of PSR J0030+0451: Millisecond Pulsar Parameter Estimation. *Astrophys. J. Lett.* **2019**, *887*, L21, DOI: 10.3847/2041-8213/ab481c.

[8] Miller, M. C.; Lamb, F. K.; Dittmann, A. J.; Bogdanov, S.; Arzoumanian, Z.; Gendreau, K. C.; Guillot, S.; Harding, A. K.; Ho, W. C. G.; Lattimer, J. M.; et al. PSR J0030+0451 Mass and Radius from NICER Data and Implications for the Properties of Neutron Star Matter. *Astrophys. J. Lett.* **2019**, *887*, L24, DOI: 10.3847/2041-8213/ab50c5.

[9] Riley, T. E.; Watts, A. L.; Ray, P. S.; Bogdanov, S.; Guillot, S.; Morsink, S. M.; Bilous, A. V.; Arzoumanian, Z.; Choudhury, D.; Deneva, J. S.; et al. A NICER View of the Massive Pulsar PSR J0740+6620 Informed by Radio Timing and XMM-Newton Spectroscopy. **2021**, arXiv: 2105.06980.

[10] Miller, M. C.; Lamb, F. K.; Dittmann, A. J.; Bogdanov, S.; Arzoumanian, Z.; Gendreau, K. C.; Guillot, S.; Ho, W. C. G.; Lattimer, J. M.; Loewenstein, M.; et al. The Radius of PSR J0740+6620 from NICER and XMM-Newton Data. **2021**, arXiv: 2105.06979.

[11] Hartle, J. B. Slowly Rotating Relativistic Stars. 1. Equations of Structure. *Astrophys. J.* **1967**, *150*, 1005–1029.

[12] Abbott, B. P.; Abbott, R.; Abbott, T. D.; Acernese, F.; Ackley, K.; Adams, C.; Adams, T.; Addesso, P.; Adhikari, R. X.; Adya, V. B.; et al. Prospects for observing and localizing gravitational-wave transients with Advanced LIGO, Advanced Virgo and KAGRA. *Living Rev Relativ* **2020**, *23*, DOI:10.1007/s41114-020-00026-9

[13] Oertel, M.; Hempel, M.; Klahn, T.; Typel, S. Equations of State for Supernovae and Compact Stars. *Rev. Mod. Phys.* **2017**, *89*, 015007, DOI: 10.1103/RevModPhys.89.015007.

[14] Margueron, J.; Hoffmann Casali, R.; Gulminelli, F. Equation of State for Dense Nucleonic Matter from Metamodeling. I. Foundational Aspects. *Phys. Rev. C* **2018**, *97*, 025805, DOI: 10.1103/PhysRevC.97.025805.

[15] Margueron, J.; Hoffmann Casali, R.; Gulminelli, F. Equation of State for Dense Nucleonic Matter from Metamodeling. II. Predictions for Neutron Star Properties. *Phys. Rev. C* **2018**, *97*, 025806, DOI: 10.1103/PhysRevC.97.025806.

[16] Carreau, T.; Gulminelli, F.; Margueron, J. Bayesian Analysis of the Crust-Core Transition with a Compressible Liquid-Drop Model. *Eur. Phys. J. A* **2019**, *55*, 188, DOI: 10.1140/epja/i2019-12884-1.

[17] Dinh Thi, H.; Carreau, T.; Fantina, A. F.; Gulminelli, F. Uncertainties in the Pasta-Phase Properties in Catalysed Neutron Stars. *Astron. Astrophys.* **2021**, *654*, A114, DOI: 10.1051/0004-6361/202141192.

[18] Dinh Thi, H.; Mondal, C.; Gulminelli, F. The Nuclear Matter Density Functional under the Nucleonic Hypothesis. *Universe* **2021**, *7*, 373, DOI: https://doi.org/10.3390/universe7100373

[19] Huang, W. J.; Audi, G.; Wang, M.; Kondev, F. G.; Naimi, S.; Xu, X. The AME2016 Atomic Mass Evaluation (I). Evaluation of Input Data; and Adjustment Procedures. *Chinese Phys. C* **2017**, *41*, 030002, DOI: 10.1088/1674-1137/41/3/030002.

[20] Drischler, C.; Hebeler, K.; Schwenk, A. Asymmetric Nuclear Matter Based on Chiral Two- and Three-Nucleon Interactions. *Phys. Rev. C* **2016**, *93*, 054314, DOI: 10.1103/PhysRevC.93.054314.

[21] LIGO Document P1800370-v5: Parameter estimation sample release for GWTC-1, DOI: https://doi.org/10.7935/KSX7-QQ51.

[22] Espinoza, C. M.; Lyne, A. G.; Stappers, B. W.; Kramer, M. A Study of 315 Glitches in the Rotation of 102 Pulsars. *Mon. Not. R. Astron. Soc.* **2011**, *414*, 1679–1704, DOI: 10.1111/j.1365-2966.2011.18503.x.

[23] Malik, T.; Alam, N.; Fortin, M.; ProvidÃªncia, C.; Agrawal, B. K.; Jha, T. K.; Kumar, B.; Patra, S. K. GW170817: Constraining the Nuclear Matter Equation of State from the Neutron Star Tidal Deformability. *Phys. Rev. C* **2018**, *98*, 035804, DOI: 10.1103/PhysRevC.98.035804.

[24] Fattoyev, F. J.; Piekarewicz, J.; Horowitz, C. J. Neutron Skins and Neutron Stars in the Multimessenger Era. *Phys. Rev. Lett.* **2018**, *120*, 172702, DOI: 10.1103/PhysRevLett.120.172702.

[25] Annala, E.; Gorda, T.; Kurkela, A.; Vuorinen, A. Gravitational-Wave Constraints on the Neutron-Star-Matter Equation of State. *Phys. Rev. Lett.* **2018**, *120*, 172703, DOI: 10.1103/PhysRevLett.120.172703.

[26] Lourenco, O.; Dutra, M.; Lenzi, C. H.; Flores, C. V.; Menezes, D. P. Consistent Relativistic Mean-Field Models Constrained by GW170817. *Phys. Rev. C* **2019**, *99*, 045202, DOI: 10.1103/PhysRevC.99.045202.

[27] Pang, P. T. H.; Tews, I.; Coughlin, M. W.; Bulla, M.; Broeck, C. Van Den; Dietrich, T. Nuclear-Physics Multi-Messenger Astrophysics Constraints on the Neutron-Star Equation of State: Adding NICER's PSR J0740+6620 Measurement. **2021**, arXiv: 2105.08688.

[28] Legred, I.; Chatziioannou, K.; Essick, R.; Han, S.; Landry, P. Impact of the PSR J0740+6620 Radius Constraint on the Properties of High-Density Matter. **2021**, arXiv: 2106.05313.

Development of enriched gadolinium targets for the measurement of cross sections of radioactive terbium production for medical applications

Yizheng WANG

SUBATECH, UMR 6457, IMT Atlantique, CNRS/IN2P3, Université de Nantes, France

Abstract — short-lived radioisotopes of Terbium family show great prospects in theranostics nuclear medicine. Nevertheless, its application is limited due to its insufficient production and high cost. To increase its availability, the scheme of producing Tb from Gd-enriched targets induced by light particles is considered in this work. Ni/Gd_2O_3 composite targets have been developed via the electrochemical co-deposition method.Uniform targets were manufactured with a thin thickness (10-20 μm) and a sufficient Gd content (up to 2.64 mg) for cross section measurement.Targets made by natural Gd_2O_3 were irradiated at GIP ARRONAX with deuteron beams (10 - 30 MeV). Cross section values measured through the stacked foils technique show a great consistency with the reference values in literature, which confirms the possibility of using enriched Gadolinium in the next step of work.

Introduction

Nuclear medicine is a branch of medicine that uses radionuclides or radiopharmaceuticals to diagnose and treat cancer cells, has been developed for decades. In recent years, a new paradigm called theranostics has emerged. It consists of coupling a given vector with different isotopes (one for imaging, another one for treatment purpose) to personalize radiopharmaceutical treatment and to monitor the early results of the treatment [1-3].

Ideally, theranostics should use radionuclides from the same chemical element to keep the same chemical properties. Isotopes from Terbium family meet this expectation [4-7]: ^{149}Tb can be used for alpha therapy, ^{152}Tb as a positron emitter can be used for positron emission tomography (PET), ^{155}Tb can be used for single photon emission tomography (SPECT) and for Auger therapy and finally ^{161}Tb can be used for beta therapy. ^{155}Tb can be used for both diagnosis and treatment and is a good example of theranoistics element[5]. At present, except for ^{161}Tb, the production of other radionuclides is mainly done through high-energy spallation reaction followed by a mass separation process [7]. Due to the low separation efficiency (1%) [7] and equipment scarcity, the production has a low production yield and high cost. Limited by its insufficient production, the application of Terbium is still a challenge.

This work proposes an alternative to use the enriched Gadolinium targets to increase the availability of Terbium according to the following reactions: ^{154}Gd (p,6n) ^{149}Tb [8], ^{152}Gd (p,n) ^{152}Tb [9] and ^{155}Gd (d,2n) ^{155}Tb [9].The energy of these light particle-induced reactions is relatively low (10 – 30 MeV), which is feasible for many biomedical accelerators. Moreover, impurity problems can be avoid by limiting the energy to a certain range.To estimate the production yield, cross sections of these reactions must be measured at the first time.

The objective of this work is to develop high quality and thin thickness ($< 20\ \mu m$) targets containing gadolinium oxide, Gd_2O_3, and to measure the production cross sections of Tb from these targets. Gd_2O_3 has been selected in this experiment because the enriched ^{155}Gd is available easily in this form. Due to the high cost of enriched gadolinium, natural gadolinium was first chosen to achieve the proof of concept of our strategy.

Target preparation

To measure production cross sections of nuclear reactions as a funciton of energy, the thickness of the targets should be limited to 20 μm to limit energy spread in thin target. Electrodeposition is a simple and efficient method of making thin nuclear targets. However, due to low reduction potential of Gd^{3+}/Gd (E = -2.28 V/SHE in acid solution [10]), good adherence Gd deposits in aqueous solutions are unattainable under hydrogen evolution reaction.

The electrochemical co-deposition method was therefore used in this work to mechanically embed gadolinium particles in a Ni matrix. Working in a Gd_2O_3-Ni electrolyte mixed bath, the principle of this method is to physically trap the insoluble Gd_2O_3 to the growing deposited Ni layer. Nickel has been selected because of it is well studied electroplating properties and it can be done in basic conditions where Gd_2O_3 stays insoluble. Inspired by the conception of SKITAL PM. et al [11], the Ni electrolyte was prepared as: 0.5

mol/L $(NH_4)_2SO_4$ + 0.5 mol/L NH_4Cl + 0.14 mol/L $NiSO_4{\cdot}6H_2O$ + 1 mol/L NH_3. The pH of the solution was adjusted by NaOH to fixe it at 9.8. Schematic diagram of experimental device used in our work is shown in Figure 1. Applied potential of expriment was -1.2 V/NHE, stirring speed was 300 rpm. For each target, 6.5 g of Gd_2O_3 was added at the beginning of the deposition.

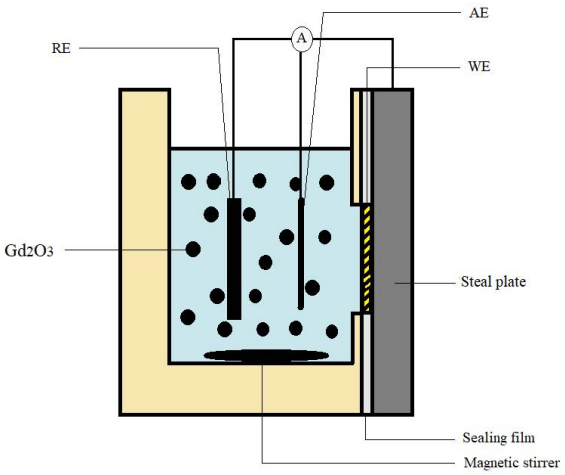

Figure 1: Schematic diagram of cell structure and electrodes positions used in our experiments: The cell contains 35 mL electrolyte solution. WE refers to the working electrode, AE to the auxiliary electrode, RE to the reference electrode. During the process, a magnetic stirring, a sealing film and a stainless steel plate are also used. Suspended Gd_2O_3 particles (black dots) were evenly distributed in the electrolyte thanks to the stirring. The schematic diagram is not drawn according to the actual scale.

Six composite Ni/Gd_2O_3 targets was deposited on gold foil of thickness equal to 50 μm. The thickness of these deposits were ranging from 13 to 18 μm for 60 min when 60 min duration of deposition was used and 3 μm when only 10 min duration of deposition was used. Morphology analysis ferformed by scanning electron microscope (SEM) shows a uniform distribution of Gd_2O_3 on the surface of the deposit (Figure 2).

These targets were irradiated for cross section measurements. After irradiation, targets were dissolved in 10 mL of 12 mol/L HCl for 4 hrs at room temperature. For each target, the dissolved solution was used for the activity measurement (section 3.1) and chemical composition analysis. The chemical composition was analyzed by Inductively Coupled Plasma - Atomic Emission Spectroscopy (ICP-AES). 0.4 to 2.64 mg Gd was trapped in deposits according to ICP-AES results depending on achieved Gd_2O_3 thickness.

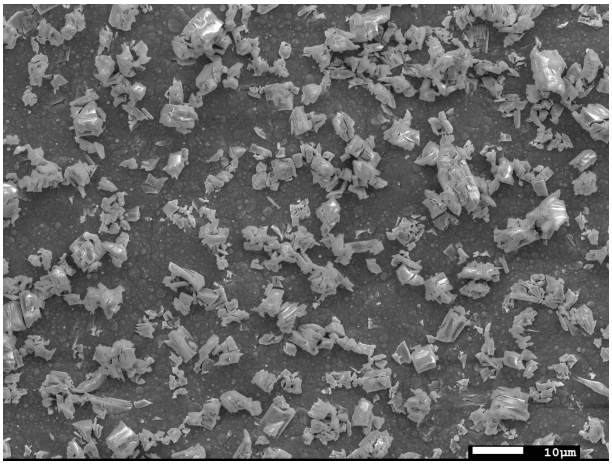

Figure 2: Microscopic images of surface morphology of the deposits.

Cross section measurements

Irradiation condition

The irradiation process was carried out at the ARRONAX cyclotron. The cyclotron can accelerate both positive ions $\left(HH^+, He^{++}\right)$and negative ions $(H^-, D^-)$with an energy up to 70 MeV for protons and alpha particles and an energy up to 34MeV for deuterons. The Stackedfoil technique [12] was used in this experiment to measure the cross section. This technique allows measuring several cross sections values at different energies simultaneously by using several thin foils. The stack assembly was composed of by Ni/Gd_2O_3 targets titanium and nickel foils as monitors and aluminum foils as degraders. Four irradiation experiments was performed for these 6 targets, the schematic diagram of one experiment (for target 4 and target 6) is illustrated in Figure 3. Foils were placed in air 6 cm from the end of the beam window made of 50μm thick Kapton foil. Targets were irradiated by deuterons with an energy range from 8MeV to 30MeV for 60 min. The choice of energies is based on a theoretical study of the ^{nat}Gd (n,x) ^{155}Tb reaction. The precise value of energy determined in the middle of each foil was obtained using the SRIM software [13], assuming that the target was composed uniformly by Gd, O and Ni, and its density was determined according to ICP-AES analysis results. The energy uncertainty is considered as the sum of beam energy uncertainty ($\pm$0.25MeV) and energy straggling.

Determination of activities

An HPGe semiconductor detector was used to detect γ rays of ^{155} Tb and ^{160} Tb produced by targets, ^{48} V produced by titanium monitors and $^{58(\ m)}$Co produced by nickel monitors. Decay data of these radionuclides are presented in Table 1. As indicated in Table 1 , among the different gamma ray emitted by ^{155} Tb we have chosen to follow the 180.08keV gamma line. This gamma line is close to that emitted by $^{198\ m}$Au $\left(T_{1/2} =\right.$

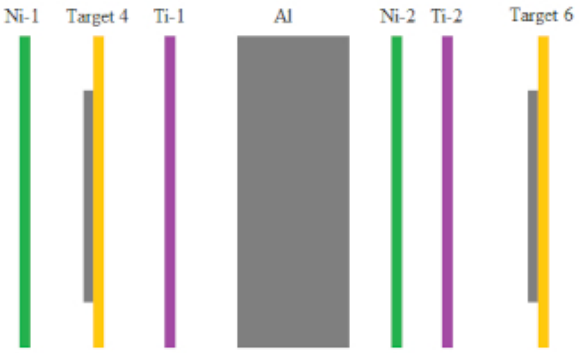

Figure 3: Schematic diagram of the stack composition used for the experiment where we irradiated target n°4 and n°6. The size and thickness of the foils arenet drawn according to the actual scale.

2.272 d, E = 180.31keV, Iγ = 0.04%) produced by the gold substrate. This is the reason why the target should be dissolved after irradiation to separate the deposit and the gold substrate. For the detection of ^{155} Tb, 5 mL of dissolved liquid sample was measured 2 days after EOB at contact ant at 19 cm from the detector. For the detection of ^{160} Tb, the same sample Was measured 2 months after EOB at contact with the detector. Concerning monitors, solid titanium monitor foils were measured by the same detector 21 days after EOB [16] to allow the full decay of ^{48}Sc ($T_{1/2}$ = 43.67 h, E = 983.526keV, Iγ = 100.1%) and avoid interferences with ^{48}V decay. Similarly, solid nickel monitor foils Jwere measured 2 months after EOB [17] to avoid interferences of ^{56}Ni $\left(T_{1/2} = 6.075 \text{ d}, E = 811.85\text{keV}, I\gamma = 86.0\%\right)$ with our monitor reaction. The distance between the solid sample and the detector was 19 cm. Liquid samples were counted for 8 hrs (^{155} Tb) or 48 hrs (^{160} Tb) while monitor foil were counted for 24 hrs. The dead time for counting was always below 5%. The Fitzpeak software [18] has been used to determine the EOB activity. Energy and efficiency calibrations were carried out with a multi-gamma liquid source and a ^{152}Eu sealed source in the same geometry as the irradiated samples.

Table 1 Decay data of detected radionuclides.

Radionuclide	Half-life (d)	E_γ (keV)	I_γ (%)
^{155} Tb	5.32(6)	180.08	7.5(4)
		298.5783(17)	26.1(6)
^{160} Tb	72.3(2)	879.378(2)	30.1(6)
		966.166(2)	25.1(5)
^{48} V	15.9735(25)	983.525	99.98(4)
$^{58(\text{ m})}$ Co	70.86(6)	810.7593(20)	99.450

Cross section calculation

Since the Gd_2O_3 particles are uniformly distributed in the composite targets, the produced cross sections at energy $E, \sigma(E)$(mb), can be calculated according to Eq. (1):

$$\sigma(E) = \frac{\text{Act}(E) \cdot S}{\phi \cdot N \cdot (1 - e^{-\lambda t})}$$

Where Act(E) (Bq) is the activity of production radionuclide at energy E, S (mb) is deposit surface, ϕ (particles s^{-1}) is the projectile flux of the target, N is the number of Gd atoms, λ (s^{-1}) is the decay constant of production radionuclide and finally t is the irradiation time. The surface was obtained by counting pixel values after scanning the deposit. The Gd atomic number was calculated according to ICP-AES results obtained for each sample.

The projectile flux ϕ of the target was calculated by the flux of monitors. For Titanium or Nickel monitors, using Eq (1) the projectile flux ϕ' of monitor foils can be determined by using the cross section $\sigma'(E')$ of the reaction ^{nat}Ti (d,x) ^{48}V or the reaction ^{nat}Ni (d,x) $^{58(m)}$Co respectively. The monitor atomic number N' was obtained by their mass, their atomic mass and the Avogadro constant. The average value of monitors flux ϕ'' was then determined as the mean flux value calculated from the two monitor reactions. Since monitor foils have the same area as targets and are located just behind the target foils, ϕ'' is considered equal to ϕ. It can be deduced Eq. (2).

$$\sigma(E) = \frac{\text{Act}(E) \cdot S}{\phi'' \cdot N \cdot (1 - e^{-\lambda t})}$$

Since all parameters in Eq. (2) are independent, estimation of cross section uncertainties is based on combined standard uncertainty, as the positive square root of the summation of squares of each parameter (Eq.(3)).

$$\frac{\Delta\sigma(E)}{\sigma(\text{E})} =$$

$$\sqrt{\left(\frac{\Delta\,\text{Act}(E)}{\text{Act(E)}}\right)^2 + \left(\frac{\Delta\phi''(E)}{\phi''(\text{E})}\right)^2 + \left(\frac{\Delta\text{S}}{\text{S}}\right)^2 + \left(\frac{\Delta\text{N}(E)}{\text{N(E)}}\right)^2}$$

measured cross section values

The Gd content in each target, their projectile energy and the cross section values of produced ^{155} Tb and ^{160} Tb arelisted in Table 2 . For target n°2, the deposition time was only 10 min, while for other targets the deposition time was 60 min. This is the reason why target n°2 only contains 0.39mg Gd while other targets contain 1.84−2.64mg Gd. However, the cross section of ^{155} Tb and ^{160} Tb produced from target n°2 were successfully measured, and the uncertainty values are still acceptable (16.92% for ^{155} Tb and 16.89% for ^{160} Tb). This indicates that using the method presented in this work, the reaction cross section values can be efficiently obtained even with a small Gd content. This gives us the possibility to adapt the Gd_2O_3 loading of the electrolyte, which is beneficial for future work on enriched $^{155}Gd_2O_3$ from the point of view of cost-saving.

Table 2 Targets information and cross section values

N°	Gd mass (mg)	Energy (MeV)	σ ^{155}Tb	σ ^{160}Tb
1	2.64	10.35 ± 0.58	20.11 ± 2.11	120.78 ± 24.09
2	0.39	13.23 ± 0.46	87.79 ± 14.86	120.44 ± 20.35
3	2.55	19.52 ± 0.55	193.89 ± 19.55	28.19 ± 6.05
4	2.30	19.78 ± 0.30	335.65 ± 84.84	54.88 ± 5.82
5	1.84	23.90 ± 0.49	329.41 ± 30.21	28.79 ± 3.60
6	2.50	29.53 ± 0.32	306.84 ± 31.17	14.73 ± 3.22

The comparison of measured ^{155}Tb cross section values and existing data in publications [19][20][21] is shown in Figure 4. Most of the measurement results are consistent with the existing data, and the error values are also similar, except for target n° 4. For target n° 4, the measurement result value is too large and so does the uncertainty value. This can be due to the fact that this target is the only one that was counted at 19 cm. Due to the long distance from the detector, the statistical data is insufficient.

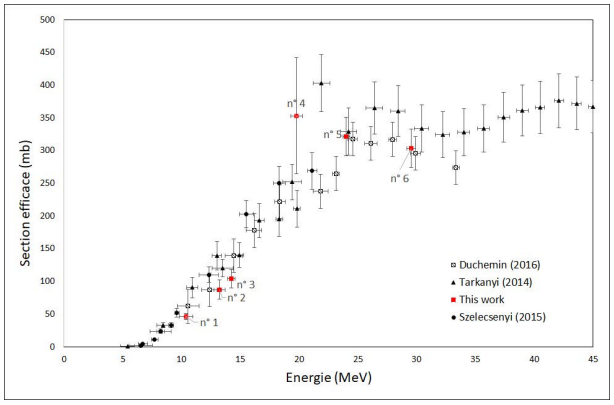

Figure 4: ^{nat} Gd(d, x)^{155}Tb cross section

Figure 5 shows the comparison of measured ^{160}Tb cross section values and the existing data of C.Duchemin[19] and F.Tarkanyi[21]. Our measured values and uncertainties are closer to the results of C.Duchemin.

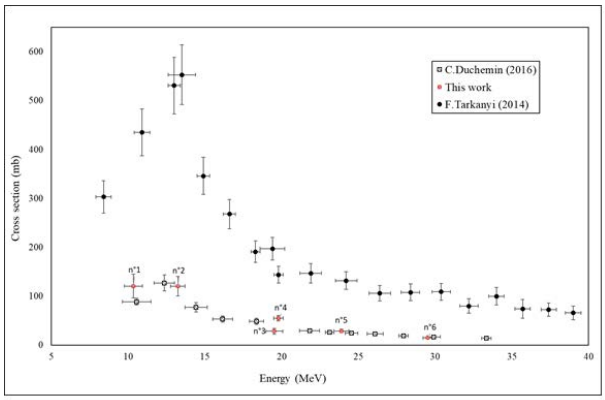

Figure 5: ^{nat}Gd(d, x)^{160}Tb cross section

Conclusions

In this study, thin Ni/Gd_2O_3 composite targets have been developed by the electrochemical method. The Gd content in the target can reach up to 2.6mg in our electroplating conditions. Using these targets, cross sections of ^{155}Tb and ^{160}Tb were measured using ^{nat}Gd to validate the whole process for cross section measurements. Most of the measured values are consistent with data from the literature. On the one hand, this work has completed the existing work of the measurement of ^{nat}Gd(d, x)^{155}Tb and ^{nat}Gd(d, x)^{160}Tb. On the other hand, this work confirms the feasibility of cross section measurement through composite targets and indicates the possibility to produce enriched gadolinium targets for the cross section measurements. In addition, this work also opens the possibility to use this technique for thin target preparation for cross section measurements when electroplating is difficult.

References

[1] Kelkar S S, Reineke T M. Theranostics: combining imaging and therapy[J]. Bioconjugate chemistry, 2011, 22(10): 1879-1903.

[2] Chen, X., Wong, S. (Eds.). (2014). Cancer theranostics. Academic Press.

[3] Cleeren F. Theranostics studies using 152/149Tb-labeled anti-CXCR4 probes in tumor mice[R]. 2021.

[4] Cavaier R F, Haddad F, Sounalet T, et al. Terbium radionuclides for theranostics applications: a focus on MEDICIS-PROMED[J]. Physics Procedia, 2017, 90: 157-163.

[5] Müller C, Fischer E, Behe M, et al. Future prospects for SPECT imaging using the radiolanthanide terbium-155 production and preclinical evaluation in tumor-bearing mice[J]. Nuclear medicine and biology, 2014, 41: e58-e65.

[6] Müller C, Zhernosekov K, Köster U, et al. A unique matched quadruplet of terbium radioisotopes for PET and SPECT and for α -and β - radionuclide therapy: an in vivo proof-of-concept study with a new receptor-targeted folate derivative[J]. Journal of nuclear medicine, 2012, 53(12): 1951-1959.

[7] Naskar N, Lahiri S. Theranostic terbium radioisotopes: challenges in production for clinical application[J]. Frontiers in Medicine, 2021, 8.

[8] Steyn, G. F., Vermeulen, C., Szelecsényi, F.,et al. Cross sections of proton-induced reactions on 152Gd, 155Gd and 159Tb with emphasis on the production of selected Tb radionuclides. Nuclear Instruments and Methods in Physics Research Section B: Beam Interactions with Materials and Atoms, 2014, 319, 128-140.

[9] Güray R T, Özkan N, Yalcin C, et al. Measurements of Gd 152 (p, γ) Tb153 and Gd 152 (p, n) Tb 152 reaction cross sections for the astrophysical γ process[J]. Physical Review C, 2015, 91(5): 055809.

[10] CRC handbook of chemistry and physics[M]. CRC press, 2004.

[11] SKITAL P M, SANECKI P T, Saletnik D, et al. Electrodeposition of nickel from alkaline NH_4OH/NH_4Cl buffer solutions [J]. Transactions of Nonferrous Metals Society of China, 2019, 29(1): 222-232.

[12] Blessing G, Bräutigam W, Böge H G, et al. Internal irradiation system for excitation function measurement via the stacked-foil technique[J]. Applied radiation and isotopes, 1995, 46(9): 955-960.

[13] Ziegler J F, Ziegler M D, Biersack J P. SRIM - The stopping and range of ions in matter (2010)[J]. Nuclear Instruments and Methods in Physics Research Section B: Beam Interactions with Materials and Atoms, 2010, 268(11-12): 1818-1823.

[14] Hermanne A, Ignatyuk A V, Capote R, et al. Reference cross sections for charged-particle monitor reactions[J]. Nuclear Data Sheets, 2018, 148: 338-382.

[15] Amjed N, Tárkányi F, Ditrói F, et al. Activation cross-sections of deuteron induced reaction of natural Ni up to 40 MeV [J]. Applied Radiation and Isotopes, 2013, 82: 87-99.

[16] Nigron, Etienne. Isotopes radioactifs produits par voies non conventionnelles. Diss. Université de Nantes-Faculté des Sciences et Techniques, 2019.

[17] Hermanne A, Takacs S, Adam-Rebeles R, et al. New measurements and evaluation of database for deuteron induced reaction on Ni up to 50 MeV[J]. Nuclear Instruments and Methods in Physics Research Section B: Beam Interactions with Materials and Atoms, 2013, 299: 8-23.

[18] Fitzgerald J et al. (2009) FitzPeaks gamma analysis and calibration software, http://www.jimfitz.demon.co.uk/fitzpeak.htm

[19] Duchemin C., Guertin A., Haddad, F., Michel N., Metivier V. (2016). Deuteron induced Tb155 production, a theranostic isotope for SPECT imaging and auger therapy. Applied Radiation and Isotopes, 118, 281-289.

[20] Szelecsényi F, Kovács Z, Nagatsu K, et al. Investigation of deuteron - induced reactions on natGd up to 30 MeV: possibility of production of medically relevant 155Tb and 161Tb radioisotopes [J]. Journal of Radioanalytical and Nuclear Chemistry, 2016, 307(3): 1877-1881.

[21] Tárkányi F, Takacs S, Ditroi F, et al. Activation cross-sections of deuteron induced reactions on natGd up to 50 MeV [J]. Applied Radiation and Isotopes, 2014, 83: 25-35.

Development of laser ionization technique coupled with mass separation for environmental and medical applications: Copper as a case study

Keerthana KAMALAKANNAN

SUBATECH, UMR 6457, 4 rue Alfred Kastler BP20722, 44307 Nantes Cedex 3 France

Abstract — A new mass separator called SMILES (Sèparation en Masse couplée à l'Ionisation Laser pour des applications Environnementales et en Santé) is being developed in SUBATECH laboratory in order to quantify, purify and separate isotopes not only for environmental but also for medical purposes. Copper is among the isotopes of interest as its isotopic composition allows to evaluate the anthropogenic source of pollution in environment. Besides, ^{64}Cu and ^{67}Cu are emerging as potential diagnostic and therapeutic tools in nuclear medicine. Resonance Ionization Mass Spectrometry (RIMS) is based on resonance laser matter interaction where resonant excitation and subsequent ionization of atoms is done using tunable lasers that is followed by a conventional spectrometry. SIMION software is used to study the ion trajectories in electromagnetic fields and to optimize mass separator parameters. RISIKO mass separator (University of Mainz, Germany) that uses dipole magnets for mass separation and Time of flight (TOF) analyser were simulated for copper ions separation, which will aide in the configuration of SMILES set up.

Introduction

A variety of laser based applications has been developed in different fields of science ever since its invention in 1960s. Among them is the mass spectroscopy. A wavelength tunable laser radiation can selectivity excite quantum transitions in atoms and molecules. A majority of laser spectroscopy methods are based on this resonance laser matter interaction [1] often referred as RIMS. Laser resonance ionization is selective according to number of charge Z even for chemically similar element like lanthanides or actinides, while the application of an electromagnetic field ensures the separation of the isotopes according to their number of mass A. This combination allows to isolate isotope with a high precision avoiding its isobars. Presently the areas of applications of mass spectrometry is diverse such as medicine, biology, pharmacology, industrial chemistry, food processing industry, nuclear science, environment, geology etc [2]. In SUBATECH and in GIP ARRONAX (Nantes), the SMILES mass separator will be used in the purification of rare isotopes, analytical measurements of radiotoxic isotopes, production of radioisotopes for medical purposes, etc. Since SMILES is in its initial stage, all possibilities are considered to achieve the mass separation. The main components that are involved in SMILES project include ionization system, beam focusing system and mass separator. The ionization can be achieved using hot cavity or laser desorption ionization method. The ions are then focused using a set of beam focusing lenses and deflectors. Finally, the mass separation can be achieved either by using an electromagnet or a time of flight mass separator (TOF MS). Simulations were made in SIMION software to study the ion trajectories and to optimize different parameters [3][4].

Key components of SMILES set up

The first key component is the laser ion source, which has very high ionization efficiency, it can be associated to a hot cavity source or a laser desorption source. In hot cavity ion source, the elements are excited/ vaporized by providing heat and then the free atoms are ionized using suitable laser, whereas in laser desorption ionization method, both vaporization and ionization are achieved using lasers. The laser system needs to be able to adapt to diverse requirement of different experiments such as element selectivity, ionization rate, spectral resolutions, etc. To ionize an element with laser, first we need to understand its excitation spectrum and ionization scheme, which are unique for each element. Precisely tuned laser are absorbed by the atoms of interest and are resonantly excited to undergo optical transitions. Then at final transition step, ionization of atoms occur. It can be based on non resonant ionization, a transition to auto ionizing state, or ionization via population of Rydberg states close to ionization potential (IP) [5].

The second key component is the mass separator. Electromagnets can be used to separate the mass as

well as to analyse it. A magnetic field is applied that separates the isotopes according to their mass. The applied magnetic field is proportional to $\sqrt{m}$ and related by equating the Lorentz force and the force due to acceleration, B (gauss) = $\sqrt{2mE}/qR$; where, m = mass of ion (kg), E = energy of ion (J), q = charge of ion (C), R = radium of curvature (m). The radius of curvature at which an ion bends under the magnetic field depends on the field applied and it increases with increasing mass. Thus, the mass are separated and can be selected using a slit and collected using a Faraday cup or a collection chamber. TOF mass spectrometry is another way of separating mass based on m/q ratio by time of flight. The linear time of flight of an ion is proportional to its $\sqrt{m/q}$ ratio and it is given by the formula; t = $\sqrt{(m/q)(1/2ES)}(S+D)$; where t = time of flight (s), m = mass of ion (kg), q = charge of ion (C), E = electric field (N/C), S = acceleration region (m) and D = field free region (m). In TOF analyzer, the ions are accelerated by applying a potential difference and travel through a field free region before it reaches the detector.

SIMION software

SIMION is an ion optics simulation software that is used to optimize electric and magnetic fields, calculate particle trajectories for a defined geometry with electrode potentials and initial particle conditions. The software is programmable that allows its users to extend its applications in novel ways. The geometry of each component can be simulated either directly or using a program in lua language which is directly embedded in SIMION. Lua can also call for programs in C/C++ or python. In SIMION each geometry is created in 2D or 3D potential array (PA) and a PA can contain up to billions of grid points. The size and potential of each grid point can be altered according to our needs. Small array solves in minutes whereas a large array could take hours depending on its conditions. PAs with different grid densities can be placed in a single "workbench" that allows us to position, size and orient them. This allows the simulation of larger geometries that cannot fit in one PA. A grid point for which potential is defined, is called an occupied or electrode point. The potentials in the space between the electrodes are determined by solving Lorentz equation, $\vec{F} = q\vec{E} + q\vec{v} \wedge \vec{B}$ where $\vec{F}$ (N) is the electromagnetic force or the Lorentz force exerted on a charged particle q (C) moving with velocity $\vec{v}$ (m/s) through an electric field $\vec{E}$ (N/C) and magnetic field $\vec{B}$ (T). SIMION solves the Lorentz equation using finite differential Laplace iteration method. This process is called "refining" of PA. Ions are then flown within the workbench volume, their trajectories are calculated by Runge-Kutta method. The results can be documented allowing us to study kinetic energy dispersion, spatial distribution, emission of ions, etc. Before proceeding with the simulations, simple tests were made to understand mirroring effects of geometry on the size of PA and the effects of superimposition of electric and magnetic fields on the ion trajectory. Mirroring reduces the size of PA significantly but it works best when the symmetrical geometries having same potentials. While studying the superimposition effects of different fields, it was observed that the software recognizes only one PA when 2 different PAs containing only electric fields were superimposed. It is because all electric field boundary conditions has to be taken into account to Solve the Lorentz equation but SIMION considers only the 1st condition. However, it recognizes both the PAs when electric and magnetic fields were superimposed.

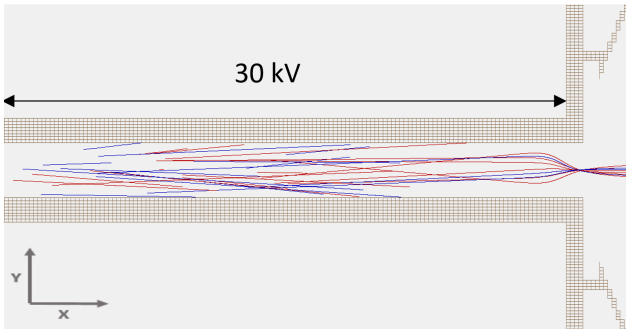

Figure 1: Ion confinement inside the source of RISIKO (50 ions) blue: ^{63}Cu and red: ^{65}Cu

Simulation studies

To better understand the parameters required for SMILES configuration, the RISIKO mass separator situated in University of Mainz has been simulated. In RISIKO, a hot cavity ion source is used in which a suitable laser beam is introduced to ionize the free atoms. The ion source is basically a small cylindrical tube of 2.5 mm inside diameter and 35 mm long. For transitional degrees of freedom, the kinetic energy of ions is given by, KE=3/2 kT; where, KE = average kinetic energy (J), k = Boltzmanns constant (1.28E28 JK^{-1}, T = Temperature (K). Usually, the temperature of a thermal source ranges from 2000 to 2400 K, so the initial kinetic energy of any ion is between 0.25 to 0.3 eV. For simulation, both ^{63}Cu and ^{65}Cu ions are randomly generated inside the source and about 65 to 85% of them are lost inside the source itself (Figure 1). The ions are then extracted into the system by the help of an extraction electrode that has an inclination of 67.5° at the beginning to accelerate the ions. The ions are then focused by the beam focusing system that consists of einzel lenses, deflectors and quadrupole lenses. The focused beam is then passes through an electromagnet where the mass separation occurs. The separated mass is then detected with a detector that is placed perpendicularly to the trajectory of the ion beam. For simulation, the geometries were created in 4 different PAs since the energy of ions at the exit of einzel lenses is same as its energy when it enters the quadrupole lens. This configuration allows to reduce the size of PA and

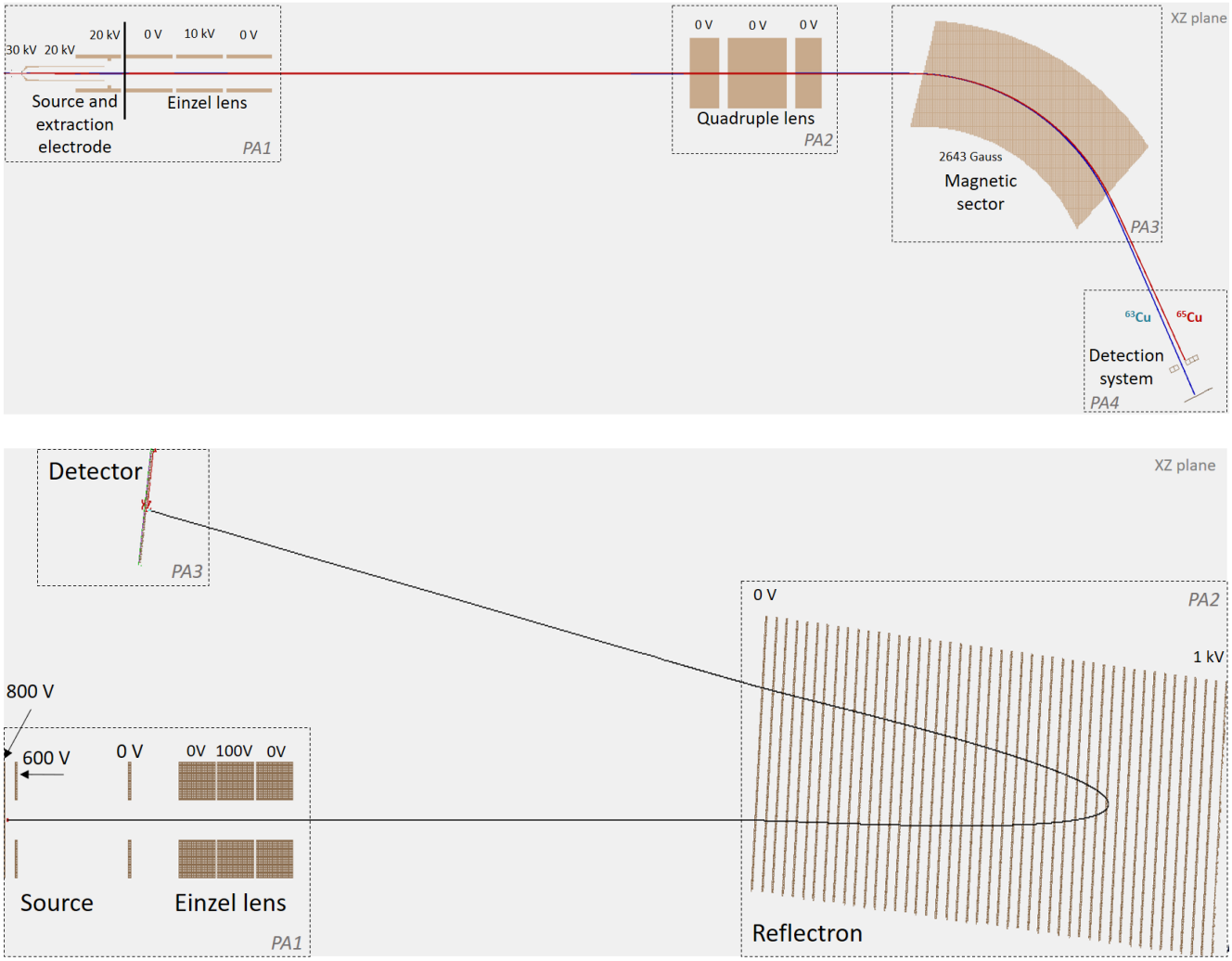

Figure 2: Simulation of RISIKO mass separator (top) and simulation of Reflectron (bottom)

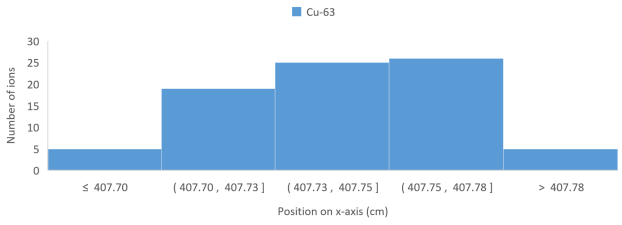

Figure 3: Number of ^{63}Cu ions detected along the x-axis

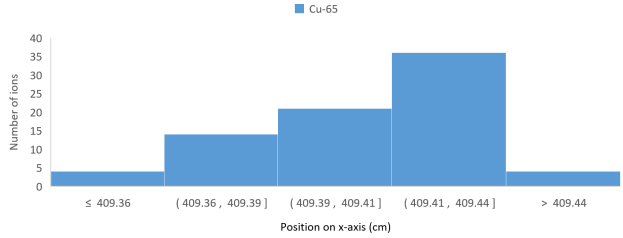

Figure 4: Number of ^{65}Cu ions detected along the x-axis

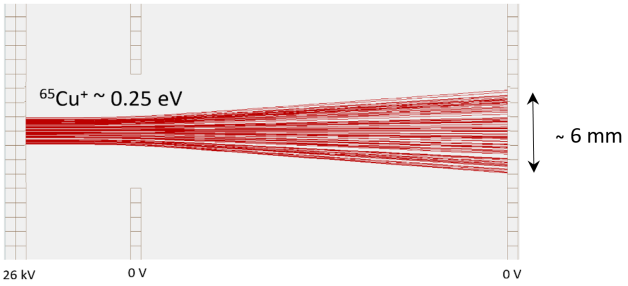

Figure 5: Linear TOF analyzer

Figure 6: 2-step voltage extraction TOF analyzer

decrease time of simulation. The 4 PAs are namely (1) source and einzel lenses, (2) quadrupole lenses, (3) magnetic sector and (4) detection system (Figure 2 top).

As mentioned earlier, TOF is another way to separate mass. Any TOF analyzer consists of an accelerating zone and a field free region. A linear TOF analyzer (Figure 5) has two electrodes to accelerate the ions where the second electrode and detector are maintained at zero potential. Linear TOF analyzer has two main drawbacks: high spatial distribution of ions on the detector and high kinetic energy dispersion. The spatial distribution of the ions at the detector can be improvised by introducing a second electrode in the acceleration zone that has a lower potential than the first electrode [6]. This type of analyzer is called as two step voltage extraction TOF analyzer (Figure 6). For simulation, 100 ^{65}Cu ions with in 0.25 eV initial kinetic energy were generated; the potentials of the acceleration electrodes are 26 kV, 20 kV and 0 V respectively. The Kinetic energy dispersion can be improved by using reflectron/ electrostatic mirrors (Figure 2 bottom). These are series of grids having homogeneous electric field that oppose the progression of ion. Ions having same mass but different velocity travel through the same distance. Depending on velocity, time travelled by the ion inside the reflectron is different. So the ion with smaller velocity enters the reflectron last but exits first. Thus the order of ions changes at the exit. For SMILES, such a TOF MS will be built. The reflectron consists of 46 electrodes with potentials increasing linearly from 0 to 1kV. A microchannel plate detector is used to measure the TOF of ions.For simulation of relectron, 3 PAs were created; 1) Source and Einzel lens, 2) reflectron and 3) detector.

Results

In the simulation of RISIKO mass separator, ^{63}Cu (Figure 4) and ^{65}Cu (Figure 4) have Gaussian distribution on the detector and they are separated by 12 mm distance. This spacing enables us to separate/ collect the mass of interest with no to minimum impurity of the other. Most of the ions of both mass can be detected with 1 mm on the detector. From the number of ions that are detected, it can be inferred that only 15-20 % of them reaches the detector and the rest are lost inside the system.

In case of TOF analyzer, 2-step voltage extraction (Figure 6) reduces the spatial distribution of ions to $\sim$ 2 mm from 6 mm that is produced in linear TOF (Figure 5) on the detector and the reflectron reduces the kinetic energy dispersion of ions on the detector. The TOF of ^{63}Cu and ^{65}Cu were recorded as 7.22E-06 s and 7.34E-06 s respectively, i.e, they are separated by a delay of 120 ns between the two masses.

Conclusions

SIMION proves to be a useful tool to study ion trajectories of different masses in electromagnetic field. The software is very flexible and enables us to calculate trajectories for a large range of mass number in various potentials and geometries. All the simulated values of SIMION are in accordance to the theoretical values. In the simulation of RISIKO mass separator, the two Cu masses are well separated at the focal point. And in case of TOF, the two Cu masses are well time separated thanks to 2-step voltage extraction that reduces spatial distribution and the reflectron that reduces kinetic energy dispersion.

References

[1] V N Fedosseev, et al; Resonance laser ionization of atoms for nuclear physics; Physica Scripta; 2012

[2] G Bouchoux, et al; Spectrométrie de masse - Applications; Techniques de l′ingénieur; 2005

[3] J L Henares et al; Hot-cavity studies for the Resonance Ionization Laser Ion Source; Nuclear Instruments and Methods in Physics Research; 2016

[4] K Blaum et al; A novel scheme for a highly selective laser ion source; Nuclear Instruments and Methods in Physics Research; 2003

[5] T Kron; Dissertation on pushing limits if resonance ionization mass spectrometry; University of Mainz; 2016

[6] D Rondeau; Spectrométrie de masse organique - Analyseurs et méthodes en tandem ou MS; Techniques de l′ingénieur; 2017

Measurement of the 72Ge(p,γ)73As cross section for the astrophysical p-process

Yasmine DEMANE

Institute of Physics of the 2 Infinities, CNRS/IN2P3/IP2I, Lyon, France

Abstract — In the framework of the so-called p-process, the final isotopic abundances of light p-nuclei are not well understood because of the propagation of uncertainties in reaction cross sections. We proposed to measure the cross section of the key reaction ^{72}Ge(p,γ)^{73}As using the activation method on a target enriched at 95%. The experimental program was carried out at the 3MV Tandetron facility at the Horia Hulubei National Institute of Physics and Nuclear Engineering. We measured a cross section of 1.59 +0.61-0.79 mb in accordance with a pre-existing study realized by F. Naqvi & al. on the same reaction. We compared the determined cross section with the Talys and the NON-SMOKER codes and the result is in good agreement with the theoretical models within the error bars.

Introduction

Astrophysical motivation

Most of the heavy nuclei in the Universe (Z $>$ 26) were formed in stars by nuclear reactions involving the capture of neutrons by fast r-process or slow s-process. About 35 proton-rich nuclei from ^{74}Se to ^{196}Hg cannot have been formed by these processes and imply the existence of another nucleosynthesis process which would intervene in explosive stellar events, the p process [1]. The conditions for the production of these "p-nuclei" are partially known, however they do not totally explain the observed abundances in the solar system. To fully understand how p-nuclei are created, it is required to modelite comprehensive reaction networks. They are believed to be mainly produced by sequences of photodisintegrations involving the reactions (γ, n), (γ, p) and (γ, α) of which it is essential to know the cross sections for the calculation of reaction rates [2].
The energies of relevance for astrophysics are situated in an interval called Gamow window, which corresponds to low energies. In the case of p-process, the Gamow window for proton reactions is located between 1 and 3.5 MeV.

Investigation reactions

Reaction rates are usually estimated by the Hauser-Feschbach statistical model or using experimental cross sections when available. In 2006, a sensitivity study realized by W. Rapp & al [3], using Hauser-Feshbach calculations, identified a list of reactions that were found to have a significant impact on light p-nuclei final abondances. It has been noticed that the proton capture rate (p,γ) as well as the inverse reactions (γ,p) are the most critical parameters in the calculations. The aim of this work will be to investigate the reaction ^{72}Ge(p,γ)^{73}As which has a direct influence on the creation and the destruction of the lightest p-nucleus ^{74}Se through the sequence : ^{72}Ge(p,γ)^{73}As(p,γ)^{74}Se. A single measurement of this reaction cross section was carried out in 2015 by F. Naqvi & al [4]. The data were obtained using the γ-summing technique on a natural target of Germanium. In this communication, we will present a measurement of the reaction cross section using the activation method on a target of ^{72}Ge enriched at 95%.
We will introduce the principle of the activation technique as well as the detail of the experiment in Sec. I. The results and the comparisons with theoretical models will be detailed in Sec. II. A summary and a conclusion will be given in Sec. III.

Experimental procedure

Activation method

The activation method consists in bombarding a target to activate it during a time t at a given energy E and determining the number of produced residual nuclei in order to get the reaction cross section at this energy. For homogeneous target of surface density N_{target} (atoms/cm^2) bombarded by a current of particles N_{inc} (1/s) the reaction cross section is expressed as follows [5] :

$$\sigma = \frac{N_{react}}{N_{target}.N_{inc}} \quad (1)$$

with N_{react} the number of produced residual nuclei (1/s). Often these nuclei carry a low kinetic energy compared to the beam particle and cannot leave the target. The number of produced nuclei is then determined by gamma detection. Two experimental techniques can be used. If the reaction product is a radioactive nucleus of relevant lifetime, we can detect after the irradiation phase the gammas emitted during the

radioactive decay of the produced nuclei. This is the activation method. Another approach is to detect the prompt gammas emitted by the excited nucleus formed by the reaction, this is the in-beam method. In the case of $^{72}Ge(p,\gamma)$, we can use the activation method. The reaction product ^{73}As decays with a half-life of 80.30 days in a daughter nucleus ^{73}Ge that decays partially by emitting intense gamma rays at 53.437 keV [6].

Target characterization

A target of ^{72}Ge enriched at least at 95% was produced at the Large Heavy Ion National Accelerator (GANIL) in France by evaporating natural metallic germanium on a thin high purity aluminium backing [6]. The thickness of the targets has been measured using the Rutherford Backscattering Spectroscopy (RBS), a non-destructive technique allowing the structure and composition of a sample to be determined using elastic collisions between atomic nuclei [7]. The thickness of the ^{72}Ge was estimated to be 3.092 ± 0.034 10^{18} atoms/cm^2.

Irradiation

The irradiation phase were carried out at the 3 MV Tandetron facility of the Horia Hulubei National Institute of Physics and Nuclear Engineering (IFIN-HH) in Romania. The target was irradiated during 9.5 hours by a proton beam with an energy of 2.5 MeV. A sketch of the setup used during the experiment is shown in Figure 1. The collected charge was measured during all the irradiation phase by a Faraday cup using a current integrator.

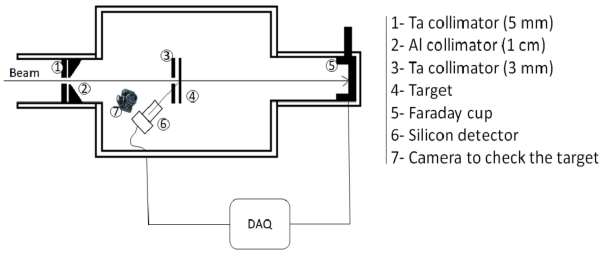

Figure 1: Schematic view of the setup used for the irradiation during the experiment.

After the irradiation phase, the sample was transported to the Slanic Prahova Salt Mine underground laboratory in Romania at 200 m underground in order to reduce background radiations. The target was placed in front of a germanium detector at 11.8 cm to start the γ-counting. A waiting time of 3.45 hours was applied between the end of the irradiation and the counting for the ^{73}As activity determination. Indeed some nuclei of the target decayed during this time and have to be considered in the calculation.

Gamma detection

The germanium detector was calibrated using five radioactive sources emitting gammas from 14 keV to 1400 keV : ^{133}Ba, ^{152}Eu, ^{57}Co, ^{137}Cs and ^{241}Am. The absolute efficiency ϵ was defined as follows:

$$\epsilon = \frac{N}{A.I_\gamma.t_{run}} \quad (2)$$

where N is the integral of the considered peak after background subtraction, A the activity of the source (1/s), I_γ the tabulated intensity of the considered gamma decays and t_{run} the acquisition time (s). The final absolute efficiency as a function of energy was then deduced from a third-degree logarithmic polynomial. During three months, the GENIE2000 data acquisition system provided time dependent spectra of the number of detected gamma as a function of energy. The area of the peak at 53.437 keV due to the disintegration of ^{73}As was extracted in all the spectra in order to obtain the activity of ^{73}As using Equation (2) taking the efficiency at the corresponding energy.

Data analysis

Activity determination

The calculation of the cross section for the reaction depends on three parameters involved in Equation (1). After determining the thickness of the target using the RBS technique and the flux of incident protons using the faraday cup, we extracted the number of produced residual nuclei from the measure of the ^{73}As activity as a function of the time (see Figure 2). To do that, we determined the number of produced nuclei just after the irradiation at t=0, called N_0. The activity curve of the ^{73}As can be fitted using the well known exponential law:

$$A(t) = A_0.e^{-\lambda.t} \quad (3)$$

where A_0 is the activity at t=0 (1/s), λ the decay constant (1/s) and t the time (s). The parameters A_0 and λ are determined by the fitting procedure, whose result is shown on Figure 2. The obtained decay constant value is in accordance with the literature value λ_{ref} = 9.991 10^{-8} s^{-1} [6]. We can now use the relation $A_0 = \lambda.N_0$ to calculate the number of produced nuclei just after irradiation. Since the decay of ^{73}As during irradiation is negligible, N_0 gives the number of reactions $Nreact$ that is used to calculate the reaction cross section according to Equation (1).

The decay measurements were carried out over a period of three months to have enough statistics to determine the activity of the residual nuclei. Each group of data represents a run of acquisition. The error bars

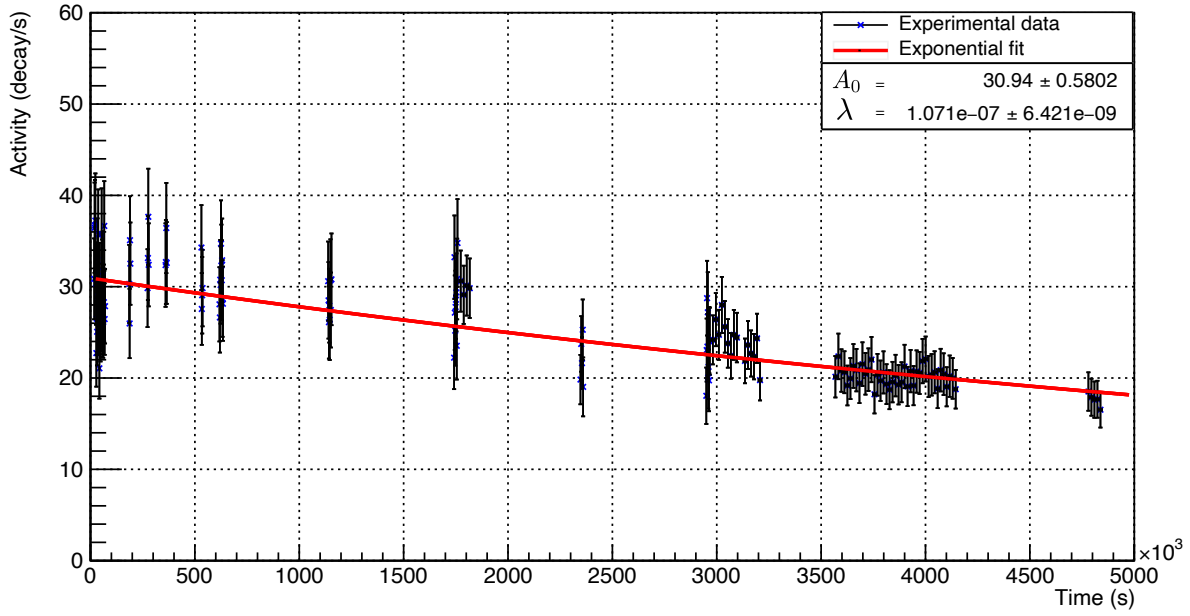

Figure 2: Activity curve of the ^{73}As over the time. The experimental data have been obtained by performing the reaction ^{72}Ge(p,γ)^{73}As at 2.5 MeV on an enriched target and measuring the gamma transition at 53.437 KeV detected after irradiation.

take into consideration the uncertainties on the efficiency, the gamma intensity, the peak area and the run time. The change around t=3000s in the size of error bars is explained by a significant increase in the acquisition time going from 30min to 4hours and thus reducing the uncertainty on the peak fits.

Hauser-Feshbach (HF) calculations with Talys

The calculation of the ^{72}Ge(p,γ)^{73}As cross section in the framework of the HF statistical model requires the knowledge of the gamma width as well as the proton width. These quantities depend on three nuclear statistical parameters : the level density, the gamma strength and the nucleon-nucleus optical potential. The modeling of these parameters require constraints from experimental data. Uncertainties in the reaction rates used for nucleosynthesis arise from the lack of experimental data at the relevant energy, especially for unstable nuclei.
To estimate theoretical reaction cross sections, we used the Talys-1.95 software, a nuclear reaction program that uses the statistical Hauser-Feshbach theory. We studied the impact of three parameters, the gamma strength function (γ-SF), the nuclear level density (NLD) and the optical model potential (OMP). For more details and references about the different models available for these parameters, see the manual of Talys-1.95 [8].

For comparison purposes, we used two different approaches, a phenomenological one ("Talys Pheno" in the Table 1) and a semi-microscopical one ("Talys Micro 1" and "Talys Micro 2" in the Table 1). Our theoretical predictions will be compared to the NON-SMOKER code [9], another Hauser-Feshbach statistical model code fully web driven which uses a different set of models for the statistical parameters.

	NON-SMOKER	Talys Pheno	Talys Micro 1	Talys Micro 2
OMP	JLM77	KD	JLM	JLM
NLD	RTK97	BSFG	HF-BCS	HF-B
γ-SF	CTT91	BA	HF-BCS	HF-B

Table 1: Theoretical models configuration used for the cross sections comparison. JLM=Jeukenne-Lejeune-Mahaux, KD=Koning-Delaroche, RTK=Rauscher-Thielemann-Kratz, BSFG=Back-Shifted-Fermi-Gas, HF-BCS=Hartree-Fock+Bardeen-Cooper-Schrieffer, HF-B=Hartree-Fock+Bogoliubov, CTT=Cowan-Thielemann-Truran, BA=Brink-Axel [8][9].

Cross sections comparison

The ^{72}Ge(p,γ)^{73}As cross sections was measured at 2.5 MeV using the activation method. In a preliminary analysis, we have obtained a result of 1.59 +0.61-0.79 mb shown by the purple dot on the Figure 3. Theoretical cross sections as well as the experimental data from F. Naqvi & al. are also shown on the figure for an energy varying from 1.5 to 4.5 MeV.

At 2.5 MeV one can see that the obtained value is compatible with those of F. Naqvi & al. although they used a different experimental approach, the in-beam γ-summing technique. Our results are also in agreement

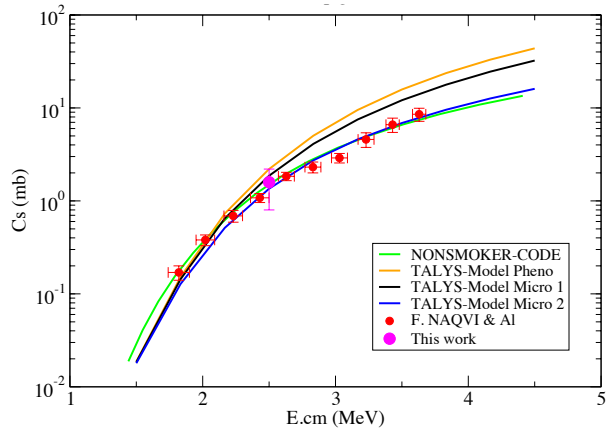

Figure 3: Cross section of the reaction ^{72}Ge(p,γ)^{73}As measured in the present work compared to the experimental data from F.Naqvi & al. and to the predictions of statistical model reaction codes.

with the four theoretical curves within the error bars. We can notice that the data points from Naqvi & al. are only compatible with TALYS micro 2 and NON-SMOKER results, which allows to rule out the two other theoretical curves. Our preliminary data point instead has too large error bars to discriminate between the four models. This is mainly due to the uncertainty in the determination of N_0, whose procedure was detailed in subsection 3.1.

Discussion and outlook

In the present work, the ^{72}Ge(p,γ)^{73}As cross section has been measured at 2.5 MeV using the activation technique on an enriched target. We obtained a result in accordance with the measurement of F. Naqvi & al. using an in-beam method on a natural germanium target. The cross section is also in agreement with Talys and NON-SMOKER code calculations within the error bars. Our analysis is in process to reduce the uncertainty on the new data point.
Five other reactions of interest for the light p-nuclei abundance calculation have also been measured following the same experimental scheme, and their analysis is in progress. Among these five reactions, three have never been experimentally measured and theoretical predictions diverge in the Gamow window. The present study is important for understanding the abundance of light p-nuclei but also to validate the experimental method in the presence of an existing data set.

Acknowledgements

This work was suported thanks to the financial support of the LabEx LIO (ANR-10-LABX-0066) of the University of Lyon, created within the framework of the future investments program bearing the reference ANR-10-LABX-0066 set up by the State and managed by the National Research Agency (ANR).

This work was carried out thanks to the following authors: L. Al Ayoubi, B. Rebeiro, G. Randisi, J. Balsamelli, B. Bastin, C. Ducoin, O. Stezowski, R.M. Magineanu, C. Borcea, R. F. Andrei, C.-O. Bacri, R.C. Badita, A.-M. Blebea Apostu, R. Borcea, S. Calinescu, B. Croitoru, H. Al Falou, G. Fremont, V. Girard Alcindor, M. C. Gomoiu, D. Iancu, F. De Oliveira, A. Pantelica, C. Petrone, F. Rotaru, M. Stanoiu, C. Stodel, M. Straticiuc, P. Stroescu, J.-C. Thomas, D. Tudor.

References

[1] T. Rauscher & al, *Constraining the astrophysical origin of the p-nuclei through nuclear physics and meteoric data*, Rep. Prog. Phys. 76 (2013).

[2] Woosley S. E. & Al, *The p-processes in supernovae*, Astrophysical Journal Supplement Series, vol. 36, p. 285-304 (1978).

[3] W. Rapp & al, *Sensitivity of p-Process Nucleosynthesis to Nuclear Reaction Rates in a 25 Mo Supernova Model*, ApJ 653 474 (2006).

[4] F. Naqvi & al, *Proton capture cross section of ^{72}Ge and astrophysical implications*, PHYSICAL REVIEW C 92, 025804 (2015).

[5] Gy. Gyürky & al, *The activation method for cross section measurements in nuclear astrophysics*, Eur. Phys. J. A 55: 41 (2019).

[6] https://www.nndc.bnl.gov/

[7] Matej Mayer, *SIMNRA User's Guide version 5.0*, master report, (1997-2002).

[8] A. Koning, S. Hilaire, S. Goriely, *Talys-1.95, A nuclear reaction program*, (2019).

[9] T. Rauscher, F. K. Thielemann, *Astrophysical Reaction Rates From Statistical Model Calculations*, At. Data Nucl. Data Tables 75 1.

Part VIII

Standard Model

session chaired by Mykola KHANDOGA

Off-shell Higgs into 4 leptons & electron tracking in ATLAS

Arnaud MAURY

Laboratoire de Physique des 2 infinis Irène Joliot-Curie - IJCLab

Abstract — The discovery of the Higgs was first made in the Higgs-to-4-lepton (H4l) decay channel. Nevertheless, new analysis possibilities are available beyond the on-shell data by studying the off-shell Higgs, defined as having a centre-of-mass energy above 220 GeV. In particular, we shall use the framework of EFTs (Effective Field Theory), which aims to better understand the deviations of data relative to the Standard Model. The goal is to generate trustworthy Monte-Carlo samples for the relevant EFT operators to fit data and measure the Wilson coefficients for those operators. In this work, we have focused on the Monte-Carlo generation process to compare and validate several software versions.
Concurrently, work has been carried out on ACTS (Acts Common Tracking Software), an experiment-independent software currently under development and under integration to the future ATLAS-ITk. Tracking is particularly challenging for the electron because of increased bremsstrahlung, as the particle loses energy as it progresses in the tracker. A new tracking algorithm is currently implemented in ACTS to better address this issue. The performance of this new algorithm must be compared with a reference one. In order to do this, pull plots are a valuable tool to gauge the physical correctness of the algorithm.

Introduction

We aim to analyse ATLAS' Run 2 data in the Higgs-to-4-lepton (H4l) channel and in the off-shell region using the framework of EFTs (Effective Field Theory), particularly the SMEFT (Standard Model EFT). In the H4l channel, the Higgs boson decays into two Z bosons, and each of those Z bosons decay into two charged leptons (e or μ). It is primordial for analysis in Particle Physics to have Monte-Carlo samples: this is what makes it possible to analyse data and compare it with the theory. After an overview of the Monte-Carlo simulation used, we compare two software versions by confronting their production for several physical observables.

When constraining theory parameters using experimental data, one typically uses the Likelihood ratio, a statistical quantity that yields the uncertainty on the measurement of theory parameters. However, problems such as those we have in Particle Physics[1] are highly-dimensional and thus have an intractable likelihood (i.e. it cannot be numerically evaluated as integrals would be of high dimension). These problems are called *inverse problems*. Simulation-based inference using Machine Learning (ML) is a method that enables us to estimate this likelihood ratio using information only accessible during simulation.

One of the upgrades scheduled for ATLAS for Run 4, circa 2026, is the upgrade of the current Inner Detector to the Inner Tracker Pixel Detector (ITk). Concurrently, after taking previously existing tracking code from ATLAS, the experiment-independent ACTS project is developing a cleaner and more efficient code for particle tracking. The goal is to integrate this software into ITk, i.e. ensure it keeps its physical fidelity and efficiency once integrated into ATLAS' software environment (Athena). Another future goal is to integrate a new fitting algorithm called Gaussian Sum Filtering (GSF) to ACTS. In these proceedings, we shall see what tools can be used to gauge (and thus compare) the relevance and correctness of various tracking algorithms.

[1] but also in fields such as meteorology or epidemiology.

EFT Monte-Carlo generation of off-shell Higgs

The off-shell Higgs

The Standard Model Higgs boson discovered at the LHC in 2012 has a mass of $m_H = 125$ GeV for a width of $\Gamma_H 0.013$ GeV. [1] Thus, the Zero-Width Approximation is often used around the 125 GeV resonance as there is not much deviation from taking the actual non-zero width of the Higgs. This simplifying assumption, however, does not hold anymore in the high-mass range (i.e. above 200 GeV), see figure 1. [2] indeed shows that the study of the off-shell Higgs is relevant in order to completely characterise the Higgs boson.

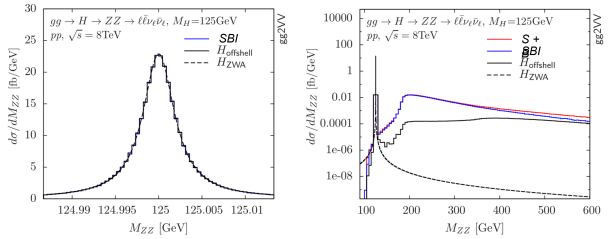

(a) Near the Higgs resonance (b) In the high-mass region

Figure 1: Differential cross-section of the $gg \to H \to ZZ$ process (a) at the Higgs resonance and (b) at the high-mass region. The Zero-Width Approximation is denoted as H_{ZWA} and the actual signal is SBI. [2]

SMEFT

Effective Field Theory (EFT) is a framework where we set an energy cut-off scale Λ, under which the SM is valid and above which it may not take into account new phenomena. In other words, if there are new phenomena at energy scales above Λ that are beyond the reach of our experimental setups (mainly the LHC), they need not be taken explicitly into account by our EFT and can be neglected. Such phenomena, however, might indirectly have an effect at energy scales below Λ, and EFTs are such that they match reality in those energy scales below Λ, typically by using perturbation theory. This makes EFTs an interesting tool to probe New Physics at energy scales lower than Λ without needing to explicitly specify which BSM (Beyond Standard Model) model we consider fundamentally: it is a theory-independent method that yields precision constraints, the indirect effect of BSM Physics phenomena.

In our case, we use the SMEFT (Standard Model EFT), which models the Standard Model with a cut-off scale of $\Lambda = 1$ TeV. Concretely, we add to the Standard Model Lagrangian (which is made up of 4-dimensional operators) 6-dimensional operators (eq. 1): operators of an odd number of dimensions break Lorentzian symmetry, while we are not taking into account 8-dimensional operators for the time being.

$$\mathcal{L}_{\text{SMEFT}} = \mathcal{L}_{\text{SM}} + \frac{1}{\Lambda^2}\sum_i c_i^{(6)} O_i^{(6)} \tag{1}$$

The c_i in eq. 1 are called Wilson coefficients and the O_i Wilson operators. The c_i are therefore the parameters that will be fitted to data to better understand the effects of unknown BSM Physics on what can observe right now at the LHC. Here, we consider three EFT operators: O_{pG}, O_{pt} and O_{tp}.

Monte-Carlo simulation for HEP

Monte-Carlo simulation of data is the bread and butter of High-Energy Physics analysis. On the one hand, it makes it possible to predict what results or distributions we should observe based on different assumptions (i.e. different theories, different values for the theory's parameters). On the other hand, simulation of events is necessary when analysing experimental data to understand the background, remove this background, or even understand in what region of phase-space to look for a signal (or absence of signal) in experimental data. Therefore, it is paramount to make sure our simulation software is reliable and produces trustworthy samples.

Simulation of events in HEP is generally done in two steps. First, the parton level process (or hard scattering): this is the crux of the process, where partons (i.e. gluons or quarks from the proton beams) interact. The various processes which are possible in this step are modelled by Feynman diagrams. These processes take place in very small length scales, in the order of the millimetre. This step is in our case carried out by MadGraph.[3] Secondly, the parton shower: particles produced at the parton level are not always stable by themselves (especially if quarks are produced). This step models their disintegration cascade (which we also call *shower*) and is in our case done by Pythia.[4]

In the work presented here, separate simulations were carried out for each operator to compare software versions for each EFT operator relevant to our study.

Comparison plots

Our goal is to compare two versions of the *SMEFTatNLO* model [5]: the v0.1 and the v1.0. For those comparisons, two versions of MadGraph were finally used: v2.7.3 and v2.9.3. The results of both MadGraph versions behave the same way, so we shall only consider the results of v2.9.3. In the work that was carried out, the following observables were used to compare distributions: $|\cos\theta^*|$ (θ^* being the angle between a Z boson and the closest proton beam axis), y_{4l} (the reconstructed pseudo-rapidity of the Higgs), $\cos\theta_1$ (the angle between the Z_1 boson[2] and the lepton of highest momentum it decays into), $\cos\theta_2$ (the angle between the Z_2 boson (the other Z boson) and the lepton of highest momentum it decays into), m_{4l} (the reconstructed mass of the Higgs), $p_T(4l)$ (the reconstructed transverse momentum of the Higgs), ϕ (the angle between the plane of decay of Z_1 and the plane of decay of Z_2).

The observable $|\cos\theta^*|$ yields the most relevant and readable plots. In figure 2, we can see that the $|\cos\theta^*|$ distributions for both SMEFTatNLO versions are statistically similar to each other, for the quadratic contributions of EFT operators O_{pG}, O_{pt} and O_{tp}.

Simulation-Based Inference

Our goal as scientists is to test our theory against experimental data and use this data to find the parameters of our theory. As mentioned in the introduction, in intractable problems such as those we have in HEP, the likelihood cannot be numerically evaluated because of the high dimensionality of the problem. Yet, likelihood enables us to deduce theory parameters from

[2] by definition the Z boson closest to its mass shell of $m_Z = 91.19$ GeV

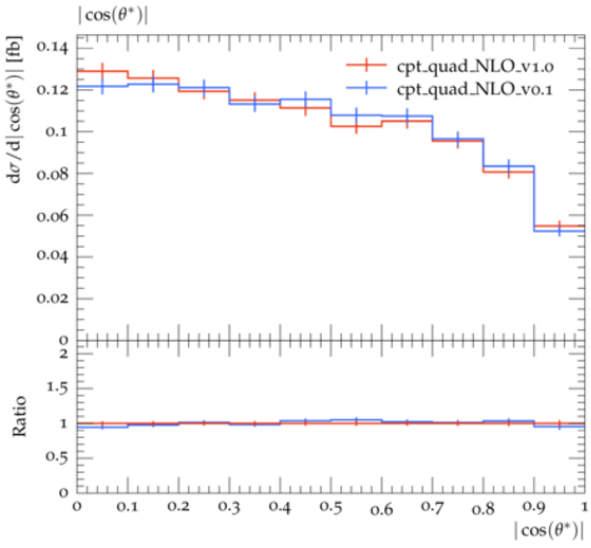

(a) Operator O_{pt}

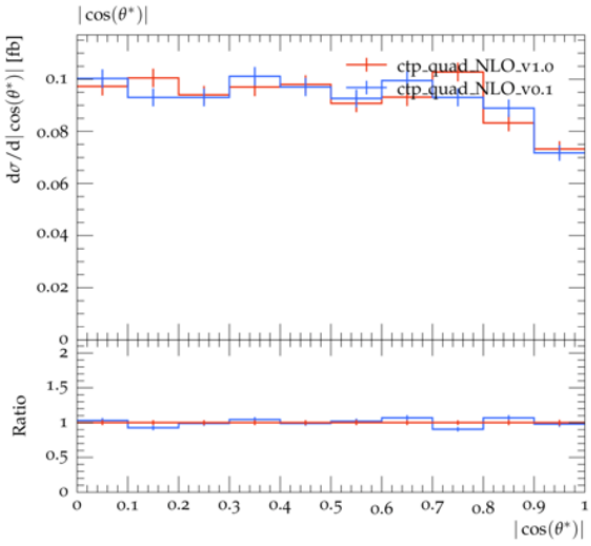

(b) Operator O_{tp}

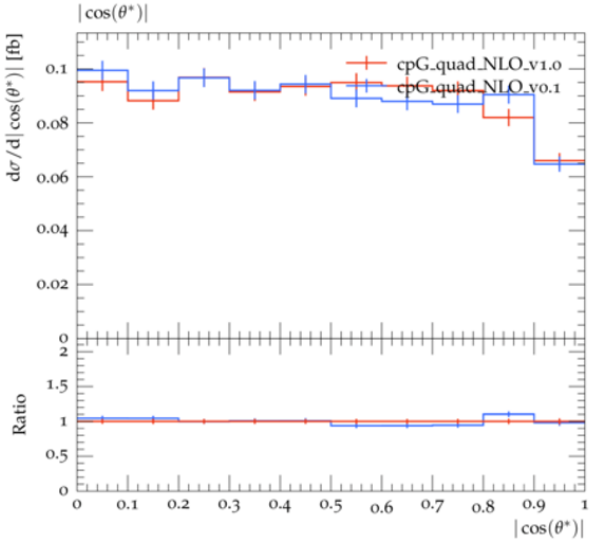

(c) Operator O_{pG}

Figure 2: Distributions of $|\cos\theta^*|$ for several different EFT operators, comparing two versions of SMEFTatNLO: v1.0 in red and v0.1 in blue.

physical observables, as simulation enables us to predict physical observables from theory parameters. The main idea, as explained in [6], is that since the likelihood ratio is tractable at the parton level (an intermediate state of the simulation) but not at the detector level (which is what is available experimentally), the likelihood ratio at parton level could be computed and stored during Monte-Carlo simulations. This quantity could then be used to train Neural Networks to estimate the likelihood ratio at detector level. Hence, we could train Neural Networks using information only available in simulations to obtain the likelihood ratio for experimental data without having access to parton level data.

Electron tracking in ITk

Tracking: finding tracks

As a particle travels through the detector, its position is recorded by each detector layer. However, as illustrated in fig. 3, we can only measure the intersection points between the detector layers and the trajectory of the particle, and not the entire trajectory. Thus, one has to find and reconstruct tracks (i.e. the trajectory of a particle) based on a limited number of points (generally, in ITk, there are about 10 hits per track).

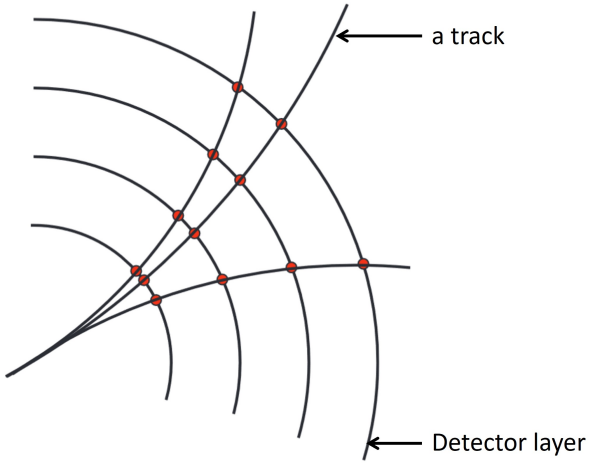

Figure 3: Illustration of the track of a charged particle going through a detector. Figure from [7].

Each track is uniquely defined by the five following parameters. To define them, it is helpful to introduce the point of closest impact (in red in fig. 3), which is the point of the track closest to the beam axis (which is the z-axis). These are: d_0 (the impact parameter, i.e. the smallest distance between the track and the beam axis), z_0 (the z coordinate of the point of closest impact), θ (the angle of the track relative to the beam axis at the point of closest impact), ϕ (the angle of the track relative to the x-y plane at the point of closest impact) and q/p (electric charge of the particle over its momentum).

In a real-life situation, more than one particle goes through the detector in the same time window. Hence,

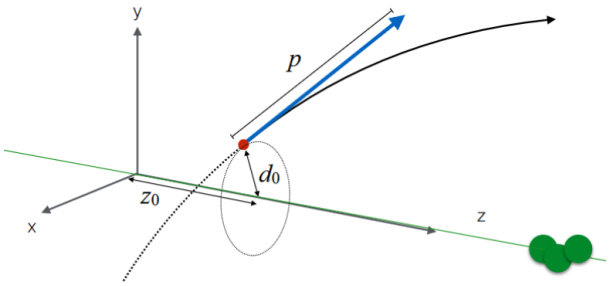

Figure 4: Illustration of the definition of track parameters. Figure from [7].

what we observe in the detector is a set of points on each detector layer, see fig. 4. From this set of points, we must find tracks. The big picture idea is to find a seed (i.e. a crude first guess) for the parameters of the track we are looking for, then refine this initial guess by propagation from the first points of the track, finally doing a chi-square minimisation.

The problem of electrons

Electrons radiate and lose much energy by bremsstrahlung, significantly more than muons, especially at relatively low energies. Therefore, the trajectory gets more curved than expected, and the measured momentum can be underestimated.

A new fitting algorithm (namely GSF, for Gaussian Sum Filter) seems better suited for this task and considers the loss of energy due to bremsstrahlung. Work in the ACTS project is currently in progress to implement this algorithm into ACTS.

The ACTS software

ACTS (A Common Tracking Software) originates from the original tracking software developed over the years in the ATLAS collaboration. A new software project was then restarted from scratch as an experiment-independent software, greatly inspired and influenced by the ATLAS original tracking software. The project in ACTS is to validate the integration of ACTS into ATLAS' common software platform called Athena, as well as to validate the integration of the GSF track fitting algorithm. Indeed, the software must remain both physically accurate and CPU efficient. Priority is put on the physical fidelity of the software. To test this, we use a (graphical representation) tool called *pull plots*.

Pull plots

For a given observable (i.e. one of the track parameters), we define the *residual* value as the difference between the fitted value and the truth value. The *pull* value is then defined as the ratio between the residual and the error value, i.e. the error related to the fit. Hence, we have a pull value for each track and for each track parameter. We then plot the histogram of these pull values. Ideally, pull plots must be Gaussian, centred, and reduced (i.e. a standard deviation of 1). Pull plots are a practical tool to, for instance, find discrepancies when tracking different tracks, e.g. with different particles or in different parts of the detector.

We compare pull plots for electrons on the one hand and for muons on the other hand, for track parameter q/p in fig. 5: the pull distributions are not centred. This shows indeed that the fitted momentum is less than the truth momentum. This effect is even more pronounced for electrons (fig. 5a) than it is for muons (fig. 5b).

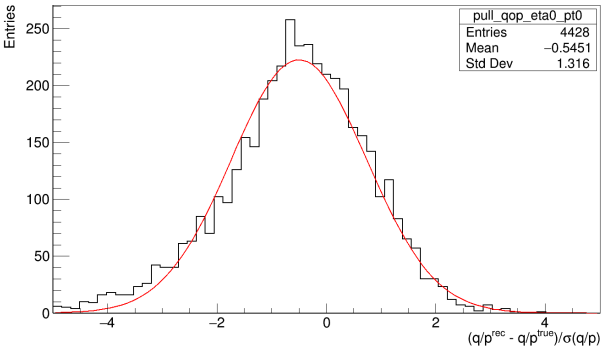

(a) Pull plot for the electron.

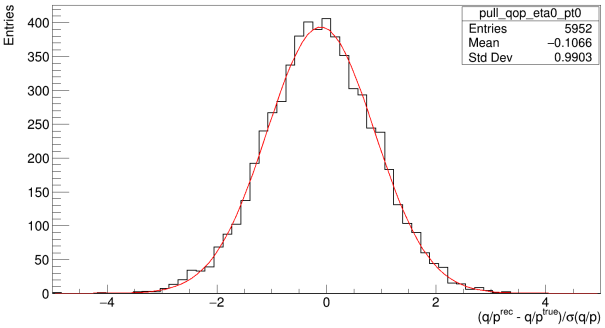

(b) Pull plot for the muon.

Figure 5: Pull plots for the track parameter q/p.

Conclusions and outlook

The study of the off-shell Higgs can be valuable and lead to precision measurement, thus increasing our knowledge and constraint on theory parameters. Monte-Carlo generation is challenging, mainly when producing samples for isolated EFT operators, as their cross-sections are very small (around 10^{-3} smaller than the Standard Model H4l process). Monte-Carlo simulation is our preliminary source of data, not only when analysing experimental data but also when developing new statistical and Machine Learning techniques. With HL-LHC coming up, aggressive R&D is a must, as computational progress alone will not keep up with the increase of luminosity and pile-up in ATLAS.

As such, Machine Learning and new statistical methods must be explored. Breakthroughs in the field of Simulation-Based Inference techniques will enable physicists to apply them to Particle Physics, enabling us to extract the most information possible from exper-

imental data. Its specific application to H4l is currently work in progress.

The ITk upgrade is coming soon to ATLAS. In addition to a hardware upgrade, a new and more efficient software will significantly increase our ability to track particles in ATLAS, particularly electrons. Validation of the software upgrade is a must to ensure the fidelity of the physical results produced. Using pull plots is a way of detecting problems impacting the Physics of the events produced by the software.

References

[1] M. Tanabashi et al. (Particle Data Group), Phys. Rev. D 98, 030001 (2018) and 2019 update

[2] *Inadequacy of zero-width approximation for a light Higgs boson signal*, N. Kauer, G. Passarino, arXiv:1206.4803 [hep-ph]

[3] Alwall, J., Herquet, M., Maltoni, F. et al. MadGraph 5: going beyond. J. High Energ. Phys. 2011, 128 (2011). https://doi.org/10.1007/JHEP06(2011)128

[4] Sjoestrand, Torbjoern; Ask, Stefan; Christiansen, Jesper R.; Corke, Richard; Desai, Nishita; Ilten, Philip; Mrenna, Stephen; Prestel, Stefan; Rasmussen, Christine O.; Skands, Peter Z. (2015), An introduction to PYTHIA 8.2, DOI: 10.17632/f5x6zvrmdh.1

[5] Degrande, Céline and Durieux, Gauthier and Maltoni, Fabio and Mimasu, Ken and Vryonidou, Eleni and Zhang, Cen; Automated one-loop computations in the standard model effective field theory, Phys. Rev. D, 103, 9, May 2021, American Physical Society, DOI: 10.1103/PhysRevD.103.096024

[6] Brehmer, Johann and Cranmer, Kyle and Louppe, Gilles and Pavez, Juan, A guide to constraining effective field theories with machine learning, Phys. Rev. D 98, 5, Sep 2018, American Physical Society, DOI:10.1103/PhysRevD.98.052004

[7] Figures from Andreas Salzburger (Track and Vertex Reconstruction - HCPSS Aug 11-22, 2014)

Boosted $H \to b\bar{b}$ Tagging in ATLAS

Yajun HE

LPNHE, Paris

Abstract — This talk is dedicated to the identification of boosted $H \to b\bar{b}$ in the ATLAS Collaboration. In current physics analyses, the large-R jets with two b-tagged associated Variable Radius (VR) track jets are taken as $H \to b\bar{b}$ events, so-called the double b-tagging method. The performance, calibrations and applications have been studied based on individual b-jet. Lots of interesting results have been produced. However, at very high energy, the two b-jets from the Higgs boson are highly collimated, with the result that the separation of the two b-jets becomes less efficient. Therefore, we're motivated to develop new and more efficient tagging techniques. The boosted $X \to b\bar{b}$ tagger, which is recently developed in ATLAS, focuses on tagging one large radius jet which contains two b-hadrons. The background rejection efficiency is significantly improved. And the calibrations of the tagger are recently published.

Introduction

The Standard Model (SM) of Particle Physics summarises the fundamental particles of nature and three of the four fundamental forces between them: strong, weak and electromagnetic forces. The SM has been so far very successful from the experimental point of view. However, the incomplete SM can not explain all fundamental phenomena like gravity and dark matter. The BSM searches employ one of two strategies: direct searches where the decays of a BSM particle are observed directly and indirect searches which look for discrepancy between experimentally measured and theoretically predicted values of the properties of SM particles.

One popular particle for both direct and indirect searches is the Higgs boson, because it plays important role for the masses of the SM particles. The Higgs boson has a $\sim 58\%$ chance to decay into $b\bar{b}$ which makes this decay channel a good probe for new physics, especially at the highly energetic regime ($p_T^H > 250\ GeV$) [1].

This talk focuses on the identification of these energetic (boosted) $H \to b\bar{b}$ in ATLAS. The current techniques and applications are presented first, followed by the new techniques and its calibration results.

Double b-tagging method

Quarks and gluons are measured with jets, which consists of the particles produced from a cascade of particles produced in the hadronisation of quarks and gluons. Jets are reconstructed using information from trackers and calorimeters of the ATLAS detector. Hence, in $H \to b\bar{b}$ tagging, we're interested in b-jets instead of b-quarks. Figure 1 shows different types of jets: b-jet (left), c-jet (middle) and light-jet (right). Due to its long lifetime and its large mass, a b-jet has measurable Secondary Vertex (SV) and high decay product multiplicity. Therefore a b-jet is distinguishable among c-jets and light-jets. To identify a b-jet, apart from the hadronic jets, the tracks associated to the jets and the primary vertices are also used as inputs. These inputs are first processed in the low level algorithms such as IP-based algorithms, SV finding algorithm, multi-vertices finding algorithm. Then, using the ouputs from the low level algorithms, the high-level algorithms are produced more intuitive discriminant. The common used high-level algorithms in ATLAS are based on machine learning techniques like MV2 and DL1(r) [3].

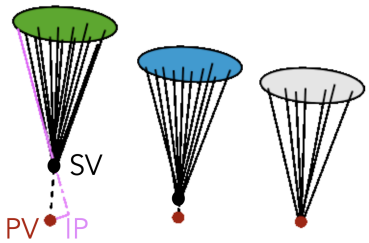

Figure 1: Graphical representation of b-jet (left), c-jet (middle) and light-jet (right). PV: Primary Vertex. IP: Impact parameter. SV: Secondary Vertex.

Since the angular distance between the two b-jets from one Higgs boson is proportional to $1/p_T^H$, for $p_T^H > 250\ GeV$, we're using the variable radius (VR) track jets for b-tagging to avoid the overlapping of the two b-jets. Thus, as shown by figure 2, the boosted $H \to b\bar{b}$ object is identified as the large-Radius ($R = 1$) jets with two b-tagged associated variable radius (VR) track jets. This is so-called the **double b-tagging method**.

The definition of the tagging efficiency and the calibrations in the double b-tagging method are based on the single isolated b-jets. By cutting the discriminant

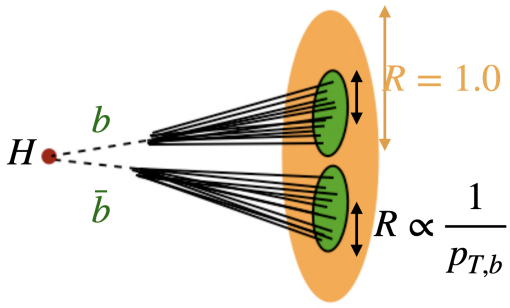

Figure 2: Graphical representation of a $H \to b\bar{b}$ object.

from high level algorithms, the tagging efficiency (ϵ) is defined as the fraction of the signal events passing the chosen cuts over the total signal events. The usage of the SFs in ATLAS analyses can be found in [2] :

All recently $H \to b\bar{b}$ related physics analyses are based on this method and lots of interesting results have been produced. However, for NP searhes where we're probing extremely high energies, the double b-tagging method is degraded. For example in the searches for heavy resonance decaying to HH via $b\bar{b}b\bar{b}$, the efficiency of the double b-tagging method is degraded from the resonance mass higher than 1.5 TeV, the tagging requirements have to be loosen [4].

New $X \to b\bar{b}$ tagger

Instead of tagging b-jets, the new $X \to b\bar{b}$ tagger tags the $H \to b\bar{b}$ object shown in figure 2. The main backgrounds are thus dijet from QCD and top jets which are eventually containing a b-quark inside the large-R jets. The new $X \to b\bar{b}$ tagger is a neural network based algorithm and uses the p_T and η of the large-R jets and the high-level b-tagging outputs of the first three VR track jets as inputs. The outputs are the probability of the large-R jets as QCD (p_{QCD}), Top (p_{Top}) and Higgs (p_{Higgs}). And the discriminant used to define work points is:

$$D_{Xbb} = \ln \frac{p_{Higgs}}{f_{Top} \cdot p_{Top} + (1 - f_{Top}) \cdot p_{QCD}} \qquad (1)$$

The new $X \to b\bar{b}$ tagger shows more powerful background rejection compared to the double b-tagging method as shown by figure 3 [5].

The first calibration results are published [6].

The signal efficiency is calibrated using $Z(\to b\bar{b})\gamma$ and $Z(\to b\bar{b})$+jets events because the tagger is flavor dependent and $Z \to b\bar{b}$ topology is similar to $H \to b\bar{b}$ one. In addition, in the analyses with $H \to b\bar{b}$, there is important contribution from $Z \to b\bar{b}$. The calibration uses the large-R jets having at least 2 ghost associated VR track jets, which is different from the double b-tagging method. The calibration is p_T-dependent. The results using $Z(\to b\bar{b})\gamma$ are for p_T in 200-450 GeV and that using $Z(\to b\bar{b})$+jets for 450-1000 GeV. Figure 4 shows the signal efficiency scale factors for the new $X \to b\bar{b}$ tagger at 60% efficiency working point. The results from $Z(\to b\bar{b})\gamma$ method and $Z(\to b\bar{b})$+jets method agrees and the tendency of the SFs agree with the fact that the MC used for the calibration overpredicts the cross-section of $Z(\to b\bar{b})$+jets at high energies.

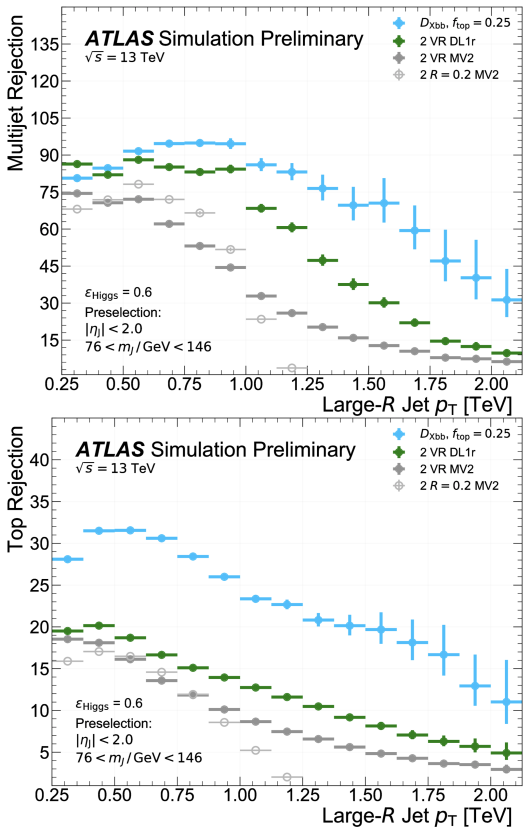

Figure 3: Dijet (up) and top (down) jet rejection as a function of large-R jet p_T with a constant 60% Higgs tagging efficiency. The error bars correspond to the statistical uncertainty. The fixed-radius track-jets with $R = 0.2$ begin to lose discriminating power when $p_T > 800$ GeV, since subjets begin to merge and resolving two independent b-jets becomes difficult. The variable-radius track-jets, by contrast, can resolve multiple subjets in boosted objects with $p_T > 1$ TeV.

The top mis-tag rate is calibrated using semi-leptonic $t\bar{t}$ events. The leptonically decaying top quark is used to tag the event and the hadronically decaying top quark is used to construct the top large-R jet. Figure 5 shows the top mis-tag rate scale factors for the new $X \to b\bar{b}$ tagger at 60% efficiency working point. The mis-tag rate for the other main background QCD is also studied using $g \to b\bar{b}$ events.

The performance of the new $X \to b\bar{b}$ tagger in physics analyses is under study, for example, in the on-going analysis on the production of Higgs associated with a vector boson (V) with $V \to qq'$ and $H \to b\bar{b}$, the new $X \to b\bar{b}$ tagger and the calibration results will be applied in the Higgs sector.

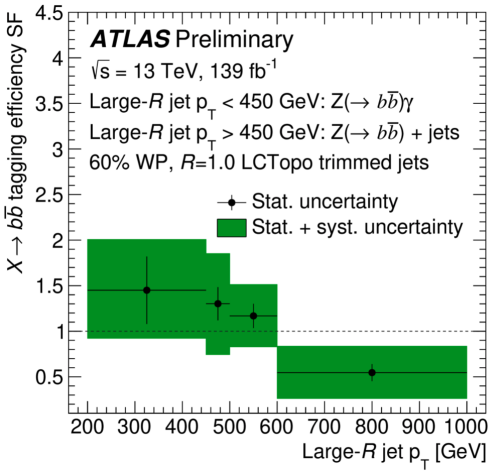

Figure 4: Signal efficiency scale factors for the new $X \to b\bar{b}$ tagger at 60% efficiency working point.

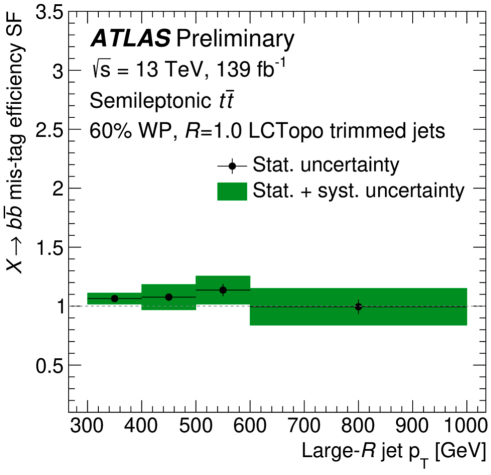

Figure 5: Top mis-tag rate scale factors for the new $X \to b\bar{b}$ tagger at 60% efficiency working point.

Summary

Boosted $H \to b\bar{b}$ tagging is an essential topic for many physics analyses in ATLAS. This talk summarises the double b-tagging method which has been used in most of analyses in ATLAS so far and lots of interesting results have been produced. The recently developed $X \to b\bar{b}$ tagger greatly improve the boosted $H \to b\bar{b}$ identification performance. Our team's work on calibration make it useful and usable by physics analyses. We're looking forward to see the performance of the $X \to b\bar{b}$ tagger and its calibrations results in physics analyses.

References

[1] Grazzini, M., Ilnicka, A. Spira, M. Higgs boson production at large transverse momentum within the SMEFT: analytical results. Eur. Phys. J. C 78, 808 (2018). https://doi.org/10.1140/epjc/s10052-018-6261-7

[2] Aad, G., Abbott, B., Abbott, D.C. et al. ATLAS b-jet identification performance and efficiency measurement with $t\bar{t}$ events in pp collisions at $sqrt(s) = 13\ TeV$. Eur. Phys. J. C 79, 970 (2019). https://doi.org/10.1140/epjc/s10052-019-7450-8

[3] ATLAS Collaboration, Optimisation and performance studies of the ATLAS b-tagging algorithms for the 2017-18 LHC run. https://atlas.web.cern.ch/Atlas/GROUPS/PHYSICS/PUBNOTES/ATL-PHYS-PUB-2017-013

[4] ATLAS Collaboration. Search for resonant pair production of Higgs bosons in the $b\bar{b}b\bar{b}$ final state using pp collisions at $\sqrt{s} = 13$ TeV with the ATLAS detector. https://atlas.web.cern.ch/Atlas/GROUPS/PHYSICS/CONFNOTES/ATLAS-CONF-2021-035.

[5] ATLAS Collaboration. Identification of Boosted Higgs Bosons Decaying Into $b\bar{b}$ With Neural Networks and Variable Radius Subjets in ATLAS. https://atlas.web.cern.ch/Atlas/GROUPS/PHYSICS/PUBNOTES/ATL-PHYS-PUB-2020-019

[6] ATLAS Collaboration. Efficiency corrections for a tagger for boosted $H \to b\bar{b}$ decays in pp collisions at $\sqrt{s} = 13$ TeV with the ATLAS detector. https://atlas.web.cern.ch/Atlas/GROUPS/PHYSICS/PUBNOTES/ATL-PHYS-PUB-2021-035

Prospectives for Higgs measurements at Future Circular Collider

Ang LI

Université de Paris, CNRS, Astroparticule et Cosmologie, F-75013 Paris, Francee

Abstract — After the Higgs boson discovery at the LHC in 2012 by the ATLAS and CMS experiments, the measurement of the properties of the Higgs boson became one of the highest priority among the experimental particle physics community. The Higgs boson mass and the third family (t, b and τ) Yukawa couplings have now been measured at the LHC. The best accuracy on the Higgs boson mass is currently 140 MeV. In order to measure the Higgs boson properties at high precision, the high energy future collider programs were proposed. In this report, the ZH cross section measurement with the "recoil mass" technique, the electron Yukawa coupling, and the Higgs boson self-coupling measurements at FCC will be discussed.

Future Colliders

Two types of e^+e^- accelerators, linear, and circular colliders, are proposed for future experiments by the particle physics community. The International Linear Collider (ILC) was proposed to be constructed in Japan while the Compact Linear Collider (CLIC) was proposed by CERN. They are both linear electron-positron collider working at different centre-of-mass (c.o.m) energies ($\sqrt{s}$). For circular colliders, CERN proposes the Future Circular Collider (FCC) while the Chinese community proposes the Circular Electron-Positron Collider (CEPC). The design of FCC and CEPC are similar. Both of them will first work as an electron-positron machine then upgrade to become hadron colliders. In this document, we will focus on the FCC.

The current strategy for FCC, agreed in 2020, sets an electron-positron Higgs boson factory as the highest priority facility after the Large Hadron Collider (LHC), along with the investigation of the technical and financial feasibility of such a Higgs boson factory, followed by a hadron collider placed in the same tunnel, about 90km long. Among the 18 years of preparation, the five-year feasibility studies of FCC will begin alongside with the LHC-Run3 in 2021. The next European Strategy will be held around 2026 to decide the approval of the project. If approved, the civil engineering, accelerator and detector constructions will begin. The whole FCC integrated program (FCC-INT) is similar to the LEP-LHC program (the Large Electron-Positron collider followed by the LHC in the same tunnel). The first stage of FCC will run as an electron-positron machine (FCC-ee) at different centre-of-mass energy points for 15 years. Then, there will be a 10 years long shutdown to upgrade the machine to FCC hadron collider (FCC-hh) including the change of magnets and detectors. FCC-hh will then take data for 25 years.

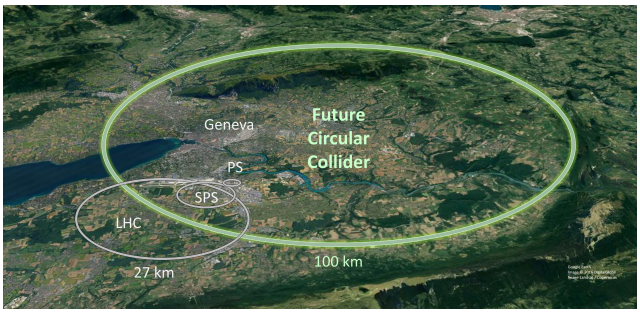

Figure 1: A schematic map showing a possible location for the Future Circular Collider (Image: CERN)

Higgs Measurements at Future Circular Colliders

The FCC-ee will operate at high luminosity at several c.o.m energy points, the Z pole at 91.2 GeV, WW threshold at 161 GeV, ZH peak at 240 GeV and close to the $t\bar{t}$ threshold at 365 GeV as shown in Figure 2. A run at the Higgs production threshold is also foreseen to measure the Higgs to electrons Yukawa coupling.

FCC-ee will produce 5×10^{12} Z boson, which is five times more than the number of Z boson produced by LEP, 10^8 WW events at WW threshold. The Higgsstrahlung (ZH) process, $e^+e^- \to ZH$, and the WW fusion process, $e^+e^- \to H\nu_e\bar{\nu}_e$, are essential for the Higgs boson measurements. The figure 3 shows the relation of cross-section to centre-of-mass of ZH and WW fusion production modes. The blue and green curve represent the higgsstrahlung (ZH) and WW-fusion respectively. The cross-section of Higgsstrahlung process is maximal at about 260 GeV, but the ZH event rate is largest at 240 GeV. About 10^6 events will be produced with the expected integrated luminosity of 5 ab^{-1}. At 365 GeV, the machine will produce 1.8×10^5 ZH and 4.5×10^4 WW-fusion events. Combining the data col-

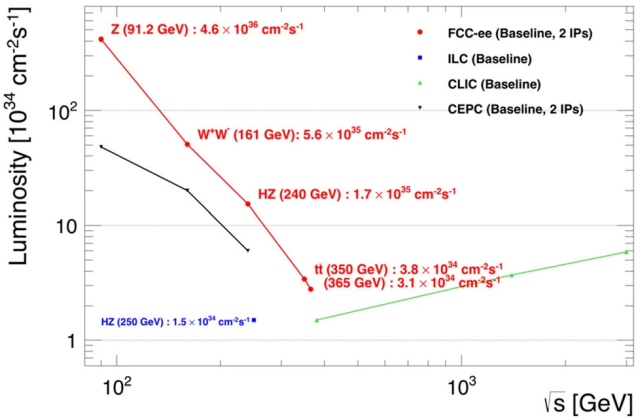

Figure 2: Luminosity as a function of centre-of-mass for the FCC-ee with two interaction points. The simulated luminosity is shown. Also shown are those estimated for ILC, CLIC and CEPC.

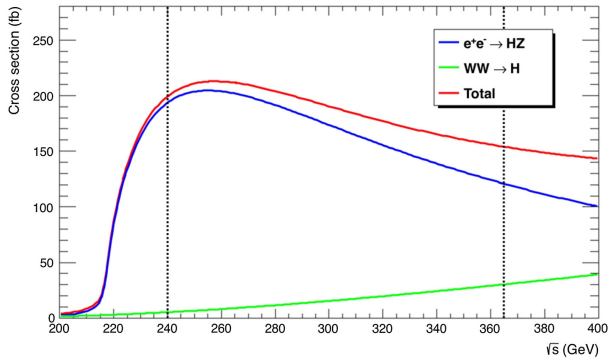

Figure 3: The Higgs boson production cross section as a function of the centre-of-mass energy in unpolarised e^+e^- collisions. The blue and green curves stand for the Higgsstrahlung and WW fusion processes, respectively, and the red curve displays the total production cross section. The vertical dotted lines indicate the centre-of-mass energies of choice at the FCC-ee for the measurement of the Higgs boson properties.[7]

lected at these two energies will improve the Higgs boson measurements significantly.

0.1 ZH cross section measurement with the Higgs boson "recoil mass" method

The progress made with the Higgs boson recoil mass method was reported in Ref. [1]. Only the leptonic decays of Z boson ($Z \to l^+l^-$, with $l = e$ or μ) are used for the cross-section measurement, as they are more precise and allow for the ZH events to be inclusively and efficiently selected independently of the Higgs boson decay mode. This choice is therefore effective towards an almost fully model-independent determination of the HZZ coupling, but the small Z di-electron and di-muon branching ratios limit the statistical precision. The mass m_{recoil} recoiling against the lepton pair is determined from total energy-momentum conservation that is shown in equation 1 and figuratively in figure 4 calculating the difference of the four-vector of centre-of-mass energy and lepton pair system.

$$m^2_{recoil} = (\sqrt{s} - E_{l\bar{l}})^2 - p^2_{l\bar{l}} = s - 2E_{l\bar{l}}\sqrt{s} + m^2_{l\bar{l}} \quad (1)$$

Since it uses the centre-of-mass energy, the recoil

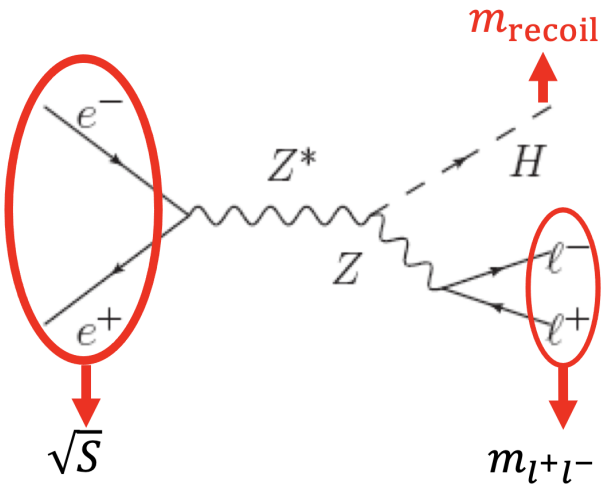

Figure 4: Feynman diagram of Higgsstrahlung process and "Recoil mass", m_{recoil}, calculation.

mass is sensitive to its precise knowledge, which can be affected by the beam energy spread (BES) and initial state radiation (ISR). The main backgrounds come from the WW, ZZ and $Z/\gamma \to l^+l^-$ processes. Figure 5 shows the m_{recoil} distribution between 40 and 160 GeV, where two peaks are present, one around 125 GeV, from the ZH process, while another is around 91 GeV, from the ZZ process. Ultimately [1], the σ_{ZH} accuracy and

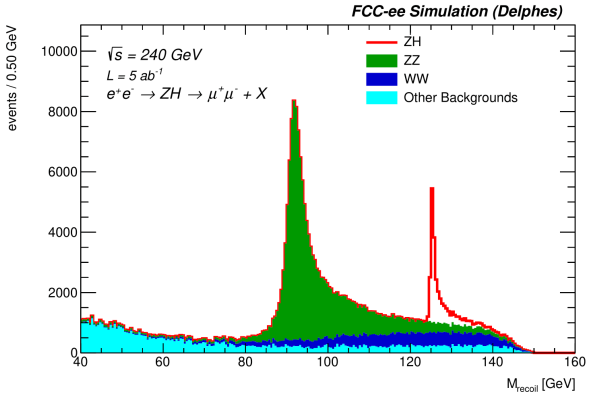

Figure 5: Inclusive m_{recoil} distribution for events with a Z decaying to $\mu^+\mu^-$, between 40 and 160 GeV. The Z peak from the ZZ background and the H peak from the ZH signal are well visible.

the Higgs boson mass are expected to achieve 0.5% and MeV level respectively. After measuring the ZH cross-section, the coupling of HZZ and Higgs boson width can be determined and are expected to achieve per mil precision.

Though the ZH recoil mass study is still on going here we show some preliminary results. We only studied

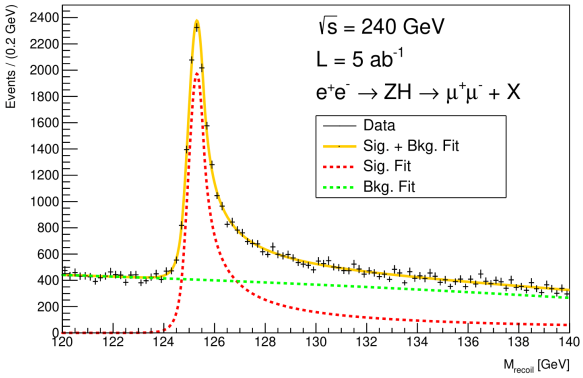

Figure 6: Zoom of the m_{recoil} distribution in the region around m_H. The ZH signal is fitted to a double-sided-crystal ball function, and the simulated background to a second-order polynomial.[1]

the $\mu^+\mu^-$ final states, applied simple selections, without applying advanced analysis techniques, and then determine the signal yield and peak position through a fit to the m_{recoil} distribution of the selected candidates. Figure 6 shows an example of the signal plus background fit. So far, we conclude that the statistical analysis yields an Higgs boson mass uncertainty of 6.7 MeV. Inclusion of the systematic uncertainties results into about 8.0 MeV and 1.9% uncertainties respectively, where the uncertainty from ISR is dominant but conservatively estimated.

0.2 Higgs-Electron Yukawa coupling

The electron Yukawa coupling measurement was studied in [2]. After achieving the MeV precision on the Higgs boson mass, the electron Yukawa coupling could be measured via the resonant s-channel $e^+e^- \to H$ by operating the FCC-ee at $\sqrt{s} = m_H$. So far, the Yukawa couplings have been measured only for top (t), bottom (b) quarks and τ lepton. At the end of the high luminosity LHC (HL-LHC) era, part of the Higgs boson Yukawa couplings to the second family fermions will be probed. But the Yukawa couplings to the first family fermion are difficult to probe since the Higgs boson branching ratio is proportional to the square of the mass of the fermion. The resonant Higgs boson production was considered so far only for a muon collider since the cross-section of $e^+e^- \to H$ is about 1.64 fb while for muon ($\mu^+\mu^- \to H$) the cross-section is 70 pb. There are several challenges for this measurement. First, we need a very accurate knowledge of the Higgs mass, which is expected to be achieved with the ZH recoil studies. Second, the ISR and BES needs to be known at about the MeV level. And finally, several backgrounds have to be known precisely. But this measurement has many fundamental physics motivations and implications. In particular, the Higgs mechanism for first family of fermions can be probed experimentally, and the existence of a particle that is quasi-degenerate with Higgs boson mass can be studied.

0.3 Trilinear Higgs self-coupling

The Higgs boson self-coupling measurement at FCC was studied in [3] and [4]. The self-coupling can be measured at FCC-ee using the loop-induced modifications to single-Higgs production. If we include all the FCC-ee running, a model-independent precision of 42% can be achieved on κ_λ. It will be reduced to 34% in combination with HL-LHC data, to 21% with 4 interaction points (IP). If we have four interaction points (IPs), the Higgs boson self-coupling could be discovered at FCC-ee. It will be reduced to 12% when only κ_λ is allowed to vary and the other parameters are taken at their SM values. The FCC-hh has the potential to reach a precision of 5% on κ_λ from di-Higgs production in combination with the precise Higgs boson decay branching ratio measurements from the FCC-ee.

Conclusions

In the Higgs boson measurements at the e^+e^- colliders, the "ZH recoil mass" method will improve the uncertainty of m_H to a few MeV level (and the Higgs boson width $\Gamma = 4.1$ MeV in the SM, could also be measured), the precision on σ_{ZH} to 0.5%, and measure the HZZ coupling as a "candle" for other Higgs boson studies. The electron Yukawa coupling could be probed via the s-channel at FCC-ee. The trilinear Higgs boson self-coupling could be discovered with four IPs at FCC-ee and will be studied precisely at FCC-hh. Results in this document are preliminary, and updated studies are ongoing.

References

[1] P. Azzurri, G. Bernardi, S. Braibant, D. d'Enterria, J. Eysermans, P. Janot, A. Li and E. Perez, Eur. Phys. J. Plus **137** (2022) no.1, 23 doi:10.1140/epjp/s13360-021-02202-4 [arXiv:2106.15438 [hep-ex]].

[2] D. d'Enterria, A. Poldaru and G. Wojcik, [arXiv:2107.02686 [hep-ex]].

[3] M. McCullough, Phys. Rev. D **90** (2014) no.1, 015001 [erratum: Phys. Rev. D **92** (2015) no.3, 039903] doi:10.1103/PhysRevD.90.015001 [arXiv:1312.3322 [hep-ph]].

[4] A. Blondel and P. Janot, [arXiv:1809.10041 [hep-ph]].

[5] F. An, Y. Bai, C. Chen, X. Chen, Z. Chen, J. Guimaraes da Costa, Z. Cui, Y. Fang, C. Fu and J. Gao, *et al.* Chin. Phys. C **43** (2019) no.4, 043002 doi:10.1088/1674-1137/43/4/043002 [arXiv:1810.09037 [hep-ex]].

[6] J. Yan, S. Watanuki, K. Fujii, A. Ishikawa, D. Jeans, J. Strube, J. Tian and H. Yamamoto, Phys. Rev. D **94** (2016) no.11, 113002 [erratum: Phys. Rev. D **103** (2021)

no.9, 099903] doi:10.1103/PhysRevD.94.113002 [arXiv:1604.07524 [hep-ex]].

[7] A. Abada *et al.* [FCC], Eur. Phys. J. C **79** (2019) no.6, 474 doi:10.1140/epjc/s10052-019-6904-3

Measurement of the Higgs self-coupling through same-charge di-leptons channel in the ATLAS experiment at the LHC

Océane PERRIN

LPC (Laboratoire de Physique de Clermont), CNRS/IN2P3

Abstract — This documents presents a search for the measurement of the Higgs self coupling through the Di-Higgs decaying in two leptons same charge ($\ell^{\pm}\ell^{\pm}$). This study is based on Monte-Carlos simulations corresponding of the LHC-Run II data collected with the ATLAS detector from 2015 to 2018 with an integrated luminosity of 139 fb^{-1}. The signal extraction has been done through a multivariate method targeting each 3 main backgrounds (Di-boson, $t\bar{t}$ and single boson productions), leading to $\mu_{95\%}$=30.1. The main instrumental backgrounds have been estimated using data Driven methods. Finally this analysis is included into a global analysis of the leptonic final state of the Higgs pair. Combining these previous channels leads to an expected limit $\mu_{95\%}$=11.35 (stat only).

Introduction

In 1964, 6 physicists proposed a mechanism to granting masses to already known particles that compose the matter. They introduced a new particle called Higgs Boson or BEH (Brout-Englert-Higgs) boson ([1][2]). In 2012, a bosonic particle with a mass equal to 125GeV has been observed by ATLAS and CMS Collaborations at the LHC. The discovery of the Higgs boson brought a first probe of the mechanism that triggers the breaking of the electroweak symmetry, called the BEH mechanism. Since, physicists are trying to probe the various properties that we confer to the Higgs boson, such as the Higgs self-interaction.

Electro-weak symmetry breaking (EWSB)

The electromagnetic force is unified with the weak force, and so called electroweak force. Yet we know that the symmetry of the electroweak force is broken (bosons W and Z are massive compared to massless photons). This symmetry has been broken by the Higgs vacuum expectation value (vev for short - [3]) due to the shape of the Higgs potential, also called mexican hat potential (see figure 1).

Searching the minimum of the Higgs potential leads to the general expression:

$$\mathcal{V}_H = \frac{1}{2}m_H^2 H^2 + \lambda_3 \nu H^3 + \lambda_4 H^4 \qquad (1)$$

With λ_3 and λ_4 corresponding respectively to trilinear and the quartic Higgs self-couplings and m_H the Higgs mass. In the Standard Model, the value of these two self-couplings have been predicted to equal $\lambda_3^{SM} = \frac{m_H^2}{2\nu^2}$ and $\lambda_4^{SM} = \frac{m_H^2}{8\nu^2}$, where μ is the expected value of the Higgs field in the vacuum.

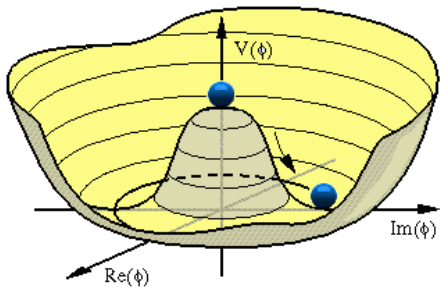

Figure 1: Higgs potential shape as function of Φ.

Di-Higgs production at LHC and decay

The trilinear Higgs self-coupling can be directly extracted from Higgs pair-production at LHC. Several mechanisms lead to di-Higgs production using proton-proton collisions [4]:

- The Gluon-gluon fusion (see figure 2)
- Vector boson fusion (WW or ZZ fusion process) (see figure 3)

The HH can decay into multiple channels summarized in figure 4. In this study, the HH production has been studied decaying into $\ell^{\pm}\ell^{\pm}$, where ℓ could be e or μ. This signature has been chosen in order to minimise the background. This channel corresponds to 3% of the decays of the di-Higgs.
A recent search of Higgs boson pair production decaying into 2 bottom quarks and two photons with ATLAS

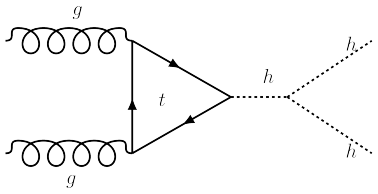

Figure 2: Feynman diagrams of Higgs boson pair production through gluon-gluon fusion

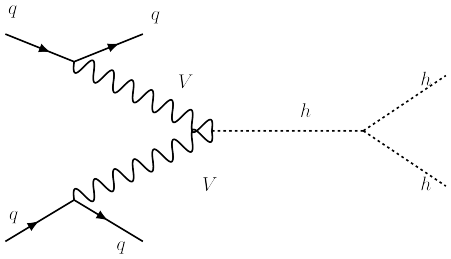

Figure 3: Feynman diagrams of Higgs boson pair production through vector boson fusion

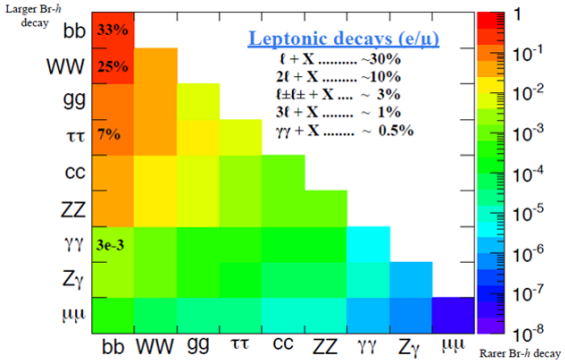

Figure 4: Branching ratios of the decay of an diHiggs pair.

detector ($\sqrt{s}$=13 TeV) shows observed (expected) upper limit at 95% on the signal strength of 5.7 [5].

Signal Extraction

The signal and backgrounds processes are simulated using MADGRAPH and POWHEG Monte Carlo generators. This analysis has been done using Monte-Carlo Simulations, corresponding of the LHC-Run II data collected with ATLAS detector from 2015 to 2018, corresponding to an integrated luminosity equals to 139 fb^{-1}.

Building BDTs

In order to define enriched regions in signal (HH decaying into $\ell^{\pm}\ell^{\pm}$), a variable called "discriminating variable" need to be produced. In this study, a boosted decision tree (BDT) method has been chosen. This method is a consecutive binary selection over various topological and kinematic properties such as impulsion, invariant mass or distance between the two leptons. In the case of $\ell^{\pm}\ell^{\pm}$, we need to deal with 3 different main backgrounds. The strategy of this analysis, is to train 3 individual BDTs respectively with VV VS HH ($t\bar{t}$ VS HH, Vjets VS HH), see figure 5. Then these BDT output variables, are combined into signal sensitivity estimate by applying a new BDT trained over all backgrounds.

Signal strength estimation

Once the final BDT output has been estimated for all backgrounds, a profile likelihood fit has been used to estimate the limit on the signal strength with a 95% confidence level, also called "$\mu_{95\%}$". At this stage, no systematic uncertainty was taken into account.
The profile likelihood fit leads to $\mu_{95\%}$=29.4.

Instrumental Background Estimation

Superposing data to Monte-Carlo simulations highlight a good agreement within 25% (see figure 6). This difference can be caused by some significant mismodeling of some processes in the Monte-Carlo simulations, including charge misassignment and non-prompt leptons backgrounds. In this study, these two backgrounds have been estimated or adjusted by data-Driven methods.

Charge mis-identification estimation

An important background process contributing to HH signal is the charge mis-assignment of one of the two leptons. This phenomenon is due to one electron having a hard bremsstrahlung ($e^{\pm} \rightarrow e^{\pm}\gamma^{*} \rightarrow e^{\pm}\, e^{+}\, e^{-}$) or due to a mis-measurement of a electron track-curvature. The aim of this charge mis-identification estimation is to determinate a rate (ϵ) and apply it to data event containing two electrons with opposite charges ($e^{+}e^{-}$) in the final state. Finally the number of same charge events N_{SS} can be written as:
for ee channel:

$$N_{SS} = \frac{\epsilon_{e1} + \epsilon_{e2} - 2\epsilon_{e1}\epsilon_{e2}}{1 - (\epsilon_{e1} + \epsilon_{e2} - 2\epsilon_{e1}\epsilon_{e2})} N_{OS} \qquad (2)$$

for eμ channel:

$$N_{SS} = \frac{\epsilon_{e}}{1 - \epsilon_{e}} N_{OS} \qquad (3)$$

The rates are evaluated for electron from QED contribution, material conversion, or electron score identification contribution and parameterised as function of p_T and η (see figure 7).

Non-prompts leptons backgrounds estimation

Non-prompts leptons backgrounds in $e^{\pm}e^{\pm}$ channel include a mixture of semileptonic heavy-flavour decays, initial and final state radiation contribution (so called Fake_QED), light-flavour hadron decays and photon

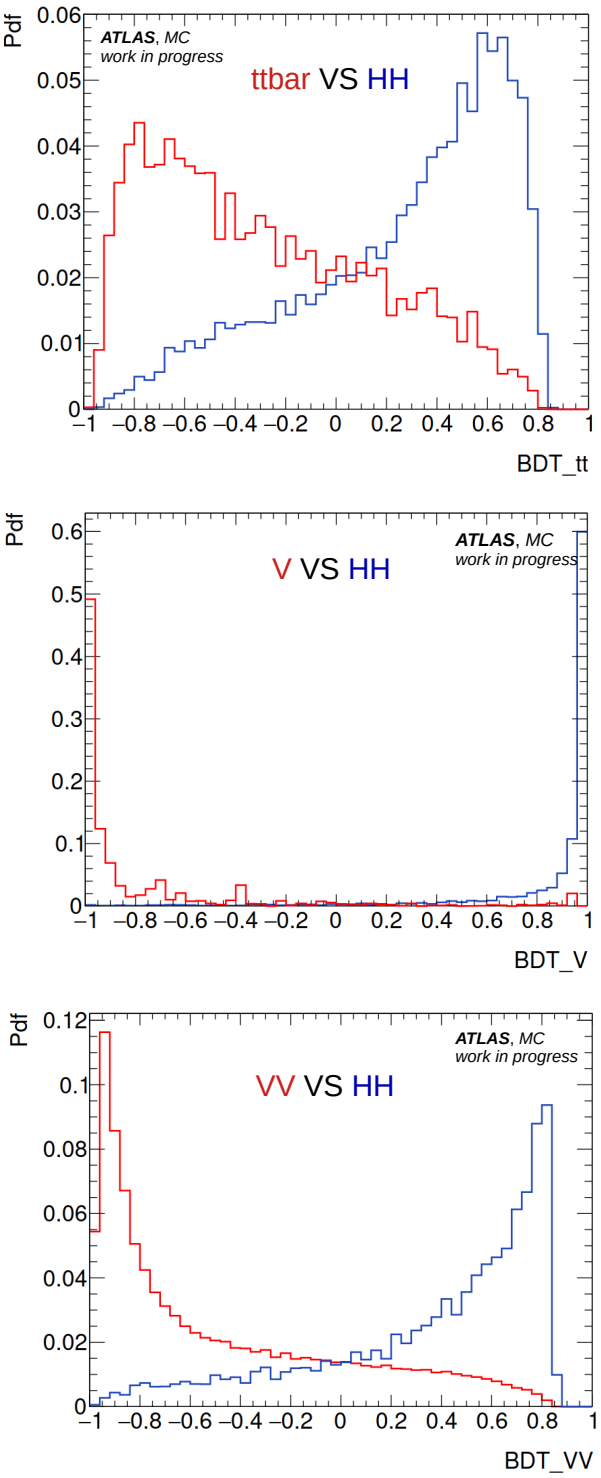

Figure 5: Distribution of each specific BDT: $t\bar{t}$ VS HH (top), VV VS HH (center), Vjets VS HH (bottom). Di-Higgs decaying into $\ell^{\pm}\ell^{\pm}$ is in red, and backgrounds are in blue.

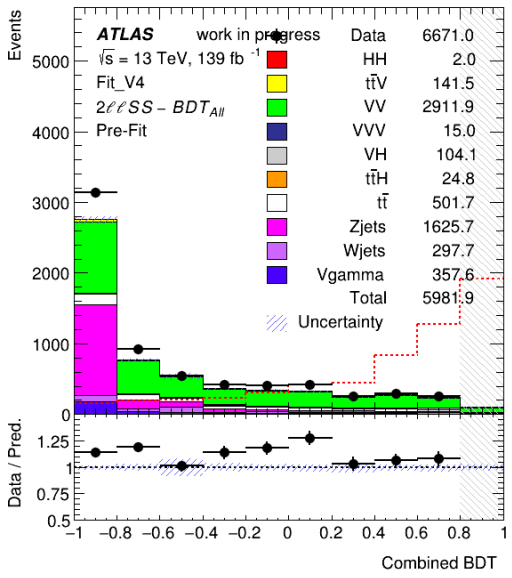

Figure 6: Distribution of the Combined BDT, colors bars for MC simulation and black dot for Data

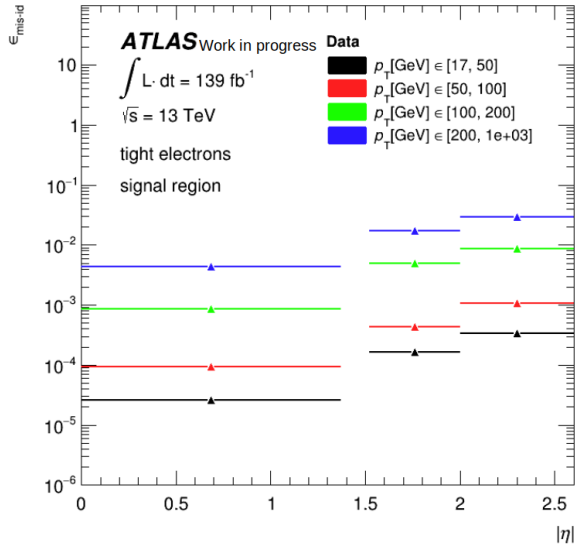

Figure 7: Charge mis-assignment rates estimated for various η and P_T in signal region for electron score identification

conversions. In order to adjust the MC simulation, a template fit method has been used. This semi-data-driven method relies on the re-normalisation of the previously quoted non-prompt contributions templates, considering all shapes given by MC simulation. The aim is to define 5 control regions enriched in each non-prompt backgrounds, and use a profile likelihood method to extract 4 normalisations factors. Figures 8 and 9 show a region enriched in electron production (μe+ee) for pre-fit and post-fit.

Then the 4 Normalization factors are applied to the template.

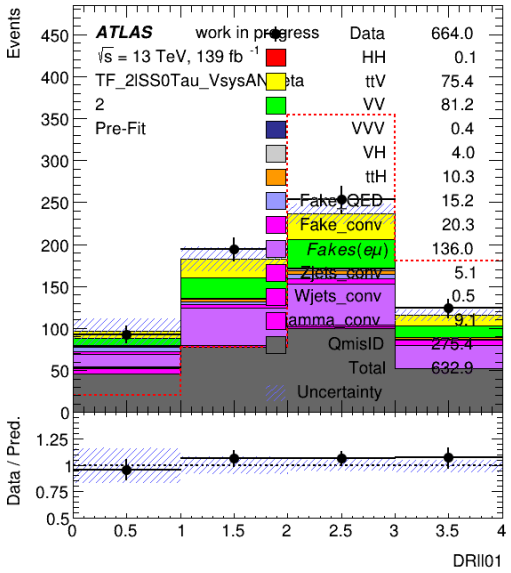

Figure 8: Distribution of the distance between two leptons for pre-fit. This region is enriched in electron production (μe+ee).

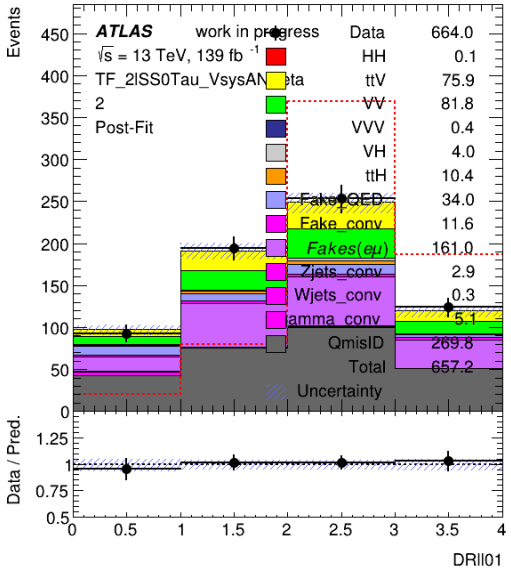

Figure 9: Distribution of the distance between two leptons for post-fit. This region is enriched in electron production (μe+ee).

Final result

Including the instrumental background estimations and the systematics related to this last background, a good agreement, Data VS Prediction, within 20% can be observed, see Figure 10. Then, a profile likelihood fit has been done over the final BDT output leading to a limit $\mu_{95\%}$= 33.2.

Combination

The result obtained in the previous section is specific to the $e^{\pm}e^{\pm}$ signature. This study is included into leptonic

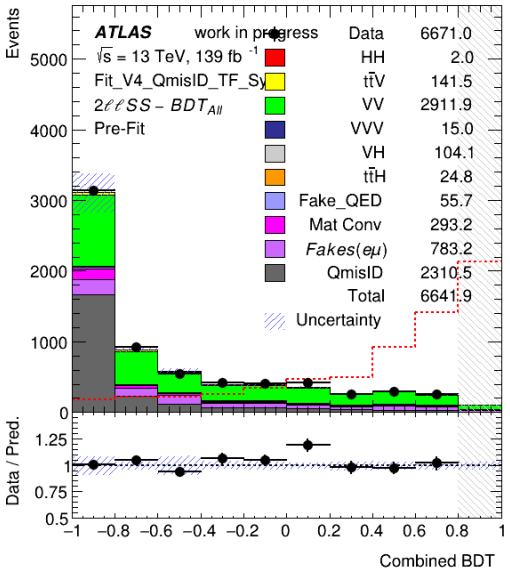

Figure 10: Distribution of the Combined BDT including instrumental background estimation. Colors bars are for MC simulation/instrumental background estimate and black dot for Data

final state analysis of the Higgs pair, itself included into a di-higgs analysis (all decays merged). Each leptonic decay channel works with its own strategy and use a BDT method to build its final discriminant variable. Then, results are combined in order to extract a limit μ_{95} = 11.50 (see figure 11). At this stage, the combination does not include data-driven adjustment or systematics.

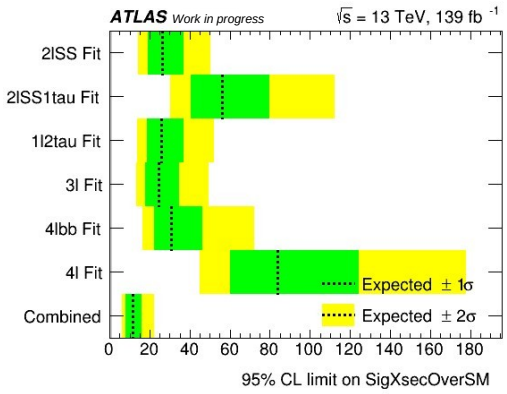

Figure 11: Expected limit ($\mu_{95\%}$) obtained from each leptonic decays channels and from the combination

Conclusions and future prospects

A introduction to search for Higgs self-coupling through Higgs boson pair decaying to two leptons same-charge ($\ell^{\pm}\ell^{\pm}$) has been presented. The signal extraction has been done by training 3 BDTs specific to the 3 main backgrounds and combined into a final discriminant variable. Then two data-driven methods have been

used to estimate instrumental backgrounds including non-prompt and charge mis-identification backgrounds. Finally a profile likelihood fit has been done, leading to a limit equals to $\mu_{95\%}$=33.2, including systematics related to instrumental backgrounds.
This analysis takes part of the HH multileptons channel. This combination leads to $\mu_{95\%}$=11.5, excluding systematics and data driven estimations. The next step will be to include all systematics into the analysis and the combination.

References

[1] Peter W.Higgs,Broken Symmetries and the Masses of Gauge Bosons, 1964, Phys. Rev. Lett. 13 (16 1964) 508

[2] F. Englert and R. Brout, Broken Symmetry and the Mass of Gauge Vector Mesons, 1964, Phys. Rev. Lett. 13 (9 1964) 321

[3] M. Tanabashi et al. (Particle Data Group), Phys. Rev. D 98, 030001 (2018)

[4] G. Degrassi et al., Probing the Higgs self coupling via single Higgs production at the LHC

[5] ATLAS Collaboration, Search for Higgs boson pair production in the two bottom quarks plus two photons final state in pp collisions at $\sqrt{s}$ = 13 TeV with the ATLAS detector (arXiv:2112.11876)

Measuring the CKM angle γ in open charm B decays at LHCb

Halime SAZAK

University Clermont Auvergne, CNRS/IN2P3, LPC, Clermont-Ferrand, France

Abstract — This note reports on the study of the CKM angle γ using the decay channel $B_s^0 \to \tilde{D}^{(*)0}\phi$, where the $\tilde{D}^0$ meson is reconstructed five modes $K\pi$, $K3\pi$, $K\pi\pi^0$, KK and $\pi\pi$, while the ϕ is reconstructed in the mode K^+K^- and the another decay channel is $B^\pm \to D^0 K^{*\pm}$, where two body final states of the D^0 meson are considered with $K\pi$, KK, and $\pi\pi$ and the K^* is reconstructed in the mode $K\pi^0$. This study is based on the total LHCb dataset of Run 1 & Run 2, accumulated over years 2011 to 2018.

Introduction

The γ angle is one of the three angles that makes up the Cabibbo-Kobayashi-Maskawa (CKM) matrix [1] defined as $\arg[-V_{ud}V_{ub}^*/V_{cd}V_{cb}^*]$. Precision measurement of the angle γ in a variety of B-meson decay modes is one of the main goals of flavour physics. The measurement can be achieved by exploiting the interference of decays that proceed via the $b \to c\bar{u}s$ and $b \to u\bar{c}s$ tree-level amplitudes, where the determination of the relative weak phase γ is not affected by theoretical uncertainties Figure 1.

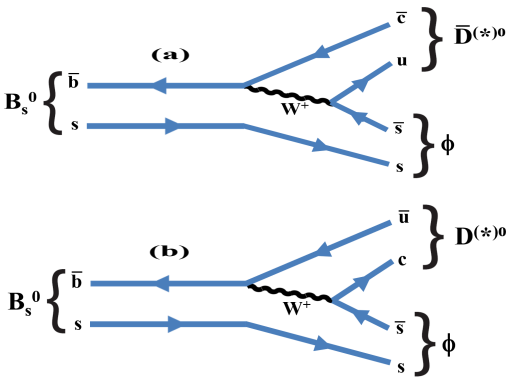

Figure 1: Feynman diagrams for (a) $B_s^0 \to \bar{D}^{(*)0}\phi$ $b \to c$ and (b) $B_s^0 \to D^{(*)0}\phi$ $b \to u$ transition.

The measurement of the γ angle in tree-level open-charm b-hadron decays is theoretically clean and provide a benchmark for the SM of the particle physics to explain the CP violation and to test the new physics contribution Beyond the Standard Model. By having precision measurement, LHCb experiment aims to improve the knowledge of γ. A measurement with a precision better than 1° challenges the Standard Model(SM) with the coherence of the KM mechanisms up to NP scales of at least 15 TeV, whatever is the scenario of New Physics(NP).

The γ angle can be measured through many different decay modes. LHCb has obtained the best precision on gamma by combining the measurements from different decay modes using the full Run 1 and Run 2 data LHCb data. The latest precision on gamma which gives $\gamma = (74.0^{+5.0}_{-5.8})°$ where the uncertainty includes both statistical and systematic uncertainties [2].

There are alternative methods to improve the sensitivity on γ. Among them a brand new analysis dealing with $B_s^0 \to \tilde{D}^{(*)0}\phi$ decays and a mode conventional one with the mode $B^\pm \to D^0 K^{*\pm}$ have the potential to make a significant impact. In this study, for the mode $B_s^0 \to \tilde{D}^{(*)0}\phi$ where D meson is reconstructed in the quasi-specific modes $K\pi$, $K3\pi$, $K\pi\pi^0$ and CP-eigenstate modes KK and $\pi\pi$ has been measured. As shown in the sensitivity paper Ref [6], the yields of these modes were estimated using realistic assumptions based on measurements from LHCb [3, 4, 5]. Among these sub-decay modes we work on optimising the $D^0 \to K\pi\pi^0$ where the combination of two tracks and photons reconstructed in π^0. And for the $B^\pm \to D^0 K^{*\pm}$ mode where K^* decays to $K^* \to K\pi^0$. The experimental difficulty of these modes is related to the neutral pion produced at LHCb. The first strategy is to fight against the combinatorial background from genuine of false π^0. The analysis including full datasets Run 1 and Run 2.

$B_s^0 \to \tilde{D}^{(*)0}\phi$ Analysis

The first part of the report shows the study on the γ angle measurement through the $B_s^0 \to \tilde{D}^{(*)0}\phi$, decay where D meson decays to 5 sub-decays: $K\pi$, $K3\pi$, $K\pi\pi^0$, KK and $\pi\pi$. The quasi flavour-specific $K^-\pi^+\pi^0$ decay mode is studied in this analysis. This mode is complicated because of the π^0. Since we are dealing with the large background coming from π^0 and we

would like to reduce the level of the background coming from genuine fake π^0 produced at LHCb. π^0 is identified by a decay of two photons detected by the Electromagnetic calorimeter (ECAL). The resolved π^0 where the two photons reconstructed separately is used and gives the precise reconstruction and the better mass resolution of the particles. Preliminary studies was done on this sub-decay mode with Run 1 and Run 2 data (2018 not included). An update of the analysis has been done with the full dataset corresponding to integrated luminosity of $3.2\,\text{fb}^{-1}$ collected with the LHCb detector at center-of-mass energies of 7 and 8 TeV from 2011 to 2012 and of $5.9\,\text{fb}^{-1}$ at center-of-mass energies of 13 TeV from 2015 to 2018 years. In this work we describe the measurement through the decay of $\text{B}_\text{s}^0 \to \tilde{D}^{(*)0}\phi$ whose observations were published by the LHCb experiment in 2018 [3] and 2021 [6]. The analysis is proceed in two steps: the first part of the study is to define the specific selections for the $K\pi\pi^0$ sub-decay mode. To get rid of the background coming from the π^0, a method based on understanding of the $D^0 \to K\pi\pi^0$ decay that goes mainly through three particles: $K^{*0}(892)$ (horizontal segment), $K^{*-}(892)$ (vertical segment) and $\rho^+(770)$ (anti-diagonal segment) which are displayed in the Figure 2 are developed. To fight against the combinatorial background forming false $\tilde{D}^0 \to \text{K}^-\pi^+\pi^0$ and to reduce the level of false π^0 as much as possible, we developed specific selections which strategy is actually to deal with the specific skin of π^0. The selection cuts that we use for the $\tilde{D}^0 \to \text{K}^-\pi^+\pi^0$ in $\text{B}_\text{s}^0 \to \text{D}^0\phi$ decays, are based on the discriminating observables (kinematic and particle identification variables). Among those discriminating variables, in order to understand the Dalitz plot structure and to keep in a large majority of the occurences we use a variable named Dalitz Weight. If there are any resonances in the decay, they will reveal as lines on the plot and their position (horizontal, vertical and diagonal) will indicate the particles come from those resonant particles. The amplitude of this decay mode was measured by E691 experiment Ref. [9] and confirmed by the CLEO-C experiment [10].

The second part of the analysis, we worked on the pre-selection optimisation on the signal mode $\text{B}_\text{s}^0 \to \tilde{D}^{(*)0}\phi$. For the studied decay channel $\text{B}_\text{s}^0 \to \tilde{D}^{(*)0}\phi$, we used the similar selections requirements which was designed for the non-resonant measurement of $\text{B}_\text{s}^0 \to \bar{\text{D}}^0\text{K}^+\text{K}^-$ branching fraction [7]. Topological and kinematical variables which are based on multivariate (MVA) analysis has been employed on the mode. After all selection requirements are applied, a fit is performed to the invariant mass distribution of Dϕ candidates. Figure 3 from the published study [3] on $\text{B}_\text{s}^0 \to \tilde{D}^{(*)0}\phi$ and $\bar{\text{D}}^0$ meson decays to $K\pi$ shows the fit to the invariant mass distribution of Dϕ candidates obtained using the sPlot technique Ref. [11].

An extended unbinned maximum-likelihood fit is performed to obtain the yields for the $\text{B}_\text{s}^0 \to \text{D}^0\phi$ and $\text{B}_\text{s}^0 \to \tilde{D}^{(*)0}\phi$. After performing fit, the number of yields obtained for $K\pi\pi^0$ are given in the Table 1, this gives the comparison for the yields from the previous analysis [6] and ongoing analysis.

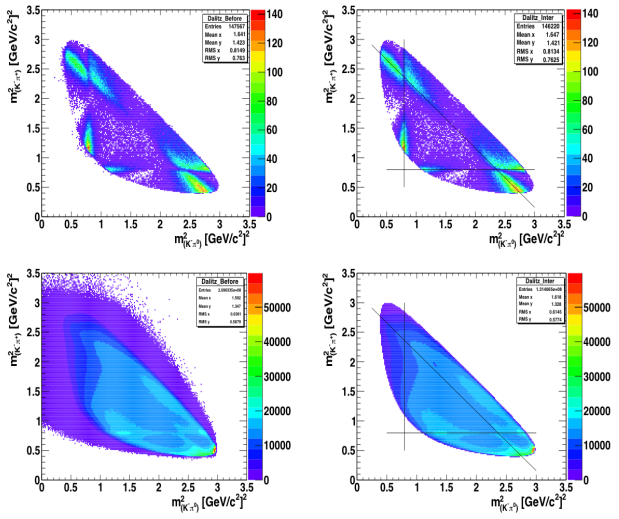

Figure 2: Dalitz Plot of the selected sample $\text{D}^0 \to \text{K}^-\pi^+\pi^0$ for signal MC Run 2 before DW selection plot (top left) and after selection (top right) for background Data Run 2 before DW selection(bottom left) and after selection (bottom right).

From the Table, it can be seen that the signal yield is improved the purity is very competitive wrt to the $K\pi$ mode. The dataset for the $\text{B}_\text{s}^0 \to \tilde{D}^{(*)0}\phi$ is multiplied by almost a factor of 2.4. Next step of the analysis will be to combine the $K\pi$, $K3\pi$, KK and $\pi\pi$ sub-decays to measure γ.

D decay mode	$\text{B}_\text{s}^0 \to \bar{\text{D}}^0\phi$	$\text{B}_\text{s}^0 \to \tilde{D}^{(*)0}\phi$
$K\pi\pi^0$ (Run 1+Run 2)	58	34
$K\pi\pi^0$ (Run 1+Run 2)	136±13	147±19

Table 1: Obtained event yields for the $K\pi\pi^0$ with Run 1 and Run 2 dataset. (Top) gives the expected event yields for the $K\pi\pi^0$ from the study in the sensitivity paper published in 2021 [6].(Bottom) gives the event yields from the ongoing study on $K\pi\pi^0$.

$\text{B}^- \to \text{D}^0\text{K}^{*-}$ Analysis

This part reports the study on more conventional $\text{B}^\pm \to \text{D}^0\text{K}^{*\pm}$ decay, where D is either a D^0 or $\bar{\text{D}}^0$ with D decays to 2 body final states ($K\pi$, KK, and $\pi\pi$). The $\text{B}^- \to \text{DK}^{*-}$ channel has previously been investigated by the BaBar collaboration using a variety of two-body D decay modes [8]. In 2017, LHCb published the $\text{B}^- \to \text{D}^0\text{K}^*$ results using two- and four-body D^0 final states using Run 1, 2015 and 2016 LHCb samples which K^{*-} decays to $\text{K}^{*-} \to \text{K}_\text{S}^0\pi^-$. This study will be improved with another mode which K^{*-} decays to $\text{K}^{*-} \to \text{K}^-\pi^0$ which has a larger branching fraction, but the π^0 reconstruction efficiency is much low. However, the two K^{*-} channels are same mode and the same physical parameters can be shared, like r_B, δ_B and γ. Therefore this mode could make a large contri-

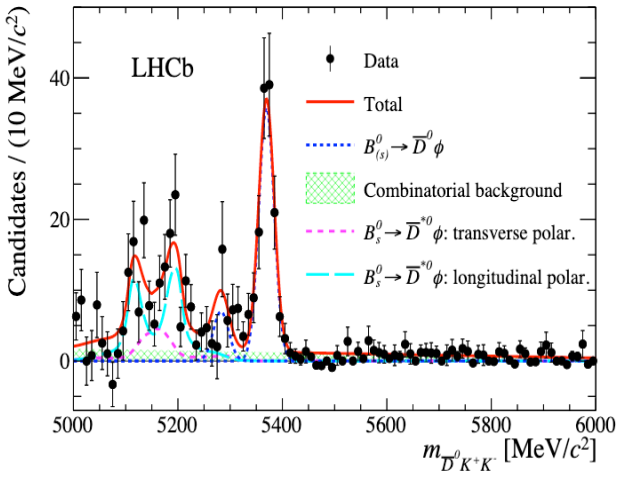

Figure 3: Fit to the $m_{\overline{\mathrm{D}}^0\mathrm{K}^+\mathrm{K}^-}$ invariant mass distribution of $\overline{\mathrm{D}}^0\phi$ candidates obtained using sPlot technique. Data is shown as black points. The total function is displayed as a red solid line. Different contributions are given dashed lines and shadowed areas. Blue dashed line is given for the $\mathrm{B}^0_\mathrm{s} \to \overline{\mathrm{D}}^0\phi$ and $\mathrm{B}^0 \to \overline{\mathrm{D}}^0\phi$ signals. Green shaded area is for the combinatorial background. $\mathrm{B}^0_\mathrm{s} \to \tilde{D}^{(*)0}\phi$ is represent with the cyan long dashed with longitudinal polarisation and pink middle dashed for transverse polarisation factor [3]

bution to the γ measurement at LHCb. Furthermore, we optimized the selection and reconstruction approach for $\mathrm{B}^- \to \mathrm{D}^0\mathrm{K}^*$ with $\mathrm{K}^{*-} \to \mathrm{K}^-\pi^0$ channel, the reconstruction efficiency is improved significantly. Figure 4 shows the contour plots of gamma angle as a function of the physics qualities : strong phase δ_B and the r_B is for the ratio of the amplitudes of the two interfering mechanism.

From the Figure 4, dashed lines are drawn at 1σ and the solid lines continue at 2σ. The dark green zone corresponds to the combination of the two channels at 1σ, the light green one at 2σ. We can see that, the result for the $\mathrm{K}^{*-} \to \mathrm{K}^-\pi^0$ is quite competitive with the published result of $\mathrm{K}^{*-} \to \mathrm{K}^0_\mathrm{S}\pi^-$ decay. This will be improved with the full Run 1 and Run 2 dataset.

Results

Updates on the measurement of γ angle through the $\mathrm{B}^0_\mathrm{s} \to \tilde{D}^{(*)0}\phi$ and the $B^\pm \to D^0 K^{*\pm}$ decays are reported. The dataset for the $\mathrm{B}^0_\mathrm{s} \to \tilde{D}^{(*)0}\phi$ is multiplied by almost a factor of 2.4 with the ongoing study. Analysis will be finalized soon for $K\pi\pi^0$ to extract the γ phase with the $K\pi$, $K3\pi$, KK and $\pi\pi$ sub-decay modes. By using the expected event yields, a precision on γ of about 8 to 19° can be achieved with Run 1 and Run 2 data. With the more data, the precision on γ of 3-8° can be reached with the LHCb Run 1 to 3 dataset($23\,\mathrm{fb}^{-1}$ in 2025).

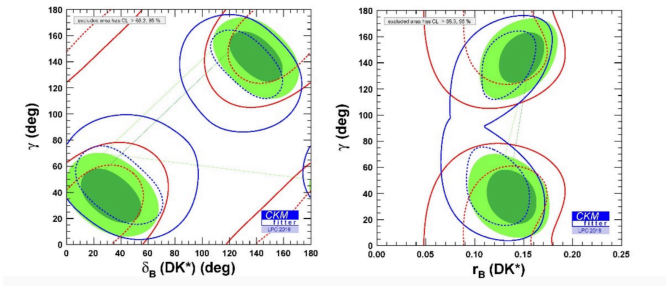

Figure 4: γ angle as a function of the value of δ_B(left) and r_B (right).The red colour is given for the $\mathrm{K}^{*-} \to \mathrm{K}^-\pi^0$ and the blue colour is for $\mathrm{K}^{*-} \to \mathrm{K}^0_\mathrm{S}\pi^-$ The combination of the two decay mode is given in green curve.

References

[1] M. Kobayashi and T. Maskawa, "CP Violation in the Renormalizable Theory of Weak Interaction," Prog. Theor. Phys. **49** (1973), 652-657 doi:10.1143/PTP.49.652

[2] M. W. Kenzie *et al.* [LHCb], "Update of the LHCb combination of the CKM angle γ," LHCb-CONF-2018-002.

[3] R. Aaij *et al.* [LHCb], "Observation of $B^0_s \to \overline{D}^{*0}\phi$ and search for $B^0 \to \overline{D}^0\phi$ decays," Phys. Rev. D **98** (2018) no.7, 071103 doi:10.1103/PhysRevD.98.071103 [arXiv:1807.01892 [hep-ex]].

[4] R. Aaij *et al.* [LHCb], "Measurement of CP observables in $B^\pm \to DK^\pm$ and $B^\pm \to D\pi^\pm$ with two- and four-body D decays," Phys. Lett. B **760** (2016), 117-131 doi:10.1016/j.physletb.2016.06.022 [arXiv:1603.08993 [hep-ex]].

[5] R. Aaij *et al.* [LHCb], "A study of CP violation in $B^\mp \to Dh^\mp$ ($h = K, \pi$) with the modes $D \to K^\mp\pi^\pm\pi^0$, $D \to \pi^+\pi^-\pi^0$ and $D \to K^+K^-\pi^0$," Phys. Rev. D **91** (2015) no.11, 112014 doi:10.1103/PhysRevD.91.112014 [arXiv:1504.05442 [hep-ex]].

[6] D. Ao, D. Decamp, W. B. Qian, S. Ricciardi, H. Sazak, S. T'Jampens, V. Tisserand, Z. R. Wang, Z. W. Yang and S. N. Zhang, *et al.* "Study of CKM angle γ sensitivity using flavor untagged $B^0_s \to \tilde{D}^{(*)0}\phi$ decays," Chin. Phys. C **45** (2021) no.2, 023003 doi:10.1088/1674-1137/abd16d [arXiv:2008.00668 [hep-ex]].

[7] R. Aaij *et al.* [LHCb], "Observation of the decay $B^0_s \to \overline{D}^0 K^+K^-$," Phys. Rev. D **98** (2018)

no.7, 072006 doi:10.1103/PhysRevD.98.072006 [arXiv:1807.01891 [hep-ex]].

[8] B. Aubert *et al.* [BaBar], "Measurement of CP violation observables and parameters for the decays $B^{\pm} \to DK^{*\pm}$," Phys. Rev. D **80** (2009), 092001 doi:10.1103/PhysRevD.80.092001 [arXiv:0909.3981 [hep-ex]].

[9] M. V. Purohit [E-691], "A Dalitz plot analysis of D –> K pi pi decays using E-691 data,"

[10] S. Kopp *et al.* [CLEO], "Dalitz analysis of the decay D0 —> K- pi+ pi0," Phys. Rev. D **63** (2001), 092001 doi:10.1103/PhysRevD.63.092001 [arXiv:hep-ex/0011065 [hep-ex]].

[11] M. Pivk and F. R. Le Diberder, "SPlot: A Statistical tool to unfold data distributions," Nucl. Instrum. Meth. A **555** (2005), 356-369 doi:10.1016/j.nima.2005.08.106 [arXiv:physics/0402083 [physics.data-an]].

Electron energy resolution corrections in the ATLAS liquid argon electromagnetic calorimeter

Juan Salvador TAFOYA VARGAS

IJCLab / Université Paris-Saclay

Abstract — The calibration of the liquid argon electromagnetic calorimeter at the ATLAS experiment is performed with Z $\rightarrow$ *ee* data and MC. While the continuous efforts of the collaboration have improved the agreement between both samples, there is a remaining non-negligible discrepancy between the data and MC dilepton invariant mass lineshape that has not been accounted for by existent corrections. As measurements coming from the tracker (and their simulation) are highly precise, the energy measurement at the calorimeter seems to be the most likely culprit. This study aims to better understand the mass lineshape discrepancy by performing energy resolution corrections on MC. These are performed on an event-by-event basis with scalings of $\Delta = E_{\text{reco}} - E_{\text{truth}}$ via some parametrization $\Delta' = f_\eta(\Delta, E^{\text{T}}_{\text{truth}})$, where the explicit dependence on $E^{\text{T}}_{\text{truth}}$ seeks to account for the changing kinematics of the electron-pair across different regions of the calorimeter. As the Δ' correction translates into a shape deformation of the energy resolution distribution, it allows to account for specific effects, such as tails and negative smearing corrections, which have an important effect on the lineshape agreement.

Introduction

In the ATLAS experiment, the energy of electrons and photons is completely determined by the Liquid Argon (LAr) electromagnetic calorimeter. Since these measurements are of fundamental importance for any other study, such as precision electroweak studies, the proper calibration of the detector is imperative, which motivates for continuous efforts to improve higher order effects.

Calibration is done sequentially by concentrating on "easily" measurable phenomena, such as $Z \rightarrow ee$, where all the sub-products can be detected within the calorimeter and the parent particle is completely reconstructed. The particular study described through this note is applied at a late stage of the calibration sequence (shown in a red rectangle in Figure 1), right before the data-driven scale validation.

The entirety of this study is described in detail in Ref. [1].

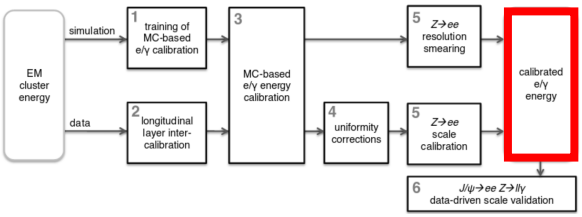

Figure 1: Calibration chain for e/γ in the ATLAS electromagnetic calorimeter.

Motivation

While many studies before this one have improved considerably the agreement between the data and MC mass lineshape, it is still not perfect (see, for instance, Figure 2). It is suspected that this disagreement may be caused primarily by a miscalibration of the simulated calorimeter, and thus many efforts have been done aiming to improve the corresponding MC sample.

This particular work aims to calibrate the MC energy resolution via scalings in order to better account for specific effects, such as tails and small/negative smearing corrections.

An initial study on this technique has already been done by the USTC group [2], which was focused towards the forward part of the calorimeter. This same study serves as the initial reference for the following work.

Energy resolution corrections

Along this study, data will be considered as a perfect sample, and thus all corrections are done on the MC side. We define the MC resolution Δ as the difference between the reconstructed energies E_{reco} (GEANT4 + energy scale correction [3]) and their corresponding values at generation E_{truth} (truth = dressed level), i.e.

$$\Delta = E_{\text{reco}} - E_{\text{truth}}. \tag{1}$$

We define then a corrected resolution value Δ' as

$$\Delta' = f(\Delta), \tag{2}$$

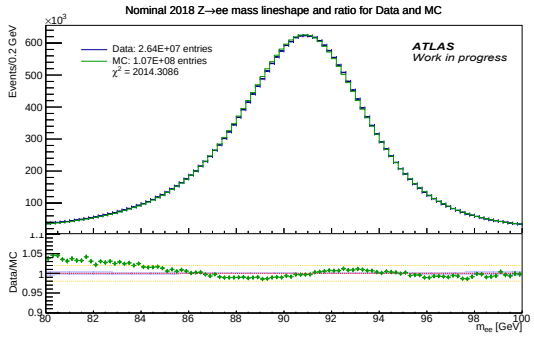

Figure 2: $Z \to ee$ invariant mass lineshape, including all the available sample, after the energy scale correction described in Ref. [3]. The bin-to-bin χ^2 value between data and MC is shown.

such that the corrected energy E'_{reco} looks like

$$E'_{\text{reco}} = E_{\text{truth}} + \Delta'. \tag{3}$$

One of the most simple parametrizations Δ' looks like

$$\Delta' = p_0\Delta + p_1\Delta^2 + p_2, \tag{4}$$

and this will in fact be the basis for the more complex forms explored ahead.

η dependency

In order to account for different effects as a function of the region of the calorimeter, this calibration study is performed in regions of pseudo-rapidity η. These are defined following the physical sections of the calorimeter, with boundaries between regions located at

$$|\eta| = 0.00, 0.60, 1.00, 1.37, 1.55, 1.82, 2.47.$$

For simplicity, we use an integer number (running, from negative to positive, from 1 to 12) to identify each of the regions, s.t. 1 corresponds to the left-most region (negative end-cap, $-2.47 < \eta < -1.82$), 6 to the center-most negative one (negative barrel, $-0.6 < \eta < 0.0$), and 12 to the right-most one (positive end-cap, $1.82 < \eta < 2.47$).

All the previous means that there are in total 12 (or 6, if the binning is defined for $|\eta|$) sets of parameters $\vec{p}_\eta = (p_0, p_1, p_2, ..)$ that must be determined in order to calibrate all the calorimeter (not to be confused with the momentum $\vec{p}$, which lacks the "η" sub-index).

Particularities of the study

Since this study looks at $Z \to ee$ samples, there are two electrons per event, both of which are affected by the resolution correction. In this study, we only differentiate electrons by their pseudo-rapidity η_1 and η_2, so the calibration runs on a grid of [η-1,η-2] bins. Figure 3 shows the mass line ratio in this grid, for the nominal data and MC. The naming convention in the grid passes on from before, e.g.:

- Region 1-1: both electrons in $-2.47 < \eta < -1.82$
- Region 6-2 = 2-6: one electron in $-1.82 < \eta < -1.55$ and the other in $-0.6 < \eta < 0.0$.

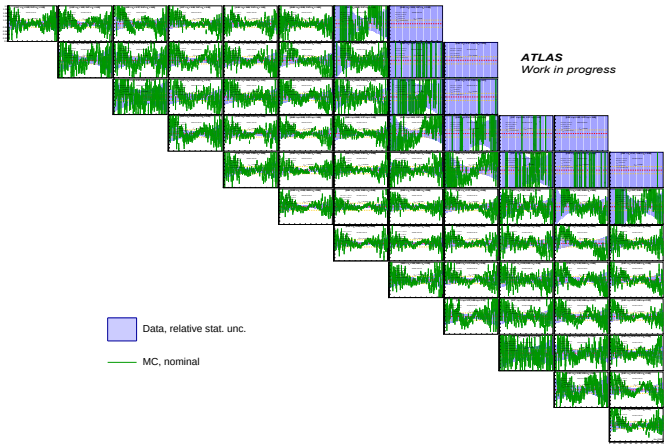

Figure 3: Nominal data/MC $Z \to ee$ invariant mass line ratios, in the [η-1,η-2] grid seen by the calibration process. All ratio plots go from 0.9 to 1.1 (vertical axis), in the 80 to 100 GeV range.

Minimization and parameter estimation

Since the purpose of this study is to improve the agreement between data and MC invariant mass lineshapes, the best parameters $\hat{\vec{p}}_\eta$ are determined by comparing the shape of both distributions with a χ^2 measurement, and minimizing this quantity.

MINUIT

Due to the nature of this study, a large amount of parameters must be determined simultaneously in order to calibrate the whole calorimeter. For this, the multi-dimensional customizable numerical minimizer `MINUIT` [4] is used through `ROOT 6.08/02` [5], using the minimization algorithm `MIGRAD`.

Minimization sequence

As mentioned, the current study aims to minimize the shape difference between the data and corrected MC mass lines. This means that, for each proposed set of parameters $\vec{p}_\eta$ (provided by MINUIT), the dilepton mass distribution must be obtained using e.g. a histogram. Nevertheless, the Δ' correction acts on the individual energy of each of the electrons E_{reco} (and their original resolution Δ), and there are 2 electrons per Z-boson event. Figure 4 shows a simplified schematic representation of this process.

Due to the nature of this study, each individual event is corrected before generating the corresponding histogram, which leads to an event migration between bins, and translates to non-physical fluctuations

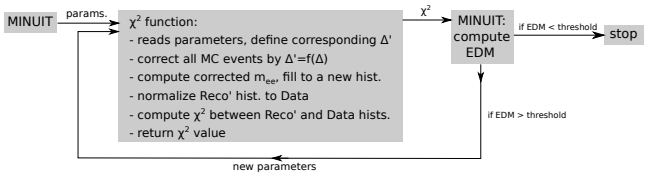

Figure 4: Schematic representation of the minimization process used to estimate the best Δ' parameters.

of the χ^2 curve (in it's typical bin-to-bin definition, i.e., $\sum$[Data - MC]^2/Unc^2). In order to overcome this, we proposed a new method capable of recovering a curve with a well defined minimum, which is described in detail in a separate note [6].

Mixing multiple channels

As the entire calorimeter is split into several [η-1,η-2] bins, each providing measurements for each set of parameters $\vec{p}_\eta$ of the Δ' correction, it generates strong correlations that call for a simultaneous estimation. This is achieved by minimizing a global χ^2 value, defined as

$$\chi^2_{\text{global}} = \chi^2_{\eta\text{-}1\text{-}1} + \chi^2_{\eta\text{-}2\text{-}1} + \chi^2_{\eta\text{-}3\text{-}1} + ..., \tag{5}$$

which includes all the relevant η-bins.

Checks on Kinematics

In order to not do blind tests, it is of use to know the quantities relevant for the mass computation, and potentially contribute to the data/MC disagreement. Thus, let us look at Eq. (6), which gives a clear insight of the relationship between the dilepton mass and individual electron kinematics:

$$\begin{aligned} m^2_{ee} &= 2E_1E_2(1-\cos\theta_{12}) \\ &= 2E^{\text{T}}_1E^{\text{T}}_2\left[\cosh(\eta_1-\eta_2)-\cos(\phi_1-\phi_2)\right]. \end{aligned} \tag{6}$$

Several checks were performed on each of the quantities, seeking to understand whether there could be other (major) sources of mis-calibration (this is described in detail in the complete report [1]). We were able to discard additional sources, such as the angular quantities measured by the tracker. Moreover, we also noticed that the transverse momentum E^{T} is a good indicator of the change in kinematics across different bins, as it remains (roughly) constant for both electrons within the same η-bin, but changes between different regions. Figure 5 shows the transverse momentum distributions for few η-bins, both for data and MC. As a consequence, E^{T} dependence is explicitly included in the definition of the Δ' correction in a polynomial manner.

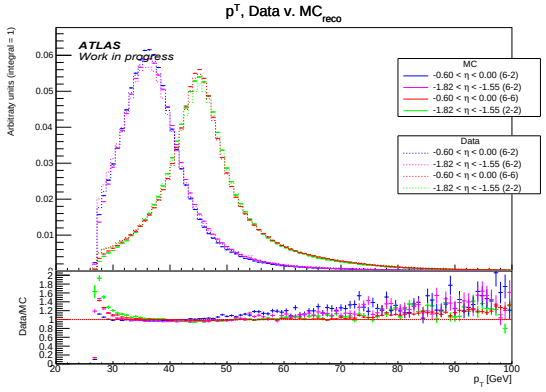

Figure 5: Data and nominal Reco MC distributions of E^{T} for regions 6-6, 2-2, and 6-2. The integral of all the distributions has been normalized to 1.

Main results

After testing several definitions of the Δ' function, the best data to MC agreement with a combined E^{T} dependence. That is, with linear E^{T} dependence in the barrel ($|\eta| < 1.37$), and cubic one in the endcap ($|\eta| > 1.37$). It is defined as:

$$\begin{aligned} \Delta' = &\left[p_0 + p_3(E^{\text{T}}_{\text{truth}} - 45\text{ GeV})\right]\Delta \\ &+ \left[p_1 + p_4(E^{\text{T}}_{\text{truth}} - 45\text{ GeV})\right]\Delta^2 \\ &+ \begin{cases} \left[p_2 + p_5(E^{\text{T}}_{\text{truth}} - 45\text{ GeV})\right] & \text{if } |\eta| < 1.37 \\ \left[p_2 + p_5(E^{\text{T}}_{\text{truth}} - 45\text{ GeV}) + p_6(E^{\text{T}}_{\text{truth}} - 45\text{ GeV})^2\right. & \\ \qquad \left. + p_7(E^{\text{T}}_{\text{truth}} - 45\text{ GeV})^3\right] & \text{if } |\eta| > 1.37. \end{cases} \end{aligned} \tag{7}$$

The effects of the resolution correction (after optimization of the parameters for all η-regions) are shown in Figure 6. The impact of this correction is seen the best in the top plot, which shows the Dada/MC mass ratio over all the calorimeter before (green) and after (red) applying Δ'.

First, it shows that it is possible to obtain an almost perfect agreement over the whole m_{ee} range, correcting both the core (around 90 GeV) and tails of the distribution (where the discrepancy goes from $\sim 5\%$ to $\sim 1.5\%$, almost within the data statistical uncertainty). Moreover, the χ^2 value between the (normalized) data and MC distributions also improves considerably: for a 100 bin histogram, it goes from $\chi^2_{\text{initial}} = 2323.70$ to $\chi^2_{\text{final}} = 122.61$.

While energy resolution corrections seem capable of explaining most of the remaining data/MC mass distribution disagreement, one must notice that the calibration is done in the 80 to 100 GeV m_{ee} range, and as such, extrapolating to higher energies must be done with care. If not, it could lead to undesired effects, such as non-physical deformation of the resolution distributions σ_E/E, or degradation of other quantities.

Finally, it is of interest to check the impact of resolution corrections on precision studies, such as the

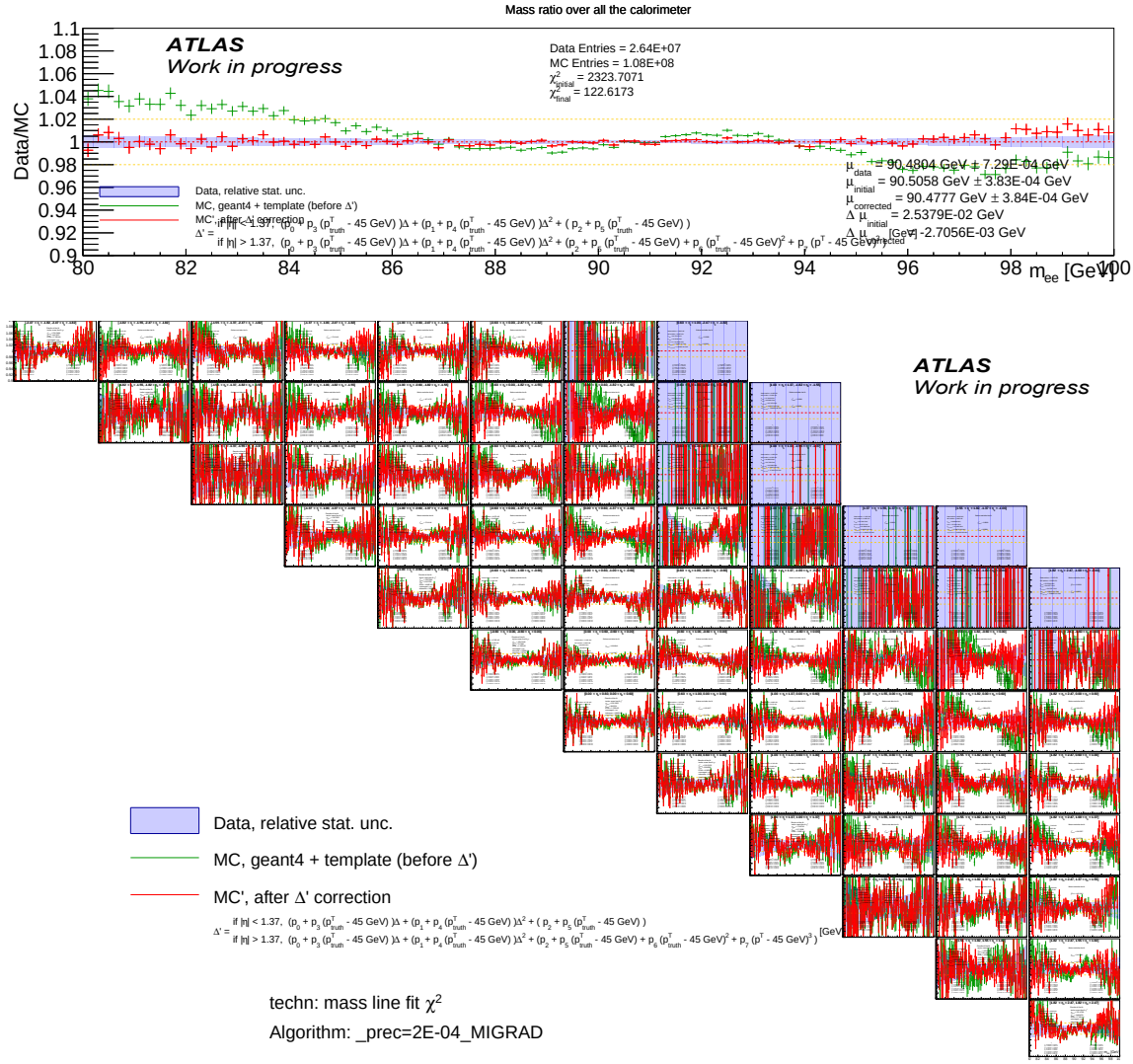

Figure 6: Data/MC mass lineshape ratios, for Δ' defined as in Eq. (7). Top: ratios and corresponding χ^2 values before (green) and after (red) the Δ' energy resolution correction, over all the calorimeter. Bottom: grid of individual [η-1,η-2] bins, before and after the same resolution correction. The relative statistical uncertainties corresponding to data are shown with blue bars (centered around 1).

W-boson mass measurements. Now that the potential of this method has been briefly explored, it could lead to further studies of interest.

Conclusions

The newly explored energy resolution corrections via scalings of $\Delta = E_{\text{reco}} - E_{\text{truth}}$ shows promising results, being capable of compensating almost perfectly the remaining discrepancy between data and MC $Z \to ee$ invariant mass.

While the parameter optimisation process is not trivial, further studies are encouraged, specially in order to inspect the impact of such calibration on precision measurements.

References

[1] Juan Salvador Tafoya Vargas; *Electron energy resolution corrections*, CERN, ATL-COM-PHYS-2021-896

[2] Siqi Yang, Cheng Wang; `https://indico.cern.ch/event/857807/contributions/3615377/attachments/1932510/3201225/ElectronCalibration.pdf`, (Online; accessed 12.08.2021)

[3] Linghua Guo; *Electron energy in-situ calibration and linearity measurements from* Z $\to$ *ee events*, CERN, ATL-COM-PHYS-2020-757

[4] Frederick James, *MINUIT Function Minimization and Error Analysis: Reference Manual Version 94.1*, CERN-D-506

[5] Rene Brun, Fons Rademakers; *ROOT: An object oriented data analysis framework*, Nucl. Instrum. Meth. A 10.1016/S0168-9002(97)00048-X

[6] Juan Salvador Tafoya Vargas; *Treatment of χ^2 fluctuations due to bin-to-bin event migration in inter-sample distribution shape comparisons*, CERN, ATL-COM-SOFT-2021-082, PUB-STAT-2021-01

Vector boson polarisation measurement in WZ production using the ATLAS detector at the LHC

Luka SELEM

LAPP, Université Savoie Mont Blanc, CNRS/IN2P3, Annecy

Abstract — The electroweak symmetry breaking mechanism being responsible for the appearance of a longitudinal polarisation mode in the massive $W^{\pm}$ and Z vector bosons, the study of their polarisation modes is an interesting probe of the Standard Model. The measurements of the polarisation modes of the $W^{\pm}$ and Z bosons are performed separately in WZ production with leptonic decay using a template fit. The data originates from pp collisions at $\sqrt{s} = 13\,\text{TeV}$ recorded in the ATLAS detector at the Large Hadron Collider (LHC) with $139\,\text{fb}^{-1}$ of integrated luminosity. These polarisation measurements are additionally performed separating in the charge of the $W^{\pm}$ boson. In all cases, no deviation from theory prediction is found.

Introduction

In spite of the discovery of the Higgs boson in 2012, the study of the Standard Model is not complete. Precision measurement of triple or quartic gauge couplings in the electroweak sector is an important physics goal, as a probe of its non-abelian structure. In particular, this is studied in di-boson processes, that is processes producing two bosons among the $W^{\pm}$ and Z vector bosons of the electroweak sector. This has been done since the Large Electron Positron collider (LEP) operated at CERN in WW production, as a means of studying anomalous triple gauge couplings. Di-boson processes are still a hot topic in particle physics as the increased energy reached in the center of mass of proton–proton collisions in the LEP successor, the Large Hadron Collider (LHC), allowed recently the quartic gauge couplings of the electroweak sector to be studied. Nevertheless, these processes are very rare, and their low cross section translates in a low production rate in the multi-purpose detectors ATLAS and CMS used to detect them at the LHC. The data collected during the Run-2 of the LHC in the years 2015-2018 now allows to perform precision measurements on these rare processes. As can be seen on Figure 1, these processes are comparable in cross-section to the total Higgs production.

Moreover, the vector bosons of the electroweak sector have an interesting property which sets them apart from the other gauge bosons of the Standard Model: they are massive. This mass could be incorporated to the Standard Model by adding an electroweak spontaneous symmetry breaking process in the form of the mechanism of Brout-Englert-Higgs (BEH). On the other hand, this mass allows these bosons to have three degrees of freedom for their polarisation vector, when massless gluons and photons can only have transverse polarisation modes. As a result, the additional longitudinal polarisation mode is a quite unique feature of $W^{\pm}$ and Z vector bosons which is ultimately linked to the BEH mechanism. This has interesting consequences, such as the Goldstone equivalence theorem [1] or amplitude zeros [2]. It is therefore of interest to study di-boson processes through the prism of their polarisation to get a more detailed test of the Standard Model.

The study of the polarisation of one boson in the di-boson WZ production has already been done in ATLAS with partial Run-2 data [3], and in CMS with full Run-2 data [4]. It will be presented here with full Run-2 ATLAS recorded data as a first step toward the simultaneous measurement of both bosons polarisations.

The WZ leptonic channel in Run-2

Among these diboson processes, the WZ process is an interesting compromise between a sizeable section and a clean experimental signature, as can be checked on Figure 1. The ZZ process can have a very clean four leptons signature in the detector, but with a comparatively low cross section. The WW process on the other hand has a higher cross section, but a signature impaired by the neutrinos or the heavy jets of the W decay, leading to an incomplete access to its final-state kinematics.

The WZ production with fully leptonic decay is studied to ensure an almost complete access to its final state kinematics. The experimental signature in proton-

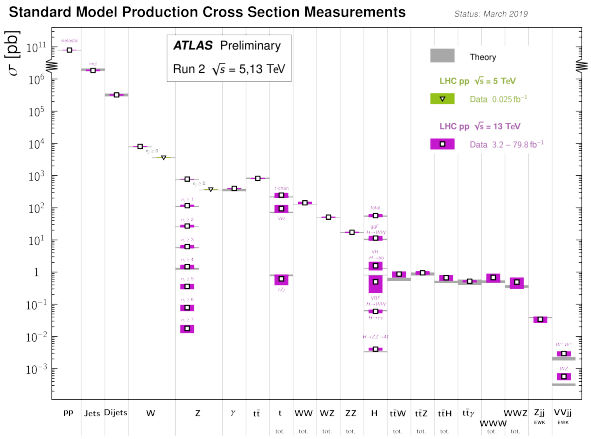

Figure 1: Cross sections as predicted by the Standard Model and measured by ATLAS.

proton collisions in ATLAS is thus the following,

$$\mathrm{pp} \rightarrow \ \ell\,\ell\,\ell\,\nu \ + \ X,$$

where the ℓ denotes either an electron or a muon, ν is a neutrino detected as missing transverse momentum in the detector, and X are other objects, typically from initial or final state radiations. Decays to τ-leptons are not considered being harder to reconstruct in ATLAS. Among the various signal Feynman diagrams, the main ones in Figure 2 feature resonant W and Z bosons. They are the diagrams of the Double Pole Approximation (DPA) used in theoretical calculations [5].

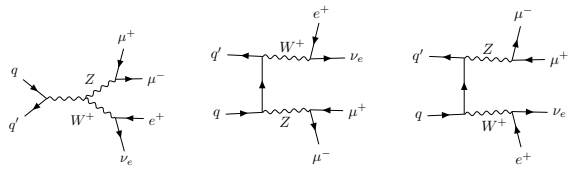

Figure 2: Main signal Feynman diagrams for the WZ production with leptonic decay.

As can be seen on Table 1, the signal over background ratio is fairly good, at 3.47. The main backgrounds originate from ZZ events where one lepton would be missed, or backgrounds producing less than two leptons but with additional *misidentified leptons* reconstructed in the detector. Other backgrounds include a top-anti-top $t\bar{t}$ pair produced with a vector boson V, a top t produced with a Z and WZ events where one decay lepton is a τ-lepton subsequently decaying to an electron or muon.

Extracting polarisation with a template fit

The inclusive WZ signal corresponds to all WZ events in leptonic decay independently of their polarisation. The next step would be to separate this signal among

Data	21 242
Total Expected	21 715
WZ in e/μ	16 861
Total Bkg.	4 855
ZZ	1 425
Misid. leptons	1 109
$t\bar{t}$+V	885
WZ in τ	618
tZ	394
Others	425
Signal/Background	3.47

Table 1: Observed and expected event yields for the $W^{\pm}Z$ signal and background processes.

all polarisations configurations to extract polarisation fractions. As a first step, only the polarisation of one boson at a time is studied. The electroweak vector bosons $W^{\pm}$ and Z have three degrees of freedom for their polarisation vector: one longitudinal mode is labelled 0 and two transverse modes are called *Left* L and *Right* R. An effect of the polarisation can be seen in the distribution of the cosine of the polar decay angle $\cos\theta^*$. As can be seen in Figure 3, θ^* is the angle between the direction in the decaying boson rest frame of the negatively charged lepton (except for W^+ decay where the positively charged lepton is used), and the boson flight direction, which has to be defined in a given frame. This is intrinsically linked to the fact that polarisations vectors are not Lorentz invariant quantities; the choice of a different frame yields different polarisation fraction. Here, the direction of the vector boson will be taken in the WZ rest frame.

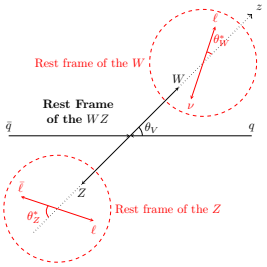

Figure 3: Definition of the polar decay angles θ^*_W and θ^*_Z in the WZ rest frame.

The theory predicts [6] for the variable $\cos\theta^*_W$ a differential cross section depending on the polarisation fractions f_0, f_{L} and f_{R}:

$$\frac{1}{\sigma_{W^{\pm}Z}}\frac{d\sigma_{W^{\pm}Z}}{d\cos\theta^*_W} = \frac{3}{8}f_{\mathrm{L}}\left(1 \mp \cos\theta^*_W\right)^2 + \frac{3}{8}f_{\mathrm{R}}\left(1 \pm \cos\theta^*_W\right)^2 + \frac{3}{4}f_0\left(1 - \cos\theta^{*\,2}_W\right). \quad (1)$$

This means that a W^+ polarised *Right* (resp. *Left*) will tend to have its decay fermion forward (resp. backward), while a longitudinally polarised W^+ will have its decay fermion more transverse. Ultimately this is only statistical: it is impossible to determine the polarisation of the boson of a given event. The definition of $\cos\theta^*_W$ depends on q_W the charge of the W boson. Still, W^+Z and W^-Z events can be combined by using

instead the variable $q_W \cdot \cos\theta^*_W$ with the formulas for a W^+ boson in equation (1).

For Z bosons the formula is similar [7] :

$$\frac{1}{\sigma_{W\pm Z}}\frac{d\sigma_{W\pm Z}}{d\cos\theta^*_Z} = \frac{3}{8}f_{\mathrm{L}}\left(1+2C_{\mathrm{w}}\cos\theta^*_Z+\cos\theta^{*\,2}_Z\right)+ \frac{3}{8}f_{\mathrm{R}}\left(1-2C_{\mathrm{w}}\cos\theta^*_Z+\cos\theta^{*\,2}_Z\right)+\frac{3}{4}f_0\left(1-\cos\theta^{*\,2}_Z\right). \quad (2)$$

where $C_{\mathrm{w}} = (2c_v c_a)/\left(c_v^2+c_a^2\right)$. This constant is expressed in terms of $c_v = -1/2 + 2\sin^2\theta_W$ and $c_a = -1/2$, the vector and axial vector couplings of the Z boson to leptons, with $\sin^2\theta_W$ the weak mixing angle, a parameter of the electroweak theory. From the formulas (1) and (2), it appears that the $\cos\theta^*$ can be used as a discriminative variable between the three polarisation modes. The distribution of the $\cos\theta^*$ observable is represented in Figure 4 (left) separately for each polarisation state of the $W^\pm$ boson.

Monte-Carlo samples are generated for unpolarised signal events and processed through detector simulation softwares to reach detector-level. Using equation (1) or (2) depending on the boson considered, fractions are extracted from the generator-level distribution of $\cos\theta^*$ of that boson with an analytical fit. These fractions can in turn be used to reweight event by event the unpolarised Monte Carlo sample to obtain three samples called polarisation templates. The generator-level distributions of the $\cos\theta^*$ from these templates can be seen for boson $W^\pm$ in Figure 4 (left). The same reweighting applied to the Monte Carlo detector-level events provides the expected $\cos\theta^*$ distributions at detector level for each polarisation state, as can be seen for boson $W^\pm$ in Figure 4 (right). These distributions can be used as templates to extract polarisation fractions from a fit to data.

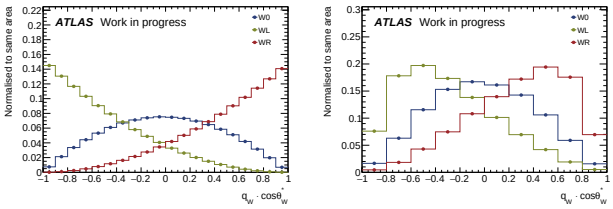

Figure 4: Distributions of $q_W \cdot \cos\theta^*_W$ normalised to the same area of the three polarisation templates at generator level (left) and at detector level (right).

Results

The polarisation templates are stacked along with Monte Carlo samples of the background processes. This gives the expected distribution of $\cos\theta^*$ in data. It is compared to the actual Run-2 data distribution of $\cos\theta^*$ and the proportion of polarisation templates are adjusted in order for the expected distribution to fit the data. This template fit is performed using a binned likelihood maximization using the `HistFactory` framework [8]. The result of such a template fit is shown for W^+ polarisation measurement in Figure 5. The ratio of a given polarisation template integral over the sum of all the templates integrals gives the corresponding polarisation fraction. The sum of fractions is normalised to one by definition. As a result, of the three fractions, only two parameters of interest are considered in the fit: f_0 and $f_L - f_R$.

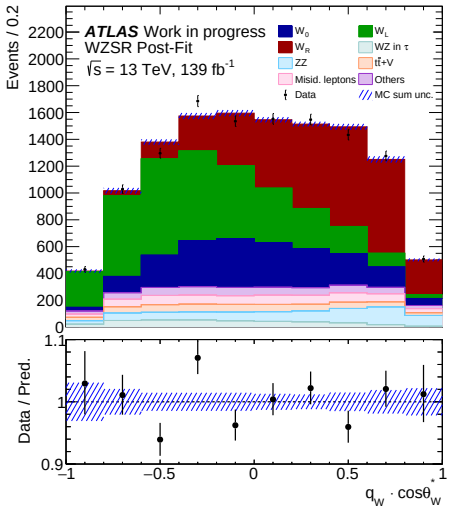

Figure 5: Post-fit distribution of $q_W \cdot \cos\theta^*_W$ in W^+Z events. The points represent the data with the error bar representing the statistical uncertainties. The solid histograms represent the polarisation template W_0, W_L and W_R scaled by the template fit. The pale histograms represent the various background processes estimated through Monte Carlo. The dashed band is the total post-fit uncertainty of the sum of these Monte Carlo predictions. The lower panel represents the ratio of the data points to the sum of Monte Carlo histograms.

Systematic uncertainties are implemented for each sample. Such systematics can be shape variations of the samples histograms due to uncertainties on the reconstruction of some particles in the detector, theoretical uncertainties of parameters used in the Monte Carlo generation, or modelling uncertainties originating from the method to obtain polarisation templates. These systematics in conjunction with the statistical uncertainties yield the total uncertainty on the parameter of interest.

The measured values of f_0 and $f_L - f_R$ is represented in Figure 6 in a plane f_0x$(f_L - f_R)$. It compares to the theoretical prediction extracted through a fit of a Monte Carlo unpolarised sample at the generator level. From these results, no deviations from theoretical predictions are found. The numerical values represented in table 2 show that the polarisation fraction f_0 is measured with a relative uncertainty below (or almost below when there is W charge separation) 20 %. Similar precisions are achieved for f_L and f_R, but the difference between them is so small that $f_L - f_R$ is measured with a poor precision. This is especially true for the Z boson where the difference between *Left* and *Right* polarisation modes is less stark in the templates.

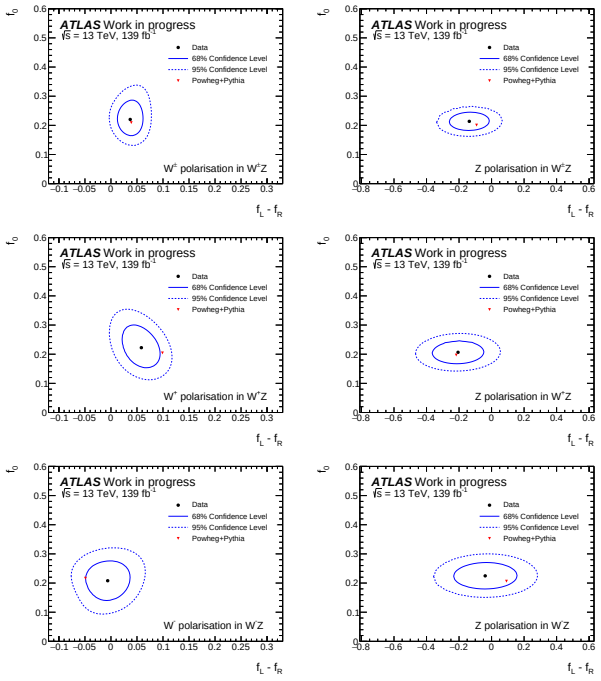

Figure 6: Measured value of f_0 and $f_L - f_R$ for boson W (left) and Z (right), for $W^{\pm}Z$ events (top plots), $W^{+}Z$ events (middle plots) and $W^{-}Z$ events (bottom plots). The black point is the measured value from the template fit. The triangular point is the theoretical predictions from `Powheg+Pythia` Monte Carlo. The solid line ellipse corresponds to the 68 % confidence level region for the joint measurement of f_0 and $f_L - f_R$. The dashed line ellipse is the 95 % confidence level region.

It seems that the sign of $f_L - f_R$ of the Z boson is the opposite as the one for the W. This could be an emergent effect of the polarisation correlations between the bosons due to angular momentum conservation. The separation with the charge of the W boson yields no significant change in the longitudinal polarisation f_0, neither in theory or data. Nevertheless, it appears that W^+ bosons favour slightly the *Left* polarisation, $f_L - f_R > 0$, while W^- bosons favour slightly the *Right* polarisation, $f_L - f_R < 0$. This is probably linked to the differences in the initial states, W^+Z events coming from $u\bar{d}$ quarks, and W^-Z events coming from $\bar{u}d$ quarks.

Conclusions

In conclusion, WZ events were studied in the leptonic channel using data from the full Run-2 recorded with the ATLAS detector. In particular, the polarisation fractions of separately the W and the Z bosons are measured through a template fit. The key step in this analysis was the generation of templates for the three polarisations of the measured bosons. This was performed through a reweighting taking advantage of the theoretical distribution of the polarisation observable $\cos\theta^*$ linked to the decay of the considered vector boson. The results of these measurement show no deviations from theory, even when separating by the charge of the $W^{\pm}$ boson.

Parameter of Interest	Value	Absolute uncertainty	Relative uncertainty
	$W^{\pm}$		
$f_0^{W^{\pm}}$	0.220	0.039	18 %
$(f_{\mathrm{L}} - f_{\mathrm{R}})^{W^{\pm}}$	0.037	0.016	43 %
height	Z with $W^{\pm}$		
$f_0^{Z\mathrm{with}W^{\pm}}$	0.214	0.021	10 %
$(f_{\mathrm{L}} - f_{\mathrm{R}})^{Z\mathrm{with}W^{\pm}}$	-0.137	0.081	59 %
height	W^{+}		
$f_0^{W^{+}}$	0.222	0.048	22 %
$(f_{\mathrm{L}} - f_{\mathrm{R}})^{W^{+}}$	0.058	0.024	41 %
height	Z with W^{+}		
$f_0^{Z\mathrm{with}W^{+}}$	0.207	0.026	13 %
$(f_{\mathrm{L}} - f_{\mathrm{R}})^{Z\mathrm{with}W^{+}}$	-0.206	0.105	51 %
height	W^{-}		
$f_0^{W^{-}}$	0.208	0.044	21 %
$(f_{\mathrm{L}} - f_{\mathrm{R}})^{W^{-}}$	-0.006	0.028	450 %
height	Z with W^{-}		
$f_0^{Z\mathrm{with}W^{-}}$	0.225	0.030	13 %
$(f_{\mathrm{L}} - f_{\mathrm{R}})^{Z\mathrm{with}W^{-}}$	-0.039	0.128	330 %
height			

Table 2: Measured polarisation fractions $f_0$and $f_L - f_R$ for both $W^{\pm}$ and Z bosons, separating by charge of the $W^{\pm}$ boson. The third column represents the absolute uncertainty. The fourth column represents the relative uncertainty.

This measurement hints at correlations between the polarisation of W and Z bosons. The next step would be the measurement of the polarisations of the W and Z bosons simultaneously. It is however more challenging as the cross section of a given polarisation configuration is typically one order of magnitude below the single boson polarisation cross section, itself one order of magnitude below the inclusive cross section.

References

[1] M. S. Chanowitz and M. K. Gaillard, *The TeV Physics of Strongly Interacting W's and Z's,* Nucl. Phys. B **261** (1985), 379

[2] U. Baur, T. Han and J. Ohnemus, *Amplitude zeros in $W^{\pm}Z$ production,* Phys. Rev. Lett. **72** (1994), 3941

[3] ATLAS Collaboration, *Measurement of $W^{\pm}Z$ production cross sections and gauge boson polarisation in pp collisions at $\sqrt{s} = 13$ TeV with the ATLAS detector,* Eur. Phys. J. C **79** (2019), 535

[4] CMS Collaboration, *Measurement of the inclusive and differential WZ production cross sections, polarization angles, and triple gauge couplings in pp collisions at $\sqrt{s} = 13$ TeV,* [arXiv:2110.11231 [hep-ex]].

[5] A. Denner and G. Pelliccioli, *NLO QCD predictions for doubly-polarized WZ production at the LHC,* Phys. Lett. B **814** (2021), 136107

[6] J. A. Aguilar-Saavedra and J. Bernabeu, *Breaking down the entire W boson spin observables from its decay,* Phys. Rev. D **93** (2016), 011301

[7] J. A. Aguilar-Saavedra, J. Bernabéu, V. A. Mitsou and A. Segarra, *The Z boson spin observables as messengers of new physics,* Eur. Phys. J. C **77** (2017), 234

[8] K. Cranmer *et al.* [ROOT], *HistFactory: A tool for creating statistical models for use with RooFit and RooStats,* CERN-OPEN-2012-016.

Measurement of the CP properties of the Higgs boson with the CMS detector

Mario SESSINI

Institut Pluridisciplinaire Hubert Curien - Strasbourg

Abstract — This paper aims to present some measurements of the CP properties of the Higgs boson through several of its couplings to other Standard Model (SM) particles. In particular, results of an analysis of the coupling to a pair of neutral Z^0 bosons will be shown, as well as studies of two Yukawa couplings, one to the top quark and the other to the τ lepton. To this day, all measurements are consistent with the SM prediction of a purely scalar neutral Higgs boson. Pure pseudo-scalar hypothesis is excluded at 3.8σ confidence level through Z^0 coupling, 3.2σ through top quark coupling and 3.0σ through τ lepton coupling.

Introduction

The discovery of a new particle with properties similar to the Higgs boson as predicted by the Standard Model [1, 2, 3, 4, 5, 6] was announced in 2012 by the CMS [7, 8] and ATLAS [9] collaborations. Further studies are now performed to give a better description of several of its properties, including mass measurements, decay width and CP properties. Even though the Higgs boson is described as a purely scalar boson by the SM, the discovery of any non-purely scalar state would have important implications in the search for new physics, as some SM extensions can also include a pseudo-scalar Higgs boson. Such properties can be studied with the CMS detector through the final products issued from the several decay channels of the Higgs boson produced in pp collisions at the LHC. The first section of this paper will aim to introduce some basic understanding of the couplings of the Higgs boson to other SM bosons and fermions. The second section will show the techniques used to performed CP measurements for three of these couplings, and at last results of these studies will be presented.

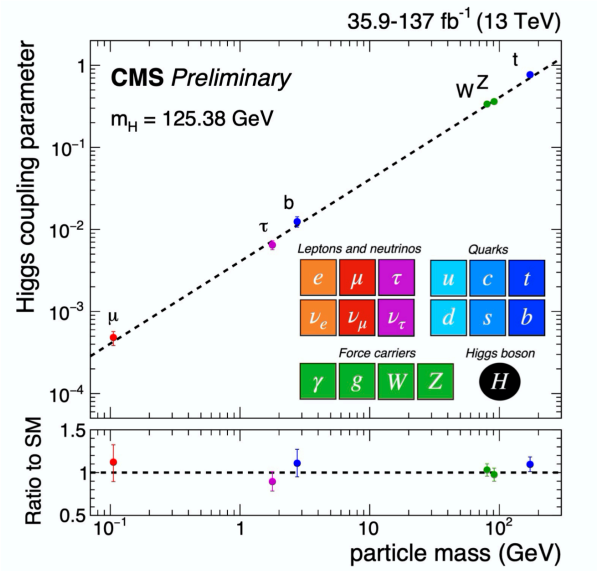

Figure 1: Measurement of the Higgs coupling parameters in pp collisions at $\sqrt{s}$=13TeV with the CMS detector.

Decay rates and couplings of the Higgs boson

In its SM description, the Higgs boson is able to couple to any massive particle with a coupling strength proportional to the particle's mass (Fig.1). As a consequence, decay rates to light particles are greatly suppressed. In addition, the Higgs boson is also able to indirectly couple to massless particles such as the photon or the gluon through virtual loops of top quarks, providing in particular the di-photon ($H^0 \to \gamma\gamma$) final state. This channel is of great interest as it offers a well measured and easy to identify final state, but also a way to measure the coupling of the Higgs boson to the top quark in the production mode $t\bar{t}H^0$ since the latter is too heavy for the decay mode $H^0 \to t\bar{t}$ to occur.

For a complete understanding of the CP properties of the Higgs boson, all of its decay channels (Fig.2) should be studied. However, the choice of the decay mode in the frame of a CP analysis at the LHC is also limited by other factors, such as the loss of spin information in the final state ($H^0 \to b\bar{b}$) or the missing observation of the decay mode ($H^0 \to c\bar{c}$). Finally, CP-violating effects are expected to have minor contributions in couplings to gauge bosons whereas they appear at tree level in Yukawa couplings. This specific type of coupling will be discussed in the following part.

Decay channel	Branching ratio [%]
$H \to b\bar{b}$	57.5 ± 1.9
$H \to WW$	21.6 ± 0.9
$H \to gg$	8.56 ± 0.86
$H \to \tau\tau$	6.30 ± 0.36
$H \to c\bar{c}$	2.90 ± 0.35
$H \to ZZ$	2.67 ± 0.11
$H \to \gamma\gamma$	0.228 ± 0.011
$H \to Z\gamma$	0.155 ± 0.014
$H \to \mu\mu$	0.022 ± 0.001

Figure 2: Various decay modes of the Higgs boson and their branching ratio.

Yukawa couplings

Every coupling of the Higgs boson with a fermion is described by a unique interaction called Yukawa coupling. This coupling can be described by a lagrangian (Eq.1) itself made of a CP-even and a CP-odd coupling. Each part is depending on a specific coupling constant κ_l and $\tilde{\kappa}_l$ respectively.

$$\mathcal{L}_Y = -\frac{m_l \phi}{v}(\kappa_l \overline{\psi}_l \psi + \tilde{\kappa}_l \overline{\psi}_l i\gamma_5 \psi_l) \quad (1)$$

In this lagrangian, m_l stands for the mass of the lepton, ψ_l for its Dirac field, ϕ for the scalar Higgs field and $v = 246$ GeV for the vacuum expecation value. From κ_l and $\tilde{\kappa}_l$ a CP-odd fraction of the Yukawa coupling can be defined (Eq.2), which can also be related to an effective mixing angle α^{Hll}.

$$f_{CP}^{Hll} = \frac{|\tilde{\kappa}_l|^2}{|\kappa_l|^2 + |\tilde{\kappa}_l|^2} = \sin^2(\alpha^{Hll}) \quad (2)$$

Therefore, the coupling appears to be purely scalar for an effective mixing angle $\alpha^{Hll} = 0°$, purely pseudo-scalar for $\alpha^{Hll} = 90°$ and a mixture of both CP states for any other value with a maximum mixing state for $\alpha^{Hll} = 45°$.

Analysis strategy

This section aims to give an overview of several strategies used to extract and measure the CP properties of the Higgs boson for three different couplings. The first analysis [10] relies on the kinematic description of the four-leptons final state in the $H^0 \to ZZ \to 4l$ decay channel. The pure pseudo-scalar Higgs boson hypothesis is tested against the SM pure scalar hypothesis. In the second analysis [11], the Yukawa coupling to the top quark is studied in the $t\bar{t}H^0$ production mode where H^0 decays to a pair of photon. At last, an analysis of the CP properties of the Higgs boson in the $H^0 \to \tau\tau$ channel [12] to which the Strasbourg CMS team contributed will be introduced.

$H^0 \to ZZ \to 4l$

The event selection for this study is performed in a way the signal is composed of events from one of the three following final states : $4e$, $2e2\mu$ or 4μ. Both Z^0 candidates must be formed with two oppositely charged leptons of same flavour, and also need to be isolated and properly identified to avoid mis-identifications due to the Z + jet and $t\bar{t}$ backgrounds.

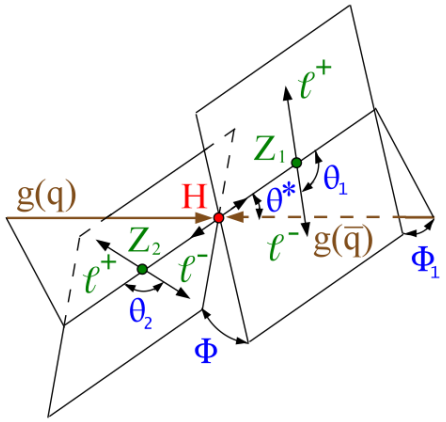

Figure 3: Production and decay of a Higgs boson in the $H^0 \to ZZ \to 4l$ decay mode. θ^* and Φ_1 stand for the production angles in the Higgs rest frame and θ_1, θ_2 and Φ for the three production angles in the Z_1, Z_2 and H rest frames respectively.

Since there is no neutrinos in this decay channel, the event kinematic can be fully described. Therefore kinematic discriminants are built from kinematic variables (Fig.3) and used to categorize events. This allows to discriminate the background from the signal in the first place but also to test several spin-parity J^D hypothesis of the Higgs boson against the 0^+ SM hypothesis.

$t\bar{t}H^0$ production mode

This analysis did not only focus on measuring the CP structure of the Yukawa coupling in the $t\bar{t}H^0$ production mode. It also focused on measuring the signal strength $\mu_{t\bar{t}H}$ of the process defined as the ratio of $\sigma_{t\bar{t}H}\mathcal{B}_{\gamma\gamma}$, the product of the cross section of the $t\bar{t}H^0$ production mode and the branching ratio of the $H^0 \to \gamma\gamma$ decay mode, and the SM expected value of this product $\sigma_{t\bar{t}H}\mathcal{B}_{\gamma\gamma}$=$1.13^{+0.08}_{-0.11}$fb [13].

By the presence of a top quark pair in the process, the final state can either be hadronic or leptonic each one with its own background. For this reason, two dedicated BDT ("BDT-bkg") are trained to separate signal events from background events. Kinematic properties of jets, leptons and photons are used as input features, as well as the jet and lepton multiplicity, the b-tagging scores of jets and the missing transverse

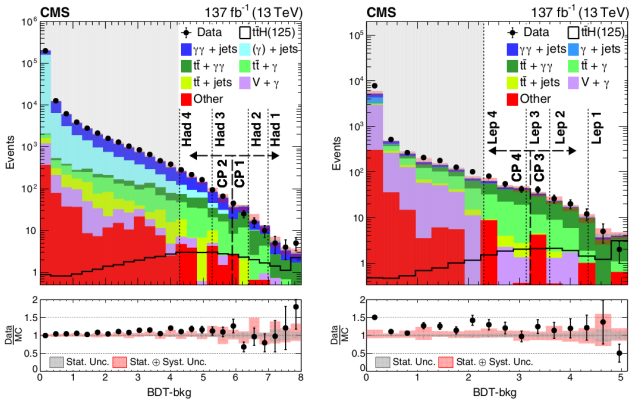

Figure 4: BDT-bkg output distributions for the hadronic final state (left) and leptonic final state (right). Events are satisfying either 100< $m_{\gamma\gamma}$ <120GeV or 130< $m_{\gamma\gamma}$ <180GeV. Events in the grey shaded regions are rejected from the analysis.

energy p_T^{miss}. The di-photon mass $m_{\gamma\gamma}$ is not used to avoid inducing bias. Non-rejected events are further on classified into eight categories, four for each final state (Fig.4), in order to maximize the expected significance. A simultaneous binned maximum likelihood fit of the distribution of the di-photon invariant mass $m_{\gamma\gamma}$ is then performed (Fig.5) to extract $\sigma_{t\bar{t}H}\mathcal{B}_{\gamma\gamma}$ and $\mu_{t\bar{t}H}$.

In the next part of the analysis, a second BDT is trained to identify CP-odd events from CP-even events. Events are then classified according to their BDT score called D_{0^-} in three separated bins (Fig.6) and a fit is performed to extract the CP-odd fraction of the coupling as defined in equation 2.

$H^0 \to \tau\tau$

In this study, a new CP sensitive observable ϕ_{CP} is introduced. Each τ will decay shortly after being produced and ϕ_{CP} is defined as the angle between the taus decay planes (Fig.7) in the Higgs boson rest frame. The $H^0 \to \tau\tau$ differential cross section can be parametrized as follow :

$$\frac{d\Gamma}{d\phi_{CP}} \sim 1 - b(E^+)b(E^-)\frac{\pi^2}{16}\cos(\phi_{CP} - 2\alpha^{H\tau\tau}). \quad (3)$$

As a result, the ϕ_{CP} distribution gives a direct information about the Higgs boson CP state (Fig.7) and a CP-even(odd) Higgs boson will be more likely to decay when the angle between the taus decay planes is 180°(0/360°) due to spin correlations. Oppositely, the Z^0 boson will produce a flat ϕ_{CP} distribution. However, in a experiment such like the LHC reconstructing the Higgs boson rest frame can be a tough task because of the composite nature of the proton and the presence of neutrinos in every tau decays. Consequently, optimized methods are needed and will be presented in what follows.

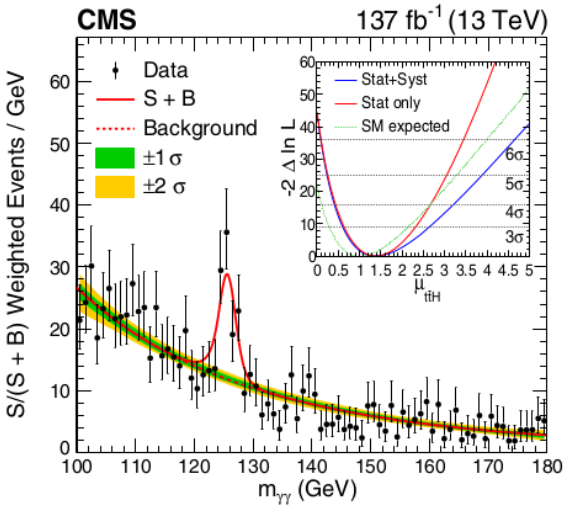

Figure 5: Invariant mass distribution for the selected events (black points) weighted by $S/(S+B)$, where $S(B)$ is the numbers of expected signal (background) events in a $\pm 1\sigma_{eff}$ mass window centered on m_H. The σ_{eff} is defined as the smallest interval containing 68.3% of the $m_{\gamma\gamma}$ distribution and ranges from 1.2% to 1.6% for different categories.

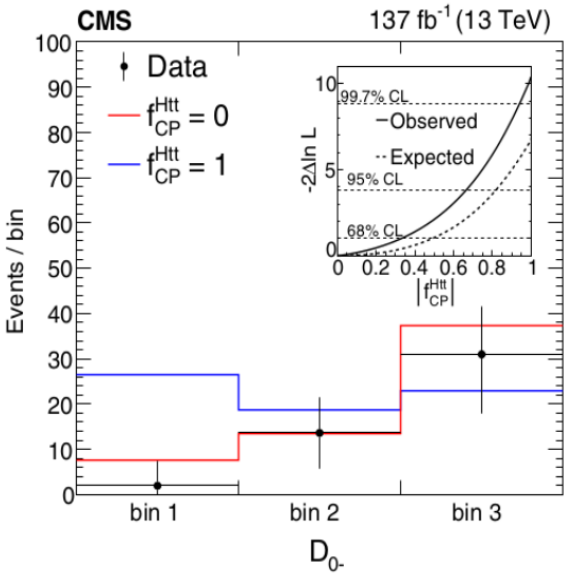

Figure 6: Distributions of events as in (Fig.5) in three bins of D_{0^-}. All previous categories are combined in the mass range 115<$m_{\gamma\gamma}$<135GeV and the background estimation determined in the previous fit is subtracted. The inner panel shows the likelihood scan for the CP-odd fraction of the coupling $|f_{CP}^{Htt}|$.

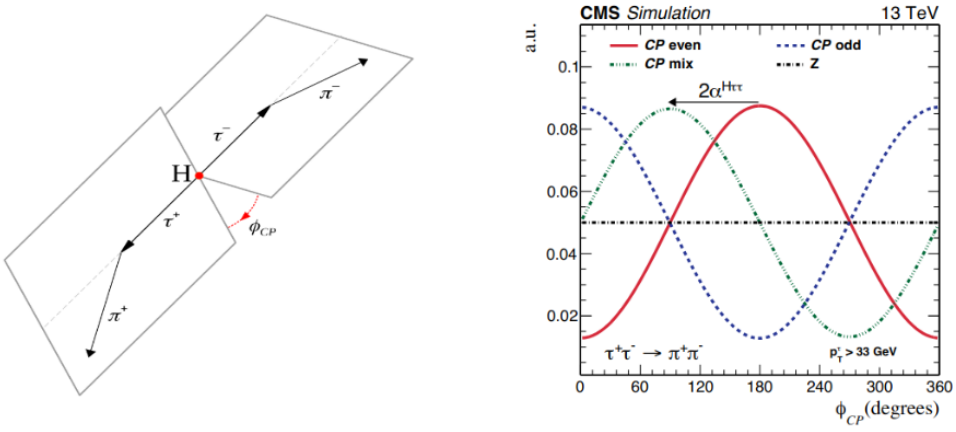

Figure 7: Representation of the taus decay planes in the Higgs boson rest frame, ϕ_{CP} represents the angle between the planes (left). Distribution of ϕ_{CP} for the CP-even scenario (solid red), CP-odd (dashed blue), maximum mixing (dash dotted green) and for Z^0 (flat black line) (right). The $\tau^+\tau^-(\nu_\tau\bar{\nu}_\tau) \to \pi^+\pi^-$ decay mode is considered.

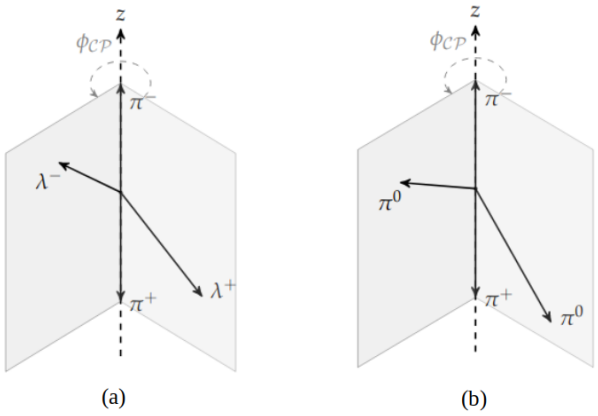

Figure 8: (a) Representation of the impact parameter (IP) method in the $\tau^{\pm}(\nu_\tau) \to \pi^{\pm}$ decay mode, each plane is spanned by the momentum of the pion and its respective IP. (b) Representation of the neutral pion method in the $\tau^{\pm}(\nu_\tau) \to \pi^{\pm} + \pi^0$ decay mode, each plane is spanned by the momentum of the charged pion and the neutral pion.

Impact parameter method

The impact parameter method is designed for decay modes where one charged track is reconstructed, like $\tau^{\pm} \to \pi^{\pm}, \mu^{\pm}$. The decay planes between which ϕ_{CP} is measured are spanned by the pions or the muons and their own impact parameter in the rest frame built from the two charged particles (Fig.8). The impact parameter of a track is defined as the vector between the primary vertex and the point of closest approach from the primary vertex on the extrapolated track.

Neutral pion method

This method offers an optimal sensitivity in the $\tau^{\pm}(\nu_\tau) \to \pi^{\pm} + \pi^0$ decay mode. It relies on the measurement of the angle between the planes spanned by the charged pions and their associated neutral pion, boosted in the rest frame of the two charged pions (Fig.8). This method can be applied in any decay mode with at least two pions in the final state. In the case of the three-prong decay mode through a charged a_1 resonance, we use the decay plane spanned by the intermediate neutral ρ resonance decaying to two charged pions with opposite charges.

Polarimetric vector method

This last method developed in Strasbourg is based on the estimation of the most probable direction of the spin from taus called the polarimetric vector. ϕ_{CP} is then calculated from the planes spanned for each tau by its polarimetric vector and its own direction in the Higgs boson rest frame. This method could be applied to any hadronic decay, but the need to reconstruct both taus makes it challenging. To this day, the polarimetric vector method combined with the Global Event Fit (GEF) algorithm [14] led to an improvement of the sensitivity in the $\tau\tau \to a_1^+ a_1^-$ decay channel [15] compared to the initial neutral pion method (Fig.9).

All of these methods can be applied separately on each tau and mixed together for decay modes where the taus are not decaying the same way. The next step for this analysis is to extract the signal from the background using a MVA with kinematic variables as input. This MVA will then give three possible output categories, namely :

- Higgs (signal)
- Genuine τ_h background (embedded samples [16])
- Fake τ_h background (misidentified jets)

The background estimation consistency is checked in the first place using the two background categories. The signal category is then "unblinded" lastly in order

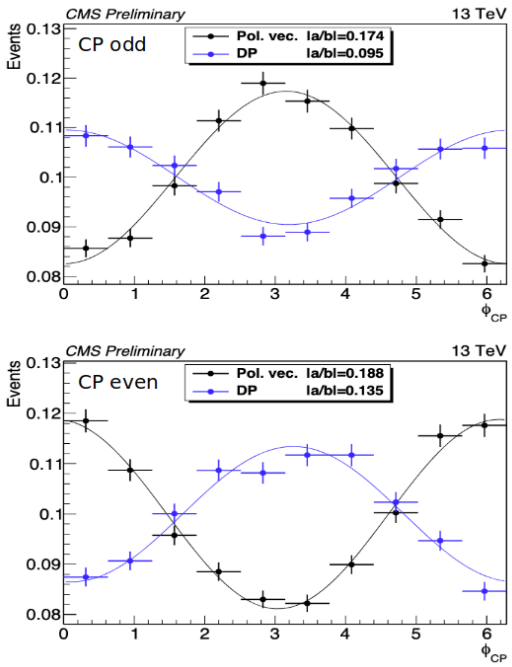

Figure 9: ϕ_{CP} distributions in the $\tau\tau \to a_1^+ a_1^-$ decay mode in the CP-odd scenario (up) and CP-even scenario (down). $|a/b|$ values are defined as the ratio of fitting parameters from the function $a\cos(x) + b$ (Results from G. Bourgatte PhD **??**).

to perform a fit of the data using a likelihood function. The parameters extremizing this function are defined as "best fit" parameters.

Results

$H^0 \to ZZ \to 4l$

From the method described in the previous section, results are summarized in Fig.10. From the first line, the pure CP-odd hypothesis 0^- is excluded at 3.8σ.

$t\bar{t}H^0$ production mode

From the fit to data performed in Fig.5, the cross section is measured to be $\sigma_{t\bar{t}H}\mathcal{B}_{\gamma\gamma}$=$1.56^{+0.4}_{-0.32}$fb with a significance of 6.6σ, leading to the first single-channel observation of the $t\bar{t}H^0$ process. The pure CP-odd hypothesis of the coupling is excluded at 3.2σ and the CPP-odd fraction of the coupling is constrained to be f_{CP}^{Htt}=0.00±0.33 at 68% CL.

$H^0 \to \tau\tau$

Following the fit to data providing the "best fit" parameters of the likelihood function $L(\alpha^{H\tau\tau}_{\text{best fit}})$, a negative log-likelihood scan is performed (Fig.11) :

$$-2\Delta \ln L = -2(\ln(L\alpha^{H\tau\tau}) - \ln(L\alpha^{H\tau\tau}_{\text{best fit}}) \quad (4)$$

J^P model	J^P production	Expected ($\mu = 1$)	Obs. 0^+	Obs. J^P	CL_s
0^-	any	2.4σ (2.7σ)	-1.0σ	$+3.8\sigma$	0.05%
0^+_h	any	1.7σ (1.9σ)	-0.3σ	$+2.1\sigma$	4.5%
1^-	$q\bar{q} \to X$	2.7σ (2.7σ)	-1.4σ	$+4.7\sigma$	0.002%
1^-	any	2.5σ (2.6σ)	-1.8σ	$+4.9\sigma$	0.001%
1^+	$q\bar{q} \to X$	2.1σ (2.3σ)	-1.5σ	$+4.1\sigma$	0.02%
1^+	any	2.0σ (2.1σ)	-2.1σ	$+4.8\sigma$	0.004%
2^+_m	$gg \to X$	1.9σ (1.8σ)	-1.1σ	$+3.0\sigma$	0.9%
2^+_m	$q\bar{q} \to X$	1.7σ (1.7σ)	-1.7σ	$+3.8\sigma$	0.2%
2^+_m	any	1.5σ (1.5σ)	-1.6σ	$+3.4\sigma$	0.7%
2^+_b	$gg \to X$	1.6σ (1.8σ)	-1.4σ	$+3.4\sigma$	0.5%
2^+_h	$gg \to X$	3.8σ (4.0σ)	$+1.8\sigma$	$+2.0\sigma$	2.3%
2^-_h	$gg \to X$	4.2σ (4.5σ)	$+1.0\sigma$	$+3.2\sigma$	0.09%

Figure 10: Results for various J^P hypothesis. The third column shows the expected separation with the signal strength value from the fit to data or the value from the Standard Model (μ=1). The observed separation columns show results for the 0^+ or J^P model with μ set as a free parameter in the fit. The last column stands for the confidence level value for the J^P model.

Observation in data led to an exclusion of the pure CP-odd hypothesis $\alpha^{H\tau\tau}$=±90° with 3.0σ. The observed (expected) value for $\alpha^{H\tau\tau}$ is -1±19° (0±21°) at the 68.3% CL, ±41° (±49°) at the 95.5% CL, and at the 99.7% CL the observed range is ±84°. Therefore, all previous measurements are consistent with the Standard Model prediction of a purely scalar Higgs boson.

References

[1] F. Englert and R. Brout, "Broken symmetry and the mass of gauge vector mesons", *Phys. Rev. Lett.* **13** (1964) 321, doi:10.1103/PhysRevLett.13.321.

[2] P. W. Higgs, "Broken symmetries, massless particles and gauge fields", *Phys. Lett.* **12** (1964) 132, doi:10.1016/0031-9163(64)91136-9.

[3] P. W. Higgs, "Broken symmetries and the masses of gauge bosons", *Phys. Rev. Lett.* **13** (1964) 508, doi:10.1103/PhysRevLett.13.508.

[4] G. S. Guralnik, C. R. Hagen, and T. W. B. Kibble, "Global conservation laws and massless particles", *Phys. Rev. Lett.* **13** (1964) 585, doi:10.1103/PhysRevLett.13.585.

[5] P. W. Higgs, "Spontaneous symmetry breakdown without massless bosons", *Phys. Rev.* **145** (1966) 1156, doi:10.1103/PhysRev.145.1156.

[6] T. W. B. Kibble, "Symmetry breaking in non-abelian gauge theories", *Phys. Rev.* **155** (1967) 1554, doi:10.1103/PhysRev.155.1554.

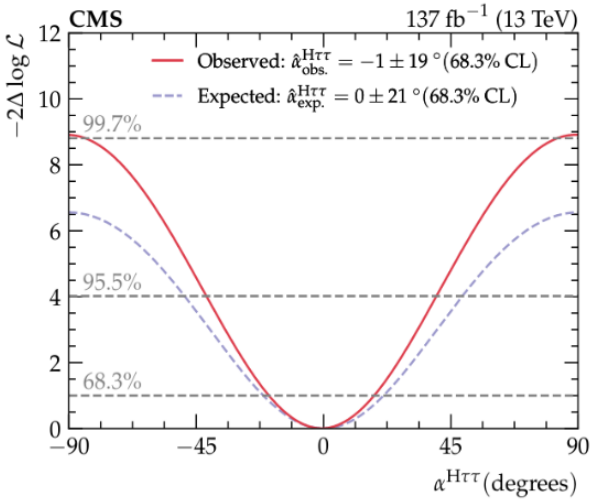

Figure 11: Negative log-likelihood scan for the combination of the $\tau_e\tau_h$, $\tau_\mu\tau_h$, $\tau_h\tau_h$ and channels.

[7] CMS Collaboration, "Observation of a new boson at a mass of 125 GeV with the CMS experiment at the LHC", *Phys. Lett. B* **716** (2012) 30, doi:10.1016/j.physletb.2012.08.021

[8] CMS Collaboration, "Observation of a new boson with mass near 125 GeV in pp collisions at $\sqrt{s}$ = 7 and 8 TeV", *JHEP* **06** (2013) 081, doi:10.1007/JHEP06(2013)081

[9] ATLAS Collaboration, "Observation of a new particle in the search for the Standard Model Higgs boson with the ATLAS detector at the LHC", *Phys. Lett. B* **716** (2012) 1, doi:10.1016/j.physletb.2012.08.020

[10] CMS Collaboration, "Measurement of the properties of a Higgs boson in the four-lepton final state", *Phys. Rev. D* **89** (2014) 092007, doi:10.1103/PhysRevD.89.092007

[11] CMS Collaboration, "Measurements of $t\bar{t}H$ Production and the CP Structure of the Yukawa Interaction between the Higgs Boson and Top Quark in the Diphoton Decay Channel", *Phys. Rev. Lett.* **125** (2020) 061801, doi:10.1103/PhysRevLett.125.061801

[12] CMS Collaboration, "Analysis of the CP structure of the Yukawa coupling between the Higgs boson and τ leptons in proton-proton collisions at $\sqrt{s}$=13 TeV", CMS-HIG-20-006, arXiv:2110.04836

[13] LHC Higgs Cross Section Working Group, "Handbook of LHC Higgs cross sections: 4. Deciphering the nature of the Higgs sector", CERN (2016), https://doi.org/10.23731/CYRM-2017-002

[14] V. Cherepanov, A. Zotz, "Kinematic reconstruction of $Z/H \to \tau\tau$ decay in proton-proton collisions" arXiv:1805.06988

[15] G. Bourgatte, "Étude des propriétés CP du boson de Higgs dans le canal tau tau dans l'expérience CMS auprès du LHC", *PhD*, (2020), http://www.theses.fr/2020STRAE029

[16] A.M. Sirunyan *et al.*, "An embedding technique to determine $\tau\tau$ backgrounds in proton-proton collision data", *JINST* **14** (2019) P06032, https://doi.org/10.1088/1748-0221/14/06/P06032

Part IX

Theoretical Physics

session chaired by Luc DARMÉ

Perturbative renormalization of the Euclidean ϕ_4^4 theory with flow equations

Majdouline BORJI

CPHT, École Polytechnique

Abstract — The flow equations of the renormalization group allow to analyse the perturbative n-point functions of renormalizable quantum field theories. Rigorous bounds obtained from the flow equations permit to control large momentum behaviour, infrared singularities and large order behaviour in the number of loops and arguments n. We use this method to give a rigorous proof of the renormalizability of the massive ϕ_4^4 theory on a half-space. We choose a suitable class of test functions and prove bounds for the amputated n-point distributions folded with these test functions. These bounds are uniform in the cutoff and thus directly lead to renormalizability.

Introduction

Quantum field theory was originally developed as a theoretical framework that combines classical field theory, special relativity, and quantum mechanics and has become the general theoretical framework to study physical systems with an infinite (or large) number of degrees of freedom.

A rigorous mathematical analysis of quantum field theories is faced with the problem that path integrals describing systems in field theory are generally not defined. There exists a complete theory of Gaussian measures that apply to free theories. However, for the interacting case, a rigorous mathematical description starts from regularized versions of the theory, where the number of degrees of freedom in space and momentum has been made finite. This is a task common to all regularizations, such as simple momentum cutoff, Pauli-Villars and lattice cutoff. One then studies correlation functions and proves that these have uniform limits in the cutoffs.

The scalar field theory in $d = 4$ (i.e ϕ_4^4) is renormalizable in the sense that when the momentum cutoff is sent to infinity, the correlation functions stay finite. Several proofs exist to prove the renormalizability of ϕ_4^4 theory [9]-[12]. Among them, the perturbative proof of renormalization based on Wilson Flow equations performed by Polchinski in the seminal paper [8] in 1984. The flow equations allow to describe theories by an effective action L^{Λ,Λ_0}, depending on a scale Λ with $0 \leq \Lambda \leq \Lambda_0 < \infty$ for Euclidean quantum field theories in the continuum with a momentum cutoff. Here Λ plays a similar role as an infrared cutoff, Λ_0 denotes the ultraviolet cutoff. L^{Λ,Λ_0} should satisfy the following conditions:

• At the ultraviolet cutoff $\Lambda = \Lambda_0$, L^{Λ,Λ_0} coincides with the bare action.

• For $\Lambda < \Lambda_0$, L^{Λ,Λ_0} is obtained upon integration of the field-degrees of freedom which propagate with momenta p between Λ and Λ_0.

• As $\Lambda \to 0$, L^{Λ,Λ_0} approaches a theory without infrared cutoff.

A promising application of the flow equations is the proof of renormalizability of quantum field theories. Conventional proofs of renormalizability are based on an approach in terms of Feynman diagrams. In perturbation theory, the correlation functions are represented as a sum of Feynman integrals. This approach is complicated for two reasons. First, the convergence of a Feynman integral is determined by a criterion called the power counting theorem. It allows one to determine the convergence of Feynman integrals in the large cutoff limit by counting suitably defined UV-divergence degrees so that the Feynman integral is absolutely convergent. Second, a systematic procedure is required to achieve convergence to all orders in perturbation theory, that is to substract the divergences from all Feynman integrals of the theory. It is the combinatorics of counting divergence degrees and of removing divergences which makes the proof rather cumbersome. The flow equations give an alternative proof based on a tight inductive scheme wherefrom bounds on the regularized Schwinger functions implying renormalizability can be deduced. Renormalizability of a quantum field theory implies that the unregularized n-point correlation functions at loop order l

$$\lim_{\Lambda\to 0,\Lambda_0\to\infty} \mathcal{L}_{l,n}^{\Lambda,\Lambda_0}(p_1,...,p_n)$$

exist in the sense that they are both IR (in the limit of very small momenta) and UV finite (in the limit of very large momenta). Finite limits are achieved by imposing a finite set of renormalization conditions on a physical scale that is independent of the UV cutoff Λ_0. For simplicity, we will consider the case in which all fields are massive to avoid any IR problems. Proving renormalizability then amounts to show the existence of the large UV-cutoff limit $\Lambda_0 \to \infty$.

In [13], we used the method of the flow equations to investigate the renormalizability of the massive ϕ_4^4

scalar field theory on the semi-infinite space, which is the simplest model to study surface effects in quantum field theory. $\mathbb{R}^3 \times \mathbb{R}^+$.

It is defined starting from the massive ϕ_4^4 model in infinite space, with the difference that it is defined on a half space bounded by a plane. In this model, three types of boundary conditions are considered in the literature, namely Dirichlet, Neumann and Robin boundary conditions.

Boundary conditions and the possible propagators

The self-adjoint extensions of the Laplacian operator in $\mathbb{R}^3 \times \mathbb{R}^+$ define all the possible boundary conditions. However, not all self-adjoint extensions lead to boundary conditions with classical interpretation. The massive propagators associated to Robin, Neumann and Dirichlet boundary conditions are defined from functional calculus by

$$C_\bullet\left((z,x);(z',x')\right) = \int_0^\infty d\lambda e^{-\lambda\left(-\Delta_\bullet + m^2\right)}\left((z,x);(z',x')\right), \tag{1}$$

where $\bullet \in \{D,R,N\}$ for respectively Dirichlet, Robin and Neumann boundary conditions. In the pz-representation, which corresponds to taking the partial Fourier transformation with respect to the variable $x \in \mathbb{R}^3$, the Dirichlet, Neumann and Robin propagators simply read

$$C_D(p;z,z') = \frac{1}{2\sqrt{p^2+m^2}}\left[e^{-\sqrt{p^2+m^2}|z-z'|} - e^{-\sqrt{p^2+m^2}|z+z'|}\right],$$

$$C_N(p;z,z') = \frac{1}{2\sqrt{p^2+m^2}}\left[e^{-\sqrt{p^2+m^2}|z-z'|} + e^{-\sqrt{p^2+m^2}|z+z'|}\right],$$

$$C_R(p;z,z') = \frac{1}{2\sqrt{p^2+m^2}}\left[e^{-\sqrt{p^2+m^2}|z-z'|} + \frac{\sqrt{p^2+m^2}-c}{\sqrt{p^2+m^2}+c}\, e^{-\sqrt{p^2+m^2}|z+z'|}\right].$$

The Dirichlet boundary condition corresponds to $c \to \infty$ and the Neumann boundary condition to $c = 0$. We study the Robin boundary condition since the other two conditions are limit cases of the former. One can easily verify that we have

$$\begin{aligned} C_D(p;0,z') &= C_D(p;z,0) = 0\,, \\ \lim_{z\to 0}\ \partial_z C_N(p;z,z') &= \lim_{z'\to 0}\ \partial_{z'} C_N(p;z,z') = 0\,, \\ \lim_{z\to 0}\ \partial_z C_R(p;z,z') &= c\ C_R(p;0,z')\,, \\ \lim_{z'\to 0}\ \partial_{z'} C_R(p;z,z') &= c\ C_R(p;z,0). \end{aligned}$$

The method of flow equations: A simple example

Here, we elucidate the method of flow equations used in the proof of perturbative renormalizability of the simple case of ϕ^4 in $\mathbb{R}^4$.

The regularized propagator

The starting point to define an Euclidean quantum field theory is the Gaussian measure, since it is the support of this measure that allow to define the field. A Gaussian measure with mean zero is uniquely defined by its covariance operator. This operator can be defined through the propagator, which plays the role of its kernel. For the massive scalar field theory in $\mathbb{R}^4$, the propagator in Fourier space is given by

$$C(p) = \frac{1}{p^2+m^2}$$

The Gaussian measure associated to this propagator has its support included in $\mathcal{S}'\left(\mathbb{R}^4\right)$ (i.e. the space of tempered distributions). The support of the Gaussian measure is what defines the space to which the field belongs. The bare interaction includes powers and derivatives of the field. However, It can not be given any mathematical meaning if the field is a distribution. Therefore, we regularize the propagator to make the support of the associated Gaussian measure included in at least $\mathcal{C}^2\left(\mathbb{R}^4\right)$ (i.e. the space of functions with continuous zeroth, first and second derivatives). We choose the following regularization

$$C^{\Lambda,\Lambda_0}(p) = \frac{1}{p^2+m^2}\left(e^{-\frac{p^2+m^2}{\Lambda_0^2}} - e^{-\frac{p^2+m^2}{\Lambda^2}}\right), \tag{2}$$

where Λ_0 is the UV-cutoff and Λ a flow paramater $0 \le \Lambda \le \Lambda_0$ which plays the role of an infrared cutoff. For $\Lambda \to 0$ and $\Lambda_0 \to 0$, the full propagator of the theory is recovered.

The flow equations

The theory we consider is the massive Euclidean ϕ^4-theory on $\mathbb{R}^4$. This means that we start from the bare interaction

$$L^{\Lambda_0,\Lambda_0}(\phi) = \int_{\mathbb{R}^4} d^4x \left(\frac{f}{4!}\phi^4(x) + a(\Lambda_0)\phi^2(x) - b(\Lambda_0)\phi(x)\Delta\phi(x) + c(\Lambda_0)\phi^4(x)\right).$$

The first term is formed of the field's self-interaction with real coupling constant f having mass dimension equal to zero. The second part contains the related counterterms, determined according to the following rule. The canonical mass dimension of the field is one, the counterterms allowed in the bare interaction are all local terms of mass dimension ≤ 4 that can be formed of the field and of its derivatives respecting the euclidean symmetries. From the bare interaction and the flowing propagator (2), we may define Wilson's flowing effective action L^{Λ,Λ_0} by integrating out momenta in the region $\Lambda \le |p| \le \Lambda_0$:

$$e^{-\frac{1}{\hbar}L^{\Lambda,\Lambda_0}(\phi)} := \mathcal{N}\int d\mu_{\Lambda,\Lambda_0}(\Phi) e^{-\frac{1}{\hbar}L^{\Lambda_0,\Lambda_0}(\Phi+\phi)} \tag{3}$$

and can be recognised to be the generating functional of the connected amputated correlation functions of the theory with propagator C^{Λ,Λ_0} and bare action L^{Λ_0,Λ_0}. For the normalization factor $\mathcal{N}$ to be finite, we have to restrict the

theory to finite volume. All subsequent formula are also valid in the thermodynamic limit since no longer involve the vacuum functional [5].
The fundamental tool for our study of the renormalization problem is the functional flow equation

$$\partial_\Lambda L^{\Lambda,\Lambda_0} = \frac{\hbar}{2}\langle\frac{\delta}{\delta\phi}, \dot{C}^{\Lambda,\Lambda_0}\frac{\delta}{\delta\phi}\rangle L^{\Lambda,\Lambda_0} - \frac{1}{2}\langle\frac{\delta L^{\Lambda,\Lambda_0}}{\delta\phi}, \dot{C}^{\Lambda,\Lambda_0}\frac{\delta L^{\Lambda,\Lambda_0}}{\delta\phi}\rangle. \tag{4}$$

where $\dot{C}^{\Lambda,\Lambda_0} := \partial_\Lambda C^{\Lambda,\Lambda_0}$. It is obtained by deriving both sides of the equation (3) with respect to Λ and performing an integration by parts in the functional integral on the RHS using the properties of the Gaussian measure [1], and finally rearranging the powers of $\hbar$ coming from $L^{\Lambda,\Lambda_0}/\hbar$ and from $\hbar\dot{C}^{\Lambda,\Lambda_0}$. To derive the flow equations verified by the n-point Schwinger (correlation) functions, we first expand L^{Λ,Λ_0} in moments with respect to ϕ,

$$\forall (p_i)_{1\le i\le n} \in \mathbb{R}^4,$$
$$(2\pi)^{4(n-1)}\delta_{\phi(p_1)}\cdots\delta_{\phi(p_n)}L^{\Lambda,\Lambda_0}|_{\phi=0} = \delta^4(p_1+\cdots+p_n)\mathcal{L}_n^{\Lambda,\Lambda_0}(p_1,\cdots,p_n)$$

and also in a formal powers series with respect to $\hbar$ to select the loop order l,

$$\mathcal{L}_n^{\Lambda,\Lambda_0} = \sum_{l=0}^{\infty}\hbar^l\mathcal{L}_{l,n}^{\Lambda,\Lambda_0} \ .$$

From the functional flow equation (4), we then obtain the perturbative flow equations for the n-point correlation functions by identifying coefficients

$$\begin{aligned}
&\partial_\Lambda\partial^w\mathcal{L}_{l,n}^{\Lambda,\Lambda_0}(p_1,\cdots,p_n)\\
&= \frac{1}{2}\int_{k\in\mathbb{R}^4}\partial^w\mathcal{L}_{l-1,n+2}^{\Lambda,\Lambda_0}(k,p_1,\cdots,p_n,-k)\partial_\Lambda C^{\Lambda,\Lambda_0}(k)\\
&\quad - \frac{1}{2}{\sum_{l_1,l_2}}'\ {\sum_{n_1,n_2}}'\sum_{w_i} c_{w_i}\Big[\partial^{w_1}\mathcal{L}_{l_1,n_1+1}^{\Lambda,\Lambda_0}(p_1,\cdots,p_{n_1},p)\\
&\quad \partial^{w_3}\partial_\Lambda C^{\Lambda,\Lambda_0}(p)\partial^{w_2}\mathcal{L}_{l_2,n_2+1}^{\Lambda,\Lambda_0}(-p,p_{n_1+1},\cdots,p_n)\Big]_{rsym}\\
&\qquad p = -p_1-\cdots-p_{n_1} = p_{n_1+1}+\cdots+p_n
\end{aligned}$$

where the prime on top of the summation imposes the restriction to $n_1+n_2=n$ and $l_1+l_2=l$ and the symbol "rsym" means summation over those permutations of the momenta $p_1,\cdots,p_n$, which do not leave invariant the (unordered) subsets $(p_1,\cdots,p_{n_1})$ and $(p_{n_1+1},\cdots,p_n)$, and, therefore, produce mutually different pairs of (unordered) image subsets.
Here we wrote the equation directly in a form where a number $|w|$ of momentum derivatives, characterized by a multi index w, act on both sides. Derivatives of the $\mathcal{L}_{l,n}^{\Lambda,\Lambda_0}$ are needed to obtain a closed inductive scheme. We set

$$\partial^w = \frac{\partial^{|w|}}{\partial p_{1,1}^{w_1}\partial p_{1,2}^{w_2}...\partial {p_{n,4}}^{w_{4,n}}} \quad |w| = w_{1,1}+...+w_{n,4}.$$

Moreover, the combinatorial factor $c_{\{w_i\}} = w!(w_1!w_2!w_3!)^{-1}$ comes from Leibniz's rule. In the loop order $l=0$, the first term on the RHS is absent.

Boundary conditions

The bare interaction implies that at $\Lambda=\Lambda_0$, we have for all $n+|w|\ge 5$,

$$\partial^w\mathcal{L}_{l,n}^{\Lambda_0,\Lambda_0}(p_1,\cdots,p_n) = 0, \quad \mathcal{L}_{l,2}^{\Lambda_0,\Lambda_0}(p,-p) = 0 \ .$$

For the relevant terms, which corresponds to $n+|w|\le 4$, they are fixed by the renormalization conditions at $\Lambda=0$

$$\mathcal{L}_4^{\Lambda,\Lambda_0}(0,\cdots,0) = f,$$
$$\mathcal{L}_2^{\Lambda,\Lambda_0}(0,0) = 0, \qquad \partial_{p^2}\mathcal{L}_2^{\Lambda,\Lambda_0}(0,0) = 0 \ .$$

The renormalization point is chosen at zero momentum for simplicity (BPHZ renormalization conditions).

Proof of perturbative renormalizability

Perturbative renormalizability of the regularized field theory (3) amounts to the following: for given coupling constant f in the bare interaction L^{Λ_0,Λ_0}, the coefficients $a(\Lambda_0)$, $b(\Lambda_0)$ and $c(\Lambda_0)$ of the counterterms can be adjusted within a loop expansion of the theory,

$$a(\Lambda_0) = \sum_{l=1}^{\infty}\hbar^l a_l(\Lambda_0),\cdots, c(\Lambda_0) = \sum_{l=1}^{\infty}\hbar^l c_l(\Lambda_0) \ ,$$

in such a way that the limits of the $n-$point correlation functions exist when Λ goes to 0 and Λ_0 goes to ∞ in every loop order l.

$$\forall\,(p_i)_{1\le i\le n}\in\mathbb{R}^4,\ n\in\mathbb{N}, l\in\mathbb{N}^*$$
$$\mathcal{L}_{l,n}^{0,\infty}(p_1,\cdots,p_n) := \lim_{\Lambda\to 0,\Lambda_0\to\infty}\mathcal{L}_{l,n}^{\Lambda,\Lambda_0}(p_1,\cdots,p_n).$$

A simple inductive proof of ϕ_4^4 theory regularized by a UV-cutoff has been exposed several times in the literature [4]-[7]. It is based on proving the following induction hypotheses. For all $l\in\mathbb{N}^*$, $n\in\mathbb{N}$, w and for $0\le\Lambda\le\Lambda_0$ holds
A) Boundedness in the UV-cutoff

$$\begin{aligned}
&\left|\partial^w\mathcal{L}_{l,n}^{\Lambda,\Lambda_0}(p_1,\cdots,p_n)\right|\\
&\le (\Lambda+m)^{4-n-|w|}\,\mathcal{P}_1\left(\log\frac{\Lambda+m}{m}\right)\mathcal{P}_2\left(\left\{\frac{|p_i|}{\Lambda+m}\right\}\right) \ .
\end{aligned} \tag{5}$$

B) Convergence in the UV-limit

$$\begin{aligned}
&\left|\partial_{\Lambda_0}\partial^w\mathcal{L}_{l,n}^{\Lambda,\Lambda_0}(p_1,\cdots,p_n)\right|\\
&\le \frac{(\Lambda+m)^{5-n-|w|}}{(\Lambda_0+m)^2}\mathcal{P}_3\left(\log\frac{\Lambda_0+m}{m}\right)\mathcal{P}_4\left(\left\{\frac{|p_i|}{\Lambda+m}\right\}\right).
\end{aligned} \tag{6}$$

Here and in the following the $\mathcal{P}$ denote polynomials with nonnegative coefficients. The coefficients depend on $l,n,|w|$ but not on $\{p_i\}$, Λ, Λ_0. For $l=0$, all polynomials $\mathcal{P}_1$ reduce to 1. The statement (6) implies for small values of Λ_0 only,

$$\begin{aligned}
&\left|\partial_{\Lambda_0}\partial^w\mathcal{L}_{l,n}^{\Lambda,\Lambda_0}(p_1,\cdots,p_n)\right|\\
&\le \Lambda_0^{-2}\,(\Lambda+m)^{5-n-|w|}\left(\log\frac{\Lambda_0+m}{m}\right)^{\nu}\mathcal{P}_4\left(\left\{\frac{|p_i|}{\Lambda+m}\right\}\right).
\end{aligned} \tag{7}$$

Integration of the bound (7) over the lattice cutoff Λ_0 im-

mediately proves the convergence of all $\mathcal{L}_{l,n}^{\Lambda,\Lambda_0}(p_1,\cdots,p_n)$ for fixed Λ to finite limits with $\Lambda_0 \to \infty$. In particular, one obtains for all $\tilde{\Lambda}_0 < \Lambda_0$,

$$\left|\mathcal{L}_{l,n}^{\Lambda_0,\infty}(p_1,...,p_n) - \mathcal{L}_{l,n}^{\tilde{\Lambda}_0,\infty}(p_1,...,p_n)\right| < \Lambda_0 m^{5-n}\left(\log\frac{\Lambda_0+m}{m}\right)^{\nu}\mathcal{P}_5\left(\left\{\frac{|p_i|}{m}\right\}\right).$$

(5)-(6) imply also that the connected amputated Schwinger (CAS) n-point functions are $\mathcal{C}^\infty$ w.r.t. momenta, Λ and Λ_0. Thus, due to the Cauchy criterion in $\mathcal{C}^\infty(\mathbb{R}^+)$ (w.r.t. to Λ_0) finite limits exist to all loop orders l.

Results: Perturbative renormalization of the massive ϕ_4^4 in the half-space $\mathbb{R}^3 \times \mathbb{R}^+$

Since the translation invariance is broken by the presence of the surface $\mathbb{R}^3 \times \{0\}$, we perform a partial Fourier transformation w.r.t. the directions in which the translation invariance is preserved ($x \in \mathbb{R}^3$). This defines what we call the mixed representation $(p,z) \in \mathbb{R}^3 \times \mathbb{R}^+$. In [13], we studied the perturbative renormalizability of the semi-infinite ϕ_4^4 theory with Robin boundary condition. It will be proved by analyzing the generating functional L^{Λ,Λ_0} of CAS distributions, which are no more functions because of the mixed pz-representation . The upper indices Λ_0 and Λ enter through the regularized propagator. We choose the following regularization

$$C_R^{\Lambda,\Lambda_0}(p;z,z') = \int_{\frac{1}{\Lambda_0^2}}^{\frac{1}{\Lambda^2}} d\lambda\; e^{-\lambda(p^2+m^2)} p_R(\lambda;z,z')\ .$$

where p_R denotes the one-dimensional Robin heat kernel

$$p_R(\lambda;z,z') := p_N(\lambda;z,z') - 2\int_0^\infty \frac{dw}{\sqrt{2\pi\lambda}}\, e^{-w}\, e^{-\frac{\left(z+z'+\frac{w}{c}\right)^2}{2\lambda}}\ .$$

Here p_N denotes the one-dimensional Neumann heat kernel

$$p_N(\lambda;z,z') := \frac{1}{\sqrt{2\pi\lambda}}\left(\frac{e^{-\frac{(z-z')^2}{2\lambda}} + e^{-\frac{(z+z')^2}{2\lambda}}}{2}\right).$$

To establish bounds on the CAS, which are distributions, they have to be folded first with test functions. In [13], a suitable class of test functions is introduced, together with tree structures that will be used in the bounds on the CAS to be derived. Let $1 \le s \le n$, we define $\tau := \inf \tau_{2,s}$ where $\tau_{2,s} = (\tau_2,\cdots,\tau_s)$ with $\tau_i > 0$ and similarly $z_{2,s} = (z_2,\cdots,z_s)$. Given $y_2,\cdots,y_s \in \mathbb{R}^+$, we define

$$\phi_{\tau_{2,s},y_{2,s}}(z_{2,s}) := \prod_{i=2}^{s} p_R(\tau_i;z_i,y_i) \prod_{i=s+1}^{n} \chi^+(z_i)\ , \quad (8)$$

where $\chi^+(z_i)$ is the characteristic function of the semi-line $\mathbb{R}^+$. This definition can be generalized by choosing any other subset of s coordinates among $z_2,\cdots,z_n$. Using these test functions, we introduced a tree structure that emerges naturally from the flow equations in the position space. After introducing all the necessary tools, we state and prove inductive bounds on the amputated Schwinger distributions folded with the introduced test functions which, being uniform in the cutoff, directly lead to renormalizability.

Conclusions

We introduced the method of the flow equations using the basic example of the massive scalar field theory with a ϕ^4 interaction in $\mathbb{R}^4$. For a boundary field theory, such as ϕ^4 in $\mathbb{R}^3 \times \mathbb{R}^+$, the first problem one encounters is that the translation invariance is broken, and we can no more work in Fourier space. This imply that the CAS are distributions rather than functions. To deduce perturbative renormalizability by proving inductive bounds, we need to introduce test functions to which the CAS are folded. An additional difficulty compared to the renormalization of the scalar field theory in a space without boundary [4] comes from the fact that the renormalization of amputated and non-amputated diagrams is not equivalent. This is a consequence of the presence of a surface.

References

[1] J. Glimm and A. Jaffe,"Quantum Physics: A Functional Integral Point of View", Springer Verlag (1987)

[2] M. Reed and L. Rosen, "Support properties of the free measure for Boson fields", Commun.Math.Phys. 36, 123-132 (1974)

[3] M. Borji and Ch. Kopper, "Perturbative renormalization of the lattice regularized ϕ_4^4 with flow equations", J. Math. Phys. 61, 112304 (2020)

[4] Ch. Kopper, V.F. Muller, "Renormalization Proof for Massive ϕ_4^4 Theory on Riemannian Manifolds", Commun.Math.Phys. 275, 331-372 (2007)

[5] G. Keller, Ch. Kopper and M. Salmhofer, "Perturbative renormalization and effective Lagrangians in ϕ^4 in four-dimensions", Helv.Phys.Acta 65, 32-52 (1992)

[6] G. Keller, Ch. Kopper and C. Schophaus, "Perturbative renormalization with flow equations in Minkowski space", Helv.Phys.Acta 70, 247-274 (1997)

[7] V. F. Muller, "Perturbative renormalization by flow equations", Rev.Math.Phys. 15, 491-558 (2003)

[8] J. Polchinski, "Renormalization and Effective Lagrang ians",Nucl.Phys.B 231, 269-295 (1984)

[9] Y. Hahn, W. Zimmermann, "An elementary proof of Dyson's power counting theorem", Commun.Math.Phys 10, 330-342 (1968)

[10] W. Zimmermann, "Convergence of Bogoliubov's method of renormalization in momentum space", Commun.Math.Phys. 15, 208-234 (1969)

[11] J. H. Lowenstein, "Convergence theorems for renormalized Feynman integrals with Zero-Mass propagators", Commun.Math.Phys. 47, 53-68 (1976)

[12] J.H. Lowenstein, W. Zimmermann, "The power counting theorem for Feynman integrals with massless propagators", Commun.Math.Phys. 44, 73-86 (1975)

[13] M. Borji and Ch. Kopper, "Perturbative renormalization of ϕ_4^4 theory on the half space $\mathbb{R}^+ \times \mathbb{R}^3$ with flow equations", Preprint. (2022)

On the B-meson decay anomalies

Jonathan KRIEWALD

Laboratoire de Physique de Clermont (UMR 6533), CNRS/IN2P3, Université Clermont-Auvergne, France

Abstract — In the Standard Model electroweak interactions are strictly lepton flavour universal. In view of the emerging hints for the violation of lepton flavour universality in several B-meson decays, we conduct a model-independent study (effective field theory approach) of several well-motivated new physics scenarios. Taking into account the most recent LHCb data, we provide updates to New Physics fits for numerous popular hypotheses. We also consider a promising model of vector leptoquarks, which in addition to explaining the B-meson decay anomalies ($R_{K^{(*)}}$ and $R_{D^{(*)}}$) would have an extensive impact for numerous flavour observables.

Introduction

In the Standard Model (SM), charged leptons are only distinguishable due to their masses. In particular, all electroweak (EW) couplings to gauge bosons are blind to lepton flavour, leading to an accidental symmetry called lepton flavour universality (LFU), whose validity has been determined to a very high accuracy for instance in $Z \to \ell^+\ell^-$ and $W^\pm \to \ell^\pm\nu$ ($\ell = e, \mu, \tau$) decays [1]. However, during the last decade, hints on the violation of LFU in $b \to c\ell\nu$ and $b \to s\ell\ell$ decays have begun to emerge, in tension with respect to the SM expectations. In particular, measurements of the "theoretically clean" ratios of branching ratios $R_{D^{(*)}} = \mathrm{BR}(B \to D^{(*)}\tau\nu)/\mathrm{BR}(B \to D^{(*)}\ell\nu)$ [2] and $R_{K^{(*)}} = \mathrm{BR}(B \to K^{(*)}\mu\mu)/\mathrm{BR}(B \to K^{(*)}ee)$ [3, 4] deviate around $2-3\,\sigma$ from the theoretical predictions, expected to be unity in the SM (up to phase space suppression). Current averages of experimental measurements and the SM predictions can be found in Table 1.

	R_K	R_{K^*}	R_D	R_{D^*}
SM	$\simeq 1$	$\simeq 1$	0.299 ± 0.003	0.258 ± 0.005
Exp.	0.845 ± 0.06	0.69 ± 0.12	0.340 ± 0.030	0.295 ± 0.014

Table 1: SM predictions and experimental measurements of the "theoretically clean" LFU observables.

Additionally, measurements of angular observables in $B^{0,+} \to K^*\mu^+\mu^-$ decays exhibit (local) deviations of $2-3\,\sigma$ in several q^2 bins [5, 6].

Very recently, the LHCb Collaboration updated their measurement of $R_K = 0.846^{+0.044}_{-0.041}$ [7] with the deviation to the SM prediction now reaching $3.1\,\sigma$, thus providing the first *evidence* of LFU violation. [1]

These curious, persisting tensions with the SM seem to indirectly hint towards the presence of new physics (NP), likely at the TeV-scale. Many different approaches have been explored to identify which NP models better succeed in reconciling theoretical predictions with experimental data. Before addressing the prospects of vector leptoquark (LQ) extensions of the SM (one of the preferred scenarios to simultaneously explain both anomalies), we will consider a model-independent effective field theory (EFT) based approach. This will allow to generically identify which classes of NP models offer the most appropriate content and interactions to explain the anomalous data.

[1] For an (animated) overview of how the fit to $b \to s\ell\ell$ data has evolved upon inclusion of the new measurements see http://moriond.in2p3.fr/2021/EW/slides/ani_fit_evo.mp4.

EFT and global fits

The EFT approach relies in parametrising NP effects in terms of higher-order non-renormalisable operators (vestigial traces in the low-energy theory of heavier states, which are integrated out). Starting from the relevant subsets of the effective Lagrangian, cast in terms of semileptonic Wilson coefficients (WC) $C^{qq';\ell\ell'}$ and effective operators, we identify scenarios of (sets of) $C^{qq';\ell\ell'}$ significantly favoured by current data.

The subset of the effective Lagrangian for charged current $d_k \to u_j\ell\nu_i$ transitions is given by

$$\mathcal{L}_{\text{eff}} \simeq -\frac{4G_F}{\sqrt{2}} V_{jk} \left[(1 + C_{V_L}^{jk\ell i})(\bar{u}_j\gamma_\mu d_k)(\bar{\ell}\gamma^\mu P_L \nu^i)\right] + \text{H.c.}\,, \tag{1}$$

where V_{jk} are elements of the Cabibbo-Kobayashi-Maskawa (CKM) quark mixing matrix. While the charged current anomalies $R_{D^{(*)}}$ can be explained with NP contributions to the left-handed vector coefficient $C_{V_L}^{cb\tau\nu}$, the neutral current ones – especially due to the deviations in the angular observables – call upon a dedicated EFT analysis to identify which operator structure (or combination of structures) is preferred by experimental data. A subset of the low energy effective Lagrangian in $b \to s\ell\ell$ transitions can be cast as

$$\mathcal{L}_{\text{eff}} \supseteq \frac{4G_F}{\sqrt{2}} V_{3j}\, V_{3i}^* \sum_{\substack{k\,=\,7,\,9,\\ 10,\,S,\,P}} \Big(C_k(\mu)\,\mathcal{O}_k(\mu) + C_k'(\mu)\,\mathcal{O}_k'(\mu) \Big)\,, \tag{2}$$

in which the relevant operators (and their chirality-flipped counterparts) are given by

$$\begin{aligned}
\mathcal{O}_7^{ij} &= \frac{e\, m_{d_j}}{(4\pi)^2}(\bar{d}_i\, \sigma_{\mu\nu}\, P_R\, d_j)\, F^{\mu\nu}\,, \\
\mathcal{O}_9^{ij;\ell\ell'} &= \frac{e^2}{(4\pi)^2}(\bar{d}_i\, \gamma^\mu\, P_L d_j)(\bar{\ell}\gamma_\mu\, \ell')\,, \\
\mathcal{O}_{10}^{ij;\ell\ell'} &= \frac{e^2}{(4\pi)^2}(\bar{d}_i\, \gamma^\mu\, P_L\, d_j)(\bar{\ell}\gamma_\mu\, \gamma_5\, \ell')\,, \\
\mathcal{O}_S^{ij;\ell\ell'} &= \frac{e^2}{(4\pi)^2}(\bar{d}_i\, P_R\, d_j)(\bar{\ell}\,\ell')\,, \\
\mathcal{O}_P^{ij;\ell\ell'} &= \frac{e^2}{(4\pi)^2}(\bar{d}_i\, P_R\, d_j)(\bar{\ell}\gamma_5\, \ell')\,, \qquad (3)
\end{aligned}$$

where the primed operators $\mathcal{O}'_{7,9,10,S,P}$ correspond to the exchange $P_L \leftrightarrow P_R$. New Physics contributions to the coefficients $C_7^{(\prime)}$ are already strongly constrained by $b \to s\gamma$ and low-q^2 $b \to see$ data and will therefore not be considered in the following. Current measurements of the $B_s \to \mu\mu$ decay disfavour NP contributions to the coefficients $C_S^{(\prime)}$ and $C_P^{(\prime)}$ (small NP contributions to $C_{10}^{(\prime)}$ are still viable). Therefore we exclusively focus on NP contributions to the coefficients C_9 and C_{10}.

NP "scenario"	best-fit	1σ range	pull_{SM}	p-value
$\Delta C_9^{bs\mu\mu}$	-0.92	$[-1.07, -0.77]$	6.1	29.2%
$\Delta C_9^{bs\mu\mu} = -\Delta C_{10}^{bs\mu\mu}$	-0.39	$[-0.47, -0.32]$	5.5	18.3%
$\Delta C_9^{bs\mu\mu}$	-0.86	$[-1.03, -0.66]$	5.8	28.7%
$\Delta C_{10}^{bs\mu\mu}$	0.10	$[-0.02, 0.22]$		
$\Delta C_9^{bs\mu\mu} = -\Delta C_{10}^{bs\mu\mu}$	-0.33	$[-0.41, -0.25]$	6.4	41.9%
$\Delta C_9^{\text{univ.}}$	-0.86	$[-1.05, -0.66]$		

Table 2: Fits of minimal New Physics hypotheses to $b \to s\ell\ell$ data inspired by model building.

In Table 2 we display our results for several hypotheses of NP present in left-handed vector operators $\mathcal{O}_9$ and $\mathcal{O}_{10}$. Sizeable NP contributions to the coefficient $C_9^{bs\mu\mu}$ are preferred by $b \to s\ell\ell$ data, leading to an improvement over the SM predictions of $\sim 6\,\sigma$. If the underlying NP exclusively couples to $SU(2)_L$-doublets, one is led to to the relation $C_9 = -C_{10}$, replicating the $V-A$ structure of the SM. This restriction gives a reasonable fit to the data, with an improvement of $\sim 5.5\,\sigma$ over the SM (see Table 2), slightly worse than assuming NP contributions to C_9 exclusively. This stems from data on the $B_s \to \mu\mu$ decay restricting NP contributions to C_{10} to small values, while larger values for C_9 are necessary to accommodate $R_{K^{(*)}}$ and the angular observables[2].

Relaxing the condition $C_9 = -C_{10}$ leads to a slight improvement of the fit. As can be seen in the top panel of Fig. 1, there is however a slight tension between the angular data and the LFU ratios $R_{K^{(*)}}$ in this scenario.

This tension can be alleviated by considering NP coupled additionally to right-handed quark currents, which is however difficult to achieve in realistic models.[3]

[2]For more information on the statistical procedure and a complete list of observables taken into account, see Appendices A and B of Ref. [13] respectively.

[3]For example in Z' and leptoquark models right-handed couplings to quarks inevitably lead to large contributions to $B_s \to \mu\mu$ decays and $B_s - \bar{B}_s$ mixing, in conflict with current experimental data.

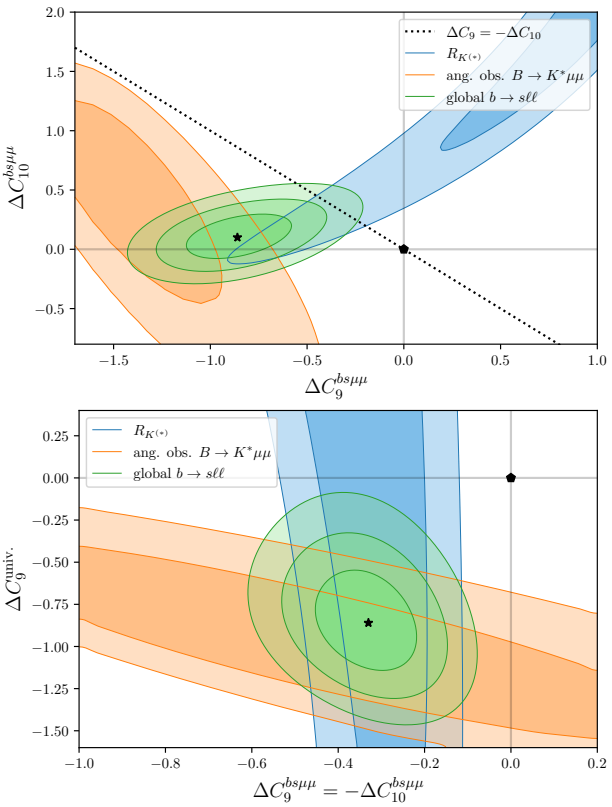

Figure 1: Results of fits to $b \to s\ell\ell$ data assuming NP coupled to left-handed quarks. The results are shown as two-dimensional likelihood contours.

A somewhat different idea, first proposed in [8], relies on introducing a lepton flavour universal contribution to C_9, in addition to $\Delta C_9^{bs\mu\mu} = -\Delta C_{10}^{bs\mu\mu}$. Thus, the relevant NP contributions to the WC are given by

$$\begin{aligned}
C_9^{bs\mu\mu\text{NP}} &= \Delta C_9^{bs\mu\mu} + \Delta C_9^{\text{univ}}\,, \\
\Delta C_{10}^{bs\mu\mu} &= -\Delta C_9^{bs\mu\mu}\,, \quad \Delta C_9^{bsee} = \Delta C_9^{\text{univ}}\,. \qquad (4)
\end{aligned}$$

As can be seen in Table 2, a fit of this scenario leads to an excellent description of the data, which is also shown in the bottom panel of Fig. 1. In principle, the universal contribution can also be envisaged in $C_9^{bs\tau\tau}$. Should this be the case, it could be mimicked by underestimated or unknown long distance charm-loop effects, a possibility that was recently studied in [9], in which a lepton flavour universal contribution to C_9 is treated as a nuisance parameter in the fit (also taking into account "look elsewhere effects").

However, a more interesting possibility is that the universal contribution arises via operator mixing due to renormalisation group evolution from a large $\Delta C_9^{bs\tau\tau}$ at the EW scale (or NP matching scale)[10]. Since tree-level matching of SMEFT preserves $SU(2)_L$, a large $\Delta C_9^{bs\tau\tau}$ at the EW scale could then be connected to the charged current $R_{D^{(*)}}$ anomalies, since $\Delta C_{9,10}^{bs\tau\tau}$ and $C_{V_L}^{cb\tau\nu}$ then depend on the same SMEFT coefficient.

In order to analyse this interesting possibility we will now consider semi-leptonic (dimension-6) SMEFT operators, focusing on the following (left-handed) operators

$$\begin{aligned}\mathcal{L}_{\text{SMEFT}} \supseteq\ & (C_1)_{\ell q}^{\alpha\beta ij}(\bar{L}_L^\alpha \gamma_\mu L_L^\beta)(\bar{Q}_L^i \gamma^\mu Q_L^j) \\ +\ & (C_3)_{\ell q}^{\alpha\beta ij}(\bar{L}_L^\alpha \gamma_\mu \tau^\alpha L_L^\beta)(\bar{Q}_L^i \gamma^\mu \tau^\alpha Q_L^j)\end{aligned} \quad (5)$$

in which Q_L and L_L respectively denote the left-handed SM quark and lepton doublets, and τ^α are the $SU(2)_L$ generators defined via the Pauli matrices as $\tau^\alpha = \sigma^\alpha/2$. Matching the SMEFT operators at tree-level onto WET [11, 12], leads to neutral and charged current WET operators, which are related by $SU(2)_L$ invariance. The matching conditions relevant for $b \to s\ell\ell$ and $b \to c\ell\nu$ transitions can be schematically written as [12] (up to the appropriate normalisations)

$$\begin{aligned} C_9^{bs\ell_\alpha\ell_\beta} = -C_{10}^{bs\ell_\alpha\ell_\beta} &\propto (C_1)_{\ell q}^{\alpha\beta 23} + (C_3)_{\ell q}^{\alpha\beta 23}\,, \\ C_{V_L}^{bc\ell_\alpha\nu_\beta} &\propto -(C_3)_{\ell q}^{\alpha\beta 23}\,. \end{aligned} \quad (6)$$

However, due to $SU(2)_L$ invariance, a sizeable contribution to $(C_1)_{\ell q}^{\alpha\beta 23}$ and $(C_3)_{\ell q}^{\alpha\beta 23}$ also leads to significant New Physics contributions in $B \to K^{(*)}\nu\bar{\nu}$. It can be shown [12] that this decay is proportional to $B \to K^{(*)}\nu\bar{\nu} \propto (C_1)_{\ell q} - (C_3)_{\ell q}$, and so we impose the condition $(C_1)_{\ell q} = (C_3)_{\ell q}$ to evade this constraint. A large LFU contribution to $C_9^{bs\ell\ell}$ is then generated via RGE above and below the EW scale by having a contribution in $(C_1)_{\ell q}^{3323} = (C_3)_{\ell q}^{3323}$, leading to a large $C_9^{bs\tau\tau}$ (below the EW scale), in addition to $C_{V_L}^{bc\tau\nu}$, which is necessary to accommodate the $b \to c\tau\nu$ data.

Motivated by the reach of LHC, we set a moderate matching scale at 2 TeV and carry out a fit combining $b \to c\ell\nu$ and $b \to s\ell\ell$ data (see Appendix B of [13]). We obtain a best fit point given by

$$\begin{aligned} (C_1)_{\ell q}^{2223} &= (C_3)_{\ell q}^{2223} = (3.0^{+0.7}_{-0.6}) \times 10^{-4}\ \text{TeV}^{-2}\,, \\ (C_1)_{\ell q}^{3323} &= (C_3)_{\ell q}^{3323} = -0.059 \pm 0.01\ \text{TeV}^{-2}\,, \end{aligned} \quad (7)$$

amounting to a pull of $7.4\,\sigma$ with respect to the SM prediction, and a p-value of 59.4%. Interestingly, as can be seen in Fig. 2, the agreement between the different observables is excellent. Should the B-meson decay anomalies be a low-energy manifestation of NP, this can be interpreted as a hint that both the charged and neutral current anomalies could be accommodated in a model with a single mediator that preserves $SU(2)_L$, and thus be taken as a guide for model building.

Despite the large number of model-building alternatives, only a few select scenarios can successfully put forward a simultaneous explanation for both charged and neutral current B-meson decay anomalies. Standard Model extensions relying on a V_1 vector leptoquark transforming as $(\mathbf{3}, \mathbf{1}, 2/3)$ under the SM gauge group have received considerable attention in the literature, being currently the only single-leptoquark solution capable of simultaneously addressing both charged and neutral current anomalies; at tree-level, V_1 generates $(C_1)_{\ell q} = (C_3)_{\ell q}$ and such constructions can be realised at sufficiently low scales.

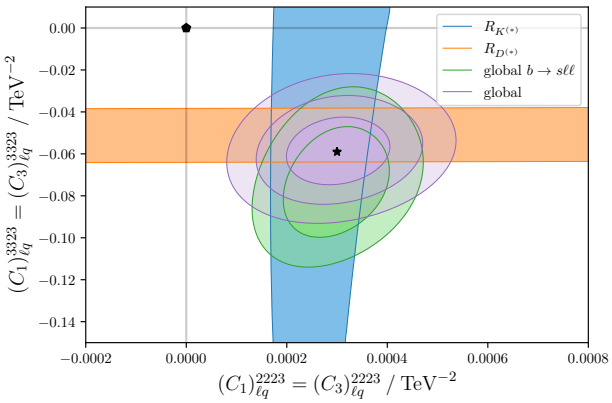

Figure 2: Results of a fit of SMEFT Wilson coefficients to $b \to s\ell\ell$ and $b \to c\tau\nu$ data assuming a minimal realistic New Physics hypothesis.

Vector leptoquarks

Gauge vector LQs, such as V_1, naturally arise in (grand) unified theories, specifically from quark-lepton unification, as it occurs in Pati-Salam models. In our study of Ref. [14], and instead of exploring a specific UV completion for V_1 leptoquarks, we chose to find requirements on the couplings of V_1 to the SM fermions in an effective way. The subset of the relevant (left-handed [4]) LQ couplings to SM fermions can be parametrised as

$$\mathcal{L} \simeq \sum_{i,j,k,l=1}^{3} V_1^\mu \left(\bar{d}_L^i \gamma_\mu K_L^{ik} \ell_L^k + \bar{u}_L^j V_{ji}^\dagger \gamma_\mu K_L^{ik} U_{kl}^P \nu_L^l \right) + \text{H.c.}\,,$$

where K_L^{ij} denote the effective LQ couplings and U^P is the Pontecorvo-Maki-Nakagawa-Sakata (PMNS) leptonic mixing matrix. The matching of the LQ couplings (at the LQ mass scale, $m_{V_1} \simeq 1.5\,\text{TeV}$) to the WCs singled out by the EFT analysis can be done as follows:

$$\begin{aligned} C_{9,10}^{ij;\ell\ell'} &= \mp \frac{\pi}{\sqrt{2} G_F\, \alpha_{\text{em}}\, V_{3j}\, V_{3i}^*\, m_{V_1}^2} \left(K_L^{i\ell'}\ K_L^{j\ell *} \right)\,, \\ C_{jk,\ell i}^{V_L} &= \frac{\sqrt{2}}{4\, G_F\, m_{V_1}^2} \frac{1}{V_{jk}} \left(V\, K_L\, U^P \right)_{ji} K_L^{k\ell *}\,. \end{aligned} \quad (8)$$

Sizeable V_1 couplings of second- and third-generation quarks to different lepton flavours can lead to strongly enhanced rates in lepton flavour violating (LFV) processes, such as $B \to K\tau\mu$, which put stringent constraints on the model's parameter space. As shown in our analysis in [14], in order to evade those bounds, effectively non-unitary couplings to the SM fermions are necessary (achieved by considering mixings of vector-like leptons to SM leptons).

In a second analysis we have taken the 9 left-handed LQ couplings as independent parameters and we have

[4] Due to the absence of strong hints suggesting non-vanishing right-handed contributions to the WET operators, we restrict the LQ couplings to be left-handed.

fit them to more than 350 observables (for a complete list see [13]), for three mass benchmark points of $m_{V_1} \in [1.5, 2.5, 3.5]$ TeV; this allows finding a region in the 9-dimensional parameter space in which the B-anomalies can be explained while evading cLFV constraints [13]. We then sampled the global likelihood in terms of the LQ couplings using Markov-Chain Monte-Carlo techniques (see [13] for details). From the Monte-Carlo samples we have then computed posterior ranges for the observables around the best fit point(s), based on the currently preferred parameter space.

Several rare B-decays involving tau-leptons and numerous LFV tau-decays are expected to be searched for by the Belle II experiment [15] with improved sensitivities. Due to sizeable couplings of the LQ to b, s- and c-quarks, and to charged leptons, a priori we expect sizeable enhancements of $b \to s\tau^+\tau^-$ and LFV processes. In Fig. 3 we show the 1σ ranges of the posterior

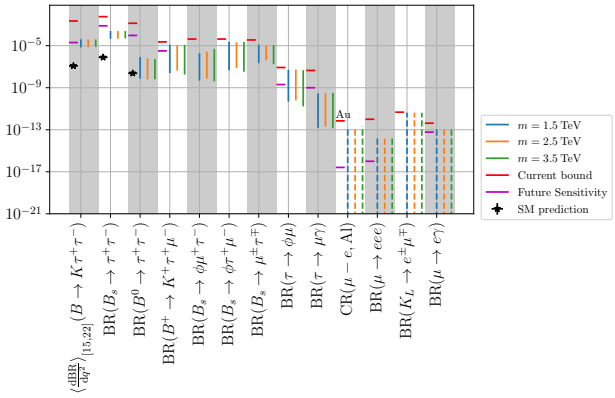

Figure 3: Posterior ranges of the vector LQ predictions for several observables searched for by Belle II, COMET and Mu2e. Figure taken from Ref. [13].

distributions for several such observables, together with current experimental limits and future sensitivities. In particular, $B \to K\tau\mu$ and $\tau \to \phi\mu$ decays are promising channels at Belle II. Additionally, the predicted range of neutrinoless $\mu - e$ in Aluminium will be (almost) fully probed by COMET and Mu2e [16, 17].

The results of this analysis are by no means a guarantee to discover LFV signals in those channels. Thus, we have studied the impact of *null* results in LFV channels at Belle II, Mu2e and COMET - thus replacing current LFV bounds with future sensitivities in our fit. Results of such a hypothetical future fit are presented in Fig. 4, where we show predictions of the LQ model for $R_{D^{(*)}}$ based on current and future LFV limits. Moreover, we have extrapolated the current measurement of $R_{D^{(*)}}$ by Belle to Belle II's anticipated accuracy with $50\,\mathrm{ab}^{-1}$ integrated luminosity, and combined it with all other measurements available, denoted via the green and purple (dashed) ellipses [13]. Curiously, in the absence of LFV signals the LQ expected best fit point (in orange) overlaps with the $1\,\sigma$ contour of the extrapolated Belle II sensitivity, although moving closer to the SM prediction. On the other hand, should future measurements coincide with the central value of the current global av-

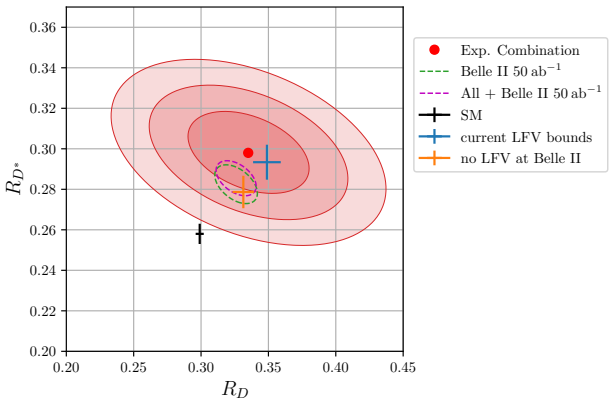

Figure 4: Posterior ranges for LQ predictions for $R_{D^{(*)}}$ based on current (future) limits on LFV processes relevant for the test of the vector LQ hypothesis presented in blue (orange). The predictions for different masses coincide. Also shown are the extrapolations of the current Belle measurement to the sensitivity of Belle II (dashed contourlines). Figure taken from Ref. [13].

erage (with improved accuracy), a V_1-LQ explanation of the $R_{D^{(*)}}$ anomalies would be in conflict with future bounds on LFV processes (again in the absence of any LFV discovery at Belle II). Thus, the evolution of future measurements of $R_{D^{(*)}}$ will prove instrumental in falsifying the vector LQ hypothesis.

Conclusions and outlook

Numerous hints for the presence of LFU violation in charged and neutral current semi-leptonic B-meson decays have recently emerged in association with several observables. Current EFT analyses appear to favour minimal models that can simultaneously address both tensions, due to a preference of *universal* contributions to $C_9^{bs\ell\ell}$ at the b-quark mass scale. This interpretation is further strengthened by the very recently updated measurement of R_K. Following the recent LHCb measurement [7], we have updated fits of several NP hypotheses leading to a good agreement with the data.

In view of the absence of tree-level couplings between down-type quarks and neutrinos, $SU(2)_L$-singlet vector LQs are excellent candidates for a combined explanation of the B-meson decay anomalies, although subject to stringent constraints from LFV observables. We have shown that a non-unitary flavour structure of the LQ couplings to SM matter is necessary in order to comply with numerous bounds from flavour observables, which have been measured to be in good agreement with the SM; such a structure can be generated via mixings of SM leptons with heavy vector-like doublet states. We have further explored the flavour phenomenology of this simple vector LQ model, carrying a dedicated statistical analysis; this allowed identifying several "*golden modes*" that have excellent chances to be observed by upcoming experiments in the near future. Finally, we highlighted the importance of future

$R_{D^{(*)}}$ measurements for the model's viability.

References

[1] P. A. Zyla *et al.* [Particle Data Group], PTEP **2020** (2020) no.8, 083C01

[2] G. Caria *et al.* [Belle], Phys. Rev. Lett. **124** (2020) no.16, 161803 [arXiv:1910.05864 [hep-ex]].

[3] R. Aaij *et al.* [LHCb], Phys. Rev. Lett. **122** (2019) no.19, 191801 [arXiv:1903.09252 [hep-ex]].

[4] R. Aaij *et al.* [LHCb], JHEP **08** (2017), 055 [arXiv:1705.05802 [hep-ex]].

[5] R. Aaij *et al.* [LHCb], Phys. Rev. Lett. **125** (2020) no.1, 011802 [arXiv:2003.04831 [hep-ex]].

[6] R. Aaij *et al.* [LHCb], Phys. Rev. Lett. **126** (2021) no.16, 161802 [arXiv:2012.13241 [hep-ex]].

[7] R. Aaij *et al.* [LHCb], "Test of lepton universality in beauty-quark decays," arXiv:2103.11769 [hep-ex].

[8] M. Algueró, B. Capdevila, S. Descotes-Genon, P. Masjuan and J. Matias, Phys. Rev. D **99** (2019) no.7, 075017 [arXiv:1809.08447 [hep-ph]].

[9] G. Isidori, D. Lancierini, P. Owen and N. Serra, Phys. Lett. B **822** (2021), 136644 [arXiv:2104.05631 [hep-ph]].

[10] A. Crivellin, C. Greub, D. Müller and F. Saturnino, Phys. Rev. Lett. **122** (2019) no.1, 011805 [arXiv:1807.02068 [hep-ph]].

[11] G. D'Ambrosio, G. F. Giudice, G. Isidori and A. Strumia, Nucl. Phys. B **645** (2002), 155-187 [arXiv:hep-ph/0207036 [hep-ph]].

[12] F. Feruglio, P. Paradisi and A. Pattori, JHEP **09** (2017), 061 [arXiv:1705.00929 [hep-ph]].

[13] C. Hati, J. Kriewald, J. Orloff and A. M. Teixeira, Eur. Phys. J. C **81** (2021) no.12, 1066 [arXiv:2012.05883 [hep-ph]].

[14] C. Hati, J. Kriewald, J. Orloff and A. M. Teixeira, JHEP **12** (2019), 006 [arXiv:1907.05511 [hep-ph]].

[15] E. Kou *et al.* [Belle-II], PTEP **2019** (2019) no.12, 123C01 [erratum: PTEP **2020** (2020) no.2, 029201] [arXiv:1808.10567 [hep-ex]].

[16] R. Abramishvili *et al.* [COMET], PTEP **2020** (2020) no.3, 033C01 [arXiv:1812.09018 [physics.ins-det]].

[17] L. Bartoszek *et al.* [Mu2e], "Mu2e Technical Design Report," arXiv:1501.05241 [physics.ins-det].

New Physics Scenarios in the Non Minimal Flavour Violating MSSM

Mohamed Amine BOUSSERJA

Université de Lyon, Université Claude Bernard Lyon 1, CNRS/IN2P3, Institut de Physique des Deux Infinis de Lyon, France

Abstract — Persistent tensions between experimental measurements and the SM predictions in $b \to s\ell^+\ell^-$ transitions are one of the most promising venues for New Physics searches. We present a study of non-minimal flavour violating MSSM scenarios contributing to the relevant Wilson coefficients to address the observed flavor anomalies using the Mass Insertion Approximation and the public code `SuperIso`. We show that after imposing theoretical constraints on the flavour violating parameters we can find scenarios in agreement with the experimental measurements.

Introduction

Tensions between the Standard Model (SM) and the experimental predictions in the $b \to sl^+l^-$ transitions have kept on increasing. A series of measurements have shown $2-3\sigma$ disagreements with the SM predictions, which started with the angular observables (in particular P_5') in the $B^0 \to K^{*0}\mu^+\mu^-$ decay (see e.g. [1]), followed by the measurement of ratios testing lepton flavour universality [2, 3, 4]. The LHCb collaboration has also recently measured the $B^+ \to K^{*+}\mu^+\mu^-$ angular observables using the full data coming from the Runs 1 & 2 corresponding to an integrated luminosity of 9 fb^{-1} [5] which confirms the previously observed tensions in the similar neutral decay modes. Model independent global fits to all available $b \to s\ell\ell$ data seem to consistently indicate New Physics (NP) compatible with a single negative shift in C_9 from its SM value by about 25% (see e.g. [6, 7, 8, 9]).

In this context of strong and persisting flavour anomalies, one promising NP model is the Minimal Supersymmetric Standard Model (MSSM). Until the recent development of computational capabilities, the full 105-dimensional MSSM parameter space was hardly explored. Instead, practical simplifications were made for instance by taking most of the parameters to be zero or assuming the so-called Minimal Flavour Violation (MFV) hypothesis. These approximations of the (R-parity conserving) MSSM have not proven to be enough to explain the B anomalies so far. Moreover, no signal predicted by such models as the constrained MSSM (cMSSM, 5 free parameters), or the phenomenological MSSM (pMSSM, 19 free parameters) has been detected so far at $\sqrt{s} = 13$ TeV at the LHC, or elsewhere. In this study we present a more general approach to $b \to sll$ transitions, by looking at the impact of the phenomenological MSSM (pMSSM, 19 free parameters) with Non Minimal Flavor Violation (NMFV) [10] through the Mass Insertion Approximation (MIA) approach [11]. We then discuss the obtained contributions, and compare them to the pMSSM.

Theoretical Context

In the search for NP models, one relevant approach is Effective Field Theory, which allows to define an effective Hamiltonian describing the underlying process by current operators and encapsulating higher scale NP effects in the so-called Wilson coefficients. The fits to these Wilson coefficients are an efficient approach to test BSM models against experimental measurements. The effective Hamiltonian for the decay $B \to X_s\ell^+\ell^-$ in the SM and in the MSSM is given by (in the basis of Ref. [12]):

$$\mathcal{H}_{\text{eff}} = -\frac{4G_F}{\sqrt{2}} V_{ts}^* V_{tb} \sum_{i=1}^{10} C_i(\mu) O_i \ , \qquad (1)$$

where G_F is the Fermi constant, V_{ts}, V_{tb} are CKM elements, and α_s is the strong coupling constant evaluated at the Z mass.
The relevant operators for $b \to s\gamma$ and $b \to s\ell\ell$ transitions are:

$$O_7 = \frac{e}{16\pi^2} m_b \bar{s}_L \sigma^{\mu\nu} b_R F_{\mu\nu} \ ,$$
$$O_9 = \frac{e^2}{(4\pi)^2} (\bar{s}_L \gamma_\mu b_L) \bar{l} \gamma^\mu l \ ,$$
$$O_{10} = \frac{e^2}{(4\pi)^2} (\bar{s}_L \gamma_\mu b_L) \bar{l} \gamma^\mu \gamma_5 l \ .$$

The global best-fit to the associated Wilson coefficients C_7, C_9, and C_{10} can be found in e.g. [7] and corresponds roughly to $\delta C_9 \sim -1$ and $\delta C_7 \sim 0$.

The pMSSM is known to be unable to shift C_9 by a sufficient amount without violating the constraints on C_7 coming from $b \to s\gamma$ [13]. Relaxing the MFV hypothesis allows for substantial new flavour changing neutral currents processes (see e.g. Figure 1) that can significantly increase the 1-loop supersymmetric contributions to C_9.

To express the new contributions, we make use of the MIA, which provides a simple way of expressing all relevant quantities [14] (amplitudes, Wilson coefficients, etc.) in term of the flavour violating off-diagonal entries of the squark soft-breaking masses. The main advantage is to allow for a study of flavour violating quantities directly at the Lagrangian level, and evades the reconstruction of flavour effects after the final sparticle spectrum mixing.

In particular for the relevant processes, the FCNC are allowed by the flavour violating entries in the squark squared mass matrices. For example for the $\tilde{u}$-sector (following the notation from [15]):

$$\mathcal{M}^2_{\tilde{\boldsymbol{d}}} = \begin{pmatrix} M^2_{\tilde{Q}} + m^2_d + D_{\tilde{d},L} & \frac{v_d}{\sqrt{2}} T^\dagger_d - m_d \mu \tan\beta \\ \frac{v_d}{\sqrt{2}} T_d - m_d \mu^* \tan\beta & M^2_{\tilde{D}} + m^2_d + D_{\tilde{d},R} \end{pmatrix}, \tag{2}$$

and similarly for the down squarks. In our study, we follow the convention in [11, 16] and define the relevant dimensionless Mass Insertions (MI) as:

$$\delta^{\tilde{f}}_{ij} \equiv \frac{(\Delta^{\tilde{f}}_{ij})_{AB}}{M_{sq}} , \tag{3}$$

where $(\Delta^{\tilde{f}}_{ij})_{AB}$ is an off-diagonal element of the $\tilde{f} = \tilde{u}, \tilde{d}$ squark squared mass matrix, while the indices $(i, j) \in \{2, 3\}$ span generation space, $(A, B) \in \{L, R\}$ are chirality indices, and M_{sq} is the average squark mass.

The MI parameters can then be considered as additional free parameters of the model. They can be constrained a posteriori and a comprehensive discussion of their experimentally allowed ranges can be found in [17]. In our case, we keep $\left\|\delta^{\tilde{f}}_{AB}\right\| < 0.85$ to avoid scenarios with tachyonic spectra, and impose the constraints from vacuum stability [16], i.e.:

$$\|(\delta^u_{23})_{LR}\| < m_t \frac{\sqrt{2M^2_{sq} + 2M^2_{sl}}}{M^2_{sq}} , \tag{4}$$

where m_t is the top quark mass, and M_{sl} is the average slepton mass.

Finally, let us say that no particular limits on the sparticle masses are considered, apart from the model independent ones in [18].

Results

We perform a uniform sampling of all the 19 parameters of the pMSSM and the 9 additional MI parameters from the ranges in Table 1 and Table 2 respectively. We compute the associated pMSSM spectrum using `Softsusy` [19] and the Wilson coefficients are obtained using `SuperIso` [12]. The MI NMFV contributions are computed from the formulae in [16, 20]. The results for the total Wilson coefficients are then run down to the m_b scale. For comparison purposes, we also compute the pMSSM Wilson coefficients for the same points by turning off the MI parameters.

Parameter	Range
M_1	$[50, 5000]$
M_2	$[50, 5000]$
M_3	$[50, 5000]$
m_A	$[50, 5000]$
$\tan\beta$	$[2, 60]$
μ	$[-10^4, 10^4]$
A_t, A_b, A_τ	$[-10^4, 10^4]$
$M_{\tilde{q}_{1L}}, M_{\tilde{q}_{3L}}$	[50,5000]
$M_{\tilde{u}_R}, M_{\tilde{d}_R}, M_{\tilde{t}_R}, M_{\tilde{b}_R}$	[50,5000]
$M_{\tilde{e}_L}, M_{\tilde{\tau}_L}, M_{\tilde{e}_R}, M_{\tilde{\tau}_R}$	[50, 5000]

Table 1: Allowed ranges for the 19 pMSSM soft-breaking parameters.

Parameter	Range
$(\delta^{\tilde{u}}_{23})_{LR}$	[-1,1]
$(\delta^{\tilde{u}}_{23})_{LL}$	[-1,1]
$(\delta^{\tilde{u}}_{33})_{LR}$	[-1,1]
$(\delta^{\tilde{d}}_{23})_{LL}$	[-1,1]
$(\delta^{\tilde{d}}_{23})_{RR}$	[-1,1]
$(\delta^{\tilde{d}}_{23})_{RL}$	[-1,1]
$(\delta^{\tilde{d}}_{23})_{LR}$	[-1,1]
$(\delta^{\tilde{d}}_{33})_{RL}$	[-1,1]
$(\delta^{\tilde{d}}_{33})_{LR}$	[-1,1]

Table 2: Additional NMFV input parameters in the MIA.

In Figure 2, the results in term of $C_9(\mu_b)$ and $C_7(\mu_b)$ for about 2 million model points are shown. We can see an **oyster**-shaped spread of the pMSSM distribution upon turning on the NMFV contributions in the (C_9, C_7) plane. The largest contribution to C_9 can be obtained by shifting C_7 significantly from its SM value, which is strongly constrained by the $b \to s\gamma$ data. However, it is clear from the impressive spread that the flavour anomalies can be given a satisfying answer using this framework, whilst still having reasonable values for C_7.

In Figure 3, a zoom in the region of interest in the $(\delta C_9, \delta C_7)$ plane is presented, together with the global best fit patches from [7], after imposing constraints for vacuum stability and tachyonic spectra. δC_i is defined as : $C_i^{\text{NMFV}} - C_i^{\text{SM}}$. The pMSSM distribution is shown in red, and the corresponding NMFV points are shown in blue. Imposing the constraints leaves 1 721 remaining points. We can see that even if the highest density of model points can be found away from the C_7 best fit region, the presented NMFV model succeeds in

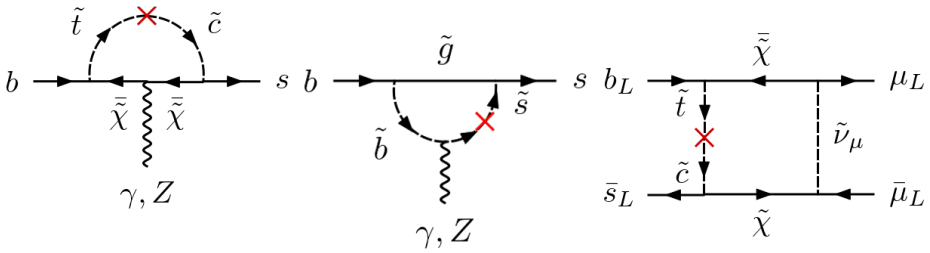

Figure 1: Examples of additional diagrams within the Mass Insertion Approximation to the NMFV MSSM. The red cross indicates a Mass Insertion and therefore a flavor change.

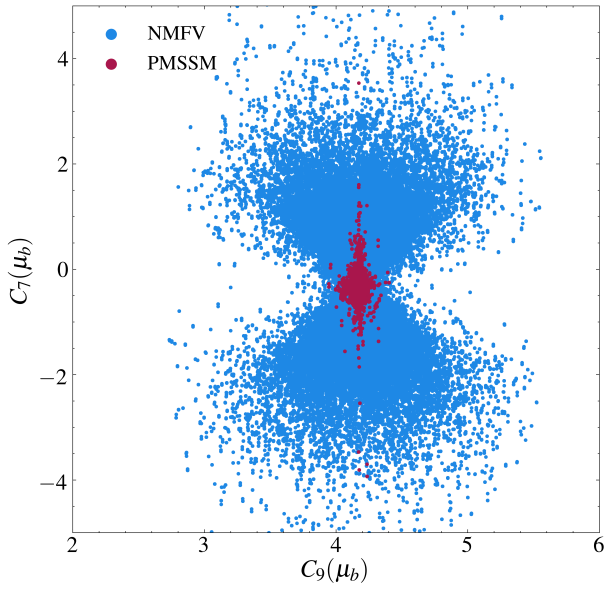

Figure 2: Distributions of sampled points in the (C_9, C_7) plane. The NMFV model points are shown in blue and the pMSSM ones in red.

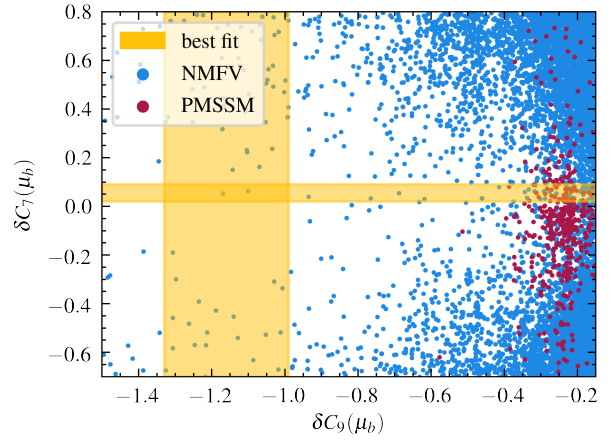

Figure 3: Distribution of the scanned model points it the $(\delta C_9, \delta C_7)$ plane. The orange bands represents the 1σ best fit region from [7].

proposing valid scenarios. In particular, several points seem to completely account for the flavour anomalies in the B sector, but further exploration of the full model spectrum is necessary.

The lightest electroweakinos mass distribution with the corresponding C_9 value is shown in Figure 4. The vast majority of the surviving points are in compressed spectra scenarios, i.e. the masses of the lightest neutralino (Dark Matter candidate) and chargino are extremely degenerate, allowing them to evade most direct search results. On the other hand, some model points can drive up the mass of lightest chargino well-in the TeV scale, which can also be challenging to exclude from direct searches.

Finally, all the previous results should be considered with particular care, as the recast of LHC limits for general MSSM models is a non trivial task [21, 22, 23], which goes beyond the scope of this study.

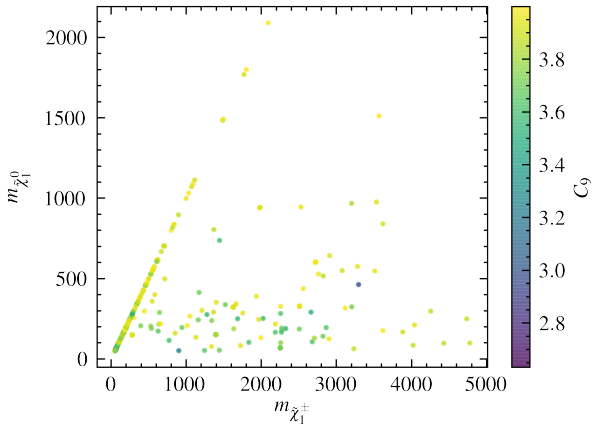

Figure 4: Distribution of the sampled points in the $(m_{\chi_1^\pm}, m_{\chi_1^0})$ plane, keeping only the points that significantly shift C_9 and satisfy tachyonic and vacuum stability constraints .

Conclusions

We presented an overview of the effect of NMFV scenarios on the pMSSM contributions to the relevant Wilson coefficients for the $b \to sll$ anomalies. The NMFV allows to shift the C_9 coefficient enough to fully explain the anomalies. Imposing theoretical constraints on the flavour violating parameters leaves compatible benchmark scenarios to further explore, in particular with respect to collider searches. This shows the interest of

NMFV models with respect to more constrained models such as the cMSSM and the pMSSM in the context of flavor anomalies. Finally, we refer the interested reader to our recent complete study of NMFV models [24].

References

[1] R. Aaij *et al.* [LHCb], JHEP **02** (2016), 104 [arXiv:1512.04442];

[2] R. Aaij *et al.* [LHCb], JHEP **08** (2017), 055 [arXiv:1705.05802].

[3] R. Aaij *et al.* [LHCb], [arXiv:2103.11769].

[4] R. Aaij *et al.* [LHCb], [arXiv:2110.09501].

[5] R. Aaij *et al.* [LHCb], Phys. Rev. Lett. **126** (2021) no.16, 161802 [arXiv:2012.13241].

R. Aaij *et al.* [LHCb], Phys. Rev. Lett. **125** (2020) no.1, 011802 [arXiv:2003.04831].

[6] M. Algueró, B. Capdevila, S. Descotes-Genon, J. Matias and M. Novoa-Brunet, [arXiv:2104.08921].

[7] T. Hurth, F. Mahmoudi, D. M. Santos and S. Neshatpour, [arXiv:2104.10058]; T. Hurth, F. Mahmoudi and S. Neshatpour, Phys. Rev. D **103** (2021), 095020 [arXiv:2012.12207].

[8] L. S. Geng, B. Grinstein, S. Jäger, S. Y. Li, J. Martin Camalich and R. X. Shi, Phys. Rev. D **104** (2021) no.3, 035029 [arXiv:2103.12738].

[9] J. Bhom, M. Chrzaszcz, F. Mahmoudi, M. T. Prim, P. Scott and M. White, [arXiv:2006.03489].

[10] Hall, L., Kostelecky, V. & Raby, *Nucl. Phys. B.* **267** pp. 415-432 (1986)

[11] E. Gabrielli, A. Masiero and L. Silvestrini, Phys. Lett. B **374** (1996), 80-86 [hep-ph/9509379].

[12] F. Mahmoudi, Comput. Phys. Commun. **178** (2008), 745-754 [arXiv:0710.2067]; Comput. Phys. Commun. **180** (2009), 1579-1613 [arXiv:0808.3144]; Comput. Phys. Commun. **180** (2009), 1718-1719; S. Neshatpour and F. Mahmoudi, [arXiv:2105.03428].

[13] F. Mahmoudi, S. Neshatpour and J. Virto, Eur. Phys. J. C **74** (2014) no.6, 2927 [arXiv:1401.2145].

[14] A. Dedes, M. Paraskevas, J. Rosiek, K. Suxho and K. Tamvakis, JHEP **06** (2015), 151 [arXiv:1504.00960].

[15] B. C. Allanach, C. Balazs, G. Belanger, M. Bernhardt, F. Boudjema, D. Choudhury, K. Desch, U. Ellwanger, P. Gambino and R. Godbole, *et al.* Comput. Phys. Commun. **180** (2009), 8-25.

[16] E. Lunghi, A. Masiero, I. Scimemi and L. Silvestrini, Nucl. Phys. B **568** (2000), 120-144.

[17] K. De Causmaecker, B. Fuks, B. Herrmann, F. Mahmoudi, B. O'Leary, W. Porod, S. Sekmen and N. Strobbe, JHEP **11** (2015), 125 [arXiv:1509.05414].

[18] Zyla, P. & Others Review of Particle Physics. *PTEP.* **2020**, 083C01 (2020)

[19] B. C. Allanach, Comput. Phys. Commun. **143** (2002), 305-331 [hep-ph/0104145].

[20] A. Behring, C. Gross, G. Hiller and S. Schacht, JHEP **08** (2012), 152. [arXiv:1205.1500].

[21] Bernigaud, J. & Herrmann, B. *SciPost Phys.*. **6**, 066 (2019) [arXiv:1809.04370]

[22] A. Chakraborty, M. Endo, B. Fuks, B. Herrmann, M. M. Nojiri, P. Pani and G. Polesello, Eur. Phys. J. C **78** (2018) no.10, 844 [arXiv:1808.07488].

[23] Alguero, G., Heisig, J., Khosa, C., Kraml, S., Kulkarni, S., Lessa, A., Reyes-GonzÃ¡lez, H., Waltenberger, W. & Wongel, A. (2021,12) [arXiv:2112.00769].

[24] Boussejra, M.A., Mahmoudi, F. & Uhlrich, G. (2022,1) [arXiv:2201.04659]

Computation of relic densities within freeze-out mechanism

Marco PALMIOTTO

Université de Lyon, Université Claude Bernard Lyon 1, CNRS/IN2P3,
Institut de Physique des Deux Infinis de Lyon, France

Abstract — Since decades, our knowledge of fundamental physics is being challenged by astrophysical and cosmological observations, thus leading us to the hypothesis of the existence of the so-called *dark matter*. In the frameworks in which dark matter is made of one or more stable particles not yet detected by particle physics experiments, a crucial aspect is the computation of its relic density. We present ongoing work to add features to the software `SuperIso Relic`, in order to study the evolution of the density of particles in new physics models and allow the computation of the evolution of the number density of more than one species.

Definition of relics

According to the ΛCDM model, the Universe has always been in an expansion phase. In the past all matter species were in thermal equilibrium as a consequence of large temperature and reduced distances. As long as the Universe expands, distances become larger and temperature decreases. This leads less interacting species to go out of equilibrium sooner than the more interacting ones. In what follows, we will refer to FLRW metric as the Friedmann-Lemaître-Robertson-Walker metric, that describes the universe in the ΛCDM model.

As an example, let us consider a stable particle X of mass m_X. Typically, X is in thermal equilibrium[1] with its anti-particle $\bar{X}$ and with the rest of the thermal bath as long as the temperature of the Universe T is greater than m_X. Moreover, being X stable, the annihilation reactions are the only ways through which its number density n_X can change. If X remains in equilibrium all the time, then its number density will eventually become negligible. Indeed, since X is in thermal equilibrium, its number density must scale with the thermal bath temperature as

$$n_X \sim (m_X/T)^{3/2} \exp(-m_X/T) \to 0 for T \to 0.$$

We call this behaviour *Boltzmann suppression*.

Therefore, if we have a New Physics model with a stable particle, it could be a candidate for dark matter only if it decouples from the other species for some temperature. Then its temperature, and its number density accordingly, evolve in a different way. We call this particle a *relic*.

[1] We define *kinematical equilibrium* as the situation in which a particle's number density follows the Maxwell-Boltzmann distribution. The *thermal equilibrium* is achieved when a particle in kinematical equilibrium has the same temperature of the thermal bath.

The Boltzmann equation

The *Boltzmann equation* is the equation that governs the evolution of the number density n of a particle X. In this section we will show how such equation is derived and how its solutions behave. To have more details about the Boltzmann equation and its derivation, see refs [1] and [2].

Let us call f the distribution function of X, thus the number of particle per unit of volume $n(t)$ that occupy a volume of phase space $(x + [3]x, p + [3]p)$ at time t can be written as

$$n(t) = f(t, x, p)[3]x[3]p.$$

Therefore, we can start from an equation for f in order to obtain n. The Boltzmann equation is

$$L[f] = C[f]$$

where $L[f]$ is the *Liouville operator* and the $C[f]$ is the *collisional operator*. The former is nothing but the total time derivative of f:

$$L[f] \equiv ft = x^\alpha tfx^\alpha + p^\alpha tfp^\alpha,$$

and it is completely determined by the FLRW metric and the assumption that f depends only on the energy $f = f(E, t)$.[2] The latter is the number of particles per phase space volume which is lost or gained per unit of time under collisions with other particles. In order to compute it, several assumptions are made:

- The species follow the Maxwell-Boltzmann distribution
- The initial chemical potential of the species under consideration is negligible.

[2] This ansatz is true for sure if we consider species in thermal equilibrium. In any case, stronger assumptions have to be made in order to write $C[f]$ in a suitable form, as we will see soon.

- Only reactions of the kind $1,2 \to 3,4$ are relevant, with X being particle 1, 2 being a new physics particle, and 3,4 being Standard Model particles
- After decoupling, the species under consideration remains in kinematical equilibrium.

After some manipulations, the Boltzmann equation reads

$$\frac{x}{Y_{\rm eq}} Y x = -\frac{\Gamma_{\rm eq}}{H}\left[\left(\frac{Y}{Y_{\rm eq}}\right)^2 - 1\right] \qquad (1)$$

where $x = m/T$ is an adimensional parameter that measures time, $Y = n/s$ is a "comoving density"[3], H is the Hubble parameter, and

$$\Gamma_{\rm eq} = n_{\rm eq}\langle\sigma v\rangle$$

is the interaction rate. We have used $n_{\rm eq}$ the number density of X at thermal equilibrium, while $\langle\sigma v\rangle$ is the average value of the products $\sigma(1,2 \to 3,4)v_{12}$, where σ is the total cross section and v_{12} is the relative velocity of the initial particles. Altogether, $\Gamma_{\rm eq}$ is the interaction rate of X with any other NP particle leading to their annihilation into SM particles. The behaviour of a solution of the equation (1) can be easily obtained by looking at the ratio $\Gamma_{\rm eq}/H$. When $\Gamma_{\rm eq}/H \gg 1$, i.e. if the particles interact faster than the Universe expands, the variation of Y is such that, at some point, Y is brought very close to the equilibrium value $Y_{\rm eq}$. On the other hand, if $\Gamma_{\rm eq}/H \ll 1$ then the right hand side of (1) is close to 0 and Y remains constant. As long as the temperature decreases, there is a moment x_F in which $\Gamma_{\rm eq}(x_F) = H(x_F)$ and we can consider the species decoupled and the Y constant.[4] We call this moment the *freeze out*. In figure 1 we show the typical behaviour of a solution of (1) computed numerically. The solid line is $Y_{\rm eq}$, and the dashed line in Y. Solving with an initial condition $Y(x_0) = Y_0 \approx Y_{\rm eq}$ we have that the two curves are superposed until the freeze-out. Then $Y_{\rm eq}$ becomes negligible due to the Boltzmann suppression and Y is roughly constant. The moment x_F where the freeze out happens is shifted later and later in time the more $\langle\sigma v\rangle$ increases, i.e. the more the species interacts.

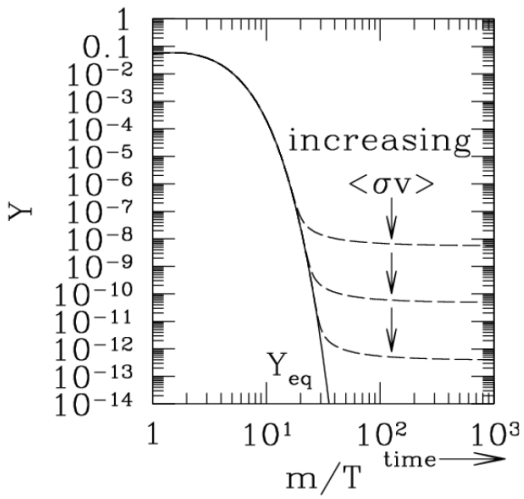

Figure 1: General behaviour of the solutions of (1) (source [3]).

Present and future of `SuperIso Relic`

In this section we will briefly mention some of the features of `SuperIso Relic` relevant to the computation of relic densities. More details can be found in refs [4] and [5]. In `SuperIso Relic`, a more general form of (1) is implemented, in order to have the following features:

- Choosing a model among the MSSM and the NMSSM
- Following the evolution of the density of the lightest supersymmetric particle (LSP)
- Considering non-thermal production of dark matter, i.e. production of dark matter particles outside of thermal equilibrium
- Considering entropy injection, i.e. fluctuations of the entropy density due to unknown properties of the early universe
- Considering variable dark energy, i.e. a cosmological constant Λ that varies in time.

Let us briefly comment these features. Concerning the choice of the model, we recall that in supersymmetric theories proton decay is in principle possible, unless a fine tuning of the parameter is made, or unless a symmetry called R-parity is imposed. Most supersymmetric models, including the MSSM and the NMSSM, posses the R-parity. This symmetry is defined as a multiplicative quantum number, conserved in all reactions, equal to $+1$ for Standard Model particles, and to -1 for new physics particles. In this way a Standard Model particle cannot decay into a supersymmetric particle and vice versa. The consequence is that the LSP is stable, and, if electrically neutral, is a candidate for dark matter. It is our goal to overcome this restriction to only two NP models and allow the computations in user-defined models.

For the second feature, since the LSP is stable, equation (1) is implemented in a way that Y contains the sum of all the number densities of all the supersymmetric species. This allows simplifications in the collisional term and thus in the computation of $\langle\sigma v\rangle$. It can be useful, however, to follow the evolution of the species separately. In fact, having direct information on when one or more specific species decouples, can give us relevant information to better explore the parameter space of the model under consideration, such

[3] We recall that for a massive particle the density scales as the third inverse power of the scale factor a^{-3}, same as the entropy density s.

[4] We would like to point out that the behaviour of H is $H \propto \sqrt{g_{\rm eff}(T)}T^4$, where $g_{\rm eff}(T)$ is the number of effective degrees of freedom at the temperature T. Moreover $\Gamma_{\rm eq}$ scales with a power of the tempertature: $\Gamma_{\rm eq} \propto \sigma \propto T^n$. So the equation $\Gamma_{\rm eq}(x_F) = H(x_F)$ admits (most of the times) a solution.

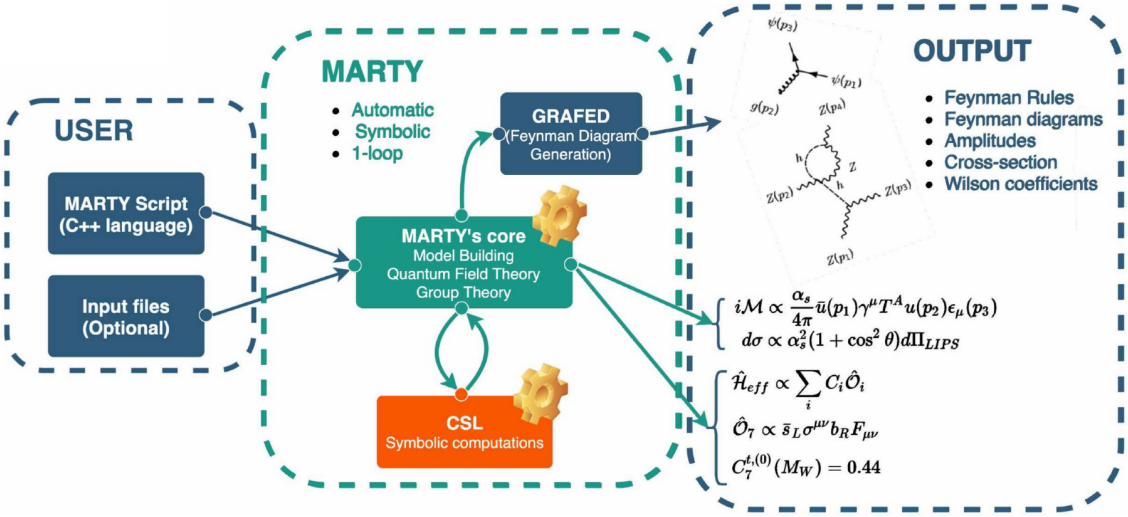

Figure 2: Schematic representation of the structure of `MARTY` .

as how couplings affect the relic density. Therefore, our current work aims to overcome this limitation. This is complicated by the fact that the term $\langle\sigma v\rangle$ is computed thanks to a self-generated `FORMcalc` code, thus hardly human readable and editable.

The last three features are all achieved by properly modifying the Boltzmann equation, since they are obtained by relaxing some of its hypothesis. For instance, the non-thermal production of DM is achieved by manual modifications of n, while for the entropy injection a manual modification of the entropy density s and variable dark energy by adding a variable dark energy density in the second Friedmann equation.

In the future version of `SuperIso Relic`, the limitations to the computation of $\langle\sigma v\rangle$ will be overcame by using `MARTY` [6]. `MARTY` is a completely open source software, whose principle of working is schematised in figure 2. Thanks to `MARTY`, the user can define a Lagrangian density in a C++ file, and then perform symbolic manipulations to get a C++ library. In our case, this library contains the code to perform the numerical computations to get squared matrix elements, that we than use to compute single cross sections or $\langle\sigma v\rangle$, by defining functions that handle kinematics. Other software that do this are already on the market. However they require passages of inputs among them, and they rely on Mathematica, which is closed-source. In the framework we are working on, the code to obtain $\langle\sigma v\rangle$ is easier to read and to modify, allowing new features. This code is written with the purpose of providing what is missing to make an interface among the libraries generated with `MARTY` and `SuperIso Relic`.

We have therefore computed $\langle\sigma v\rangle$ in the MSSM using this technique and validated it against the existent `FORMcalc` code. On the about 3400 squared amplitudes needed for the calculations, only about 15 disagree, and only at the 10% level. Once these discrepancies are fixed, the same setup will be used to reproduce the code for the NMSSM. Next, the new code will be integrated into `SuperIso Relic` to replace the old one. We will eventually implement in `SuperIso Relic` the possibility to solve the different Boltzmann equations independently for different particles in the thermal bath. Furthermore, once this is done, the feature to get the DM density in user-defined NP models can be added.

Conclusions

Studying the relic density of a stable particle of a Beyond Standard Model (BSM) theory tells us if such a particle can be a dark matter candidate or not. Among the BSM scenarios, the ones in the framework of supersymmetry with R-parity have been and still are studied because in such theories the lightest supersymmetric particle is stable, thus, if chosen to be neutral, it is a candidate for dark matter. `SuperIso Relic`, in its current version, gives the evolution of the total density of supersymmetric particles until today. In the future versions, separate equations will be solved for separate species, providing more detailed information on the model under consideration and its parameters. This goal will be achieved thanks to the software `MARTY`, that allows to get quantities starting from the Lagrangian density. This feature provides a high flexibility that we hope to use further in the future, for instance to give the user the chance to work in models different from supersymmetric ones, or maybe even user-defined. The flexibility of the code may be used also to add more predictions related to direct and indirect detection of dark matter. Finally, we will handle performance optimisation in a better way, since the code will be easier to modify and effectively parallelise.

Acknowledgments

I would like to thank Grégoire Uhlrich for his incredible support with `MARTY`.

References

[1] Gondolo, P. and Gelmini, G., *Cosmic abundances of stable particles: Improved analysis*, Nucl. Phys. B **360**, 1991, doi:10.1016/0550-3213(91)90438-4

[2] Gondolo, P. and Edsjo, J., *Neutralino relic density including coannihilations*, Phys. Atom. Nucl. **61**, 1998

[3] Peter, P. and Uzan, J.P., *Primordial Cosmology*, Oxford University Press, 2013

[4] A. Arbey and F. Mahmoudi, *SuperIso Relic v3.0: A program for calculating relic density and flavour physics observables: Extension to NMSSM*, Comput. Phys. Commun. **182** (2011), doi:10.1016/j.cpc.2011.03.019

[5] A. Arbey, F. Mahmoudi and G. Robbins, *SuperIso Relic v4: A program for calculating dark matter and flavour physics observables in Supersymmetry*, Comput. Phys. Commun. **239** (2019), doi:10.1016/j.cpc.2019.01.014

[6] G. Uhlrich, F. Mahmoudi and A. Arbey, *MARTY - Modern ARtificial Theoretical phYsicist A C++ framework automating symbolic calculations Beyond the Standard Model*, Comput. Phys. Commun. **264** (2021), 107928 doi:10.1016/j.cpc.2021.107928

Solving $(g-2)_\mu$ with a new light gauge boson

Emanuelle PINSARD

Laboratoire de Physique de Clermont

Abstract — Focusing on the tensions associated with the anomalous magnetic moment of charged leptons (muon and electron), we minimally extend the Standard Model via a new light gauge boson (Z') and work under the hypothesis of strictly flavour violating couplings to leptons. Taking into account several flavour observables, we derive stringent constraints on the model's parameter space, and subsequently carry out predictions for several observables.

Introduction

Despite its success, the Standard Model (SM) cannot account for neutrino oscillation phenomena, dark matter and the origin of the baryon asymmetry of the Universe. The first also implies that Lepton Flavour Violation (LFV) occurs in the neutral lepton sector. Furthermore, numerous tensions between SM predictions and observations have emerged, such as those regarding the anomalous magnetic moment of charged leptons (a_ℓ), the Cabibbo-angle anomaly, B-meson decay anomalies,.... Many of these deviations, pointing towards the need of New Physics (NP), are related to the flavour sector.

Numerous extensions of the SM have been studied to explain the long-standing tensions in the anomalous magnetic moments (see [1] for a detailed review on NP scenarios for a_μ). Among them, minimal Beyond the Standard Model (BSM) constructions extending the SM gauge group via $U(1)$ gauge groups are very appealing as they offer a particularly simple solution to these anomalies. Focusing on Z' boson extensions, several models can successfully account for the observed discrepancies in $a_{\mu,e}$. The new boson can then be heavy [2] or light, with flavour conserving and/or violating interactions (see for instance Refs. [3, 4, 5]).

Here we will discuss the implications of a light Z' with strictly flavour violating couplings to leptons, considering all the three leptonic generations [6]. We first review the magnetic moment and the observed tensions, then describe the minimal model under consideration. The third section will be devoted to the NP contributions and the constraints from flavour observables. Finally we will present the results before summarising with the concluding remarks.

Magnetic moment

The magnetic moment of a charged lepton measures its tendency to align with a magnetic field and is given by:

$$\vec{\mu_\ell} = g_\ell \frac{e}{2m_\ell}\vec{s}, \tag{1}$$

where $\vec{s}$, m_ℓ are the spin and the mass of the lepton and g_ℓ is the Landé factor. The latter can be computed from Dirac equation, leading to $g_\ell \equiv g_{\text{Dirac}} = 2$. In order to take quantum corrections into account, let us first start with the electromagnetic lepton current:

$$\mathcal{J}_\mu = \overline{\ell}(p')\left[\gamma_\mu F_1(q^2) + \frac{i\sigma_{\mu\nu}q^\nu}{2m_\ell}F_2(q^2) + \gamma_5\frac{i\sigma_{\mu\nu}q^\nu}{2m_\ell}F_3(q^2) + \gamma_5(q^2\gamma_\mu - \not{q}q_\mu)F_4(q^2)\right]\ell(p), \tag{2}$$

with q the photon momentum, F_i the electromagnetic form factors and $g_\ell = 2(F_1(0) + F_2(0))$. Computing these form factors at tree level leads to $g_\ell = g_{\text{Dirac}}$; the higher order contributions will arise from corrections to $F_2(0)$ at the loop level. Defining the anomalous magnetic moment:

$$a_\ell \equiv \frac{g_\ell - g_{\text{Dirac}}}{g_{\text{Dirac}}} = \frac{g_\ell - 2}{2} = F_2(0)\,, \tag{3}$$

the first correction at next-to-leading order in Quantum Electrodynamics (QED), was obtained in 1948. Currently, QED contributions to $(g-2)_\mu$ are known at 5-loops, the electroweak ones (interactions involving W, Z and Higgs bosons) at 2-loops; the non perturbative Quantum Chromodynamics (QCD) contributions arise from light-by-light scattering and hadronic vacuum polarization.

The SM expectation for the muon anomalous magnetic moment given by the "Muon $g-2$ Theory initiative" [7] is:

$$a_\mu^{\text{SM}} = 116\,591\,810\,(43) \times 10^{-11}. \tag{4}$$

The combined measurements from the BNL E821 experiment [8] and the recent "g-2" E989 experiment at FNAL [9] give the experimental average:

$$a_\mu^{\text{exp}} = 116\,592\,061\,(41) \times 10^{-11}, \tag{5}$$

leading to the 4.2σ discrepancy

$$\Delta a_\mu \equiv a_\mu^{\text{SM}} - a_\mu^{\text{exp}} = 251\,(59) \times 10^{-11}. \tag{6}$$

The accuracy of both theoretical predictions and experimental measurements render this observable very sensitive to NP and it can then be used to test and constrain BSM models.

Even if less precise, the electron anomalous magnetic moment also suffers from tensions between theory and observation: Δa_e is known from the precise measurement of the electromagnetic fine structure constant α_e with Caesium atoms [10, 11]. The theory prediction [12] based on Cs exhibits a -2.5σ tension with observation:

$$\Delta a_e^{\rm Cs} \sim -0.88\,(36) \times 10^{-12}, \tag{7}$$

while a more recent measurement using Rubidium atoms [13] shows a 1.7σ deviation:

$$\Delta a_e^{\rm Rb} = 0.48\,(30) \times 10^{-12}. \tag{8}$$

Explaining both the muon and the electron discrepancies turns out to be difficult, since the ratio $\Delta a_\mu/\Delta a_e$ does not exhibit the behaviour which would be expected from the scaling of effective dipole operators (m_μ/m_e), or from symmetry arguments (m_μ^2/m_e^2). Moreover, considering $\Delta a_e^{\rm Cs}$, there is also a sign difference between the two anomalous magnetic moments.

To account for these tensions, one can extend the SM content by a single field (scalar leptoquark, dark photon, or Z' as we will discuss in the next section), two or three-fields (such as vector-like leptons or scalar(s) plus fermion(s)), or even consider supersymmetric models.

The model

We consider here a minimal extension of the SM via one new light neutral gauge boson Z' (without specifying the new gauge group). Such a model is subject to stringent constraints from direct searches and electroweak precision observables (EWPO). The non-observation of a Z' at electron beam dump experiments (SLAC E141, Orsay, NA64 [14, 15]), in dark photon production searches (KLOE-2 experiment [16], BaBar [17]) or at parity-violation experiments (SLAC E158 [18]) sets severe bounds on $Z'ee$ couplings. The other diagonal couplings are also constrained by neutrino-electron scattering.

In order to evade these severe bounds one can consider strictly flavour violating couplings to leptons (not considering quark couplings allows circumventing hadronic constraints). Gauge kinetic mixing then only arises as a 2 loop effect and is neglected in the following.

In what follows, we study an intermediate mass $m_{Z'} = 10$ GeV and consider the interaction Lagrangian:

$$\mathcal{L} = Z'_\mu \left[\bar{\ell}_i \gamma^\mu (g_X^{ij} P_X) \ell_j + \bar{\nu}_i \gamma^\mu (g_L^{ij} P_L) \nu_j\right] + \text{H.c.}\,, \tag{9}$$

where the sum runs over the indices $i, j = e, \mu, \tau$, with $i \neq j$; $P_X = P_{L,R}$ are the chiral projectors and $g_X^{ij} = g_{L,R}^{ij}$ are the new coupling constants. Notice that we only consider left-handed (LH) neutrinos, which couple to the Z' as LH charged leptons, due to $SU(2)_L$ gauge invariance.

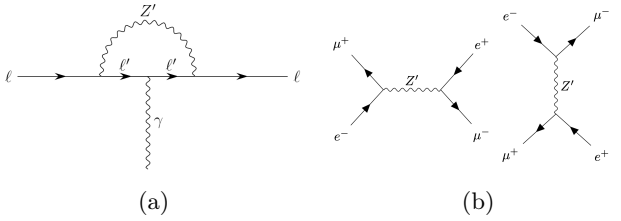

(a) (b)

Figure 1: Feynman diagrams for: (a) the one-loop contribution to charged lepton anomalous magnetic moment mediated by a Z'; (b) the tree-level contributions to Muonium oscillations mediated by a Z'.

We can see from the Lagrangian in Eq.(9) that the neutral boson couples to charged leptons with both left and right couplings, potentially at the source of sizeable contributions to the different anomalous magnetic moments.

NP contributions and constraints

We now proceed with the new physics contributions induced by this model, as well as the constraints set by the different processes under consideration.

Anomalous magnetic moment

The new physics contribution to a_ℓ from an additional neutral Z' boson arises at one-loop (see Fig. 1a) and, following [19, 20, 21], can be expressed as:

$$\Delta a_\ell = \sum_i \left[\frac{|g_V^{\ell i}|^2}{4\pi^2}\frac{m_\ell^2}{m_{Z'}^2} F(\lambda, \epsilon_i) + \frac{|g_A^{\ell i}|^2}{4\pi^2}\frac{m_\ell^2}{m_{Z'}^2} F(\lambda, -\epsilon_i)\right], \tag{10}$$

with $g_V, g_A = (g_L \pm g_R)/2$ the hermitian vector and axial-vector couplings, $m_{Z'}$ the mass of the exchanged vector boson, and with the sum running over the internal leptons. The function $F(\lambda, \epsilon_i)$ is defined:

$$F(\lambda, \epsilon_i) = \frac{1}{2}\int_0^1 dx \left[\frac{2x(1-x)[x - 2(1-\epsilon_i)]}{(1-x)(1-\lambda^2 x) + \epsilon_i^2 \lambda^2 x} + \frac{\lambda^2 x^2 (1-\epsilon_i)^2 (1 + \epsilon_i - x)}{(1-x)(1-\lambda^2 x) + \epsilon_i^2 \lambda^2 x}\right], \tag{11}$$

with $\epsilon_i = m_i/m_\ell$, m_i being the mass of the internal fermion and $\lambda = m_\ell/m_{Z'}$. The different sign between the vector and axial-vector loop functions leads to partial cancellations, allowing for an explanation of both Δa_μ and Δa_e.

From the known measurements of a_ℓ we will be able to constrain the Z' LFV couplings to leptons $g_{L,R}^{\ell,\ell'}$, depending on the internal fermion ℓ'.

Muonium oscillations

Another relevant observable to consider is the spontaneous Muonium-anti-Muonium oscillation. Muonium is a bound state of an electron and an anti-muon,

Mu $= \mu^+ e^-$. In presence of charged lepton flavour violation (cLFV), this system can oscillate into anti-Muonium $\overline{\text{Mu}} = \mu^- e^+$. In the model under consideration $\text{Mu} - \overline{\text{Mu}}$ conversion can occur at tree-level (as shown in Fig. 1b), from s and t-channels, so one can expect stringent bounds on $g^{e\mu}$. Indeed the PSI experiment [22] set bound on the oscillation probability

$$P < 8.3 \times 10^{-11} \,. \tag{12}$$

The relevant effective Lagrangian can be cast as [23]:

$$-\mathcal{L}_{\text{Mu}-\overline{\text{Mu}}} = \sum_{i=1,\ldots,5} \frac{G_i}{\sqrt{2}} Q_i, \tag{13}$$

where Q_i are the four-fermion operators inducing $\text{Mu} - \overline{\text{Mu}}$ transitions

$$\begin{aligned} Q_{1(2)} &= 4\left(\overline{\mu}\gamma_\alpha P_{L(R)} e\right)\left(\overline{\mu}\gamma^\alpha P_{L(R)} e\right), \\ Q_3 &= 4\left(\overline{\mu}\gamma_\alpha P_R e\right)\left(\overline{\mu}\gamma^\alpha P_L e\right), \\ Q_{4(5)} &= 4\left(\overline{\mu} P_{L(R)} e\right)\left(\overline{\mu} P_{L(R)} e\right). \end{aligned} \tag{14}$$

The presence of an external magnetic field will also induce an energy splitting, leading to $\text{Mu} - \overline{\text{Mu}}$ mixing. The transition probability in our model (i.e. considering only vector couplings so that $Q_4, Q_5 = 0$) can be written as

$$P = \frac{2.57 \times 10^{-5}}{G_F^2} \left\{ |c_{0,0}|^2 \left| -G_3 + \frac{G_1 + G_2 - \frac{1}{2} G_3}{\sqrt{1 + X^2}} \right|^2 + |c_{1,0}|^2 \left| G_3 + \frac{G_1 + G_2 - \frac{1}{2} G_3}{\sqrt{1 + X^2}} \right|^2 \right\}, \tag{15}$$

where $|c_{F,m}|^2$ denote the population of Muonium states and the factor X encodes the magnetic flux density. For hermitian couplings $g^{e\mu}_{L,R}$, one finds

$$\frac{G_{1(2)}}{\sqrt{2}} = \frac{|g^{e\mu}_{L(R)}|^2}{4 m^2_{Z'}}, \qquad \frac{G_3}{\sqrt{2}} = \frac{2 g^{e\mu}_L g^{e\mu,*}_R}{4 m^2_{Z'}}, \tag{16}$$

suggesting that $\text{Mu} - \overline{\text{Mu}}$ oscillations can indeed play a relevant role in constraining $g^{e\mu}_{L,R}$.

Z-boson decays

Z-decays to charged leptons offer another experimental probe of the new boson. At one-loop level, Z' mediates lepton flavour conserving (LFC) decays $Z \to \ell^+ \ell^-$ and LFV ones $Z \to \ell_i^+ \ell_j^-$.

In both cases, one has to consider loop diagrams which are ultraviolet (UV)-divergent and must thus be renormalized. For this purpose we follow the fermion diagonal (for LFC decays) and off-diagonal (for LFV decays) self-energy renormalizations from [24, 25, 26]. The remaining divergences are then taken into account in the vertex counter-term in the $\overline{\text{MS}}$ scheme.

LFC Z-decays and lepton flavour universality (LFU): Even if the NP contribution occurs at one-loop (versus tree-level in the SM) the interference between NP and SM processes is non-negligible and sets constraints on all off-diagonal new boson couplings. Besides, the one-loop contribution of the Z' induces modifications of the Z coupling constants.

To constrain both effects, we will study the ratio of LFC decays (allowing the cancellation of the QED corrections). Since the quantum charges are the same, both the Z boson and the photon have universal couplings to leptons. Thus the LFU of Z decays will allow constraining NP contributions due to the existing tight bounds [27]:

$$\begin{aligned} \frac{\Gamma(Z \to \mu^+ \mu^-)^{\text{exp}}}{\Gamma(Z \to e^+ e^-)^{\text{exp}}} &= 1.0001 \pm 0.0024, \\ \frac{\Gamma(Z \to \tau^+ \tau^-)^{\text{exp}}}{\Gamma(Z \to e^+ e^-)^{\text{exp}}} &= 1.0020 \pm 0.0032. \end{aligned} \tag{17}$$

LFV Z-decays: The presence of the new boson allows for cLFV Z-decays (also at the loop-level). The current limits from ATLAS on $Z \to e^\pm \mu^\mp$ [28] and OPAL on $Z \to e^\pm \tau^\mp$ and on $Z \to \mu^\pm \tau^\mp$ [29] are not sufficiently strong to constrain the different Z' couplings due to the loop suppression. The NP contributions to the decay rate turn out to be small: $\text{BR}(Z \to \ell_i^+ \ell_j^-) \sim \mathcal{O}(10^{-14})$.

Leptonic τ decays

In the SM, $\tau \to \ell \nu_\tau \overline{\nu}_\ell$ decays are mediated by a W-boson and occur at tree-level. In the present SM extension, these decays can also be mediated by a Z' at tree level, thus potentially competing with the SM processes. The measured τ leptonic decay ratio R_τ from ARGUS [30], CLEO [31], BaBar [32] is found to be consistent with the SM, allowing to set bounds on BSM scenarios. The HFLAV collaboration global fit [33] is given by:

$$R_\tau \equiv \frac{\Gamma(\tau^- \to \mu^- \nu_\tau \overline{\nu}_\mu)}{\Gamma(\tau^- \to e^- \nu_\tau \overline{\nu}_e)} = 0.9761 \pm 0.0028. \tag{18}$$

Experimentally, it is not possible to disentangle the different neutrino flavours, so any LFV tree-level decay $\tau \to \ell \nu_i \overline{\nu}_j$, with $i, j = e, \mu, \tau$, mediated by the Z' will contribute to this observable.

cLFV

Since neutrino oscillations break the lepton flavour symmetry in the neutral sector, it is natural to look for processes that violate this symmetry in the charged lepton sector. The non-observation of such processes, and the several experimental upper bounds on cLFV, can be used to constrain NP models. Among these observables, one has muon and tau three-body decays ($\mu \to 3e$, $\tau \to 3e$, $\tau \to 3\mu$, $\tau^- \to \mu^- e^+ e^-$, $\tau^- \to \mu^- e^+ \mu^-$, $\tau^- \to e^- \mu^+ \mu^-$ and $\tau^- \to e^- \mu^+ e^-$), most of them being mediated by Z and photon-penguin, and the more stringent radiative decays ($\mu \to e\gamma$, $\tau \to e\gamma$ and $\tau \to \mu\gamma$). In the muon sector, there are also Muonium oscillations (as previously discussed) and decays, as well as $\mu - e$ conversion (not considered here).

At high energies, cLFV can appear in Z-decays (as

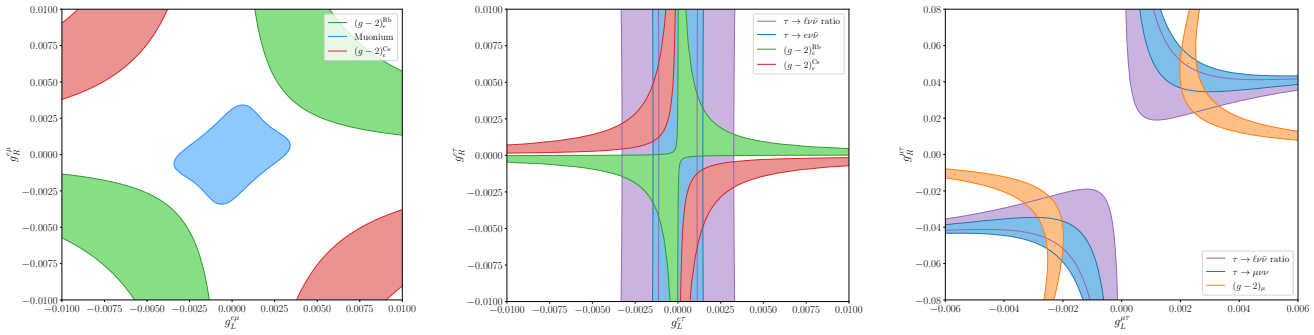

(a) $e-\mu$ couplings. (b) $e-\tau$ couplings. (c) $\mu-\tau$ couplings.

Figure 2: From left to right, $g_R^{\alpha\beta}$ vs. $g_L^{\alpha\beta}$ (with $\alpha\beta = e\mu, e\tau$ and $\mu\tau$), setting all other couplings to zero. Coloured surfaces correspond to the regions in agreement with experimental constraints at 1σ: $\Delta a_e^{\rm Rb}$ in green, $\Delta a_e^{\rm Cs}$ in red, $(g-2)_\mu$ in orange, the blue areas are those allowed by $\tau \to \mu\nu\overline{\nu}$ and $\tau \to e\nu\overline{\nu}$ while the purple ones are allowed by the ratio of leptonic τ decays. The cyan region in Fig.2a denotes those allowed by Muonium oscillations.

previously mentioned) and in Higgs-decays, also mediated by loop diagrams. As for the Z-boson, due to the loop suppression, the NP contributions to Higgs LFV decays will be negligible. Concerning LFC Higgs-decays, the new boson will also contribute at one-loop, but even if enhanced by the tau Yukawa couplings, the branching ratios receive small corrections from the Z'. Altogether, we thus found that the NP contributions to the LFC Z and Higgs boson-decays, $Z/H \to \ell^+\ell^-$ are not sizeable enough to impose significant constraints on the flavour-changing gauge couplings.

Results

Having discussed the several contributions, as well as the constraints, we now address the viable parameter space for the Z' couplings (see [6] for a full discussion). Muonium oscillations constrain the $e\mu$ couplings to be smaller than 3×10^{-3}, and $g_L^{e\mu}$ and $g_R^{e\mu}$ can be of the same or opposite sign. Unfortunately in order to explain the electron anomalous magnetic moment, one needs these couplings to be of opposite sign and larger than what is allowed by the bounds on $\mathrm{Mu}-\overline{\mathrm{Mu}}$ transitions (see Fig. 2a). Moreover these couplings lead to a negative shift in $(g-2)_\mu$, making the discrepancy worse than in the SM.

To account for the deviation in $(g-2)_e$ one can also consider a τ in the loop, i.e. relying on the $e\tau$ couplings to the new gauge boson. Considering only $g_X^{e\tau} \neq 0$, the τ-decays set stringent bounds. Explaining $\Delta a_e^{\rm Cs}$ then requires left/right couplings of opposite-sign or one of them to be zero, while the explanation of $\Delta a_e^{\rm Rb}$ demands same-sign couplings. Combining the τ-decays and the anomalous magnetic moment, one can nevertheless find some allowed regions, as can be seen in Fig. 2b. (These couplings also induce a negative contribution to Δa_τ of order $\mathcal{O}(10^{-9})$.)

Concerning a_μ, we have seen that $g^{e\mu}$ cannot account for the observed positive discrepancy, but this process can also be mediated by a Z' and a τ in the loop. In this case, one should explore the $g^{\mu\tau}$ parameter space. As for the $e\tau$ couplings, τ-decays set stringent limits, but there exists a tiny window allowing to explain the tension of the muon magnetic moment. As can be seen in Fig. 2c, the left and right couplings need to be non-zero and of the same sign (also leading to a negative contribution to $(g-2)_\tau$). The couplings needed to explain Δa_μ being bigger than $g^{e\tau}$, the NP contribution to the tau magnetic moment will be driven by $\mu\tau$ couplings.

Finally we can also attempt to explain both the charged lepton magnetic moment anomalies, with two different couplings $e\tau$ and $\mu\tau$, each one giving the necessary contribution to a_e (from CS or Rb) and a_μ. Unfortunately, if we consider the couplings to be simultaneously non-zero, the contribution to the cLFV $\mu \to e\gamma$ decay (mediated by the Z' and a τ in the loop) is excessively large, rendering the explanation of both a_e and a_μ impossible within this minimal model.

Conclusions

We have considered a minimal NP Z' model, with flavour-changing interactions to SM leptons. The constraints from several flavour observables (such as radiative and three-body cLFV decays, boson decays and $\mathrm{Mu}-\overline{\mathrm{Mu}}$ oscillations) imply that we can only explain one of the muon or electron anomalous magnetic moment. In particular, the joint explanation of both electron and muon $g-2$ requires sizeable $g^{e\tau}$ and $g^{\mu\tau}$ which turn out to be excluded by the bounds on $\mu \to e\gamma$ branching ratio.

The next step will be to extend this model, including a new scalar responsible for symmetry breaking and thus giving mass to the Z' boson. The Yukawa couplings will then contribute to the processes described above, and one should investigate if one can then solve both of the $(g-2)_{e,\mu}$ without an extremely large $\mathrm{BR}(\mu \to e\gamma)$.

Further extensions are also possible in the fermion sector, such as introducing RH neutrinos (and a potential neutrino mass mechanism and/or dark matter candidate) or exploring the couplings to quarks.

References

[1] P. Athron, C. Balázs, D. H. J. Jacob, W. Kotlarski, D. Stöckinger and H. Stöckinger-Kim, JHEP **09** (2021), 080 [arXiv:2104.03691 [hep-ph]].

[2] P. Langacker, Rev. Mod. Phys. **81** (2009), 1199-1228 [arXiv:0801.1345 [hep-ph]].

[3] J. Heeck, Phys. Lett. B **758** (2016), 101-105 [arXiv:1602.03810 [hep-ph]].

[4] R. Foot, X. G. He, H. Lew and R. R. Volkas, Phys. Rev. D **50** (1994), 4571-4580 [arXiv:hep-ph/9401250 [hep-ph]].

[5] W. Altmannshofer, C. Y. Chen, P. S. Bhupal Dev and A. Soni, Phys. Lett. B **762** (2016), 389-398 [arXiv:1607.06832 [hep-ph]].

[6] J. Kriewald, J. Orloff, E. Pinsard, A. M. Teixeira, "Flavour-constraining light Z' extensions of the Standard Model," in preparation.

[7] T. Aoyama, N. Asmussen, M. Benayoun, J. Bijnens, T. Blum, M. Bruno, I. Caprini, C. M. Carloni Calame, M. Cè and G. Colangelo, *et al.* Phys. Rept. **887** (2020), 1-166 [arXiv:2006.04822 [hep-ph]].

[8] G. W. Bennett *et al.* [Muon g-2], Phys. Rev. D **73** (2006), 072003 [arXiv:hep-ex/0602035 [hep-ex]].

[9] B. Abi *et al.* [Muon g-2], Phys. Rev. Lett. **126** (2021) no.14, 141801 [arXiv:2104.03281 [hep-ex]].

[10] R. H. Parker, C. Yu, W. Zhong, B. Estey and H. Müller, Science **360** (2018), 191 [arXiv:1812.04130 [physics.atom-ph]].

[11] C. Yu, W. Zhong, B. Estey, J. Kwan, R. H. Parker and H. Müller, Annalen Phys. **531** (2019) no.5, 1800346

[12] D. Hanneke, S. Fogwell and G. Gabrielse, Phys. Rev. Lett. **100** (2008), 120801 [arXiv:0801.1134 [physics.atom-ph]].

[13] L. Morel, Z. Yao, P. Cladé and S. Guellati-Khélifa, Nature **588** (2020) no.7836, 61-65

[14] D. Banerjee *et al.* [NA64], Phys. Rev. Lett. **120** (2018) no.23, 231802 [arXiv:1803.07748 [hep-ex]].

[15] D. Banerjee *et al.* [NA64], Phys. Rev. D **101** (2020) no.7, 071101 [arXiv:1912.11389 [hep-ex]].

[16] A. Anastasi, D. Babusci, G. Bencivenni, M. Berlowski, C. Bloise, F. Bossi, P. Branchini, A. Budano, L. Caldeira Balkeståhl and B. Cao, *et al.* Phys. Lett. B **750** (2015), 633-637 [arXiv:1509.00740 [hep-ex]].

[17] J. P. Lees *et al.* [BaBar], Phys. Rev. Lett. **113** (2014) no.20, 201801 [arXiv:1406.2980 [hep-ex]].

[18] P. L. Anthony *et al.* [SLAC E158], Phys. Rev. Lett. **95** (2005), 081601 [arXiv:hep-ex/0504049 [hep-ex]].

[19] M. Lindner, M. Platscher and F. S. Queiroz, Phys. Rept. **731** (2018), 1-82 [arXiv:1610.06587 [hep-ph]].

[20] F. Jegerlehner and A. Nyffeler, Phys. Rept. **477** (2009), 1-110 [arXiv:0902.3360 [hep-ph]].

[21] J. P. Leveille, Nucl. Phys. B **137** (1978), 63-76

[22] L. Willmann, P. V. Schmidt, H. P. Wirtz, R. Abela, V. Baranov, J. Bagaturia, W. H. Bertl, R. Engfer, A. Grossmann and V. W. Hughes, *et al.* Phys. Rev. Lett. **82** (1999), 49-52 [arXiv:hep-ex/9807011 [hep-ex]].

[23] T. Fukuyama, Y. Mimura and Y. Uesaka, "Models of the Muonium to Antimuonium Transition," arXiv:2108.10736 [hep-ph].

[24] K. I. Aoki, Z. Hioki, M. Konuma, R. Kawabe and T. Muta, Prog. Theor. Phys. Suppl. **73** (1982), 1-225

[25] D. Espriu, J. Manzano and P. Talavera, Phys. Rev. D **66** (2002), 076002 [arXiv:hep-ph/0204085 [hep-ph]].

[26] A. Denner, Fortsch. Phys. **41** (1993), 307-420 [arXiv:0709.1075 [hep-ph]].

[27] P. A. Zyla *et al.* [Particle Data Group], PTEP **2020** (2020) no.8, 083C01

[28] G. Aad *et al.* [ATLAS], Phys. Rev. D **90** (2014) no.7, 072010 [arXiv:1408.5774 [hep-ex]].

[29] R. Akers *et al.* [OPAL], Z. Phys. C **67** (1995), 555-564

[30] H. Albrecht *et al.* [ARGUS], Z. Phys. C **53** (1992), 367-374

[31] A. Anastassov *et al.* [CLEO], Phys. Rev. D **55** (1997), 2559-2576 [erratum: Phys. Rev. D **58** (1998), 119904]

[32] B. Aubert *et al.* [BaBar], Phys. Rev. Lett. **105** (2010), 051602 [arXiv:0912.0242 [hep-ex]].

[33] Y. S. Amhis *et al.* [HFLAV], Eur. Phys. J. C **81** (2021) no.3, 226 [arXiv:1909.12524 [hep-ex]].

Analytic and Numerical Bootstrap for One-Matrix Model and "Unsolvable" Two-Matrix Model

Zechuan ZHENG

ENS Ulm

Abstract — We propose the relaxation bootstrap method for the numerical solution of multi-matrix models in the large N limit. It gives rigorous inequalities on the single trace moments of the matrices up to a given "cutoff" order (length) of the moments. The method combines usual loop equations on the moments and the positivity constraint on their correlation matrix. We have a rigorous proof of applicability of this method in the case of the one-matrix model.

Introduction

Matrix integrals play an important role in numerous physical and mathematical subjects. A rather general class of matrix integrals has the form

$$Z = \int d^{N^2}A\, d^{N^2}B\, d^{N^2}C \dots\, e^{-\mathrm{tr}\mathcal{V}(A,B,C,\dots)} \qquad (1)$$

where $A, B, C, \dots$ are Hermitian $N \times N$ matrices with $U(N)$ invariant integration measure and the potential $\mathcal{V}(x, y, z, \dots)$ is an analytic function (often a polynomial) of the variables $x, y, z, \dots$.

The $N \to \infty$ limit, with the appropriately adjusted parameters of the potential and of the averaged quantity, is of a special importance in multiple applications since it describes the thermodynamical limit of macroscopically many degrees of freedom for various physical systems. Such a limit deals with an infinite number of integrals, thus the matrix integral becomes a functional integral.

Virtually the only universal general method of numerical computation of functional integrals is the Monte-Carlo (MC) method. It has been applied to some matrix integrals with more or less of success. Its main drawbacks are well known: i) the result comes with a statistical error; ii) it is sometimes difficult to reach the numerical equilibrium state in a reasonable time; iii) MC is bad for the systems with sign-changing Boltzmann weights or non-local interactions; iv) the size of the system (the number of integrals) is limited by computational facilities v) The precision is usually rather modest, maximum about 3-4 digits.

For a alternative, recently, an impressive progress has been made in the computations of multi-point correlators in conformal field theories in various dimensions, due to the conformal bootstrap method [1]. It appeared to be far more efficient and precise than other numerical approaches, giving the critical exponents of 3d Ising model with the record 6-digits precision.

Inspired by this success a few authors applied the philosophy of the numerical bootstrap to the computations of various matrix integrals [3, 4] and even of the lattice multi-color QCD and $\mathcal{N} = 4$ SYM theory [2]. Instead of the direct study of the matrix integrals they proposed to study the large N Schwinger-Dyson equations which are often also called loop equations. They are easily obtained by the obvious Ward identities resulting from insertion of the full matrix derivative under the matrix integral:

$$0 = \int d^{N^2}A\, d^{N^2}B \dots\, \frac{1}{N}\mathrm{tr}\Big(\frac{\partial}{\partial A}A^m B^n \dots\Big) e^{-\mathrm{tr}\mathcal{V}(A,B,\dots)} \qquad (2)$$

where the matrix derivative inside the trace $\frac{\partial}{\partial A}$ acts on all A-matrices, including the potential. All other loop equations correspond to all possible "words" of matrices under the trace and to all insertions of various matrix derivatives at any place in the "words".[1] Then the positivity conditions are imposed stating that the inner product[2] of any operator with itself is positive. Rigorous bounds on the dynamical quantities of the theory can be derived from these positivity conditions and loop equations.

This new approach has, in our opinion, a great potential for the precision computations of physically important matrix integrals in the 't Hooft limit. But at the same time it is very much perfectible at this stage.

Firstly, the numerical matrix bootstrap approach based on the loop equations and positivity constraint, is not well understood analytically. Its efficiency, and the power of positivity, still looks quite mysterious. Secondly, the matrix bootstrap has a very distinguished feature comparing to most of the other bootstrap problems commonly addressed in the literature: it is in gen-

[1] In the 't Hooft limit, the single trace "words" are enough due to the factorization property which we will describe in the next section.

[2] Here inner product of an operator $\mathcal{O}$ means $\langle \mathrm{tr}\mathcal{O}^\dagger\mathcal{O}\rangle$.

eral non-convex. Generally solving a large scale non-convex optimization problem is pretty challenging.

In our recent work [5], we advance the matrix bootstrap approach trying, on the one hand, to understand analytically the role of positivity conditions, and on the other hand, to overcome, at least partially, the above-mentioned limitations of the method. The report given in JRJC contains basic introduction to the element of our work.

Toy model

For a illustration of the bootstrap framework, we consider the following single-variable integral:

$$Z = \int_{-\infty}^{\infty} \exp\left(-\frac{x^2}{2} - g\frac{x^4}{4}\right) \mathrm{d}x, \quad g > 0, \tag{3}$$

We want to compute its k-moment for a given g:

$$\mathcal{W}_k = \frac{1}{Z}\int_{-\infty}^{\infty} x^k \exp(-\frac{x^2}{2} - g\frac{x^4}{4})\mathrm{d}x \tag{4}$$

It is straightforward to notice that all the moments are related with $\mathcal{W}_2$ by the partial integration:

$$(k+1)\mathcal{W}_k = \mathcal{W}_{k+2} + g\mathcal{W}_{k+4}, \tag{5}$$

which we call **loop equations** in the bootstrap framework.

For $\mathcal{W}_2$, we have the known closed-form solution:

$$\frac{-I_{-\frac{1}{4}}\left(\frac{1}{8g}\right) + (4g+1)I_{\frac{1}{4}}\left(\frac{1}{8g}\right) - I_{\frac{3}{4}}\left(\frac{1}{8g}\right) + I_{\frac{5}{4}}\left(\frac{1}{8g}\right)}{2\sqrt{2}gK_{\frac{1}{4}}\left(\frac{1}{8g}\right)/\pi} \tag{6}$$

A crucial element of bootstrap method is that the expectations of square of polynomials are always positive semi-definite:

$$\frac{1}{Z}\int_{-\infty}^{\infty}(\sum \alpha_i x^i)^2 \exp(-\frac{x^2}{2} - g\frac{x^4}{4}) \geq 0, \ \forall \alpha \tag{7}$$

This is a quadratic form in α, its positivity is equivalent to:

$$\mathbb{W} = \begin{pmatrix} \mathcal{W}_0 & \mathcal{W}_1 & \mathcal{W}_2 & \dots \\ \mathcal{W}_1 & \mathcal{W}_2 & \mathcal{W}_3 & \dots \\ \mathcal{W}_2 & \mathcal{W}_3 & \mathcal{W}_4 & \dots \\ \vdots & \vdots & \vdots & \ddots \end{pmatrix} \succeq 0 \tag{8}$$

This condition will be referred as the positivity of **correlation matrix**.

We can solve the Semi-Definite Programming (SDP) maximizing or minimizing $\mathcal{W}_2$ constrained by a truncation of the positivity of correlation matrix:

$$\min \text{or} \max \ \mathcal{W}_2 \tag{9}$$

$$\mathbb{W}_\Lambda \succeq 0 \tag{10}$$

Here $\mathbb{W}_\Lambda$ is the top $(\Lambda+1)\times(\Lambda+1)$ sub-matrix of $\mathbb{W}$.

For $g = 1$, $\Lambda = 10$, we can get the numerical bootstrap result:

$$0.4679137 \leq \mathcal{W}_2 = 0.4679199170 \leq 0.4679214 \tag{11}$$

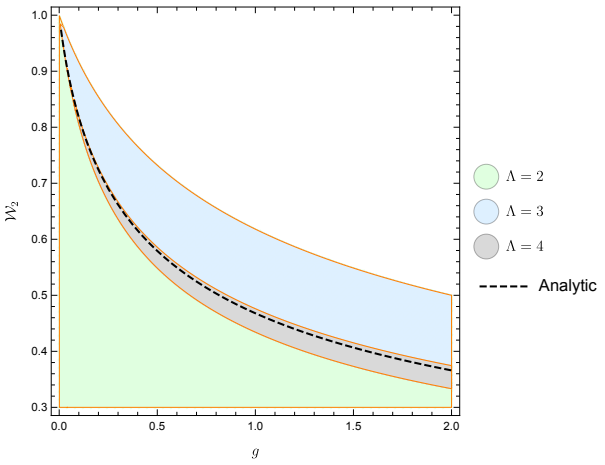

Figure 1: The bootstrap result for quartic integrals.

Large N one-matrix model

We first briefly review the main points of Ref. [3], the Hermitian one-matrix model is defined by matrix integral:

$$Z_N = \int d^{N^2}M \, e^{-N\mathrm{tr}V(M)} \tag{12}$$

where the invariant Hermitian measure is $d^{N^2}M = \prod_{i,j}^{N} dM_{ij}$. The potential is usually taken polynomial :

$$V(x) = \sum_{k=2}^{d+1} \frac{g_k}{k} x^k. \tag{13}$$

The main "physical observable" is the k-th moment:

$$\mathcal{W}_k = \langle \mathrm{Tr}M^k \rangle = \int \frac{d^{N^2}M}{Z_N} \frac{1}{N} \mathrm{tr}M^k e^{-N\mathrm{tr}V(M)}. \tag{14}$$

The bootstrap method works exactly in parallel to the previous example of toy model, except the loop equation is now quadratic:

$$\sum_{j=1}^{d} g_j \ \mathcal{W}_{k+j} = \sum_{l=0}^{k-1} \mathcal{W}_l \ \mathcal{W}_{k-l+1}. \tag{15}$$

Non-linear equation is non convex, so this will grow into a serious problem when the level of difficulty goes up. But for the quartic model $V(z) = \frac{1}{2}z^2 + \frac{g}{4}z^4$, this is not a problem since all higher moments are polynomials of the lowest moments $\mathcal{W}_2$. Using the bootstrap method, we get the Figure 2 which shows perfect agreement between bootstrap results and analytic results.

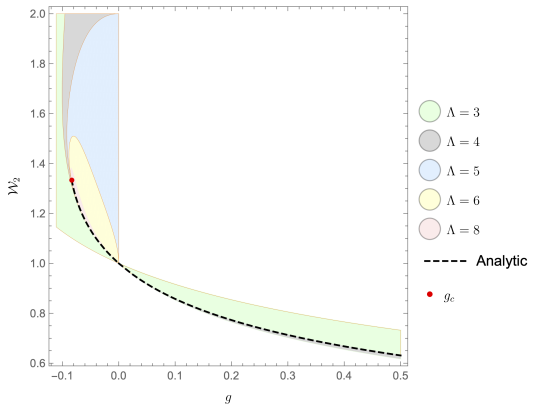

Figure 2: The allowed region for quartic model $V(z) = \frac{1}{2}z^2 + \frac{g}{4}z^4$ for different cutoff Λ, compared with the analytic solution. Here we assuming $\mathcal{W}_1 = 0$, we also note that for $g > 0$, we didn't plot $\Lambda \geq 5$ since they are almost indistinguishable from the analytic solution on the figure. Here g_c is the critical value of this model beyond which we cannot define a sensible large N matrix model.

Relaxation

Very few large N matrix models share the same simplicity as the above one matrix model, so the non-convexity will eventually make the bootstrap method intractable. [3] So we proposed the relaxation method to relax the non-linearities in the loop equations to convex inequalities.

More precisely, we make in the loop equation the substitution $\langle \mathrm{Tr}\mathcal{O}_i\rangle\langle \mathrm{Tr}\mathcal{O}_j\rangle = X_{ij}$, or in matrix notations:

$$X = xx^{\mathrm{T}} \tag{16}$$

where again x is the column vector whose components are $\langle \mathrm{Tr}\mathcal{O}_i\rangle$. Formally, this changes the loop equations to a linear form:

$$\mathrm{Tr}X\mathcal{A}_i + b_i^{\mathrm{T}}x + a_i = 0\,. \tag{17}$$

To apply the relaxation method, we relax (16) by imposing the inequality:

$$(\alpha^{\mathrm{T}}x)^2 \leq \alpha^{\mathrm{T}}X\alpha, \quad \forall\alpha \in \mathbb{R}^L \tag{18}$$

which is equivalent to:

$$X \succeq xx^{\mathrm{T}}\,. \tag{19}$$

By Schur's complement, this can be re-arranged into a more compact form:

$$\mathcal{R} = \begin{pmatrix} 1 & x^{\mathrm{T}} \\ x & X \end{pmatrix} \succeq 0. \tag{20}$$

Here we introduced the relaxation matrix by $\mathcal{R}_{ij} = X_{ij}$ and $\mathcal{R}_{0i} = \mathcal{R}_{i0} = \langle \mathrm{Tr}\mathcal{O}_i\rangle = x_i$. This step concludes our translation of the nonlinear bootstrap problem into an SDP. This SDP takes now a numerically much more tractable, convex form:

$$\begin{aligned} \text{minimize} \quad & c^{\mathrm{T}}x \\ \text{such that} \quad & {}_X\mathcal{A}_i + b_i^{\mathrm{T}}x + a_i = 0\,, \\ \text{and} \quad & M_0 + \sum_{j=1}^{L} M_j x_j \succeq 0\,, \\ \text{and} \quad & \begin{pmatrix} 1 & x^{\mathrm{T}} \\ x & X \end{pmatrix} \succeq 0\,. \end{aligned} \tag{21}$$

It has now two types of variables to bootstrap: a column vector variable x and a symmetric matrix variable X.

"Unsolvable" two-matrix model

In this section, we implement the relaxation bootstrap method described in the previous section to the case of generically unsolvable large N two-matrix model:

$$\lim_{N\to\infty} \int dAdB\, e^{-N\mathrm{tr}\left(-h[A,B]^2/2 + A^2/2 + gA^4/4 + B^2/2 + gB^4/4\right)} \tag{22}$$

where the integration goes over Hermitian matrices A and B. This model is unsolvable analytically for generic parameters h and g, at least with the known methods, such as reduction to eigenvalues or the character expansion. It is still analytically solvable for some particular values: for $g = 0$ it can be reduced to a specific one-matrix model and solved via saddle point method or via the reduction to a KP equation [6]; for $h = 0$ it reduces to two decoupled one-matrix models; for $h = \infty$ we have $[A, B] = 0$ and it reduces again explicitly to another eigenvalue problem. These particular solvable cases are useful to test the power of our numerical method.

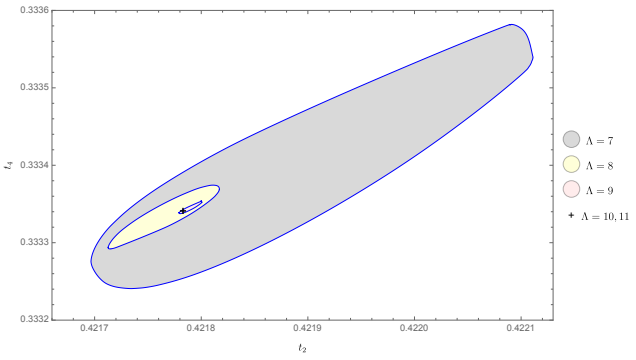

Figure 3: The allowed region of $t_2 - t_4$ of model (22) with parameter $g = 1, h = 1$ for the cutoff $\Lambda = 7, 8, 9, 10, 11$. We recall the definition of Λ: the longest operators in the correlation matrix and in the loop equations have the length 2Λ.

Let us demonstrate our results for various values of the length cutoff Λ. We summarized the allowed regions for the first two correlators $t_2 = \langle \mathrm{Tr}A^2\rangle$ and $t_4 = \langle \mathrm{Tr}A^4\rangle$ in Fig 3. The regions for $\Lambda = 10$ and

[3] In general, the non-convex optimization problem is a NP hard problem

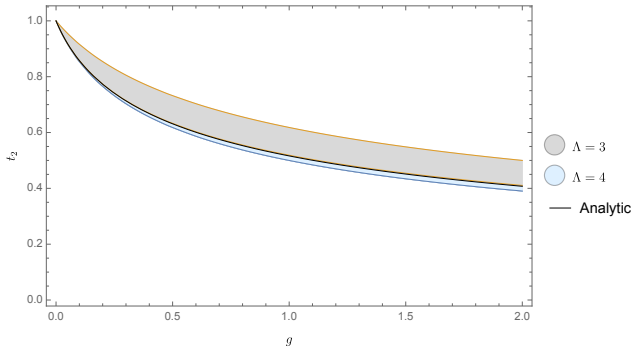

Figure 4: Comparison with the exact analytic solution of model (22) with $h = 0$, i.e. two decoupled quartic one-matrix model. The lower plot is for $\Lambda = 8$.

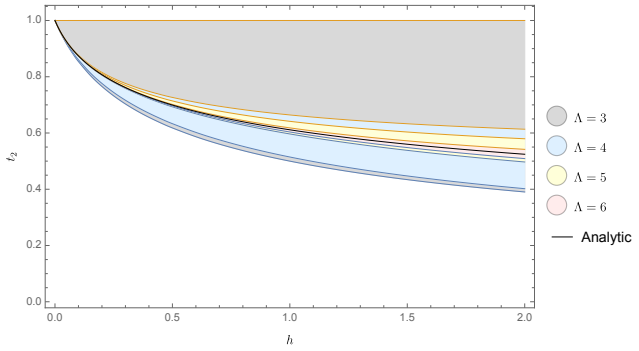

Figure 5: Comparison of the numerical bootstrap results with the exact analytic solution of the model with $g = 0$. The lower plot is for $\Lambda = 8$.

$\Lambda = 11$ are too small to be plotted on the figure, so we give here the upper and lower bound of t_2 and t_4. For $\Lambda = 10$:

$$\begin{cases} 0.421780275 \leq t_2 \leq 0.421785491 \\ 0.333339083 \leq t_4 \leq 0.333343006 \end{cases} \tag{23}$$

and for $\Lambda = 11$:

$$\begin{cases} 0.421783612 \leq t_2 \leq 0.421784687 \\ 0.333341358 \leq t_4 \leq 0.333342131 \end{cases} \tag{24}$$

We see here that for $\Lambda = 11$ we already have a six digits precision at $g = h = 1$.

The comparison of our numerical results with analytic result is presented on Fig 4 and Fig 5. Indeed, we see that our numerical results nicely agree with the analytic formula. An apparent feature of these plots is that when $g < 0$ or $h < 0$, the allowed region is much larger than the one for the positive coupling case, thus giving less of precision. In general we have the worst convergence in the neighborhood of critical values.

Conclusions

In this work, we develop further the matrix bootstrap method pioneered in the papers [2, 3] and propose a crucial improvement – the relaxation procedure – applicable to a large class of multi-matrix problems and allowing to bootstrap them with a much higher precision. The relaxation transforms a Non-linear SDP, with the non-linearity due to the structure of loop equations, to the usual, linear SDP. We demonstrate the efficiency of our approach on the analytically unsolvable two-matrix model and establish its phase structure with rather high precision.

References

[1] R. Rattazzi, V. S. Rychkov, E. Tonni and A. Vichi, JHEP **12**, 031 (2008) doi:10.1088/1126-6708/2008/12/031 [arXiv:0807.0004 [hep-th]].

[2] P. D. Anderson and M. Kruczenski, "Loop Equations and bootstrap methods in the lattice," Nucl. Phys. B **921**, 702-726 (2017) doi:10.1016/j.nuclphysb.2017.06.009 [arXiv:1612.08140 [hep-th]].

[3] H. W. Lin, "Bootstraps to strings: solving random matrix models with positivite," JHEP **06**, 090 (2020) doi:10.1007/JHEP06(2020)090 [arXiv:2002.08387 [hep-th]].

[4] X. Han, S. A. Hartnoll and J. Kruthoff, "Bootstrapping Matrix Quantum Mechanics," Phys. Rev. Lett. **125**, no.4, 041601 (2020) doi:10.1103/PhysRevLett.125.041601 [arXiv:2004.10212 [hep-th]].

[5] V. Kazakov and Z. Zheng, "Analytic and Numerical Bootstrap for One-Matrix Model and "Unsolvable" Two-Matrix Model," [arXiv:2108.04830 [hep-th]].

[6] V. A. Kazakov, I. K. Kostov and N. A. Nekrasov, Nucl. Phys. B **557**, 413-442 (1999) doi:10.1016/S0550-3213(99)00393-4 [arXiv:hep-th/9810035 [hep-th]].

Microscopic Effective Interactions for the Nuclear Shell Model

Zhen LI, ***with Nadezda A. Smirnova***

LP2i Bordeaux (Laboratoire de Physique des Deux Infinis de Bordeaux), Université de Bordeaux

Abstract — We present the formalism and numerical implementation of many-body perturbation theory as an approach to derive microscopic effective interactions for the nuclear shell model. The *sd*-shell microscopic effective interactions are derived from N^{3}LO, CD-Bonn and Daejeon16 potentials using many-body perturbation theory with up to second-order Feynman-Goldstone diagrams. The centroids of the derived microscopic effective interactions are too attractive, which results in too small sub-shell gaps. This deficiency leads to overbinding problems in the description of neutron-rich nuclei, and poor spectroscopy of nuclei in the vicinity of sub-shell closures. By comparing different microscopic effective interactions, we found the effective interaction derived from Daejeon16 is better than N^{3}LO and CD-Bonn. It is worth investigating further with Daejeon16.

Introduction

To describe the structure and decay of an atomic nucleus with A nucleons at low energies one needs to solve a (possibly non-relativistic) quantum-mechanical A-body problem, starting from the nucleon-nucleon interaction. Several high-precision nucleon-nucleon potentials are currently available. Among them are more phenomenological potentials, obtained within the meson-exchange concept, such as Bonn potentials [1], or Argonne potential [2], together with the modern potentials derived within the chiral effective field theory [3] (e.g., N^{3}LO potential [4]). The latter are advantageous because of their clear connection to quantum chromodynamics, as well as due to their capacity to provide three- and higher-body interactions in a systematic way and to estimate theoretical uncertainties at a given order of low-energy chiral expansion. To solve the A-body Schrödinger equation, there have been developed several *ab initio* approaches, namely, Quantum Monte-Carlo methods [5], the no-core shell model (NCSM) [6], Coupled Cluster (CC) theory [7], In-Medium Similarity Renormalization Group (IM-SRG) [8], self-consistent Green's function methods [9], many-body perturbation theory (MBPT) [10], etc. Most of these approaches are applicable either to light nuclei, or to closed-shell nuclei. The exact and accurate treatment of intermediate-mass open-shell nuclei is still a challenge.

The NCSM, being a full configuration-interaction approach, solves the A-body Schrödinger equation by exact diagonalization of the Hamiltonian matrix constructed in a spherically-symmetric many-body basis. Usually a harmonic-oscillator basis is used because of its remarkable symmetry properties. The size of the model space grows, however, very quickly, making a solution computationally tractable only for nuclei with $A \lesssim 20$. For heavier nuclei, approximations have to be made. Among them, the interacting shell model [11] reduces the A-body problem to a valence-particle problem, considering only a few valence nucleons moving in a restricted model space (usually being one major harmonic-oscillator shell) outside an inert closed-shell core. Because of this severely truncated model space, one must use a so-called *effective* nucleon-nucleon interaction, and not a bare nucleon-nucleon interaction that would be appropriate for the NCSM.

An effective valence-space Hamiltonian is a one- and two-body operator fully defined by a set of single-particle energies and two-body matrix elements. The single-particle energy for an effective Hamiltonian can be extracted from experimental spectra of core-plus-valence-nucleon systems. To get two-body matrix elements of an effective interaction is more difficult. They can either be established empirically, from a fit to a large wealth of data on spectra of nuclei from the model space, or derived microscopically from the nucleon-nucleon interaction. While the former approach is able to provide excellent agreement with experiment, the latter, however, is still challenging today. Several methods were elaborated to construct microscopically valence-space effective interactions, such as MBPT (see [12, 13] and references therein), or the recently proposed non-perturbative techniques based on the NCSM calculations [14, 15, 16], CC solution [17, 18, 19] and IM-SRG [20, 21].

In this work, we use MBPT to derive *sd*-shell microscopic effective interactions from different bare (or renormalized) nucleon-nucleon potentials — CD-Bonn, N^{3}LO and Daejeon16 [22]. We use the derived interactions to compute effective single-particle energies, oxygen isotope ground-state energies and spectra of selected *sd*-shell nuclei. A comparison of our results with those obtained from an empirical effective inter-

action USDB [23] and with the experimental data is performed.

Formalism

An effective shell-model Hamiltonian can be written as

$$H_{\rm eff} = \sum_{\alpha} \varepsilon_{\alpha} c_{\alpha}^{\dagger} c_{\alpha} + \frac{1}{4} \sum_{\alpha\beta\gamma\delta} \langle \alpha\beta | V_{\rm eff} | \gamma\delta \rangle c_{\alpha}^{\dagger} c_{\beta}^{\dagger} c_{\delta} c_{\gamma}, \quad (1)$$

where c_{α} ($c_{\alpha}^{\dagger}$) is the annihilation (creation) operator in the harmonic-oscillator basis, while the Greek letters (α, β, γ and δ) denoting the full set of single-particle quantum numbers in the valence space, i.e. $\alpha \equiv \{n_{\alpha} l_{\alpha} j_{\alpha} m_{\alpha}\}$. The single-particle energies, ε_{α}, can be extracted from experiment. The effective two-body interaction $V_{\rm eff}$ can be obtained via the Lee-Suzuki similarity transformation [24]

$$V_{\rm eff}^{(n)} = \hat{Q}(\omega) + \sum_{m=1}^{\infty} \hat{Q}_m(\omega) \left\{ V_{\rm eff}^{(n-1)} \right\}^m, \; n \geq 1, \quad (2)$$

where $V_{\rm eff}^{(n)}$ is the effective interaction after n-th iteration, and $V_{\rm eff}^{(0)}(\omega) = \hat{Q}(\omega)$. $\hat{Q}(\omega)$ is the so-called $\hat{Q}$ box, which can be calculated using MBPT [25]

$$\langle \alpha\beta | \hat{Q}(\omega) | \gamma\delta \rangle = \langle {\rm C} | c_{\beta} c_{\alpha} H_1 U(0, -\infty) c_{\gamma}^{\dagger} c_{\delta}^{\dagger} | {\rm C} \rangle_{\rm v}, \quad (3)$$

where $H_1 = V - U_{\rm aux}$ is the residual interaction, $U_{\rm aux}$ is an auxiliary one-body potential (the harmonic oscillator potential in our work), $U(0, -\infty)$ is the time evolution operator, and $|{\rm C}\rangle$ is the unperturbed nuclear core comprised of completely filled lowest harmonic oscillator states. The $\hat{Q}$ box is given by a sum of irreducible and valence-linked diagrams, indicated by the subscript 'v', in the above formula. The corresponding $\hat{Q}$-box first- and second-order Feynman-Goldstone diagrams are shown in Fig. 1. The wave lines represent a bare (or softened[1]) nucleon-nucleon interaction. The lines with upward (downward) arrows stand for particles (holes). $\hat{Q}_m(\omega)$ is related to the m-th order derivative of $\hat{Q}(\omega)$ over the starting energy ω of the diagrams as

$$\hat{Q}_m(\omega) = \frac{1}{m!} \frac{{\rm d}^m \hat{Q}(\omega)}{{\rm d}\omega^m}. \quad (4)$$

From Fig. 1 we can see clearly that a valence-space shell-model effective interaction is not just the bare interaction. It must effectively incorporate nucleonic excitations between the restricted model space and the excluded part of Hilbert space. The bare (or softened) nucleon-nucleon interaction is the lowest-order approximation for an effective interaction from the point of view of perturbation theory. The diagrams beyond the lowest order provide important contributions.

[1] A softening is needed to remove the hard core at short distances in order to facilitate convergence of a many-body approach.

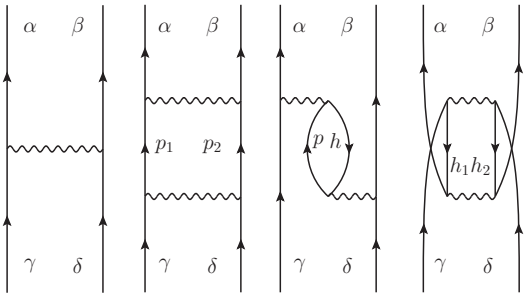

Figure 1: First- and second-order $\hat{Q}$-box Feynman-Goldstone diagrams.

In this work, we use N^{3}LO, CD-Bonn and Daejeon16 to derive the *sd*-shell effective interaction. The *G*-matrix evolved N^{3}LO and CD-Bonn are used as input in Feynman-Goldstone diagrams, whereas Daejeon16 is used directly in the calculation, since it is already softened by a similarity renormalization group technique.

Effective Interactions for the *sd* Shell

The *sd*-shell microscopic effective interactions N^{3}LO-2, CD-Bonn-2 and DJ16-2 (DJ16-4) are derived from the realistic nucleon-nucleon interactions N^{3}LO, CD-Bonn and Daejeon16 respectively, using MBPT with up to second order Feynman-Goldstone diagrams. When referring to an effective interaction, the number following the dash is $N_{\rm max}$, with $N_{\rm max}\hbar\Omega$ being the maximum unperturbed excitation energy of the intermediate states in Feynman-Goldstone diagrams. For instance, $N_{\rm max} = 2$ is used in the derivation of N^{3}LO-2, CD-Bonn-2 and DJ16-2, whereas $N_{\rm max} = 4$ is used in DJ16-4.

In order to assess the quality of the derived interactions, we study first one-neutron separation energies obtained from a valence-space Hamiltonian for nuclei with closed sub-shells using a normal filling approximation. These quantities, referred to as effective single-particle energies (ESPEs) [26, 27, 28], are known to carry important information on the interaction centroids. Fig. 2 shows neutron ESPEs for O-isotopes obtained from the above derived microscopic effective interactions and from USDB. The slopes of the segments are given by the centroids of the two-body matrix elements, defined as

$$\overline{V}_{ab} = \frac{\sum_{m_{\alpha} m_{\beta}} \langle \alpha\beta | V | \alpha\beta \rangle}{\sum_{m_{\alpha} m_{\beta}} 1} \quad (5)$$

where summations run over Pauli allowed states, and $a \equiv \{n_{\alpha} l_{\alpha} j_{\alpha}\}$, i.e. $\alpha \equiv \{a m_{\alpha}\}$. As seen from the figure, the ESPEs from microscopic interactions indicate two deficiencies compared to the USDB results. First, the sub-shell gaps between $1s_{1/2}$ and $0d_{5/2}$ at $N = 14$, 16 and 20 are too small. Second, the slopes of $1s_{1/2}$ and $0d_{3/2}$ effective single-particle orbitals are very steep,

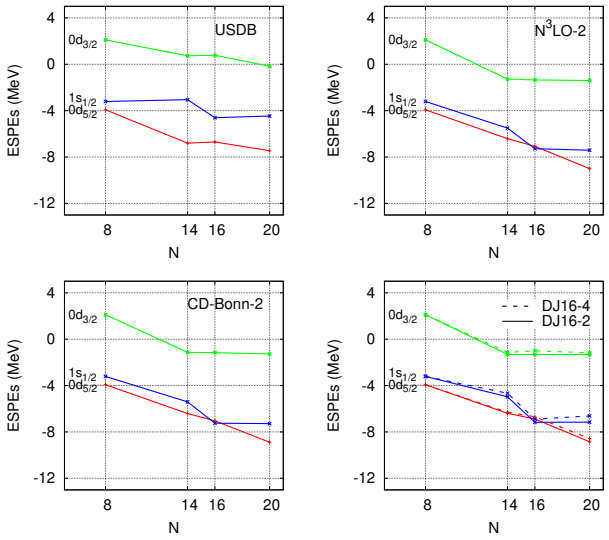

Figure 2: Neutron ESPEs (effective single-particle energies) for oxygen isotopes calculated from microscopic effective interactions (N^{3}LO-2, CD-Bonn-2, DJ16-2 and DJ16-4) and the phenomenological USDB effective interaction.

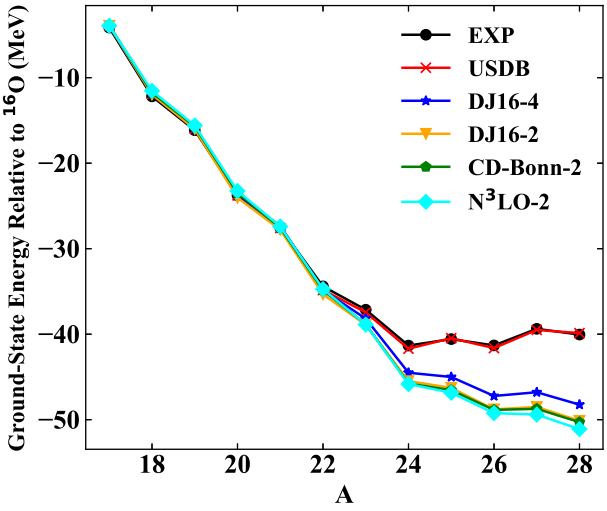

Figure 3: Oxygen isotope ground-state energies relative to ^{16}O calculated from microscopic effective interactions (N^{3}LO-2, CD-Bonn-2, DJ16-2 and DJ16-4) and the phenomenological USDB effective interaction.

indicating that the corresponding centroids $\overline{V}_{1s_{1/2}0d_{5/2}}$ and $\overline{V}_{0d_{3/2}0d_{5/2}}$ of the microscopic interactions are too much attractive. These are general problems of microscopic interactions derived from two-nucleon potentials as was recognized first by Poves and Zuker [29]. Their consequences for the structure of nuclei will be discussed below.

We also observe that centroids of DJ16s are slightly better than those of N^{3}LO-2 and CD-Bonn-2, and similarly, we notice that centroids of DJ16-4 are slightly better than those of DJ16-2.

Next, using the shell-model code Antoine [30], we have calculated ground-state energies of O isotopes ($A = 17 - 28$) and spectra of a few *sd*-shell nuclei starting from the microscopic effective interactions and from USDB. The results are consistent with the conclusions based on the ESPE's analysis. The oxygen isotope ground state energies relative to ^{16}O are shown in Fig. 3. We observe that USDB provides a very good agreement with experiment, whereas larger and larger deviations appear as more and more nucleons are involved in the calculations with microscopic effective interactions. This kind of overbinding arises from too much attractive centroids, as was discussed above. Again, we remark that DJ16s work slightly better than N^{3}LO-2 and CD-Bonn-2, and more precisely, DJ16-4 overbinds O isotopes less than DJ16-2. The spectra of several *sd*-shell nuclei are shown in Fig. 4. It is remarkable that for $A = 18$, all interactions show a very good agreement with experiment. Interestingly, the agreement stays fair for ^{24}O because of the large $N = 16$ sub-shell gap. For ^{21}O and ^{23}O, however, we notice that our microscopic effective interactions cannot reproduce the ground state spin and parity for the former and a sufficiently large excitation energy of the first excited states for the latter. This is due to the small sub-shell gaps between $0d_{5/2}$ and $1s_{1/2}$, as shown in Fig. 2. The same reason underlies a certain discrepancy observed for ^{22}O (the spectrum is too much compressed). For all nuclei, USDB sets a benchmark, being in very good agreement with the data.

Summary

In this work, we have derived *sd*-shell microscopic effective interactions N^{3}LO-2, CD-Bonn-2, DJ16-2 and DJ16-4 from realistic nucleon-nucleon interactions using MBPT with up to second order Feynman-Goldstone diagrams.

The neutron ESPEs for O isotopes, oxygen ground-state energies and spectra of selected *sd*-shell nuclei obtained with the newly derived effective interactions are presented. The results confirm that microscopic effective interactions obtained from two-nucleon potential have several deficient centroids, that are too attractive and, in addition, result in too small sub-shell gaps. This leads to overbinding of neutron-rich nuclei and to poor spectroscopy of nuclei in the vicinity of sub-shell closures. According to a number of recent studies, introduction of three-nucleon forces can improve this situation [31, 32, 33, 34, 35, 36].

By comparing the results from different microscopic effective interactions, we found that the effective interaction derived from Daejeon16 is slightly better than those constructed from N^{3}LO and CD-Bonn. Enlarging the value of $N_{\max}$ improves the overbinding problem, but it is still far away from experiment.

Further investigations of the convergence properties as a function of $N_{\max}$ and the role of third-order diagrams in MBPT are in progress, especially for the effective interaction derived from Daejeon16.

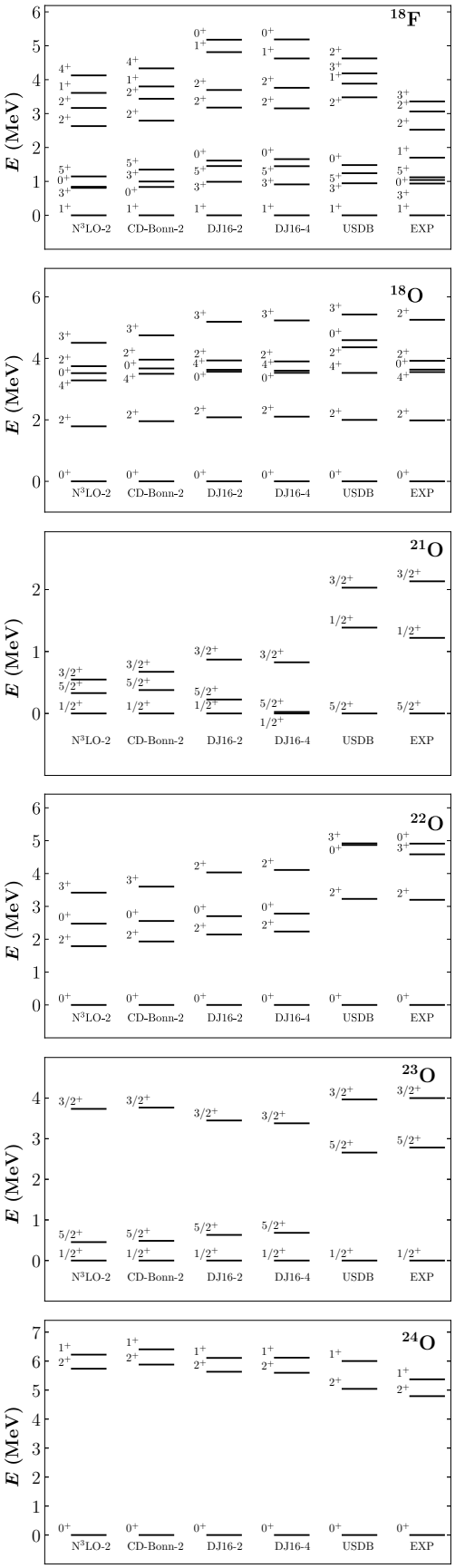

Figure 4: Energy levels of some *sd*-shell nuclei calculated from microscopic effective interactions (N^3LO-2, CD-Bonn-2, DJ16-2 and DJ16-4) and the phenomenological USDB effective interaction.

Acknowledgments

The work was supported within the Master Project "Exotic Nuclei, Fundamental Interactions and Aastrophysics" by IN2P3/CNRS, France.

References

[1] R. Machleidt, Phys. Rev. C 63, 024001 (2001).

[2] R. B. Wiringa, V. G. J. Stoks and R. Schiavilla, Phys. Rev. C 51, 38 (1995).

[3] R. Machleidt and D. R. Entem, Phys. Rep. 503, 1 (2011).

[4] D. R. Entem and R. Machleidt, Phys. Rev. C 68, 041001 (2003).

[5] J. Carlson, S. Gandolfi, F. Pederiva, S. C. Pieper, R. Schiavilla, K. E. Schmidt and R. B. Wiringa, Rev. Mod. Phys. 87, 1067 (2015).

[6] B. R. Barrett, P. Navrátil and J. P. Vary, Prog. Part. Nucl. Phys. 69, 131 (2013).

[7] G. Hagen, T. Papenbrock, M. Hjorth-Jensen and D. J. Dean, Rep. Prog. Phys. 77, 096302 (2014).

[8] H. Hergert, S. K. Bogner, T. D. Morris, A. Schwenk and K. Tsukiyama, Phys. Rep. 621, 165 (2016).

[9] W. H. Dickhoff and C. Barbieri, Prog. Part. Nucl. Phys. 52, 377 (2004).

[10] A. Tichai, R. Roth and T. Duguet, Front. Phys. 8, 164 (2020).

[11] E. Caurier, G. Martínez-Pinedo, F. Nowacki, A. Poves and A. P. Zuker, Rev. Mod. Phys. 77, 427 (2005).

[12] M. Hjorth-Jensen, T. T. Kuo, and E. Osnes, Phys. Rep. 261, 125 (1995).

[13] L. Coraggio, A. Covello, A. Gargano, N. Itaco and T. T. S. Kuo, Prog. Part. Nucl. Phys. 62, 135 (2009).

[14] A. F. Lisetskiy, B. R. Barrett, M. K. G. Kruse, P. Navratil, I. Stetcu and J. P. Vary, Phys. Rev. C 78, 044302 (2008).

[15] E. Dikmen, A. F. Lisetskiy, B. R. Barrett, P. Maris, A. M. Shirokov and J. P. Vary, Phys. Rev. C 91, 064301 (2015).

[16] N. A. Smirnova, B. R. Barrett, Y. Kim, and I. J. Shin, A. M. Shirokov, E. Dikmen, P. Maris and J. P. Vary, Phys. Rev. C 100, 054329 (2019).

[17] G. R. Jansen, J. Engel, G. Hagen, P. Navratil and A. Signoracci, Phys. Rev. Lett. 113, 142502 (2014).

[18] G. R. Jansen, M. D. Schuster, A. Signoracci, G. Hagen and P. Navratil, Phys. Rev. C 94, 011301 (2016).

[19] Z. H. Sun, T. D. Morris, G. Hagen, G. R. Jansen and T. Papenbrock, Phys. Rev. C 98, 054320 (2018).

[20] S. K. Bogner, H. Hergert, J. D. Holt, A. Schwenk, S. Binder, A. Calci, J. Langhammer and R. Roth, Phys. Rev. Lett. 113, 142501 (2014).

[21] S. R. Stroberg, A. Calci, H. Hergert, J. D. Holt, S. K. Bogner, R. Roth, and A. Schwenk, Phys. Rev. Lett. 118, 032502 (2017).

[22] A. M. Shirokov, I. J. Shin, Y. Kim, M. Sosonkina, P. Maris and J. P. Vary, Phys. Lett. B 761, 87 (2016).

[23] B. Alex Brown and W. A. Richter, Phys. Rev. C 74, 034315 (2006).

[24] K. Suzuki, and S. Y. Lee, Prog. Theor. Phys. 64, 2091 (1980).

[25] T. T. S. Kuo and E. Osnes, Folded-Diagram Theory of the Effective Interaction in Atomic Nuclei, Springer Lecture Notes in Physics, (Springer, Berlin, 1990) Vol. 364.

[26] R. K. Bansal and J. B. French, Phys. Lett. 11, 145 (1964).

[27] T. Otsuka, M. Honma, T. Mizusaki, N. Shimizu, and Y. Utsuno, Prog. Part. Nucl. Phys. 47, 319 (2001).

[28] N. A. Smirnova, B. Bally, K. Heyde, F. Nowacki, and K. Sieja, Phys. Lett. B 686, 109 (2010).

[29] A. Poves and A. Zuker, Phys. Rep. 70, 235 (1981).

[30] E. Caurier and F. Nowacki, Acta Phys. Pol. B 30, 705 (1999).

[31] A. P. Zuker, Phys. Rev. Lett. 90, 4 (2003).

[32] T. Otsuka, T. Suzuki, J. D. Holt, A. Schwenk, and Y. Akaishi, Phys. Rev. Lett. 105, 3 (2010).

[33] J. D. Holt, T. Otsuka, A. Schwenk, T. Suzuki, J. Phys. G: Nucl. Phys. 39, 085111 (2012).

[34] J. D. Holt, J. Menendez, J. Simonis, A. Schwenk, Phys. Rev. C 90, 024312 (2014).

[35] T. Fukui, L. De Angelis, Y. Z. Ma, L. Coraggio, A. Gargano, N. Itaco and F. R. Xu, Phys. Rev. C 98, 044305 (2018).

[36] Y. Z. Ma, L. Coraggio, L. De Angelis, T. Fukui, A. Gargano, N. Itaco and F. R. Xu, Phys. Rev. C 100, 034324 (2019).

Shapes of heavy and super-heavy atomic nuclei with Skyrme Energy Density Functionals

Philippe DA COSTA, ***with M. Bender, K. Bennaceur and J. Meyer***

Université Claude Bernard Lyon 1, CNRS, IP2I, UMR 5822, France

Abstract — In this contribution, we present a snapshot on a work-in-progress parameter adjustment of Skyrme-type effective interactions tailored for an improved description of the properties of heavy and super-heavy nuclei. We will show that a slight modification of the fit protocol together with the inclusion of the often-neglected two-body contribution to the center-of-mass correction greatly improves the results for shapes, barriers heights and binding energies of heavy nuclei.

Introduction

The self-consistent mean-field approach and its extensions such as the Random Phase Approximation (RPA) and Generator Coordinate Method (GCM) allow for the systematic study of properties and phenomena for all, but the lightest, systems throughout the chart of nuclei [1]. Using a universal energy density functional (EDF) for the effective in-medium nucleon-nucleon interaction, these techniques give access to numerous observables concerning ground and excited states of nuclei, such as binding energies, deformations shape coexistence phenomena, isomeric states, rotational bands, as well as the large-amplitude collective motion.

It is well established that a correct description of shape isomeric states and fission barriers of heavy nuclei is strongly correlated with the value of the surface energy coefficient $a_{\rm surf}$ [5, 2, 3, 4] and also with the surface symmetry energy coefficient $a_{\rm ssym}$ [14].

The correlation between $a_{\rm surf}$ calculated from an EDF and deformation properties of nuclei has recently been revisited [3]. It was shown that the computational-friendly surface energy coefficient $a_{\rm surf}^{\rm MTF}$ obtained from semi-infinite nuclear matter in the Modified Thomas-Fermi (MTF) approximation [6] can be used to tune the deformation properties during a parameter fit.

The optimal parameterization obtained in Ref. [3], denoted SLy5s1, and having $a_{\rm surf}^{\rm MTF} = 18.0\,\text{MeV}$, is not the first one that is adjusted with the aim of improving the description of the surface properties of nuclei. One can cite the Skyrme parameterizations SkM* [5] and UNEDF2 [7] as well as the Gogny force D1S [8] as major milestones from the past.

The work described here is in the continuity of the one done for the adjustment of the SLy5sX series of parameterizations that SLy5s1 is part of [3]. Compared to the earlier SLy5 parameterization [9], SLy5s1 represents a significant advancement for the description of deformation properties of heavy and super-heavy nuclei [4]. This improvement, however, comes at the price of deteriorating the predictive power for nuclear masses.

A possible route out of this dilemma is to reconsider the treatment of the effect of spurious center-of-mass (CM) motion [10]. This latter is usually done by subtracting the average value of the kinetic energy of the nucleus in its CM frame. The corresponding operator reads [9]

$$\frac{1}{2Am}\Big(\sum_i \hat{\mathbf{p}}_i\Big)^2 = \sum_i \frac{\hat{\mathbf{p}}_i^2}{2Am} + \sum_{i<j} \frac{\hat{\mathbf{p}}_i \cdot \hat{\mathbf{p}}_j}{Am} \qquad (1)$$

where the sums run over single-particle states. The first term in Eq. (1) is a one-body operator and leads to a very simple modification of the functional which is a scaling of the kinetic energy by a factor $1 - \frac{1}{A}$. The second term, however, is a two-body operator that leads to a non-local contribution to the total energy [10]. The implementation of this term is quite cumbersome, and its calculation comparatively costly in terms of CPU time. Therefore, it has been omitted for the vast majority of parameterizations of Skyrme-type EDFs adjusted so far, examples being SLy5s1 [3], SkM* [5] as well as SLy4 and SLy5 [9]. These parameterizations only consider the one-body part of the operator (1). Other parameterizations that aim at describing nuclear dynamics were adjusted without any CM correction at all, examples being SLy4d [11] and UNEDF2 [7]. The motivation for the latter practice is that, because of the $1/A$ factor, the CM correction cannot be consistently defined for processes where two nuclei fuse or one nucleus splits apart. Among the few Skyrme parameterizations that were adjusted considering the full CM correction (1) are SLy6 and SLy7 [11], and the parameterizations of Refs. [12, 13]. The same was done for the Gogny force D1S [8]. Not for all of these the full correction has been included in the variational equations, but was added perturbatively to the total energy after convergence.

It has been pointed out that the choices made for the CM correction during a parameter fit have an impact on the resulting surface properties [10]. Parameterizations

that consider the complete operator (1) give systematically smaller fission barriers than parameterizations that keep only the one-body part, but are otherwise adjusted within the same fit protocol [3, 10, 14]. This finding is not related to the deformation dependence of the CM correction itself, which in general is quite small [10]. Instead, the interaction part of the EDF has to absorb the absent contributions from Eq. (1) to the total binding energy. These roughly scale as $A^{2/3}$, which explains why considering or not terms in Eq. (1) during the fit changes $a_{\rm surf}$ [10].

The Strutinski theorem [15] relates deformation energies and the actual deformation of energetic minima and barriers to the evolution of the bunching of single-particle levels around the Fermi energy with deformation. As the overall level density scales with effective mass, deformation properties might also be correlated to the latter.

These observations have motivated the construction of a new series of parameterizations that are adjusted with each of the three different treatments of the CM correction terms mentioned above, and this for three different values of the isoscalar effective mass, $m_0^*/m = 0.70$, 0.80 and 0.85. Their thorough analysis is underway [16]; below we will report on preliminary results obtained for the subset with $m_0^*/m = 0.80$.

The energy density functional

We consider the EDF generated from a standard central+spin-orbit Skyrme effective interaction with a density-dependent term

$$\begin{aligned} V_{\rm Sky}(\mathbf{x}_1,\mathbf{x}_2;\mathbf{x}_3,\mathbf{x}_4) = \Big[& t_0\,(\delta_{s_1s_3}\delta_{s_2s_4} + x_0\delta_{s_1s_4}\delta_{s_2s_3}) \\ & + \tfrac{1}{2}\,t_1\,(\delta_{s_1s_3}\delta_{s_2s_4} + x_1\delta_{s_1s_4}\delta_{s_2s_3})\,(\mathbf{k}_{12}^{*2} + \mathbf{k}_{34}^2) \\ & + t_2\,(\delta_{s_1s_3}\delta_{s_2s_4} + x_2\delta_{s_1s_4}\delta_{s_2s_3})\,\mathbf{k}_{12}^* \cdot \mathbf{k}_{34} \\ & + \tfrac{1}{6}\,t_3\,(\delta_{s_1s_3}\delta_{s_2s_4} + x_3\delta_{s_1s_4}\delta_{s_2s_3})\,\rho_0^\alpha(\mathbf{R}_{12}) \\ & + \mathrm{i}\,W_0\,(\boldsymbol{\sigma}_{s_1s_3}\delta_{s_2s_4} + \boldsymbol{\sigma}_{s_2s_4}\delta_{s_1s_3})\cdot(\mathbf{k}_{12}^* \times \mathbf{k}_{34})\Big] \\ & \times \delta(\mathbf{r}_3 - \mathbf{r}_1)\delta(\mathbf{r}_2 - \mathbf{r}_4)\delta(\mathbf{r}_2 - \mathbf{r}_1)\,\delta_{q_1q_3}\,\delta_{q_2q_4}\,, \end{aligned} \quad (2)$$

where we use standard notations for the generalized coordinates $\mathbf{x} \equiv (\mathbf{r}sq)$ for a nucleon at position $\mathbf{r}$ with spin and isospin projections s and q, relative momenta $\mathbf{k}_{ij} = \frac{1}{2}\,(\mathbf{k}_j - \mathbf{k}_i)$, CM position of two nucleons $\mathbf{R}_{ij}$ and matrix elements of the vectors of Pauli matrices $\boldsymbol{\sigma}_{s_is_j}$. The particle-hole part of the EDF can be written as

$$E_{\rm ph} = E_{\rm kin} + E_{\rm Sky} + E_{\rm Coul} + E_{\rm corr} \quad (3)$$

where $E_{\rm kin}$ is the kinetic term and $E_{\rm Sky}$ is the part of the EDF that models the strong interaction and that is generated by (2). All particle-hole-type terms are kept, in particular the ones bilinear in the spin-current density, which is not always done as for example for SkM* [5], SLy4 and SLy6 [9]. The term $E_{\rm Coul}$ is the Coulomb energy, and the term $E_{\rm corr}$ approximately removes the excitation energy owing to spurious motions caused by broken symmetries. In the present work, it is limited to the correction for CM motion $E_{\rm corr} = E_{\rm cm}^{(1)} + E_{\rm cm}^{(2)}$ as obtained from (1) with

$$E_{\rm cm}^{(1)} = -\sum_i \frac{\langle \hat{\mathbf{p}}_i^2 \rangle}{2Am} \quad (4)$$

and

$$E_{\rm cm}^{(2)} = -\sum_{i<j} \frac{\langle \hat{\mathbf{p}}_i \cdot \hat{\mathbf{p}}_j \rangle}{Am}\,. \quad (5)$$

Where $\langle \hat{O} \rangle = \langle \psi | \hat{\rm O} | \psi \rangle$ correspond to the mean value of an operator $\hat{\rm O}$ [23]. The actual parameter fit only considers doubly-magic nuclei that are calculated in HF approximation. For the HFB calculations of open-shell nuclei and deformation energies reported below, an isovector contact pairing EDF with suitable coupling constants has been added [16].

Adjustment of the parameters

We have adjusted three sets of parameterizations with different treatment of the CM correction. For the first set, we have omitted the terms (4) and (5) altogether, such that there is no CM correction at all. These will be labeled by 1F2F in what follows. For the second set of parameterizations, the correction was limited to its one-body part only, *i.e.* the term (4). These will be labeled by 1T2F in what follows. Finally, the third set of parameterizations was adjusted considering both the one-body and two-body terms in the CM correction. These will be labeled by 1T2T. For each choice for the CM correction and for each value for the effective mass, we have adjusted a series of parameterizations with a constraint on the surface energy coefficient calculated at the MTF level with target values from 15.5 MeV to 20.0 MeV. The other constraints used in the fit are on

- binding energies of ^{40}Ca, ^{48}Ca, ^{56}Ni, ^{100}Sn, ^{132}Sn and ^{208}Pb with a tolerance of 1 MeV and the (extrapolated) one for ^{78}Ni with a tolerance of 2 MeV;
- binding energy difference between ^{40}Ca and ^{56}Ni with a tolerance of 1 MeV;
- energy per neutron in infinite neutron matter (taken from [17]) below a density of 0.45 fm^{-3} with a tolerance of 25 %;
- energy per nucleon in polarized symmetric and neutron matter at density 0.1 fm^{-3} (taken from [18]) with a tolerance of 25 %;
- properties in infinite nuclear matter at the saturation point: energy per nucleon $B_{\rm sym} = -16.0 \pm 0.1$ MeV, symmetry energy coefficient $J = 32 \pm 1$ MeV and its slope $L = 50 \pm 5$ MeV;
- response functions [19] in all spin and isospin channels in order to avoid the appearance of finite-size instabilities [19, 20].

In addition, two linear combinaisons of parameters from the interaction (2) fix the saturation density at $\rho_{\rm sat} =$

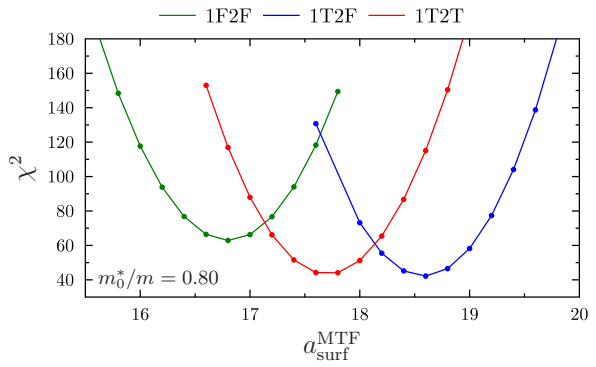

Figure 1: Penalty function obtained for the series of parameterizations using the recipes for CM correction as indicated.

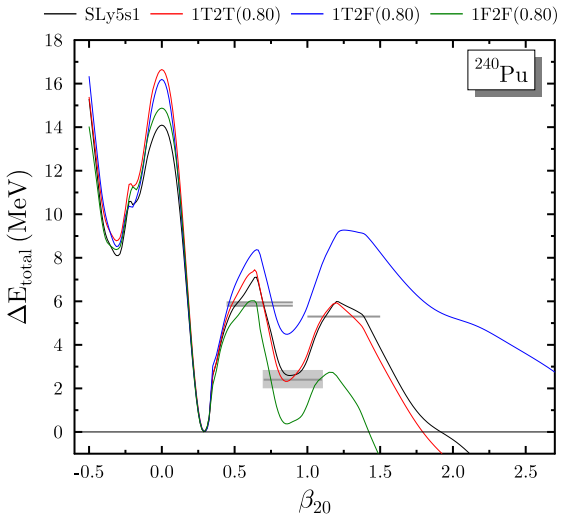

Figure 2: Deformation energy curve of ^{240}Pu as a function of β_{20} as defined in Ref. [4] for the parameterizations as indicated. The energies are normalized to the respective ground-state energy. The horizontal grey bars indicate experimental values for the excitation energy of the shape isomer and the height of the inner and outer saddle points as used before in Refs. [3, 4], and whose deformation is not known.

0.16 fm^{-3} and the isoscalar effective mass m_0^*/m to the desired value. The power of the density dependence in Eq. (2) is set to $\alpha = 1/6$, such that the EDF contains in total seven free parameters that have to be adjusted.

We emphasize that the constraints on linear responses were not used for any of the parameterizations mentioned above other than the SLy5sX series, with the consequence that SLy5 and SLy7 exhibit finite-size instabilities in the spin channels when all time-odd terms are kept in the same way as done here.

Results

Penalty function

As will be discussed in detail elsewhere [16], the optimal results are obtained with an isoscalar effective mass of 0.80. The values of the penalty functions for the parameterizations of type 1F2F, 1T2F and 1T2T and $m_0^*/m = 0.80$ are plotted on Fig. 1 as functions of the MTF surface energy coefficient $a_{\rm surf}^{\rm MTF}$.

Previous studies that we have conducted [3, 4] have shown that the optimal values of $a_{\rm surf}^{\rm MTF}$ for a satisfying description of the deformation properties of heavy nuclei fall in an interval between 17.6 and 18.0 MeV. It is striking to see that the minimum of the penalty function χ^2 as a function of $a_{\rm surf}^{\rm MTF}$ is precisely in this interval for the parameterizations of the 1T2T type while it is well above (near 18.6 MeV) for parameterizations 1T2F and well below (near 16.8 MeV) for parameterizations 1F2F. This explains why existing parameterizations whose surface properties are not constrained and that do not use the 1T2T recipe systematically fail to describe fission barriers [3]: those of 1T2F type (SLy4, SLy5, ...) tend to overestimate them, while those of 1F2F type (SLy4d) underestimate them. This also explains why the SLy5s1 parameterization, which is of 1T2F type and very similar to the parameterization with $a_{\rm surf}^{\rm MTF} = 18.0$ MeV on Fig. 1 performs rather poorly for binding energies of nuclei: bringing $a_{\rm surf}^{\rm MTF}$ to a realistic value has been done at the expense of other features, mainly binding energies of nuclei.

Energy landscape of ^{180}Hg and ^{240}Pu

Since the optimization of the parameters for the EDFs of type 1T2T gives the lowest χ^2 for a value of $a_{\rm surf}^{\rm MTF}$ that is close to the expected optimal value, we have decided to produce one additional parameterization of each type without a constraint on $a_{\rm surf}^{\rm MTF}$ in the penalty function. For the rest of the discussion, we will use these parameterizations, labeled 1F2F(0.80), 1T2F(0.80), 1T2F(0.80), along with the previously adjusted parameterization SLy5s1.

Figures 2 and 3 show the deformation energy of ^{240}Pu and ^{180}Hg as a function of the quadrupole deformation parameter β_{20}. The calculations allow for non-axial and reflection-asymmetric shapes along the path in the same way as described in Ref. [4].

For all four parameterizations, the ground-state shape of ^{240}Pu corresponds to $\beta_{20} \simeq 0.3$ in agreement with data [4], while the isomeric state is at $\beta_{20} \simeq 0.8$. The plot illustrates the correlation between the scheme for CM correction used during the fit and deformation properties: the parameterization 1T2F(0.80) (with $a_{\rm surf}^{\rm MTF} \simeq 18.6$ MeV) grossly overestimates the height of the fission barrier, while 1F2F(0.80) (with $a_{\rm surf}^{\rm MTF} \simeq 16.8$ MeV) underestimates it. By contrast, the parameterization 1T2T(0.80) (with $a_{\rm surf}^{\rm MTF} \simeq 17.8$ MeV) gives a fair description of the empirical values for the saddle point heights and the excitation energy of the isomeric state that is very similar to what is found for SLy5s1 (with $a_{\rm surf}^{\rm MTF} \simeq 18.0$ MeV) [3, 4].

The energy landscape for ^{180}Hg, which is among the most neutron-deficient nuclei for which information about the fission barrier is available, is displayed

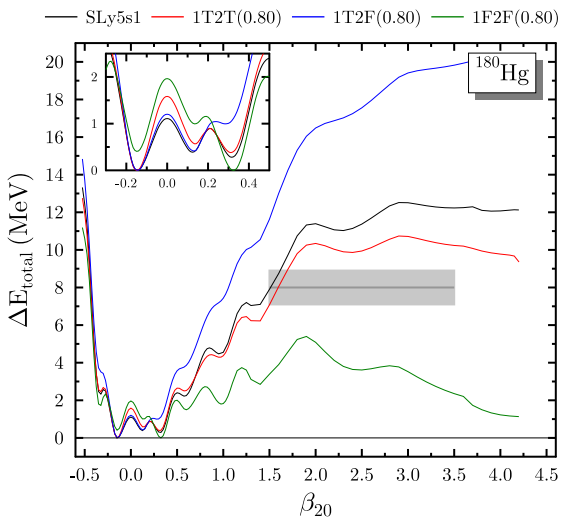

Figure 3: Same as Fig. 2 for ^{180}Hg. See Ref. [4] for the estimate of the experimental barrier height indicated by the grey horizontal bar. The energy curves end at the deformation at which the calculation jumps to a solution with two separate fragments. The inset is a zoom on the energy curve at small deformation that allows to identify the shape of the absolute minimum.

on Fig. 3. The structure of the fission barrier of this nucleus is quite different from the one of ^{240}Pu: there is one broad barrier that extends to very large deformations. Again, 1T2F(0.80) dramatically overestimates the barrier height, whereas 1F2F(0.80) underestimates it. The 1T2T(0.80) parameterization predicts a barrier height that is reasonably close to the empirical data, performing even better than SLy5s1. As will be discussed elsewhere [16], 1T2T(0.80) and SLy5s1 differ in $a_{\rm surf}$ and $a_{\rm ssym}$, which leads to a similar effective surface energy coefficient in the very asymmetric ^{240}Pu, but a noticeable difference in the more symmetric ^{180}Hg.

At small deformations, ^{180}Hg also exhibits shape coexistence with an oblate minimum at $\beta_{20} \simeq -0.15$ and a prolate minimum at $\beta_{20} \simeq 0.32$. Experimental data consistently point to an oblate shape of the ground state [21], while many effective interactions predict a prolate shape instead. Predicting the correct ground-state shape for even-even Hg isotopes and providing a fair description of the odd-even staggering of radii of Hg isotopes is one of the successes of SLy5s1 [21] that we hope to preserve for future fits. As can be seen from the inset of Fig. 3, this is indeed the case for 1T2T(0.80) and 1T2F(0.80), but not 1F2F(0.80).

Binding energies of spherical nuclei

As mentioned before, the improved deformation properties of SLy5s1 compared to SLy4 and SLy5 come at the expense of a diminished predictive power for total binding energies. The results discussed so far indicate that 1T2T(0.80) performs even slightly better than SLy5s1 for deformation energies without compromising standard observables for spherical nuclei. It is

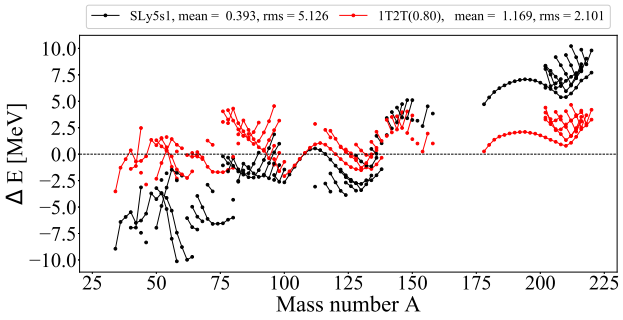

Figure 4: Binding energy residuals for a set of 214 spherical or nearly spherical nuclei. Results in red are for calculations done using the parameterization SLy5s1 and results in black using 1T2T(0.80).

therefore instructive to compare predictions for binding energies obtained with these two parameterizations.

To make this comparison, we have used a list of 214 nuclei which are expected to be spherical, or nearly spherical, and for which the binding energies are either known or extrapolated from experiment (see [22] and references therein). The results are shown on Fig. 4. The values of the mean and root mean square (rms) deviation are indicated on the figure. On can see that the 1T2T(0.80) parameterization, by far, gives a better agreement with experimental data.

Summary and Conclusions

In this contribution, we reported on an ongoing work that aims at an improved the description of the deformation properties of very heavy nuclei. We have built a series of parameterizations of the standard Skyrme EDF that is free from finite-size instabilities, using three different recipes for the CM correction. Results obtained with this series of fits unambiguously demonstrate that the inclusion of both the one- and two-body contributions to the CM energy results in quite realistic deformation properties of standard Skyrme EDFs without the need to constrain the surface energy coefficient, at least within our present fit protocol. Conversely, to achieve the same good description of deformation energies with one of the other two schemes requires to constrain $a_{\rm surf}$ during the fit, which inevitably compromises the predictive power for binding energies and possibly also other observables. A more detailed article with results for even-even as well as odd-even nuclei is in preparation [16].

Acknowledgments

We thank W. Ryssens for fruitful discussions during the writting of this article. This work was supported by the french Agence Nationale de la Recherche under grant No. 19–CE31–0015–01 (NEWFUN). The computations were performed using HPC resources from the computing center of the IN2P3/CNRS.

References

[1] M. Bender *et al.*, Rev. Mod. Phys. 75, 121 (2003).

[2] M.Brack *et al.*, Phys. Rep. 23, 275 (1985)

[3] R. Jodon *et al.*, Phys. Rev. C 94, 024335 (2016).

[4] W. Ryssens *et al.*, Phys. Rev. C 99, 044315 (2019).

[5] J. Bartel *et al.*, Nucl. Phys. A 386, 79 (1982).

[6] K. Krivine and J. Treiner, Phys. Lett. B 88, 212 (1979).

[7] M. Kortelainen *et al.*, Phys. Rev. C 85, 024304 (2012).

[8] J.-F. Berger *et al.*, Comp. Phys. Comm. 63, 365 (1991).

[9] E. Chabanat *et al.*, Nucl. Phys. A 635, 231 (1998) .

[10] M. Bender *et al.*, Eur. Phys. J. A 7, 467 (2000).

[11] C. Simenel and B. Avez, Int. J. Mod. Phys. E 17, 31 (2008).

[12] P.-G. Reinhard and H. Flocard, Nucl. Phys. A 584, 467 (1995).

[13] P. Klüpfel *et al.*, Phys. Rev. C 79, 034310 (2009).

[14] N. Nikolov *et al.*, Phys. Rev. C 83, 034305 (2011).

[15] S.G. Nilsson and I. Ragnarsson, *Shapes and Shells in Nuclear Structure* (Cambridge University Press, Cambridge, England, 1995)

[16] Ph. Da Costa *et. al.*, in preparation.

[17] R.B. Wiringa *et. al.*, Phys. Rev. C 38, 1010 (1988).

[18] G.H. Bordbar and M. Modarres, Phys. Rev. C 57, 714 (1998).

[19] A Pastore *et al.*, Phys. Rep. 563, 1 (2015).

[20] V. Hellemans *et al.*, Phys. Rev. C 88, 064323 (2013).

[21] S. Sels *et al.*, Phys. Rev. C 99, 044306 (2019).

[22] K. Bennaceur *et al.*, J. Phys. G: Nucl. Part. Phys. 47, 105101 (2020).

[23] P.A.M. Dirac, Mathematical Proceedings of the Cambridge Philosophical Society, (1939), 35(3), pp 416-418.